Studying Turbulence Using Numerical Simulation Databases - III

Proceedings of the 1990 Summer Program

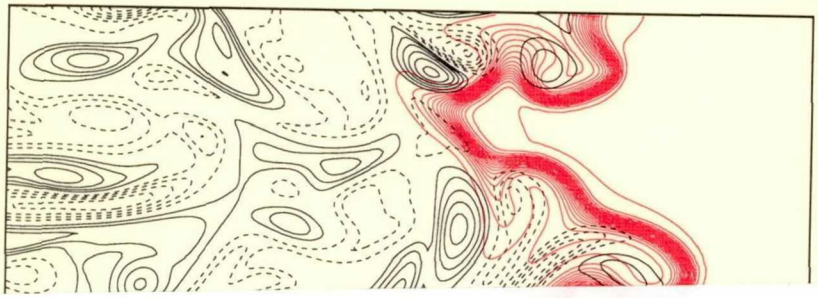

Center for Turbulence Research

December 1990

NASA

Ames Research Center

Stanford University

Studying Turbulence Using Numerical Simulation Databases - III

Proceedings of the 1990 Summer Program

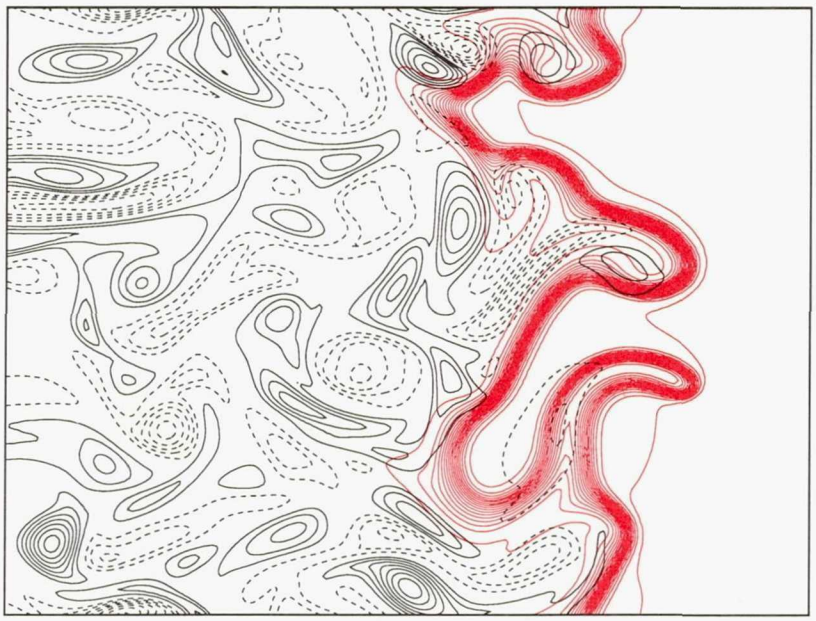

Center for Turbulence Research

December 1990

NASA

Ames Research Center

LELAND STANFORD JUNIOR UNIVERSITY
ORGANIZED 1891

Stanford University

ORIGINAL PAGE
BLACK AND WHITE PHOTOGRAPH

CONTENTS

Preface

The third Summer Program of the Center for Turbulence Research was held during the four week period July 16 to August 10, 1990. As in the past Summer programs, direct numerical simulation databases were used to study turbulence physics and modeling issues. Twenty seven participants from seven countries were selected based on their research proposals. They joined twenty eight local participants from Stanford and NASA-Ames Research Center who devoted virtually all their time during the Program to this activity. Noteworthy features of this Summer Program were a special emphasis on subgrid scale modeling for large eddy simulations and a relatively large effort devoted to turbulent reacting flows and combustion. The remaining projects were rather independent, but some unplanned collaborative efforts developed among the participants in different groups during the course of the Program.

The databases consisted of a turbulent mixing layer (past the mixing transition), turbulent and transitional channel flow with passive scalar, 3-D boundary layer and channel flow, homogeneous shear flow, compressible homogeneous turbulence, compressible free-shear flows, and reacting flows. In a few cases, the need for additional data arose which led to additional direct simulations; in some instances, however, time did not permit obtaining sufficient integration times to accumulate high quality statistical samples.

As part of the program five review tutorials were given on *wall turbulence and the Kolmogorov region* (A. Perry), *combustion modeling* (C. Donaldson), *compressible turbulence and shocks* (S. Lee), *small scale in turbulent mixing layers* (M. Rogers), and *renormalization group analysis of turbulence* (L. Smith).

This report contains twenty five papers that resulted from the 1990 Summer Program. The papers are divided into six groups and are preceded by an overview written by each group coordinator. This report provides an account of a short term, but intensive, study of the physics and models of turbulent flows. Therefore, the results should be considered as preliminary. It is hoped that the studies that began during the Program will be continued and in due course the results will be presented in the archival literature. Early reporting of some of the projects occurred at the Forty-Third Meeting of the Fluid Dynamics Division of the American Physical Society in Ithaca, New York, November 18-20, 1990. Fifteen abstracts based on the work accomplished during the Summer Program were presented at this meeting.

Thanks are due to Ms. Debra Spinks for the compilation of this report and her invaluable assistance in the organization of the Summer Program.

Parviz Moin
William C. Reynolds
John Kim

I. The subgrid scale modeling group

Subgrid-scale models are used in large-eddy simulation of turbulent flows, where the large-scale field is computed directly via the filtered Navier-Stokes equations and the small scale-field is modeled. The subgrid-scale model then represents the effects of the small scales on the large-scale motions. Relatively little effort has been devoted to subgrid scale modeling, despite its purported importance as an alternative to single-point closures for solving engineering problems. The Smagorinsky (1963) model remains as the most widely used model for large-eddy simulations. Several modifications to this model have been proposed to account for mean-flow complexities, but they are generally based on *ad hoc* foundations. Improvements have also been sought in analogy with single-point closure models by using moment equations for the subgrid-scale stresses (Deardorff, 1973, *J. Fluids Eng.* **95**; Schumann, 1975, *J. Comp. Phys.* **18**).

The key element that has been missing in most subgrid scale modeling efforts has been the effective utilization of the large-scale field which is computed directly. This rather rich spectral information is not available in methods based on Reynolds-averaged equations and should be brought to bear in large eddy simulations. The model of Bardina *et al.* (1980, *AIAA 80-1357*) is a rare example where an attempt is made to extrapolate from the computed large-scale field to model the small scales; however, this model still relies on a supplementary Smagorinsky model to provide the necessary subgrid-scale dissipation. Several improved subgrid-scale models have been developed in Fourier space based on statistical theories of homogeneous turbulence. Although they are appealing because of their more rigorous theoretical foundations, they are of little use for inhomogeneous flows, where the problems are formulated in physical space, and where accurate subgrid-scale models are really needed.

The problems with the Smagorinsky model (or its variants) are: 1) The optimal model constant must be changed in different flows; 2) the model does not have the correct limiting behavior near the wall; 3) the model does not vanish in laminar flow, and it is demonstrated to be too dissipative in the laminar/turbulent transition region; 4) the model does not account for backscatter of energy from small scales to large scales, which has been shown to be of importance in the transition regime; and 5) compressibility effects are not included in the model. The objective of the subgrid-scale modeling group was to address these issues.

The group concentrated on four projects: Three were devoted to the development, implementation, and testing of subgrid-scale models, and one was an attempt to quantify the subgrid-scale backscatter using direct numerical simulation databases. Germano, Piomelli, Moin & Cabot used the scale-similarity ideas of Bardina *et al.* and Germano (1990, *CTR Manuscript 116*) to derive an eddy viscosity model. The model uses the strain fields at *two different scales* and thus utilizes spectral information in the large-scale field to extrapolate the small-scale stresses. Using an algebraic identity derived by Germano (1990), and using the Smagorinsky model to

represent the subgrid-scale stresses at both scales, an expression for the Smagorinsky "constant" is derived which is a function of space and time. The constant can be negative in some regions and thus does not totally exclude backscatter, it provides for the proper asymptotic behavior of the stresses near the wall without *ad hoc* damping functions, and it vanishes in laminar flow without *ad hoc* intermittency functions. Large-eddy simulations of the transitional and turbulent channel flows using this model performed during the Summer Program were very encouraging. Essentially, the agreements with the direct simulation results were as good or better than those obtained with variants of the Smagorinsky model but without the fine-tuning and the *ad hoc* components that such models have required. I believe that this model represents a major advance in subgrid-scale modeling and should be tested in more complex turbulent flows.

Eddy viscosity models are absolutely dissipative; that is, energy is transferred from large scales to the small scales. Although this is the correct behavior in the mean, it is not necessarily true instantaneously and at each point in space. In fact, recent computations by Piomelli *et al.* (1990, *Phys. Fluids A*, **2**) have indicated that backscatter may be dynamically critical in the transition region. Piomelli, Cabot, Moin & Lee investigated the scope of backscatter using direct numerical simulation databases of turbulent and transitional channel flow and compressible isotropic turbulence at different Reynolds numbers and Mach numbers. It was very surprising to find that at any instant about 50% of the grid points were in the state of energy transfer from small to large scales when sharp cut-off filters were used. Although the mean transfer is from large to small scales, it results from the small difference between large forward and backward components.

Comte, Lee & Cabot tested and modified the structure-function-based model of Métais & Lesieur (1990, preprint). The main appeal of the model is its rigorous roots in wave space. The model is formulated in physical space, however, and is directly applicable to inhomogeneous flows. It was tested using the database from direct numerical simulation of channel flow. Its asymptotic behavior near the wall was not correct and modifications were implemented to improve it. This model was also incorporated in a large-eddy simulation of compressible isotropic decay, and, as expected, its performance was satisfactory.

Squires & Zeman developed an eddy viscosity model for compressible flows. The model is essentially a modification of the Smagorinsky model with a parameterization of turbulence kinetic energy that must now be accounted for separately. In the limit of incompressible flow, the Smagorinsky model is recovered. They also obtained an expression for the eddy diffusivity *tensor*. The stress-similarity ideas of Germano *et al.* can be applied in a straightforward manner to this model for dynamic computation of the space- and time-dependent model coefficient. This extension to the model of Squires & Zeman should provide an attractive subgrid-scale model for compressible flows. Other improvements would be to account for the effects of eddy shocklets. Some ideas in this direction are presented by Squires & Zeman, but they have not been tested.

Parviz Moin

Center for Turbulence Research
Proceedings of the Summer Program 1990

A dynamic subgrid-scale eddy viscosity model

By Massimo Germano,[1] Ugo Piomelli,[2]
Parviz Moin[3] AND William H. Cabot[3]

One major drawback of the eddy viscosity subgrid-scale stress models used in large-eddy simulations is their inability to represent correctly with a single universal constant different turbulent fields in rotating or sheared flows, near solid walls, or in transitional regimes. In the present work a new eddy viscosity model is presented which alleviates many of these drawbacks. The model coefficient is computed dynamically as the calculation progresses rather than input *a priori*. The model is based on an algebraic identity (Germano 1990) between the subgrid-scale stresses at two different filtered levels and the resolved turbulent stresses. The subgrid-scale stresses obtained using the proposed model vanish in laminar flow and at a solid boundary, and have the correct asymptotic behavior in the near-wall region of a turbulent boundary layer. The results of large-eddy simulations of transitional and turbulent channel flow that use the proposed model are in good agreement with the direct simulation data.

1. Introduction

In large-eddy simulations (LES) the effect of the large scales is directly computed, and only the small subgrid scales are modeled. Since small scales tend to be more isotropic than the large ones, it should be possible to parameterize them using simpler and more universal models than standard Reynolds stress models. Thus, most subgrid-scale (SGS) stress models are based on an eddy viscosity assumption. In the most commonly used model, due to Smagorinsky (1963), the eddy viscosity ν_T is obtained by assuming that the small scales are in equilibrium, so that energy production and dissipation are in balance. This yields an expression of the form

$$\nu_T = (C_S\Delta)^2\,|\overline{S}|, \tag{1}$$

where Δ is the filter width (which, unless otherwise noted, is assumed to be equal to the grid size), C_S is the Smagorinsky constant, $|\overline{S}| = (2\overline{S}_{ij}\overline{S}_{ij})^{1/2}$ is the magnitude of large-scale strain rate tensor

$$\overline{S}_{ij} = \frac{1}{2}\left(\frac{\partial \overline{u}_i}{\partial x_j} + \frac{\partial \overline{u}_j}{\partial x_i}\right), \tag{2}$$

1 Politecnico di Torino, Italy
2 University of Maryland
3 Center for Turbulence Research

and $\overline{u}_i$ is the large-scale velocity.

Lilly (1966) determined that, for homogeneous isotropic turbulence with cutoff in the inertial subrange, $C_S \simeq 0.17$. In the presence of mean shear, however, this value was found to cause excessive damping of large-scale fluctuations, and in his simulation of turbulent channel flow, Deardorff (1971) used $C_S = 0.094$. *A priori* tests by McMillan, Ferziger & Rogallo (1980) on homogeneous turbulence confirmed that C_S decreases with increasing strain rate. Mason & Callen (1986), however, found that the value $C_S = 0.2$ gave good results if the grid resolution was sufficiently fine, and concluded that values of C_S lower than 0.2 are required if the numerical resolution is insufficient. Their results, however, were not confirmed by Piomelli, Moin & Ferziger (1988), who found the optimum value of C_S to be around 0.1 even with meshes much finer than those used by Mason & Callen (1986).

Additional modifications to the Smagorinsky model were made in the near-wall region of plane channels to force the subgrid-scale stresses to vanish at the solid boundary. Moin & Kim (1982), for example, used damping functions to account for near-wall effects. Piomelli *et al.* (1988) chose the damping function to ensure the proper asymptotic behavior for the SGS shear stresses near the wall, but found little difference with the results obtained with the standard Van Driest (1956) damping used by Moin & Kim (1982) and others.

Yakhot *et al.* (1989) used a subgrid-scale model based on the Renormalization Group theory of Yakhot & Orszag (1986) in the large-eddy simulation of channel flow. Although the stresses predicted by the model in its original formulation go to zero without requiring any damping function, Yakhot *et al.* (1989) included an *ad hoc* factor to take into account the anisotropy of the small-scales in the near-wall region. The asymptotic behavior of the stresses predicted by this model depends on the grid distribution in the wall-normal direction; for the grids commonly used, an incorrect asymptotic behavior is obtained.

Large-eddy simulations of transition in boundary layers (Piomelli *et al.* 1990a) and plane channel (Piomelli & Zang 1990b) show that during the early stages of transition the Smagorinsky model predicts excessive damping of the resolved structures, leading to incorrect growth rates of the initial perturbations. To overcome this difficulty they introduced additional empiricism in the form of an intermittency function which modified the Smagorinsky constant by effectively setting it to zero during the linear and early nonlinear stages of transition.

This brief survey of the existing literature indicates that, although modifications of the Smagorinsky model have been successfully applied to the LES of transitional and turbulent flows, it is not possible to model effectively with a single, universal constant the variety of phenomena present in the flows examined. The *ad hoc* manner in which the SGS eddy viscosity has been extrapolated to the wall is far from desirable. In addition the Smagorinsky model cannot account for energy flow from small scales to large scales (backscatter), which can be significant (Piomelli *et al.* 1990c).

In this work a new, dynamic SGS stress model is proposed that attempts to overcome these deficiencies by locally calculating the eddy viscosity coefficient to

reflect closely the state of the flow. This is done by sampling the smallest resolved scales and using this information to model the subgrid scales. The model presented here requires a single input parameter and exhibits the proper asymptotic behavior near solid boundaries or in laminar flow without requiring damping or intermittency functions. The model is also capable of accounting for backscatter.

In the next Section, the model will be presented and its characteristics discussed. The model was tested both *a priori*, taking advantage of existing direct numerical simulation (DNS) databases, and *a posteriori* using the model in an LES calculation. The results of these tests will be discussed in Section 3. Concluding remarks will be made in Section 4.

2. Mathematical formulation

In large-eddy simulation, the large scale quantities are defined by the convolution of the velocity and pressure fields with a filter function. For the purposes of this work we define two filtering operators: one is the *grid* filter, $\overline{G}$, denoted by an overbar:

$$\overline{f}(\mathbf{x}) = \int f(\mathbf{x}')\overline{G}(\mathbf{x},\mathbf{x}')d\mathbf{x}', \tag{3}$$

while the other, the *test* filter, $\widetilde{G}$, is denoted by a tilde:

$$\widetilde{f}(\mathbf{x}) = \int f(\mathbf{x}')\widetilde{G}(\mathbf{x},\mathbf{x}')d\mathbf{x}'; \tag{4}$$

finally, let $\widetilde{\overline{G}} = \overline{G}\widetilde{G}$.

By applying the grid filter to the dimensionless continuity and Navier-Stokes equations one obtains the filtered equations of motions

$$\frac{\partial \overline{u}_i}{\partial x_i} = 0, \tag{5}$$

$$\frac{\partial \overline{u}_i}{\partial t} + \frac{\partial}{\partial x_j}(\overline{u}_i\overline{u}_j) = -\frac{\partial \overline{p}}{\partial x_i} - \frac{\partial \tau_{ij}}{\partial x_j} + \frac{1}{Re}\frac{\partial^2 \overline{u}_i}{\partial x_j \partial x_j}. \tag{6}$$

In the following, x or x_1 is the streamwise direction, y or x_2 the wall-normal direction and z or x_3 is the spanwise direction. The effects of the small scales appear in the subgrid-scale stress term

$$\tau_{ij} = \overline{u_i u_j} - \overline{u}_i\overline{u}_j, \tag{7}$$

which must be modeled.

Consider now the subgrid-scale stress obtained by applying the test filter to the filtered equations of motion (5) and (6)

$$T_{ij} = \widetilde{\overline{u_i}\overline{u}_j} - \widetilde{\overline{u}}_i\widetilde{\overline{u}}_j, \tag{8}$$

and the resolved turbulent stress $\mathcal{L}_{ij}$ defined as

$$\mathcal{L}_{ij} = \widetilde{\overline{u}_i\overline{u}_j} - \widetilde{\overline{u}}_i\widetilde{\overline{u}}_j. \tag{9}$$

The resolved turbulent stresses are representative of the contribution to the Reynolds stresses by the scales whose length is intermediate between the grid filter width and the test filter width, i.e. the small resolved scales. It is easy to see that these quantities are related by the algebraic relation (Germano 1990)

$$\mathcal{L}_{ij} = T_{ij} - \widetilde{\tau}_{ij}, \tag{10}$$

which relates the resolved turbulent stress $\mathcal{L}_{ij}$, which can be calculated explicitly, to the subgrid-scale stresses at the test and grid levels, T_{ij} and τ_{ij}.

The identity (10) can be exploited to derive more accurate SGS stress models by determining, for example, the value of the Smagorinsky coefficient most appropriate to the instantaneous state of the flow. Assuming that the same functional form can be used to parameterize both T_{ij} and τ_{ij} (the Smagorinsky model, for example), let M_{ij} and m_{ij} be the models for the anisotropic parts of the T_{ij} and τ_{ij}:

$$\tau_{ij} - \frac{\delta_{ij}}{3}\tau_{kk} \simeq m_{ij} = -2C\overline{\Delta}^2|\overline{S}|\overline{S}_{ij}, \tag{11}$$

$$T_{ij} - \frac{\delta_{ij}}{3}T_{kk} \simeq M_{ij} = -2C\widetilde{\overline{\Delta}}^2|\widetilde{\overline{S}}|\widetilde{\overline{S}}_{ij}, \tag{12}$$

where

$$\widetilde{\overline{S}}_{ij} = \frac{1}{2}\left(\frac{\partial\widetilde{\overline{u}}_i}{\partial x_j} + \frac{\partial\widetilde{\overline{u}}_j}{\partial x_i}\right), \qquad |\widetilde{\overline{S}}| = \sqrt{2\widetilde{\overline{S}}_{mn}\widetilde{\overline{S}}_{mn}}, \tag{13}$$

$\overline{\Delta}$ is the characteristic filter width associated with $\overline{G}$, and $\widetilde{\overline{\Delta}}$ is filter width associated with $\widetilde{\overline{G}}$. Substitution of (11) and (12) into (10) and contracting with $\overline{S}_{ij}$ (or $\widetilde{\overline{S}}_{ij}$) gives

$$\mathcal{L}_{ij}\overline{S}_{ij} = -2C\left(\widetilde{\overline{\Delta}}^2|\widetilde{\overline{S}}|\widetilde{\overline{S}}_{ij}\overline{S}_{ij} - \overline{\Delta}^2\widetilde{|\overline{S}|\overline{S}_{ij}}\overline{S}_{ij}\right), \tag{14}$$

from which $C(x,y,z,t)$ can, apparently, be easily obtained. The quantity in parentheses, however, can become zero which would make C indeterminate or ill-conditioned. *A priori* tests in turbulent channel flow have shown this to be indeed the case. For the channel flow, therefore, it was assumed that C is only a function of y and t. To this end, the average of both sides of (14) is taken over a plane parallel to the wall (indicated by $<.>$) to yield

$$C(y,t) = -\frac{1}{2}\frac{<\mathcal{L}_{kl}\overline{S}_{kl}>}{\widetilde{\overline{\Delta}}^2 <|\widetilde{\overline{S}}|\widetilde{\overline{S}}_{mn}\overline{S}_{mn}> - \overline{\Delta}^2 <\widetilde{|\overline{S}|\overline{S}_{pq}}\overline{S}_{pq}>}; \tag{15}$$

the new dynamic eddy viscosity subgrid-scale stress model is then given by

$$m_{ij} = \frac{<\mathcal{L}_{kl}\overline{S}_{kl}>}{\left(\widetilde{\overline{\Delta}}/\overline{\Delta}\right)^2 <|\widetilde{\overline{S}}|\widetilde{\overline{S}}_{mn}\overline{S}_{mn}> - <\widetilde{|\overline{S}|\overline{S}_{pq}}\overline{S}_{pq}>}|\overline{S}|\overline{S}_{ij}. \tag{16}$$

In more general situations, the plane average should be replaced with appropriate local space and time averages.

A few remarks are in order regarding the properties and the character of the subgrid-scale stress model given by (16). First, the model gives zero SGS stress everywhere $\mathcal{L}_{ij}$ vanishes (as long as the denominator remains finite). Such is the case in laminar flow or at solid boundaries. Furthermore, it is easy to show that in the near-wall region m_{ij} is proportional to the cube of the distance from the wall y_w, regardless of the choice of $\overline{\Delta}$ or $\widetilde{\Delta}$. This is the correct asymptotic behavior for the (1,2) component of the subgrid-scale stress tensor, which, in this region, is the most significant one. To the authors' knowledge, this is the only model which satisfies this property without the use of *ad hoc* damping functions. Finally, the use of (16) implies that the modeled subgrid-scale dissipation, $\epsilon_{sgs} = m_{ij}\overline{S}_{ij}$, is proportional to the average dissipation of the resolved turbulent stresses, $<\mathcal{L}_{ij}\overline{S}_{ij}>$, which can be either positive or negative. Thus, the model does not rule out backscatter. In the present formulation backscatter is not localized, and may (or may not) occur at every point in a plane; the use of local averaging in (14), however, would allow the model to provide localized backscatter as well.

The only adjustable parameter in the model is the ratio $\alpha = \widetilde{\Delta}/\overline{\Delta} > 1$. The resolved turbulent stresses calculated using small values of α can be contaminated by numerical errors; on the other hand, large values of α imply that the stresses due to large energy carrying structures are used to determine the contribution of the subgrid scales. If the optimal value of α varies greatly from one flow to another, the applicability of the model is reduced. In the next Section, the optimal value of α obtained from a turbulent channel flow database will be used for the large-eddy simulation of transitional and turbulent channel flow at higher Reynolds numbers to address this issue. Finally, the model (16) implicitly assumes similarity between the SGS stresses at the grid and test levels, which are modeled using the same functional expression, namely, the Smagorinsky model.

3. Results and discussion

A priori tests of the dynamic subgrid-scale stress model (16) were carried out to determine the best choice for α and the accuracy with which the model predicts the SGS stresses and dissipation. The tests were performed using the DNS database of Kim, Moin & Moser (1987) for turbulent channel flow, and that of Zang, Gilbert & Kleiser (1990) for transitional flow. Reynolds numbers are respectively $Re = 3300$ (based on the centerline velocity U_c and channel halfwidth δ) for the turbulent case, and $Re = 8000$ for the transitional case (based on initial centerline velocity and channel halfwidth).

The first task accomplished by these tests was to determine the optimal value of the ratio α. The sharp cutoff filter was applied as both grid and test filter in the streamwise and spanwise directions. No explicit filtering was applied in the wall-normal direction. The length scales were defined as

$$\overline{\Delta}^3 = \overline{\Delta}_1\overline{\Delta}_2\overline{\Delta}_3, \qquad \widetilde{\Delta}^3 = \widetilde{\Delta}_1\widetilde{\Delta}_2\widetilde{\Delta}_3, \tag{17}$$

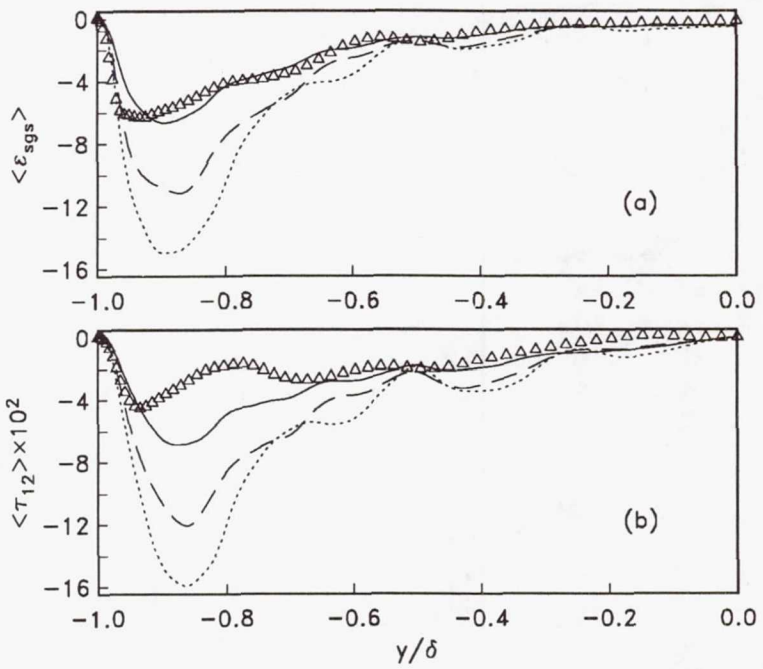

FIGURE 1. Plane-averaged subgrid-scale shear stress $<\tau>_{12}$ and dissipation $<\epsilon_{sgs}>$; $Re = 3300$ turbulent channel flow. △ exact; ——— $\alpha = 2$; - - - - $\alpha = 4/3$; ····· $\alpha = 8/7$. (a) Dissipation; (b) SGS shear stress.

where $\overline{\Delta}_i$ and $\widetilde{\overline{\Delta}}_i$ are the filter widths in each coordinate direction associated with $\overline{G}$ and $\widetilde{\overline{G}}$ respectively.

The mean subgrid-scale shear stress $<\tau>_{12}$ and dissipation $<\epsilon_{sgs}>$ are compared with the modeled ones in Figure 1 for various filter widths in the turbulent channel flow case. The choice $\alpha = 2$ was found to yield the best results. With this choice $\overline{\Delta}$ corresponds to a wavenumber in the decaying region of the one-dimensional energy spectrum, while $\widetilde{\overline{\Delta}}$ represents a wavenumber in the flat region. In Figure 2, C is plotted as function of the wall coordinate $y^+ = u_\tau y_w/\nu$ [where $u_\tau = (\tau_w/\rho)^{1/2}$ is the friction velocity, τ_w is the wall shear and ρ the fluid density] ; the expected y^{+3} behavior is evident. At the channel center $C \simeq 2.5 \times 10^{-3}$; the square root of this value is about half the commonly used value for the Smagorinsky constant, $C_S = 0.1$. The model was also tested in transitional flow, where the choice $\alpha = 2$ appeared to be the best, at least for the prediction of the subgrid-scale dissipation

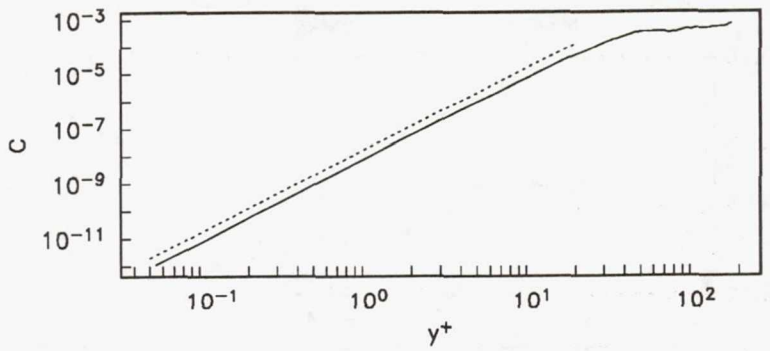

FIGURE 2. Variation of C [defined in Eqn. (16)] with distance from the wall; $Re = 3300$ turbulent channel flow, $\alpha = 2$. —— C obtained from DNS (Kim *et al.* 1987); ····· $C \sim y^{+3}$.

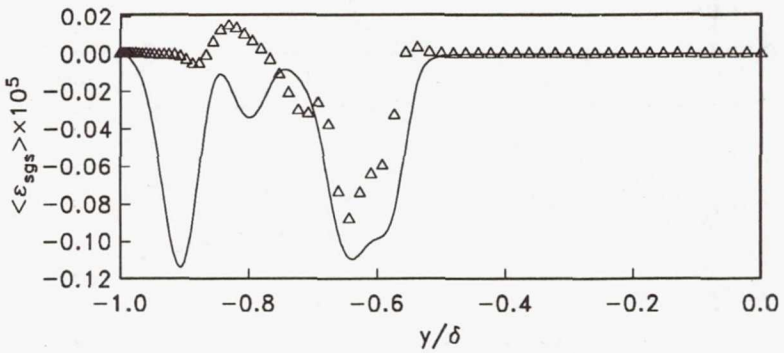

FIGURE 3. Plane-averaged subgrid-scale dissipation $<\epsilon_{sgs}>$; transitional flow, $t = 176$. △ exact; —— $\alpha = 2$.

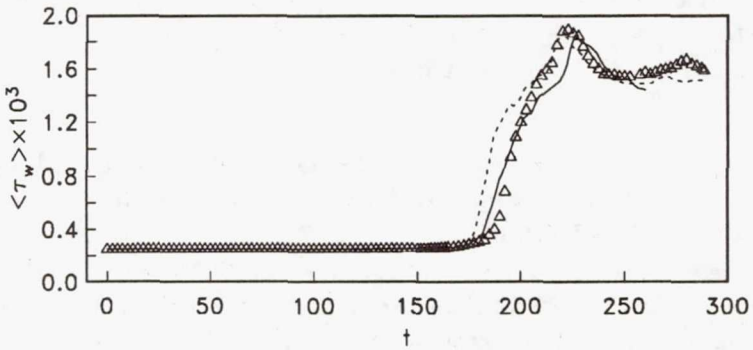

FIGURE 4. Time development of the plane-averaged wall shear stress $<\tau_w>$ in $Re = 8000$ transitional channel flow. △ DNS (Zang *et al.* 1990); —— present results; ····· LES (Piomelli & Zang 1990b).

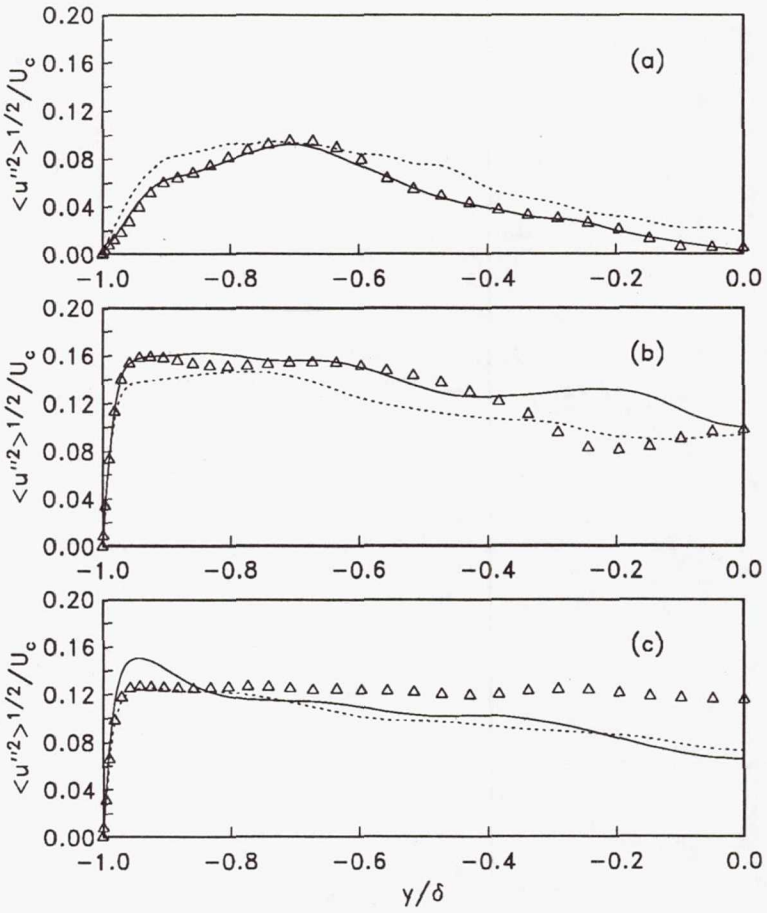

FIGURE 5. Turbulence intensities $<u_i''^2>^{1/2}$ in transitional channel flow. △ Filtered DNS (Zang *et al.* 1990); ——— present calculation; ····· LES results of Piomelli & Zang (1990b). (a) $t = 176$; (b) $t = 200$; (c) $t = 220$.

(Figure 3). The SGS dissipation predicted by the Smagorinsky model, by contrast, is many orders of magnitude larger, and peaks much closer to the wall than the exact one (Piomelli *et al.* 1990a).

To further determine the accuracy of the dynamic SGS model (16), it was also tested *a posteriori* in the LES of transitional and fully developed turbulent channel flow. Initial conditions consisted of the parabolic mean flow, on which a 2D Tollmien-Schlichting (TS) mode of 2% amplitude and a 3D TS mode of 0.02% amplitude were superimposed. The initial conditions and Reynolds number matched those of the direct simulation of Zang, Gilbert & Kleiser (1990). The governing equations (5) and (6) were integrated in time using a pseudo-spectral Fourier-Chebyshev

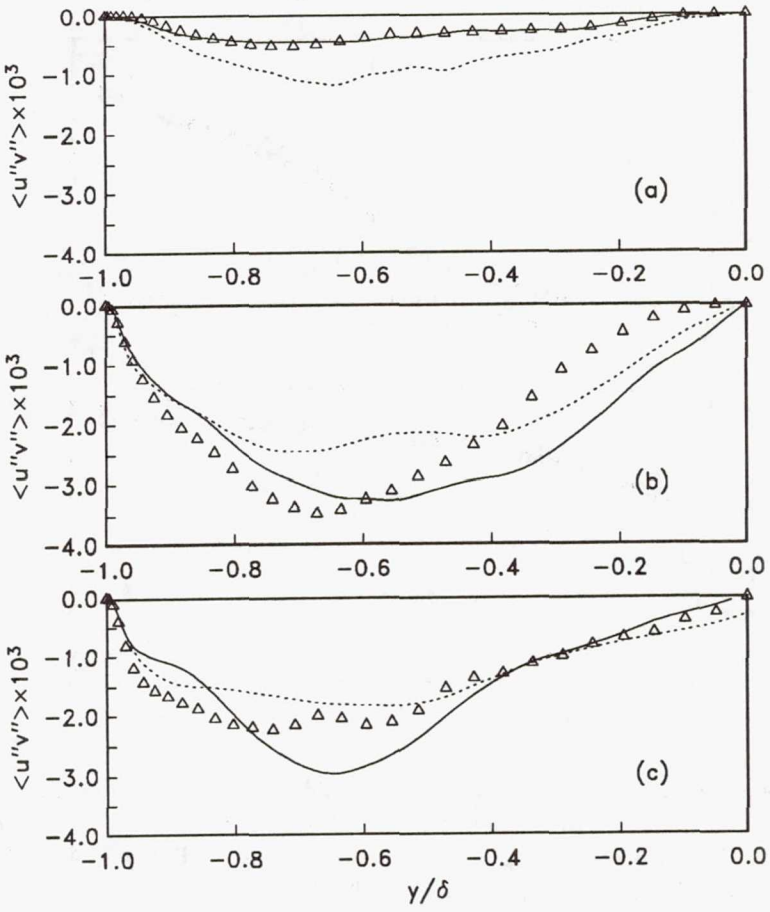

FIGURE 6. Plane-averaged Reynolds stress $<u''v''>$ in transitional channel flow. △ Filtered DNS (Zang *et al.* 1990); ——— present calculation; ····· LES results of Piomelli & Zang (1990b). (a) $t = 176$; (b) $t = 200$; (c) $t = 220$.

collocation method (Zang & Hussaini 1987). The ratio $\alpha = 2$ was chosen. At the initial stages $8\times49\times8$ grid points were used; the mesh was then progressively refined up to $48\times65\times64$ points; the dimensions of the computational domain were $2\pi\delta$ in the streamwise direction, and $4\pi\delta/3$ in the spanwise direction. Periodic boundary conditions were applied in the streamwise and spanwise directions; no-slip conditions were applied at the walls.

The time development of the mean wall shear stress $<\tau_w>$ is compared in Figure 4 with the DNS results of Zang, Gilbert & Kleiser (1990) and with the results of the LES of Piomelli & Zang (1990b), which used a Smagorinsky model including

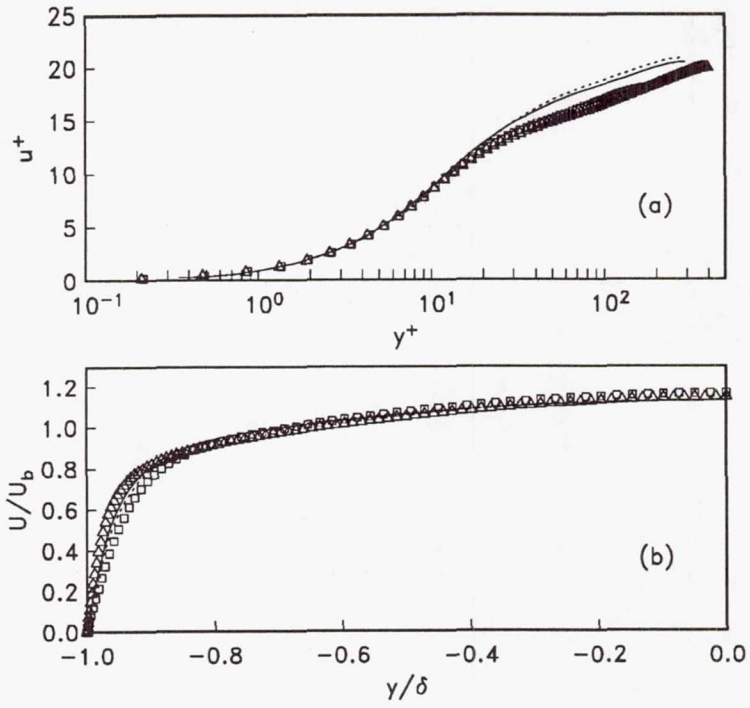

FIGURE 7. Mean velocity profile in fully developed turbulent channel flow. △ $Re_\tau = 395$ Filtered DNS (Kim *et al.* 1987); □ $Re_\tau = 180$ filtered DNS (Kim *et al.* 1987); ——— present calculation ($Re_\tau = 295$); ····· LES results of Piomelli & Zang (1990b) ($Re_\tau = 293$). (a) Global coordinates; (b) wall coordinates.

Van Driest damping and an *ad hoc* intermittency function; the present results compare very well with the finely resolved DNS. A coarse direct simulation which can adequately resolve the early stages of transition (up to $t \simeq 170$) cannot predict the drag crisis and the breakdown process with any accuracy (Piomelli & Zang 1990b). The root-mean-square fluctuation of $<u''^2>^{1/2}$ (where $u_i'' = \overline{u}_i - <\overline{u}_i>$) and the Reynolds shear stress $<u''v''>$, shown in Figures 5 and 6, are in fair agreement with the DNS results. The DNS results have been filtered using the same filter employed in the LES calculation. Discrepancies between the LES and DNS results at late stages of transition may be due to the fact that, at these times, slight differences in the prediction of the onset of transition may result in significant differences in the instantaneous fields. The capability of the model to predict average backscatter is evidenced by the fact that for $t \leq 185$ the eddy viscosity was negative for significant regions of the channel.

Once fully developed turbulent flow was achieved, statistics were accumulated.

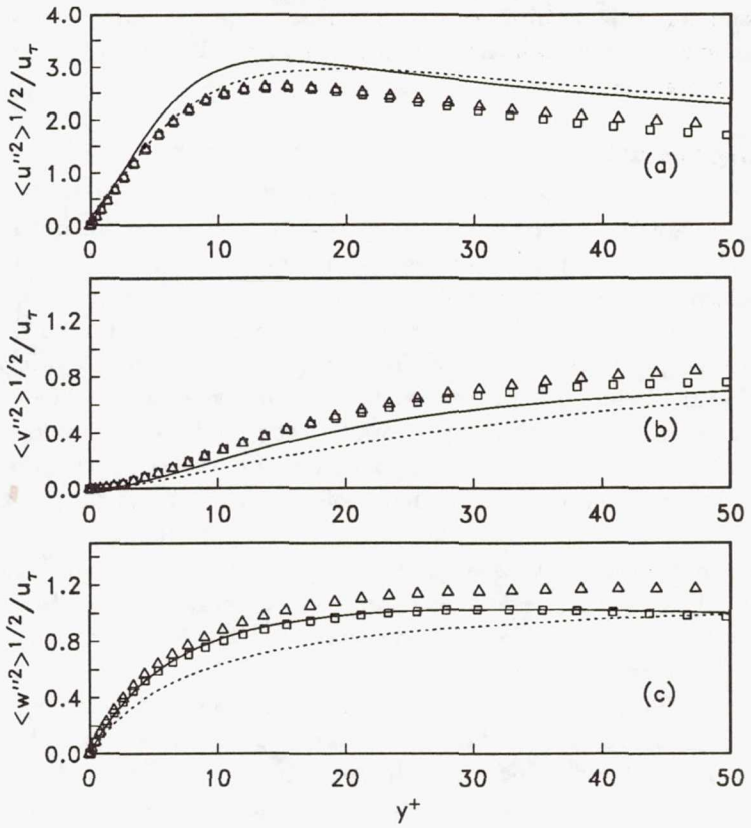

FIGURE 8. Turbulence intensities $<u_i''^2>^{1/2}$ in fully developed turbulent channel flow. $\triangle$ $Re_\tau = 395$ Filtered DNS (Kim *et al.* 1987); $\square$ $Re_\tau = 180$ filtered DNS (Kim *et al.* 1987); ——— present calculation ($Re_\tau = 295$); ····· LES results of Piomelli & Zang (1990b) ($Re_\tau = 293$). (a) u; (b) v, (c) w.

The Reynolds number of the turbulent flow was $Re_\tau = 295$ based on friction velocity u_τ and channel halfwidth. The mean velocity profile is shown in Figure 7, normalized by the friction velocity u_τ and by the bulk velocity U_b

$$U_b = \frac{1}{2\delta}\int_{-\delta}^{\delta} <\overline{u}> dy. \tag{18}$$

Although an inadequate resolution of the wall layer results in a low value of wall stress, which is reflected in a high value of the intercept of the logarithmic layer in Figure 7b, agreement of the LES results with the DNS data is fairly good. The turbulence intensities $<u_i''^2>^{1/2}$ normalized by the friction velocity u_τ are shown in Figure 8. The DNS results have been filtered using the same filter employed in the LES calculation. In general, the dynamic model gives more accurate results than the Smagorinsky model used by Piomelli & Zang (1990b). The peak of the

streamwise turbulent kinetic energy occurs near $y^+ = 12$, a value also obtained by experiments and numerical simulations; the mean streak spacing was found to be $\lambda^+ = 140$, somewhat larger than the established value of 100, which is also expected of large-eddy simulations.

4. Concluding remarks

A new eddy viscosity subgrid-scale stress model has been presented in which the smallest resolved scales are dynamically tested to predict the behavior of the subgrid scales. This model is based on the algebraic identity (10) between the resolved turbulent stresses and the subgrid-scale stresses obtained using two filters, the grid filter and the test filter. The model coefficient was obtained dynamically as the calculations progress. This procedure exploits the spectral information on the energy content of the smallest resolved scales provided by LES calculations to dynamically adjust the model. The only input to the model is the ratio of test filter width to grid filter width, which was optimized using a numerical turbulent channel flow database. Among the useful properties of the model is its proper asymptotic behavior near the wall without the use of *ad hoc* damping functions.

Large-eddy simulations of transitional and fully developed turbulent channel flow were also carried out. The results were in good agreement with those of direct simulations, and better than those of LES that used the Smagorinsky model with *ad hoc* damping and intermittency functions.

Investigation of the properties of this model when the box filter is employed is desirable. The robustness of the choice $\alpha = 2$ should also be examined by applying the model to flow configurations much different from those studied here. Finally, the use of local space and time averages instead of the plane average used to obtain (16) should be attempted.

REFERENCES

DEARDORFF, J.W. 1970 A numerical study of three-dimensional turbulent channel flow at large Reynolds numbers. *J. Fluid Mech.* **41**, 453–480.

GERMANO, M. 1990 Averaging invariance of the turbulent equations and similar subgrid-scale modeling. *CTR Manuscript 116.*

KIM, J., MOIN, P. & MOSER, R. 1987 Turbulence statistics in fully developed channel flow at low Reynolds number. *J. Fluid Mech.* **177**, 133–166.

LILLY, D.K. 1966 On the application of the eddy viscosity concept in the inertial sub-range of turbulence. *NCAR Manuscript 123.*

MASON, P.J. & CALLEN, N.S. 1986 On the magnitude of the subgrid-scale eddy coefficient in large-eddy simulation of turbulent channel flow. *J. Fluid Mech.* **162**, 439–462.

MCMILLAN, O.J., FERZIGER, J.H. & ROGALLO, R.S. 1980 Tests of new subgrid-scale models in strained turbulence. *AIAA Paper No. 80-1339.*

MOIN, P. & KIM, J. 1982 Numerical investigation of turbulent channel flow. *J. Fluid Mech.* **118**, 341–377.

PIOMELLI, U., MOIN, P. & FERZIGER, J.H. 1988 Model consistency in large eddy simulation of turbulent channel flows. *Phys. Fluids* **31**(7), 1884–1891.

PIOMELLI, U., ZANG, T.A., SPEZIALE C.G. & HUSSAINI, M.Y. 1990a On the large-eddy simulation of transitional wall-bounded flows. *Phys. Fluids A* **2**(2), 257–265.

PIOMELLI, U. & ZANG, T.A. 1990b Large-eddy simulation of transitional channel flow. *1st IMACS Conf. on Computational Physics*, Boulder, June 1990.

PIOMELLI, U., CABOT, W.H., MOIN, P. & LEE, S. 1990c Subgrid-scale backscatter in transitional and turbulent flows. This volume.

SMAGORINSKY, J. 1963 General circulation experiments with the primitive equations. I. The basic experiment. *Mon. Weather Rev.* **91**, 99–164.

VAN DRIEST, E.R. 1956 On the turbulent flow near a wall. *J. Aero. Sci.* **23**, 1007–1011.

YAKHOT, A., ORSZAG, S.A., YAKHOT, V. & ISRAELI, M. 1989 Renormalization Group formulation of large-eddy simulations. *J. Sci. Comput.* **4**, 139–158.

YAKHOT, V. & ORSZAG, S.A. 1986 Renormalization Group analysis of turbulence. *J. Sci. Comput.* **1**, 3–51.

ZANG, T.A. & HUSSAINI, M.Y. 1987 Numerical simulation of nonlinear interactions in channel and boundary-layer transition. In *Nonlinear wave interactions in fluids,* R.W. Miksad, T.R. Akylas and T. Herbert, eds., ASME, New York, 131–145.

ZANG, T.A., GILBERT, N. & KLEISER, L. 1990 Direct numerical simulation of the transitional zone. In *Instability and transition,* M.Y. Hussaini and R.G. Voigt eds., Springer-Verlag, New York, 283-299.

Center for Turbulence Research
Proceedings of the Summer Program 1990

Subgrid-scale backscatter in transitional and turbulent flows

By Ugo Piomelli,[1] William H. Cabot,[2] Parviz Moin[2] AND Sangsan Lee[2]

Most subgrid-scale (SGS) models for large-eddy simulations are absolutely dissipative (that is, they remove energy from the large scales at each point in the physical space). The actual SGS stresses, however, may transfer energy to the large scales (backscatter) at a given location. Direct numerical simulations of turbulent channel flow and compressible isotropic turbulence are used to study the backscatter phenomena. In all flows considered roughly 50% of the grid points were experiencing backscatter when a Fourier cutoff filter was used. The backscatter fraction was less with a Gaussian filter, and intermediate with a box filter in physical space. Moreover, the backscatter and forward scatter contributions to the SGS dissipation were comparable, and each was often much larger than the total SGS dissipation. The SGS dissipation (normalized by total dissipation) increased with filter width almost independently of filter type and Reynolds number. The amount of backscatter showed an increasing trend with Reynolds numbers. In the near-wall region of the channel, events characterized by strong Reynolds shear stress correlated fairly well with areas of high SGS dissipation (both forward and backward). In compressible isotropic turbulence similar results were obtained, independent of fluctuation Mach number.

1. Introduction

Large-eddy simulation (LES) is based on the assumption that the modeled small scales are nearly homogeneous and isotropic. Most of the commonly used subgrid-scale (SGS) models, moreover, assume that the main function of subgrid scales is to remove energy from the large scales and dissipate it through the action of the viscous forces. It has been known for some years, however, that while on average energy is transferred from the large to the small scales ("forward scatter"), reversed energy flow ("backscatter") from the small scales to the large ones may also occur intermittently.

The most commonly used subgrid-scale stress model, the Smagorinsky (1963) model, is absolutely dissipative, i.e., can only account for forward scatter. This model has been reasonably successful in simulations of simple turbulent flows; its success is probably due to its ability to predict the global energy drain by the small scales even if the details of the model are incorrect (Rogallo & Moin 1984).

1 University of Maryland
2 Center for Turbulence Research

Very few of the SGS models used in the past are capable of providing backscatter. The mixed model of Bardina, Ferziger & Reynolds (1980), for example, has a part that is not absolutely dissipative, the scale-similar part; in channel flow this term provides backscatter (Horiuti 1989).

Recent work on the LES of transitional flows (Piomelli *et al.* 1990) has shown that, during the early nonlinear stages of transition energy is transferred from small scales to large scales even in the mean, and that failure to account for this phenomenon can cause inaccurate prediction of the growth of the perturbations. The Smagorinsky model predicted decay of the perturbations even in instances in which the flow should have been unstable. Acceptable results were obtained, however, by introducing an intermittency factor which turned off the eddy viscosity model until the perturbations had grown to finite amplitude and altered the mean velocity profile.

Leith (1990) proposed an SGS stress model including a stochastic backscatter force that was used for the LES of two-dimensional mixing layer. Although his results show the correct growth rate of the layer, no comparison is made with calculations in which the stochastic force is omitted.

Chasnov (1990) presented an SGS stress model which includes a stochastic backscatter force. Use of this model in a LES computation of freely-decaying isotropic turbulence gave results in good agreement with theoretical predictions. By contrast, use of an eddy viscosity model did not yield the expected spectral decay in the inertial subrange.

Although backscatter modeling has recently received some attention, little effort has been made to actually quantify this phenomenon, especially in wall-bounded flows. In this study, the velocity fields obtained from direct numerical simulations (DNS) of the Navier-Stokes equations will be used to calculate subgrid-scale dissipation and backscatter. Although this work will concentrate on transitional and turbulent plane channel flows, compressible homogeneous isotropic turbulence has also been examined. In the next Section the equations relevant to the problem will be presented; in Section 3 results of *a priori* tests performed on the numerical simulations will be shown and discussed. Finally, in Section 4 conclusions and suggestions for future work will be made.

2. Mathematical formulation

In large-eddy simulation the large-scale quantities (indicated by an overbar) are defined by the filtering operation

$$\overline{f}(\mathbf{x}) = \int f(\mathbf{x}')G(\mathbf{x},\mathbf{x}')d\mathbf{x}', \tag{1}$$

in which G is the filter function and the integral is extended to the entire domain. Applying the filtering operation to the Navier-Stokes equations yields the dimensionless filtered continuity and Navier-Stokes equations

$$\frac{\partial \overline{u}_i}{\partial x_i} = 0, \tag{2}$$

$$\frac{\partial \overline{u}_i}{\partial t} + \frac{\partial}{\partial x_j}(\overline{u}_i\overline{u}_j) = -\frac{\partial \overline{p}}{\partial x_i} - \frac{\partial \tau_{ij}}{\partial x_j} + \frac{1}{Re}\frac{\partial^2 \overline{u}_i}{\partial x_j \partial x_j}. \tag{3}$$

Equations (2-3) govern the evolution of the large scales. The effects of the small scales appear in the subgrid-scale (SGS) stress

$$\tau_{ij} = \overline{u_i u_j} - \overline{u}_i \overline{u}_j, \tag{4}$$

which must be modeled.

To examine the effect of the SGS stress model on the resolved scales, consider the transport equation for the resolved energy $\overline{q}^2 = \overline{u}_i \overline{u}_i$

$$\frac{\partial \overline{q}^2}{\partial t} + \frac{\partial}{\partial x_j}\left(\overline{q}^2 \overline{u}_j\right) = \frac{\partial}{\partial x_j}\left(-2\overline{p}\,\overline{u}_j - 2\overline{u}_i \tau_{ij} + \frac{1}{Re}\frac{\partial \overline{q}^2}{\partial x_j}\right) - \frac{2}{Re}\frac{\partial \overline{u}_i}{\partial x_j}\frac{\partial \overline{u}_i}{\partial x_j} + 2\tau_{ij}\overline{S}_{ij}, \tag{5}$$

in which $\overline{S}_{ij}$ is the large scale strain-rate tensor

$$\overline{S}_{ij} = \frac{1}{2}\left(\frac{\partial \overline{u}_i}{\partial x_j} + \frac{\partial \overline{u}_j}{\partial x_i}\right). \tag{6}$$

One half of the last term on the right-hand side of (5) will be referred to as "subgrid-scale dissipation", $\epsilon_{sgs} = \tau_{ij}\overline{S}_{ij}$; it represents the energy transfer between resolved and subgrid scales. If it is negative, the subgrid scales remove energy from the resolved ones (forward scatter); if it is positive, they release energy to the resolved scales (backscatter). The backward and forward scatter components of ϵ_{sgs}, respectively denoted by ϵ_+ and ϵ_-, are defined as

$$\epsilon_+ = \frac{1}{2}\left(\epsilon_{sgs} + |\epsilon_{sgs}|\right), \qquad \epsilon_- = \frac{1}{2}\left(\epsilon_{sgs} - |\epsilon_{sgs}|\right). \tag{7}$$

It is easy to see that eddy viscosity SGS stress models of the Smagorinsky type are absolutely dissipative, since they assume that the eddy viscosity ν_T is positive, which gives

$$\tau_{ij}\overline{S}_{ij} = -2\nu_T \overline{S}_{ij}\overline{S}_{ij} < 0. \tag{8}$$

To investigate the character of backscatter in turbulent flows the velocity fields obtained from the direct numerical simulation (DNS) of the Navier-Stokes equations were filtered to yield the exact resolved and subgrid-scale velocities, and the exact subgrid-scale dissipation. The filter functions used in this work are the Gaussian filter, the box filter in physical space and the sharp cutoff filter. The Gaussian filter is given by

$$G_i(x_i, x_i') = \left(\frac{6}{\pi \Delta_i}\right)^{1/2} \exp\left[6(x_i - x_i')^2/\Delta_i^2\right], \tag{9}$$

the box filter is defined as

$$G_i(x_i, x_i') = \begin{cases} 1/\Delta_i & \text{for } |x_i - x_i'| < \Delta_i/2 \\ 0 & \text{otherwise,} \end{cases} \tag{10}$$

while the cutoff filter is most conveniently defined in Fourier space:

$$\widehat{G}_i(k_i) = \begin{cases} 1 & \text{for } k_i \le K_i \\ 0 & \text{otherwise,} \end{cases} \tag{11}$$

where $\widehat{G}_i$ is the Fourier coefficient of the filter function in the ith direction, G_i, $K_i = \pi/\Delta_i$ is the cutoff wavenumber and Δ_i is the filter width in the ith direction.

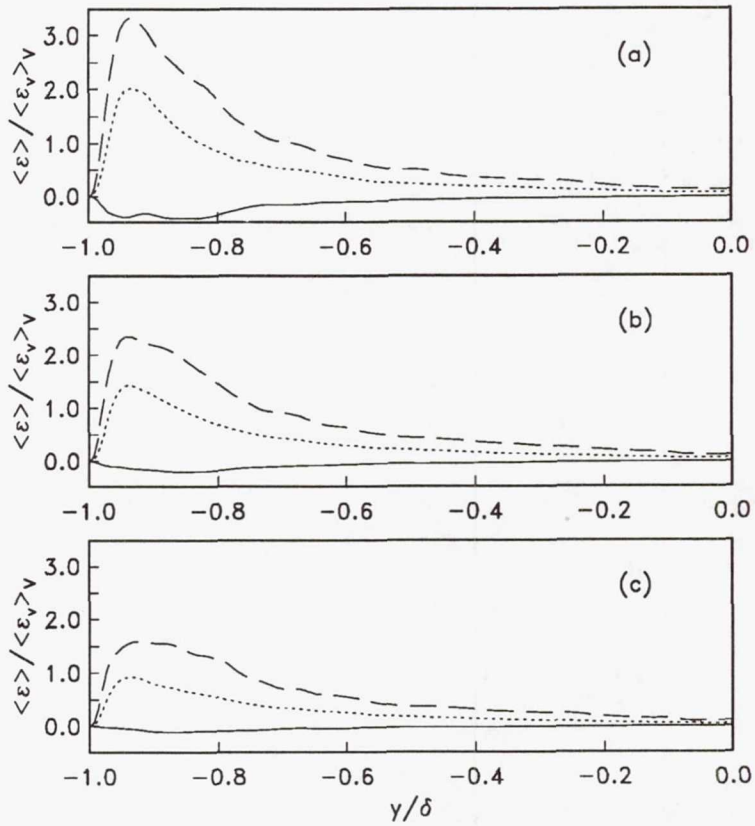

FIGURE 1. Subgrid-scale dissipation normalized by $<\epsilon_v>_V$; $Re = 3300$ turbulent channel flow; cutoff filter. —— Plane-averaged dissipation $<\epsilon_{sgs}>$; ---- r.m.s. fluctuation of ϵ_{sgs}; ····· plane-averaged backscatter $<\epsilon_+>$. (a) $\Delta_i = 4\Delta x_i$, $\alpha = 0.10$; (b) $\Delta_i = 8\Delta x_i/3$, $\alpha = 0.04$; (c) $\Delta_i = 2\Delta x_i$, $\alpha = 0.02$.

3. Results and discussion

The direct simulation results used for the study of backscatter in channel flows were those of Kim, Moin & Moser (1987) for turbulent channel flow, and those of Zang, Gilbert & Kleiser (1990) for the transitional channel flow case. In all cases x or x_1 is the streamwise direction, y or x_2 the direction normal to the walls, which are located at $y = \pm 1$, and z or x_3 is the spanwise direction; u, v and w are the velocity components along the coordinate directions. Reynolds numbers are respectively $Re = 3300$ and 7900 (based on centerline velocity U_c and channel halfwidth) for the turbulent cases and $Re = 8000$ for the transitional case (based on initial centerline velocity and channel halfwidth).

In Figure 1 the plane-averaged and root-mean-square subgrid-scale dissipation are shown for the $Re = 3300$ case. In the following, $<.>$ indicates averaging over a plane parallel to the wall, while $<.>_V$ indicates averaging over the entire computational

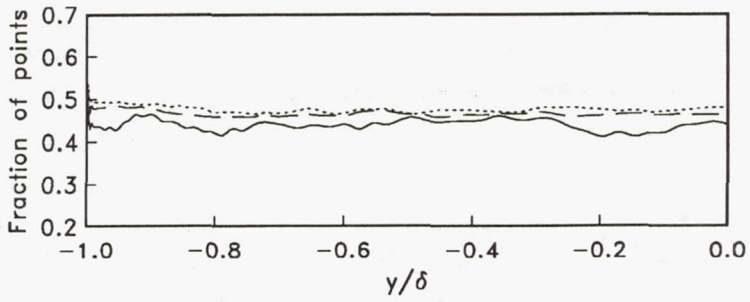

FIGURE 2. Fraction of grid points at which $\epsilon_{sgs} > 0$; $Re = 3300$ turbulent channel flow; cutoff filter. —— $\Delta_i = 4\Delta x_i$, $\alpha = 0.10$; ---- $\Delta_i = 8\Delta x_i/3$, $\alpha = 0.04$; ····· $\Delta_i = 2\Delta x_i$, $\alpha = 0.02$.

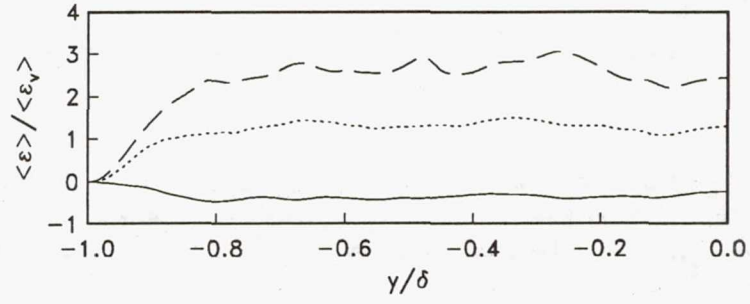

FIGURE 3. Subgrid-scale dissipation normalized by $<\epsilon_v>$; $Re = 3300$ turbulent channel flow; $\Delta_i = 4\Delta x_i$, $\alpha = 0.10$; cutoff filter. —— Plane-averaged dissipation $<\epsilon_{sgs}>$; ---- r.m.s. fluctuation of ϵ_{sgs}; ····· plane-averaged backscatter $<\epsilon_+>$.

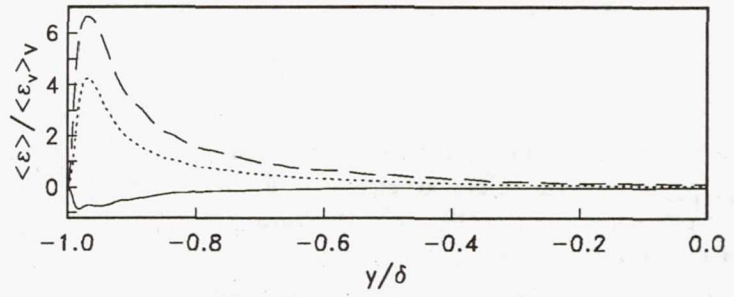

FIGURE 4. Subgrid-scale dissipation normalized by $<\epsilon_v>_V$; $Re = 7900$ turbulent channel flow; $\Delta_i = 4\Delta x_i$, $\alpha = 0.04$; cutoff filter. —— Plane-averaged dissipation $<\epsilon_{sgs}>$; ---- r.m.s. fluctuation of ϵ_{sgs}; ····· plane-averaged backscatter $<\epsilon_+>$.

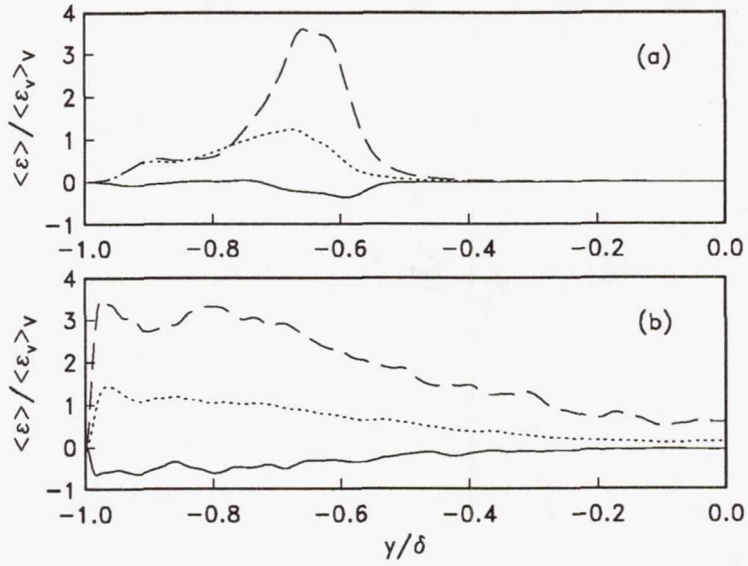

FIGURE 5. Subgrid-scale dissipation normalized by $<\epsilon_v>_V$; $Re = 8000$ transitional channel flow; cutoff filter. —— Plane-averaged dissipation $<\epsilon_{sgs}>$; ---- r.m.s. fluctuation of ϵ_{sgs}; ····· plane-averaged backscatter $<\epsilon_+>$. (a) $\Delta_i = 8\Delta x_i$, $\alpha = 0.01$, $t = 170$; (b) $\Delta_i = 4\Delta x_i$, $\alpha = 0.03$, $t = 200$

domain. The SGS dissipation and backscatter will be normalized by either the volume- or plane-averaged *absolute value* of the viscous dissipation, defined as

$$\epsilon_v = \frac{2}{Re} S_{ij} S_{ij}, \tag{12}$$

where

$$S_{ij} = \frac{1}{2}\left(\frac{\partial u_i}{\partial x_j} + \frac{\partial u_j}{\partial x_i}\right). \tag{13}$$

The amount of filtering will be characterized by α, the ratio of subgrid-scale kinetic energy $<q^2_{sgs}>_V$ to total turbulent kinetic energy $<q^2>_V$. Since filtering was only applied in the plane parallel to the wall, the ratios of filter width Δ_i to grid size Δx_i reported here only refer to the streamwise and spanwise directions.

Figure 1 indicates that the backscatter contribution to ϵ_{sgs} is much larger than the mean for all filter widths examined. While the subgrid scales extract energy from the large scales in the mean, large values of ϵ_+ and ϵ_- can be expected. The fraction of points in each plane which experience backscatter (shown in Figure 2) is close to 50% almost independent of filter width and distance from the wall. This

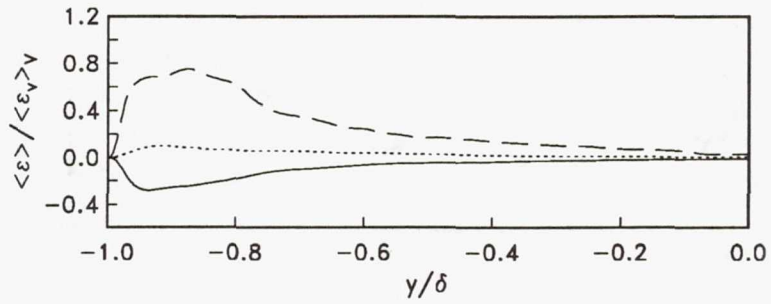

FIGURE 6. Subgrid-scale dissipation normalized by $<\epsilon_v>_V$; Re = 3300 turbulent channel flow; $\Delta_i = 4\Delta x_i$, $\alpha = 0.22$; Gaussian filter. —— Plane-averaged dissipation $<\epsilon_{sgs}>$; ---- r.m.s. fluctuation of ϵ_{sgs}; ····· plane-averaged backscatter $<\epsilon_+>$.

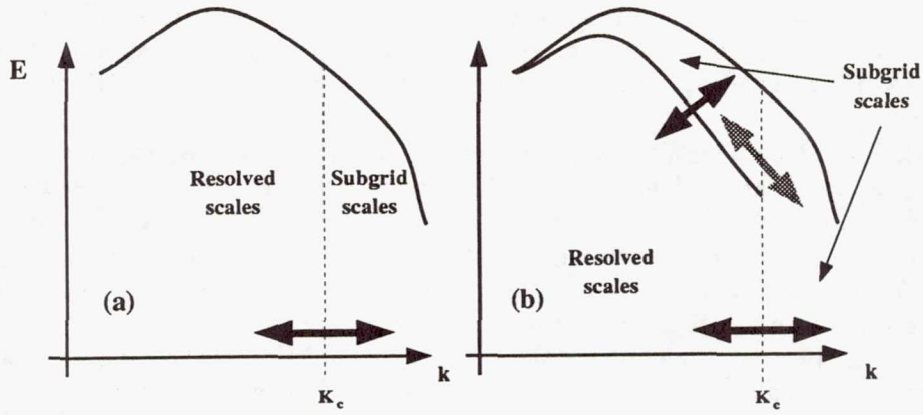

FIGURE 7. Sketch of the interactions between large and small scales in spectral space. (a) Cutoff filter; (b) Gaussian filter.

result was found to hold for all flows examined, including the transitional channel flow and the compressible isotropic decay.

Both backward and forward scatter peak in the near-wall region, at approximately $y^+ = 12$ (variables indicated by a superscript + are normalized by the kinematic viscosity ν and the friction velocity u_τ). In the near-wall region of the channel, events characterized by strong Reynolds shear stress correlate fairly well with areas of high SGS dissipation (both forward and backward). The unconditioned correlation coefficient between ϵ_{sgs} and uv is only 0.28 at $y^+ = 7$, but decays to zero above $y^+ = 15$. This value increases to 0.45 at $y^+ = 7$ if the correlation coefficient is conditioned on the value of uv being larger than its rms. The subgrid-scale dissipation normalized by the plane-averaged viscous dissipation (Figure 3) increases

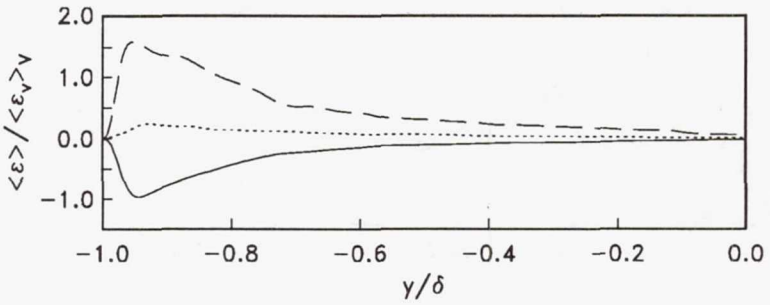

FIGURE 8. Subgrid-scale dissipation normalized by $<\epsilon_v>_V$; $Re = 3300$ turbulent channel flow; $\Delta_i = 4\Delta x_i$, $\alpha = 0.29$; box filter. ——— Plane-averaged dissipation $<\epsilon_{sgs}>$; ---- r.m.s. fluctuation of ϵ_{sgs}; ····· plane-averaged backscatter $<\epsilon_+>$.

monotonically with distance from the wall and levels off at midchannel (see below).

Similar results were obtained from the $Re = 7900$ channel flow (Figure 4) and from the transitional cases examined (Figure 5). At the early stages of transition (for $t < 180$), however, backscatter was found to occur in the mean (Piomelli *et al.* 1990).

When the Gaussian filter was used the magnitude of ϵ_+ was very much reduced over that found using the cutoff filter (Figure 6), although backscatter still occured at approximately 30% of the grid points. In practice, the Gaussian filter is usually coupled with a sharp cutoff filter, so that the subgrid-scale velocity has a contribution from the small scales (those beyond the cutoff) and from the scales resolved on the grid. The subgrid-scale dissipation, therefore, accounts for part of the energy transferred between scales above the cutoff, and a portion of the energy transferred between scales above the cutoff and those below it (the interaction indicated by the dark arrows in Figure 7). Another portion of the energy transferred by this interaction between large scale and small scales (indicated by the lighter arrow), however, appears as an energy transfer between subgrid scales in the transport equation for q^2_{sgs} with the Gaussian filter, while it contributes to backscatter with the cutoff filter.

When the box filter is used the SGS dissipation and backscatter are intermediate between those obtained with the Gaussian and the cutoff filters (Figure 8). This reflects the character of the box filter, which separates large and small scales more precisely than the Gaussian, but not as clearly as the cutoff filter.

The volume-averaged subgrid-scale dissipation and fraction of backscatter points for the turbulent channel flows examined are shown in Figure 9. The SGS dissipation (normalized by total dissipation) increased with filter width almost independently of filter type and Reynolds number. The amount of backscatter (Figure 10) appears to slightly increase with Reynolds number, a trend confirmed by the finding that $<\epsilon_+>/<\epsilon_v>$ also increases with distance from the wall (see Figure 3).

The results obtained from the compressible isotropic decay simulations exhibit the

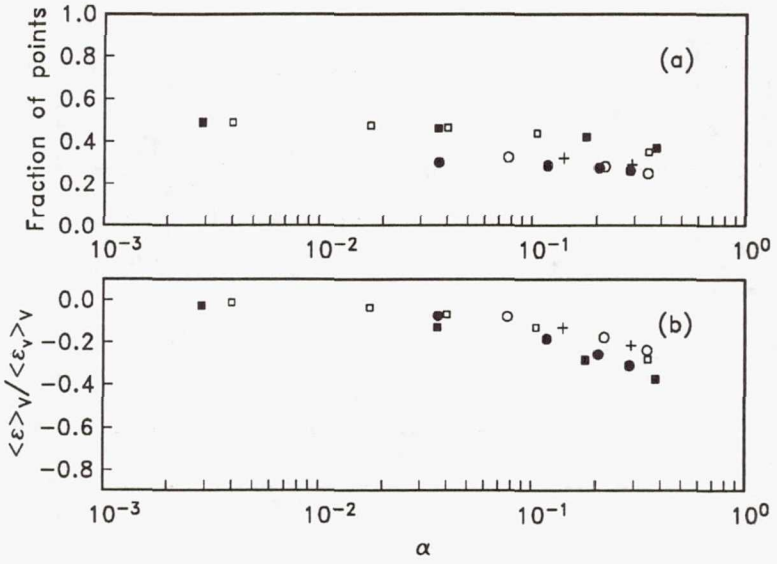

FIGURE 9. Volume-averaged (a) fraction of backscatter points and (b) subgrid-scale dissipation. □ Re = 3300 turbulent channel flow, cutoff filter; ■ Re = 7900 turbulent channel flow, cutoff filter; ○ Re = 3300 turbulent channel flow, Gaussian filter; ● Re = 7900 turbulent channel flow, Gaussian filter; + Re = 3300 turbulent channel flow, box filter.

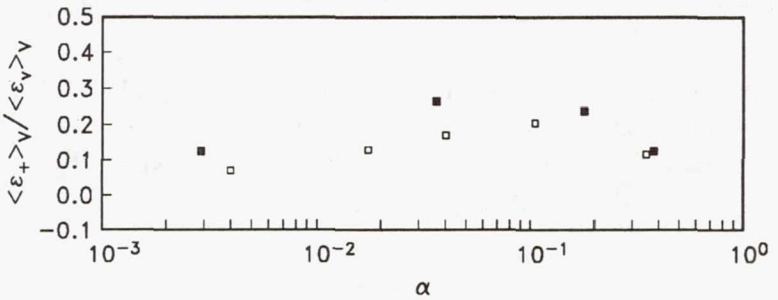

FIGURE 10. Volume-averaged backscatter. □ Re = 3300 turbulent channel flow, cutoff filter; ■ Re = 7900 turbulent channel flow, cutoff filter.

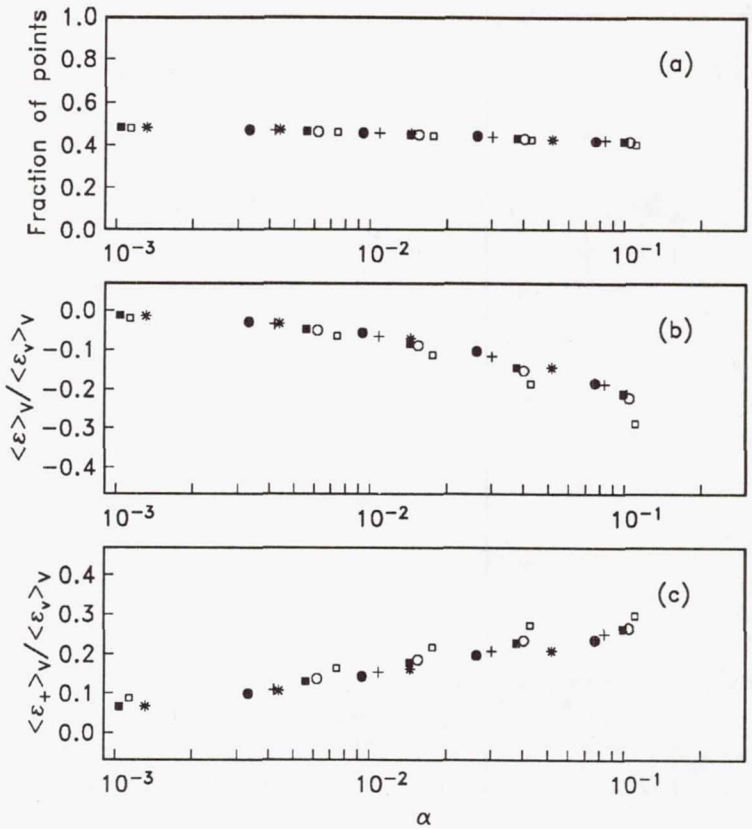

FIGURE 11. Volume-averaged (a) fraction of backscatter points, (b) subgrid-scale dissipation and (c) backscatter. Compressible isotropic turbulence,cutoff filter. $Re_o = 35.1$ for all cases. □ $Re = 22.5$, $M = 0.132$, $M_o = 0.173$; ○ $Re = 19.8$, $M = 0.113$, $M_o = 0.173$; ■ $Re = 19.4$, $M = 0.220$, $M_o = 0.346$; ● $Re = 17.3$, $M = 0.182$, $M_o = 0.346$; + $Re = 18.0$, $M = 0.289$, $M_o = 0.519$; × $Re = 15.0$, $M = 0.213$, $M_o = 0.519$.

same trends observed above. The direct simulation data were taken from the results of Lee, Lele & Moin (1990). For the compressible flow simulations the subgrid-scale stresses τ_{ij} and dissipation ϵ_{sgs}, and the viscous dissipation ϵ_v are defined as

$$\tau_{ij} = \overline{\rho}\left(\widetilde{u_i u_j} - \widetilde{u}_i \widetilde{u}_j\right), \tag{14}$$

$$\epsilon_{sgs} = \tau_{ij}\widetilde{S}_{ij}, \tag{15}$$

$$\epsilon_v = \frac{4}{3}\overline{\mu}\overline{\left(\frac{\partial u_i}{\partial x_i}\right)^2} + \overline{\mu}\ \overline{\omega_i \omega_i}, \tag{16}$$

where the tilde denotes Favre-filtering, and ω_i is the ith component of the vorticity vector $\omega_i = \epsilon_{ijk}\partial u_k/\partial x_j$ (in which ϵ_{ijk} is the alternating tensor). The results from

three simulations were examined with initial turbulent Mach numbers $M_o = 0.173$, 0.346 and 0.519, respectively (based on rms velocity and mean speed of sound). The initial Reynolds number Re_o for the three cases (based on Taylor microscale and rms velocity) was 35.1. Various stages of the decay were examined, and the volume-averaged fraction of backscatter points, subgrid-scale dissipation and backscatter are shown in Figure 11. The magnitude of the subgrid-scale dissipation increases with filter width; within the range of filter widths examined, the subgrid-scale backscatter also increases with filter width, a result consistent with the turbulent channel flow. No dependence on the Mach number was observed.

4. Concluding remarks

A numerical investigation of subgrid-scale backscatter has been conducted to determine the extent and magnitude of the energy transfer from small to large scales. It has been found that, when a cutoff filter is used, backscatter occurs at nearly half of the points in the flow. The mean subgrid-scale dissipation, which is usually negative, is the sum of two large quantities: energy transfer from large to small scales and backscatter. Each of these events is many times the mean SGS dissipation. Strong backward and forward scatter events are fairly well correlated with regions of high Reynolds stress, at least in the near-wall region.

When the Gaussian filter is used the amount of backscatter decreases, since part of the energy transfer between large and small scales is accounted for as an interaction between subgrid scales. The results obtained with the box filter in real space, which is implicitly applied by finite difference schemes, are intermediate between those obtained with the cutoff and Gaussian filters.

While the magnitude of the SGS dissipation (normalized by the volume-averaged viscous dissipation) increases with filter width independently of Reynolds number and filter type, backscatter increases slightly with Reynolds number. Similar results were observed in compressible isotropic turbulence.

REFERENCES

BARDINA, J., FERZIGER, J.H. & REYNOLDS, W.C. 1980 Improved subgrid-scale models for large-eddy simulation. *AIAA Paper No. 80-1357.*

CHASNOV, J.R. 1990 Simulation of the Kolmogorov inertial subrange using an improved subgrid model. Submitted to *Phys. Fluids A.*

HORIUTI, K. 1989 The role of the Bardina model in large eddy simulation of turbulent channel flow. *Phys. Fluids A* **1**(2), 426–428.

KIM, J., MOIN, P. & MOSER, R. 1987 Turbulence statistics in fully developed channel flow at low Reynolds number. *J. Fluid Mech.* **177**, 133–166.

LEE, S., LELE, S.K. & MOIN, P. 1990 Eddy-shocklets in decaying isotropic turbulence. *CTR Manuscript 117.*

LEITH, C.E. 1990 Stochastic backscatter in a subgrid-scale model: Plane shear mixing layer. *Phys. Fluids A* **2**(3), 297–299.

PIOMELLI, U., ZANG, T.A., SPEZIALE C.G. & HUSSAINI, M.Y. 1990 On the large-eddy simulation of transitional wall-bounded flows. *Phys. Fluids A* **2**(2), 257–265.

ROGALLO, R.S. & MOIN, P. 1984 Numerical simulation of turbulent flows. *Ann. Rev. Fluid Mech.* **16**, 99–137.

SMAGORINSKY, J. 1963 General circulation experiments with the primitive equations. I. The basic experiment. *Mon. Weather Rev.* **91**, 99–164.

ZANG, T.A., GILBERT, N. & KLEISER, L. 1990 Direct numerical simulation of the transitional zone. In *Instability and transition,* M.Y. Hussaini and R.G. Voigt eds., Springer-Verlag, New York, 283-299.

A subgrid-scale model based on the second-order velocity structure function

By P. Comte[1], S. Lee[2] AND W. H. Cabot[3]

A series of tests were performed to help extend the use of a subgrid-scale model to compressible and wall-bounded flows. *A priori* tests were done in the case of the incompressible turbulent channel flow. They showed that a one-dimensional formulation of the structure-function model is more appropriate, leading to a satisfactory behavior of the model at the walls without requiring any damping function. This model is consistent with the original formulation of Métais & Lesieur (1990). In large-eddy simulations of compressible isotropic turbulence, both models performed well up to an initial *rms* Mach number of 0.6.

1. Introduction

It is well known that, even with the largest supercomputers available, one cannot simulate all the scales involved in most flows encountered in nature or in practical applications. It is often chosen to resolve as accurately as possible the largest scales, and to model the scales which are smaller than the computational mesh.

In the case of freely decaying incompressible isotropic turbulence, Chollet & Lesieur (1981) have developed a subgrid-scale model based on the concept of spectral eddy viscosity introduced by Kraichnan (1976). The normalized eddy viscosity $\nu_t(t)$ is given in terms of the kinetic energy spectrum at the cutoff wavenumber k_c:

$$\nu_t(k|k_c,t) = \nu_t^+(k|k_c)\,\sqrt{\frac{E(k_c,t)}{k_c}}. \tag{1}$$

The dimensionless eddy viscosity ν_t^+ is evaluated assuming that k_c lies in the Kolmogorov subrange. This formulation ensures that ν_t remains equal to zero as long as there is no energy at the cutoff. In the limit of infinite Reynolds number, the energy balance for the resolved scales is

$$\int_0^{k_c} 2\,\nu_t\,k^2\,E(k,t)\,dk \;=\; \varepsilon\,(t). \tag{2}$$

For the Kolmogorov spectrum

$$E(k,t) \;=\; C_k\,\varepsilon^{2/3}\,k^{-5/3}\;\;,\quad C_k \;\approx\; 1.4, \tag{3}$$

1 Grenoble Institute of Mechanics, Grenoble, France
2 Stanford University
3 Center for Turbulence Research

this yields

$$\nu_t(t) \left[\frac{E(k_c,t)}{k_c}\right]^{-1/2} \equiv \nu_t^+ = \frac{2}{3} C_k^{-3/2} \approx 0.402, \tag{4}$$

assuming that ν_t depends only on time.

In fact, Chollet & Lesieur (1981) proposed a more complicated expression for ν_t^+ which involved the ratio k/k_c, but the expression proposed in (4), justified by Leslie & Quarini (1979), proved to give acceptable results (Métais & Lesieur 1990). Chollet (1984, 1985) also applied the same methodology to parametrize the passive-temperature-variance transfer across the cutoff, and proposed a spectral eddy diffusivity κ_t proportional to the eddy viscosity ν_t, with a constant turbulent Prandtl number $Pr_t = \nu_t/\kappa_t \approx 0.6$. The Chollet-Lesieur model has also been used in the case of non-isotropic flows, such as stably stratified homogeneous turbulence (Métais & Chollet 1989; Métais & Lesieur 1990) and the mixing layer (Comte *et al.*, 1989). In the latter case, after the first pairing, the model has permitted to reach a regime of fully developed turbulence with $k^{-5/3}$ spectrum in the smallest resolved scales and with velocity fluctuation profiles in very good agreement with their experimental counterparts. Furthermore, the simulations reproduced the fine details of the turbulence structures, including the streamwise secondary vortices.

Métais & Lesieur (1990) then proposed another model which computes a time-dependent eddy viscosity and eddy diffusivity in the physical space at each point, and which is consistent with the Chollet-Lesieur model. This new model is based on the second-order isotropic velocity structure function

$$F_2(\mathbf{x},r,t) = \left\langle [\mathbf{u}(\mathbf{x}+\mathbf{r},t) - \mathbf{u}(\mathbf{x},t)]^2 \right\rangle_{\|\mathbf{r}\|=r}, \tag{5}$$

which is related in the case of the incompressible turbulence to the energy spectrum by (Batchelor 1953)

$$F_2(r,t) = \langle F_2(\mathbf{x},r,t)\rangle_{\mathbf{x}} = 4\int_0^\infty E(k,t)\left[1 - \frac{\sin kr}{kr}\right] dk, \tag{6}$$

where $\mathbf{u},\mathbf{x},\mathbf{r}$ is the velocity vector, the position vector and the separation vector, respectively; $\|.\|$ denotes for the norm of a vector; and r is the distance between two points. Henceforth, this new model will be referred to as *the structure-function model.* It will be described in more detail in Section 2. Low-resolution tests (48^3) have led to more accurate predictions than with the Chollet-Lesieur model, which may be explained by the fact that the structure-function model takes intermittency into account better by defining ν_t and κ_t locally.

The structure-function model proved superior to the Smagorinsky (1963) model in the case of the flow past a backward-facing step (Silveira *et al.* 1990). It has also been utilized by Normand (1990) (see also Normand & Lesieur 1990) to simulate weakly-compressible isotropic turbulence and compressible boundary layer over a flat plate at an external Mach number of 5. The objective of the present work is to test this model and try to improve upon it in the two cases of incompressible channel flow and compressible isotropic turbulence at higher Mach number than before.

2. Structure-Function Model

A sharp cutoff at k_c in the Fourier space corresponds in the physical space to a filter function $G(\mathbf{x})$ defined by

$$G(x_i) = \frac{2\ \sin(\pi x_i/\Delta_c)}{\pi x_i}, \tag{7}$$

with

$$\Delta_c = \pi/k_c. \tag{8}$$

For the Kolmogorov spectrum (3) extending from $k = 0$ to ∞, the associated structure function F_2^a yields the original formulation of Kolmogorov's (1941) law

$$F_2^a(r) = \frac{9}{5}\,\Gamma\left(\frac{1}{3}\right)\ C_k\ \varepsilon^{2/3}\ r^{2/3} \approx 4.822\ C_k\ \varepsilon^{2/3}\ r^{2/3}, \tag{9}$$

where we have used the identity

$$\int_0^\infty x^{-8/3}\ [x - \sin x]\ dx = \frac{9}{10}\int_0^\infty x^{-2/3}\ \sin x\ dx = \frac{1}{2}\Gamma(\tfrac{1}{3}). \tag{10}$$

A relationship between $E(k_c,t)$ and $F_2^a(r,t)$ is obtained for all r by eliminating $C_k\ \varepsilon^{2/3}$ in (3) and (9). Hence, (4) yields

$$\begin{aligned}\nu_t(t) &= \frac{\frac{2}{3}\ C_k^{-3/2}}{\pi^{4/3}\sqrt{\frac{9}{5}\ \Gamma\left(\frac{1}{3}\right)}}\ \left(\frac{r}{\Delta_c}\right)^{-4/3}\ \Delta_c\ \sqrt{F_2^a\ (r,t)} \\ &\approx 0.0398\ \left(\frac{r}{\Delta_c}\right)^{-4/3}\ \Delta_c\ \sqrt{F_2^a\ (r,t)}\ .\end{aligned} \tag{11}$$

The Métais-Lesieur model is obtained by assuming

$$F_2^a(r,t) = \overline{F_2}(r,t) + C_0(r,t), \tag{12}$$

where $\overline{F_2}$ is the structure function computed from the resolved-velocity field $\overline{\mathbf{u}}(\mathbf{x},t)$, and C_0 is defined by

$$C_0(r,t) \equiv 4\int_{k_c}^\infty E(k,t)\left[1 - \frac{\sin kr}{kr}\right] dk \tag{13}$$

for a Kolmogorov spectrum extending from k_c to ∞. The validity of this assumption has been checked by Métais & Lesieur (1990) and proved to be valid provided r is

not too far from the cutoff scale $\Delta_c = \pi/k_c$ (see their Figure 20). Using (3) and (9), the spectrum $E(k,t)$ arising in (13) is related to $F_2^a(r,t)$ by

$$E(k,t) = \frac{1}{\frac{9}{5}\,\Gamma\left(\frac{1}{3}\right)}\, F_2^a(r)\; r^{-2/3}\; k^{-5/3}. \tag{14}$$

This yields

$$C_0 = F_2^a(r)\,\left(\frac{r}{\Delta_c}\right)^{-2/3} H\left(\frac{r}{\Delta_c}\right), \tag{15}$$

with

$$\begin{aligned} H(\zeta) &= \frac{4}{\frac{9}{5}\,\Gamma\left(\frac{1}{3}\right)} \int_\pi^\infty s^{-5/3}\left[1 - \frac{\sin s\zeta}{s\zeta}\right] ds \\ &= \frac{4}{\frac{9}{5}\,\Gamma\left(\frac{1}{3}\right)} \left[\frac{3}{2}\pi^{-2/3} + \zeta^{2/3}\Im\mathrm{m}\left\{e^{5i\pi/6}\Gamma(-5/3, i\pi\zeta)\right\}\right]. \end{aligned} \tag{16}$$

Using (12) and (15), one can estimate $F_2^a(r,t)$ in terms of the structure function $\overline{F_2}(r,t)$ of the resolved-velocity field:

$$F_2^a(r,t) = \left[1 - \left(\frac{r}{\Delta_c}\right)^{-2/3} H\left(\frac{r}{\Delta_c}\right)\right]^{-1} \overline{F_2}(r,t). \tag{17}$$

Substituting this expression into (11) yields

$$\nu_t(t) = A\left(\frac{r}{\Delta_c}\right)\,\Delta_c\,\sqrt{\overline{F_2}(r,t)} \tag{18}$$

with

$$A\left(\frac{r}{\Delta_c}\right) = \frac{\frac{2}{3}\,C_k^{-3/2}}{\pi^{4/3}\sqrt{\frac{9}{5}\Gamma\left(\frac{1}{3}\right)}} \left(\frac{r}{\Delta_c}\right)^{-4/3}\left[1 - \left(\frac{r}{\Delta_c}\right)^{-2/3} H\left(\frac{r}{\Delta_c}\right)\right]^{-1/2}. \tag{19}$$

Numerical values for A in terms of its argument r/Δ_c are given in Table 1.

ζ	$A(\zeta = r/\Delta_c)$
1	0.063
2	0.020
3	0.011
4	0.0071
5	0.0052

Table 1. $C_k = 1.4$

In practice, one has to bear in mind that assumption (12) is valid only for $\zeta \leq 2$ and that there are some uncertainties in the value of C_k.

The structure-function model is eventually made local by suppressing the averaging over $\mathbf{x}$, which yields

$$\nu_t(\mathbf{x},t) = A\left(\frac{r}{\Delta_c}\right)\,\Delta_c\,\sqrt{\overline{F_2}(\mathbf{x},r,t)}, \tag{20}$$

where $\overline{F_2}(\mathbf{x},r,t)$ is the resolved structure function defined by

$$\overline{F_2}(\mathbf{x},r,t) = \left\langle [\overline{\mathbf{u}}(\mathbf{x}+\mathbf{r},t) - \overline{\mathbf{u}}(\mathbf{x},t)]^2 \right\rangle_{\|\mathbf{r}\|=r}. \tag{21}$$

For the incompressible isotropic turbulence simulations, the computational grid was a uniform cubic mesh. The best results were obtained with $\zeta = r/\Delta x = 1$ and $\overline{F_2}(\mathbf{x},r,t)$ was calculated at each grid point by averaging over the six closest surrounding points.

3. A Priori Tests of Incompressible Channel Flow

We now consider a velocity field $\mathbf{u}(\mathbf{x})$ resulting from the direct simulation of a turbulent incompressible channel flow. This has a periodic horizontal field (x-z plane) at the resolution of 128^3 grid points, and all the scales of the motion are explicitly resolved. By convolution with a sharp filter in Fourier space, a large-scale field $\overline{\mathbf{u}}(\mathbf{x})$ is obtained at a resolution of $32 \times 128 \times 32$. No explicit filter was applied in the y-direction, normal to the walls.

By filtering the velocity field $\mathbf{u}(\mathbf{x})$ obtained from direct numerical simulations, we can compute $\overline{\mathbf{u}}(\mathbf{x})$. Since $\mathbf{u}(\mathbf{x})$ is known, one can compute the actual subgrid-scale stresses

$$\tau_{ij}^a = \overline{u_i u_j} - \overline{u_i}\,\overline{u_j} \tag{22}$$

and the actual subgrid-scale dissipation

$$\varepsilon^a = \tau_{ij}^a\,\overline{S}_{ij}, \tag{23}$$

$\overline{S}_{ij}$ being the large-scale strain-rate tensor defined by

$$\overline{S}_{ij} \equiv \frac{1}{2}\left(\frac{\partial \overline{u}_i}{\partial x_j} + \frac{\partial \overline{u}_j}{\partial x_i}\right). \tag{24}$$

The technique known as *a priori* test, first applied by Clark, Ferziger & Reynolds (1979) in the case of isotropic turbulence, is to compare the subgrid-scale values τ_{ij}^m and ε_{ij}^m, predicted by the model, to the actual values τ_{ij}^a and ε_{ij}^a. It is applied here to test the structure-function model defined in Section 2, in comparison with the Smagorinsky model. However, one has to bear in mind that the structure-function model is based on the assumption that turbulence is fully developed at small scale with a $k^{-5/3}$ energy spectrum. This is approximately verified in the high Reynolds

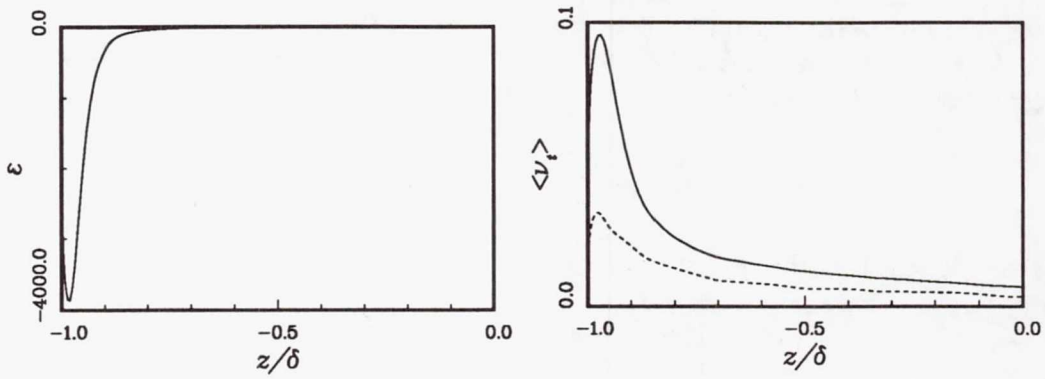

FIGURE 1. Left plot : ——— Smagorinsky dissipation, ---- *actual* dissipation (collapsed on the axis). Right plot : Smagorinsky eddy viscosity ——— mean, ---- *rms*.

number experiments (see Perry & Chong 1982, where slopes between -1 and $-5/3$ are found), but certainly not in the case of the field $\mathbf{u}(\mathbf{x})$, which was obtained from a direct numerical simulation at a moderate Reynolds number. It is thus likely that the *actual subgrid-scale dissipation* ε^a defined by (23) is smaller than if it had been computed from a high-Reynolds-number turbulent field. The aim of the *a priori* tests presented here is more to qualitatively investigate the behavior of the structure-function model in the presence of walls and to develop a way to account for the anisotropy of both the turbulence and the mesh than to try to match the *actual dissipation* ε^a and the modeled dissipation

$$\varepsilon^m = \tau_{ij}^m \, \overline{S}_{ij}. \tag{25}$$

Here the modeled residual stress τ_{ij}^m is related to the strain-rate tensor $\overline{S}_{ij}$ through the eddy viscosity ν_t:

$$\tau_{ij}^m = -2 \, \nu_t \, \overline{S}_{ij}; \tag{26}$$

ν_t is defined by (20) in the case of the structure-function model. In the case of the Smagorinsky model, ν_t is defined by

$$\nu_t = l^2 \, \sqrt{2 \overline{S}_{ij} \overline{S}_{ij}}, \tag{27}$$

where the subgrid-scale length l is related to the filter width (the size of the coarse grid) by

$$l = C_s (\Delta x \, \Delta y \, \Delta z)^{1/3}. \tag{28}$$

The value of the constant C_s is set equal to 0.1, as advised by Deardorff (1970). This value was also used by Piomelli *et al.* (1990), but with a damping function (Van Driest 1956), which is not used here.

We present profiles averaged over the x-z plane and the two statistically symmetric sides of the channel. Figure 1 corresponds to the Smagorinsky model. $\langle \varepsilon^m \rangle$ peaks at about -4000, whereas $\langle \varepsilon^a \rangle$, which peaks at about -6, does not even appear in the figure. Note that no damping function is used in (27).

The results in Figure 1 are rather insensitive to the scheme used to compute the derivatives arising in (24): we used both a spectral scheme and a centered second-order finite-difference scheme and found almost the same result (no visible difference on the plots). This is thus another confirmation that, in the channel flow, the Smagorinsky model requires an additional treatment, such as a damping function.

In order to apply the structure-function model to the channel flow, it is necessary to assume some properties of homogeneity or isotropy. Several different options are possible, each of them leading to a definition of the resolved structure function $\overline{F_2}$:

(a) Homogeneity and isotropy at small scales, in all x-z planes (parallel to the walls). This yields a structure function, which will be called here *the 2-D structure function*, computed at any point M as a function of the velocities at M, and the four neighboring points M_N, M_S, M_W and M_E in the same x-z plane as M. In this case, the length scale Δ_c corresponds to the horizontal mesh size $\Delta x \approx \Delta z$, which is constant over the entire computational domain. This option was chosen by Normand (1990) (see also Normand & Lesieur 1990) for his simulation of a supersonic, spatially growing boundary layer.

(b) Three-dimensional homogeneity and isotropy of the small-scale turbulence within the computational cell. In this case, the resolved structure function is calculated, as it was above for the isotropic turbulence, with

$$\Delta_c = (\Delta x\ \Delta y\ \Delta z)^{1/3} \tag{29}$$

by analogy with the length scale l of the Smagorinsky model. Δy, which depends on y, is defined by

$$\Delta y = \frac{y_{M_T} - y_{M_B}}{2}, \tag{30}$$

where M_T and M_B are the two neighbors of M which have the same horizontal (x, z) coordinates. This structure function will be henceforth referred to as *the 3-D structure function.*

(c) Homogeneity and isotropy at the smallest resolved scale in one direction, *viz.* Δy, which depends on y. Here, Δ_c is chosen to be equal to Δy. The structure function at M will be called *the 1-D structure function* and computed as a function of the velocities at M, M_T and M_B.

Let us first consider option (a): if Δx equals Δz, we take $\Delta_c = \Delta x = \Delta z$ and the resolved structure function is

$$\overline{F}_{2_{2D}}(\Delta_c, M) = \frac{1}{4}\Big[\|\mathbf{u}(M) - \mathbf{u}(M_E)\|^2 + \|\mathbf{u}(M) - \mathbf{u}(M_W)\|^2 + \|\mathbf{u}(M) - \mathbf{u}(M_N)\|^2 + \|\mathbf{u}(M) - \mathbf{u}(M_S)\|^2\Big]. \tag{31}$$

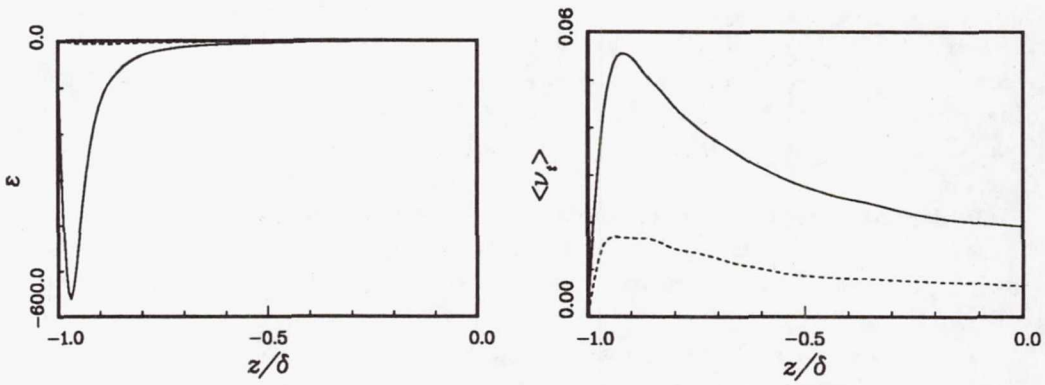

FIGURE 2. Left plot : —— 2-D structure-function dissipation, ---- *actual* dissipation (almost collapsed on the axis). Right plot : 2-D structure-function eddy viscosity —— mean, ---- *rms*.

In fact, for the grid used in the simulation of channel flow, Δx was different from Δz. We thus set $\Delta_c = \min(\Delta x, \Delta z)$ and applied (31) with linear interpolation:

$$\overline{F}_{2_{2D}}(\Delta_c, M) = \frac{1}{4}\left[\left(\frac{\Delta_c}{\Delta x}\right)^2 \left(\|\mathbf{u}(M) - \mathbf{u}(M_E)\|^2 + \|\mathbf{u}(M) - \mathbf{u}(M_W)\|^2\right) + \left(\frac{\Delta_c}{\Delta y}\right)^2 \left(\|\mathbf{u}(M) - \mathbf{u}(M_N)\|^2 + \|\mathbf{u}(M) - \mathbf{u}(M_S)\|^2\right)\right]. \quad (32)$$

Figure 2 shows $\langle \varepsilon^m \rangle$ and $\langle \nu_t \rangle$ for a resolved structure function computed after (32). This model is still much too dissipative with peak $\langle \varepsilon^m \rangle$ of about -560. However, the behavior near the wall is better than that with the Smagorinsky model.

Option (b) was tested, with a resolved structure function

$$\overline{F}_{2_{3D}}(\Delta_c, M) = \frac{1}{6}\Big[\|\mathbf{u}(M) - \mathbf{u}(M_E)\|^2 + \|\mathbf{u}(M) - \mathbf{u}(M_W)\|^2 + \|\mathbf{u}(M) - \mathbf{u}(M_N)\|^2 + \|\mathbf{u}(M) - \mathbf{u}(M_S)\|^2 + \|\mathbf{u}(M) - \mathbf{u}(M_T)\|^2 + \|\mathbf{u}(M) - \mathbf{u}(M_B)\|^2\Big] \quad (33)$$

with Δ_c defined by (29). Figure 3 shows the results: the profiles have the same shape as before, with slightly better peak values.

Option (c) yields the resolved structure function

$$\overline{F}_{2_{1D}}(\Delta_c, M) = \frac{1}{2}\left[\left(\frac{\Delta_c}{\Delta y_T}\right)^2 \|\mathbf{u}(M) - \mathbf{u}(M_T)\|^2 + \left(\frac{\Delta_c}{\Delta y_B}\right)^2 \|\mathbf{u}(M) - \mathbf{u}(M_B)\|^2\right] \quad (34)$$

with $\Delta y_T = |y_{M_T} - y_M|$, $\Delta y_B = |y_{M_B} - y_M|$, and $\Delta_c = \min(\Delta y_T, \Delta y_B)$. Figure 4 shows better agreement between the peak values of $\langle \varepsilon^m \rangle$ and $\langle \varepsilon^a \rangle$.

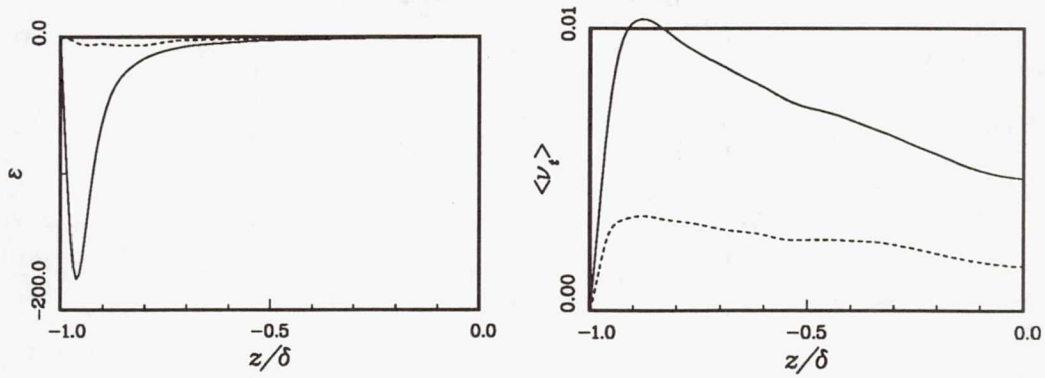

FIGURE 3. Left plot : —— 3-D structure-function dissipation, ---- *actual* dissipation. Right plot : 3-D structure-function eddy viscosity —— mean, ---- *rms*.

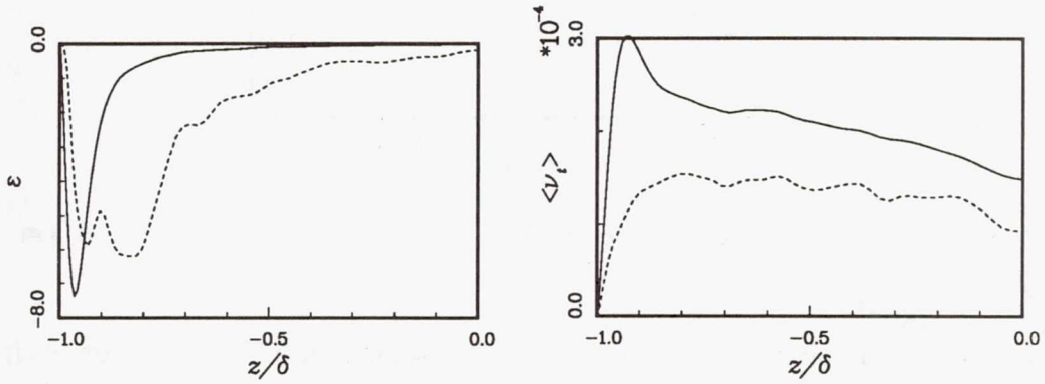

FIGURE 4. Left plot : —— 1-D structure-function dissipation, ---- *actual* dissipation. Right plot : 1-D structure-function eddy viscosity —— mean, ---- *rms*.

4. Compressible Isotropic Turbulence

Among the previous attempts for the development of subgrid-scale models for compressible flows is the work of Erlebacher *et al.* (1987). They Favre-filtered the Navier-Stokes and energy equations. They proposed to close the system by introducing several Smagorinsky models and determined the corresponding constants by use of the results from direct numerical simulations of compressible isotropic turbulence. Yoshizawa (1986) developed a subgrid-scale model through asymptotic expansions about an incompressible state. The applications of this model are limited to weakly compressible turbulence. In the case of boundary layers, "Morkovin's hypothesis" (Morkovin 1962; Bradshaw 1977) assumes that small-scale turbulence is not affected by compressibility if the free-stream Mach number does not exceed 5. This means that, in this case, there is no feedback from the acoustic and entropy modes onto the turbulent velocity field. Small-scale energy and temperature fluctuations can thus be considered as passive scalars, which justifies the use of subgrid-scale models

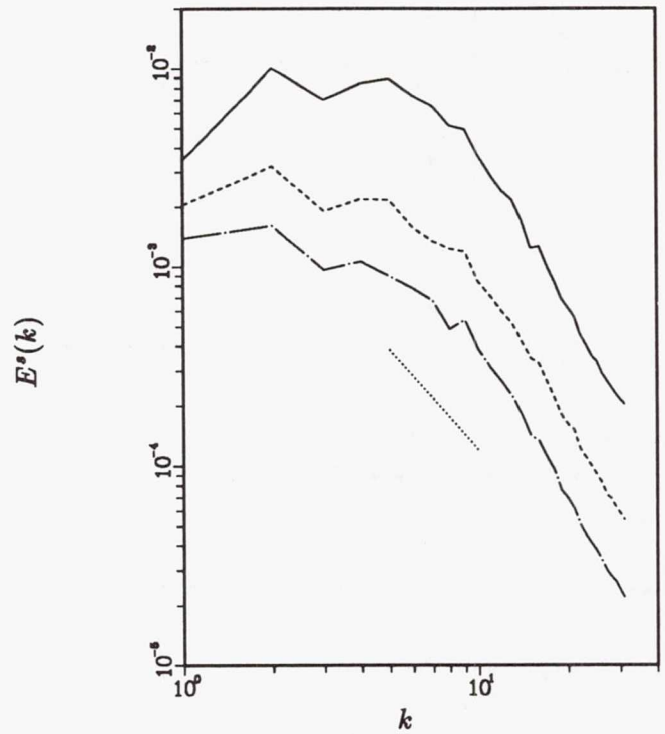

FIGURE 5. Evolution of the solenoidal energy spectrum : —— $t/\tau_t = 3.46$, - - - - $t/\tau_t = 7.77$, —·— $t/\tau_t = 12.4$, ····· $k^{-5/3}$.

developed for incompressible turbulent flows. Following this idea, Normand (1990) and Normand & Lesieur (1990) used the 2-D structure-function model in a compressible code and simulated a spatially growing boundary layer at a free-stream Mach number of 5 and a Reynolds number (based on the upstream displacement thickness) of 10^4.

In the present study, the large-eddy momentum and energy equations are solved in conservative variables (density, momentum, and total energy) for freely decaying compressible, isotropic turbulence at infinite Reynolds number, *i.e.* with molecular viscosity and diffusivity set to zero. This formulation involves the Favre-filtering of the equations, which leaves several terms that must be modelled (see Erlebacher *et al.* 1987). The contribution of these terms is parametrized by the structure-function model.

We first test the ability of the model to allow a $k^{-5/3}$ range to build up in the solenoidal kinetic energy spectrum, starting from a non-divergent initial field whose spectrum decays exponentially beyond a given k_i. In the incompressible case, Métais & Lesieur (1990) obtained, with the resolution of 48^3, a range of slopes between $-5/3$ and -2, starting from $t = 8\ \tau_0$, where $\tau_0 = (u_0\ k_i)^{-1}$ is the large-scale-eddy turnover time, and u_0 is the initial *rms* velocity.

In Figure 5, the temporal evolution of solenoidal energy spectrum is shown for

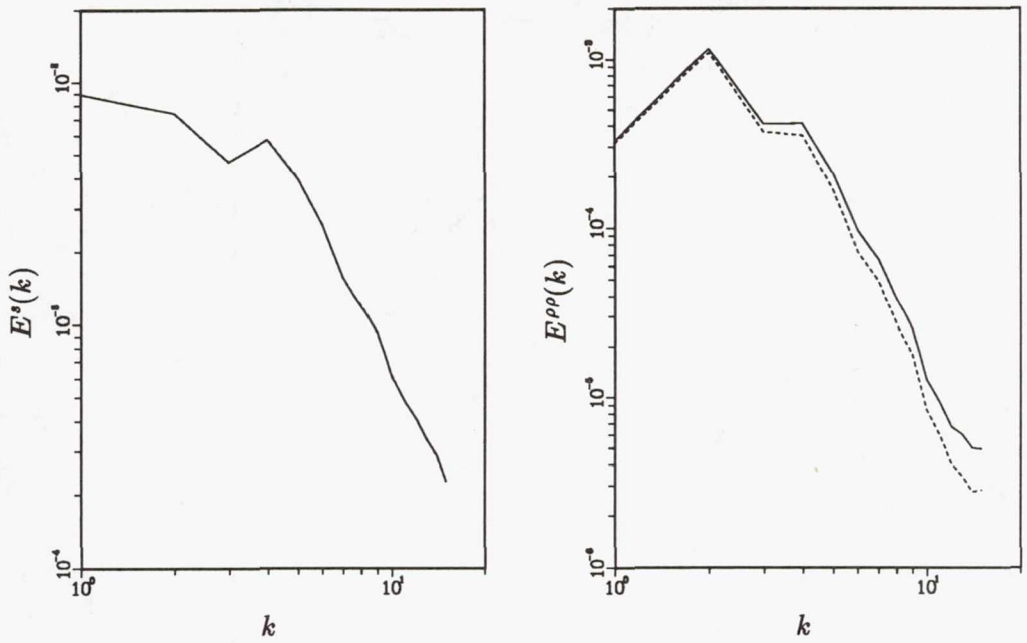

FIGURE 6. Solenoidal energy spectra (left) and density power spectra (right) for two different turbulent Prandtl numbers : ——— $Pr_t = 0.70$, ---- $Pr_t = 0.40$.

a compressible simulation at a resolution of 64^3 and an initial *rms* Mach number $M_o = u_0/c = 0.3$. Here, the unit of time is the Taylor-microscale-eddy turnover time $\tau_e = \lambda/u_o$, somewhat smaller than τ_0. At $t = 12\ \tau_e$, which corresponds to the end of the simulation, a range of slopes between $-5/3$ and -2 is found around $k = 10$. This is, at least, consistent with the incompressible results of Métais & Lesieur (1990) at a comparable stage of temporal evolution, *i.e.* earlier than $t = 8\ \tau_0$.

By investigating the DNS database, Erlebacher *et al.* (1987) found that, in compressible turbulence, the turbulent Prandtl number Pr_t is about 0.4, *viz.* smaller than the commonly accepted incompressible value (≈ 0.7) approximately by a factor of the specific heat ratio γ. We thus tested the effect of Pr_t on the evolution of the solenoidal energy and density power spectra (Figure 6). As expected, decreasing Pr_t brings about more dissipation of density variance, and this is also visible in temperature and pressure power spectra. However, the evolution of the solenoidal energy spectrum does not show any appreciable dependence on Pr_t ; this supports the aforementioned statement that the feedback from the acoustic and entropy modes into the turbulent velocity field can be neglected, at least when the turbulent Mach number is not very high.

We also compared the predictions of the 1-D and the 3-D structure-function formulations. Figure 7 shows a slight difference between the two predictions, which may be due to the reduction of the sample size when using the 1-D formulation.

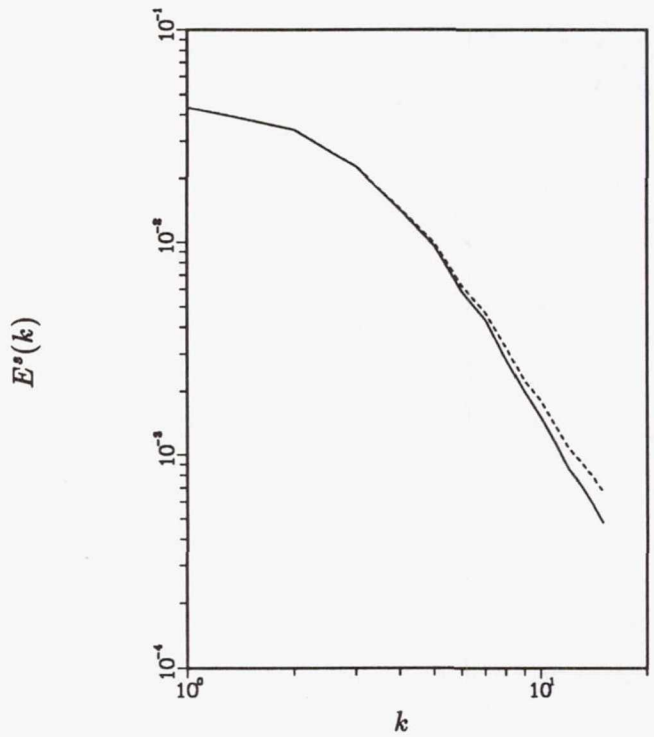

FIGURE 7. Comparison of 1-D energy spectra for the 1-D and 3-D formulation of the structure function : ——— 1-D formulation, - - - - 3-D formulation.

5. Conclusion

The aim of the present work was to investigate the extension of the structure-function SGS model developed by Métais & Lesieur (1990) to compressible flows in the presence of mean shear. The study was split into two parts:

First, *a priori* tests were performed in the case of an incompressible turbulent channel flow. In all three formulations (3-D, 2-D or 1-D), the eddy viscosity and dissipation approached zero at the walls, without requiring any damping function; this is a considerable improvement over the Smagorinsky model. The formulation of the structure-function model strongly resembles that of the Smagorinsky model when the derivatives arising in the latter are computed by means of a second-order centered scheme. The computational cost of the two models are thus comparable. Several attempts to recover correct peak values for the subgrid-scale dissipation have suggested the use of a 1-D formulation of the structure function, although the reduction of the sample size (as compared to the 3-D formulation) introduces some scatter in the estimate of the energy concentrated locally at small scale.

Second, simulations of freely decaying compressible isotropic turbulence at infinite Reynolds number led to spectra of developed turbulence, up to an initial *rms* Mach number of 0.6. This, together with the insensitivity of the solenoidal energy spectra to the value of the turbulent Prandtl number, suggests that such simple models

derived from incompressible turbulence can be applied to large-eddy simulations of compressible flows, provided the turbulent Mach number and the density gradients are not very high. For initial *rms* Mach numbers larger than 0.8, the model fails, probably due to formation of eddy shocklets. In this case, the solution may be to refine the model to take into account the additional dissipation due to these shocklets (Zeman 1990).

The main conclusion of this work is that the concept of structure functions can provide a valuable subgrid-scale model for simulation of compressible shear flows with non-cubic meshes. *A priori* tests are quick and economical tools to qualitatively check the behavior of a model, *e.g.* at the walls; however, they may not give quantitatively accurate results, since they strongly depend on the turbulence level in the sample field **u**. Thus, the fact that the Smagorinsky model and the 2-D and 3-D structure-function models all predict much greater dissipations than ε^a does not necessarily mean that these models are worthless. One could for instance invoke the spatially growing supersonic boundary-layer simulation performed by Normand (1990) with the aid of the 2-D structure-function model. The level of turbulence reached in this simulation could not have been obtained if the model had been as dissipative as suggested by the present *a priori* test (see Figure 2). Consequently, the global result of this *a priori* test has to be interpreted as an encouragement to carry on the validation of the different formulations of the structure-function model by performing large-eddy simulations and comparing the results with experimental results at high Reynolds numbers.

The first author would like to thank the CTR for selecting him for this Summer Research Program, which proved most fruitful.

REFERENCES

BATCHELOR, G. K. 1953 *The Theory of Homogeneous Turbulence*, Cambridge University Press, p. 197.

BRADSHAW, P. 1977 Compressible turbulent shear layers. *Ann. Rev. Fluid Mech.* **9**, 33-54.

CHOLLET, J.-P. 1984 Turbulence tridimensionnelle isotrope: modélisation statistique des petites échelles et simulation numérique des grandes échelles. *Thèse de Doctorat d'Etat*, Grenoble.

CHOLLET, J.-P. 1985 Two-point closure used for sub-grid scale model in large-eddy simulations. In *Turbulent Shear Flows 4* (eds. L. J. S. Bradbury *et al.*), Springer-Verlag, pp.62-72.

CHOLLET, J.-P. & LESIEUR, M. 1981 Parameterization of small scales of three-dimensional isotropic turbulence utilizing spectral closures . *J. Atmos. Sci.* **38**, 2747-2757.

CLARK, R. A., FERZIGER, J. H. & REYNOLDS, W. C. 1979 Evaluation of subgrid-scale models using an accurately simulated turbulent flow . *J. Fluid Mech.* **91**, 1-16.

COMTE, P. 1989 Etude par simulation numérique de la transition à la turbulence en écoulement cisaillé libre. *Thèse* de l'Institut. National Polytechnique de Grenoble

COMTE, P., LESIEUR, M. & FOUILLET, Y. 1989 Coherent structures of mixing layers in large-eddy simulation. In *Topological Fluid Mechanics* (eds. H. K. Moffatt & A. Tsinober), Cambridge University Press, pp.649-658.

DEARDORFF, J. 1970 A numerical study of three-dimensional turbulent channel flow at large Reynolds numbers. *J. Fluid Mech.* **41**, 453-480.

ERLEBACHER, G., HUSSAINI, M. Y., SPEZIALE, C. G. & ZANG, T. A. 1987 Towards the large-eddy simulations of compressible turbulent flows. *ICASE Rep.* 87-20.

KOLMOGOROV, A. N. 1941 The local structure of turbulence in incompressible viscous fluids for very large Reynolds numbers. *Dokl. Akad. Nauk SSSR.* **30**, 301-305.

KRAICHNAN, R. H. 1976 Eddy viscosity in two and three dimensions . *J. Atmos. Sci.* **33**, 1521-1536.

LESLIE, D. C. & QUARINI, G. L. 1979 The application of turbulence theory to the formulation of subgrid modeling procedures. *J.Fluid Mech.* **91**, 65-91.

MÉTAIS, O. & CHOLLET, J.-P. 1989 Turbulence submitted to stable density stratification: large-eddy simulations and statistical theory. In *Turbulent Shear Flows 6* (eds. J.-C. Andre *et al.*), Springer-Verlag, pp.398-415.

MÉTAIS, O. & LESIEUR, M. 1990 Spectral large-eddy simulation of isotropic and stably-stratified turbulence. Submitted to *J. Fluid Mech.*

MORKOVIN, M. V. 1962 Effects of compressibility on turbulent flows. In *Mécanique de la turbulence*, colloque CNRS n° 108, Aug. 28-Sept. 2 1961, Marseille, France, pp.367-380.

NORMAND, X. 1990 Transition à la turbulence dans les écoulements cisaillés compressibles et pariétaux. *Thèse* de l'Institut National Polytechnique de Grenoble.

NORMAND, X. & LESIEUR, M. 1990 Numerical experiments on transition in the compressible boundary layer over an insulated flat plate. To appear in *Theor. Comp. Fluid Dyn.*

PERRY, A. E. & CHONG, M. S. 1982 On the mechanism of wall turbulence. *J. Fluid Mech.* **119**, 173-217.

PIOMELLI, U., ZANG, T. A., SPEZIALE, C. G. & HUSSAINI, M. Y. 1990 On the large-eddy simulation of transitional wall-bounded flows. *Phys. Fluids A.* **2**, (2), 257-265.

SILVEIRA, A., GRAND, D., MÉTAIS, O. & LESIEUR, M. 1990 Large-eddy simulation of the turbulent flow in the downstream region of a backward-facing step. Submitted to *Phys. Rev. Letters.*

SMAGORINSKY, J. S. 1963 General circulation experiments with the primitive equations. I. The basic experiment. *Mon. Weath. Rev.* **91**, 99-163.

VAN DRIEST, E. R. 1956 On turbulent flow near the wall. *J. Aero. Sci.* **23**, 1007-1011.

YOSHIZAWA, A. 1986 Statistical theory for compressible turbulent shear flows, with the application to subgrid modeling. *Phys. Fluids.* **27**, (7), 2152-2164.

ZEMAN, O. 1990 Dilatation dissipation: The concept and application in modeling compressible turbulence. *Phys. Fluids A.* **2**, (2), 178-188.

Center for Turbulence Research
Proceedings of the Summer Program 1990

On the subgrid-scale modeling of compressible turbulence

By Kyle Squires[1] AND Otto Zeman[1]

A new sub-grid scale model is presented for the large-eddy simulation of compressible turbulence. In the proposed model, compressibility contributions have been incorporated in the sub-grid scale eddy viscosity which, in the incompressible limit, reduce to a form originally proposed by Smagorinsky (1963). The model has been tested against a simple extension of the traditional Smagorinsky eddy viscosity model using simulations of decaying, compressible homogeneous turbulence. Simulation results show that the proposed model provides greater dissipation of the compressive modes of the resolved-scale velocity field than does the Smagorinsky eddy viscosity model. For an initial r.m.s. turbulence Mach number of 1.0, simulations performed using the Smagorinsky model become physically unrealizable (i.e., negative energies) because of the inability of the model to sufficiently dissipate fluctuations due to resolved scale velocity dilatation. The proposed model is able to provide the necessary dissipation of this energy and maintain the realizability of the flow. Following Zeman (1990), turbulent shocklets are considered to dissipate energy independent of the Kolmogorov energy cascade. A possible parameterization of dissipation by turbulent shocklets for Large-Eddy Simulation is also presented.

1. Introduction

Compressibility effects in turbulent flows depend mainly on the r.m.s. fluctuating Mach number, M_t, defined as the ratio of the r.m.s. fluctuating velocity to the mean field sonic velocity. Direct numerical simulations (DNS) of homogeneous turbulence indicate that, in general, the direct compressibility effects on turbulence are insignificant if $M_t = O(10^{-1})$ in the sense that the solenoidal (rotational) part of the fluctuating velocity field and the acoustic (irrotational) field are decoupled. The acoustic field, which is determined mainly by initial conditions, plays only a passive role in the overall turbulence dynamics (Blaisdell 1990, Zeman and Blaisdell 1990). Only when M_t exceeds a value of about 0.3 does compressibility begin to noticeably influence turbulence dynamics and structure. Further increase in M_t may lead to formation of shock-like structures or turbulent shocklets. Shocklet formation has been detected in the DNS of decaying turbulence when the initial value of M_t exceeded 0.5 (Lee, *et al.* 1990). In the DNS of homogeneous shear turbulence, Blaisdell (1990) detected shocklets for $M_t \geq 0.7$. Zeman (1990) suggested that weak shocklets may be responsible for the growth rate attenuation in shear layers and proposed a physical model for shocklet formation and the associated (dilatation) dissipation.

1 Center for Turbulence Research

On the basis of the DNS results and experimental evidence in mixing layers (e.g., Papamoschou and Roshko 1987), compressibility effects may be broadly classified by the magnitude of M_t. Thus, we shall refer to the range $0.3 < M_t < 0.6$ as moderate Mach numbers whereby the compressibility effects are observable but with no formation of shock-like structures (which signifies interactions between compressive (acoustic) and solenoidal fields). At larger Mach numbers, $M_t > 0.6$, a full scope of compressibility-induced effects may be expected, such as shocklet and baroclinic vorticity generation and significant solenoidal/compressive field interactions.

In large eddy simulation (LES) techniques, the r.m.s. velocity of subgrid-scale turbulence is smaller by the order $O(\triangle x/L)^{1/3}$ than that of the energy containing eddies of scale L. The lower limit on the mesh size $\triangle x$ is set by the computer. In the LES calculations presented later in section 4, $L/\triangle x \approx 30$, and it follows that the r.m.s. Mach number associated with subgrid scales is $(M_t)_{sg} = M_t(\triangle x/L)^{1/3} \approx 0.3M_t$. Thus, for realistic resolved-scale Mach numbers $M_t < 1$, the subgrid scale turbulence can be considered as incompressible but acted on by the large-scale compression and/or expansion and by inhomogeneities in the resolved thermal field as well. In section 2, we describe a formulation of a Smagorinsky-type SGS model which incorporates these compressibility contributions.

The possibility of occurrence of shocklets (at larger-than-moderate Mach numbers) presents a problem which must be treated separately from the SGS modeling. We can envisage that in the real flow a shocklet will have formed whose cross-section is sketched in figure 1. Because the shocklet is formed by the large-scale motions, it is expected to span an area of several mesh sizes, but since the shock thickness (λ_s) scales on viscosity, the gradients and dissipation associated with the shock front cannot be resolved in LES. It may be shown that the ratio $\lambda_s/\triangle x$ is proportional to $(\rho/\triangle\rho)(L/\triangle x)Re_L^{-1}$, where Re_L is the large scale (turbulent) Reynolds number and $\triangle\rho/\rho$ is a relative density jump across the shock. Because Re_L is arbitrarily large, λ_s will always be a negligible fraction of $\triangle x$ and, therefore, the actual shock front will be smeared over several mesh points and the shocklet dissipation underestimated by the order $O(\lambda_s/\triangle x)$ (Zeman 1990). The shocklet dissipation rate is locally very high and is independent of the Kolmogorov energy cascade and of the SGS turbulence. Therefore, it cannot be made a part of the SGS mode, and the only alternative is to represent the shocklet-induced effects by means of added (virtual) stresses in the resolved-scale governing equations. This approach is described in section 3. The LES numerical method is described in section 4, and computational results of LES of decaying compressible turbulence are presented in section 5. Section 6 concludes the report.

2. Large-scale compressibility effects on SGS energy and viscosity

The set of compressible LES equations obtained by Favre filtering the governing equations are

$$\frac{\partial\overline{\rho}}{\partial t} + \frac{\partial\overline{\rho}\widetilde{U}_i}{\partial x_i} = 0 \tag{1}$$

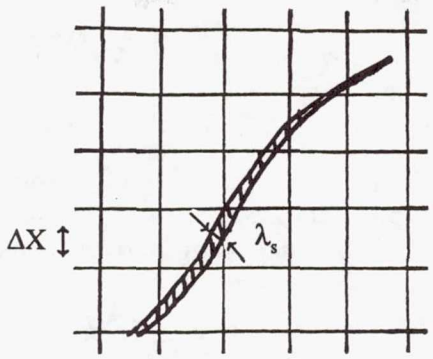

FIGURE 1. Schematic of a shocklet in a computational grid.

$$\frac{\partial}{\partial t}(\overline{\rho}\widetilde{U}_i) + \frac{\partial}{\partial x_j}(\overline{\rho}\widetilde{U}_j\widetilde{U}_i) = -\frac{\partial \overline{P}}{\partial x_i} + \frac{\partial \overline{\sigma}_{ij}}{\partial x_j} - \frac{\partial \tau_{ij}}{\partial x_j} \tag{2}$$

$$\frac{\partial}{\partial t}(\overline{\rho}\widetilde{E}) + \frac{\partial}{\partial x_j}(\overline{\rho}\widetilde{U}_j\widetilde{E}) = -\frac{\partial \overline{P}\widetilde{U}_j}{\partial x_j} + \frac{\partial \overline{U_i\sigma_{ij}}}{\partial x_j} + \frac{\partial}{\partial x_j}\left(\overline{\kappa\frac{\partial T}{\partial x_j}}\right) - \frac{\partial \pi_j}{\partial x_j} - \frac{\partial q_j}{\partial x_j} \tag{3}$$

$$\tau_{ij} = (\overline{\rho U_i U_j} - \overline{\rho}\widetilde{U}_i\widetilde{U}_j) \approx \overline{\rho}\widetilde{u_i u_j} \tag{4}$$

$$q_j = c_v(\overline{\rho T U_j} - \overline{\rho}\widetilde{T}\widetilde{U}_j) \approx c_v\overline{\rho}\widetilde{tu_j} \tag{5}$$

$$\pi_j = \overline{PU_j} - \overline{P}\widetilde{U}_j \approx \overline{pu_j} \tag{6}$$

Here, U_i, P, T are velocity, pressure, and temperature and $E = c_vT + U_jU_j/2$ is the total energy per unit mass. The viscous stress tensor is represented as σ_{ij} in equations (2) and (3). The field decomposition is $X = \widetilde{X} + x$, where $\widetilde{X} = \overline{\rho X}/\overline{\rho}$ is the filtered (resolved) quantity and, as opposed to incompressible flows, is obtained through Favre filtering. The sub-grid component of the variable X is denoted as x. The proposed Smagorinsky-type closures to the stress tensor τ_{ij} and heat flux q_j are

$$\frac{\tau_{ij}}{\overline{\rho}} = \widetilde{u_iu_j} = -2\nu_T S^*_{ij} + \frac{1}{3}q^2\delta_{ij} \tag{7}$$

$$\frac{q_i}{c_v\overline{\rho}} = \widetilde{tu_i} = -\alpha_{ij}\frac{\partial \widetilde{T}}{\partial x_j} \tag{8}$$

where

$$S^*_{ij} = \frac{1}{2}(\widetilde{U}_{i,j} + \widetilde{U}_{j,i} - \frac{2}{3}\nabla\cdot\widetilde{\mathbf{U}}\delta_{ij}) \tag{9}$$

is the trace-free strain rate tensor, $q^2 = \widetilde{u_ju_j}$ is (twice) the Favre-averaged kinetic energy of SGS turbulence, and ν_T and α_{ij} are, respectively, eddy viscosity and (tensor) eddy diffusivity due to SGS turbulence. Now our task is to parameterize

the effect of the resolved compressive field on the SGS viscosity and diffusivity in a functional form

$$\nu_T = \nu_{To} F(M_t, \nabla \cdot \widetilde{\mathbf{U}}, \nabla T, \nabla P), \tag{10a}$$

$$\alpha_{ij} = Pr_t^{-1} \nu_{To} H_{ij}(M_t, \nabla \cdot \widetilde{\mathbf{U}}, \nabla T, \nabla P), \tag{10b}$$

where $\nu_{To} \propto (\triangle x)^2 |S_{ij}|$ is the (Smagorinsky) viscosity, and Pr_t is the turbulent Prandtl number in the incompressible limit $M_t = 0$. Also, in this limit $F \to 1$, and $H_{ij} \to \delta_{ij}$. With the aid of the fluctuating part of the equation of state, the pressure-flux term $\pi_i = \overline{pu_i}$ can be expressed as

$$\pi_i = R(\overline{\rho} \widetilde{tu_i} + \widetilde{T} \overline{\rho' u_i}). \tag{11}$$

As mentioned already, it is justified to treat the SGS turbulence as incompressible; therefore, π_i is negligible compared to either of the terms on the RHS of (11) and $\widetilde{tu_i}/T \approx -\overline{\rho' u_i}/\overline{\rho}$. In order to determine the functions F and H_{ij} in equations (10a) and (10b), we shall approximate the conservation equations for SGS turbulence energy q^2 and heat flux $\widetilde{tu_i}$ as in second-order closure schemes, with the resolved scale motions acting as the mean (input) field. Neglecting the third-order correlations, the transport equations for q^2 and $\widetilde{tu_i}$ may be expressed as (e.g., see Zeman 1990)

$$\frac{Dq^2}{Dt} = -2\widetilde{u_i u_j} S^*_{ij} - \frac{2}{3} q^2 \nabla \cdot \widetilde{\mathbf{U}} - 2\overline{u}_j \frac{\partial \overline{P}}{\partial x_j} \frac{1}{\overline{\rho}} - 2\frac{q^3}{\Lambda} + \frac{2}{\overline{\rho}} \overline{p u_{j,j}} \tag{12}$$

$$\frac{D\widetilde{tu_i}}{Dt} = -\widetilde{u_i u_j} \frac{\partial \widetilde{T}}{\partial x_j} - \widetilde{tu_j} \frac{\partial \widetilde{U}_i}{\partial x_j} - C_h \widetilde{tu_i} \frac{q}{\Lambda}. \tag{13}$$

The average of the fluctuating velocity u_i is by definition, $\overline{u}_i = -\overline{\rho' u_i}/\overline{\rho}$ and according to (11) (with $\pi_i = 0$) it is approximated as $\overline{u}_i \approx \widetilde{tu_i}/\widetilde{T}$. The fourth term in (12) represents the SGS solenoidal dissipation $\epsilon_s = q^3/\Lambda$; the dissipation scale Λ scales on the mesh size $\triangle x$ and will be determined later. The constant C_h in the heat flux equation (13) is the tendency-to-isotropy constant and its value is dictated by the Prandtl number Pr_t; typically, $C_h \approx 6.5$. Employing the inertial subrange relations, we find that the convective derivative terms in (12) and (13) are of order $O(\triangle x/L)^{2/3}$ smaller compared with the principal right-hand-side (RHS) terms and are neglected. Since the convective derivative terms are small and the sub-grid scale turbulence Mach number is also small, the last term in equation (12) representing the pressure dilatation correlation of the sub-grid scales may also be neglected. It should be remarked, however, that the convective-term discard may not be justified in the regions containing shock-like structures (see section 3).

In order to obtain expressions in the form (10), we shall recast (12) and (13) in terms of the SGS viscosity ν_T and write

$$\nu_T = \beta \Lambda q \tag{14}$$

where β is presently an undetermined constant. With the aid of (7) and (14), equations (12) and (13) can now be solved for ν_T, α_{ij}, q^2, and Pr_t. To first order in $\nabla \cdot \widetilde{\mathbf{U}}$ we obtain

$$q^2 = 2\beta\Lambda^2 \left|S^*_{ij}\right|^2 + \beta\Lambda^2 \frac{\nabla\overline{P}\cdot\nabla\widetilde{T}}{\overline{\rho}\widetilde{T}Pr_t} - \frac{\sqrt{2\beta}}{3}\Lambda^2 \left|S^*_{ij}\right| \nabla\cdot\widetilde{\mathbf{U}}, \tag{15}$$

and

$$\alpha_{ij} = \frac{\nu_T}{Pr_t}\delta_{ij} - \frac{\nu_T}{3}\frac{\Lambda}{q}S^*_{ij}. \tag{16}$$

As mentioned earlier, Pr_t is related to the tendency-to-isotropy constant C_h; from the second-order closure equations we obtain $Pr_t \approx C_h/8.12 = 0.8$ (Zeman 1990). The viscosity constant β in (14) must be such that in the incompressible limit $M_t = 0$, the SGS viscosity approaches a well-tested Smagorinsky value $\nu_{To} = (C_s\triangle x)^2|S^*_{ij}|$. The obvious choice here is $\Lambda = \triangle x$ and, hence, $\beta = C_s^{4/3}$. An accepted value for the Smagorinsky constant is $C_s = 0.2$, and this gives $\beta = 0.12$. A more accurate analysis, based on the inertial subrange relations (e.g. Tennekes and Lumley 1972), gives

$$\epsilon_s = \frac{q^3}{\Lambda} \approx \frac{q^3(k)k}{(2\alpha)^{3/2}}, \tag{17}$$

where $k \approx \pi/\triangle x$ is the smallest SGS wavenumber and $\alpha \approx 1.5$ is the Kolmogorov constant. From (17), $\Lambda = (2\alpha)^{3/2}\triangle x/\pi \approx 1.65\triangle x$ and then $\beta = 0.06$. Tests of the SGS model represented by the closure equations (7), (8), and (14)-(16) showed a reasonable insensitivity to the choice of β and, therefore, the results presented in this paper were obtained using $\Lambda = \triangle x$.

3. Virtual shocklet stresses

As mentioned earlier, in LES the information on shocklet occurrence is lost due to a lack of resolution, and the total energy dissipation is likely to be underestimated. The would-be shock front is numerically diffused and may manifest itself by numerical instability. Here, an approach is suggested to reconstruct the shocklet effects through inclusion of additional (virtual) stresses in the resolved scale equations. These virtual stresses depend on the local Mach number $m = (\widetilde{U}_j\widetilde{U}_j)^{1/2}/a(\widetilde{T})$, the density (or pressure) gradients, and possibly on molecular properties. The principal purpose of this stress reconstruction is to recover some part of the dissipation associated with the possible shock structures.

The idea of the virtual stress parameterization is based on the model and theory of shocklet dissipation developed by Zeman (1990) and on the assumption that although the actual-flow shock structure cannot be resolved in the LES, the actual and LES fields share statistical properties of energy containing motions. Thus, we assume that the actual (or DNS) and LES fields have the same pdf $p(m)$ of the fluctuating Mach number $m(\mathbf{x},t)$ and that the local density (or pressure) gradients and $\nabla\cdot\widetilde{\mathbf{U}}$ are, in combination with $m(\mathbf{x},t)$, sufficient indicators of an unresolved

shock event. Then, one of the plausible ways to express the virtual stress divergence due to an unresolved shocklet (to be added to the RHS of equation (2)) is

$$(\tau_{ij,j})_{shk} \propto -\nabla\overline{\rho}a^2(\frac{m^2-1}{m})^2 p_s(m, \nabla\cdot\widetilde{\mathbf{U}}, \nabla\overline{\rho}), \tag{18}$$

where $p_s(x,y,z)$ is a conditional, shock probability function which is an indicator of the virtual shock occurrence; the necessary but not sufficient condition for the shock occurrence is $m > 1$ and$\nabla\cdot\widetilde{\mathbf{U}} < 0$. According to (18) the shock stress divergence is in the direction of the density front $\nabla\overline{\rho}$, and we convince ourselves that equation (18) gives a correct magnitude of shocklet dissipation by forming the kinetic energy equation for the resolved scales, $K = \widetilde{U}_j\widetilde{U}_j/2$. With $(\tau_{ij,j})_{shk}$ added to the RHS of (2), we obtain

$$\frac{DK}{Dt} = -((\tau_{ij})_{shk}\widetilde{U}_i)_{,j} + (\tau_{ij})_{shk}\widetilde{U}_{i,j} + \text{ other terms.} \tag{19}$$

The (dilatation) dissipation due to the virtual shocklet is the second term in (19) and with (18) we obtain

$$\frac{DK}{Dt} \propto +\nabla\cdot\widetilde{\mathbf{U}}\overline{\rho}a^2(\frac{m^2-1}{m})^2 p_s(m, \widetilde{\mathbf{U}}, \nabla\overline{\rho}) = -\epsilon_{shk}. \tag{20}$$

Note that the differential operation is not to be applied to the scalar function in m and to p_s, since these serve only as rescaling and probability measures.

The proposed parameterization of shocklet dissipation in LES will have to be verified by comparing DNS of shocklet turbulence with a corresponding LES field. The comparison might be difficult to interpret in nonstationary (decaying) turbulence simulations. To this end, we shall attempt in the future to generate a stationary turbulence field at sufficiently high r.m.s. Mach number by random forcing applied at the largest scales.

As a final point, we should keep in mind that the large-scale shock front may have a significant effect on the (presently neglected) convective terms in the kinetic energy budget of SGS turbulence (12). Since the average velocity $\widetilde{U}_s$ normal to the shock front must be of the order of the sonic speed a, then the advective derivative $\widetilde{U}_j q^2_{,j}$ in (12) could be of order $aq^2/\triangle x$ and, therefore, larger than the primary terms such as the dissipation $\epsilon_s \propto q^3/\triangle x$. Inclusion of these shock front advection effects in the SGS models has not so far been considered.

4. Simulation methods and parameters

The Favre-filtered equations for a compressible fluid (equations 1-3) were solved for the case of temporally evolving homogeneous turbulence. Since homogeneous turbulence is in principle unbounded, numerical simulation of these flows employ periodic boundary conditions in a finite computational domain. The application of periodic boundary conditions typically permits extremely accurate schemes for

the evaluation of spatial derivatives. In the numerical method used for the present work, spatial derivatives are evaluated using high-order accurate compact finite differences. These difference schemes possess spectral-like resolution (see Lele 1990), and the formal order of accuracy of the scheme used in the present work is sixth order. The discretized equations were solved using 32^3 grid points and were time advanced using a third-order Runge Kutta method.

It should be remarked that the filtered momentum and energy equations shown in section 2 contain terms which may not be greatly simplified following the filtering of the governing equations. For example, no appreciable simplification of the viscous stresses in the momentum equations or the viscous dissipation terms in the energy equation is obtained by filtering equations (2) and (3). In fact, since the energy of the flow is computed using the transport equation for *total* energy, a number of additional terms arise following the filtering operation. It is important to remember, however, that many of these terms, e.g., the viscous dissipation terms in the energy equation, are negligible at high Reynolds numbers (at least away from solid boundaries). Other terms are assumed to be represented by the sub-grid scale model.

The initial conditions for all simulations were identical to those used by Lee, *et al.* (1990), i.e., the initial velocity field is constrained to be divergence free, and there are no initial density or temperature fluctuations. The velocity fluctuations were also constructed from an initial energy spectrum of the form

$$E(k) = Ak^4 \exp\left[-2(k/k_0)^2\right]. \tag{21}$$

Simulations were performed using the SGS model shown in section 2 and compared to results obtained using an 'incompressible' Smagorinsky-type model, i.e., a sub-grid scale model neglecting corrections for resolved-scale velocity dilatation. This model will be referred to as the Smagorinsky model and is summarized below

$$\frac{\tau_{ij}}{\overline{\rho}} = -2\nu_T S^*_{ij} + \frac{1}{3} q^2 \delta_{ij}, \tag{22}$$

$$\frac{q_i}{c_v \overline{\rho}} = -\alpha_{ij} \frac{\partial T}{\partial x_j} \tag{23}$$

where

$$\nu_T = \sqrt{2\beta^3}\Lambda^2 \left|S^*_{ij}\right|, \tag{24}$$

$$\alpha_{ij} = \frac{\nu_T}{Pr_t}\delta_{ij} - \frac{\nu_T}{3}\frac{\Lambda}{q} S^*_{ij}, \tag{25}$$

and

$$q^2 = 2\beta\Lambda^2 \left|S^*_{ij}\right|^2. \tag{26}$$

As mentioned in section 2, the value of the constant β was determined by considering an incompressible limit, i.e., the limit which yields the Smagorinsky model shown above. Following this limit process, the value of the constant β used for the

simulations presented in this paper was 0.12. The reader is referred to section 6 for further discussion considering determination of the constant. This value of β corresponds to a value of the Smagorinsky constant, C_s, of 0.2. It is should be remarked, however, that a value of $C_s = 0.2$ is larger than the value of 0.092 determined by Erlebacher, *et al.* (1990). Erlebacher, *et al.* determined the constant from direct numerical simulations of compressible homogeneous turbulence by correlating exact and modelled stresses.

The remaining parameter for the sub-grid scale model is the value of the turbulent Prandtl number, Pr_t. As shown in section 2, Pr_t is related to the tendency-to-isotropy constant, C_h. Using the second-order closure equations, a value of $Pr_t = 0.8$ is then obtained. Alternatively, one can also show that filtering the pressure-work term in the energy equation gives rise to an additional sub-grid scale heat flux (i.e., other than that arising from filtering the convective terms). This additional flux augments the overall SGS heat flux by a factor of γ. If the ratio of the sub-grid scale fluxes of momentum and heat are considered to be the same as in incompressible turbulence, then the turbulent Prandtl number for compressible turbulence must then be reduced by a factor of γ. A widely accepted value of Pr_t for simulations of incompressible turbulence is 0.7. Accounting for the reduction of Pr_t by the additional sub-grid scale heat flux from the pressure-work term, the value of the turbulent Prandtl number for compressible turbulence is then $Pr_t = 0.5$. It is interesting to note that this value is the same as that determined by Erlebacher, *et al.* (1990) using their DNS database. No tests were conducted in the present study to investigate the influence of Pr_t on the computed flow fields, and a value of $Pr_t = 0.5$ was used for the results presented in section 5.

Since the initial density and temperature fields were considered to be uniform and the initial velocity field was solenoidal, the properties of the initial fields may be specified by the Taylor-microscale Reynolds number, Re_λ $(= u'\lambda/\nu)$, and the turbulence Mach number, M_t. The values of M_t for the three cases investigated in the present work were 0.61, 0.8, and 1.0. The corresponding values of the Taylor-microscale Reynolds number were 50, 65, and 83. For each of these Mach numbers, simulations were performed using both the Smagorinsky eddy viscosity model and the proposed model that incorporates additional terms representing the effect of compressibility.

5. Results

Shown in figure 2 is the time development of twice the resolved-scale turbulence energy for an initial turbulence Mach number of 0.8. The time axis in figure 2, as well as figure 4, has been made dimensionless by the eddy turnover time, τ_e, in the initial field. The two curves shown in figure 2 correspond to the Smagorinsky eddy viscosity model and the proposed model which incorporates corrections due to resolved scale compressibility. As is evident from the figure, there is negligible difference between the resolved-scale energy obtained using either the Smagorinsky model or the proposed model. This result is consistent with that obtained at the lower turbulence Mach number, $M_t = 0.61$.

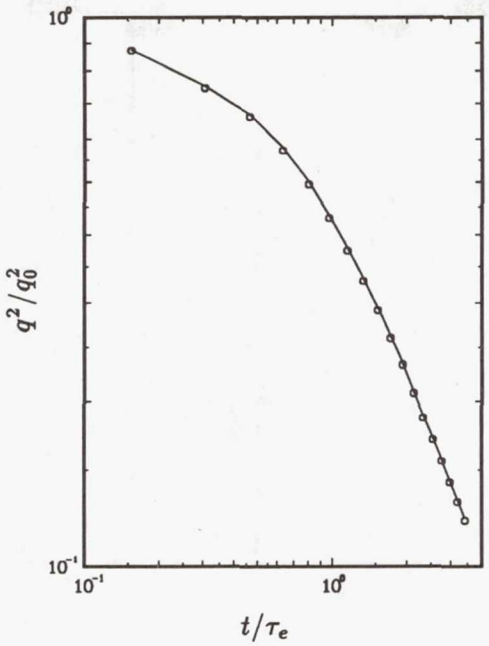

FIGURE 2. Time development of turbulence kinetic energy for an initial $M_t = 0.8$. ——— , Smagorinsky; o , proposed.

Shown in figures 3a and 3b are the radial energy spectra of the velocity and dilatation fields at $t/\tau_e = 1.3$ for an initial $M_t = 0.8$. Consistent with the results observed in figure 2, it can be seen from figure 3a that there is negligible difference between the velocity spectrum obtained using either sub-grid scale model. Figure 3b shows, however, that there is greater energy in the resolved-scale dilatation field at higher wavenumbers from the computation using the Smagorinsky model than for the proposed model. Figures 3a and 3b clearly show that the model more significantly affects the compressive modes of the velocity as opposed to the solenoidal velocity components.

The time development of the resolved-scale turbulence energy is shown in figure 4 for both the Smagorinsky and proposed models for an initial $M_t = 1.0$. As was also observed for the lower Mach number cases, this figure shows that at early times, the resolved scale energy is virtually identical for both cases. It was also found, however, that the flow field becomes physically unrealizable using the Smagorinsky model. The solid line in figure 4 has been drawn up to the instant in time in which the resolved-scale temperature becomes negative.

The radial energy spectra of the resolved scale velocity at the time step immediately preceding the instant at which the flow field computed using the Smagorinsky model becomes unrealizable has been shown in figure 5a. It may be observed from this figure that the spectra of the velocity fields obtained using both the Smagorinsky and proposed model are virtually identical. The mean-square energy obtained by integrating the spectra were found to differ by only 0.06 percent. The spectra of

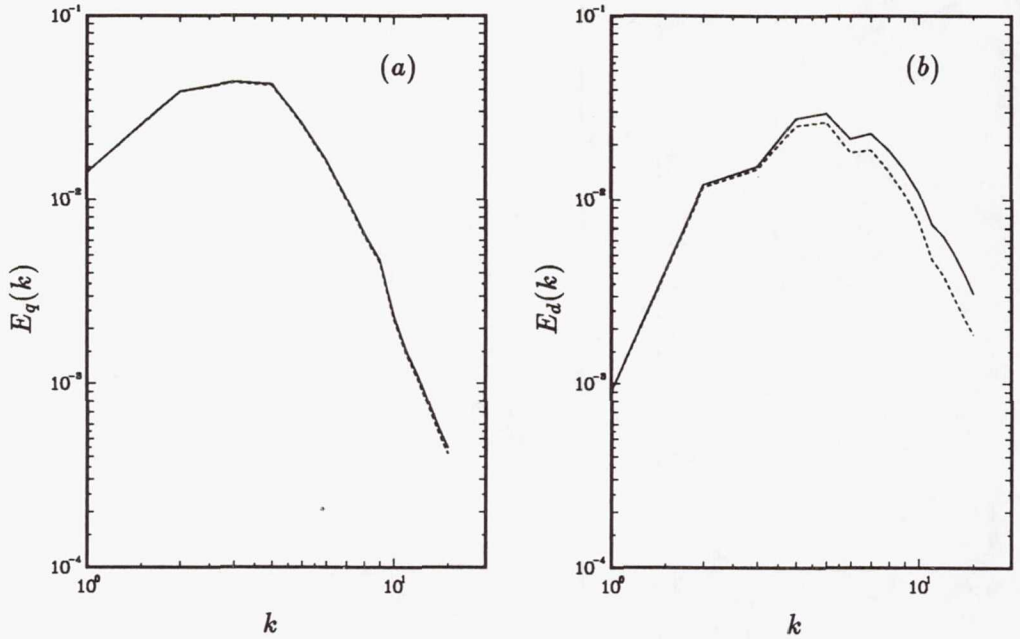

FIGURE 3. Radial spectra at $t/\tau_e = 1.3$ of (a) velocity, and (b) dilatation for an initial $M_t = 0.8$. ——— , Smagorinsky; - - - - , proposed.

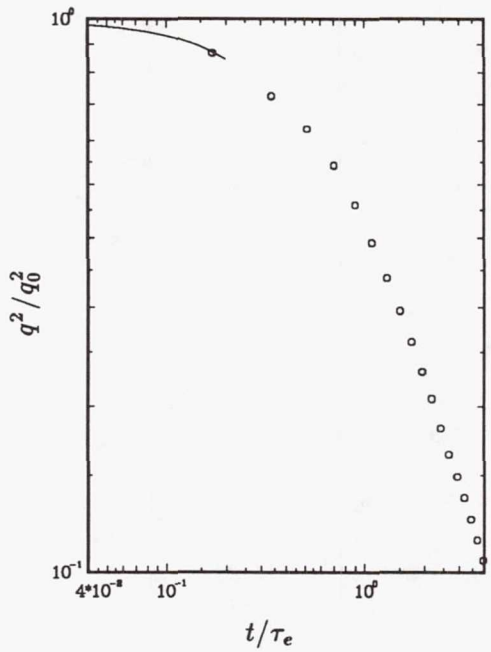

FIGURE 4. Time development of turbulence kinetic energy for an initial $M_t = 1.0$. ——— , Smagorinsky; o , proposed.

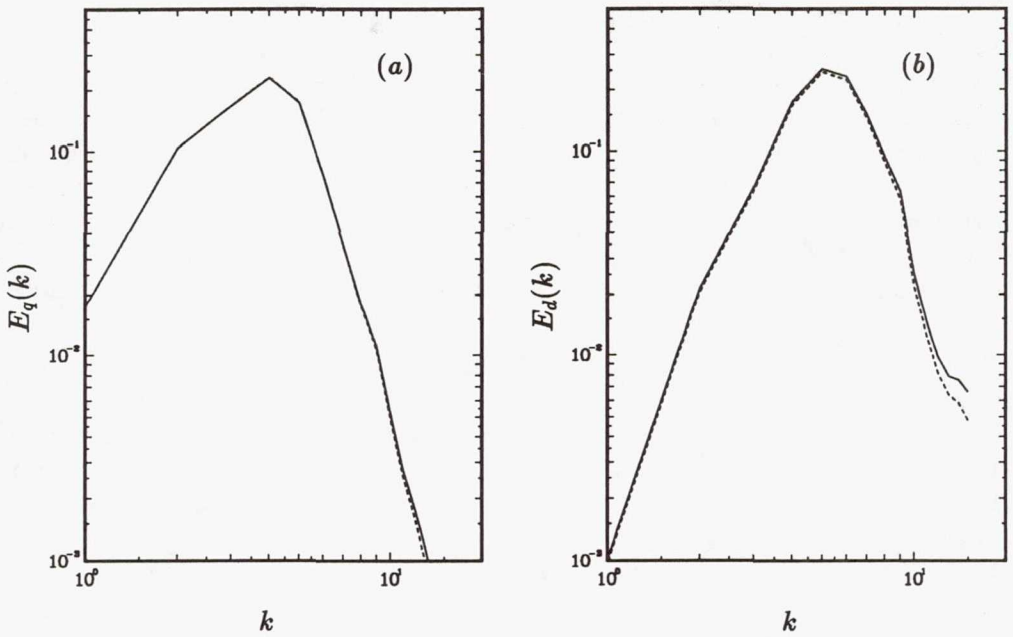

FIGURE 5. Radial spectra at $t/\tau_e = 0.2$ of (a) velocity, and (b) dilatation for an initial $M_t = 1.0$. ——— , Smagorinsky; - - - - , proposed.

the resolved-scale dilatation field is shown in figure 5b. As could also be observed in the dilatation spectra from the $M_t = 0.8$ case, the dilatation spectra obtained using the proposed model is below that of the Smagorinsky model at the higher wavenumbers. The mean-square, resolved-scale dilatation at this instant in time differs by approximately 6 percent for simulations performed using the two models. This excess in the dilatation field obtained using the Smagorinsky model is sufficient to cause the flow field to become physically unrealizable. Locally, dilatation fluctuations can become extremely large. The proposed model provides sufficient dissipation in these regions to prevent the resolved-scale temperature from becoming negative. These results also illustrate that the differences in the resolved scales obtained using the two models occur primarily in the high-wavenumber end of the spectrum. It is precisely in this region in which resolved-scale compression and expansion are most significant.

6. Summary and future work

A new sub-grid scale model for the Large-Eddy Simulation of compressible turbulence has been developed and tested using numerical simulations of temporally-evolving compressible turbulence. The development of the model was guided by concepts employed in second-order closure modeling of compressible turbulence. The proposed model reduces to Smagorinsky's (1963) model for the LES of incompressible turbulence in the limit $M_t \to 0$ and also requires only one adjustable constant. The constant is determined from the incompressible limit in which case it must reduce to a value widely used in LES of incompressible turbulence ($C_s \approx 0.2$).

Simulation results obtained using both the proposed model as well as the Smagorinsky model showed that at turbulence Mach numbers of 0.61 and 0.8 there is negligible difference between the resolved scale solenoidal velocity fields obtained using either model. For an initial $M_t = 1.0$, it was found that the Smagorinsky model was unable to provide sufficient dissipation in regions of large compression and/or expansion. This inability to provide the necessary dissipation in these regions in turn caused the flow to become physically unrealizable (i.e., negative temperature). The proposed model, which incorporates the effect of large-scale velocity dilatation, does provide the necessary dissipation in these regions and maintains the physical realizability of the flow.

While the usefulness of the proposed model over the Smagorinsky model has been demonstrated at high turbulence Mach numbers, important issues remain to be resolved. The effect of shocklet dissipation was not incorporated into the sub-grid scale model for the simulation results presented in this report. Before incorporating the virtual shocklet stress (see section 3) into the simulations, the parameterization should first be verified by correlating modelled shocklet dissipation against actual shocklet dilatational dissipation. As was mentioned in section 3, such a comparison may be difficult to interpret in simulations of decaying turbulence. To alleviate this difficulty, one may apply a body force at the largest scales of the flow in order to obtain a quasi-stationary state. An advantage of applying an external body force is that it is possible to maintain a reasonably steady value of the turbulence Mach number. Comparison of the shocklet stress from simulations of compressible turbulence which has been artificially forced at the largest scales should be more meaningful than that obtained from decaying turbulence. Such an effort will be undertaken in the near future.

Another issue to be resolved is the effect of Reynolds number on the simulation results. All of the results presented in this report were obtained from simulations which included molecular effects, i.e., finite Reynolds number. Thus, the role of the eddy viscosity was to primarily provide the extra dissipation needed in regions of high dilatation. Since the philosophy behind LES is to compute high-Reynolds number turbulent flow fields the model should be tested in simulations at infinite Reynolds number, i.e., zero molecular viscosity and thermal conductivity. Such simulations will provide a more rigorous test of the proposed model as well as better demonstrate differences between the proposed model and the Smagorinsky model.

Finally, a new sub-grid scale model has been presented by Germano, Piomelli, Moin, and Cabot during this summer program which does not require an *a priori* choice of the model constant(s) and also allows backscatter from the small to the large scales. The formulation of the model is based upon an algebraic identity between the subgrid-scale stresses at two different levels and the resolved filtered stresses. This formulation is general enough so that it may be applied to the LES of compressible turbulence. Therefore, another direction of future work will be to incorporate the proposed model presented in this paper with the dynamic sub-grid scale model presented by Germano, *et al.*

REFERENCES

BLAISDELL, G. A. 1990 Numerical simulations of compressible homogeneous turbulence. Ph.D. dissertation, Department of Mechanical Engineering, Stanford University, Stanford, California.

ERLEBACHER, G., HUSSAINI, M. Y., SPEZIALE, C. G., & ZANG, T. A. 1990 Toward the Large-Eddy Simulation of compressible turbulent flows. *ICASE report 90-76.*

LEE, S., LELE, S. K., & MOIN, P. 1990 Eddy shocklets in decaying compressible turbulence. *Physics of Fluids.* in press.

LELE, S. K. 1990 Compact finite difference schemes with spectral-like resolution. *CTR Manuscript 107.* also submitted to the Journal of Computational Physics.

PAPAMOSCHOU, D. & ROSHKO, A. 1987 The compressible turbulent shear layer: an experimental study. *J. Fluid Mech.* **197,** 453.

SMAGORINSKY, J. 1963 General circulation experiments with the primitive equations. *Monthly Weather Review.* **93,** 99.

TENNEKES, H. L., & LUMLEY, J. L. 1972 *A first course in turbulence.* The MIT press.

ZEMAN, O., & BLAISDELL, G. A. 1990 New physics and models for compressible turbulence. to appear in *Advances in Turbulence.* Springer-Verlag.

ZEMAN, O. 1990 Dilatation dissipation: the concept and application in modeling compressible mixing layers. *Physics of Fluids.* **2,** 178-188.

II. The turbulence modeling group

The turbulence modeling effort was carried out by three separate teams. Aupoix, Blaisdell, Reynolds, and Zeman used Blaisdell's simulations of homogeneous compressible isotropic turbulence and homogeneous compressible shear flow to examine various aspects of modeling the energy equation in these flows. Bradshaw and Sendstad used simulations of channel flow with a spanwise pressure gradient and a 3-D boundary layer to study aspects of three-dimensional turbulent boundary layers. Rodi and Mansour used simulations of channel flow to evaluate various aspects of $k - \epsilon$ modeling in the near-wall region, producing two contributions to this volume. These studies again demonstrate the powerful uses that can be made of simulation databases in guiding the development of turbulence modeling.

Aupoix *et al.* showed that the dilatation dissipation and pressure-dilatation terms are important in the kinetic energy equation and should not be neglected in turbulence models. In decaying isotropic turbulence, these terms depend critically on the initial conditions, specifically on the strength of the initial density fluctuations. However, in homogeneous shear flow, these terms approach limiting behavior that is independent of the initial conditions. The simulations show that the limiting value of the ratio of dilatational dissipation to solenoidal dissipation is about 0.1 and hint that there may be a limiting turbulent Mach number of approximately 0.7. Models for evolution of the *rms* pressure fluctuation and for key terms in the transport equation for pressure-velocity gradient term were also explored.

Bradshaw and Sendstad studied the simulation of channel flow with a suddenly-imposed cross-stream pressure gradient. They showed that the main effects occur in the viscous region and found some support for ideas about toppling suggested earlier by Bradshaw and Pontikos. They initiated a three-dimensional spatially-developing boundary layer calculation similar to an earlier Bradshaw experiment and show some preliminary results from calculations not yet well-developed. These preliminary results indicate that the shear stress vector and velocity gradient vector are not aligned in the outer region of the boundary layer. More detailed conclusions must await the completed calculation.

Rodi and Mansour's first paper on low Reynolds number (near-wall) modeling of the $k - \epsilon$ equation concentrated on the evaluation of various "damping function" models. They show that the treatment of the eddy viscosity coefficient C_μ as a constant (0.09) is at best a rough approximation, and significant tempering of that coefficient as a function of the production/dissipation ratio is required. They proposed improved damping functions for use in standard models. Perhaps the most significant result came from their investigation of Durbin's suggestion for use of $\overline{v'^2}$ instead of k to set the velocity scale. They showed that with this change it is not necessary to use empirical damping functions; hence, this approach gives a cleaner and more physical model. They made a detailed study of the various terms in the ϵ budget, using the results to make a careful assessment of existing models. They identified areas of weakness in the models and proposed new models for the

important terms in the ϵ equation, parameterized by the local non-dimensional strain rate and Reynolds number. Their new model is clearly an improvement in the case of channel flow. Subsequent work will test these models in more general situations.

Rodi and Mansour's second paper focuses on one-equation modeling, especially Durbin's ideas on the use of $\overline{v'^2}$ instead of k to give the velocity scale. As noted above, this model does not require damping functions used in existing near-wall models. When used in a one-equation model it requires a correlation for $\overline{u'v'}/\overline{v'^2}$ and $\overline{v'^2}/k$, for which they provide models based on the channel flow simulations. Together with simple linear length scale prescriptions and the k equation, these correlations provide a simple one-equation approach very deserving of further evaluation in more complex flows.

During the summer school, this author gave an informal workshop in which a new type of turbulence model based on a one-point "eddy structure tensor" that contains two-point information was described. This model has since been shown to do remarkably well in predicting the rapid distortion behavior of a very wide variety of homogeneous turbulent flows and a good job in homogeneous shear flow with either weak or strong shear. Working notes giving the current status of this model are available upon request to the author.

W. C. Reynolds

Modeling the turbulent kinetic energy equation for compressible, homogeneous turbulence

By B. Aupoix[1], G. A. Blaisdell[2], W. C. Reynolds[3], AND O. Zeman[3]

The turbulent kinetic energy transport equation, which is the basis of turbulence models, is investigated for homogeneous, compressible turbulence using direct numerical simulations performed at CTR. It is shown that the partition between dilatational and solenoidal modes is very sensitive to initial conditions for isotropic decaying turbulence but not for sheared flows. The importance of the dilatational dissipation and of the pressure-dilatation term is evidenced from simulations and a transport equation is proposed to evaluate the pressure-dilatation term evolution. This transport equation seems to work well for sheared flows but does not account for initial condition sensitivity in isotropic decay. An improved model is proposed.

1. Introduction

1.1 Turbulent kinetic energy equation

Industrial turbulence models, i.e. one-point closures, commonly use transport equations for averaged quantities. The first equation to be considered in one- or two-equation models is the turbulent kinetic energy equation.

For compressible flows, it is convenient to use Favre averaging. We use $\bar{}$ and $'$ to denote respectively an ensemble average and the fluctuation with respect to the ensemble average, $\tilde{}$ and $''$, a Favre average, and fluctuations with respect to the Favre average.

From the continuity and momentum equations, it is possible to deduce a transport equation for the turbulent kinetic energy per unit mass, $k = \frac{1}{2}\widetilde{u_i'' u_i''}$,

$$\underbrace{\frac{\partial \bar{\rho} k}{\partial t} + \frac{\partial \bar{\rho} \tilde{u}_j k}{\partial x_j}}_{(1)} = \underbrace{-\bar{\rho}\widetilde{u_i'' u_j''}\frac{\partial \tilde{u}_i}{\partial x_j}}_{(2)} \underbrace{-\overline{\tau_{ij}\frac{\partial u_i''}{\partial x_j}}}_{(3)} \underbrace{+\overline{p'\frac{\partial u_i''}{\partial x_i}}}_{(4)} + \underbrace{\overline{u_i''}\frac{\partial \bar{p}}{\partial x_i}}_{(5)} + \underbrace{\frac{\partial}{\partial x_k}\left[-\frac{1}{2}\overline{\rho u_i'' u_i'' u_k''} + \overline{u_i''\tau_{ik}} - \overline{p' u_k''}\right]}_{(6)} \tag{1.1}$$

1 ONERA/CERT Department of Aerothermodynamics
2 Stanford University
3 Center for Turbulence Research

Term (1) is the advection term, while term (2) represents the turbulent kinetic energy production due to the action of the mean velocity gradients upon the turbulent stresses. These terms are exact and do not require modeling, besides a way to compute the turbulent stresses.

The terms to be modelled are (3), which is the dissipation due to the work of the viscous stress

$$\tau_{ij} = \mu \left[\frac{\partial u_i}{\partial x_j} + \frac{\partial u_j}{\partial x_i} - \frac{2}{3} \delta_{ij} \frac{\partial u_k}{\partial x_k} \right] \quad ; \tag{1.2}$$

the pressure-dilatation term, (4); the mean pressure gradient term, (5); and the diffusion term, (6).

The dissipation and diffusion terms already exist in incompressible flows, while the pressure terms (4 and 5) are due to the flow compressibility. We shall, however, see in section 2 that flow compressibility also affects the form of the dissipation term.

1.2 Data bases for the modeling of the turbulent kinetic energy equation

Direct numerical simulations (DNS) of compressible, homogeneous turbulence are underway at CTR. For compressible flows, homogeneity requires that the mean pressure, temperature, and density be constant over space and that the mean velocity gradient satisfies the constraint

$$\frac{\partial}{\partial t} \frac{\partial \tilde{u}_i}{\partial x_j} + \frac{\partial \tilde{u}_i}{\partial x_k} \frac{\partial \tilde{u}_k}{\partial x_j} = 0 \tag{1.3}$$

Examples of allowed mean flows include constant flow, shear flow, and time-dependent irrotational strained flows.

DNS of isotropic decaying turbulence and of sheared flows have been performed by Blaisdell [1990]. Since turbulent statistics are point-independent for homogeneous flows, the diffusion term, (6), is null. As the mean pressure is constant over space, no direct information is available for the pressure gradient term, (5). We shall, however, see in section 3 that this term can be modelled together with the pressure-dilatation term.

1.3 Motivation

Homogeneous flows can be used to investigate models for the dissipation term, (3), and the pressure-dilatation term, (4). The turbulent kinetic energy balance of a sheared flow plotted in figure 1 shows that the pressure-dilatation term, often neglected, is about 10% of the dissipation and is thus important when compared with the time derivative of the turbulent kinetic energy.

Section 2 is devoted to the modeling of the dissipation term, while section 3 deals with the pressure-dilatation term modeling.

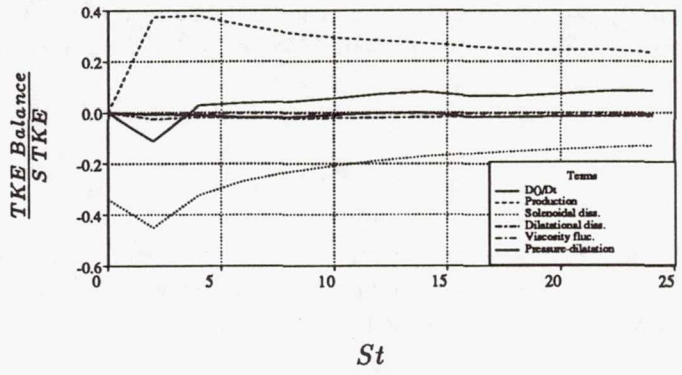

FIGURE 1. Turbulent kinetic energy balance for shear flow.

2. Modeling of the dissipation term

2.1 Decomposition of the dissipation term

As shown in figure 1, DNS confirms the *a priori* idea that the contribution of viscosity fluctuations to the dissipation is negligible. For homogeneous flows, the dissipation term can thus be written as

$$\overline{\rho}\overline{\varepsilon} = \overline{\tau_{ij}\frac{\partial u_i''}{\partial x_j}} \simeq \underbrace{\overline{\mu}\overline{\omega_i''\omega_i''}}_{\overline{\rho}\overline{\varepsilon}_s} + \underbrace{\frac{4}{3}\overline{\mu}\overline{\frac{\partial u_i''}{\partial x_i}\frac{\partial u_j''}{\partial x_j}}}_{\overline{\rho}\overline{\varepsilon}_d} \tag{1.4}$$

where ω is the vorticity.

The solenoidal dissipation, ε_s, represents the contribution of the vorticity, i.e. the usual form of the dissipation term in incompressible homogeneous turbulence. The dilatational dissipation, ε_d, is due to the flow compressibility.

For homogeneous flows, it is possible to split the velocity field into a solenoidal part (normal to the wave number vector in Fourier space) and a dilatational part (parallel to the wave number vector). The above splitting of the dissipation term then reflects the splitting of the velocity field. It must be pointed out that this splitting of the velocity is not unique in inhomogeneous flows. However, for inhomogeneous flows, the dissipation term, (3), can still be split into solenoidal and dilatational parts *plus* a diffusion term.

The solenoidal and dilatational dissipations are plotted as part of the balance presented in figure 1. The dilatational contribution is small compared with the solenoidal one, about 10%, but is not negligible in the balance.

2.2 Existing models

Sarkar *et al.* [1989] confirmed, from DNS of isotropic decaying turbulence, the results of their asymptotic analysis which predicts the existence of an equipartition of energy between the variance of the pressure associated with the dilatational

velocity field and the dilatational contribution to the kinetic energy. Then, assuming that the dilatational pressure variance scales with the square of the turbulent Mach number, $M_t = \sqrt{q^2}/a$, and that the solenoidal and dilatation velocity fields have similar Taylor microscales, they obtain

$$\varepsilon_d = M_t^2 \, \varepsilon_s \tag{2.1}$$

Zeman [1990] assumes that the dilatation is mainly due to shock-like structures embedded within the energetic turbulent eddies. From shock relations and an assumed Gram-Charlier pdf for the velocity fluctuations, he states

$$\varepsilon_d = c_D F(M_t, K) \varepsilon_s \qquad c_D \sim 0.75 \tag{2.2}$$

where K is the kurtosis of the velocity fluctuations.

Both Sarkar and Zeman assume that the evolution of the solenoidal dissipation is given by the same transport equation as for incompressible flows.

2.3 Comparison with DNS results

In the simulations performed by Blaisdell, the ratio of the dilatational dissipation to the total dissipation is insensitive to initial conditions in sheared flows but is very sensitive to initial conditions in isotropic decay. This is shown in figure 2.

It seems that the flow keeps a memory of the initial dissipation partition for isotropic decay but not for sheared flows. This is at variance with the above analysis, at least for isotropic decay, but Erlebacher *et al.* [1990] have shown, from linear acoustics, that the compressible part of the flow, i.e. the acoustic part, can decouple from the solenoidal part for isotropic decay and reach various asymptotic levels according to the initial conditions. This analysis holds only for isotropic flows and low turbulent Mach numbers. From DNS of low Reynolds number ($Re_\lambda \sim 20$), two-dimensional isotropic turbulence, Erlebacher [1990] evidenced a sensitivity to initial flow conditions.

Another explanation for this behavior is that turbulence remembers its initial conditions in the final period of decay. As shown in figure 3, the Reynolds number, Re_λ, based upon the Taylor microscale λ_{11} and q, becomes very small for the isotropic decay case.

To check the influence of the low Reynolds numbers, two new isotropic decaying turbulence runs were performed. To avoid low Reynolds numbers, the initial Reynolds number was held constant at $Re_\lambda \simeq 50$ during the turbulence development period by decreasing the viscosity, after which teh viscosity was held constant. The initial turbulent Mach number is 0.5. The sensitivity to initial conditions is still observed. Consequently, it seems important to keep information about initial conditions in isotropic decay while a unique equilibrium behavior seems to be achieved in the presence of shear.

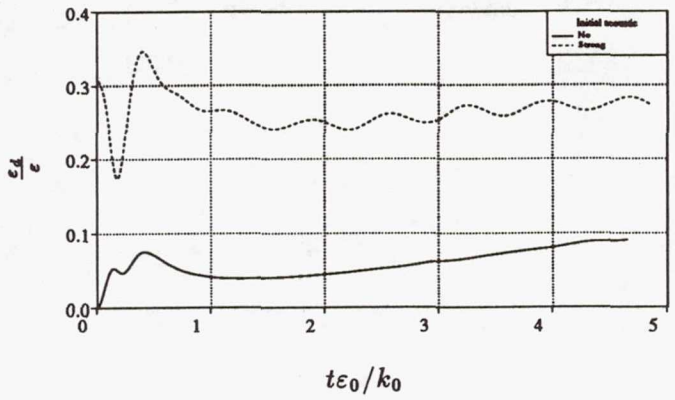

a. Isotropic decaying turbulence $M_{t_0} = 0.7$

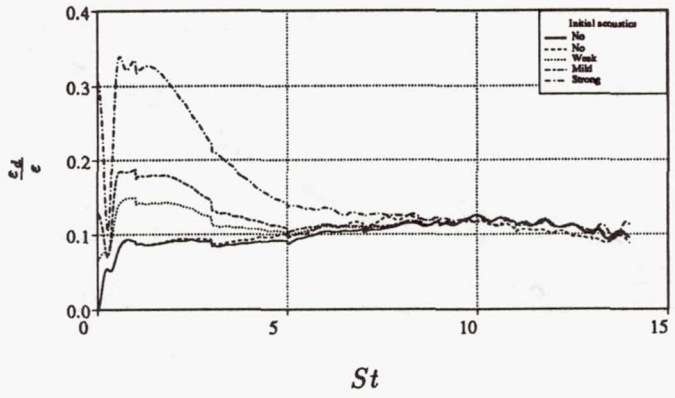

b. Sheared turbulence $M_{t_0} = 0.5$

FIGURE 2. Dissipation partition time evolution.

3. Modeling the pressure-dilatation term

3.1 Existing models

Sarkar *et al.* [1989] proposed to include the pressure-dilatation term in the expression for the dilatational dissipation as, from their isotropic decay simulations, this term is small and its fluctuations are larger than its average.

The same approach has been used by Zeman [1990] who later proposed to relate this term to the pressure-variance evolution. He uses a return law in which the pressure variance is assumed to return to an equilibrium value on an acoustic time scale. Zeman's model [1990a] reads

$$\overline{p\frac{\partial u_i''}{\partial x_i}} = -\frac{1}{2}\frac{1}{\overline{\rho}a^2}\frac{D\overline{p'^2}}{Dt} \tag{3.1}$$

$$\frac{D\overline{p'^2}}{Dt} = \frac{\overline{p_e^2} - \overline{p'^2}}{\tau_a} \tag{3.2}$$

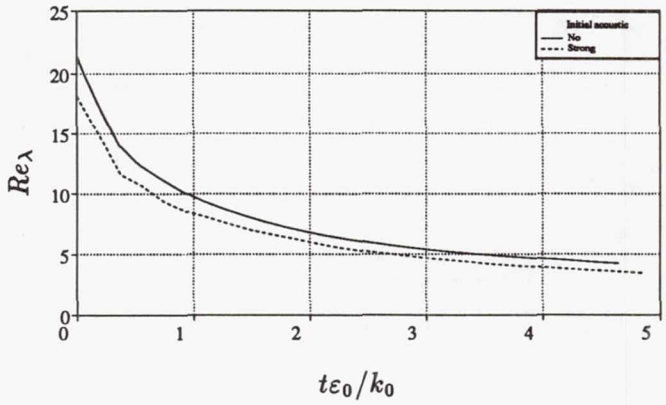

a. Isotropic decaying turbulence $M_{t_0} = 0.7$

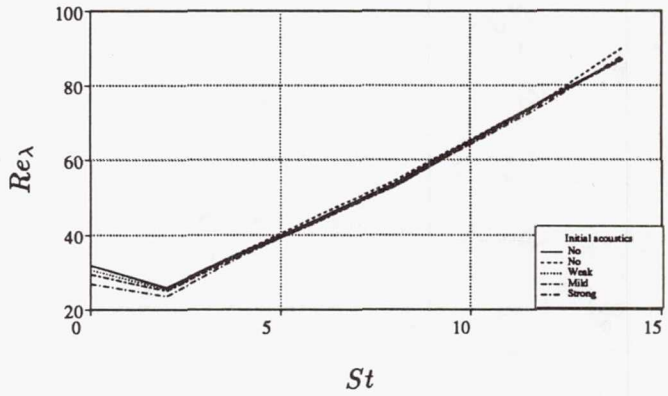

b. Sheared turbulence $M_{t_0} = 0.5$

FIGURE 3. Taylor microscale Reynolds number time evolution.

$$\overline{p_e^2} = \overline{\rho}^2 q^2 a^2 \frac{\alpha M_t^4}{1 + \alpha M_t^4} \tag{3.3}$$

where equation (3.1), which is given by linear acoustics, has been shown to have a wider range of validity. Zeman [1990b] also proposed a revised version of equation (3.3) in which the right hand side (RHS) varies as M_t^2 instead of M_t^4.

3.2 Modeling of the pressure-dilatation term

DNS of sheared flows have shown that the mean value of the pressure-dilatation term is comparable to the dilatational dissipation and thus gives a significant contribution to the kinetic energy budget. Moreover, this term exhibits oscillations which seem to scale on an acoustic time scale and are difficult to model. It appears, however, from comparisons of two runs with identical initial spectra but different seeds in the initial random field generation, that these oscillations are due to the noise of the biggest eddies for which only a small statistical sample is obtained in a single

simulation. Consequently, we only try to reproduce a smoothed pressure-dilatation evolution, not its oscillations.

3.2.1 Transport equation for the velocity-pressure gradient term

Instead of using linear acoustics and scaling relations, we first investigated the transport equation for the pressure-dilatation term. The three pressure terms which appear in the turbulent kinetic energy equation, (1.1), i.e. the pressure-dilatation term, (4); the mean pressure gradient term, (5); and the contribution of pressure to the diffusion term, (6), are an expansion of the initial term $-\overline{u_i'' \frac{\partial p}{\partial x_i}}$.

It is easier to derive an equation for $-\overline{u_i'' \frac{\partial p}{\partial x_i}}$ than for the pressure-dilatation term. Moreover, *only* for homogeneous flows can the pressure-dilatation term be interpreted as an energy exchange term between turbulent kinetic energy and potential pressure fluctuation energy $\overline{p'^2}/2\gamma\bar{p}$. However, the term $-\overline{u_i'' \frac{\partial p}{\partial x_i}}$ always represents the reversible energy exchange between the turbulent kinetic energy and the internal energy.

Assuming that the fluid is a perfect gas, the pressure can be linked to the internal energy per unit mass, e, as $p = (\gamma - 1)\rho e$ so that the energy equation can be written as a pressure evolution equation. From this equation, together with the momentum and continuity equations, the transport equation for $\overline{u_i'' \frac{\partial p}{\partial x_i}}$ can be derived as

$$
\begin{aligned}
\underbrace{\frac{\partial}{\partial t}\overline{u_i''\frac{\partial p}{\partial x_i}} + \tilde{u}_l \frac{\partial}{\partial x_l}\overline{u_i''\frac{\partial p}{\partial x_i}}}_{(a)} &= \underbrace{-2\overline{u_l''\frac{\partial p}{\partial x_i}}\frac{\partial \tilde{u}_i}{\partial x_l}}_{(b)} \underbrace{-\gamma\overline{u_i''\frac{\partial p}{\partial x_i}}\frac{\partial \tilde{u}_l}{\partial x_l} - \gamma\overline{p u_i''}\frac{\partial^2 \tilde{u}_l}{\partial x_i \partial x_l}}_{(c)} \\
&\quad \underbrace{+p\overline{\frac{\partial u_i''}{\partial x_l}\frac{\partial u_l''}{\partial x_i}} + (\gamma-1)p\overline{\frac{\partial u_i''}{\partial x_i}\frac{\partial u_l''}{\partial x_l}} - \overline{\frac{1}{\rho}\frac{\partial p}{\partial x_i}\frac{\partial p}{\partial x_i}}}_{(d)} \\
&\quad \underbrace{+\frac{1}{\bar{\rho}}\frac{\partial \bar{p}}{\partial x_i}\frac{\partial \bar{p}}{\partial x_i} - \frac{1}{\bar{\rho}}\frac{\partial}{\partial x_l}\left[\overline{\tau_{il}} - \bar{\rho}\widetilde{u_i'' u_l''}\right]\frac{\partial \bar{p}}{\partial x_i}}_{(e)} \\
&\quad \underbrace{+\overline{\frac{1}{\rho}\frac{\partial \tau_{il}}{\partial x_l}\frac{\partial p}{\partial x_i}} - (\gamma-1)\overline{\left(\tau_{lk}\frac{\partial u_l''}{\partial x_k} - \frac{\partial q_l}{\partial x_l}\right)\frac{\partial u_i''}{\partial x_i}}}_{(f)} \\
&\quad \underbrace{-\frac{\partial}{\partial x_l}\left[\overline{u_i''\frac{\partial p u_l''}{\partial x_i}} - (\gamma-1)\overline{p u_l''\frac{\partial u_i''}{\partial x_i}} + (\gamma-1)\overline{u_l''\left(\tau_{ij}\frac{\partial u_i''}{\partial x_j} - \frac{\partial q_i}{\partial x_i}\right)}\right]}_{(g)}
\end{aligned}
\tag{3.4}
$$

where (a) represents the advection by the mean flow, (b) the mean velocity gradient effects, (c) the mean dilatation and mean dilatation gradient effects, (d) third order effects, and (e) the mean pressure gradient effect, while (f) are the viscous terms and (g) the diffusion terms.

For homogeneous flows, terms (e) and (g) are zero. Moreover, for isotropic decay or sheared flows, term (c) is zero. It must also be pointed out that the three terms

$$-2\overline{u_l''\frac{\partial p}{\partial x_i}\frac{\partial \tilde{u}_i}{\partial x_l}} + \overline{p\frac{\partial u_i''}{\partial x_l}\frac{\partial u_l''}{\partial x_i}} - \overline{\frac{1}{\rho}\frac{\partial p}{\partial x_i}\frac{\partial p}{\partial x_i}}$$

exactly cancel in incompressible flows thanks to the Poisson equation for the pressure.

3.2.2 Closure of the transport equation

The first two terms in (d) can be approximated as

$$\overline{p\frac{\partial u_i''}{\partial x_l}\frac{\partial u_l''}{\partial x_i}} \simeq \overline{p}\,\overline{\frac{\partial u_i''}{\partial x_l}\frac{\partial u_l''}{\partial x_i}} \simeq \overline{p}\,\overline{\frac{\partial u_i''}{\partial x_i}\frac{\partial u_l''}{\partial x_l}} = \frac{\overline{p}}{\overline{\mu}}\varepsilon_d$$

i.e. these terms blow up as the Reynolds number tends towards infinity. Consequently, the pressure-dilatation budget is the balance of terms which tend towards infinity while their difference remains finite. A term by term modeling approach cannot be applied. Using an equation for $\overline{p\frac{\partial u_i''}{\partial x_i}}$ leads to the same behavior at high Reynolds numbers.

As with the dissipation equation, a heuristic approach is used to include the physics in a modelled equation. However, equation (3.4) does provide information about the rôle of the compressibility terms. The modeling of the equation will be discussed only for homogeneous flows so that we turn back to the pressure-dilatation term. This term should tend towards zero for incompressible flows, i.e. it must be damped on an acoustic time scale. All terms on the RHS of (3.4) cancel in the incompressible limit. On the other hand, DNS are in good agreement with (3.1) and show that the pressure-dilatation term tends, after some transients, to be positive for decaying turbulence and negative for sheared flows, i.e. to scale upon the turbulent kinetic energy temporal evolution. At last, assuming that the pressure level scales upon M_t^2 and that the production term scales upon an acoustic time scale leads to the form

$$\frac{d}{dt}\overline{p\frac{\partial u_i''}{\partial x_i}} = -C_1\rho\frac{1}{\tau_a}M_t^2\frac{dk}{dt} - C_2\frac{1}{\tau_a}\overline{p\frac{\partial u_i''}{\partial x_i}} \tag{3.5}$$

$$\text{with} \qquad \tau_a = \frac{k^{3/2}}{\varepsilon a} \qquad C_1 = 0.25 \qquad C_2 = 0.2$$

It must be mentioned that Zeman's model can be rewritten as a transport equation for the pressure-dilatation term. A somewhat different form, including turbulent kinetic energy and dissipation time derivatives and a similar damping term is thus obtained.

3.2.3 Comparison with DNS and Zeman's model

The evolution of the pressure-dilatation term given by DNS is compared with predictions from the above model, (3.5), and from Zeman's model, assuming either an M_t^4 or M_t^2 behavior in (3.3). Only the evolution of the pressure-dilatation term is predicted, using the DNS values of kinetic energy, dissipation, and other quantities. The comparison starts at a time when the turbulent flow is developed. The aim is to reproduce the mean evolution of the pressure-dilatation term, not its oscillations which are the signature of the biggest eddies of the DNS.

The comparisons for some sheared flows are plotted in figure 4. Case (4.a), which is the run with the most gridpoints and the longest development, has been used to calibrate the coefficients C_1 and C_2. Particular attention has been paid to the initial evolution of the pressure-dilatation term to avoid the increase predicted by Zeman's model. As the turbulent Mach number varies weakly, there are several possible sets of coefficients. However, they eventually lead to similar results for the other flows. Zeman's models give a good prediction of the pressure-dilatation level but not of its time derivative; the M_t^4 assumption here seems to be the best.

For case (4.b), the model seems to slightly overestimate the pressure-dilatation term, but the agreement is fair. Zeman's best model is now the M_t^2 assumption.

For case (4.c), all models predict an unrealistic initial increase of the pressure-dilatation term. Both the present model and Zeman's M_t^2 model give good levels; the present model seems to better estimate the time derivative.

The comparison for isotropic decaying turbulence is plotted in figure 5. No model is able to give good predictions of the isotropic decay case. Zeman's M_t^2 model gives good prediction of the strong acoustics case while the M_t^4 model gives good predictions of the low acoustics cases. It is possible to tune the coefficients of our model to have a fair prediction of case (5.b), but then prediction of the other flows is poor. This seems again to be due to the sensitivity of isotropic decaying flows to the initial conditions.

4. Proposals for model improvement

A simple way to improve the modeling of isotropic decaying flows is to account for the initial partition between solenoidal and compressible modes by using transport equations for both the pressure-dilatation term and the dilatational dissipation. A way to extend the above model could be

$$\frac{d}{dt}\overline{p\frac{\partial u_i''}{\partial x_i}} = -C_1\frac{\varepsilon_d}{k}P + C_2\frac{\varepsilon_s}{\tau_a} - C_3\frac{1}{\tau_a}\overline{p\frac{\partial u_i}{\partial x_i}}$$

$$\frac{d\varepsilon_d}{dt} = W_1\frac{\varepsilon_d}{k}P + W_2\frac{\varepsilon_s}{\tau_a} - W_3\frac{\varepsilon_d}{\tau_a}$$

where information about the constants and their Mach number dependency could be deduced from the equilibrium solutions for isotropic decay and sheared flows.

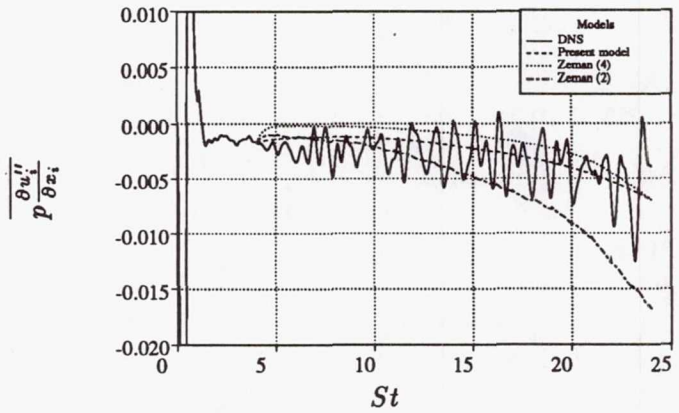

a. $M_{t_0} = 0.4$ No initial acoustics

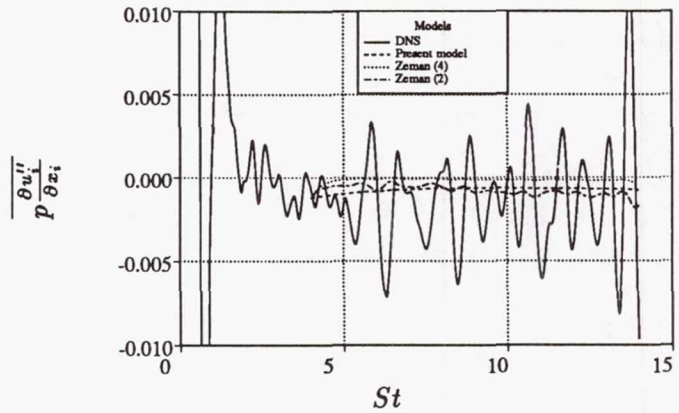

b. $M_{t_0} = 0.5$ Strong initial acoustics

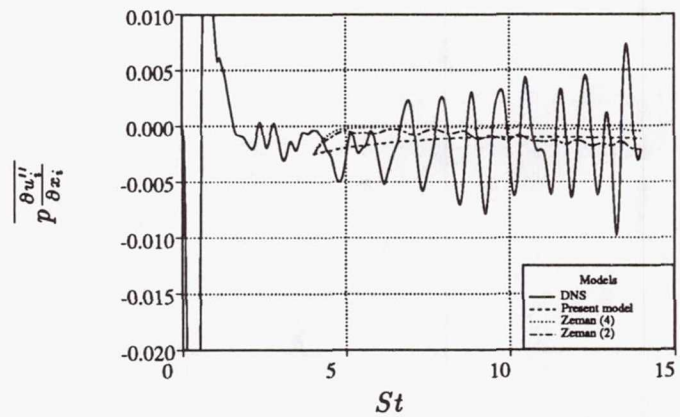

c. $M_{t_0} = 0.5$ No initial acoustics

FIGURE 4. Evolution of the pressure-dilatation term for sheared turbulence.

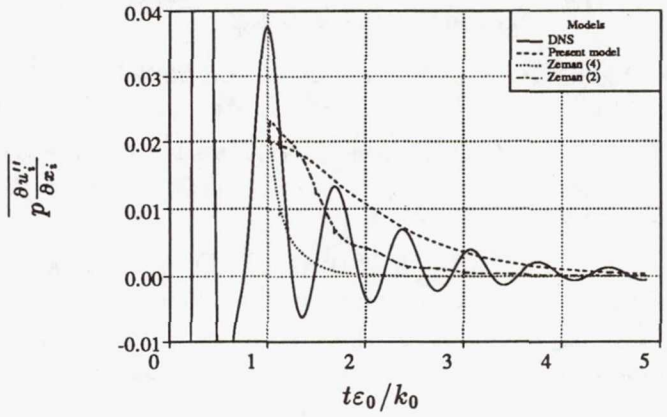

a. $M_{t_0} = 0.7$ Strong initial acoustics

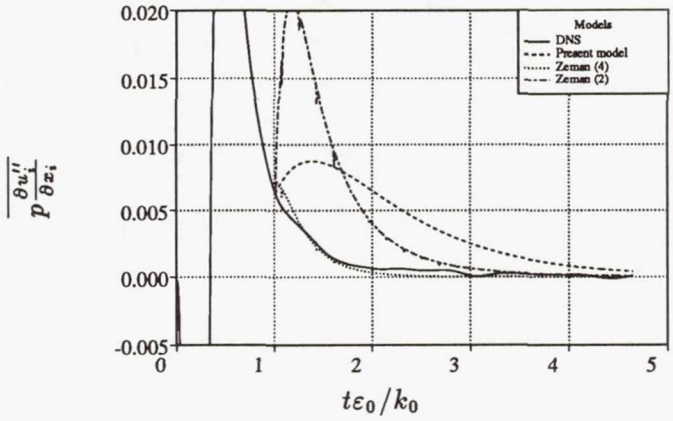

b. $M_{t_0} = 0.7$ No initial acoustics

FIGURE 5. Evolution of the pressure-dilatation term for isotropic decaying turbulence.

5. Conclusions

The dilatational dissipation and the pressure-dilatation term play important rôles in the kinetic energy budget and should not be neglected. The dilatational dissipation scales with the solenoidal dissipation and the turbulent Mach number, but this scaling also depends upon the initial conditions for isotropic decaying turbulence. A model to predict the evolution of the pressure-dilatation term has been proposed. It seems to work well for sheared flows but still requires validation and needs improvement to account for initial condition sensitivity.

Moreover, other important points such as turbulent stress, turbulent heat flux, and turbulent scalar flux modeling should be investigated. Homogeneous flows can provide helpful information, e.g. about the role of mean flow dilatation, but inhomogeneous flows are to be looked at to investigate the role of density or temperature gradients.

REFERENCES

BLAISDELL, G. A. 1990 Numerical Simulation of Compressible Homogeneous Turbulence, Ph.D. Thesis in preparation, Dept. of Mech. Eng., Stanford University.

ERLEBACHER, G. 1990 Direct simulation of compressible turbulence. *IMACS 1st international conference on computational physics. Univ. of Boulder, Boulder, Colorado. June 1990.*

ERLEBACHER, G., HUSSAINI, M. Y., KREISS, H. O. & SARKAR, S. 1990 The analysis and simulation of compressible turbulence. *ICASE Report No. 90–15.*

SARKAR, S., ERLEBACHER, G., HUSSAINI, M. Y., & KREISS, H. O. 1989 The analysis and modeling of dilatational terms in compressible turbulence. *ICASE Report No. 89–79.*

ZEMAN, O. 1990 Dilatation dissipation: The concept and application in modeling compressible mixing layers. *Phys. Fluids.* **A 2,** 178–188.

ZEMAN, O. & BLAISDELL, G. A. 1990a New physics and models for compressible turbulent flows. *European Turbulence Conference, Stockholm July 1990.*

ZEMAN, O. 1990b On the decay of isotropic compressible turbulence. *CTR Manuscript 115.* Center for Turbulence Research, NASA Ames Research Center/ Stanford University

Structure of three-dimensional turbulent boundary layers

By P. Bradshaw[1] and O. Sendstad[1]

The changes that occur in the Reynolds-stress-producing motion when a cross-stream pressure gradient is applied to an initially two-dimensional turbulent flow are discussed. Two main examples are used; (i) a temporal simulation of a channel flow with crossflow applied by a spanwise pressure gradient for $t > 0$, and (ii) a spatial simulation of the boundary layer on an infinite swept wing, which is still in progress. Evidence examined to date suggests that the structural changes in the two cases are similar, but the mechanisms may be significantly different, even if effects peculiar to the viscous wall region are ignored. The results from (ii) are provisional, based on too short a time series for accurate statistical averages to be obtained. We treat turbulence "simulations" (solutions of the Navier-Stokes equations in three space dimensions and time) in the same way as experiments: both have limitations of accuracy but both are acceptable representations of real fluid flows.

1. Introduction

Several experiments and simulations have shown significant differences in turbulence structure between two-dimensional and three-dimensional turbulent wall flows; similar effects are likely to occur in free shear layers but there are no sufficiently detailed data. (Note: here, "2-D" and "3-D" refer to the statistical-average properties of the flow; instantaneously, turbulence is always 3-D.) There are two main types of 3-D flow, those where large gradients occur in only one direction (normal to the wall in the case of a boundary layer) and those where large gradients occur in both directions in the plane normal to the general flow direction (as in wing-body junction flows or vortex/boundary-layer interactions). Here we deal only with the former type. With the exception of the simulations of the Ekman layer (Coleman, Ferziger & Spalart 1990) and the related 3-D "scrubbing" flow (Spalart 1989), most work relates to the more-or-less sudden application of crossflow to an initially two-dimensional flow by the action of spanwise pressure gradient or spanwise motion of a wall. This is a convenient idealization of a typical wing boundary layer in which crossflow gradually increases with downstream distance, and has the conceptual advantage of giving the impulse response of the (non-linear) system. Despite the facts that turbulence is always instantaneously three-dimensional and that individual turbulent eddies do not see the mean flow as such, noticeable structural changes can be produced by differences of as little as 10 degrees between the direction of the external flow and that of the flow near the wall.

1 Stanford University

These structural changes imply that changes may be needed in the dimensionless empirical coefficients used in Reynolds-averaged prediction methods (since the coefficients are, by definition, structural parameters). The examples most frequently quoted are that the eddy viscosity for the component of shear stress in the "cross-stream" direction is smaller than that for the streamwise direction, and that even the latter is less than in two-dimensional flow. In general, it is incorrect to correlate empirical coefficients with the mean-flow direction because that depends on the velocity of the observer, but it is legitimate to regard the direction of the initial 2-D flow as "special" and examine perturbations in axes aligned with the initial flow direction. For long times after the start of crossflow, the initial flow direction ceases to be relevant and should in principle be replaced by some fading-memory integral of (say) the direction of the resultant shear stress. Judging from the smallness of the structural changes in the Ekman and "scrubbing" flows, compared to those in flows where crossflow is suddenly applied, the changes are mainly transient. The simplest explanation is that the eddy structure set up in a two-dimensional flow takes some time to adjust to a three-dimensional mean strain field, but when it has done so, structural parameters like the ratio of shear-stress magnitude to turbulent energy return to something near their "two-dimensional" values.

Here we offer preliminary comments on the mechanisms that lead to the structural changes. The data set which we aimed to analyze is the simulation of the spatially-varying boundary layer on a 35° "infinite" swept wing initiated at NASA Ames Research Center by Dr P. R. Spalart (now of Boeing Commercial Airplane Co.); unfortunately, fully converged statistics are not available at the time of writing. Therefore, we have devoted some time to the analysis of a time-dependent ("transient") simulation, the initially 2-D channel (closed duct) flow with spanwise pressure gradient applied for $t > 0$ (Moin, Shih, Driver & Mansour 1990). As will be shown below, the duct flow is not closely related to wing boundary layers with spanwise pressure gradients. However, the effects of mean shear in the crossflow plane, $\partial W/\partial y$, are likely to be broadly similar in the two cases.

2. The Channel Flow with Spanwise Pressure Gradient

The main results of the simulation are reported by Moin *et al.* (1990). The initial 2-D flow is the same as that of Kim, Moin & Moser (1987), with $u_\tau \delta/\nu = 180$. At $t = 0$, a spanwise pressure gradient ten times as large as the streamwise pressure gradient is applied to produce a positive z-component mean velocity, which in the central part of the flow (where W is unaffected by viscous or turbulent stresses) is just $-t(1/\rho)\partial p/\partial z$. Because $\partial W/\partial x = 0$, there is no quasi-inviscid skewing of initially-spanwise vorticity into the spanwise direction, as predicted by the Squire-Winter-Hawthorne (SWH) secondary flow theorem. Therefore, turbulence quantities are affected only in the internal layers near the walls, in which streamwise vorticity $\partial W/\partial y$ spreads out from the surface by viscous and turbulent diffusion. In the Gruschwitz/Johnston "triangular" plot of W against U in axes aligned with the centerline velocity, the slope in the outer layer is nominally half that in a spatially-developing flow which has skewed through the same angle in inviscid flow. (In the inviscid secondary-flow approximation, half the outer-layer slope in the triangular

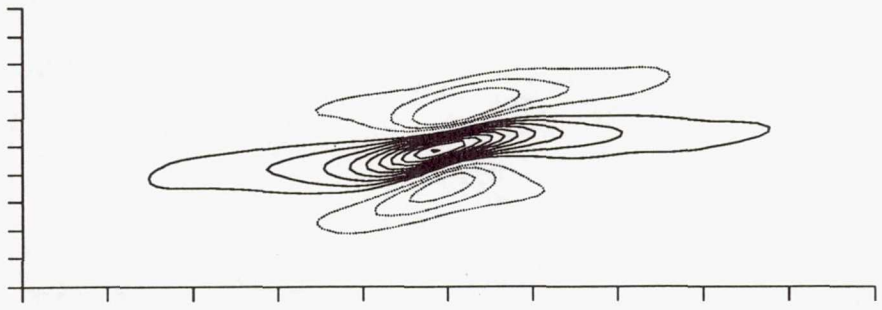

FIGURE 1. R_{12} correlation contours in channel: $x - z$ plane. In figures 1–3, negative contours are shown dotted.

plot comes from the change in coordinates from the initial x, y and half from the skewing of spanwise vortex lines to produce $\partial W/\partial y$.) After a time $t = 0.6\delta/u_\tau$, the thickness of the internal layer is about 60 wall units (one-third of the half-width of the channel), the z-component surface shear stress is about 0.68 of the original x-component surface shear stress, while the x-component surface shear stress has fallen to about 0.93 of its original value and is still decreasing; the magnitude of the surface shear stress is about 1.15 times the initial value.

The following discussion is based mainly on the two-point correlations at $t = 0.6\delta/u_\tau$ and $y^+ = 19.2$, near the peak in $-\overline{vw}$, and on budgets for various components of Reynolds stress. The correlation data are too close to the wall to be quantitatively representative of fully turbulent flow, and the bulk Reynolds number is so low that the total shear stress at $y^+ \approx 20$ in the initial flow is only 0.9 of the wall value, while the maximum in $-\rho\overline{uv}$ is less than 0.7 of the wall shear stress.

As pointed out by Moin *et al.*, the reduction in $-\overline{uv}$ seems to begin with a fall in $\overline{v\partial p/\partial y}$, which presumably implies a fall in $\overline{p\partial v/\partial y}$, the rate of transfer of turbulent kinetic energy from the u component, where it is generated, to the v component. The *last* quantity one would expect to be affected by crossflow is one that contains no z-component quantities!

Sample correlation contours in the $x - z$ and $z - y$ planes are shown in figures 1–3. At $t = 0$, the correlations are nominally symmetrical or antisymmetrical in z. At later t they are skewed in plan view and tilted in end view, by markedly differing amounts. The lengths of the axes marked on these plots are:– x, three channel half-heights or 540 wall units; y and z, one half-height or 180 wall units. For reference, the flow angle at the wall is at 36 deg. to the x axis, while at the fixed point of the correlations, $y^+ = 19.2$, the resultant mean shear and the resultant shear stress

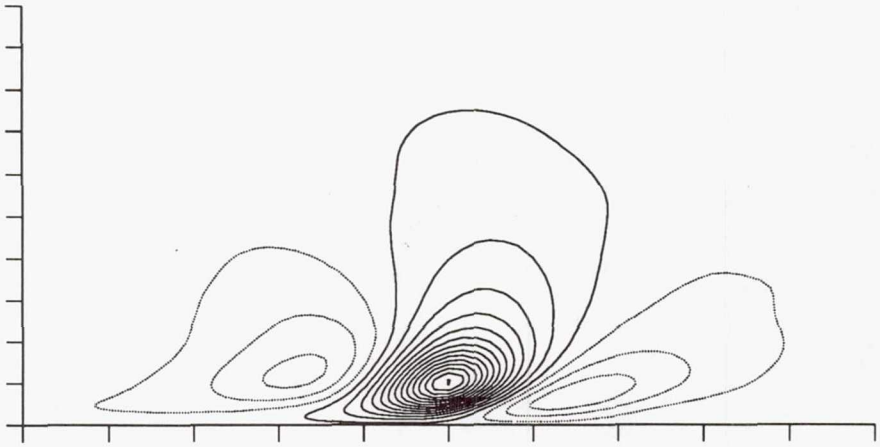

FIGURE 2. R_{11} correlation contours in channel: $z - y$ plane.

are at 13.2 deg. and 9.5 deg. to the x axis, respectively. (A large fraction of the skew in any 3-D flow occurs in the viscous wall region.) Viewed in the $x - z$ plane, the central parts of the R_{11} and R_{12} correlations (and also the R_{21} correlation, not shown here) line up with the stress angle, whereas the R_{22} correlation contours are inclined at nearly 17 deg. to the x axis and the R_{33} contours are inclined at over 20 deg. At large positive or negative separation in the x direction, the correlation contours tend to line up with the original x axis. This demonstrates quite neatly that the correlations at large separations are dominated by the unaltered eddies in the central part of the channel; this is the "inactive" motion, so called by Townsend (1961) because it is supposed to have such a small v component that it does not contribute significantly to $\overline{uv}$, and indeed the regions of R_{22} that line up with the x axis are quite small. The behavior of the negative regions that appear at large $\pm z$ in all correlations except R_{33} is interesting. In most cases, the positions of the minima are only slightly rotated away from the z axis and the contours are aligned with the central ridge, but the side extrema in R_{12} are more noticeably asymmetrical. This may give a clue to the structural alterations that reduce $\overline{uv}$.

Correlation contours in the $z - y$ plane show a wide range of behavior. R_{11} looks almost as if contours were convected passively by the w-component motion (at this time, the core fluid has moved a distance 1.8δ in the positive z direction). However, the negative side lobes have different shapes, that on the negative-z side having become slightly weaker than the other and risen above its original position ($\partial v/\partial z$ is, of course, zero, so this is not the result of passive convection). The lobe on the positive-z side seems to have been slightly flattened. The same features of shearing, upward drift of the negative-z lobe and flattening of the positive-z lobe are found in R_{12} and R_{21} (where the negative-z lobe has become slightly stronger) but are only just detectable in R_{22}.

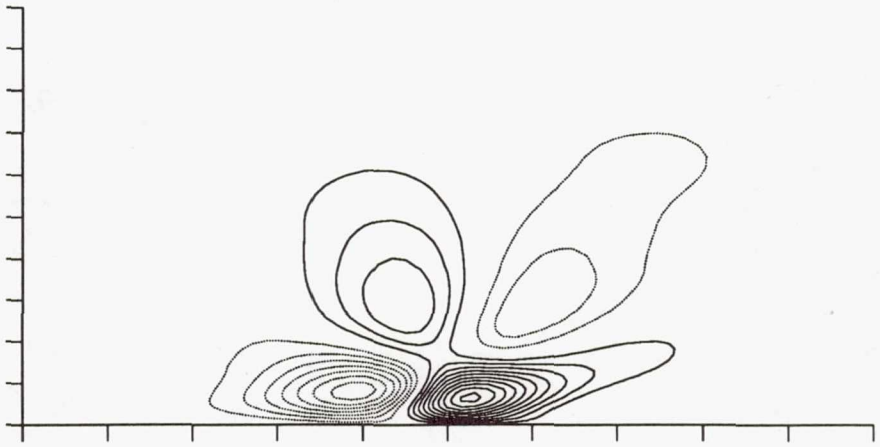

FIGURE 3. R_{13} correlation contours in channel: $z - y$ plane.

3. Simulation of the Boundary Layer on an "Infinite" Swept Wing

This simulation is intended as an approximation to the experiment of Bradshaw & Pontikos (1985) in a wind-tunnel test rig approximating a 35° "infinite" swept wing (large span and constant chord, so that mean gradients along the 35° swept generators are nominally zero).

Below, axes aligned normal and parallel to the generators are denoted by x' and z', while axes aligned with the initial flow direction ("tunnel axes") are denoted by x and z. The boundary layer initially flowed in the x direction and was then deflected in the z direction by the pressure gradient in the x' direction. This configuration is convenient experimentally because measurements need be made at only one spanwise position, and is also convenient computationally because averages can be taken along the generators as well as in time.

The numerical method and the arrangements of boundary conditions will be reported separately. Briefly, the periodic upstream and downstream boundary conditions were imposed by "fringes" in the $y - z'$ plane: the downstream fringe ingested the flow from the computational domain, removed some of its mass flow rate, and excreted the downstream. The upstream fringe was identical to the downstream one – that is, the inlet boundary layer is a greatly-thinned version of the outlet one. The run of two-dimensional flow before the onset of pressure gradient and crossflow was long enough for the perturbed boundary layer at entry to regain normal structure.

To specify the streamwise pressure gradient in the boundary layer, the normal-component velocity on the upper surface of the computational domain was chosen so that *according to an inviscid flow calculation* the pressure distribution on the lower (solid) surface was nominally the same as in the experiment. In two-dimensional flow, the representative dimensionless pressure gradient, equal to the ratio of the

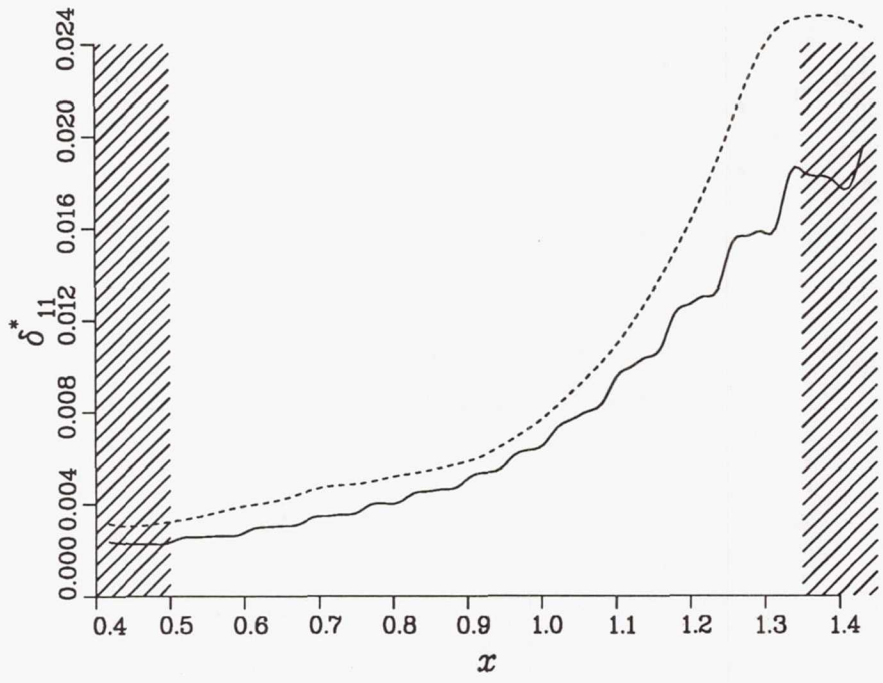

FIGURE 4. Displacement-thickness distribution in boundary layer: provisional results. Dotted line is "vorticity" definition.

two terms on the right-hand side of the momentum-integral equation

$$\frac{d(\rho_e U_e^2 \theta)}{dx} = \tau_w + \delta^* \frac{dp}{dx}, \tag{1}$$

is $(\delta^*/\tau_w)dp/dx$. Similar parameters apply in 3-D flow. The Reynolds number of the simulation is less than a tenth of that in the experiment, so typical skin-friction coefficients are larger by a factor of about two and, therefore, dp/dx must be larger by a factor of about two to reproduce the experimental distribution of $(\delta^*/\tau_w)dp/dx$.

A first estimate of the required pressure gradient gave somewhat smaller crossflow than in the experiment, but a second, larger, pressure gradient unexpectedly caused the flow to separate (i.e. the component of surface shear stress in the x' direction fell to zero). The reason was that the y-wise pressure gradient in the boundary layer is smaller than in the inviscid calculation used to determine the required normal-component velocity on the upper boundary, and as a result, the surface pressure in the retarded region is higher than in the inviscid flow; this causes increased boundary-layer growth, which further reduces $\partial p/\partial y$ and increases $\partial p/\partial x$, which causes ... and so on. The final, compromise, pressure gradient was chosen late

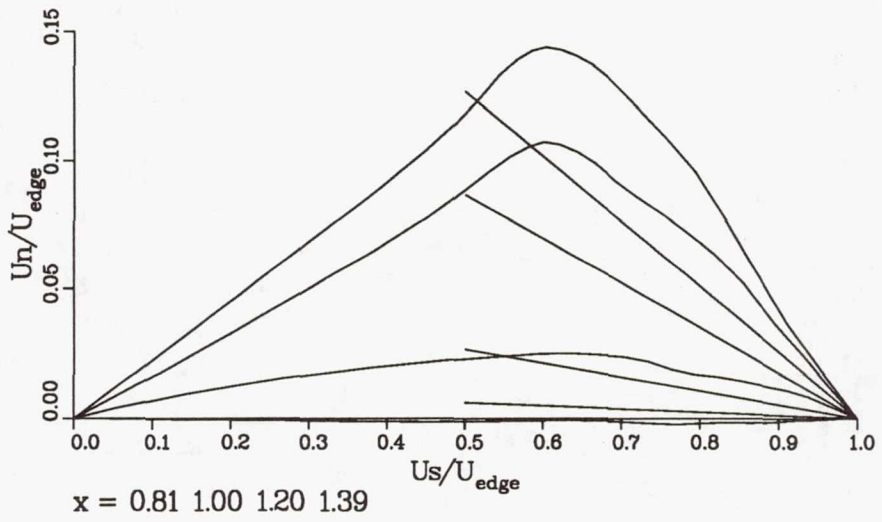

FIGURE 5. Gruschwitz/Johnston "triangular" plots in boundary layer: provisional results. x increases from lowest to highest profile.

in the summer program period, and adequately converged results for higher-order structure parameters have not been obtained at the time of writing.

Figure 4 shows the displacement thickness, which is itself not very well converged, and figure 5 the triangular plot; the adverse pressure gradient begins at about $x =$ 0.8m, where the total boundary-layer thickness is about 0.04m, and the pressure coefficient rises to just under 0.4 at the end of the useful part of the computational domain at x =1.4m.

An accompanying simulation of the 2-D boundary layer experiment of Watmuff (1990), with roughly the same distribution of $(\delta^*/\tau_w)dp/dx$, has run into unrelated numerical difficulties and is also incompletely converged. It is hoped that comparisons of the structural parameters in the 2-D and 3-D cases will allow the effects of low Reynolds number to be subtracted out, leaving an estimate of the effects of crossflow.

4. Effects of Crossflow on Turbulence Structure

Several experiments (v.d. Berg *et al.* 1975, Bradshaw & Pontikos 1985, Anderson & Eaton 1987) have shown that when a spanwise component of pressure gradient forces an initially 2-D boundary layer into crossflow, (i) the direction of the shear-stress vector $(-\overline{uv}, -\overline{vw}$ changes more slowly than the direction of the velocity-gradient vector $\partial U/\partial y, \partial W/\partial y)$ (implying that the spanwise component of eddy viscosity is smaller than the streamwise component for any reasonable definition of the arbitrary "spanwise" direction), and (ii) the ratio of shear-stress magnitude to

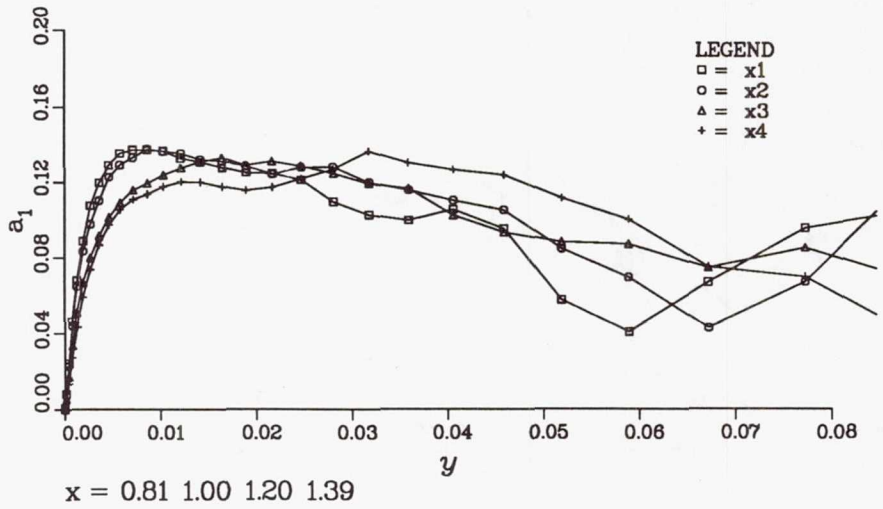

FIGURE 6. Ratio of shear stress magnitude to turbulent energy, a_1, in boundary layer: provisional results.

turbulent kinetic energy decreases (leading to a shortfall in turbulent energy production and thus to a decrease in the absolute values of turbulent energy and shear stress). Qualitatively similar results have been obtained with hot-wire anemometers and laser-doppler velocimeters, so that instrument error is not responsible. Previous low-Reynolds-number simulations of near-equilibrium flows (above) showed smaller effects, plausibly attributable to the transience of the structural changes.

The 3-D boundary-layer simulations certainly show this lag in shear-stress direction, which is qualitatively deducible directly from the Reynolds-stress transport equations (if compensating behavior of the pressure-strain redistribution term is discounted), and which is qualitatively reproduced by most transport-equation turbulence models. It is not necessarily a universal phenomenon: Johnston (1970) showed an advance, rather than a lag, in the shear-stress direction in flow over a swept step, where large values of streamline curvature, $\partial V/\partial x$, may have intervened. In the present boundary layer, $-\overline{vw}$ in the outer layer seems to be of the opposite sign to that in the inner layer; *ipso facto* this cannot be explained by turbulent transport of $-\overline{vw}$ from below.

The 3-D boundary-layer simulation which proceeded to separation showed a pronounced decrease in the ratio of shear-stress magnitude to turbulent kinetic energy, a_1, but at the time of writing, the latest statistics for the non-separating run shows no significant decrease in this structural parameter (figure 6). Roughly the same

small decrease in a_1 in the inner layer near separation occurs in the 2-D simulation, probably as the results of contributions to turbulent energy near the wall by the "inactive motion" mentioned above. Since the maximum crossflow (W/U) is almost as large in the present 3-D simulation (figure 5) as in the experiment, the absence of the decrease in stress-energy ratio cannot be explained away by hypothesizing that $a_1$is a rapidly-increasing function of crossflow.

In the experiments, the reduction in stress/energy ratio is accompanied by a reduction in the dimensionless ratio of triple products to (turbulent energy)$^{3/2}$; simulation results are not adequately converged to confirm this finding but are not in disagreement with it.

Complete budgets for all six Reynolds stresses are being accumulated. Shear-stress budgets appear to be close to equilibrium between the "generation" terms (involving mean velocity gradients) and the pressure-strain terms. This is partly misleading, because the "rapid" part of the pressure-strain term also depends on the mean velocity gradient and can be interpreted as an immediate opposition to the generation terms. If the generation terms and the "rapid" term (of opposite sign) are lumped together, their net sum is roughly equal to the "slow" part of the pressure-strain term and is not an order of magnitude larger than the mean and turbulent transport terms. Then, the shear-stress budget looks rather like the turbulent energy budget. Unfortunately, the "slow" and "rapid" parts of the pressure-strain term have not been evaluated separately in the present simulation.

5. Conclusions

Study of a previous simulation of 3-D duct flow (Moin *et al.* 1990) have shown that the distortion of the isocorrelation contours by crossflow, to first order explicable by pure convection in the crossflow shear plane, in fact involves rotation as well as shearing of the correlation pattern. In this simulation, crossflow is generated by Reynolds-stress gradients rather than by skewing of the initial spanwise vorticity, and strong crossflow is found only within the viscous wall region. Therefore, although the rotation of the correlation pattern is compatible with the idea of eddy "toppling" in crossflow advanced by Bradshaw & Pontikos (1985), it cannot be regarded as proof.

A spatially-varying boundary layer simulation is now being run in the same geometry as an (idealized) 3-D wing experiment of 10 years ago (Pontikos 1980, Bradshaw & Pontikos 1985). Again, the Reynolds number of the simulation is low enough to raise doubts about quantitative results, but the numerical accuracy of the output is not in dispute. The simulation has not yet been run long enough for statistical averages to be reliable, but when the simulation and its 2-D counterpart have run to convergence, they will provide test cases for Reynolds-averaged prediction methods and/or data for the refinement of such methods.

The 3-D boundary layer results available at the time of writing suggest that the decrease in the ratio of shear-stress magnitude to turbulent energy with increasing crossflow is not as large as has been found in several experiments; however, a previous simulation which proceeded to self-induced separation and thus incurred

significant numerical errors did show reductions of the same order as found in experiment. The present simulation suggests that the shear-stress vector in the outer layer rotates in the opposite direction to the velocity-gradient vector.

Triple products take longer to converge than second-order products; the current simulation has not run long enough for meaningful turbulent-transport terms (*derivatives* of triple products) to be extracted.

6. Acknowledgements

We are grateful to Dr. Parviz Moin for encouraging us to study the 3-D duct simulation, and to Dr. Philippe Spalart, both for planning the 3-D boundary-layer simulation and for his patient advice and guidance at all stages of this work. PB is fairly grateful to Dr. Spalart for showing that the time-lag between experiment (Pontikos 1980) and simulation is now only 10 years.

REFERENCES

ANDERSON, S. D. & EATON, J. K. 1987 Experimental study of a pressure-driven, three-dimensional, turbulent boundary layer. *AIAA J.* **25,** 1086.

V.D. BERG, B., ELSENAAR, A., LINDHOUT, J. P. F. & WESSELING, P. 1975 Measurements in an incompressible three-dimensional turbulent boundary layer, under infinite swept wing conditions, and comparisons with theory. *J. Fluid Mech.* **70,** 127.

BRADSHAW, P. & PONTIKOS, N. S. 1985 Measurements in the turbulent boundary layer on an 'infinite' swept wing. *J. Fluid Mech.* **159,** 105.

COLEMAN, G. N., FERZIGER, J. H. & SPALART, P. R. 1990 A numerical study of the turbulent Ekman layer. *J. Fluid Mech.* **213,** 313.

KIM, J., MOIN, P., & MOSER, R. 1987 Turbulence statistics in fully developed channel flow at low Reynolds number. *J. Fluid Mech.* **177,** 133.

MOIN, P., SHIH, T. H., DRIVER, D. M. & MANSOUR, N. N. 1990 Direct numerical simulation of three-dimensional turbulent boundary layer. *Phys. Fluids A.* **2** (10), 1846.

PONTIKOS, N. S. 1980 PhD thesis, Imperial College, London.

SPALART, P. R. 1989 Theoretical and numerical study of a three-dimensional turbulent boundary layer. *J. Fluid Mech.* **205,** 319.

TOWNSEND, A. A. 1961 Equilibrium layers and wall turbulence. *J. Fluid Mech.* **11,** 97.

WATMUFF, J. H. 1989 An experimental investigation of a low Reynolds number turbulent boundary layer subject to an adverse pressure gradient. *Ames/Stanford CTR Annual Research Briefs, 1988* 153.

Center for Turbulence Research
Proceedings of the Summer Program 1990

Low Reynolds number k-ϵ modeling with the aid of direct simulation data

By W. Rodi[1] AND N. N. Mansour[2]

The constant C_μ and the near-wall damping function f_μ in the eddy-viscosity relation of the k-ϵ- model are evaluated from direct numerical simulation (DNS) data for developed channel and boundary layer flow at two Reynolds numbers each. Various existing f_μ- model functions are compared with the DNS data, and a new function is fitted to the high-Reynolds-number channel flow data. The ϵ-budget is computed for the fully developed channel flow. The relative magnitude of the terms in the ϵ-equation is analyzed with the aid of scaling arguments, and the parameter governing this magnitude is established. Models for the sum of all source and sink terms in the ϵ-equation are tested against the DNS data, and an improved model is proposed.

1. Introduction

The k-ϵ model has become one of the most popular turbulence models used regularly in many calculations of flows of practical interest. In the past, k-ϵ model calculations were mostly carried out in conjunction with wall functions bridging over the viscosity-affected near-wall region. Recently, however, low-Reynolds-number (low-Re) versions of the k-ϵ model are being used in which the near-wall region is resolved. These versions contain damping functions and extra terms in order to account for the observed near-wall effects, and, in most cases, these terms and functions have been made to depend on the viscosity. A wide variety of model versions has been proposed in the literature. The pre-1984 models were reviewed in Patel *et al.* (1985). Since then, a number of newer proposals have emerged (see *e.g.* Shih and Mansour, 1990).

The extra terms and functions in low-Re k-ϵ models have not been derived on the basis of data but on various modeling arguments, and they have only been subjected to indirect testing by calculating various flows with the models. The same is true for the entire ϵ-equation, even the high Reynolds number (high-Re) version, which must be considered empirical. Direct numerical simulation (DNS) data are now available with which the individual model assumptions can be tested directly. The data can also be used as a basis for the development of improved models. The DNS data available are still for flows at fairly low Reynolds numbers, but they are suitable for examining the near-wall behavior of models and for aiding the development of realistic models in this region.

1 University of Karlsruhe, F. R. Germany
2 NASA Ames Research Center

In the work reported here, two main issues were investigated with the aid of DNS data. The first one is the behavior of the coefficient in the eddy-viscosity expression in k-ϵ models, particularly near walls. The second issue is the model form of the ϵ-equation. For high Reynolds numbers, where the energy-containing and dissipative motions are very different in scale, the exact ϵ-equation provides little if any guidance. But in low-Reynolds-number regions near walls the situation is different because the scales of energy-containing motions and the scales of dissipative motions are the same (Launder, 1986). In this case, the exact ϵ-equation is useful for identifying and describing the various near-wall influences on ϵ. The terms in the exact ϵ-equation cannot be measured and therefore information on these terms can only be obtained from DNS data. The data used in this work were for developed channel flow (Kim et al., 1987, and Kim, 1990) and for boundary layers in zero pressure gradient (Spalart, 1988) at two Reynolds numbers each. The dissipation rate budget could only be computed for the developed channel flow case. For the lower Reynolds number ($Re_\tau = 180$ based on friction velocity and channel half width), Mansour *et al.* (1988) have already provided the ϵ-budget and tested some model approximations. Here, the ϵ-budget is provided for Kim's (1990) new channel flow calculations at $Re_\tau = 395$. Some of the model versions considered more successful in Patel *et al.*'s (1985) review are tested against these data and new model proposals are made for the source/sink terms in the ϵ-equation.

2. Form of low-Reynolds-number k-ϵ models

The k-ϵ model employs the eddy viscosity concept, and for the various low-Re k-ϵ models proposed so far the relations for determining the eddy viscosity ν_t can be written for 2D shear layers in the following form

$$\nu_t = C_\mu f_\mu \frac{k^2}{\tilde{\epsilon}} \tag{1}$$

$$\frac{D}{Dt}k = \left[(\nu + \frac{\nu_t}{\sigma_k}k_{,y}\right]_{,y} + \nu_t(U_{,y})^2 - \epsilon \tag{2}$$

$$\frac{D}{Dt}\tilde{\epsilon} = \left[(\nu + \frac{\nu_t}{\sigma_\epsilon})\tilde{\epsilon}_{,y}\right]_{,y} + C_{\epsilon 1} f_1 \frac{\tilde{\epsilon}}{k}\nu_t(U_{,y})^2 - C_{\epsilon 2} f_2 \frac{\tilde{\epsilon}^2}{k} + E \tag{3}$$

$$\tilde{\epsilon} = \epsilon - D \tag{4}$$

The various models differ through the use of different functions f_μ, f_1, f_2 and different terms D and E. In the eddy-viscosity relation (1), C_μ is a constant coefficient while f_μ is a damping function reducing the eddy viscosity near the wall. Some models use as turbulence time scale k/ϵ and solve an equation for ϵ itself (effectively putting D to zero), while other models use as time scale $k/\tilde{\epsilon}$ and solve an equation for $\tilde{\epsilon}$ which, in contrast to ϵ, goes to zero at the wall. The function f_2 in the $\tilde{\epsilon}$-equation is usually effective only very close to the wall and is introduced to simulate the change in the decay rate of homogeneous turbulence as the

Model	Code	D	$\tilde{\epsilon}_w$ - B.C.	C_μ	$C_{\epsilon 1}$	$C_{\epsilon 2}$	σ_k	σ_ϵ	E
Launder-Sharma	LS	$2\nu\left(\sqrt{k}_{,y}\right)^2$	0	0.09	1.44	1.92	1.0	1.3	$2\nu\nu_t\left(U_{,yy}\right)^2$
Chien	CH	$2\nu k/y^2$	0	0.09	1.35	1.8	1.0	1.3	$-2\nu\tilde{\epsilon}/y^2\exp(-0.5y^+)$
Lam-Bremhorst	LB	0	$\nu k_{,yy}=0$ or $\epsilon_{,y}=0$	0.09	1.44	1.92	1.0	1.3	0

Table 1a. Summary of Constants, terms and boundary conditions used in existing low-Reynolds number k-ϵ models.

Model	Code	f_μ	f_1	f_2
Launder-Sharma	LS	$\exp(-3.4/(1+Re_t/50)^2)$	1.	$1-0.3\exp(-Re_t^2)$
Chien	CH	$1-\exp(-0.0115y^+)$	1.0	$1-0.22\exp[-(Re_t/6)^2]$
Lam-Bremhorst	LB	$[1-\exp(-0.0165y^*)]^2\times(1+20.5/Re_t)$	$1+(0.05/f_\mu)^3$	$1-\exp(-Re_t^2)$

Table 1b. Summary of damping functions used in existing low-Reynolds number k-ϵ models ($Re_t=k^2/\nu\epsilon$, $y^+=U_\tau y/\nu$, $y^*=k^{1/2}y/\nu$).

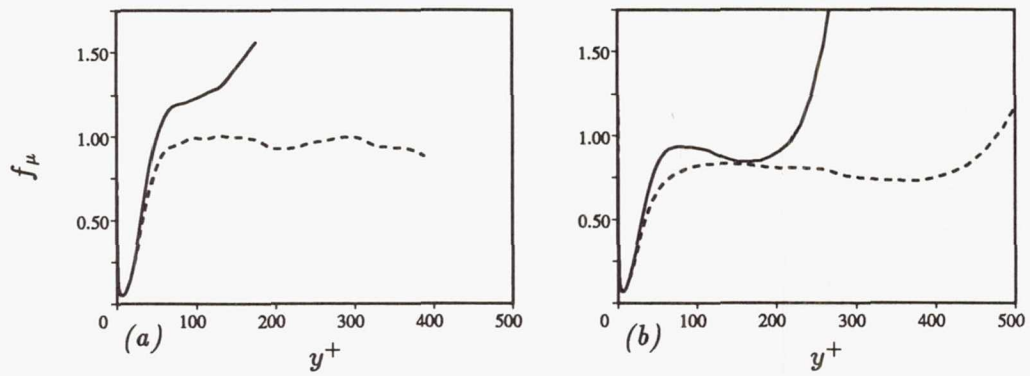

FIGURE 1. f_μ-distribution ($f_\mu = \nu_t\epsilon/C_\mu k^2$ with $C_\mu = 0.09$). *(a)* Channel flow at —— $Re_\tau = 180$, ---- $Re_\tau = 395$. *(b)* Boundary layer at —— $Re_\theta = 670$, ---- $Re_\theta = 1416$.

Reynolds number $Re_t(= k^2/\nu\epsilon)$ becomes small. The extra term E or alternatively the function f_1 were introduced to increase the ϵ-production near the wall. A general discussion on the functions and extra terms in the various models proposed until 1984 can be found in Patel *et al.* (1985). Here, attention is focused on the damping function f_μ and on the ϵ-equation (3), and with the aid of DNS data the performance of the three low-Re k-ϵ models rated best in the review of Patel *et al.* (1985) is examined. These are the models due to Launder and Sharma (1974 - hereafter referred to as LS), Lam and Bremhorst (1981 - hereafter referred to as LB) and Chien (1982 - hereafter referred to as CH). The constants and functions used in these three models are compiled in Table 1.

All of the models considered are of the form such that when f_μ, f_1, f_2 are set to 1, and terms D and E are set to zero, the standard high-Re version of the k-ϵ model is recovered.

3. C_μ-constant and f_μ-function

With $C_\mu = 0.09$ chosen as used in standard k-ϵ models, the function f_μ in the eddy-viscosity relation (1) was determined from DNS data for developed channel flow and boundary-layer flow at two Reynolds numbers each. The resulting f_μ-distributions are plotted versus $y^+ = U_\tau y/\nu$ in Fig. 1. Away from the wall, the f_μ-distribution gives an indication of the value of C_μ, which should be constant ($f_\mu = 1.0$ when $C_\mu = 0.09$). Indeed, Fig. 1a shows, for the higher Reynolds number channel flow, that C_μ is roughly .09 over more than three quarters of the channel depth. It should be noted that this is in contrast to Rodi's (1975) evaluation of Laufer's (1954) experimental pipe-flow data which show C_μ to increase towards the pipe axis where the ratio of production to dissipation of turbulence energy, P/ϵ, goes to zero. For the channel with $Re_\tau = 180$, a higher C_μ-value results in the central part of the channel. In contrast, the C_μ-value in the boundary layer, not too close to the wall, is approximately only .075. The behavior of C_μ (or rather $C_\mu f_\mu$) can be explained via the distributions of $\overline{u'v'}/k$ and P/ϵ since (1) and (2)

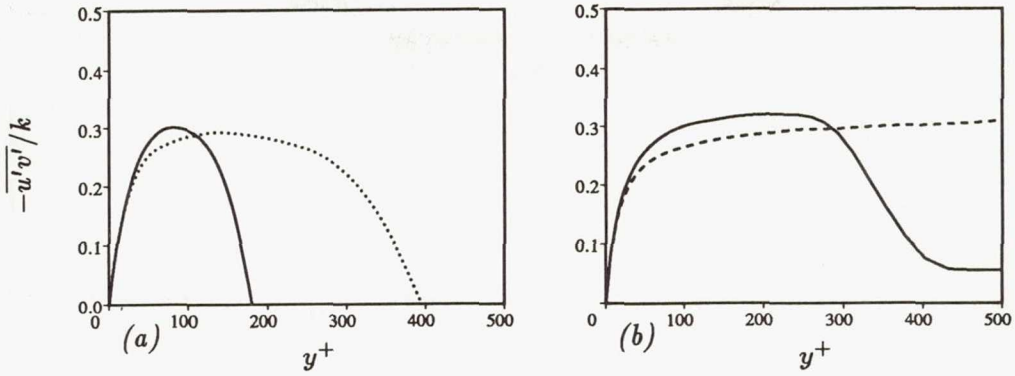

FIGURE 2. Distribution of the structure parameter $-\overline{u'v'}/k$. *(a)* Channel flow at —— $Re_\tau = 180$, ---- $Re_\tau = 395$. *(b)* Boundary layer at —— $Re_\theta = 670$, ---- $Re_\theta = 1416$.

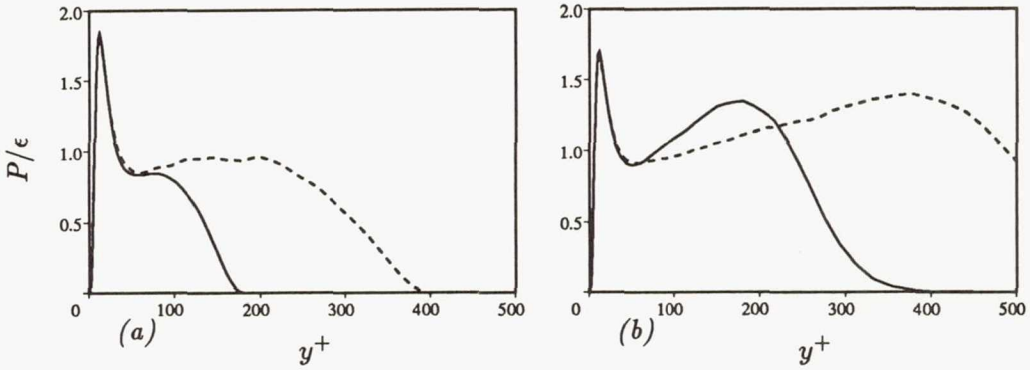

FIGURE 3. Distribution of the ratio of production to dissipation of turbulent kinetic energy, P/ϵ. *(a)* Channel flow at —— $Re_\tau = 180$, ---- $Re_\tau = 395$. *(b)* Boundary layer at —— $Re_\theta = 670$, ---- $Re_\theta = 1416$.

can be combined to yield

$$f_\mu C_\mu = \left(\frac{\overline{u'v'}}{k}\right)^2 / \frac{P}{\epsilon} \tag{5}$$

$C_\mu = 0.09$ (with $f_\mu = 1$) corresponds to $P/\epsilon = 1$ (local equilibrium) and the often measured value of the structure parameter $-\overline{u'v'}/k = 0.3$. Figs. 2 and 3 show respectively, again for channel and boundary-layer flows, the distributions of the parameters $-\overline{u'v'}/k$ and P/ϵ determining $C_\mu f_\mu$ according to relation (5). In the low-Re channel, the ratio P/ϵ has only a value of about 0.85 in the region where $-\overline{u'v'}/k \approx .3$, which explains the higher $C_\mu f_\mu$-value. In the high-Re channel, P/ϵ drops faster than $-\overline{u'v'}/k$ towards the channel center so that $(\overline{u'v'}/k)^2/P/\epsilon \approx$ constant which explains the constant value of $C_\mu f_\mu$ in the central portion of the channel. In the boundary layer, $-\overline{u'v'}/k$ approaches 0.3 only where the ratio P/ϵ is

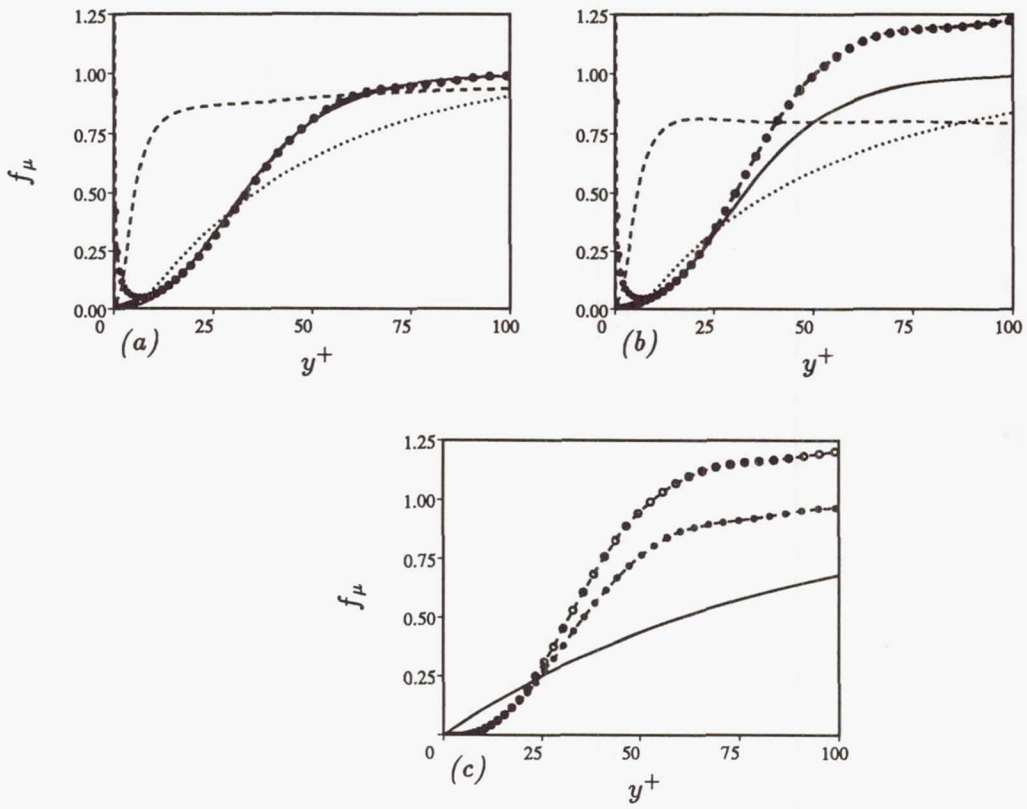

FIGURE 4. Comparison of various f_μ-model functions with DNS data for channel flow. *(a)* •-•-• DNS $Re_\tau = 395$, —— new correlation, ---- LS, ····· LB. *(b)* •-•-• DNS $Re_\tau = 180$, —— new correlation, ---- LS, ····· LB. *(c)* ⊖-⊖-⊖ DNS $Re_\tau = 180$, •-•-• DNS $Re_\tau = 395$, —— CH.

significantly larger than 1, which leads to the relatively low value of $C_\mu f_\mu \approx 0.075$ over larger parts of the boundary layer. More towards the edge of the boundary layer, where P/ϵ tends to zero, $C_\mu f_\mu$ increases.

The foregoing has shown that the use of a constant value of $C_\mu = 0.09$ can generally be only a rough approximation. When this value is chosen and when f_μ is introduced to represent the damping of the eddy viscosity near the wall, then f_μ must take a value of 1 away from the wall, which of course cannot agree with all the DNS data. For the near-wall region ($y^+ < 100$) in channel flow, Fig. 4 compares the f_μ-functions due to LS, LB and CH with the DNS data for both Reynolds numbers, and Fig. 5 provides a similar comparison for the higher Reynolds number boundary-layer flow. Very near the wall, two sets of DNS data have to be distinguished: one using ϵ itself in the eddy-viscosity relation (1) which causes f_μ to behave as $1/y$ since ϵ is finite at the wall; the other set of data is based on the use of the modified dissipation rate $\tilde{\epsilon}$ which varies as y^2 very near the wall so that f_μ goes to zero at the wall as y. The LS and CH models use $\tilde{\epsilon} \neq \epsilon$ so that their f_μ-functions should

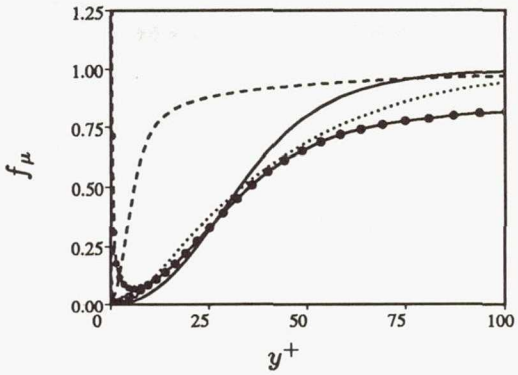

FIGURE 5. Comparison of various f_μ-model functions with DNS data for boundary layer ($Re_\theta = 1416$). •–•–• DNS, —— new correlation, - - - - LS, ····· LB.

and do go to zero at the wall.[1] However, the CH function can be seen to rise and approach the value of unity far too slowly, while the LS function initially rises far too quickly but then also has a rather slow approach to the value of 1. That the f_μ-function due to LS never rises beyond 0.8 for the low-Re channel case is due to the fact that the argument of the f_μ-function, Re_t, rises to a maximum at $y^+ \approx 20$ and then falls again. The model of LB uses ϵ and hence f_μ should increase very close to the wall; but this f_μ-function also goes to zero at the wall, which causes ν_t to behave as y^4 instead of y^3. The following increase in f_μ is simulated fairly well by the LB function, but then it approaches unity somewhat too slowly. The fairly good agreement for the boundary layer (Fig. 5) is somewhat misleading because the far-wall value of the data is lower than 1. There seems to be some influence of the Reynolds number on the f_μ-distribution in an f_μ vs. y^+-plot, but in view of the differences between various wall-bounded flows, the inclusion of such effects in a single model is not warranted. Hence, a y^+-dependent f_μ-function based on the data for the high-Re channel flow appears as a reasonable compromise, and by curve-fitting, the following f_μ-function has been determined:

$$f_\mu = \frac{(1 - \exp(-0.048y^+))^2}{(1 + 6.\exp(-0.085y^+))} \tag{6}$$

This relation, which is also included in Figs. 4 and 5, is only suitable for attached flows, while in separated flows the argument y^+ should be replaced by $Re_y = k^{1/2}y/\nu$.

Durbin (1990) suggested to use the normal fluctuations $(\overline{v'^2})^{1/2}$ as velocity scale in the eddy-viscosity relation (1) instead of $k^{1/2}$ and argued that a damping function would not be needed in this case. His eddy-viscosity relation reads:

$$\nu_t = C_\mu \overline{v'^2} T \tag{7}$$

[1] The f_μ-function due to CH had to be presented on a different graph because CH uses a different D and hence a different definition of $\tilde{\epsilon}$, resulting also in different DNS data curves.

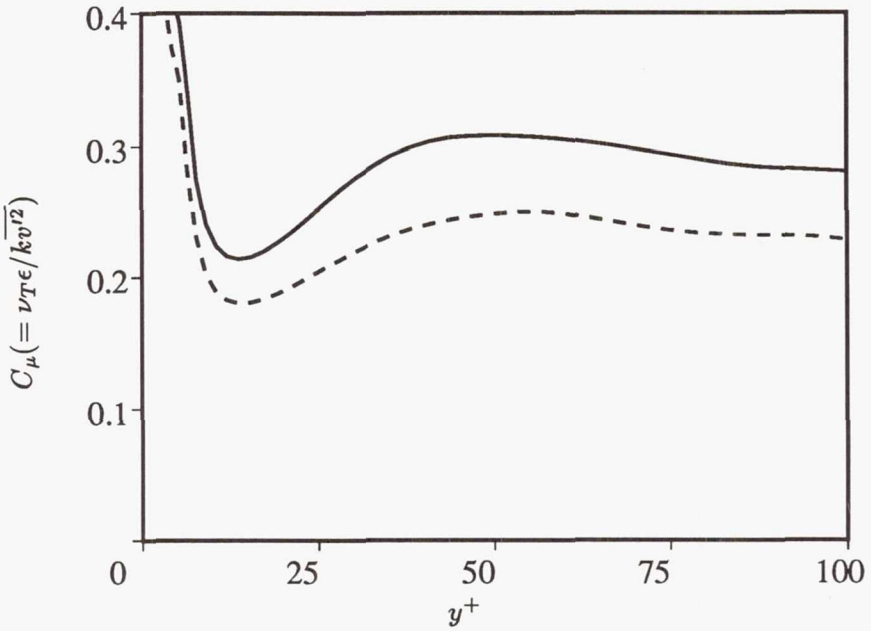

FIGURE 6. Distribution of C_μ in Durbin's (1990) model. —— $Re_\tau = 395$; ---- $Re_\tau = 180$.

with the time scale T determined from

$$T = \max\left(\frac{k}{\epsilon}, 6\left(\frac{\nu}{\epsilon}\right)^{1/2}\right) \tag{8}$$

It has been shown before by Launder (1986) that the near-wall damping expressed through the function f_μ in (1) is not so much due to viscous effects but mainly due to the damping of the normal fluctuations v' by the pressure-reflection mechanism and that f_μ therefore correlates very well with $\overline{v'^2}/k$. Hence it is interesting to test Durbin's model proposal (7) with the aid of DNS data. Fig. 6 shows C_μ in relation (7) determined from the channel-flow data at two Reynolds numbers. It can be seen that C_μ is indeed fairly constant down to $y^+ \approx 10$. The C_μ-value depends somewhat on the Reynolds number as was noted already above in the context of C_μ appearing in (1). Very close to the wall, where the time scale T according to (8) adopts a finite value, C_μ behaves as $1/y$. The use of a constant C_μ leads to $\nu_t \propto y^4$, and the correct ν_t-distribution near the wall ($\nu_t \propto y^3$) can only be obtained by introduction of a damping function in this region.

4. ϵ-budget

The exact equation for $\epsilon (= \nu\overline{u'_{i,j}u'_{i,j}})$ derived from the Navier-Stokes equations can be written in tensor form as

$$\frac{D}{Dt}\epsilon = P_\epsilon^1 + P_\epsilon^2 + P_\epsilon^3 + P_\epsilon^4 + T_\epsilon + \Pi_\epsilon + D_\epsilon - \Upsilon \tag{9}$$

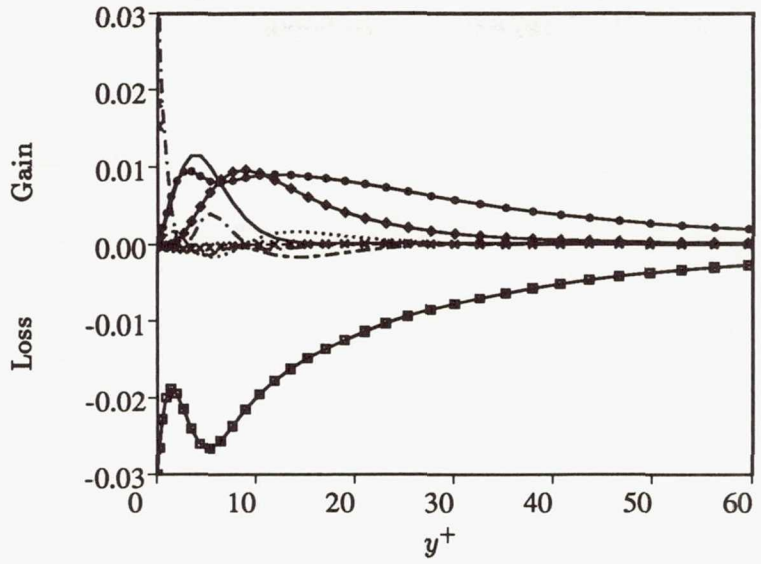

FIGURE 7. ϵ-budget for channel flow $Re_\tau = 395$. —— P_ϵ^1; ◇◇◇ P_ϵ^2; ····· P_ϵ^3; ●–●–● P_ϵ^4; – – – T_ϵ; – – – – Π_ϵ; —·— D_ϵ; ▫▫▫▫ Υ; × × × × sum of all terms.

where the individual terms on the right-hand side are defined and identified as

$P_\epsilon^1 = -\nu 2\overline{u'_{i,j}u'_{k,j}}S_{ik}$	Mixed production
$P_\epsilon^2 = -\nu 2\overline{u'_{i,k}u'_{i,m}}S_{km}$	Production by mean velocity gradient
$P_\epsilon^3 = -\nu 2\overline{u'_k u'_{i,m}}U_{i,km}$	Gradient production
$P_\epsilon^4 = -\nu 2\overline{u'_{i,k}u'_{i,m}u'_{k,m}}$	Turbulent production
$T_\epsilon = -\nu(\overline{u'_k u'_{i,m}u'_{i,m}})_{,k}$	Turbulent transport
$\Pi_\epsilon = -\nu\frac{2}{\rho}(\overline{p'_{,m}u'_{k,m}})_{,k}$	Pressure transport
$D_\epsilon = \nu\epsilon_{,kk}$	Viscous diffusion
$\Upsilon = \nu^2 2\overline{u'_{i,km}u'_{i,km}}$	Dissipation

and $S_{ij} = (U_{i,j} + U_{j,i})/2$ is the mean strain rate. For developed channel flow, the left-hand side is zero so that the terms on the right-hand side should balance each other. Mansour *et al.* (1988) have calculated the ϵ-budget from the DNS data for the low-Re channel flow. The ϵ-budget evaluated from the data for the channel with $Re_\tau = 395$ is given in Fig. 7. All terms have been made dimensionless with U_τ^6/ν^2. The imbalance in the budget (crosses) is also given; this is a measure of the errors in the budget terms due to discretization and limited sample size. As can be seen, the

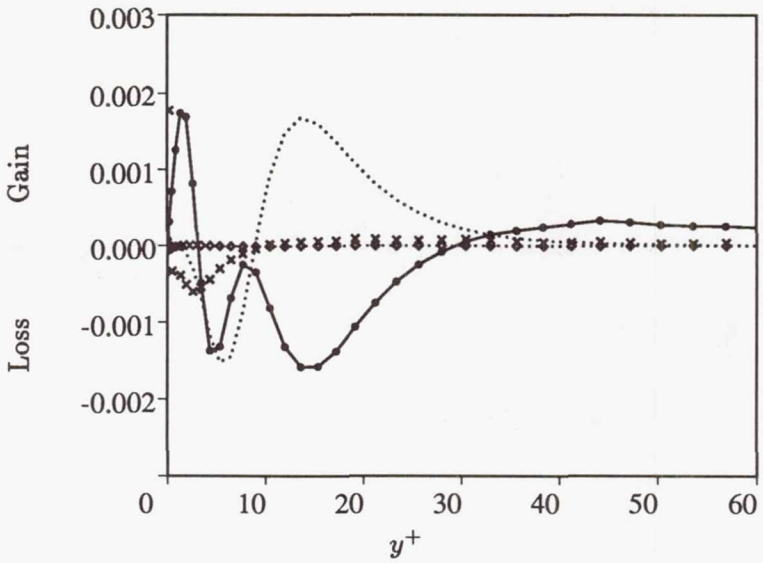

FIGURE 8. Small terms in ϵ-budget for channel flow $Re_\tau = 395$. ····· P_ϵ^3; ●–●–● T_ϵ; ◇–◇–◇ Π_ϵ; × × × × sum of all terms.

imbalance is fairly small except very close to the wall ($y^+ < 8$) so that the ϵ-budget determined from the DNS data can be considered accurate for $y^+ > 8$. As was to be expected from the order of magnitude analysis of Tennekes and Lumley (1972), the turbulent production rate P_ϵ^4 due to vortex stretching and the viscous destruction Υ dominate the balance equation in the high-Reynolds-number region away from the wall. However, near the wall, the production terms P_ϵ^1 and P_ϵ^2 become equally important, and at the wall itself viscous destruction is balanced by viscous diffusion and pressure transport. The smaller terms P_ϵ^3, T_ϵ and Π_ϵ are shown in Fig. 8 on an expanded scale. The imbalance can be seen to be small even compared with these small terms for $y^+ > 8$, and the pressure diffusion Π_ϵ can be seen to be negligible everywhere. On the other hand, the relatively small production term P_ϵ^3 is of the same order of magnitude as the turbulent diffusion T_ϵ.

The terms P_ϵ^4 and Υ increase with increasing Reynolds number, but their difference remains independent of Reynolds number (once this is sufficiently high); the latter is true also for the rate of change and transport terms, of which in the channel flow situation only the diffusion term is non-zero. According to Tennekes and Lumley (1972), the terms P_ϵ^1 and P_ϵ^2 relative to the difference $(P_\epsilon^4 - \Upsilon)$ are of order $1/Re^{1/2}$. Fig. 9 shows the sum $P_\epsilon^1 + P_\epsilon^2$ and the difference $P_\epsilon^4 - \Upsilon$ for channel flow at both Reynolds numbers investigated. With the non-dimensionalization chosen, there is no noticeable Reynolds-number influence on either group of terms away from the wall. Near the wall, both groups go up somewhat with the Reynolds number. Also, it is clear that the destruction term Υ adjusts to the increase of ϵ-production due to P_ϵ^1 and P_ϵ^2 near the wall and in fact tends to overreact somewhat. The sum of all source and sink terms (i.e. $P_\epsilon^1 + P_\epsilon^2 + P_\epsilon^3 + P_\epsilon^4 - \Upsilon$) is also

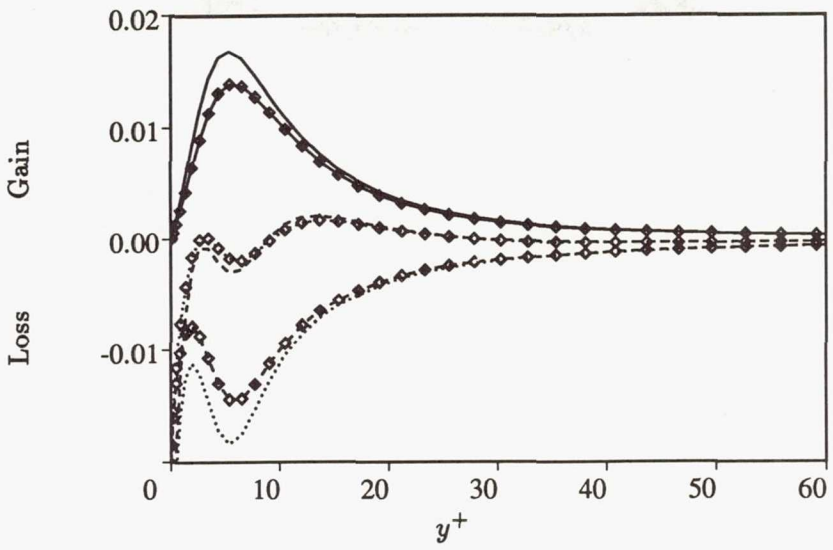

FIGURE 9. Distribution of $P_\epsilon^1 + P_\epsilon^2$, $P_\epsilon^4 - \Upsilon$ and sum of all source and sink terms in channel flow. —— $P_\epsilon^1 + P_\epsilon^2$, $Re_\tau = 395$; ····· $P_\epsilon^4 - \Upsilon$, $Re_\tau = 395$; ---- $P_\epsilon^1 + P_\epsilon^2 + P_\epsilon^3 + P_\epsilon^4 - \Upsilon$, $Re_\tau = 395$; ◇-◇-◇ $P_\epsilon^1 + P_\epsilon^2$, $Re_\tau = 180$; ◇-◇-◇ $P_\epsilon^4 - \Upsilon$, $Re_\tau = 180$; ◇·◇·◇ $P_\epsilon^1 + P_\epsilon^2 + P_\epsilon^3 + P_\epsilon^4 - \Upsilon$, $Re_\tau = 180$.

included in Fig. 9. This sum, which is little influenced by the Reynolds number, is very small compared with the actual terms in the ϵ-equation. It is this sum which, in general, balances the rate of change, convective and diffusive transport terms in the ϵ-equation and therefore governs the magnitude of ϵ. Hence it is only this sum that really matters and has to be modelled. Because of the small magnitude of the net source compared with the original terms in the ϵ-equation, the usefulness of the exact ϵ-equation has sometimes been considered doubtful. However, even though this source is small it is still finite and balances the rate of change and transport of ϵ. At high Reynolds numbers, where an inertial subrange exists, the source/sink terms are given by the integral over the low-wave number part of the spectrum of the spectral transfer function multiplied by the wave number squared (see *e.g.* Rodi, 1971). This shows that ϵ is governed by the larger-scale turbulent motions which are independent of Reynolds number.

5. Scaling arguments

Tennekes and Lumley (1972) made an order of magnitude analysis of the terms in the vorticity-fluctuation equation. The order of magnitude was expressed in terms of the velocity scale u, the macro-length-scale l and the Taylor micro-scale λ. They found that the relative magnitude of the individual terms and hence also the importance of the production terms P_ϵ^1 and P_ϵ^2 depends on the Reynolds number $Re_l = ul/\nu$. In a study of homogeneous shear flow, Bardina (1988) argued that the Reynolds number is not the only parameter determining the relative importance of the P_ϵ^1 and P_ϵ^2 production terms but that the mean shear number $S_n = Sk/\epsilon$ plays

also a role (S is the mean shear rate). His conclusions are of interest here, but his derivation seems not to be quite correct and also does not allow direct insight into the Re-dependence of the terms in the ϵ-equation. Hence, scaling arguments are elaborated here once more.

Because of the close relation between the dissipation rate ϵ and the fluctuating vorticity $\overline{\omega_i'\omega_i'}$ (with $\epsilon = \nu\overline{\omega_i'\omega_i'}$ in homogeneous flows) the scaling arguments of Tennekes and Lumley can be applied directly to the ϵ-equation. When the strain rate in the terms P_ϵ^1 and P_ϵ^2 is not expressed as u/l but is retained as a strain-rate parameter S (which in channel flow is equal to the shear rate $\partial U/\partial y$) and with $\epsilon \propto \nu u^2/\lambda^2 \propto u^3/l$ and the velocity scale $u = k^{1/2}$, there follows the order of magnitude of the various terms as

$$P_\epsilon^1, \quad P_\epsilon^2 = O\left(S\frac{k^{3/2}}{l}\cdot\frac{\lambda}{l}\right) \tag{10}$$

$$P_\epsilon^4, \quad \Upsilon = O\left(\frac{k^2}{l^2}\cdot\frac{l}{\lambda}\right) \tag{11}$$

$$P_\epsilon^4 - \Upsilon, \quad \frac{D}{Dt}\epsilon, \quad T_\epsilon = O\left(\frac{k^2}{l^2}\right) \tag{12}$$

Since $l/\lambda \propto Re_l^{1/2} \propto Re_t^{1/2}$, the terms P_ϵ^1 and P_ϵ^2 decrease as Re_t increases while the terms P_ϵ^4 and Υ increase. The difference of the latter terms, $P_\epsilon^4 - \Upsilon$, and also the rate of change and transport terms are independent of Reynolds number, as was mentioned already. The magnitude of the production terms P_ϵ^1 and P_ϵ^2 relative to the main terms in the model ϵ-equation (difference $P_\epsilon^4 - \Upsilon$ and transport terms) can now be established as:

$$\frac{P_\epsilon^1, \quad P_\epsilon^2}{P_\epsilon^4 - \Upsilon} = O\left(\frac{Sk}{\epsilon}\cdot\frac{1}{Re_t^{1/2}}\right) \tag{13}$$

The relative order of magnitude of P_ϵ^1 and P_ϵ^2 is therefore determined by the parameter

$$R = \frac{Sk}{\epsilon}\,\frac{1}{Re_t^{1/2}} = \frac{S}{(\epsilon/\nu)^{1/2}} \tag{14}$$

which indeed involves the parameter $S_n = Sk/\epsilon$. Relation (14) shows that the parameter R is the ratio of the time scale of the dissipative motion to the time scale of the mean strain field. Bardina (1988) also arrived at this parameter, but his derivation concerns the ratio of order of magnitudes of terms P_ϵ^1 and P_ϵ^2 to P_ϵ^4 and Υ, while here it represents the magnitude relative to the difference of the latter terms. The scaling arguments show that the production terms P_ϵ^1 and P_ϵ^2 are important when the parameter $R > 1$. Bardina (1988) examined two sets of homogeneous shear-flow data obtained by direct numerical simulations. For low shear cases with typically $R < .3$ the terms P_ϵ^1 and P_ϵ^2 were found small compared

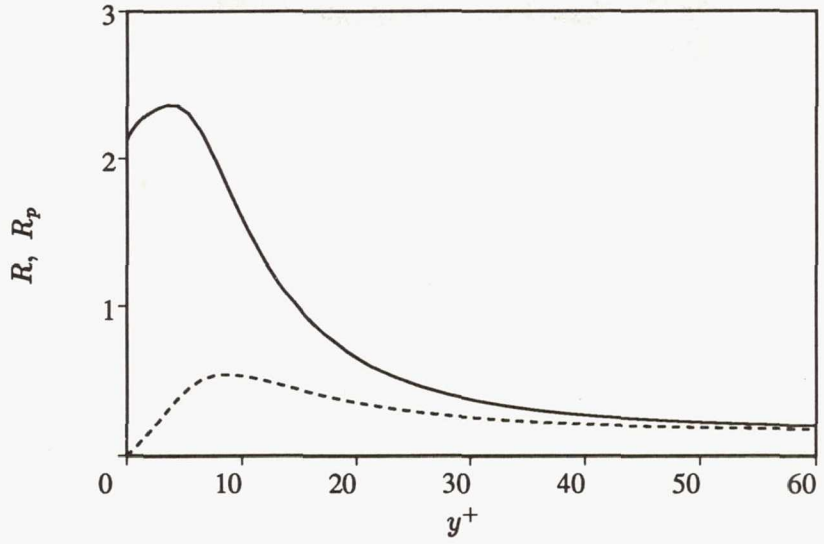

FIGURE 10. Distribution of parameters R and R_p in channel flow at $Re_\tau = 395$. —— R; ---- R_p.

with P_ϵ^4 while for the case with high shear (and low Reynolds number) characterized by $R = 6 - 15$, the terms P_ϵ^1 and P_ϵ^2 were found to be larger than P_ϵ^4.

The distribution of the parameter R in the channel flow with $Re_\tau = 395$ is shown in Fig. 10. It can be seen that in the bulk of the channel flow the parameter is substantially below 1 ($\approx .25$). In the near-wall region, where the terms P_ϵ^1 and P_ϵ^2 become important, the parameter R increases strongly and reaches a maximum value of 2.4.

6. Modeling the terms in the ϵ-equation

In order to turn the exact ϵ-equation into an equation that can be used in a turbulence model, the source and sink terms as well as the turbulent diffusion term need to be modelled. As was mentioned already, the sum of the source and sink terms is much smaller than the actual terms but it is still finite and in channel flow it is balanced by the equally small diffusion term. Models for the source and sink terms are considered first, and the starting point is the generally used basic model for high Reynolds number (or low R) situations where only $P_\epsilon^4 - \Upsilon$ is left. This difference is modelled as (see e.g. Launder *et al.*, 1975):

$$P_\epsilon^4 - \Upsilon = \left(C_{\epsilon 1} \frac{P}{\epsilon} - C_{\epsilon 2} \right) \frac{\epsilon^2}{k} \tag{15}$$

where P is the production of turbulent energy, that is the energy input into the low-wave-number part of the spectrum. The model relation (15) is compared in Fig. 11 with $P_\epsilon^1 + P_\epsilon^2 + P_\epsilon^4 - \Upsilon$ and in Fig. 14 with the sum of all source and sink terms ($C_{\epsilon 2}$ is multiplied by the damping function f_2 according to Table 1, but f_2

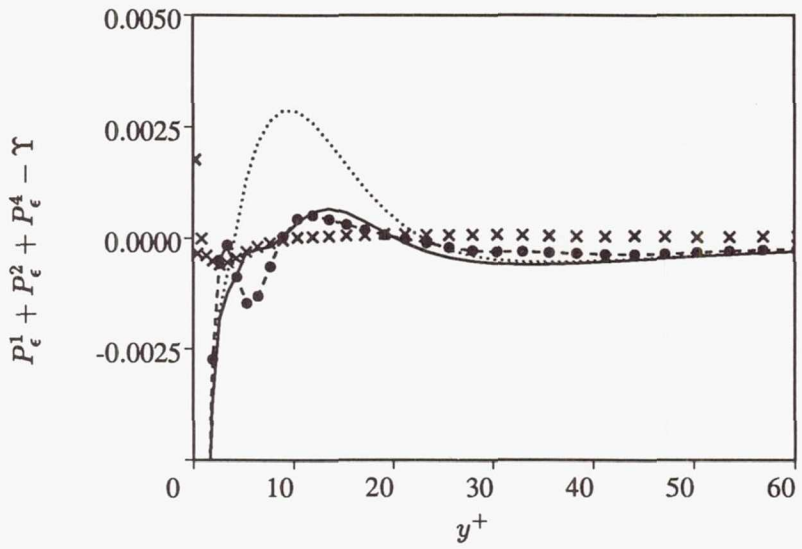

FIGURE 11. New model for source/sink terms $P_\epsilon^1 + P_\epsilon^2 + P_\epsilon^4 - \Upsilon$ compared with DNS data ($Re_\tau = 395$). •—•—• DNS data; ——— new model; ····· High-Re model; × × × sum of all terms.

is effective only for $y^+ < 5$). Depending somewhat on the constants $C_{\epsilon 1}$ and $C_{\epsilon 2}$ used, the basic model can be seen to simulate fairly well the sum of source and sink terms away from the wall, where P_ϵ^1, P_ϵ^2 and P_ϵ^3 are unimportant. The question is now how to bring in the influence of the production terms P_ϵ^1, P_ϵ^2 and P_ϵ^3 and the consequential increase in the destruction term Υ. The terms P_ϵ^1 and P_ϵ^2 involving the mean strain rate (first derivatives of velocities) are treated separately from the term P_ϵ^3 involving second derivatives.

6.1 Modeling the effect of P_ϵ^1 and P_ϵ^2.

One possibility would be to add modelled terms of P_ϵ^1 and P_ϵ^2. P_ϵ^1 can be expressed as $-\epsilon_{ij} U_{i,j}$, where ϵ_{ij} is the dissipation rate of the Reynolds-stress component $\overline{u_i' u_j'}$; this term is therefore closely related to $\epsilon^2/k \times P/\epsilon$ and hence effectively increases the value of the coefficient $C_{\epsilon 1}$ in (15), depending on P/ϵ. With such modeling of P_ϵ^1, and similar one for P_ϵ^2, the sink term would have to be cranked up drastically in order to account for the adjustment of Υ due to the extra production by P_ϵ^1 and P_ϵ^2. As an alternative, the suggestion is therefore made here to model the influence of the combined effect of P_ϵ^1 and P_ϵ^2 and Υ, which is to increase somewhat the sink term in the ϵ-equation. First the time-scale ratio R seemed to be a suitable parameter as it governs the relative importance of the terms P_ϵ^1 and P_ϵ^2, but it was found not to correlate too well. The close relation of P_ϵ^1 to the ratio of production to dissipation, P/ϵ, suggests that this ratio is an important parameter and was therefore taken to replace the strain-rate parameter kS/ϵ in (14). Of course the influence of the Reynolds number Re_t must be retained. The resulting parameter

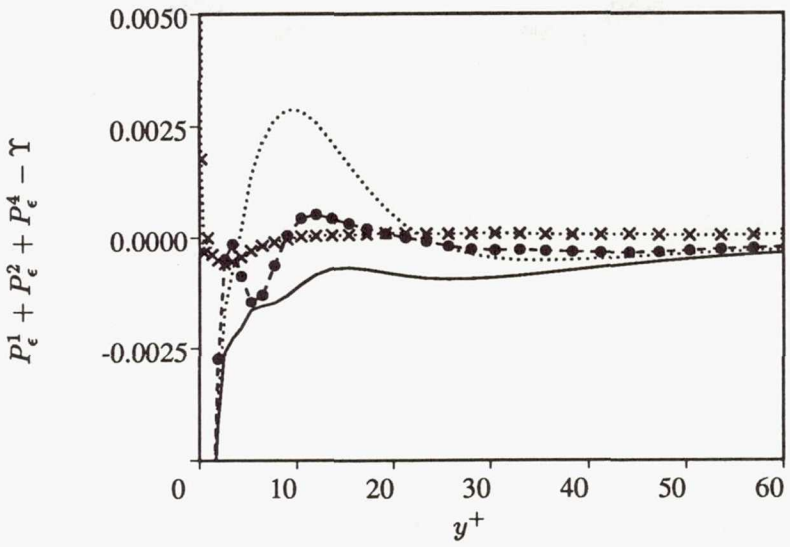

FIGURE 12. Bardina's model for source/sink terms $P_\epsilon^1+P_\epsilon^2+P_\epsilon^4-\Upsilon$ compared with DNS data ($Re_\tau = 395$). •–•–• DNS data; —— Bardina's model;····· High-Re model; × × × sum of all terms.

is

$$R_p = \frac{P/\epsilon}{.3Re_t^{1/2}} = \frac{P/k}{.3(\epsilon/\nu)^{1/2}} \tag{16}$$

which is also a time-scale ratio, namely the ratio of the time scale of the dissipating motion to the time scale P/k involving the production of turbulence. The variation of the parameter R_p in channel flow is shown in Fig. 10.

The combined effect of P_ϵ^1, P_ϵ^2 and the increase in Υ is accounted for in the new model by multiplying the coefficient $C_{\epsilon 2}$ in the sink term of (15) by the following function:

$$f_3 = \exp(2R_p^3) \tag{17}$$

This was obtained by fitting the exponential function to the DNS data of Fig. 11. The effect of this function can be seen in Fig. 11; it is restricted to the near-wall region of $y^+ < 30$. The new model simulates quite well the distribution of the source and sink terms $P_\epsilon^1 + P_\epsilon^2 + P_\epsilon^4 - \Upsilon$ down to $y^+ \approx 8$, below which the DNS results are not very reliable anyway.

6.2 Bardina's model.

Bardina (1988) suggested to account for the influence of high shear characterized by high values of the parameter R by adding an extra term to the ϵ-equation which involves the mean rotation Ω. This model suggestion is based on his previous work on turbulence under the influence of rotation (Bardina *et al.*, 1983). The extra term is

$$-\left(C_{\Omega 1}\frac{P}{\epsilon} + C_{\Omega 2}\right)\frac{\Omega k}{\epsilon}\,\frac{\epsilon^2}{k} \tag{18}$$

In his study on homogeneous shear layers, Bardina (1988) found that with this extra term (with constants $C_{\Omega 1} = 0.015$ and $C_{\Omega 2} = 0.15$) the sum of the source and sink terms ($P_\epsilon^1 + P_\epsilon^2 + P_\epsilon^4 - \Upsilon$) are modelled quite well also for the high shear case; without the extra term, only the low-shear situation was simulated well. It should be added here that the high-shear case was at a rather low Reynolds number. Bardina's model, with his constants, was tried on the channel flow, and the results are shown in Fig. 12. The model can be seen to have the correct trend, namely to reduce the sum of source and sink terms in the ϵ-equation near the wall, but the reduction is somewhat excessive. Hence there appears to be too much sensitivity to the mean rotation, which in the present case is the velocity gradient $U_{,y}$. Perhaps this oversensitivity could be remedied by multiplying the extra term (18), which does not include any Reynolds-number dependence, by a suitable function of the turbulent Reynolds number Re_t.

6.3 Modeling of P_ϵ^3.

The production term P_ϵ^3 involving second derivatives of the mean velocity is small compared with the other source and sink terms, but it is comparable with their sum and also with the turbulent diffusion term (see Fig. 8). Hence it is important to represent realistically also this term in a model. Hanjalić and Launder (1976) used a generalized gradient approximation for the fluctuating velocity gradients $u'_{i,j}$ appearing in the turbulence correlation in the P_ϵ^3 term and expressed these gradients in terms of second derivatives of the mean velocity. They arrived at a model expression which reads for the special case of channel flow:

$$P_\epsilon^3 = C_{\epsilon\nu} 2\nu \frac{\overline{v'^2} k}{\epsilon} (U_{,yy})^2 \tag{19}$$

With $\overline{v'^2}$ replaced by k and $\nu_t \propto k^2/\epsilon$, there results the model used by LS:

$$P_\epsilon^3 = 2\nu\nu_t (U_{,yy})^2 \tag{20}$$

The P_ϵ^3-distribution resulting from this model is compared in Fig. 13 with the DNS data. The model can be seen to have two problems: One is that the level of P_ϵ^3 is significantly overpredicted; this could be fixed by using a different constant. The other more fundamental problem is that the LS model predicts P_ϵ^3 to be always positive while the DNS data show that P_ϵ^3 goes negative near the wall. It can be shown from a series expansion of the fluctuating velocities u' and v' as given in Mansour *et al.* (1988) that the correlation $\overline{v'u'_{,y}}$, which is the only contribution to P_ϵ^3 in channel flow, should behave as $(\overline{u'v'})_{,y}$ near the wall, i.e. as y^2, and should be negative. This confirms the behavior resulting from the DNS data.

Because of the fundamental problems with the LS model for P_ϵ^3, an improved model was developed. To this end, an exact equation for the correlation $\overline{u'_k u'_{i,j}}$ appearing in the P_ϵ^3-definition was derived by manipulating the Navier-Stokes equations (see Appendix). For modeling purposes, it was then assumed that the correlation is related to the source terms in the exact equation involving mean velocity

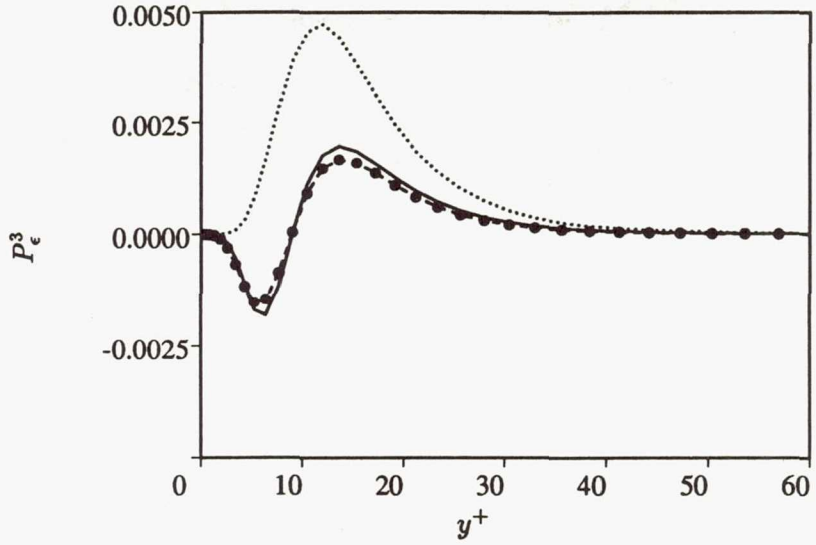

FIGURE 13. Model for P^3_ϵ-production compared with DNS data ($Re_\tau = 395$). •-•-• DNS data; —— new model; ····· LS model.

derivatives. For channel flow only the correlation $\overline{v'u'_{,y}}$ is of interest, and the main source terms in the equation for this correlation are

$$-\overline{v'^2}U_{,yy} - \frac{1}{2}\overline{v'^2}_{,y}U_{,y} \tag{21}$$

Multiplying these terms by a time scale $k/\tilde{\epsilon}$ for dimensional reasons and assuming $\overline{v'^2} \propto k$ and $k^2/\tilde{\epsilon} \propto \nu_t$ in the context of a k-ϵ eddy-viscosity model, and allowing for different multiplying constants for each of the terms in (21), the following model is obtained for shear-layer flows:

$$P^3_\epsilon = -2\nu\overline{v'u'_{,y}}U_{,yy} = C^3_1 2\nu\nu_t (U_{,yy})^2 + C^3_2 \nu \frac{k}{\epsilon} k_{,y} U_{,y} U_{,yy} \tag{22}$$

The first term can be seen to be the model of LS which is always positive. The second term is negative near the wall as desired and turns positive further away from the wall. This term also has the correct near-wall behavior, namely it approaches the wall as y^2. Adjusting the constants C^3_1 and C^3_2 to best fit the DNS data ($C^3_1 = 0.5$, $C^3_2 = 0.006$) there follows the curve given in Fig. 13. The fit can be seen to be very good.

6.4 Model performance for sum of all source/sink terms.

The model for P^3_ϵ is now put together with the previously discussed model for the other source and sink terms, including the R_p-function (17). The performance of the resulting model for the sum of all source and sink terms is shown in Fig. 14a.

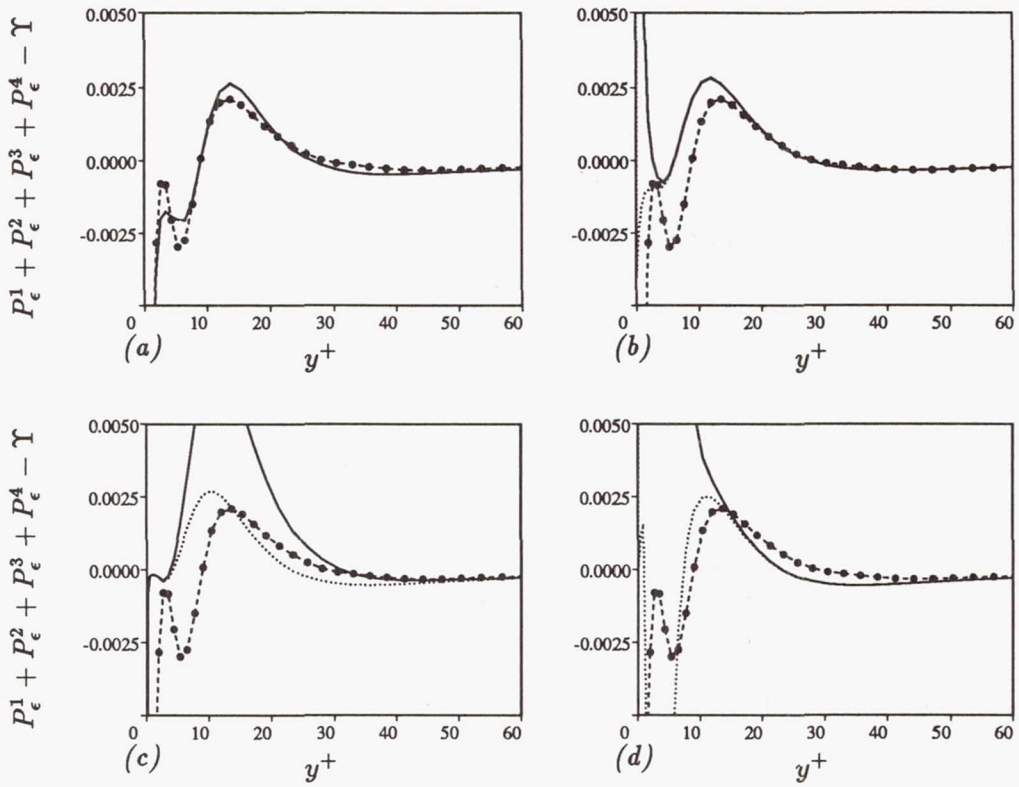

FIGURE 14. Models for all source/sink terms in ϵ-equation compared with DNS data for channel flow ($Re_\tau = 395$) •–•–• DNS data; ——— model. *(a)* New model. *(b)* CH model; ····· CH model with $E = 0$. *(c)* LS model; ····· LS model with $E = 0$. *(d)* LB model; ····· LB model with $f_1 = 1$.

The agreement between the model prediction and the DNS data is good down to $y^+ \approx 8$, below which the DNS data are not so reliable anyway.

It is of interest to see how this performance compares with that of the three selected existing models CH, LS and LB. Hence, in Figs. 14b - d the models for the sum of all source and sink terms in the ϵ-equations due to CH, LS and LB are compared with the DNS data. For $y+ \geq 40$, all models behave basically the same, because here the extra terms E and functions f_1 and f_2 are not effective. In the range $20 \leq y^+ \leq 40$, the CH model is superior because it uses different constants $C_{\epsilon 1}$ and $C_{\epsilon 2}$ than the other models (see Table 1), which seem to be more suitable in channel flow. However, these constants may not be so suitable for other flows, *e.g.* free shear layers, for which the constants $C_{\epsilon 1}$ and $C_{\epsilon 2}$ used in the other models were optimized. Even below $y^+ = 20$, the CH model is quite reasonable, but it is not as accurate as the new model, for which results are shown in Fig. 14a. The E-term in the CH model is effective only below $y^+ \approx 5$ which shows that the basic model of equation (15) without an extra E-term or f_1-function is quite reasonable, especially when suitable $C_{\epsilon 1}$ and $C_{\epsilon 2}$ constants are chosen. Fig. 14c shows that the

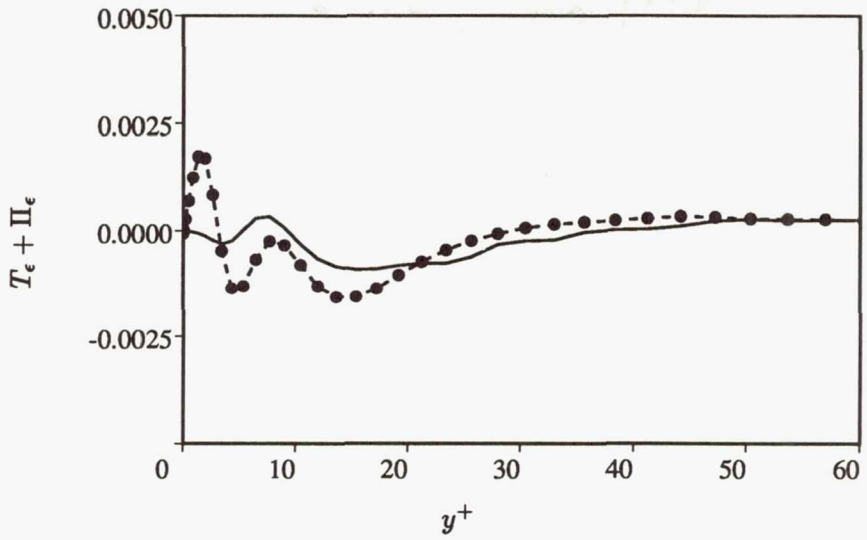

FIGURE 15. Model for diffusion term $T_\epsilon + \Pi_\epsilon$ in ϵ-equation compared with DNS data ($Re_\tau = 395$). •-•-• DNS data; —— model.

LS model predicts far too high values of the source/sink terms near the wall which is due to the E-term in their model ϵ-equation representing the P_ϵ^3-production (see also Fig. 13). Overall, the model behavior is better without this term. Similarly, the f_1-function in the LB model which increases the production of ϵ has the wrong effect because f_1 assumes very large values near the wall. Again, the model behavior is better without this function.

6.5 Diffusion model.

Finally, the diffusion model generally used in the ϵ-equation is tested against the DNS data in Fig. 15. In the channel flow considered, the diffusion model reads

$$T_\epsilon = \left(\frac{\nu_t}{\sigma_\epsilon}\epsilon_{,y}\right)_{,y} \tag{23}$$

and the adjustable constant σ_ϵ is normally taken as 1.3. Fig. 15 shows that this model simulates the distribution of the diffusion term fairly well, even though the accuracy is marginal near the wall.

7. Conclusions

From the evaluation of DNS data for channel and boundary-layer flow it was found that away from the wall the coefficient C_μ depends both on the type of flow and on the Reynolds number and varies in the bulk of the flows in the range 0.07 to 0.12. Considering only regions where the structure parameter $\overline{u'v'}/k$ is approximately constant, there is a clear dependence of C_μ on P/ϵ as given by relation (5). A fixed value of $C_\mu = 0.09$ is therefore not very accurate for all situations and a damping

function f_μ designed to recover this value away from the wall cannot be in good agreement with all DNS data examined. Nevertheless, some general conclusions can be drawn on existing model functions. The f_μ-function of Chien (CH) rises considerably too slowly, the function due to Launder and Sharma (LS) increases far too fast with distance from the wall, and the function due to Lam and Bremhorst (LB) performs best but also approaches unity too slowly. A new function of the dimensionless wall distance y^+ is proposed by fitting the DNS data for the higher-Re channel flow. A damping function was found unnecessary except very close to the wall ($y^+ < 10$) when $(\overline{v'^2})^{1/2}$ is used as velocity scale instead of $k^{1/2}$ in the eddy-viscosity relation, as suggested by Durbin (1990).

The ϵ-budget was determined from Kim's (1990) data for channel flow at $Re_\tau = 395$. This was found reliable down to a wall distance of $y^+ \approx 8$, as the calculated imbalance term is very small for $y^+ > 8$. As expected, the main terms in the ϵ-budget are the vortex-stretching-production term P_ϵ^4 and the viscous destruction term Υ, but near the wall the production terms P_ϵ^1 and P_ϵ^2 involving the mean strain rate are of similar magnitude. These production terms were found to cause the viscous destruction term to increase near the wall so that the sum of all source and sink terms is small compared with the main individual source and sink terms over the whole channel depth. The turbulent diffusion and the P_ϵ^3 term involving second derivatives of the mean velocity are of the same small magnitude. Through scaling considerations it was shown that the difference of the main source/sink terms, $P_\epsilon^4 - \Upsilon$, and the transport terms (here only turbulent diffusion) are independent of Reynolds number and also that the ratio of P_ϵ^1 and P_ϵ^2 to these terms is given by a parameter R involving the strain rate and the Reynolds number Re_t. This parameter represents the ratio of the time scale of the dissipating motion to the time scale of the mean strain field.

A new model was proposed and tested against the DNS channel data which simulates the net effect of the production terms P_ϵ^1 and P_ϵ^2 and the consequential increase in the destruction term Υ. In this new model, the sink term in the ϵ-equation is increased slightly near the wall through a parameter R_p involving the ratio of production to dissipation, P/ϵ, and the turbulent Reynolds number Re_t. A new model for the source term P_ϵ^3 was also derived, based on the production terms in the exact equation for the turbulence correlation appearing in P_ϵ^3. Altogether, the new models simulate the sum of all source and sink terms in the channel flow very well down to $y^+ \approx 8$. Judging from the comparison with the DNS data, the new model is better than the existing models investigated. The CH model is not as accurate near the wall, but it is still quite reasonable, while the LS and LB models produce too large source terms near the wall. The new model proposals comprising a new f_μ-function and new suggestions for the source/sink terms in the ϵ-equation should now be tested in actual flow calculations.

The authors are grateful to Dr. J. Kim for providing the unpublished direct simulation data for the channel flow at $Re_\tau = 395$. The second author (NNM) likes to acknowledge valuable discussions with Dr. A. Wray. The first author (WR) likes to acknowledge the generous support of the Center for Turbulence Research.

Appendix. Modeling the $\overline{u'_k u'_{i,j}}$-correlation

An exact equation for the $\overline{u'_k u'_{i,j}}$-correlation appearing in the P^3_ϵ-term can be derived by differentiating the momentum equation for the fluctuating component u'_i with respect to x_j, multiplying this equation by u'_k and averaging. The result is as follows:

$$\begin{aligned}&(\overline{u'_k u'_{i,j}})_{,t} - \overline{u'_{i,j} u'_{k,t}} + U_l(\overline{u'_k u'_{i,j}})_{,l} - U_l\overline{u'_{i,j} u'_{k,l}} \\ &+\overline{u'_k u'_{i,l}}U_{l,j} + \overline{u'_k u'_l}U_{i,l,j} - \overline{u'_k u'_{l,j}}U_{i,l} + \overline{u'_k(u'_i u'_l)_{,lj}} = -\frac{1}{\rho}\overline{p'_{,ij} u'_k} + \nu\overline{u'_k u'_{i,llj}}\end{aligned} \tag{A.1}$$

It is now assumed that the terms involving gradients of the mean velocity act to produce the correlation $\overline{u'_k u'_{i,j}}$. When put to the right-hand side of the equation, these terms read:

$$-\overline{u'_k u'_{i,l}}U_{l,j} - \overline{u'_k u'_l}U_{i,lj} - \overline{u'_k u'_{l,j}}U_{i,l} \tag{A.2}$$

For developed channel flow, the only correlation in P^3_ϵ is $\overline{v'u'_{,y}}$, and the velocity gradient production terms for this correlation are

$$-\overline{v'u'_{,x}}U_{,y} - \overline{v'^2}U_{,yy} - \overline{v'v'_{,y}}U_{,y} \tag{A.3}$$

The correlation appearing in the first term can be written as:

$$\overline{v'u'_{,x}} = (\overline{u'v'})_{,x} - \overline{u'v'}_{,x} \tag{A.4}$$

In developed channel flow, $(\overline{u'v'})_{,x}$ is zero and $\overline{u'v'_{,x}}$ is neglected to first approximation. The correlation $\overline{v'v'_{,y}}$ can be written as $1/2(\overline{v'^2})_{,y}$. The velocity-gradient production terms of the correlation $\overline{v'u'_{,y}}$ therefore are approximately:

$$\overline{v'^2}U_{,yy} - \frac{1}{2}(\overline{v'^2})_{,y}U_{,y} \tag{A.5}$$

REFERENCES

BARDINA, J. 1988 Turbulence modeling based on direct simulation of the Navier-Stokes equations. *First National Fluid Dynamics Conference, Cincinnati, Ohio,* AIAA 88-3747-CP.

BARDINA, J., FERZIGER, J. H. & REYNOLDS, W. C. 1983 Improved turbulence models based on large-eddy simulation of homogeneous incompressible, turbulent flows. *Report No. TF-19,* Thermosciences Div., Dept. of Mech. Eng., Stanford University, Stanford, California.

CHIEN, K.-Y. 1982 Predictions of channel and boundary-layer flows with a low-Reynolds-number turbulence model. *AIAA J.* **20,** 33-38.

DURBIN, P. A. 1990 Near-wall turbulence closure modeling without "damping functions". *CTR manuscript 112,*Center for Turbulence Research, Stanford University.

HANJALIC, K. & LAUNDER, B. E. 1976 Contribution towards a Reynolds-stress closure for low-Reynolds-number turbulence. *J. Fluid Mech.* **74,** 593-610.

KIM, J. 1990 private communication.

KIM, J., MOIN, P. & MOSER, R. 1987 Turbulence statistics in fully developed channel flow at low Reynolds number. *J. Fluid Mech.* **177,** 133-166.

LAM, C. K. G. & BREMHORST, K. A. 1981 Modified form of the k-ϵ model for predicting wall turbulence. *J. Fluids Eng.* **103,** 456-460.

LAUFER, J. 1954 The structure of turbulence in fully developed pipe flow. *NACA Report. 1174.*

LAUNDER, B. E. 1986 Low-Reynolds-number turbulence near walls. *Report TFD-/86/4,*UMIST, Manchester, U.K.

LAUNDER, B. E. & SHARMA, B. I. 1974 Application of the energy-dissipation model of turbulence to the calculation of flow near a spinning disk. *Letter in Heat and Mass Transfer.* **1,** 131-138.

LAUNDER, B. E., REECE, G. J. & RODI, W. 1975 Progress in the development of a Reynolds-stress turbulence closure. *J. Fluid Mech.* **68,** 537-566.

MANSOUR, N. N., KIM, J. & MOIN, P. 1988 Reynolds-stress and dissipation rate budgets in a turbulent channel flow. *J. Fluid Mech.* **194,** 15-44.

PATEL, V. C., RODI, W. & SCHEUERER, G. 1985 Turbulence models for near-wall and low-Reynolds-number closure: A review. *AIAA J.* **23**(9), 1308-1319.

RODI, W. 1971 On the equation governing the rate of turbulent energy dissipation. *Report TM/TN/A/14,* Imperial College of Science and Technology, Dept. of Mech. Eng., London, U.K.

RODI, W. 1975 A note on the empirical constant in the Kolmogorov-Prandtl eddy-viscosity expression. *ASME J. of Fluids Eng.* **97,** 386-389.

SHIH, T.-H. & MANSOUR, N. N. 1990 Modeling of near-wall turbulence. In *Engineering Turbulence Modeling and Experiments.* eds. W. Rodi and E.N. Ganić, Elsevier, New York.

SPALART, P. R. 1988 Direct simulation of a turbulent boundary layer up to $R_\theta = 1410$. *J. Fluid Mech.* **187,** 61-98.

TENNEKES, H. & LUMLEY, J. L. 1972 A First Course in Turbulence. The MIT Press, Cambridge, Massachusetts.

One-equation near-wall turbulence modeling with the aid of direct simulation data

By W. Rodi[1] AND N. N. Mansour[2]

The length scales appearing in the relations for the eddy viscosity and dissipation rate in one-equation models were evaluated from direct numerical simulation data for developed channel and boundary-layer flow at two Reynolds numbers each. To prepare the ground for the evaluation, the distribution of the most relevant mean-flow and turbulence quantities is presented and discussed, also with respect to Reynolds-number influence and to differences between channel and boundary-layer flow. An alternative model is also examined in which $(\overline{v'^2})^{1/2}$ is used as velocity scale instead of $k^{1/2}$. With this velocity scale, the length scales now appearing in the model follow very closely a linear relationship near the wall so that no damping is necessary. For the determination of $\overline{v'^2}$ in the context of a one-equation model, a correlation is provided between $\overline{v'^2}/k$ and $\overline{u'v'}/k$.

1. Introduction

One-equation eddy-viscosity models have recently regained popularity as components of two-layer turbulence models (see *e.g.* Rodi, 1991). In these, one-equation models are used only near walls in the viscosity-affected region, say up to wall distances where the ratio of eddy viscosity to molecular viscosity takes values of 20 to 40, which corresponds to wall distances of up to $y^+ \approx 80$ in boundary-layer flow. Outside this near-wall region, other, more general models are employed such as the two-equation k-ϵ model or Reynolds-stress-equation models.

In existing one-equation models, the local state of the turbulence is characterized by the velocity scale $k^{1/2}$ and the length scale l. The turbulent kinetic energy k is calculated from a transport equation, while the l-distribution is prescribed empirically. In attached near-wall flows, the only Reynolds stress of importance in the momentum equations is the shear stress $-\overline{u'v'}$, which is determined from the eddy-viscosity relation

$$-\overline{u'v'} = \nu_t U_{,y} \tag{1}$$

In one-equation models, the eddy viscosity is calculated from

$$\nu_t = C_\mu k^{1/2} l_\mu \tag{2}$$

1 University of Karlsruhe, F. R. Germany
2 NASA Ames Research Center

and the distribution of k from the following transport equation for k:

$$Uk_{,x} + Vk_{,y} = \left[\left(\nu + \frac{\nu_k}{\sigma_k}\right) k_{,y}\right] - \overline{u'v'}U_{,y} - \epsilon \tag{3}$$

The dissipation rate ϵ appearing in this equation is determined from

$$\epsilon = k^{3/2}/l_\epsilon \tag{4}$$

When the coefficient C_μ in (2) is chosen as the square of the structure parameter $\overline{u'v'}/k$ under local equilibrium conditions, the length scales l_μ and l_ϵ are the same in the log-law region, but they may differ very close to the wall. They are usually prescribed empirically by formulae of the following type

$$l_\mu = C_l y(1 - \exp(-y^*/A_\mu^*)) \tag{5}$$

$$l_\epsilon = C_l y(1 - \exp(-y^*/A_\epsilon^*)) \tag{6}$$

where

$$y^* = k^{1/2}y/\nu \tag{7}$$

and A_μ^* and A_ϵ^* are empirical constants. Hence, the length scales basically increase linearly with distance from the wall at the same rate, but their magnitude is reduced near the wall by exponential damping functions, which are similar to the van Driest damping function in the mixing-length model and are different for l_μ and l_ϵ. This is basically the model due to Wolfshtein (1969), while Norris and Reynolds (1975) used a function $(1 + C_\epsilon y^*)^{-1}$ to damp the dissipation scale l_ϵ near the wall. Of course, the length scales grow linearly only near the wall; altogether a ramp function is assumed with a uniform l-distribution in the outer part of the flow. However, in this paper we are concerned only with the near-wall region. The argument in the damping functions is taken as $y^* = k^{1/2}y/\nu$ and not $y^+ = U_\tau y/\nu$ because the functions should also work for separated flows where U_τ can go to zero.

The length-scale prescriptions (5) and (6) are based on compatibility with the universal logarithmic velocity distribution and lean heavily on experience with the mixing-length distribution near the wall, *i.e.* on the van Driest damping law. So far, the validity of the prescriptions could not be checked directly with the aid of data but only indirectly through their use in flow calculations. Direct numerical simulation (DNS) data are now available to test the length-scale relations directly and to form the basis for developing improved prescriptions if necessary. To this end, l_μ- and l_ϵ-distributions are calculated in this paper from DNS data for developed channel (Kim *et al.*, 1987 and Kim, 1990) and boundary-layer (Spalart, 1988) flows at two Reynolds numbers each, and these data are compared with the existing empirical relations. The influence of the Reynolds number is thereby also examined. Alternative modeling with the normal fluctuations $(\overline{v'^2})^{1/2}$ as velocity scale instead of $k^{1/2}$ is also investigated, and $\overline{v'^2}/k$ is correlated with $\overline{u'v'}/k$ so that no extra equation need be solved for $\overline{v'^2}$ and the one-equation-model character is retained.

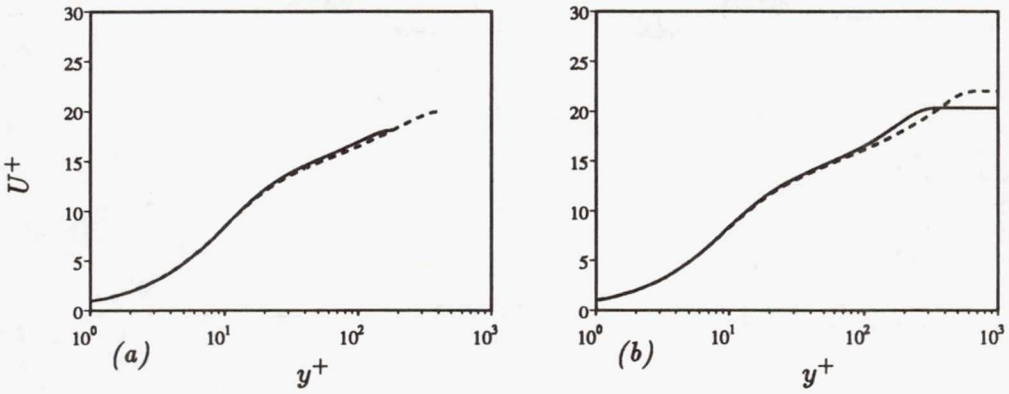

FIGURE 1. Velocity profiles in wall coordinates.
(a) Channel: —— $Re_\tau = 180$; ---- $Re_\tau = 395$.
(b) Boundary layer: —— $Re_\theta = 670$; ---- $Re_\theta = 1416$.

2. Basic quantities needed for model evaluation

The ground for the model evaluation needs to be prepared first by providing distributions of basic quantities in channel flow and boundary layers as computed from the DNS data. Here, the influence of the Reynolds number and of the flow situation (channel flow versus boundary layer) is examined with the quantities plotted in wall coordinates, *i.e.* they are made dimensionless with U_τ and ν. As components of two-layer models, one-equation models are mostly used for globally high-Reynolds-number situations and hence the model relations should correspond closely to such situations; the tuning of the model to data stemming from rather low Reynolds-number flows is therefore not desirable. Hence, it is important to examine how closely the DNS data obtained for the highest Reynolds numbers correspond to experimental data achieved at high Reynolds numbers.

All quantities to be presented in the following are made dimensionless with the friction velocity U_τ and with ν, and they are plotted against $y^+ = U_\tau y/\nu$. First, the velocity distribution is given in the usual semi-log plot in Fig. 1. For channel flow (Fig. 1a), there appears to be a reasonably well established log law for both Reynolds numbers, but for the lower Reynolds number ($Re_\tau = 180$) the constant C in the log law is above the standard value 5, while for $Re_\tau = 395$ the velocity distribution follows the standard log law over a significant part of the channel half-width. At fairly low Reynolds numbers, the increase in the log-law constant C with decreasing Reynolds number is a well known phenomenon (see *e.g.* Launder, 1986). For the boundary layer at the lower Reynolds number ($Re_\theta = 667$), the velocity distribution follows the log law in a small region only, while at the higher Reynolds number ($Re_\theta = 1416$) this region is fairly extensive (up to nearly $y^+ \approx 100$). For both channel and boundary-layer flows, the von Kármán constant derived from the data is $\kappa = 0.41$. Hence, in the higher-Reynolds-number cases, the velocity distribution corresponds to the observed distribution at much higher Reynolds numbers over a significant portion of the flow. The deviation from the log

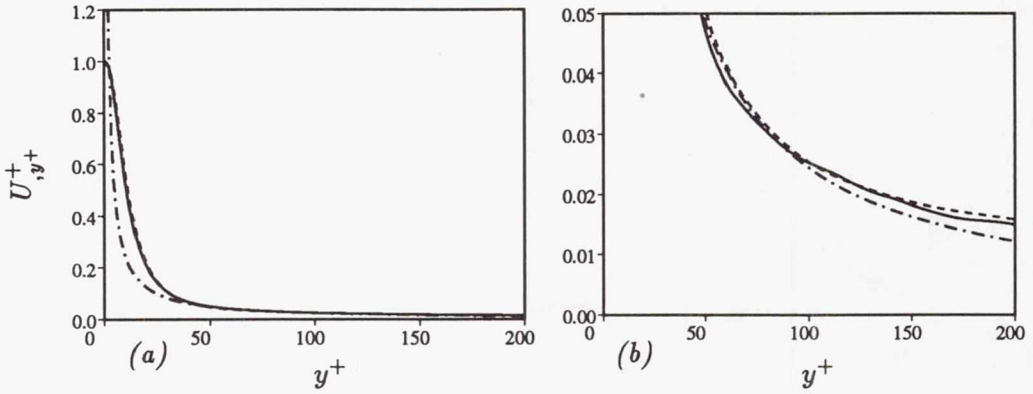

FIGURE 2. Distribution of velocity gradient. —— Channel $Re_\tau = 395$; ---- Boundary layer $Re_\theta = 1416$; —·— $1/.41y^+$. *(a)* Vertical scale between 0 and 1.2. *(b)* Expanded vertical scale between 0. and 0.05.

law can be seen more clearly in Fig. 2 where the velocity gradient $U^+_{,y^+}$ is plotted. According to the log law this gradient should follow the curve $1/\kappa y^+$, Fig. 2 shows that for both higher-Reynolds-number flows (channel flow and boundary layer) the velocity gradient starts to deviate from this curve at $y^+ \approx 30$.

Fig. 3 shows for channel flow the distribution of the RMS values of the fluctuating velocity components u, v and w compared with measurements of various experiments at high Reynolds numbers, as compiled by Myong and Kasagi (1988). The measurements show considerable scatter, and extreme data points should not be considered trustworthy. The DNS data exhibit a surprising dependence on the Reynolds number even close to the wall, particularly so for the component w. However, there is a clear trend with increasing Reynolds number towards the mean of the experimental data, and the DNS data for $Re_\tau = 395$ are already a fairly good representation of the high-Reynolds-number experimental data. Hence it may be concluded that the higher-Re channel flow data correspond closely to high-Re channel flow for which the quantities considered are independent of Reynolds number. In Fig. 4, the corresponding DNS data for the boundary layer are presented at two Reynolds numbers. Here a similar Re-dependence is found, and it is interesting to note that, except very close to the wall, the fluctuating velocities in the boundary layer are somewhat higher than in the channel flow. This may be due partly to the differences in the flow situation with the shear stress $-\overline{u'v'}$ falling more quickly with distance from the wall in the channel flow than in the boundary layer, but to some extent it is also due to the fact that the boundary-layer flow at $Re_\theta = 1416$ represents a higher Reynolds-number case than the channel flow at $Re_\tau = 395$. This can be inferred from the higher y^+- and ν_t/ν-values in the boundary layer (see Figs. 1 and 9).

The ratios $\overline{u'^2}/k$, $\overline{v'^2}/k$ and $\overline{w'^2}/k$ needed in section 4 are shown for both flows in Fig. 5. Up to $y^+ \approx 100$, there is generally little influence of the Reynolds number on these ratios, and there is also fairly good agreement between channel

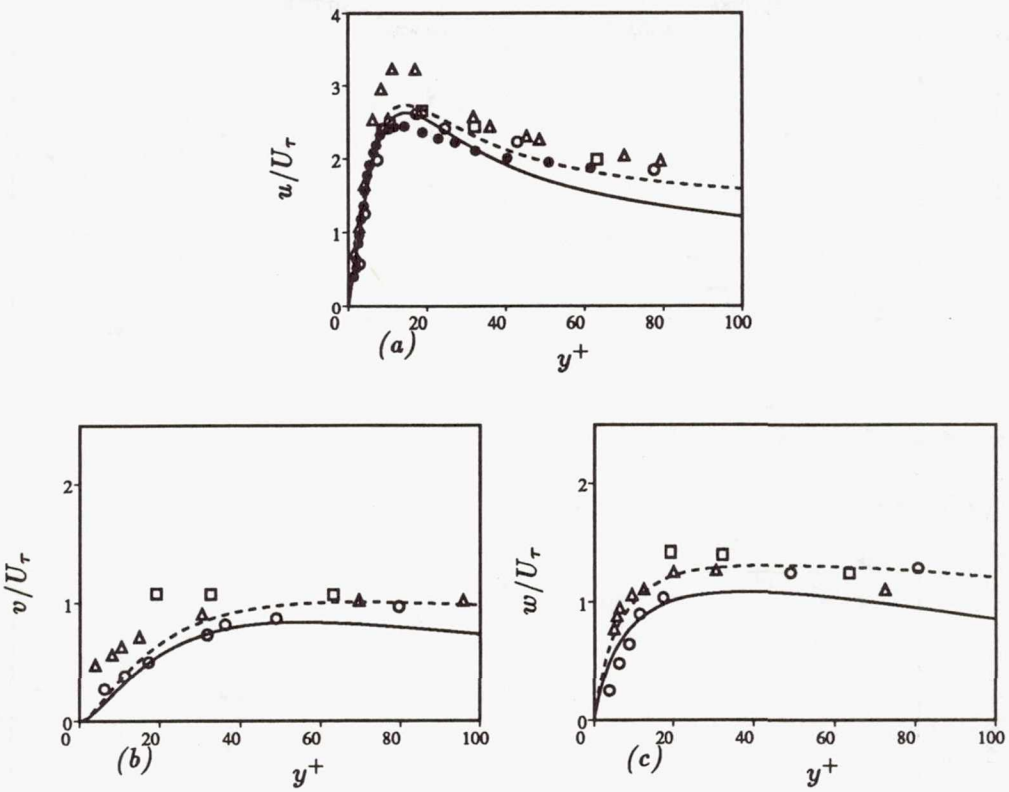

FIGURE 3. RMS fluctuations in developed channel flow, comparison with high-Reynolds-number data compiled by Myong and Kasagi (1988). —— DNS, $Re_\tau = 180$; ---- DNS, $Re_\tau = 395$; ○ Laufer (1954), $Re = 50,000$; △ Clark (1968), $Re = 30,400$; □ Kastrinakis & Eckelmann (1983), $Re = 25,200$; • Hussain & Reynolds (1975), $Re = 27,600$.

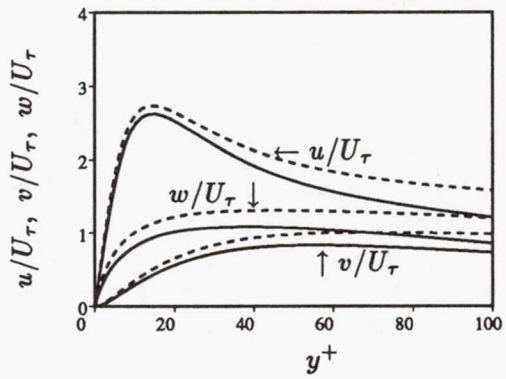

FIGURE 4. RMS fluctuations in boundary layers. —— $Re_\theta = 667$; ---- $Re_\theta = 1416$.

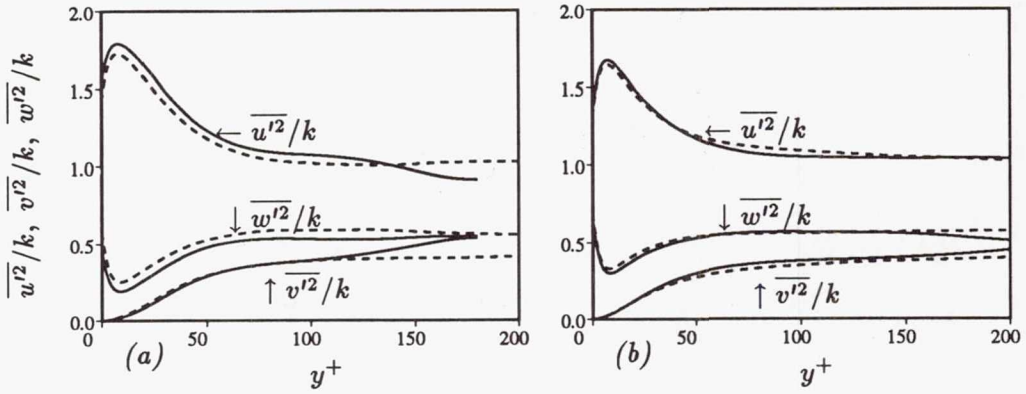

FIGURE 5. Distribution of $\overline{u'^2}/k$, $\overline{v'^2}/k$, $\overline{w'^2}/k$.
(a) Channel: —— $Re_\tau = 180$; ---- $Re_\tau = 395$.
(b) Boundary layer: —— $Re_\theta = 670$; ---- $Re_\theta = 1416$.

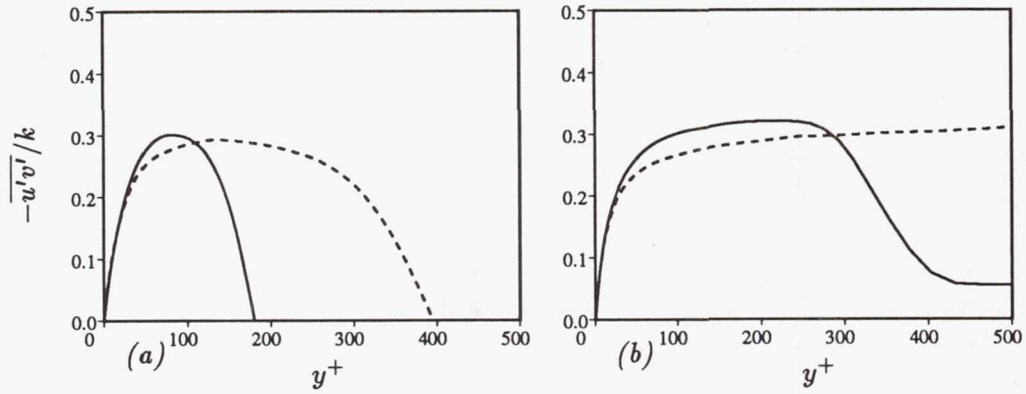

FIGURE 6. Distribution of structure parameter $-\overline{u'v'}/k$.
(a) Channel: —— $Re_\tau = 180$; ---- $Re_\tau = 395$.
(b) Boundary layer: —— $Re_\theta = 670$; ---- $Re_\theta = 1416$.

and boundary-layer flow. An exception is $\overline{w'^2}/k$, which has a larger dip near the wall in the channel-flow case. For the higher-Reynolds-number cases, constant values are a reasonable approximation to the data for $y^+ \geq 80$, with $\overline{u'^2}/k \approx 1$, $\overline{v'^2}/k \approx .41$ and $\overline{w'^2}/k \approx 0.59$. The distribution of the structure parameter $-\overline{u'v'}/k$ is given in Fig. 6. For the channel flow, the range where this parameter assumes approximately the standard value of 0.3 is much narrower than for the boundary layer. However, in the higher Re case the value of 0.3 is reached in the boundary layer only at fairly large y^+-distances. The correlation coefficient $-\overline{u'v'}/(\overline{u'^2}\ \overline{v'^2})^{1/2}$ plotted in Fig. 7 can be seen to be much more uniform over the width of the shear layers. Of course, this coefficient drops to zero at the channel center, and it also decreases very close to the wall, but overall a value of .42 is well supported by the DNS data.

The ratio of production to dissipation of turbulent kinetic energy, P/ϵ, which

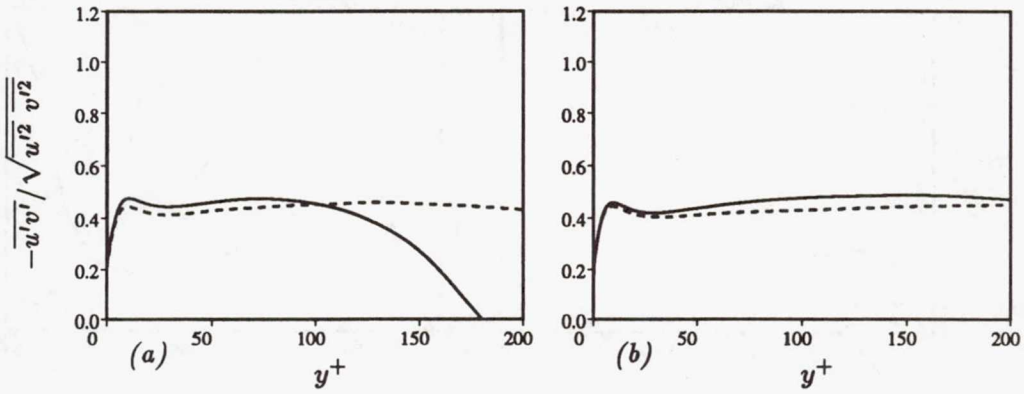

FIGURE 7. Distribution of correlation coefficient $-\overline{u'v'}/\sqrt{\overline{u'^2}\ \overline{v'^2}}$.
(a) Channel: —— $Re_\tau = 180$; ---- $Re_\tau = 395$.
(b) Boundary layer: —— $Re_\theta = 670$; ---- $Re_\theta = 1416$.

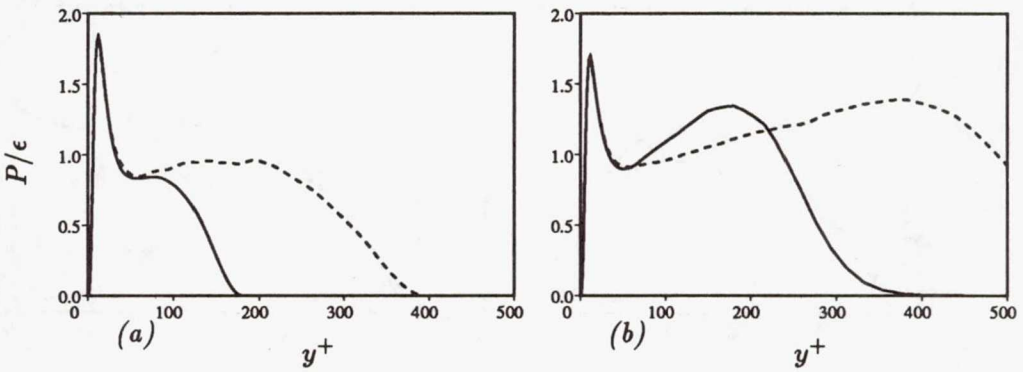

FIGURE 8. Distribution of ratio of production rate to dissipation rate of turbulent kinetic energy P/ϵ.
(a) Channel: —— $Re_\tau = 180$; ---- $Re_\tau = 395$.
(b) Boundary layer: —— $Re_\theta = 670$; ---- $Re_\theta = 1416$.

plays an important role in modeling, is given in Fig. 8. In channel flow, a substantial region with local equilibrium ($P/\epsilon \approx 1$) is present only in the higher-Reynolds number case. For the boundary-layer situation, such a region is limited to $y^+ \approx 80$ – 100, while further away from the wall, production dominates dissipation and P/ϵ reaches a maximum of about 1.4.

Finally, in Fig. 9, the ratio of turbulent to molecular viscosity, ν_t^+, is presented. The level of this quantity reached is a good indicator of the influence of viscous effects on the flow, that is whether the Reynolds number is high enough for these effects to be unimportant. Clearly the low-Re channel flow does not satisfy this criterion with ν_t^+ reaching values of only about 15. The higher-Re boundary layer reaches the highest levels of ν_t^+, as was to be expected. In the log-law region with

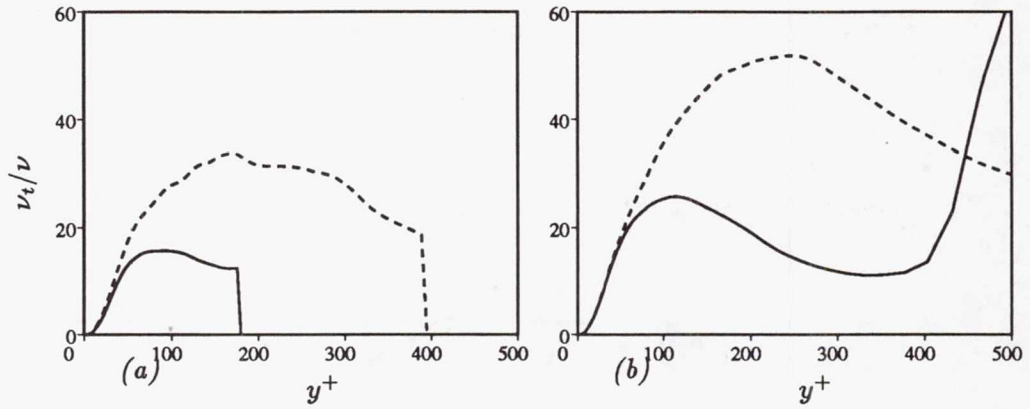

FIGURE 9. Distribution of dimensionless eddy viscosity ν_t/ν.
(a) Channel: —— $Re_\tau = 180$; ---- $Re_\tau = 395$.
(b) Boundary layer: —— $Re_\theta = 670$; ---- $Re_\theta = 1416$.

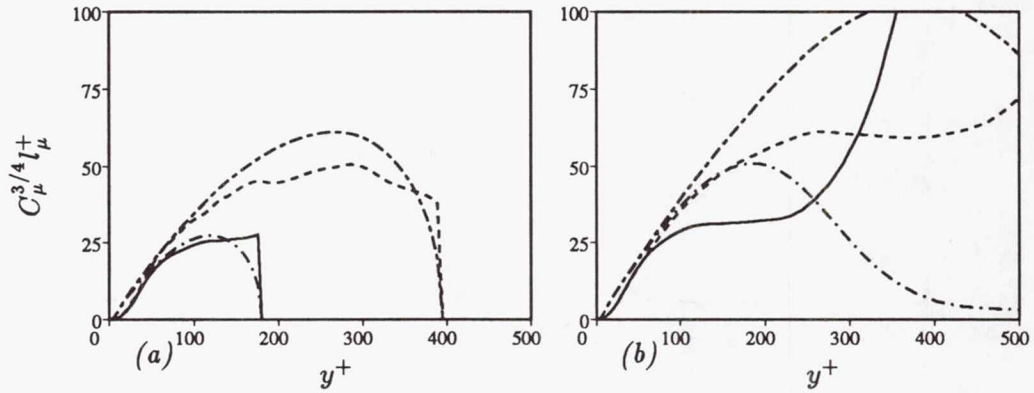

FIGURE 10. Distribution of length scale $C_\mu^{3/4} l_\mu^+$.
(a) Channel: $Re_\tau = 180$ —— DNS, —·— Eq. (11); $Re_\tau = 395$ ---- DNS, —·— Eq. (11).
(b) Boundary layer: $Re_\theta = 667$, —— DNS, —·— Eq. (11); $Re_\theta = 1416$ ---- DNS, —·— Eq. (11).

$U^+_{,y^+} = 1/\kappa y^+$, there follows from (1):

$$\nu_t^+ = -\overline{u'v'}^+ \kappa y^+ \tag{8}$$

Near the wall, ν_t^+ from the DNS data has the gradient κ, but it does not follow exactly $\nu_t^+ = \kappa y^+$ but falls below this relation because this is based on $-\overline{u'v'}^+ = 1$ while the actual shear stress is below the wall shear stress. Very near the wall, the damping of the eddy viscosity is visible, which needs to be accounted for in any turbulence model.

3. One-equation models based on $k^{1/2}$ as velocity scale

Length scale l_μ. The non-dimensional length-scale l_μ^+ defined by

$$l_\mu^+ = \frac{l_\mu U_\tau}{\nu} = \frac{\nu_t^+}{C_\mu k^{+1/2}} \tag{9}$$

was determined from the DNS data and is presented in Fig. 10. When ν_t^+ in this relation is determined from (8) based on the log law and when k^+ is assumed proportional to the shear stress $-\overline{u'v'}^+$ via

$$k^+ = \frac{-\overline{u'v'}^+}{C_\mu^{1/2}} \tag{10}$$

the following relationship for the length scale l_μ^+ results:

$$C_\mu^{3/4} l_\mu^+ = (-\overline{u'v'}^+)^{1/2} \kappa y^+ \tag{11}$$

In relation (10), $C_\mu^{1/2}$ is the structure parameter, for which a standard value of .3 has been taken so that $C_\mu = 0.09$. In Fig. 10, actually $C_\mu^{3/4} l_\mu^+$ is plotted which corresponds to the Prandtl mixing length usually assumed to be κy^+ in the log-law region. The distribution of l_μ^+ according to (11) is also included in Fig. 10. As this relation assumes the log law to hold and the structure parameter $-\overline{u'v'}/k$ to have a value of 0.3, the DNS data agree fairly well with this distribution in regions where these assumptions are approximately valid. Further away from the wall, these assumptions are not even approximately valid, so that there are considerable differences in the distributions, particularly so for the boundary layer. The differences in the curves for the various Reynolds numbers can be much reduced when l_μ/δ is plotted versus y/δ, where δ is the shear-layer thickness (channel half-width or boundary-layer thickness). $C_\mu^{3/4} l_\mu/\delta = C_\mu^{3/4} l_\mu^+ / Re_\tau$ then is approximately 0.13 in the outer region of channel flow ($y/\delta > 0.4$) and 0.095 for boundary layers in the region $.4 < y/\delta < .8$. Equation (11) can be seen to approximate the l_μ-distribution reasonably well in the near-wall region, but not too close to the wall. There, l_μ falls below the distribution (11) because of the near-wall damping of turbulent momentum transfer. A damping function à la van Driest is therefore required in this region. Fig. 11 shows the distribution of the damping function f_μ defined by

$$f_\mu = \frac{C_\mu^{3/4} l_\mu}{\kappa y} \tag{12}$$

as determined from the DNS data. f_μ is plotted versus the dimensionless wall distance y^* defined in (7), which is generally used as argument in damping functions (see equations (5) and (6)). f_μ defined by (12) following from the data does not quite reach a value of 1 as it does in models because l_μ is always below the linear

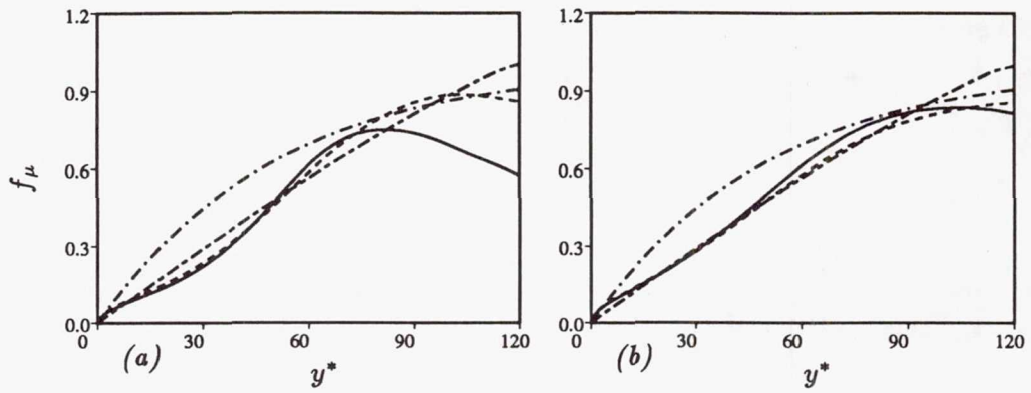

FIGURE 11. Distribution of damping function f_μ.
(a) Channel: ——— DNS $Re_\tau = 180$; - - - - DNS $Re_\tau = 395$; —·— Eq. (5) with $A_\mu^* = 50.5$; —·— Eq. (13).
(b) Boundary layer: ——— $Re_\theta = 667$; - - - - $Re_\theta = 1416$; —·— Eq. (5) with $A_\mu^* = 50.5$; —·— Eq. (13).

distribution κy (see Fig. 10). Perhaps it would be better to determine the damping function with the right-hand side of (11) in the denominator.

Commonly used exponential damping functions, *e.g.* relation (5), approach 1 further away from the wall, but they are not very accurate in the region up to $y^+ \approx 50$. An exponential function with $A_\mu^* = 50.5$ is included in Fig. 11. The DNS data are better approximated by the following power-law formula

$$f_\mu = 1 - \left(1 - \frac{y^*}{120}\right)^{1.2} \tag{13}$$

which forces f_μ to become 1 at $y^* = 120$. This relation simulates the near-wall damping quite well but approaches unity somewhat too quickly.

Dissipation length l_ϵ. The non-dimensional length scale l_ϵ^+ used for determining the dissipation rate which is defined by

$$l_\epsilon^+ = \frac{k^{+3/2}}{\epsilon^+} \tag{14}$$

is plotted in Fig. 12. When k^+ in this relation is eliminated with the aid of (10) and ϵ^+ is determined from

$$\epsilon^+ = P^+ = -\overline{u'v'}^+ U^+_{,y^+} = \frac{-\overline{u'v'}^+}{\kappa y^+} \tag{15}$$

assuming local equilibrium and the log law to hold, there results the following relation for l_ϵ^+:

$$C_\mu^{3/4} l_\epsilon^+ = (-\overline{u'v'}^+)^{1/2} \kappa y^+ \tag{16}$$

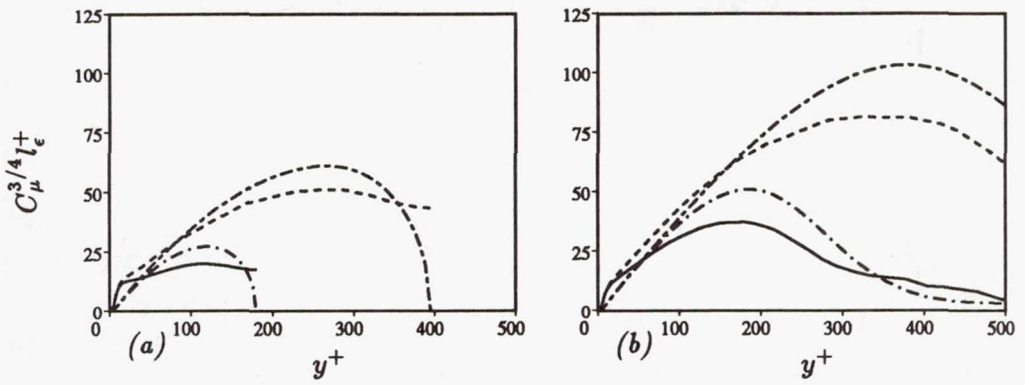

FIGURE 12. Distribution of dissipation length scale $C_\mu^{3/4} l_\epsilon^+$.
(a) Channel: $Re_\tau = 180$, —— DNS, —·— Eq. (16); $Re_\tau = 395$, ---- DNS, —·— Eq. (16).
(b) Boundary layer: $Re_\theta = 667$, —— DNS, —·— Eq. (16); $Re_\theta = 1416$, ---- DNS, —·— Eq. (16).

This is identical to relation (11) for the length scale l_μ^+ showing that, under the assumptions involved in these relations, both length scales are the same. Not too close to the wall, the behavior of l_ϵ is similar to that of l_μ, but this similarity does not extend to the channel center or the boundary-layer edge. Also, close to the wall significant differences are obvious which depend strongly on the Reynolds number. (this dependence does not disappear when l_ϵ/δ is plotted versus y/δ). A sizable region exists where l_ϵ^+ is larger than described by equation (16) or even larger than the linear relation κy^+. The maximum deviation occurs at $y^+ \approx 15$, where the distribution of the dissipation rate ϵ has a plateau (see Fig. 13). Here, existing one-equation models using a linear l_ϵ-distribution modified by a damping function according to (6) predict a peak in ϵ as shown also in Fig. 13. This ϵ-distribution with a peak away from the wall was also deduced from experiments (Patel *et al.*, 1985), but measurements of ϵ must be considered unreliable very near the wall.

As there is a considerable Reynolds-number influence on the l_ϵ-distribution, this is difficult to prescribe with a simple model relation. An alternative possibility is to introduce a model for ϵ directly via relation (15). This is plotted in Fig. 13 together with the ϵ-distribution calculated from the DNS data. It is clear that very close to the wall the behavior is very different as the right-hand side of (15) goes to zero at the wall while ϵ rises to a maximum value according to the data. Near the wall, relation (15) corresponds much closer to a modified dissipation rate $\tilde{\epsilon}$ defined by:

$$\tilde{\epsilon} = \epsilon - \nu \left(k_{,y}^{1/2} \right)^2 \tag{17}$$

In low-Reynolds-number k-ϵ models, $\tilde{\epsilon}$ is often used in the time scale k/ϵ instead of ϵ in order to keep the time scale finite at the wall. Both $\tilde{\epsilon}$ and $-\overline{u'v'}^+/\kappa y^+$ go to zero at the wall and both do so as y^2 so that relation (15) simulates correctly

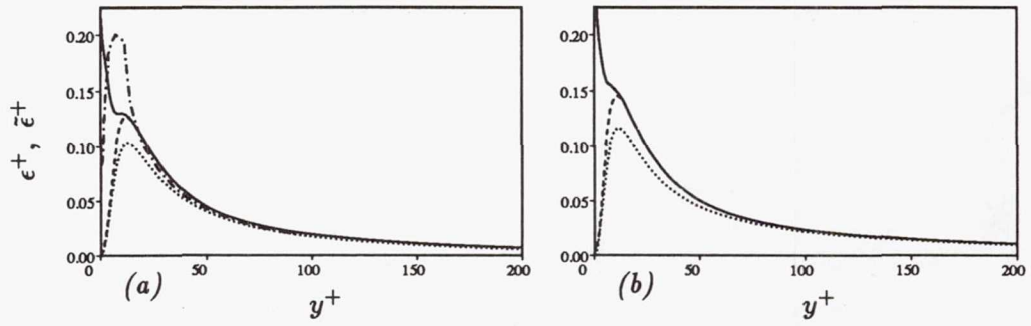

FIGURE 13. Distribution of dissipation rate ϵ^+ and $\tilde{\epsilon}^+$: —— ϵ^+; ---- $\tilde{\epsilon}^+$; ····· Eq. (15); —·— One-equation model (Cordes, 1991). *(a)* Channel, $Re = 395$. *(b)* Boundary layer, $Re_\theta = 1416$.

the behavior of $\tilde{\epsilon}$ near the wall. Relation (15) is based on the assumption of local equilibrium and on the validity of the logarithmic velocity distribution and can be seen to be a reasonably good approximation to ϵ in the y^+-range 100 – 200. However, in the case of the boundary layer deviations already increase at the larger y^+-values in this range as the velocity profile starts to deviate from the logarithmic distribution (see Fig. 2). Closer to the wall, $\tilde{\epsilon}$ (which is different from ϵ only for $y^+ \leq 12$) is also quite well simulated by (15), particularly so the shape. The peak, however, is predicted somewhat too low. In this region, the actual velocity gradient is larger than $1/\kappa y^+$, but dissipation is smaller than production (see Fig. 8). These two influences compensate each other to a large extent, but not 100% so that $\tilde{\epsilon}$ is somewhat underpredicted. A pragmatic approach to the simulation of $\tilde{\epsilon}$ is to multiply the right-hand side of relation (15) by a factor of about 1.2 which then yields $\tilde{\epsilon}$-distributions which are approximately correct for all cases considered here.

4. One-equation model based on $(\overline{v'^2})^{1/2}$ as velocity scale

Durbin (1990) suggested that, in near-wall shear layers, the normal fluctuations $(\overline{v'^2})^{1/2}$ may be a better velocity scale for characterizing the turbulent motion than $k^{1/2}$ and that no damping functions may be needed when this velocity scale is used. Hence, it is intriguing to examine whether this choice of velocity scale leads to corresponding length scales which are easier to prescribe empirically. Of course, the question then also needs to be answered as to how $\overline{v'^2}$ can be related to other known quantities in the context of a one-equation model.

Length-scale $l_{\mu,v}$. When $k^{1/2}$ is replaced by $(\overline{v'^2})^{1/2}$ in the eddy-viscosity relation (2), there follows:

$$\nu_t = (\overline{v'^2})^{1/2} l_{\mu,v} \tag{18}$$

It should be noted that any constant that may occur has been absorbed in $l_{\mu,v}$. In Fig. 14, the distribution of the dimensionless length scale $l^+_{\mu,v}$ as determined from the DNS data is compared with the distribution from the following approximate

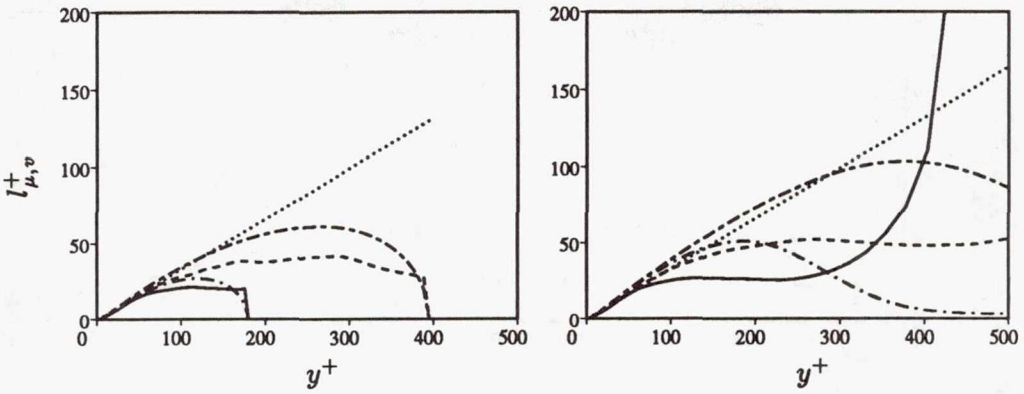

FIGURE 14. Distribution of length scale $l^+_{\mu,v}$: ····· Eq. (20).
(a) Channel: $Re_\tau = 180$, —— DNS, —·— Eq. (19); $Re_\tau = 395$, ---- DNS, —·— Eq. (19).
(b) Boundary layer: $Re_\theta = 667$, —— DNS, —·— Eq. (19); $Re_\theta = 1416$, ---- DNS, —·— Eq. (19).

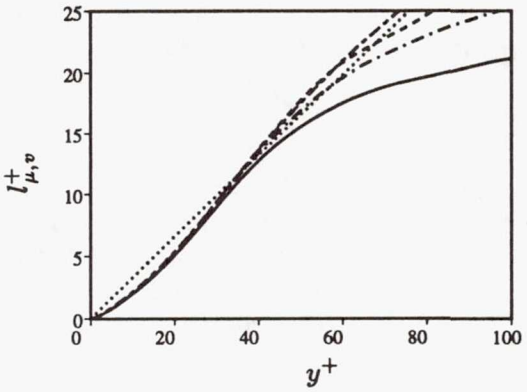

FIGURE 15. Distribution of length scale $l^+_{\mu,v}$, near the wall: ····· Eq. (20); —— Channel $Re_\tau = 180$; ---- Channel $Re_\tau = 395$; —·— Boundary layer $Re_\theta = 667$; —·— Boundary layer $Re_\theta = 1416$.

formula:

$$l^+_{\mu,v} = \frac{\nu_t^+}{(\overline{v'^2}^+)^{1/2}} = \frac{-\overline{u'v'}^+ \kappa y^+}{(\overline{v'^2}^+)^{1/2}} \tag{19}$$

This formula is again obtained by replacing the eddy viscosity by relation (7) based on the log law. Further, it can be seen from Fig. 3 that $\overline{v'^2}^+$ is approximately 1, and this value was inserted in relation (19) for the curve shown in Fig. 14. The figure indicates that, for larger y^+-values, the DNS data deviate more from the approximation curve than in the case of l_μ (see Fig. 10). However, close the wall ($y^+ < 60$) the data follow much closer the approximate relation, which is virtually

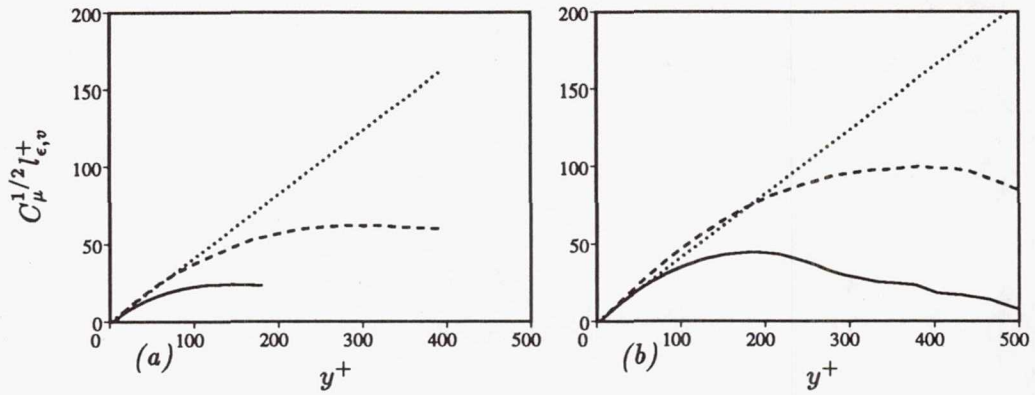

FIGURE 16. Distribution of dissipation length $C^{1/2}l^+_{\epsilon,v}$: ····· κy^+;
(a) Channel;—— $Re_\tau = 180$;---- $Re_\tau = 395$.
(b) Boundary layer; —— $Re_\theta = 667$; ---- $Re_\theta = 1416$.

linear in this region. Hence there is considerably less damping than in the case of l_μ. This is due to the fact that $\overline{v'^2}/k$ decreases near the wall (see Fig. 5) and that right at the wall $l_{\mu,v} \propto y$ while $l_\mu \propto y^2$. There appears to be some damping, but to first approximation the data can be described by

$$l_{\mu,v} = C_{l,\mu} y \tag{20}$$

where the factor $C_{l,\mu}$ is somewhat smaller than κ. As can be seen from Fig. 15, the linear distribution with $C_{l,\mu} = 0.33$ approximates the data fairly well up to $y^+ \approx 60$. It may be also of interest that $l_{\mu,v}/\delta = l^+_{\mu,v}/Re_\tau$ is approximately 0.12 in the outer part of channel flow and 0.08 in boundary-layer regions with $.4 < y/\delta < .8$.

Dissipation length $l_{\epsilon,v}$. When $(\overline{v'^2})^{1/2}$ is used as velocity scale, the dissipation relation corresponding to (4) reads:

$$\epsilon = \frac{(\overline{v'^2})^{1/2} k}{l_{\epsilon,v}} \tag{21}$$

which is practically a relation between a velocity scale, a length scale and the time scale k/ϵ. The dimensionless length scale $l^+_{\epsilon,v}$ can be approximated as

$$l^+_{\epsilon,v} = \frac{k^+}{\epsilon^+}(\overline{v'^2}^+)^{1/2} = \frac{1}{C_\mu^{1/2}} \kappa y^+ (\overline{v'^2}^+)^{1/2} \tag{22}$$

which again results from the elimination of k^+ with the aid of (10) and of ϵ^+ with the aid of (15), involving local-equilibrium and log-law assumptions. In Fig. 16, $C_\mu^{1/2} l^+_{\epsilon,v}$ determined from the DNS data is plotted together with the line κy^+ resulting from (22) by assuming again that $\overline{v'^2}^+$ has a value of 1. Fig. 16 shows that this linear relation approximates the channel flow data near the wall very well, while the data

indicate a somewhat larger slope for the boundary layer. This is due to the fact that in the boundary layer $\overline{v'^2}^+$ is somewhat larger than 1 in the region considered (see Fig. 3). Further, the lower-Reynolds-number cases follow the linear distribution only up to rather small y^+-values. In the bulk of the flow at larger y^+ distances, constant values of $l^+_{\epsilon,v}$ are approached. When $l^+_{\epsilon,v}$ is made dimensionless with δ, $C_\mu^{1/2} l_{\epsilon,v}/\delta \approx 0.14$ for both channel and boundary layer flows. Near the wall, the following linear distribution can be recommended:

$$l_{\epsilon,v} = C_{l,\epsilon} y \tag{23}$$

with $C_{l,\epsilon} \approx 1.43$ as an average value. This linear relation is a reasonable approximation up to $y/\delta \approx 0.2$.

Determination of $\overline{v'^2}$. When $(\overline{v'^2})^{1/2}$ is used as velocity scale in the turbulence model, the distribution of $\overline{v'^2}$ needs to be determined. The most direct way to obtain $\overline{v'^2}$ would be to solve a transport equation for $\overline{v'^2}$ and this is what Durbin (1990) proposed when he introduced $(\overline{v'^2})^{1/2}$ as velocity scale. However, the pressure-strain term in the $\overline{v'^2}$-equation has then to be modeled and, especially for near-wall regions, this is a difficult and an unresolved problem. Further, for a simple near-wall model for use in practical calculations, it is desirable to keep the model at the one-equation level and not to add further equations. Hence, the suggestion of Hanjalić and Launder (1976) is followed here to introduce a simple relation between $\overline{v'^2}/k$ and $\overline{u'v'}/k$. Hanjalić and Launder based their simple relation on two assumptions. First, they assumed that the shear-stress correlation coefficient is constant, *i.e.*

$$\frac{-\overline{u'v'}}{(\overline{u'^2}\ \overline{v'^2})^{1/2}} = \text{constant} \tag{24}$$

They further assumed that the kinetic energy is related to the components $\overline{u'^2}$ and $\overline{v'^2}$ by

$$k = a(\overline{u'^2} + \overline{v'^2}) \tag{25}$$

where a is a constant, which also implies that the ratio $\overline{w'^2}/k = \text{constant}$. The first assumption is well supported by the DNS data, as can be seen from Fig. 7. Fig. 5 shows that the second assumption is also well supported away from the wall while near the wall $\overline{w'^2}/k$ has a dip which however recovers at the wall itself. This dip is stronger in the channel flow than in the boundary layer. Combining relations (24) and (25) yields:

$$\frac{\overline{v'^2}}{k} = \frac{a}{c^2}\left(\frac{\overline{u'v'}}{k}\right)^2 + a\left(\frac{\overline{v'^2}}{k}\right)^2 \tag{26}$$

which is a quadratic equation for $\overline{v'^2}/k$. Hanjalić and Launder (1976) linearized this equation by omitting the second term on the right-hand side and compensating for this by suitably choosing the coefficient in front of the first term. Their final model relation reads:

$$\frac{\overline{v'^2}}{k} = 4\left(\frac{\overline{u'v'}}{k}\right)^2 \tag{27}$$

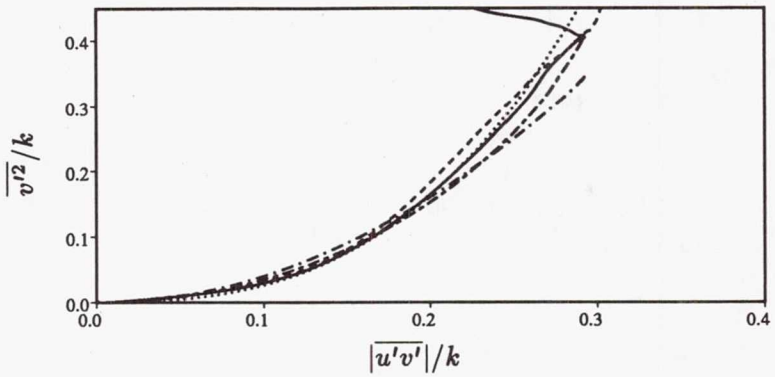

FIGURE 17. Variation of $\overline{v'^2}/k$ versus $|\overline{u'v'}|/k$: ——— channel DNS $Re_\tau = 395$; - - - - Boundary layer DNS $Re_\theta = 1416$; —·— Eq. (27); —··— Eq. (28); ····· Eq. (29).

This relation is compared in Fig. 17 with the DNS data and shows that altogether it is not a bad fit but underpredicts $\overline{v'^2}/k$ as $\overline{u'v'}/k$ approaches 0.3. When the quadratic equation (26) is solved for $\overline{v'^2}/k$, there results:

$$\frac{\overline{v'^2}}{k} = \frac{1}{2a}\left(1 - \sqrt{1 - 4\left(\frac{a}{c}\right)^2\left(\frac{\overline{u'v'}}{k}\right)^2}\right) \tag{28}$$

With $a = 0.7$ and $c = 0.42$ as a consensus of the data (see Figs. 5 and 7) the resulting curve is also included in Fig. 17. This provides a better fit at the larger $\overline{u'v'}/k$-values, but the relation still underpredicts $\overline{v'^2}/k$ in the range $.2 < |\overline{u'v'}|/k < .25$. A better representation over the entire range of $\overline{u'v'}/k$ can be obtained by the following fit to the data:

$$\frac{\overline{v'^2}}{k} = 1.13\left(\frac{\overline{u'v'}}{k}\right)^2 + 14.67\left(\frac{|\overline{u'v'}|}{k}\right)^3 \tag{29}$$

This curve is also included in Fig. 17 and can be seen to represent the relation between $\overline{v'^2}/k$ and $\overline{u'v'}/k$ with sufficient accuracy for use in a one-equation model restricted to the near-wall region.

5. Conclusions

The direct simulation data have shown that, for the Reynolds number investigated, there is still considerable influence of the Reynolds number on the quantities plotted in wall coordinates. However, for the higher Reynolds numbers simulated, the quantities are already close to those observed in experiments at much higher Reynolds numbers. On the other hand, for both channel and boundary layer the lower-Reynolds-number cases are subject to considerable viscous effects. It was also found that, except very close to the wall, the normal stresses are somewhat higher in boundary-layer than in channel flow because of the different shear-stress behavior.

The length scale l_μ in the eddy-viscosity relation of existing one-equation models follows a near-linear behavior near the wall, but very close to the wall it falls below this distribution and requires the introduction of a damping function similar to that for the mixing-length distribution. Damping functions were evaluated with the aid of the DNS data, and the existing ones were found not to be accurate. Based on the data, a new damping function was proposed. The distribution of the length scale l_ϵ in the dissipation relation shows a pronounced hump at $y^+ \approx 15$ and lies considerably above the linear distribution near the wall. This behavior is not easy to describe in a simple relation, but the distribution of the modified dissipation rate $\tilde{\epsilon}$ itself can be fairly accurately modeled in terms of shear stress and wall distance.

When the normal fluctuations $(\overline{v'^2})^{1/2}$ are introduced as velocity scale instead of $k^{1/2}$, the corresponding length scales are better behaved, *i.e.* the dissipation length $l_{\epsilon,v}$ does not have a hump and the length $l_{\mu,v}$ is subject to much less damping. Near the wall, both length scales can be approximated quite well by linear relations and no damping functions are needed. It was found that $\overline{v'^2}/k$ and $\overline{u'v'}/k$ correlate quite well near the wall, and a correlation was proposed for use in one-equation models which avoids solving an additional equation of $\overline{v'^2}$. Together with the length-scale relations introduced this forms a new one-equation model which should now be tested in actual flow calculations.

The authors are grateful to Dr. Kim for providing the unpublished direct simulation data for the channel flow at $Re_\tau = 395$. The first author (WR) would like to acknowledge the generous support of the Center for Turbulence Research.

REFERENCES

CLARK, J. A. 1968 A study of incompressible turbulent boundary layers in channel flow. *ASME J. Basic Eng.* **90**, 455-468.

CORDES, J. 1991 Entwicklung und Anwendung eines Zweischichten-Turbulenzmodells für abgelöste dreidimensionale Strömungen. *Ph.D. Thesis,* University of Karlsruhe.

DURBIN, P. A. 1990 Near-wall turbulence closure modeling without "damping functions". *CTR Manuscript 112,* Center for Turbulence Research, Stanford University.

HANJALIĆ, K. & LAUNDER, B. E. 1976 Contribution towards a Reynolds-stress closure for low-Reynolds-number turbulence. *J. Fluid Mech.* **74**, 593-610.

HUSSAIN, A. K. M. F. & REYNOLDS, W. C. 1975 Measurement of fully developed turbulent channel flow. *ASME J. Fluids Eng.* **97**, 568-580.

KASTRINAKIS, E. G. & ECKELMANN, H. 1983 Measurement of streamwise vorticity fluctuations in a turbulent channel flow. *J. Fluid Mech.* **137**, 165-186.

KIM, J. 1990 private communication.

KIM, J., MOIN, P. & MOSER, R. 1987 Turbulence statistics in fully developed channel flow at low Reynolds number. *J. Fluid Mech.* **177**, 133-166.

LAUFER, J. 1954 The structure of turbulence in fully developed pipe flow. *NACA Rept. 1174.*

MYONG, H. K. & KASAGI, N. 1988 An anisotropic k-ϵ model taking into account the near-wall limiting behavior of turbulence. Proc. 20th Turbulence Symposium, Tokyo.

NORRIS, L. H. & REYNOLDS, W. C. 1975 Turbulent channel flow with a moving wavy boundary. *Rept. No. FM-10,* Stanford University, Dept. of Mech. Eng.

PATEL, V. C., RODI, W. & SCHEUERER, G. 1985 Turbulence models for near-wall and low-Reynolds number closure: A review. *AIAA J.* **23**(9), 1308-1319.

RODI, W. 1991 Experience with two-layer models combining the k-ϵ model with a one-equation model near the wall. *paper AIAA 91-0216,* Reno, 1991.

SPALART, P. R. 1988 Direct simulation of a turbulent boundary layer up to $R_\theta = 1410$. *J. Fluid Mech.* **187**, 61-98.

WOLFSHTEIN, M. 1969 The velocity and temperature distribution in one-dimensional flow with turbulence augmentation and pressure gradient. *Int. J. Heat Mass Transfer.* **12**, 301-118.

III. Turbulence structure and control group

There are 5 papers in this somewhat loosely coupled group. The common theme of the group was to address various questions on turbulence structures and control, and to resolve issues and controversies arising from existing practices, analyses, and experimental data. Despite the short duration of the summer program, most projects met the objectives, and some highlights of these findings are given below:

Berkooz performed an evaluation of a dynamical systems approach to the wall-layer turbulence. This work was instigated by the recent work of Aubry *et al.* (1988, see the ref. in Berkooz), in which they reported that all essential features of the wall-layer dynamics were reproduced in their model of the wall-layer turbulence using a low dimensional system. In an attempt to relate these results obtained by the dynamical systems approach to those observed in a direct numerical simulation, Berkooz analyzed the computed flow fields by projecting them into the eigenfunctions defined by the proper orthogonal decomposition. A few statistics in the phase space were examined, but the evidence presented in the present paper is rudimentary at best. Further work is needed to draw any definite conclusions on the subject, and to examine whether this approach is a viable tool for developing a practical control scheme as suggested by the author in the concluding remark.

Chen *et al.* investigated the topology of small scales in mixing layers by examining the invariants of the velocity-gradient and the strain-rate tensor. This study was based on a previous work which demonstrated that flow structures can be concisely described in the space of invariants of the velocity-gradient tensor. Both compressible and incompressible flow fields were examined. Flow structures obtained in the invariant space were compared with those obtained in the physical space. Similarities and dissimilarities in the information contained in the two approaches were discussed. It was shown that a remarkable compression of information was achieved by presenting flow structures in the invariant space. For example, the flow topologies visualized in the invariant space showed how the vorticity in the rib region of a mixing layer was first stretched and then compressed as it was wrapped up by the main vortex. A strong correlation between the second and third variants (the first invariant is zero for incompressible flow and small relative to the others for compressible flow) for motions associated with high rates of dissipation was observed, suggesting that the triple products of velocity gradients may be related to the double products in a simple manner.

Guezennec *et al.* investigated the scalar transport in a turbulent channel flow. One of the objectives of this study was to address whether the heat-tagging for vorticity as commonly done in laboratory experiments is indeed accurately marking the vorticity. It was found that the correlation between the heat and vorticity was high in the wall region, where heat was released, but low away from the wall, suggesting that there exists considerable uncertainty in the use of passive markers for

vorticity. Differences between the heat and momentum transport were examined by analyzing the terms that appear in the transport equations. The pressure gradient term in the momentum equations (there is no pressure term in the heat equation) was found to be the dominant term except in the near-wall region where the viscous term becomes as significant as the pressure term. It was found that the mixing of momentum was more efficient than that of heat because of the pressure term, consistent with visual observations that passive scalars tend to wrap around more along the edge of coherent vortical motions. It should be noted that there was no high Schmidt (or Peclet) number effect since the numerical experiments were performed at $Pr = 0.1, 0.71, 2$. In the laboratory experiments where smoke or dye is used to tag the vorticity, the Schmidt number effect also plays a role in addition to the pressure effect discussed in the present paper.

Itsweire *et al.* examined the effect of shear and stratification on homogeneous turbulence. They examined, *inter alia*, the nature of the microstructure patches observed in ocean. This is an important problem in oceanic mixing, and there exists controversy on the nature of these microstructure patches among oceanographers, whether these patches consist of active turbulence or fossilized turbulence. They were able to show the effect of buoyancy on various turbulence length scales, and presented criteria for the onset and complete fossilization of turbulence. They presented a hydrodynamic phase diagram that describes the evolution of turbulence from the active to the fossil region. They also performed an evaluation of existing eddy diffusivity models using the direct simulation data, a step forward toward developing a better turbulence model correctly accounting for the buoyancy effects.

Tam and Lele investigated possible resonant instability of a supersonic shear layer. Tam came to the Summer Program to examine whether his asymptotic analysis, in which he suggested the use of resonant instability to destabilize supersonic mixing layers in a duct, can be realized in a simulated experimental environment other than the idealized condition of the perturbation analysis. Although the outcome was negative, i.e., they failed to observe any enhancement of mixing due to the resonant instability (albeit the parameters they used were not the optimal ones), this was a good example how theories and numerical simulations hand in hand can be utilized to advance our understanding of turbulence. In the second part of their paper, they also examined possible feedback instability as a mechanism for mixing enhancement involving a supersonic and a subsonic stream. Some evidence of feedback oscillations was observed, which was consistent with an existing feedback theory. These results are encouraging, but more work is required to resolve issues involving such as non-physical feedback and the short run time, etc., before a definite conclusion can be drawn.

John Kim

The structure of turbulent channel flow with passive scalar transport

By Y. Guezennec[1], D. Stretch[2] & J. Kim[3]

The simulations of a turbulent channel flow with various passive markers were examined to investigate the local mechanisms of passive scalar transport. We found significant differences between the local transport of heat and momentum, even when the molecular and turbulent Prandtl numbers are of order one. These discrepancies can be attributed to the role of the pressure. We also found that the heat is a poor marker of the vorticity field outside of the near wall region and that scalar transport over significant distances results from the aggregate effect of many turbulent eddies.

1. Introduction

Our objective was to make use of the direct numerical simulations of a turbulent channel flow with passive scalars (Kim & Moin, 1989) to investigate the relationship between the transport of a passive scalar and the underlying turbulent eddy structures. Specifically, our objectives were fourfold:

1. The validation of experimental techniques such as heat tagging and smoke visualization often used by experimentalists to "mark" turbulent structures.

2. The investigation of the role of the coherent structures in a turbulent channel flow for the transport of a passive scalar.

3. The modeling of the scalar transport based on the mechanistic understanding of the coherent structures.

4. The study of the interaction between large scales and the wall layer, and the relation, if any, between the two wall layers.

The data bases examined were those described by Kim & Moin (1989), with additional cases subsequently obtained by J. Kim. More specifically, all cases correspond to a turbulent channel flow at a Reynolds number $Re_\tau = 180$ with fully developed hydrodynamics. The simulations were performed with three scalars simultaneously with $Pr = 0.1, 0.7$ and 2.0, respectively. For this study, we concentrated our efforts on the $Pr = 0.7$ case unless otherwise noted. The various simulations differed by their boundary conditions for the thermal field and the state of their thermal development. Case I corresponded to a fully developed thermal field with uniform heat generation throughout the channel and both walls cold. Case II corresponded

1 The Ohio State University
2 Center for Turbulence Research
3 NASA Ames Research Center

to a fully developed thermal field with one hot wall and one cold wall. It was chosen because the *average* heat flux remains constant at any distance from the wall. The remaining three cases were time developing thermal fields, with time history available with a time spacing $\Delta t^+ = 3$. Case III corresponds to a cold channel flow where one wall was suddenly heated at $t = 0$. Case IV was similar but with a heat source at the center line instead of a hot wall and Case V was similar to Case III with one wall heated and the other cooled. These latter three cases were intended for the study of the development of the thermal field and for using the heat as a marker to study the interaction between various regions of the flow.

The notation used in this report is as follows: u, v, w denote streamwise, vertical and spanwise velocity fluctuations respectively. In the text θ is used to denote temperature fluctuations while the character t is used for temperature in the diagrams.

2. Validation of the Heat as a Marker of Vorticity

The underlying motivation for this task is the extensive use by experimentalists of passive markers (heat, smoke or dye) to study the structure of turbulent wall bounded flows. We wanted to investigate what the scalar really marks and how that varies with the distance from the wall. To address this important question, we correlated the temperature field (or the gradients of the temperature field) with various components of the vorticity or enstrophy field. Not only did we examine pointwise correlation coefficients but also conditional correlation coefficients and spatial correlations. The data from case II were used for this investigation.

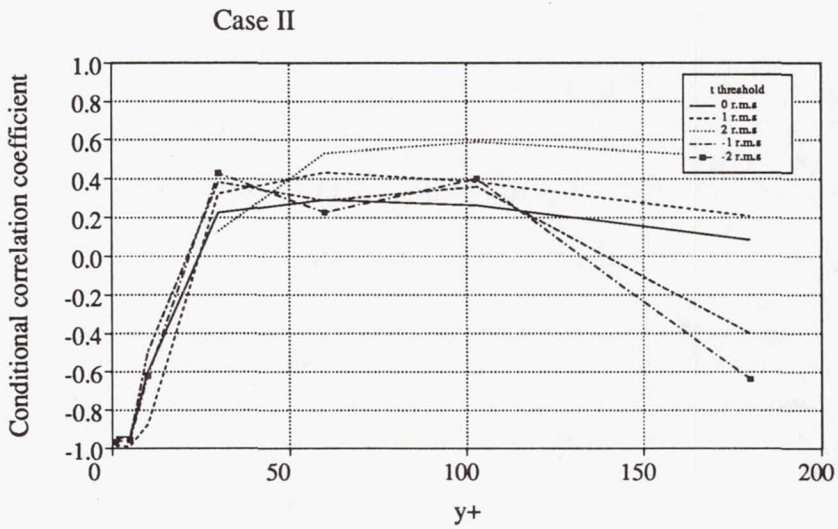

FIGURE 1. Conditional correlation coefficients between the temperature and the vorticity magnitude as a function of the distance from the wall. Temperature thresholds are ——— ,0; - - - - ,σ_θ; ····· ,$2\sigma_\theta$; — - — ,$-\sigma_\theta$; — · — ,$-2\sigma_\theta$.

Figure 1 shows a sample of the results where the temperature fluctuations were correlated pointwise with the magnitude of the vorticity vector. The various curves

correspond to different threshold values on the temperature fluctuations : a threshold of zero is an unconditional correlation, whereas non-zero values correspond to correlation coefficients conditional on the temperature exceeding that threshold value. It can be noted that very near the wall ($y^+ < 15$), there is a strong negative correlation between the temperature and the vorticity magnitude. This is linked to the fact that the largest contribution to the vorticity fluctuation comes from the u' fluctuations which are strongly correlated with the temperature (see figure 2). In that region, the conditioning on strong temperature fluctuations does not significantly affect the correlations. For $y^+ > 30$, the unconditional correlation coefficient becomes mildly positive but low in magnitude, implying that the temperature (pointwise) becomes a poor marker of vortical fluid outside of the wall region. However, by conditioning the correlation on the magnitude of the temperature fluctuations, the correlation improves somewhat in particular for large positive temperature fluctuations (threshold value of 2 σ_θ).

The rapid decorrelation of the temperature and the vorticity magnitude with increasing distances from the wall partly stems from a loss of spatial phase information. This is particularly true at $y^+ = 25$ where the pointwise correlation coefficient becomes zero and changes sign. By examining the spatial correlation maps (not shown here), one notices that the strong negative correlation observed near the wall shifts in the downstream direction and that a positive correlation peak appears upstream. This continuous change of the phase relationship between the temperature and the vorticity magnitude renders the interpretation of the passive marker difficult except near the wall. In the buffer region, the vorticity magnitude is better marked by the streamwise temperature gradient, while further away from the wall the vorticity magnitude becomes weakly correlated with the strong temperature fluctuations.

Other combinations of temperature, temperature gradients and vorticity components were investigated. Away from the wall region temperature gradients correlate slightly better with the vorticity magnitude, but we did not find a particular combination that gives a high correlation. These results suggest that there is considerable uncertainty in the use of temperature as a marker for the vortical structures originating from the wall region. The reason for this will become clear later in this report.

3. The Structure of the Heat and Momentum Flux

To investigate this aspect of the problem, Case II was chosen since it had the property that the average total heat flux $q = -\overline{v\theta} + \frac{1}{ReP_r}\frac{d\bar{\theta}}{dy}$ was constant at any distance from the wall. This allowed us to examine how this same average heat flux was distributed in space and what underlying eddy structure was responsible for it as a function of the distance from the wall.

Figure 2 shows the turbulent heat and momentum fluxes as a function of the distance from the wall. As mentioned earlier the streamwise velocity is well correlated (negatively) with the temperature through a significant part of the channel. As observed before (Kim & Moin, 1989), the $\overline{uv}$ and $\overline{v\theta}$ have comparable magnitudes

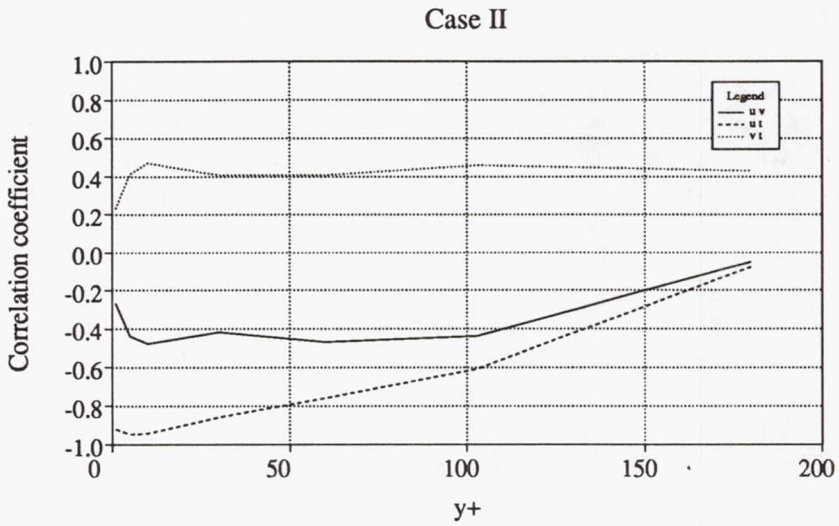

FIGURE 2. Turbulent heat and momentum fluxes as a function of the distance from the wall. Curves are ——— , $\frac{\overline{uv}}{\sigma_u \sigma_v}$; ····· , $\frac{\overline{v\theta}}{\sigma_v \sigma_\theta}$; - - - - , $\frac{\overline{u\theta}}{\sigma_u \sigma_\theta}$.

(and opposite signs) in the wall and log region, which means that the turbulent Prandtl number Pr_T is nearly unity. The molecular Prandtl number Pr is also of order one (0.7) in this case. However, the fluctuations in the products uv and $v\theta$ as measured by their root mean square values σ_{uv} and $\sigma_{v\theta}$, are quite different. The turbulent heat flux has a fluctuation level more than twice that of the momentum flux, despite their nearly equal mean values. This difference led us to believe that the turbulent transport of a passive scalar may be significantly different from the momentum transport locally and instantaneously, despite being associated with the same eddy structures, and despite the average transport $\overline{uv}$ and $\overline{v\theta}$ being similar.

Figures 3 and 4 show the contributions of the individual velocity and temperature fluctuations to the turbulent momentum and heat flux, respectively. For the case of the momentum, it can be observed that both u and v fluctuations are equally correlated (but with opposite sign) with contributions to the momentum flux. The change of sign around $y^+ = 20$ corresponds to the point where the momentum flux changes from being dominated by fourth quadrant motions (sweeps) near the wall to second quadrant motions (ejections) away from the wall. For the scalar field near the wall ($y^+ < 25$), the heat flux contributions are predominantly from cold fluid moving towards the wall, corresponding to fourth quadrant motions in the velocity field. Both v and θ are equally correlated with $v\theta$ in this region. It should be noted that this is also the region where σ_{uv} is approximately equal to $\sigma_{v\theta}$. In the region away from the wall ($y^+ > 25$) the individual correlations between v and θ and the turbulent heat flux are quite different. The temperature fluctuations have near zero correlation with the turbulent heat flux. This seems to indicate significant local countergradient transport. It should also be noted that this is the region where the fluctuations in the instantaneous turbulent heat flux are considerably higher

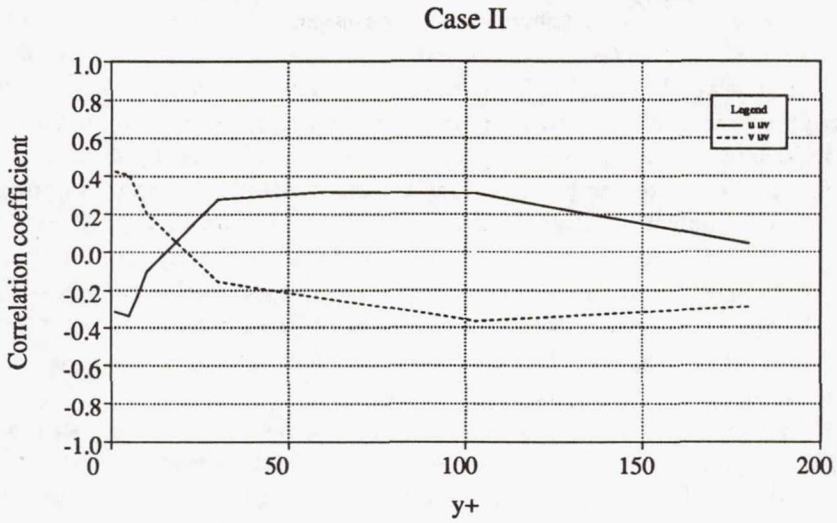

FIGURE 3. Contributions of u and v to the turbulent momentum flux as a function of the distance from the wall. Curves are ——— ,u–uv correlation; - - - - ,v–uv correlation.

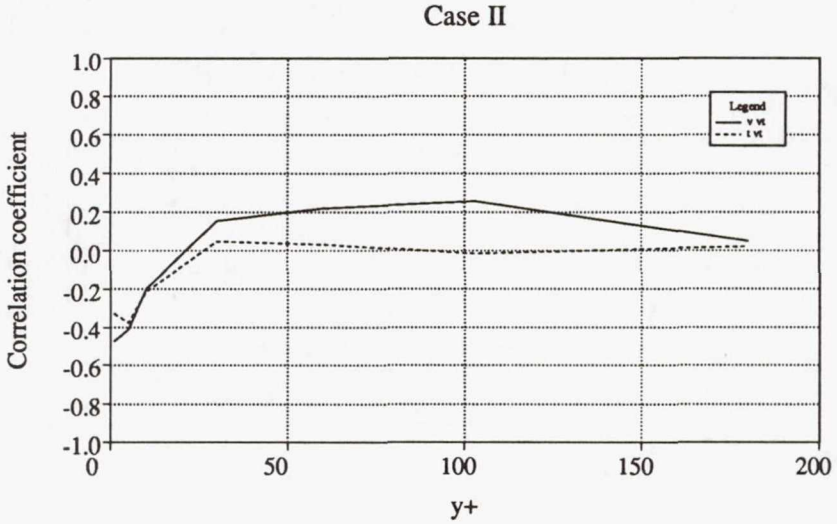

FIGURE 4. Contributions of v and θ to the turbulent heat flux as a function of the distance from the wall. Curves are ——— ,v–$v\theta$ correlation; - - - - ,θ–$v\theta$ correlation.

than those of the turbulent momentum flux. There is therefore a lot of "churning" of the scalar field by the eddies, but little actual mixing. This point is further illustrated by examining the instantaneous velocity and temperature field. Figure 5 represents a cut of the channel perpendicular to the flow (yz plane). The spanwise and normal velocity components are shown as a vector plot and the color contours

represent iso-levels of streamwise velocity fluctuations u on the top or temperature fluctuations θ on the bottom. The same number of contours was used for both fields. It can be seen that for the same eddy structures, the temperature field seems to be "wrapped" around the eddies more than the streamwise momentum. In other words, a fluid particle being displaced in the normal direction by an eddy keeps its temperature marking longer than it does its momentum marking. Figure 5 is for a case where the molecular Prandtl number is of order one (0.7), but examination of scalar fields corresponding to $Pr = 0.1$ and 2.0 indicated that the observed effects are not sensitive to Prandtl number. The high Prandtl number case exhibits sharper temperature interfaces but no significant changes in terms of the "wrapping" around. Hence, the more rapid loss of momentum marking by a fluid particle cannot be attributed to diffusive effects.

If one examines the instantaneous transport equations for momentum and temperature, one significant difference is the absence of the pressure gradient term on the right hand side of the temperature equation. Since the diffusive terms are similar for both equations, the pressure must be responsible for the difference in behavior between the two fields. To further quantify this point, the correlation coefficients between the acceleration terms in the Navier-Stokes equations and the pressure and viscous terms was calculated for each of the components. These are shown as a function of the distance from the wall in figure 6. Similarly, the root mean square values for those terms were also calculated and are shown in figure 7.

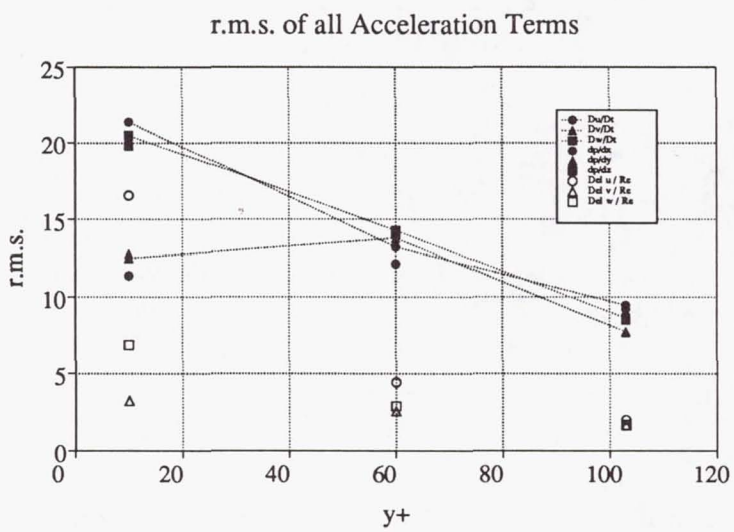

FIGURE 7. Root mean square fluctuations of the various terms contributing to the total accelerations as a function of the distance from the wall.

It can be observed that for the streamwise acceleration, the viscous terms are slightly dominant in terms of magnitude and correlation near the wall ($y^+ < 30$), but that away from the wall, the pressure gradient term is almost the sole contributor to the streamwise acceleration. More surprisingly, the normal and spanwise

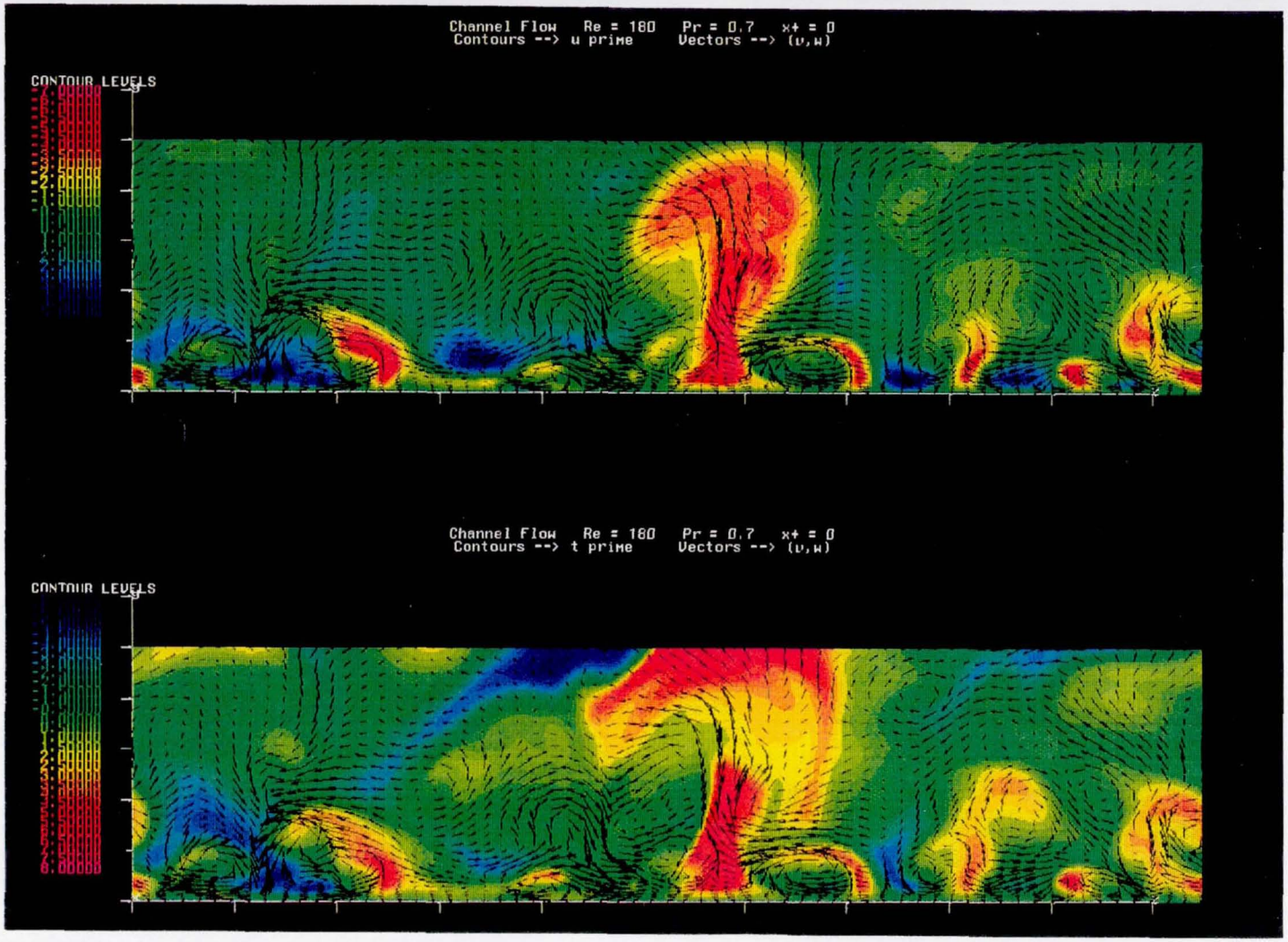

FIGURE 5. Comparison between the instantaneous streamwise velocity fluctuation field (top) and temperature fluctuation field (bottom), highlighted with the vector plot of the spanwise and normal velocity components.

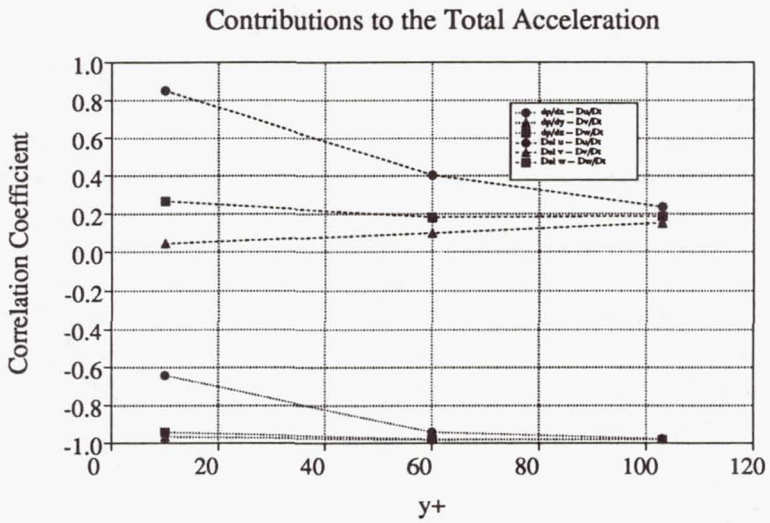

FIGURE 6. Correlation coefficients between the total accelerations and the corresponding pressure and viscous terms as a function of the distance from the wall.

acceleration terms are completely dominated by the pressure gradient term, even in the so-called viscous region at $y^+ = 10$. In other words, the *cross-stream dynamics are essentially inviscid!* The viscous terms only play an indirect role through the streamwise convection which ties in the normal and spanwise velocity component through the incompressibility constraint. The dominant role played by the pressure in the momentum transport explains the differences observed between the momentum and scalar field. The absence of any significant effect of the molecular Prandtl number mentioned earlier is consistent with the small contribution to the acceleration terms by the viscous forces. In other words, once a fluid element has been displaced in the normal direction by a turbulent eddy, it retains most of its heat marking due to the lack of a strong diffusive effect (on the time scale of the eddy dynamics) until it is "churned" again by the next eddy. On the other hand, the same fluid element loses its streamwise momentum marking very fast, as strong pressure gradient forces are generated locally to exchange the momentum of that fluid element with its surroundings. The turbulence is thus more efficient at "mixing" the momentum than the heat, while the temperature retains a higher degree of unmixedness and appears to "wrap" around the eddies as described earlier. These observations are consistent with the fact that for the same net average heat flux as momentum flux ($Pr_T = 1$), there is a higher level of fluctuations ($\sigma_{v\theta} > \sigma_{uv}$). There is significantly more local heat transfer in both directions (i.e. down-gradient and counter-gradient transport) for a small net gradient transfer. This was further verified by comparing the p.d.f. of the instantaneous heat and momentum fluxes (not shown here).

4. Pattern Recognition of the Dominant Eddy Structure

In order to further quantify the above observations regarding the structure of the scalar flux, we applied an automated pattern eduction method to analyze the flow. Details of the method are reported elsewhere (Stretch, 1989 ; Stretch, Kim and Britter, 1990). It is based on an iterative convolution between a reference pattern and the data.

A sample of the results obtained is shown in figure 8(a). The diagnostics used in this example were the vertical and spanwise velocity fluctuations. The basic ensemble averaged flow structure educed by the analyses consists of attached eddies spanning the flow from the wall to near the centerline of the channel (see Stretch, 1989 and Stretch, Kim and Britter, 1990 for further details). Ensemble averages of the streamwise velocity fluctuations and the temperature fluctuations were computed at the pattern locations and are included in figures 8(b) and (c). As expected the large streamwise velocity fluctuations are associated with the upwelling and downwelling motions which are in turn associated with the attached eddy structures. It is further apparent from the ensemble averages that the scalar perturbations have a greater vertical extent than the streamwise momentum fluctuations. The scalar field also shows a slightly greater tendency to be wrapped around the vortical structures. These results are consistent with the instantaneous fields shown in figure 5 and further support the conclusions we have drawn above.

5. Time Evolution of the Temperature Field in a Developing Flow.

To quantify the effective net transport of heat by the turbulent eddies, the data from Case III was examined. Since the fluid was initially cold, the effectiveness of the net turbulent transport was judged by tracking in time the deepest penetration of the temperature disturbance. This was repeated for various levels of temperature disturbances.

The results are summarized in figure 9 for 10 different magnitudes of the temperature disturbance. Naturally, the smallest temperature disturbance penetrates the farthest and the fastest. For reference, the average penetration speed, V_p, was calculated from the initial slope of these curves. For $\theta = 0.05$, this speed is $1.23u_\tau$, while it is $0.4u_\tau$ for $\theta = 0.5$. As a reference, the r.m.s. of the normal velocity fluctuations σ_v is of the order of $0.8u_\tau$ for the bulk of that region. Those penetration speeds computed represent an upper bound since they are calculated for the fastest penetrating disturbances. The speeds are typical of the velocity magnitudes which are induced around the vortical structures in the flow. This is consistent with our previous observation that the scalar transport is associated with these structures. However these vortices or eddies have diameters typically much smaller than the channel half width ($d^+ \simeq 20$ and $\delta^+ = 180$), a distinction which is expected to increase with Reynolds number. It therefore seems that the turbulent transport across significant distances in the normal direction results from the aggregate effect of many eddies, each transporting a material element over a distance of order their diameter at a speed of order u_τ, but not necessarily always in the right direction

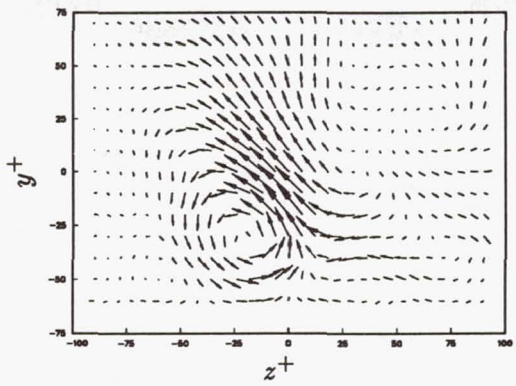

(a)

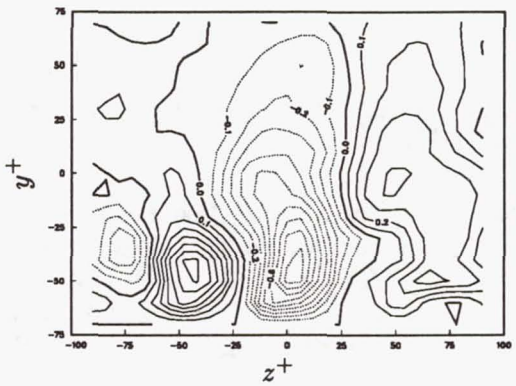

(b)

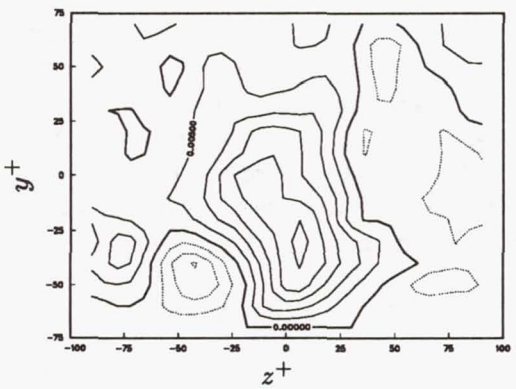

(c)

FIGURE 8. Samples of the pattern analysis results: zy plane views of ensemble averaged (a) velocity vectors; (b) streamwise momentum fluctuations; (c) temperature fluctuations.

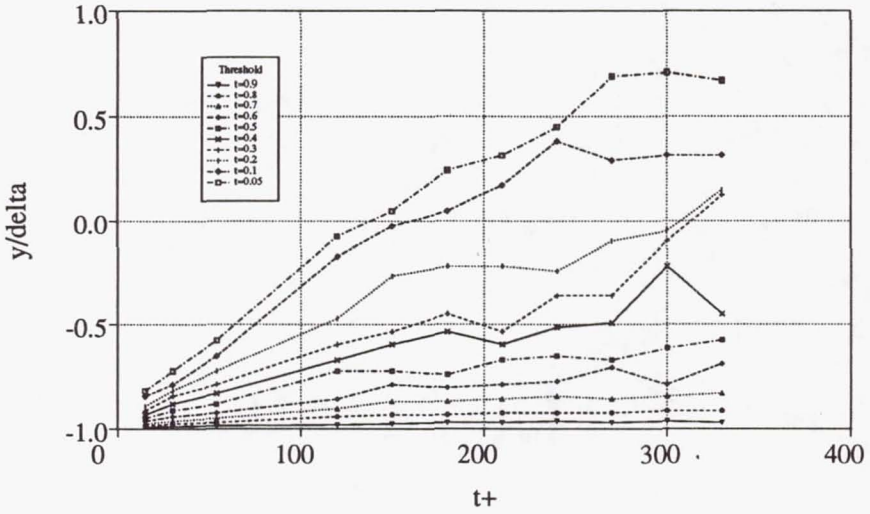

FIGURE 9. Outmost penetration of the turbulent heat flux as a function of time for various levels of temperature disturbances.

as was discussed in section 3. Hence, it may take many interactions between a material element and the turbulent eddies before it is "transported" over a significant distance (say of the order of a few hundred of wall units). However, this process is still far more efficient than a strictly diffusive effect. This aggregate transport process also explains the poor marking of the vorticity field by the passive scalar.

6. Conclusions

In summary, the following conclusions were reached:

1. Outside the near wall region $y^+ < 20$, one must be very careful in interpreting the passive scalar concentration in terms of the underlying vortical eddy structure.

2. There are significant differences between the transport of momentum and heat, even when the molecular and turbulent Prandtl numbers are of order one. These differences are linked to the role of the pressure.

3. The transport of passive scalar over significant distances appears to result from the aggregate interaction of many eddies.

REFERENCES

KIM, J. & MOIN, P. 1989 *Turbulent Shear Flows 6*, 85-96. Springer-Verlag

STRETCH, D. D. 1989 Patterns in simulated turbulent channel flow. *Annual Research Briefs - 1989* Center for Turbulence Research, Stanford, CA 94305-3030

STRETCH, D. D., KIM, J. & BRITTER, R. E. 1990 Patterns in simulated turbulent channel flow. *Unpublished manuscript to be submitted*

A study of the topology of dissipating motions in direct numerical simulations of time-developing compressible and incompressible mixing layers

By J. H. Chen[1], M. S. Chong[2], J. Soria[3], R. Sondergaard[4], A. E. Perry[2], M. Rogers[5], R. Moser[5] AND B. J. Cantwell[4]

A preliminary investigation of the geometry of flow patterns in numerically simulated compressible and incompressible mixing layers was carried out using 3-D critical point methodology. Motions characterized by high rates of kinetic energy dissipation and/or high enstrophy were of particular interest. In the approach the partial derivatives of the velocity field are determined at every point in the flow. These are used to construct the invariants of the velocity gradient tensor and the rate-of-strain tensor (P, Q, R, and P_s, Q_s, R_s respectively). For incompressible flow the first invariant is zero. For the conditions of the compressible simulation, the first invariant is found to be everywhere small, relative to the second and third invariants, and so in both cases the local topology at a point is mainly determined by the second and third invariants. The data at every grid point is used to construct scatter plots of Q versus R and Q_s versus R_s. Most points map to a cluster near the origin in Q–R space. However, fine scale motions, that is motions which are characterized by velocity derivatives which scale with $\sqrt{R_\delta}$, tend to map to regions which lie far from the origin. Definite trends are observed for motions characterized by high enstrophy and/or high dissipation. The observed trends suggest that, for these motions, the second and third invariants of the velocity gradient and rate-of-strain tensors are strongly correlated. Motions corresponding to high rates of dissipation are found to be characterized by a 3-D rate-of-strain topology which is of the type saddle-saddle-*unstable*-node; the topology saddle-saddle-*stable*-node is not observed for these motions. The second and third invariants of the rate-of-strain tensor are related by $R_s \cong K(-Q_s)^{3/2}$, which is consistent with the above scaling of velocity derivatives. The quantity K appears to depend on Reynolds number with an upper limit $K = 2\sqrt{3}/9$ corresponding to locally axisymmetric flow. For both the compressible and incompressible mixing layer, regions corresponding to high rates of dissipation are found to be characterized by comparable magnitudes of $R_{ij}R_{ij}$ and $S_{ij}S_{ij}$. For the incompressible mixing layer, regions characterized by the highest values of enstrophy are found to have relatively low strain rates.

---

1 Sandia National Laboratories
2 Dept. of Mech. Eng., The University of Melbourne, Australia
3 CSIRO, Highett, Australia
4 Dept. of Aero/Astro, Stanford University
5 NASA Ames Research Center

1. Background

The high wavenumber motions of turbulence are not well understood. The classical Kolmogorov theory for the inertial and dissipation subrange claims that such motions are locally isotropic and that kinetic energy flows from the low wavenumber end of the spectrum to the high wavenumber end by a cascade process. These ideas have been questioned for many decades, and no satisfactory physical picture has emerged which will support or refute the Kolmogorov model. For a recent appreciation of this problem see Frisch and Orzag (1990), who note that less is known about the fine scale structure of turbulence than about the structure of atomic nuclei. The purpose of this project is to initiate a study of the geometry of high wavenumber motions using data from recent direct numerical simulations of free shear layers. The cases studied included the time developing compressible mixing layer computed by Chen (1990) and the time developing incompressible mixing layer computed by Moser and Rogers (1990). The conditions of the two simulations are as follows:

	incompressible	compressible
$M_{\text{convective}}$	0	0.8
Initial R_δ	500	800
Final R_δ	3000	1600
Grid	$128 \times 256 \times 64$	$384 \times 201 \times 192$

where R_δ is the Reynolds number based on the layer velocity difference, $U_1 - U_2 = 2U$ and vorticity thickness, $R_\delta = (U_1 - U_2)\delta/\nu$. The actual data in both computations is normalized by the half-velocity difference, U, and the *initial* vorticity thickness of the layer, δ_0. The final Reynolds number of the incompressible computation is here estimated in terms of the instantaneous vorticity thickness which fluctuates considerably with time. A more stable length scale is the momentum thickness which increases by a factor of 6.5 over the course of the computation. Results for the incompressible case at $R_\delta = 3000$ are shown in Figures 3–11. Results for the compressible case at $R_\delta = 1600$ are shown in Figures 3–5 and Figures 12–14. All results presented in this paper are normalized by U and δ_0.

These simulations, particularly the incompressible case, are at Reynolds numbers which begin to approach values for which the layer would be regarded as simulating turbulent flow. At the late stages following a vortex pairing in the simulation by Moser and Rogers, the mixing layer exhibits tertiary instabilities similar in structure to the so-called "mixing transition" observed in laboratory experiments (Bernal and Roshko, 1986).

2. Approach

Topological methods are useful in the description of fields and are coming increasingly into use as a means to study large data sets generated by direct numerical simulation. In a previous summer program of the Center for Turbulence Research,

Hunt, Wray, and Moin (1988) developed criteria based on the invariants of the velocity gradient tensor and properties of the local pressure field to identify important characteristics of flow zones in direct numerical simulations of homogeneous turbulence and turbulent channel flow. Recently Chong, Perry, and Cantwell (1990) have carried out a classification of the various types of linear three-dimensional flow patterns which can occur in compressible and incompressible flow. This classification was used by Cantwell, Chen, and Lewis (1989) and Chen, Cantwell, and Mansour (1989) to analyze the topology of the flow structure in direct numerical simulations of a compressible plane wake and in experimental measurements of a pulsed low-speed diffusion flame. The method is based on concisely summarizing the flow structure in the space of invariants of the velocity gradient tensor.

The velocity gradient tensor may be broken up into a symmetric and an antisymmetric part, $A_{ij} = \partial u_i/\partial x_j = S_{ij} + R_{ij}$, where $S_{ij} = (\partial u_i/\partial x_j + \partial u_j/\partial x_i)/2$ and $R_{ij} = (\partial u_i/\partial x_j - \partial u_j/\partial x_i)/2$ are the rate-of-strain and rate-of-rotation tensors respectively. The eigenvalues of A_{ij} satisfy the characteristic equation

$$\lambda^3 + P\lambda^2 + Q\lambda + R = 0 \tag{1}$$

where the matrix invariants are:

$$P = -(a_{11} + a_{22} + a_{33}) = -\text{trace}\,[A] = -S_{ii} \tag{2}$$

$$\begin{aligned} Q &= \begin{vmatrix} a_{11} & a_{12} \\ a_{21} & a_{22} \end{vmatrix} + \begin{vmatrix} a_{11} & a_{13} \\ a_{31} & a_{33} \end{vmatrix} + \begin{vmatrix} a_{22} & a_{23} \\ a_{32} & a_{33} \end{vmatrix} \\ &= \frac{1}{2}\left[P^2 - \text{trace}[A^2]\right] \\ &= \frac{1}{2}\left[P^2 - S_{ij}S_{ji} - R_{ij}R_{ji}\right] \end{aligned} \tag{3}$$

and

$$\begin{aligned} R &= -\begin{vmatrix} a_{11} & a_{12} & a_{13} \\ a_{21} & a_{22} & a_{23} \\ a_{31} & a_{32} & a_{33} \end{vmatrix} = -\det[A] \\ &= \frac{1}{3}(-P^3 + 3PQ - \text{trace}[A^3]) \\ &= \frac{1}{3}(-P^3 + 3PQ - S_{ij}S_{jk}S_{ki} - 3R_{ij}R_{jk}S_{ki}). \end{aligned} \tag{4}$$

During the course of the work, it was decided to focus attention on the symmetric part of the velocity gradient tensor, the second invariant of which is proportional to the negative of the kinetic energy dissipation. The invariants of the rate-of-strain tensor, P_s, Q_s, and R_s, are generated by setting the components of R_{ij} to zero in the above relations.

It can be shown that, in the P-Q-R space of matrix invariants, the surface which divides real solutions from complex solutions is

$$27R^2 + (4P^3 - 18PQ)\,R + (4Q^3 - P^2Q^2) = 0. \tag{5}$$

A detailed discussion of the properties of this surface is given in Chong, Perry, and Cantwell (1990) along with a guide to the various possible elementary flow patterns which can occur in different domains.

The method used to classify the flow structure was as follows:

(i) Evaluate the nine partial derivatives of the velocity gradient tensor at every point in the computed field.

(ii) Determine the invariants P, Q, and R and P_s, Q_s, and R_s at every point. For incompressible flow $P = 0$ and, for the compressible case considered, P turned out to be quite close to zero over the whole flow. This is consistent with the fact that, at the convective Mach number of the compressible simulation, eddy-shocklets are not observed (Sandham and Reynolds, 1989).

(iii) Create a scatter plot of the results in the space of tensor invariants Q versus R and Q_s versus R_s.

Figure 1 indicates the various flow topologies which can occur in the plane $P = 0$. The intersection of this plane with the surface (5) is given by

$$R = \pm\frac{2\sqrt{3}}{9}(-Q)^{3/2} \tag{6}$$

which divides real solutions from complex solutions as indicated in Figure 1.

For the case $P = 0$ the second invariant is

$$Q = \frac{1}{2}[R_{ij}R_{ij} - S_{ij}S_{ij}] \tag{7}$$

where the indices of one of the rotation terms and one of the strain terms have been switched to indicate that Q is formed from two terms, each of which is a sum of squares. The local topology has complex or real eigenvalues depending on whether the (Q, R) pair, evaluated at a given point in the flow, lies above or below (6). The mechanical dissipation of kinetic energy due to viscous friction is

$$\phi = 2\nu S_{ij}S_{ij} = -4\nu Q_s. \tag{8}$$

Large negative values of Q_s correspond to large rates of dissipation of kinetic energy. Large negative values of Q indicate regions where the strain is both large and strongly dominant over the enstrophy. Large positive values of Q indicate the reverse.

Figures 2a and 2b show typical instantaneous local streamline patterns in canonical coordinates corresponding to either real (Figure 2a) or complex (Figure 2b) eigenvalues. These are the flow patterns which would be seen by an observer moving with the fluid velocity at the point where P, Q, and R are being evaluated.

Figure 2c illustrates a flow which can occur only in a compressible flow. The patterns illustrated in these figures represent the stable and unstable cases where only the direction of the flow along the streamlines is reversed.

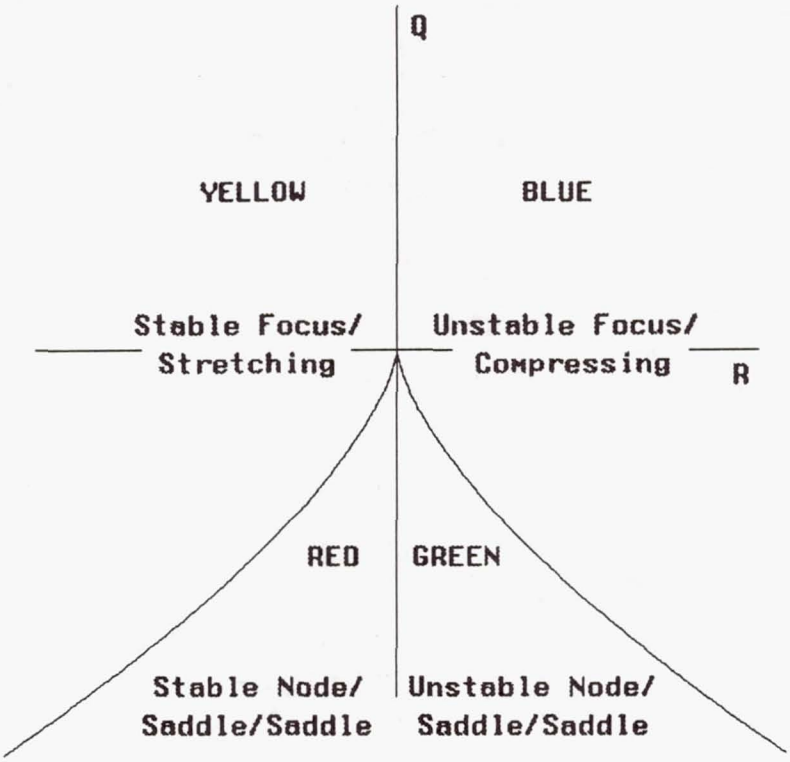

FIGURE 1. Identification of local flow topologies in the plane $P = 0$.

3. Incompressible time developing mixing layer

3.1 Flow structure in physical space

Figures 3a, 3b and 4a, 4b show contour plots of the enstrophy and dissipation respectively in two planes through the mixing layer computation of Moser and Rogers (1990). The flow depicted is at a late stage in the development of the layer when the Reynolds number based on the current vorticity thickness has reached approximately 3000 ($tU/\delta_0 = 29.8-$ after vortex pairing). At this point, well developed streamwise vortices (ribs) have formed and the layer has undergone a tertiary breakdown similar to the mixing transition observed in experiments. Two planes are chosen to illustrate the flow because, as can be seen, the observed plots are quite different depending on whether or not the plane passes through the center of one of the streamwise vortices. The main points to note are that high values of the enstrophy and high rates of dissipation occur in relatively isolated regions which tend to be highly elongated in the streamwise direction. At first sight, they appear to occur in approximately the same regions, although this is more obvious

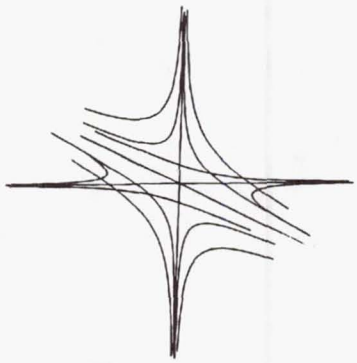

(a)

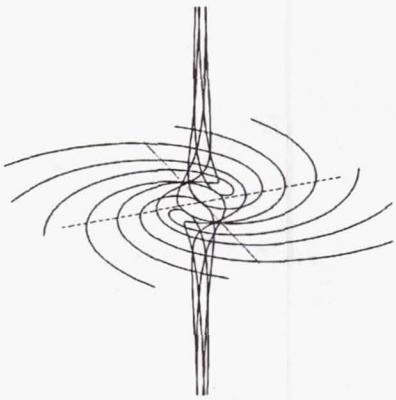

(b)

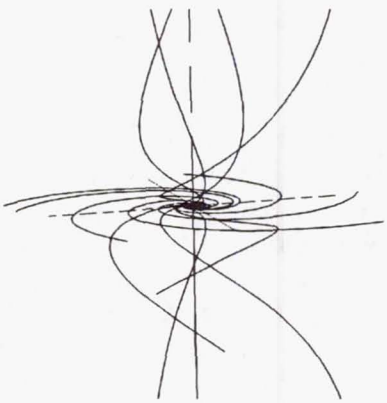

(c)

FIGURE 2. Local flow patterns in canonical coordinates: (a) stable-node-saddle-saddle, (b) stable-focus-stretching, (c) stable-focus-compressing (compressible case only).

FIGURE 3. Maps of the enstrophy field in two planes: (a) vertical rib plane, incompressible case, (b) vertical in-between plane, incompressible case, (c) horizontal plane at the middle of the layer, compressible case.

(a)

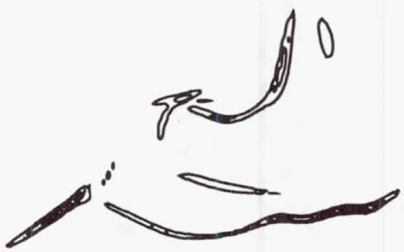

(b)

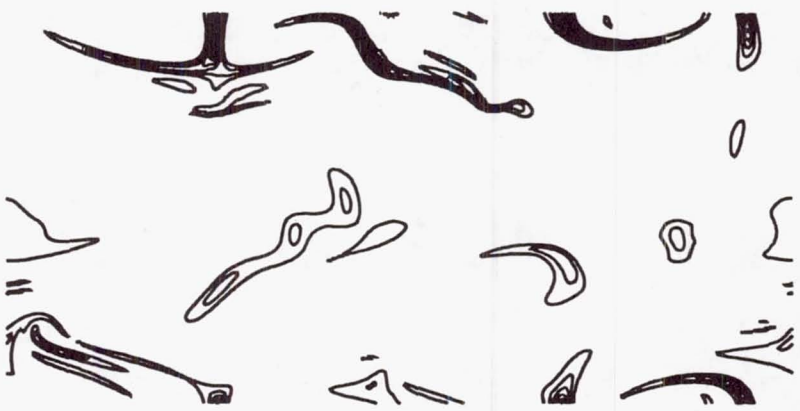

(c)

FIGURE 4. Maps of the dissipation field in two planes: (a) vertical rib plane, incompressible case, (b) vertical in-between plane, incompressible case, (c) horizontal plane at the middle of the layer, compressible case.

FIGURE 5. Maps of the local flow topology in two planes: (a) vertical rib plane, incompressible case, (b) vertical in-between plane, incompressible case, (c) horizontal plane at the middle of the layer, compressible case. See Figure 2 for color code.

in comparing Figures 3b and 4b than in comparing Figures 3a and 4a.

3.2 Flow structure in invariant space

Figures 5a and 5b depict in a new way the same two planes of data as Figures 3 and 4. In these figures, the flow is colored according to the local topology as determined by the values of the second and third invariants of the velocity gradient tensor, Q and R. To understand the color code in Figure 5, it is helpful to refer back to Figures 1 and 2 where the various possible topologies are identified. There is an incredible compression of information which has been achieved in producing Figure 5 which effectively summarizes the local topology at every point in the chosen plane of data. There is a high degree of correspondence between regions of constant topology and the enstrophy contours in Figure 3a.

When information from Figures 3 and 5 is combined, one can get some understanding of where the vorticity is being stretched and where it is being compressed. For example, following the yellow ribs from the left and right sides of the plot, one encounters elongated islands of blue which are roughly centered above and below the main vortex. In terms of the topology, there has been a change from stable-focus-stretching (yellow) to unstable-focus-compressing (blue) in this region. Combining Figures 3, 4, and 5, one can see that the region where compression of the vortex is taking place coincides closely with maxima in the energy dissipation which lie above and below the main vortex. Vorticity in the ribs is first stretched and then compressed as it is wrapped up by the main vortex with high rates of kinetic energy dissipation being generated in the process.

3.2.1 Rate-of-strain tensor, definition of fine scales

Figure 6 shows a scatter plot of Q_s versus R_s for the entire flow field. The figure was produced by plotting Q_s versus R_s for every grid point in the computation. Before discussing this figure, a slight digression is in order to see how it might help to reveal the nature of the fine scale structure in this flow.

Classical arguments, based on the idea that dissipation of turbulent kinetic energy scales with production, lead to the following estimate of the rate of dissipation of turbulent kinetic energy in a time developing turbulent shear flow.

$$\epsilon = 2\nu\overline{S'_{ij}S'_{ij}} \cong -\overline{u'v'}\frac{\partial \overline{U}}{\partial y} \cong 0.158\,U^3/\delta_0 \qquad (9)$$

where the last equality is taken from the dissipation rate calculated at $tU/\delta_0 = 29.8$ by Moser and Rogers (1990). Typical data for fully developed shear layers gives $-\overline{u'v'}/(U_1 - U_2)^2 = 0.012$, which is consistent with the right hand side of (9) when the factor of 2 in the velocity normalization is taken into account. The data in Figures 3–11 correspond to a time when the layer has increased in thickness by a factor of approximately 6.5. Since the normalization of the raw data is based on the initial vorticity thickness, this has to be accounted for in using (9) to get an

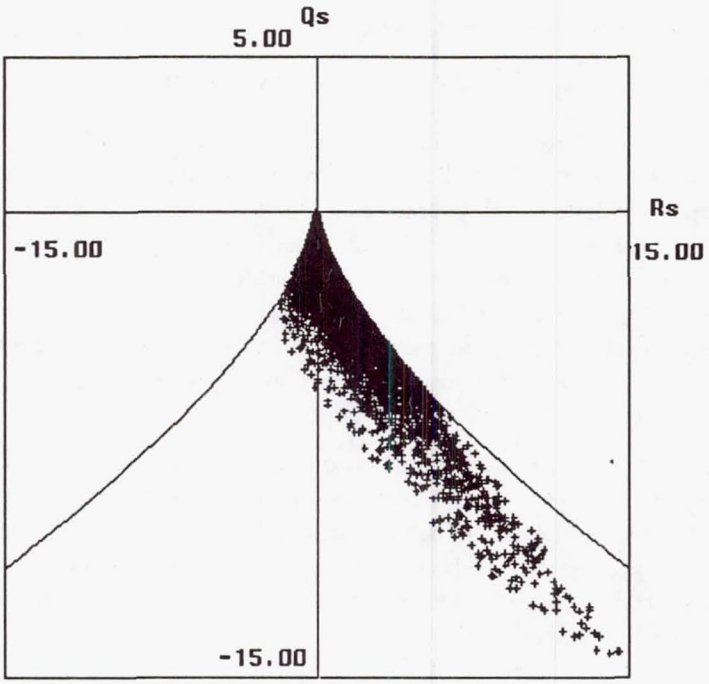

FIGURE 6. Scatter plot of Q_s versus R_s for the incompressible case at $tU/\delta_o = 29.8$.

idea of the instantaneous strain rate magnitude required to balance the production of kinetic energy at the time corresponding to $R_\delta = 3000$. The result is

$$\frac{\overline{S'_{ij}S'_{ij}}\delta_0{}^2}{U^2} \cong 0.04\left(\frac{\delta_0}{\delta}\right) R_\delta = .04\left(\frac{1}{6.5}\right) 3000 \cong 18.2 \tag{10}$$

where the Reynolds number is based on $2U$ and the current vorticity thickness, δ. Equation (10) implies that the fluctuating strain rates are larger than the mean strain rates by a factor of only about ten to twelve at a Reynolds number of 3000. To a rough approximation the relation (10) will be taken as a fair estimate of the instantaneous rate-of-strain compared to the mean rate-of-strain. Equations (9) and (10) imply that fluctuating velocity gradients scale with $(R_\delta)^{1/2}$; therefore, we would expect that, in a region where the dissipation is large,

$$\begin{aligned} Q_s &\approx R_\delta \\ R_s &\approx (R_\delta)^{3/2}. \end{aligned} \tag{11}$$

We will define fine scale motions as represented by those points which lie far from the origin in (Q_s, R_s) space according to the scaling in Equation (11).

Based on the estimate given in (10), values of Q_s on the order of -9.1 or less ought to be regarded as contributing significantly to the energy dissipation (compared with values of Q_s on the order of $-(2/6.5)^2 = -0.09$ characterizing the largest

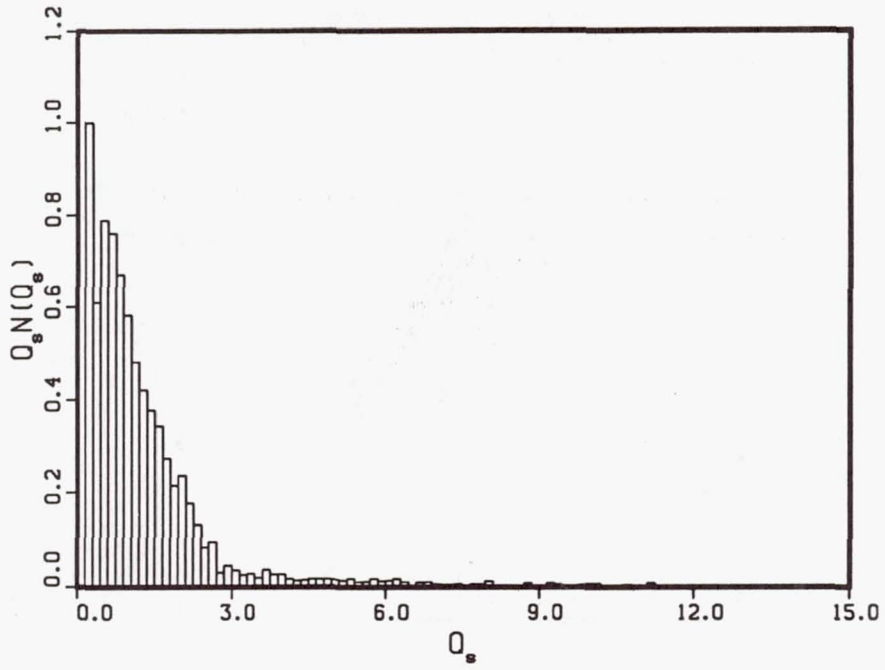

FIGURE 7. Distributions of Q_s over the volume of the incompressible mixing layer: histogram $Q_s N(Q_s)$.

scales). The assumption which underlies (9) and (11) is that the fluctuating strain rates are distributed uniformly throughout the flow. Values of Q_s on the order of -9.1 and lower are observed in Figure 6. Figure 7 shows the weighted probability distribution of Q_s. The integral under the curve in Figure 7 is proportional to the total dissipation of kinetic energy. As can be seen, the main contribution to the integral is from motions characterized by Q_s less than about 3, which is somewhat inconsistent with the estimate given in (11). The explanation for this discrepancy is that fine scale motions which contribute to the overall dissipation are not distributed uniformly throughout the volume of the flow; there is significant spatial intermittency with the occasional occurrence of very strongly dissipating events with values of Q_s as low as minus 10 to 14, as can be seen in Figure 6. It should be noted in this regard that the scattering of points with Q_s less than 5 to 6 constitutes a small fraction of the whole data set and that the major portion of the total dissipation is accounted for by events with Q_s between 0.5 and 5.

Combining the relations in (11) gives

$$|R_s| \cong (|Q_s|)^{3/2} \tag{12}$$

where absolute values are used to avoid inconsistencies in the sign. Equation (12) describes the scaling of R_s with Q_s for fine scale motions which one might expect

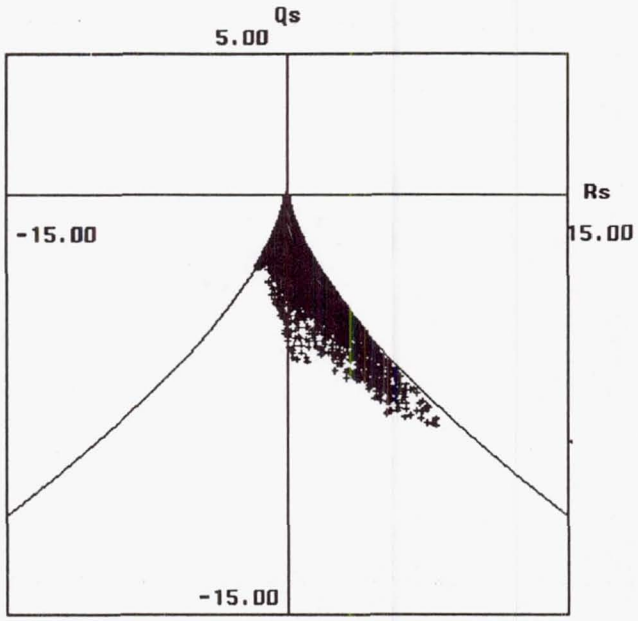

FIGURE 8. Scatter plot of Q_s versus R_s for the incompressible case at $tU/\delta_0 = 19.3$.

based purely on dimensional reasoning. There is no reason to expect that Q_s and R_s should be related to one another in any simple way since there is no restriction on either quantity save that imposed by the symmetry of the strain tensor and by the Navier-Stokes equations themselves. In principle, (Q_s, R_s) points can lie anywhere as long as they are below the curves given in Equation (6).

The unexpected result depicted in Figure 6 is that motions characterized by very high rates of dissipation (large negative Q_s) clearly show a preference for the right half plane of Figure 6 corresponding to a local topology (with the rotational part removed) which is saddle-saddle-unstable node (cf. Figure 2a). It is important to note that this preferred local topology is based on the rate-of-strain tensor. The corresponding local topology based on the velocity gradient tensor admits all possible incompressible topologies. Not only is the basic scaling (12) observed, but it appears that, with a modest amount of scatter, the fine scale motions follow a relation of the form

$$R_s \cong K(-Q_s)^{3/2}. \tag{13}$$

The positive quantity K is expected to be a function of the Reynolds number with an upper limit of $K = 2\sqrt{3}/9$ corresponding to locally axisymmetric flow. A sampling of the computation at an earlier time in Figure 8 ($tU/\delta_0 = 19.3$, before vortex pairing) reveals a substantially less developed structure, although the strong preference for the right half plane is still apparent.

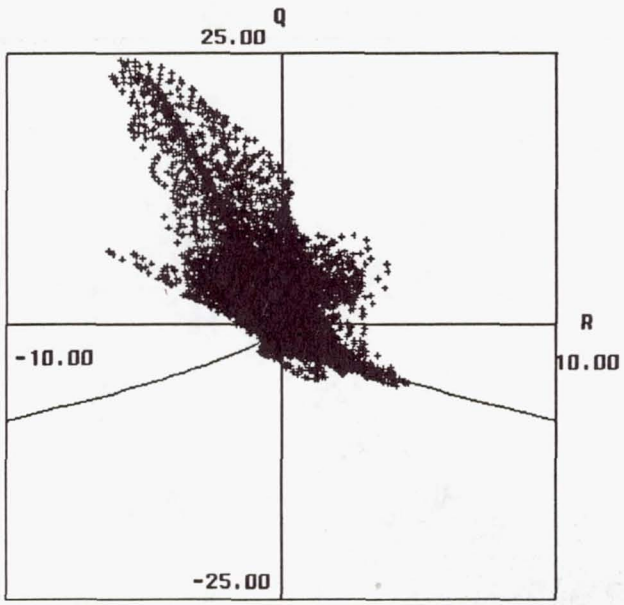

FIGURE 9. Scatter plot of Q versus R for the incompressible case at $tU/\delta_0 = 29.8$.

3.2.2 Velocity gradient tensor, regions of high enstrophy

Figure 9 shows a scatter plot of Q versus R for the entire flow field. The figure was produced in the same manner as Figure 6. For the velocity gradient tensor all of the possible topologies in the plane $P = 0$ can and do occur although, once again, the fine scales (points farthest from the origin) show a strong preference.

With reference to Figure 1, the motions with largest enstrophy show a clear tendency to a topology which is of the type stable-focus-stretching which is consistent with the expectation that the mixing layer is dominated by streamwise vortices undergoing stretching.

A question which immediately arises is whether the motions with highest enstrophy are the same motions which contain the highest dissipation rates. To address that question, it is necessary to split Q into its component parts $R_{ij}R_{ij}$ and $S_{ij}S_{ij}$. Figure 10 shows these two quantities plotted against each other for the same sample as in Figure 9. The most remarkable feature in this figure is the concentration of points along the horizontal axis.

Points of highest enstrophy tend to be characterized by low rates of strain. The larger the enstrophy, the lower the associated rate of strain. In contrast, points characterized by high rates of dissipation tend to lie on a 45 degree line in Figure 10 i.e., they tend to have comparable magnitudes of $R_{ij}R_{ij}$ and $S_{ij}S_{ij}$. This explains

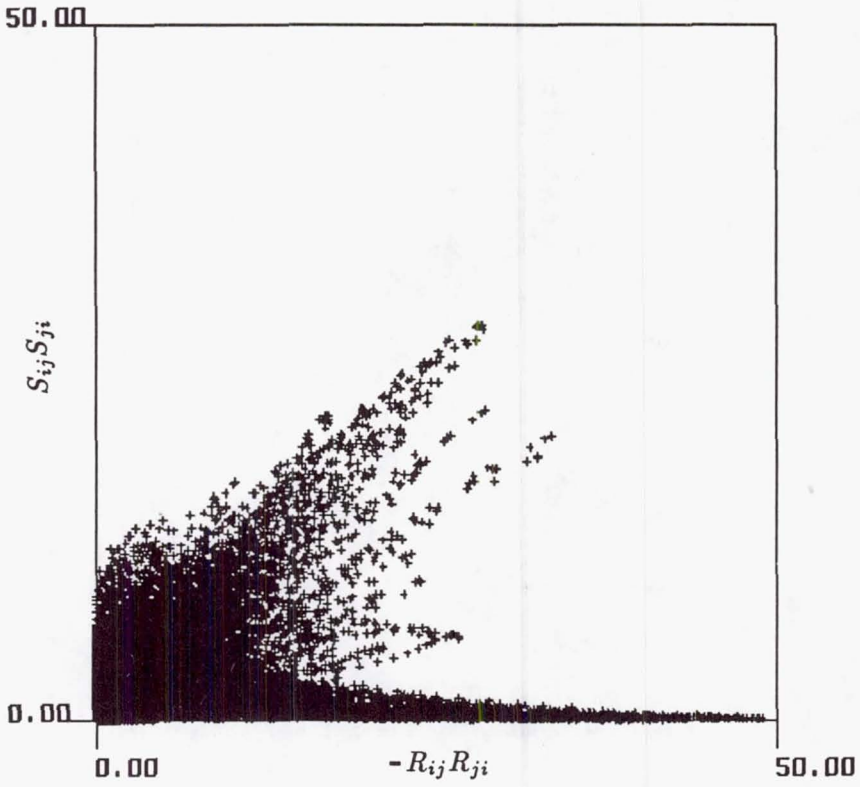

FIGURE 10. Plot of $S_{ij}S_{ij}$ versus $R_{ij}R_{ij}$ for the incompressible case at $tU/\delta_0 = 29.8$.

the absence of large negative values of Q in Figure 9.

It remains now to associate the structures found in the scatter plots with physical features of the flow field. Figures 11a and b are contour plots of the enstrophy field corresponding to the two planes shown in Figures 3 and 4 to typify the flow: one passing through the center of the main streamwise vortices (the rib plane), the other passing between the streamwise vortices (the "between plane" using the designation of Moser and Rogers). The sample space for plots of $S_{ij}S_{ij}$ versus $R_{ij}R_{ij}$ in Figures 11c and d is restricted to these two planes. A comparison of Figures 11c and 10 shows that regions of highest enstrophy occur in the rib plane. From Figure 11a, note that regions of highest enstrophy (blackened regions) occur in the streamwise vortices and do not coincide with regions of highest dissipation (cross-hatched regions). The streamwise vortices appear to be undergoing near solid-body rotation.

A comparison of Figures 11d and 10 shows that the highest values of dissipation occur in the in-between plane with dissipation and enstrophy at a given point having comparable values. Figure 11b confirms this with highest enstrophy regions (blackened regions) coincident with highest dissipation regions (cross-hatched regions).

The physical process suggested by these observations is that streamwise vorticity in the ribs is increased as it is stretched until it begins to be wrapped into the main spanwise vortex when, having reached a maximum, the stretching is reduced, undergoing a change of sign causing the vortex to contract axially while expanding radially, leading to a dissipating event which resembles the change of flow topology which occurs in vortex breakdown (Brown and Lopez, 1990). Although the details of this process need considerable further study, this description is consistent with the observed flow topology.

4. Compressible time developing mixing layer

Figures 3c and 4c are contour plots of the enstrophy and dissipation in a horizontal plane through the compressible mixing layer computation of Chen (1990). Note that in this case the chosen plane is perpendicular to the planes in Figures 3a and 3b used to study the incompressible layer. At a convective Mach number of 0.8, the plane mixing layer is more unstable to oblique disturbances than to spanwise disturbances, and as a result the flow is not dominated by well defined spanwise rollers as in the incompressible case. Note that high values of enstrophy and high rates of dissipation occur in relatively isolated regions. It appears that regions having high values of enstrophy also tend to have high values of dissipation.

Figure 5c shows the color coded topology corresponding to the same plane shown in Figures 3c and 4c. Although compressibility effects in this case would be considered to be fairly strong, the topologies observed in this plane are for the most part the same as those summarized in Figure 1 for $P = 0$. Exceptions, indicated in black (stable-focus-compressing) and cyan (unstable-focus-stretching), tend to occur in narrow regions separating commonly occurring zones of stable-focus-stretching and unstable-focus-compressing.

Figure 12 shows the scatter plot of Q_s versus R_s for this case. The $P = 0$ boundaries between real and complex solutions have been plotted on this figure, although it must be kept in mind that deviations from $P = 0$ do occur (as shown in Figure 13b), and a few points near the origin end up outside the apparent zone of real eigenvalues. Needless to say, these points do lie in the correct place with respect to the surface (6).

The Reynolds number of this case is somewhat lower than the incompressible case and the presence of compressibility tends to suppress instability; nevertheless, we see in Figure 12 the same strong tendency for points to lie in the right half plane that we saw in the incompressible case.

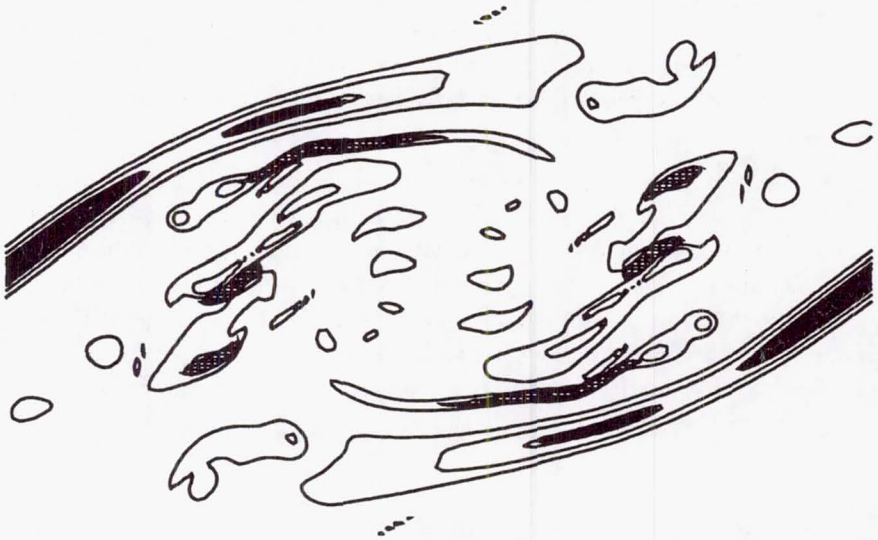

(a)

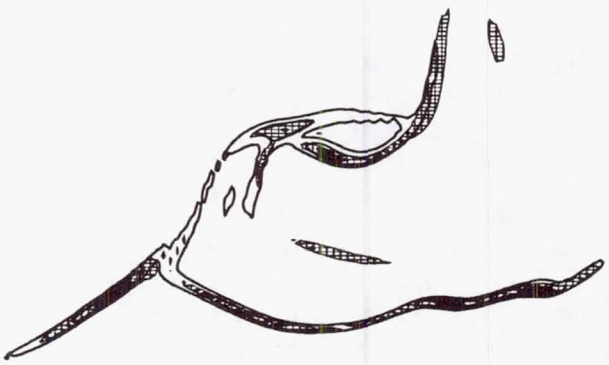

(b)

FIGURE 11A, B. Association between physical space and invariant space: (a) enstrophy field in a rib plane, (b) enstrophy field in an in-between plane.

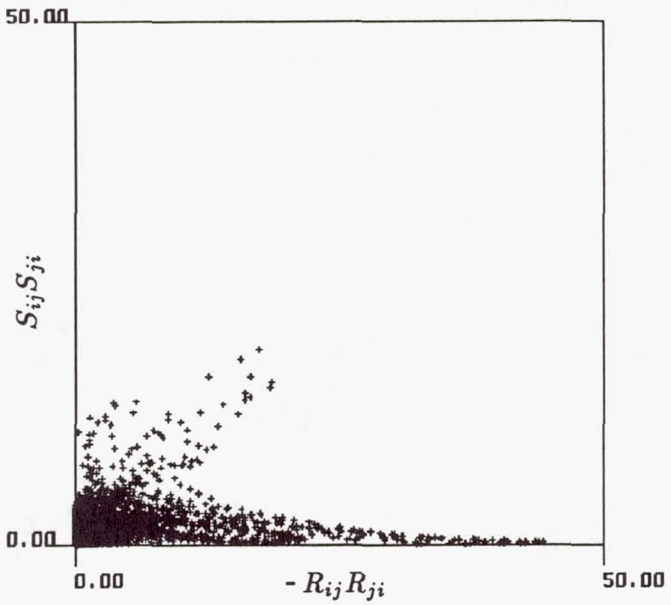

(c)

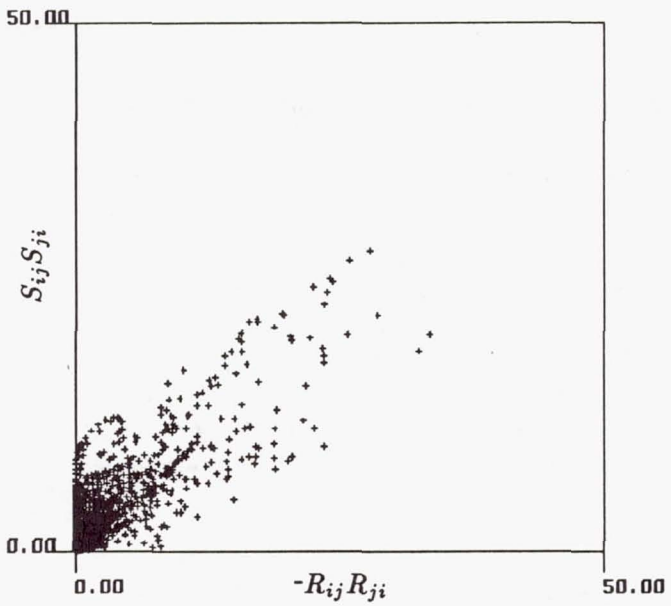

(d)

FIGURE 11C, D. Association between physical space and invariant space: (c) plot of $S_{ij}S_{ij}$ versus $R_{ij}R_{ij}$ for the data in (a), (d) plot of $S_{ij}S_{ij}$ versus $R_{ij}R_{ij}$ for the data in (b).

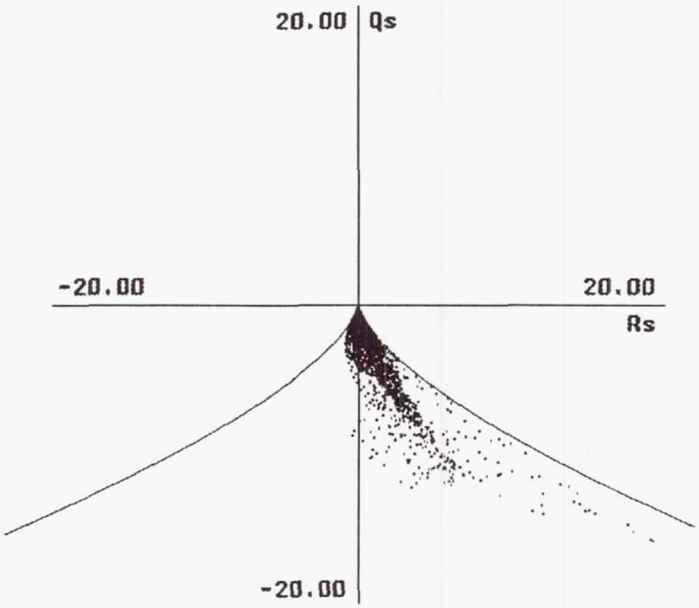

FIGURE 12. Scatter plot of Q_s versus R_s for the compressible case.

The scatter plot of Q versus R is shown in Figure 13a. Regions with complex eigenvalues still tend, as before, to lie in the second quadrant (stable-focus-stretching). However, well developed structures with large enstrophy are not observed. This is supported by Figure 14 where $S_{ij}S_{ij}$ is plotted versus $R_{ij}R_{ij}$.

Points with high dissipation tend to lie on a 45 degree line and, hence, are associated with comparable levels of strain and rotation as in the incompressible case, but the long tail of nearly strain-free high enstrophy does not occur. The conclusion from this is that well developed streamwise vortices are not a necessary condition for the breakdown to dissipating motions which follow the trend given in (13). In this respect, the discussion at the end of the previous section only describes one possible route to the formation of dissipating motions.

5. Concluding remarks

The fine scale motions in direct numerical simulations of time developing incompressible and compressible mixing layers appear to be characterized by relatively simple relations between the second and third invariants of the velocity gradient and/or rate-of-strain tensor. The prospect that triple products of velocity gradients may be related to double products is significant in that it could eventually form the basis of a closure hypothesis for the contribution of the fine scale motions to momentum and energy transport in an under-resolved computation of the flow.

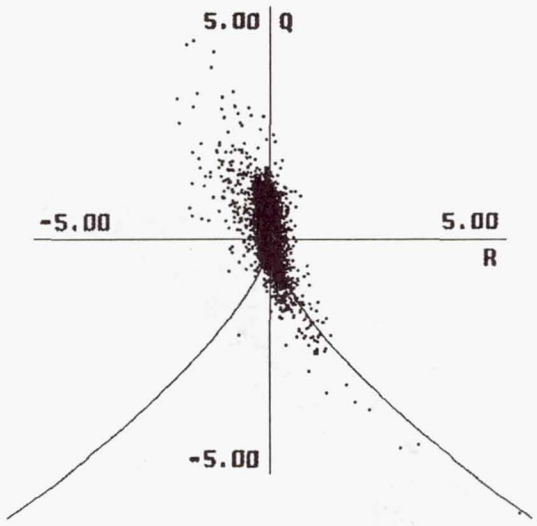

(a)

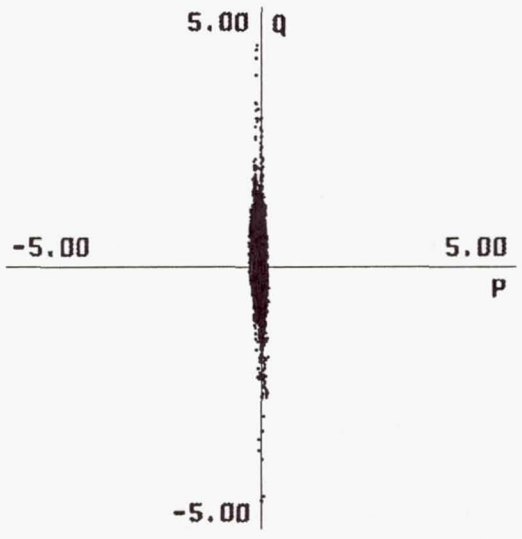

(b)

FIGURE 13. Scatter plots for the compressible case: (a) Q versus R, (b) Q versus P.

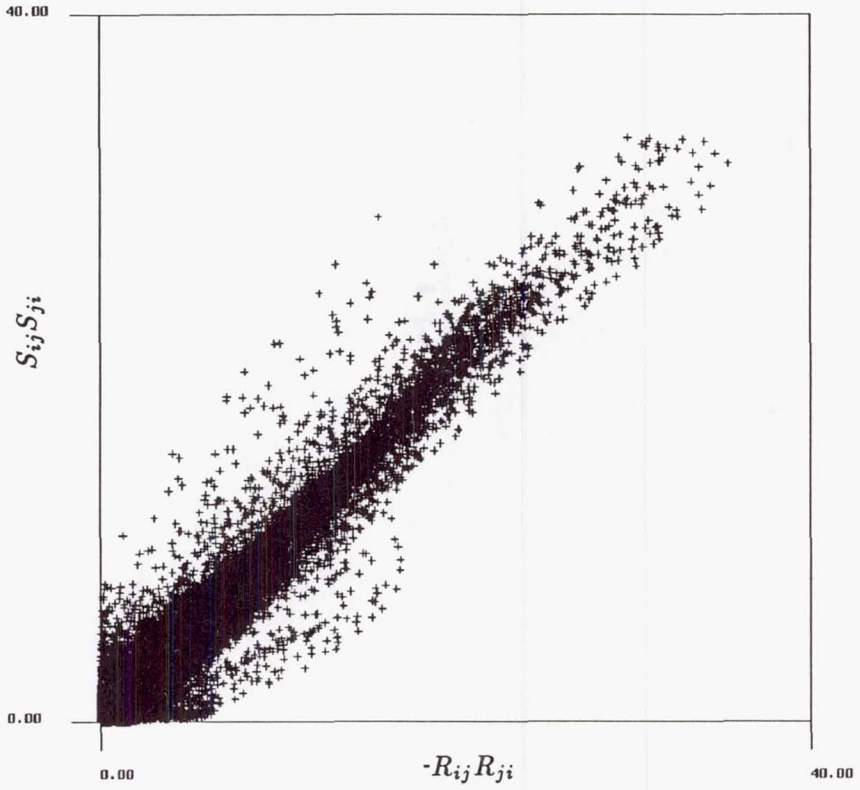

FIGURE 14. Plot of $S_{ij}S_{ij}$ versus $R_{ij}R_{ij}$ for the compressible case.

Whether such a closure can be accomplished depends on the outcome of further studies in this area.

The procedure outlined in section II needs to be applied to a variety of direct simulations including wakes, jets, homogeneous turbulence, and simulations of wall bounded flows to see if the observed relationships between Q_s and R_s and Q and R are universal. Our expectation is that there is a good chance that they are; however, this will not be known for certain until further studies are completed.

In the present study, the fine scale motions for which $R_s = K(-Q_s)^{3/2}$ only account for a modest fraction of the total dissipation of kinetic energy. Higher Reynolds number studies are needed to see whether this is a consequence of the low Reynolds number of the present simulations.

If the trends seen in the present study are found to be universal, and if at high Reynolds number these trends are found to characterize the motions which accomplish a significant fraction of the total dissipation of kinetic energy, then this will constitute a significant step on the path toward a theory of the fine scale

structure of turbulence. A great deal of theoretical work is needed to discover why high Reynolds number solutions of the Navier-Stokes equations tend to follow these trends, to account for the spatial intermittency of the fine scale structure, and to generate theoretical support for closure relations founded on fundamental physical principles.

Acknowledgements

This work was supported by the Center for Turbulence Research, DOE contract DE-AC04-76DP00789 and ONR Grant N00014-90-J-1976. J. Soria was supported by a CSIRO postdoctoral fellowship.

REFERENCES

BERNAL, L. & ROSHKO, A. 1986 Streamwise Vortex Structure in Plane Mixing Layers. *J. Fluid Mech.* **179**, 499.

BROWN, G. & LOPEZ, J. 1990 Axisymmetric vortex breakdown, part 2. physical mechanisms. *J. Fluid Mech.* (to appear).

CANTWELL, B., CHEN, J. & LEWIS, G. 1989 Topology of three-dimensional, variable density flows. *Proceedings of the Tenth Australasian Fluid Mechanics Conference.* Melbourne, Australia, December.

CHEN, J. 1990 Scalar mixing in a compressible plane mixing layer. *Sandia Report 90–8766.*

CHEN, J., CANTWELL, B. & MANSOUR, N. 1989 The topology and vorticity dynamics of a three-dimensional plane compressible wake. *Proceedings of the Tenth Australasian Fluid Mechanics Conference.* Melbourne, Australia, December.

CHONG, M., PERRY, A. & AND CANTWELL, B. 1990 A general classification of three-dimensional flow fields. *Physics of Fluids A.* **2**(5), 765–777.

FRISCH, U. & ORZAG, S. 1990 Turbulence: challenges for theory and experiment. *Physics Today.* **43, No.1,** 24-32.

HUNT, J., WRAY, A. & MOIN, P. 1988 Eddies, streams and convergence zones in turbulent flows. *Proceedings of 1988 Summer Program.* Center for Turbulence Research, Stanford Univ. and NASA Ames Research Center, p. 193

MOSER, R. & ROGERS, M. 1990 Mixing transition and the cascade to small scales in a plane mixing layer. *Proceedings of the IUTAM Symposium on Stirring and Mixing.* UCSD, La Jolla, CA, August 20–24.

SANDHAM, N. & REYNOLDS, W. 1989 *Thermosciences Report TF-45*, Dept. of Mech. Eng., Stanford University.

Direct numerical simulations of stably-stratified sheared turbulence: implications for oceanic mixing

By E. C. Itsweire,[1] S. E. Holt,[2] J. R. Koseff [2] AND J. H. Ferziger[3]

Direct numerical simulations of the time evolution of homogeneous stably stratified turbulent shear flows have been performed for several Richardson numbers Ri and Reynolds numbers R_λ by Holt (1990). The results show excellent agreement with length scale models developed from laboratory experiments to characterize oceanic turbulence. When the Richardson number Ri is less than the stationary value Ri_s, the turbulence intensity grows at all scales, and the growth rate appears to be a function of Ri. The size of the vertical density inversions also increases. On the other hand, when $Ri \geq Ri_s$ the largest turbulent eddies become vertically constrained by buoyancy when the Ellison (turbulence) scale L_E and the Ozmidov (buoyancy) scale L_O are equal. At this point, the mixing efficiency is maximal and corresponds to a flux Richardson number $R_f = 0.20$. The vertical mass flux becomes counter-gradient when $\epsilon = 19\nu N^2$, and vertical density overturns are suppressed in less than half a Brunt-Väisälä period. The results of the simulations have also been recast in terms of the Hydrodynamic Phase Diagram introduced in fossil turbulence models (Gibson, 1980, 1986). The so-called *point of fossilization* occurs when $\epsilon = 4DCN^2$; Gibson proposed $13DCN^2$. This value is in agreement with indirect laboratory observations (Itsweire *et al.*, 1986) and field observations (Dillon, 1984). Finally, the validity of the steady-state models to estimate vertical eddy diffusivities in the oceanic thermocline is discussed.

1. Introduction

The behavior of homogeneous turbulence subjected to both mean shear and a stable density gradient is complex as two processes compete. Turbulence energy is extracted from the mean flow by shear production and is mostly transferred to the streamwise velocity component, while stabilizing buoyancy forces tend to suppress energy in the vertical direction by converting turbulent kinetic energy into available potential energy. This potential energy is available for mixing. Therefore, through distinct mechanisms, both shear and buoyancy act to make turbulence more anisotropic. Depending on the ratio of the mean shear to the mean stratification, expressed as the Richardson number Ri, both growth and decay are possible (Rohr

1 Chesapeake Bay Institute, The Johns Hopkins University
2 Department of Civil Engineering, Stanford University
3 Department of Mechanical Engineering, Stanford University

et al. 1987, 1988, hereafter referred to as RHIV and RIHV; Gerz *et al.*, 1989; Holt *et al.*, 1990). A net balance between production, buoyancy and dissipation is only achieved when Ri is equal to the stationary Richardson number Ri_s. In that case, Holt *et al.* (1990) showed that low wavenumbers gain kinetic energy from the mean shear while high wavenumbers have a net loss of energy to viscous dissipation.

The temporal evolution of homogenous turbulence subjected to constant mean velocity and density gradients was numerically simulated by Holt (1990) using the pseudo-spectral method developed by Rogallo (1981). The Boussinesq form of the Navier-Stokes equations were solved for the three dimensional velocity and density fields in a 128×128×128 box. The velocity fields were initially isotropic, with initial Reynolds numbers R_λ varying from 45 to 140 and Richardson numbers Ri from 0.0575 to 1. In the results presented in this paper, the Prandtl number Pr was 1 for the low Reynolds number cases and 2 for the high Reynolds number case that simulates the laboratory experiments of Rohr *et al.* (1987, 1988). Further details on the numerical procedures and the choice of initial conditions can be found in Holt (1990).

2. Theoretical framework for stratified shear flows

2.1 Equations of motion

The coordinate system is chosen as follows: x is the streamwise direction, y the transverse direction, and z the vertical direction (up being positive), in which there are mean velocity and density gradients. For homogeneous flows satisfying the Boussinesq approximation, the evolution equations for the velocity and scalar fluctuations become:

$$\frac{\partial}{\partial t}(\overline{q^2}/2) = -\overline{uw}\frac{\partial \overline{U}}{\partial z} - \frac{g}{\rho_0}\overline{\rho w} - \epsilon \tag{1}$$

and

$$\frac{\partial}{\partial t}(\overline{\rho^2}/2) = -\overline{\rho w}\frac{\partial \bar{\rho}}{\partial z} - \chi \tag{2}$$

where $\overline{q^2} = \overline{u^2} + \overline{v^2} + \overline{w^2}$ is twice the turbulent kinetic energy, ρ_0 is the background density, $\epsilon = \nu\overline{(\partial u_i/\partial x_k)(\partial u_i/\partial x_k)}$ is the dissipation rate of turbulent kinetic energy, $\chi = D\overline{(\nabla\rho)^2}$ is the rate of destruction of density fluctuations due to molecular diffusion, and D is the molecular diffusivity of the scalar. The overbar ($\overline{\quad}$) designates an ensemble average over the computational box. Note that most oceanographers define χ as twice this quantity (e.g., Dillon, 1982; Gargett *et al.*, 1984; Gregg, 1989). These two equations can be rewritten as evolution equations for the kinetic $[E_K = \frac{1}{2}\overline{q^2}]$ and potential $[E_P = \frac{1}{2}(g/\rho_0)\overline{\rho^2}/(\partial\bar{\rho}/\partial z)]$ energies as:

$$\frac{\partial E_K}{\partial t} = P - B - \epsilon \tag{3}$$

and

$$\frac{\partial E_P}{\partial t} = B - DCN^2 \tag{4}$$

where the turbulent production due to the mean shear is

$$P = -\overline{uw}\partial\bar{U}/\partial z,$$

the buoyancy flux is

$$B = (g/\rho_0)\overline{\rho w},$$

the Brunt-Väisälä frequency is

$$N = \left(-\frac{g}{\rho_0}\frac{\partial\bar{\rho}}{\partial z}\right)^{\frac{1}{2}},$$

and

$$C = \frac{\overline{(\nabla\rho)^2}}{(\partial\bar{\rho}/\partial z)^2}$$

is the isotropic Cox number. The vertical eddy diffusivities for mass and momentum, K_ρ and K_m respectively are defined via:

$$\overline{\rho w} = -K_\rho\frac{\partial\bar{\rho}}{\partial z} \tag{5}$$

and

$$\overline{uw} = -K_m\frac{\partial\bar{U}}{\partial z} \tag{6}$$

These eddy diffusivities are proportional to the buoyancy flux and turbulent production respectively.

2.2. Relevant length scales

The behavior of stably stratified turbulent flows can be interpreted in terms of the relative strength of three forces: the buoyancy, inertial, and viscous forces. Buoyancy forces act directly on the largest scales of vertical motion, thus creating an upper bound for the size of turbulent eddies, while viscous forces determine the size of the smallest eddies. The action of these forces can be quantified using length scales obtained from dimensional analysis and physical arguments. Dougherty (1961) and Ozmidov (1965) independently suggested that buoyancy effects are important on a scale proportional to the Ozmidov scale:

$$L_O = (\epsilon/N^3)^{\frac{1}{2}} \tag{7}$$

If the vertical velocity fluctuations due to internal waves are small compared to those due to turbulence, the buoyancy scale $L_b = (\overline{w^2})^{\frac{1}{2}}/N$ can be used instead of the Ozmidov scale. On the other end of the scale domain, viscous effects are felt by turbulent eddies of size comparable to the Kolmogorov scale:

$$L_K = (\nu^3/\epsilon)^{\frac{1}{4}} \tag{8}$$

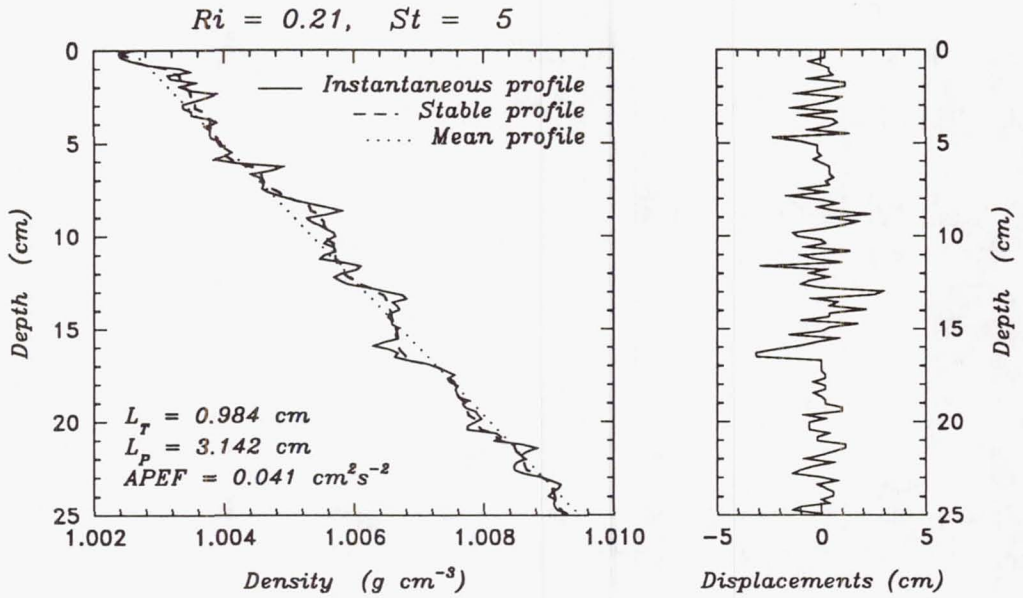

FIGURE 1. Example of an instantaneous density profile used to calculate the Thorpe scale L_T. The mean (·····), instantaneous (———) and reordered or gravitationally stable (----) density profiles are shown on the left and the vertical Thorpe displacements $d(z)$ on the right.

Finally, we require a length scale that characterizes turbulent motions to be compared with L_O and L_K. Several turbulent scales can be defined depending on whether one is interested in the energy-containing eddies that are directly related to density overturns or in the dissipative eddies related to mixing. Ellison (1957) proposed the following scale:

$$L_E = -\frac{(\overline{\rho^2})^{\frac{1}{2}}}{\partial\bar{\rho}/\partial z} \tag{9}$$

known as the overturning scale or Ellison scale, using the density fluctuations as an indicator of turbulent motions. Thorpe (1977) presented a way to compute a scale directly related to density overturns from instantaneous density (or temperature in his case) profiles. The technique is best illustrated with the help of Fig. 1.

The instantaneous density profile (———) contains gravitationally unstable inversions. Thorpe's method consists of rearranging this density profile until each fluid element is gravitationally stable (----) and keeping track of the vertical (Thorpe) displacements $d(z)$ associated with the sorting. The typical signature of an overturn is a Z pattern in both density and Thorpe displacements like the overturns observed at depths of 9, 15, and 22 cm in the example of Fig. 1. The rms value of the Thorpe displacements (over a region of constant density gradient) is called the

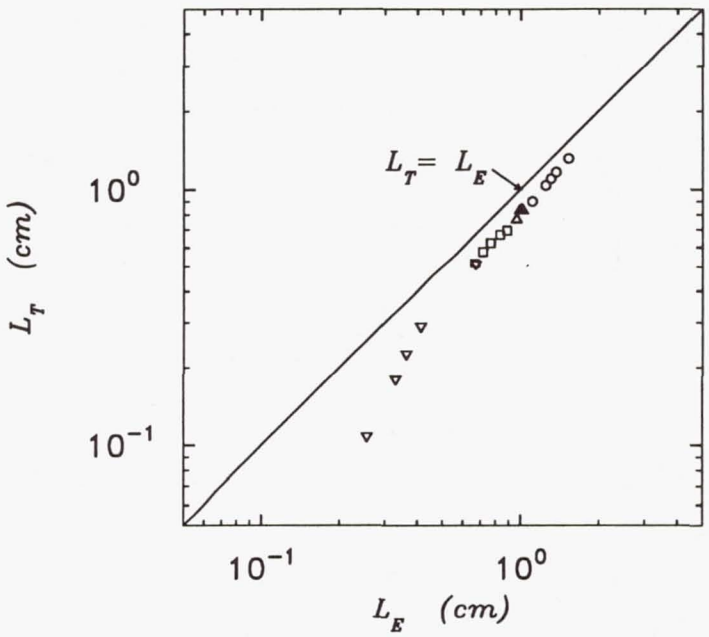

FIGURE 2. Comparison of the (rms) Thorpe Scale L_T with the Ellison scale L_E, ○ $Ri = 0.075$; △ $Ri = 0.21$; □ $Ri = 0.37$; ▽ $Ri = 1$.

Thorpe scale (Dillon, 1982; Itsweire, 1984):

$$L_T = < d(z)^2 >^{\frac{1}{2}} \tag{10}$$

where $< >$ denotes a vertical average. For homogeneous flows, the maximum Thorpe displacement

$$L_{Tmax} = L_P = max[d(z)] \tag{11}$$

is a measure of the largest turbulent overturns and, for inhomogeneous flows it can be interpreted as the size a turbulent patch. In the present case, both L_T and L_P have been ensemble-averaged over 4096 vertical profiles in order to reduce the variance.

Figure 2 shows the comparison between the Ellison and the Thorpe scales for the high Reynolds number numerical simulations ($R_\lambda = 140$). The two scales are linearly related except in the high Richardson number case ($Ri = 1$, the three leftmost ▽ correspond to dimensionless times $St = 5$, 6 and 8, where $S = \partial \bar{U}/\partial z$ is the imposed mean shear. At $Ri = 1$, internal waves motions could contribute significantly to L_E, but would not affect L_T (Itsweire, 1984). The observed relationship $L_T = 0.8 L_E$ is not significantly different from the $L_T = L_E$ relation observed in the laboratory (Itsweire, 1984), if one accounts for the differences in the vertical resolution attainable in the laboratory and the direct simulations.

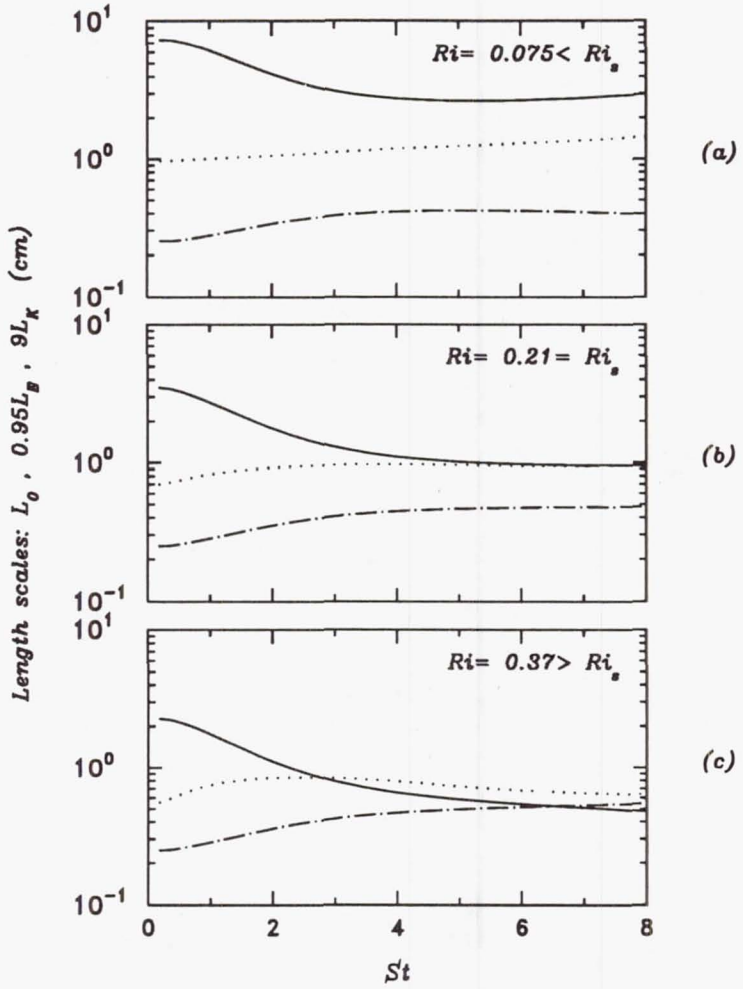

FIGURE 3. Evolution of the Ozmidov scale L_O, the Ellison scale L_E, and the Kolmogorov scale L_K as a function of dimensionless shear time St for different Richardson numbers Ri: —— L_O; ····· $0.95L_E$; —·— $9L_K$.

3. Length scale evolution as a function of Ri

The effects of mean shear and stratification on the evolution of the turbulence is illustrated in Fig. 3, where three length scales, L_O, L_E, and L_K, are compared. According to Itsweire *et al.* (1986) and RIHV, the onset of buoyancy effects occurs when $L_O = (1.15 \pm 0.05)L_E$ and complete fossilization (the point at which the buoyancy flux first goes to zero) takes place when $L_O = (8.75 \pm 1.2)L_K$. In the direct numerical simulations, these two transition points occur when $L_O = (0.95 \pm 0.05)L_E$ and when $L_O = (9 \pm 0.5)L_K$ respectively, in excellent agreement with the laboratory experiments. In order to facilitate the comparison, L_E and L_K have been multiplied

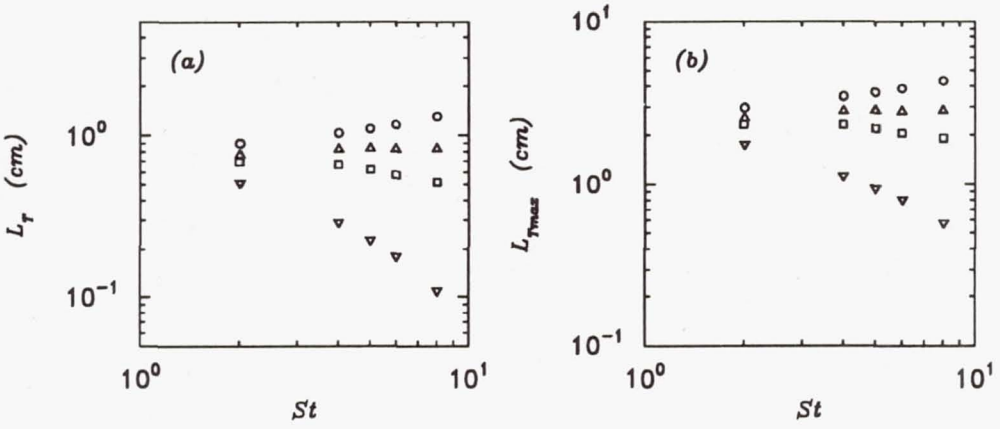

FIGURE 4. Evolution of the size of vertical overturns vs. dimensionless shear time St, (a) (rms) Thorpe scale L_T; (b) maximum Thorpe scale L_{Tmax}. ○ $Ri = 0.075$; △ $Ri = 0.21$; □ $Ri = 0.37$; ▽ $Ri = 1$.

by the appropriate constants in Fig. 3.

When the Richardson number Ri is less than the stationary Richardson number $Ri_s = 0.21$ (Fig. 3a), both the Ozmidov and the Ellison length scales grow when the flow is fully developed ($St \geq 4$). The opposite is true when $Ri > Ri_s$ (Fig. 3c) and the range of overturning turbulent scales decreases until $L_O = 9L_K$. When $Ri = Ri_s$ (Fig. 3b) it appears that all three length scales may reach constant values and that $L_O = 0.95L_E$ for large St. The size of the vertical overturns is then determined by the balance buoyancy and shear.

Given the linear relationship between the Ellison scale L_E and the Thorpe scale L_T (Fig. 2), one would expect both length scales to have the same time evolution. Figure 4a demonstrates that this assumption is correct. When $Ri > Ri_s$, both scales decrease. On the other hand, they grow if $Ri < Ri_s$. L_{Tmax} behaves similarly as illustrated in Fig. 4b. In fact, the rms and maximal values of the density overturns are related as $L_T = 3.33L_{Tmax}$. This relation shows that, at least in homogeneous flows, either L_T or L_{Tmax} is a good measure of the size of vertical overturns.

4. How do shear and stratification affect turbulence?

The length scale evolution of Fig. 3 shows that both mean shear and stratification are important in determining the fate of the turbulence. The buoyancy forces affect the turbulence by controlling the growth of the largest turbulent eddies when $Ri \leq Ri_s$ or suppressing them when $Ri > Ri_s$, so one might expect the ratio of the overturning scale (either L_E or L_T) to the Ozmidov scale L_O to be a function of the Richardson number Ri for fully developed shear flows. This interpretation is supported by both laboratory and direct simulation experiments as shown in Fig.

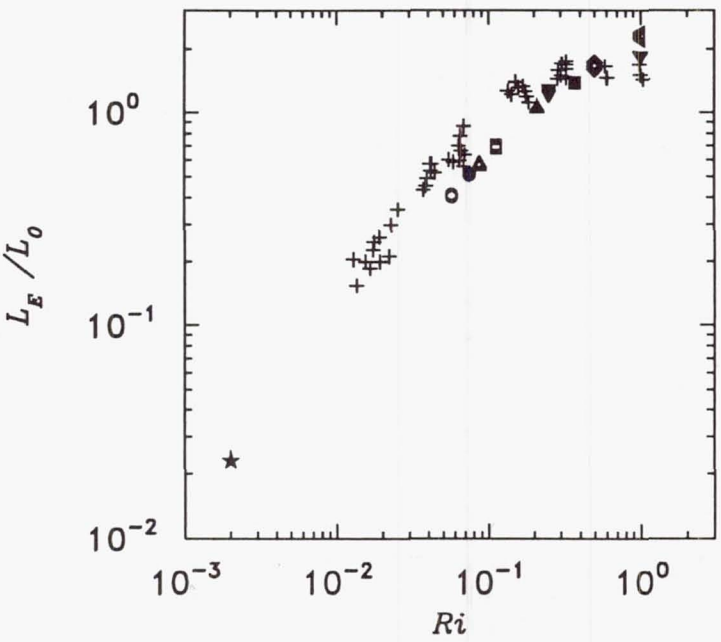

FIGURE 5. Evolution of the L_E/L_O as a function of Richardson number Ri for large development times St. Open and closed symbols refer to the direct numerical simulations, + to RIHV and $\star$ to Tavoularis & Corrsin (1981).

5, where the L_E/L_O is plotted versus Ri. The wider scatter that is observed for the stable case ($Ri \geq Ri_s$) can be attributed to the fact that L_E includes a contribution from internal wave motions. When both L_T and L_E are available, it would be better to plot L_T/L_O instead of L_E/L_O. Since L_T was not measured in the laboratory experiments of RIHV, we elected to plot L_E/L_O for a fair comparison of the two data sets.

The physical interpretation of the length scale evolution, that buoyancy forces control ($Ri \leq Ri_s$) or suppress ($Ri > Ri_s$) the largest turbulent eddies, suggests that active (sheared) turbulence exists at smaller scales. Indeed, Hunt *et al.* (1989) argue that the mean shear should control the fate of eddies smaller than L_T for Richardson number $Ri \leq 0.5$. They introduce a dissipation length scale

$$L_\epsilon = \frac{w'^3}{\epsilon} \tag{12}$$

where w' is the rms value of the vertical velocity fluctuation, and propose that, for homogeneous flows, it should be proportional to w'/S.

Our results, presented in Fig. 6, show a very clear relation between these two length scales. The $L_\epsilon = 2.22w'/S$ line corresponds to the constant proposed by Hunt *et al.* (1988). The largest departures from that line are observed at the

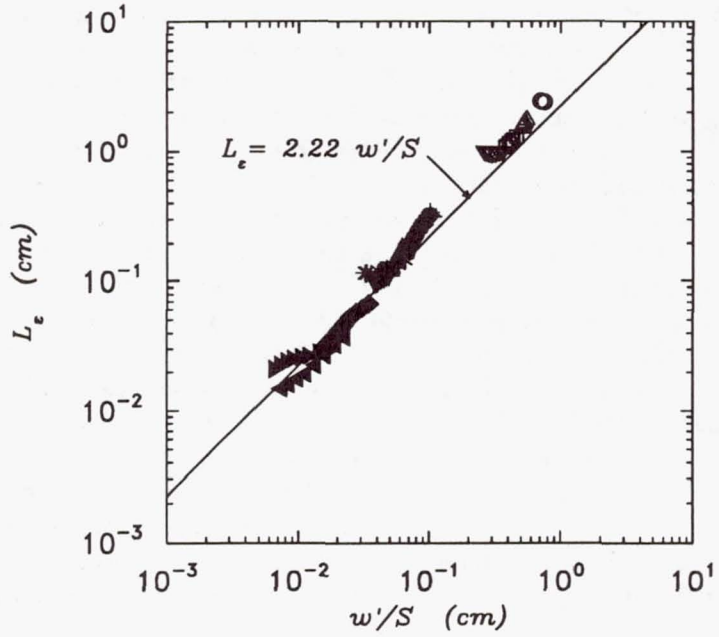

FIGURE 6. Relationship between the turbulent dissipative scale L_ϵ and the shear length scale w'/S for $Ri \leq 1$ for turbulent Reynolds numbers R_λ varying from 35 to 120. Open symbols: $R_\lambda = 140$, ○ $Ri = 0.075$, △ $Ri = 0.21 = Ri_s$, □ $Ri = 0.37$, ▽ $Ri = 1$; cross symbols: $R_\lambda = 76$, + $Ri = 0.15 = Ri_s$, × $Ri = 0.5$, * $Ri = 1$; closed symbols: $R_\lambda = 32$, • $Ri = 0$, ▲ $Ri = 0.0575$, ■ $Ri = 0.0875 = Ri_s$, ▼ $Ri = 0.1125$, ◆ $Ri = 0.25$, ◀ $Ri = 0.5$, ▶ $Ri = 1$.

largest Richardson number ($Ri = 1$), which is outside the range where the relation is supposed to be valid. The postulate of Hunt *et al.* (1988) that the mean shear strongly influences the dissipative scales is consistent with the results of Holt (1990). In these simulations, the mean shear has a strong effect on the energetics and flux development at all Richardson numbers. Holt (1990) found that the effect of the mean shear diminishes somewhat at the transition Richardson number where counter-gradient fluxes appear. The transition Richardson number is approximately 0.5 for the high Reynolds number simulations.

5. Classification of oceanic microstructure

An important problem in oceanic mixing is to determine how much mixing the observed microstructure patches produce. Many oceanographers (e.g. Dillon, 1982, 1984; Gargett *et al.*, 1984; Gregg, 1989) have argued that most microstructure patches in the thermocline are the result of weak shear instabilities and internal wave straining (the continuous creation scenario advanced by Caldwell, 1983). Gregg (1989) even proposes that the dissipation rate of kinetic energy ϵ in the

thermocline scales with the local internal wave field. These scenarios assume some sort of equilibrium between production, buoyancy, and dissipation, i.e., Richardson number must be close to the stationary value. According to these oceanographers, most of the microstructure observations are of *active* turbulence which produces vertical mixing. In this paper *active* turbulence refers to a state of motion where buoyancy forces are small compared to inertial forces and, therefore, do not prevent eddies from overturning. For homogeneous turbulence, this requires $Ri < Ri_s$.

On the other hand, Gibson (1980, 1986) proposes that most observed microstructure are the remnants of powerful but rare mixing events (the big bang scenario). At any given scale, the velocity and density fluctuations that persist when the fluid is no longer actively turbulent are referred to as fossil turbulence. In this case, the measured dissipation rates ϵ are not representative of the average dissipation rate in the thermocline, resulting in severe underestimates of vertical diffusivities.

As pointed out by Caldwell (1983), the classification of oceanic microstructure patches as *active* or *fossil* turbulence goes beyond semantics because the generating mechanisms for the two interpretations are different. Using the direct numerical simulation results, the constants in Gibson's fossil turbulence model can be calculated. The two transitions of interest are: the onset of buoyancy effects or point of fossilization and complete fossilization beyond which vertical turbulent mixing is negligible.

5.1 Onset of buoyancy effects or point of fossilization

The onset of buoyancy effects can be quantified in two different ways following Gibson (1980). Both approaches use the fact that the scalar (temperature, salinity, or density) fluctuations in a fluid with Prandtl number $Pr > 1$ will persist for longer times than the velocity fluctuations; consequently, the vertical scalar profile will retain *memory* of previous overturning events.

The first method examines the ratio of an overturning scale (L_E, L_T or L_{Tmax}) to the Ozmidov scale. Gibson interprets the Ozmidov scale L_O as the maximum turbulent length scale allowed by buoyancy at the point of fossilization and relates it to a patch size $L_O \sim L_P = L_{Tmax} \sim L_T$. This expression can be rewritten in terms of the dissipation rate $\epsilon = L_O^2 N^3 \sim {L_T}^2 N^3$. As an alternate approach to estimating the point of fossilization, Gibson (1980, 1986) argues that at transition, the largest eddy (of size $\approx L_O$) will overturn with a time scale N^{-1} and that the temperature (or density) variance ($\overline{\delta T^2}$) is of the order of $(\partial \bar{T}/\partial z)^2 L_O^2$. Therefore, the rate of destruction of temperature variance χ should be $\sim \overline{\delta T^2} N$. These relationships can be combined with the definition of the Ozmidov scale to give $\epsilon \sim DCN^2$. Gibson (1980, 1986) derives the proportionality constants from the shape of the temperature gradient spectrum and overturn models to show that the following relations hold at the point of fossilization

$$\epsilon = 13DCN^2 = 16.5{L_T}^2 N^3 \tag{13}$$

Values of the dissipation rate ϵ less than the right-hand-side of Eq. (13) indicate that the largest scales (of order L_{Tmax}) of the turbulence have been affected by buoyancy and are no longer overturning.

Dillon (1984) and Itsweire *et al.* (1986) argue from field and laboratory experiments that the coefficients in Eq. (13) are too large. By using the definition of the Ozmidov scale L_O, its relation to L_E and L_T determined in Section 3, and the value of the Cox number at transition, an equation similar to Eq. (13) can be obtained from the numerical simulations:

$$\epsilon = (4 \sim 5)DCN^2 = (1.4 \pm 0.15){L_T}^2 N^3 \tag{14}$$

This result is in much better agreement with the constants derived from laboratory measurements (Itsweire, 1984; Itsweire *et al.*, 1986):

$$\epsilon = (5.5 \pm 2)DCN^2 = (1.4 \pm 0.2){L_T}^2 N^3 \tag{15}$$

than with Gibson's model (Eq. 13). From an energetics point of view, the $\epsilon = (4 \sim 5)DCN^2$ is equivalent to a mixing efficiency of $0.20 \sim 0.25$.

5.2 Complete fossilization

Once the fossilization process starts, laboratory experiments (Stillinger *et al*, 1983; Itsweire *et al*, 1986) show that all turbulent scales are suppressed by buoyancy in a fraction of a Brunt-Väisälä period. Motion at all scales is *wavelike* and has been characterized as saturated internal waves (Gibson, 1980). In this state of motion, little vertical mixing takes place. Gibson refers to this transition as complete fossilization or buoyant-inertial-viscous transition, i.e., a state of fluid motion where buoyancy, inertial, and viscous forces are equal. As stated in Section 3, this transition can be characterized by the ratio of the Ozmidov scale to the Kolmogorov scale. Using the definitions of the length scales, this ratio L_O/L_K can be expressed in terms of a minimal dissipation rate, necessary for the existence of turbulence:

$$\epsilon = 30\nu N^2 \tag{16}$$

This criteria is in qualitative agreement with laboratory observations without shear $\epsilon = (15 \sim 21)\nu N^2$ (Stillinger *et al*, 1983; Itsweire *et al*, 1986) and with shear $\epsilon = 16\nu N^2$ (RHIV and RIHV). For the present data, the $L_O = 9L_K$ relation of Section 3 can be rewritten as:

$$\epsilon = 19\nu N^2 \tag{17}$$

which falls within the range of experimental values. It is not clear at this point whether the ratio $\epsilon/\nu N^2$ is a universal constant or depends on Reynolds number or the type of turbulence (homogeneous vs. inhomogeneous). More numerical and experimental data are needed to answer this question.

5.3 Hydrodynamic Phase Diagram

The relations derived in the preceding sections, Eqs. (14) and (17), can be used to describe the evolution of turbulence in a stratified shear flow in terms of a Hydrodynamic Phase Diagram (see Fig. 7). This diagram is another way to describe the length scale evolution of Fig. 3. It offers the advantage of using quantities that can

be directly measured by vertical profilers in the ocean. The horizontal axis $\epsilon/\nu N^2$ is a Reynolds number based on the Ozmidov scale and an associated velocity scale $(\epsilon/N)^{\frac{1}{2}}$ and the vertical axis ϵ/DCN^2 is the ratio of the dissipation rate of kinetic energy to the dissipation rate of potential energy, which Gibson (1986) interprets as a turbulent Froude number $Fr^{\frac{1}{3}}$. The evolution of turbulence can be interpreted as follows. The upper right quadrant is the *active* region, the lower left quadrant is the *fossil* region, while the lower right quadrant is a mixture *active+fossil*. When $Ri < Ri_s$ (○), all data lies in the *active* region as expected, and when $Ri > Ri_s$ (□, ▽), the turbulence undergoes a transition from *active* to a mixture *active+fossil* to completely *fossil*. This classification can be related to the length scale evolution described in Fig. 3 as follows. Let us consider the case where $Ri = 0.37$ (see Fig 3c). When $St \approx 2.8$, $L_O = 0.95L_E$ and the turbulence undergoes transition from the *active* region to the *active+fossil* region (see □ symbols in Fig. 7). Later, when $St \approx 6.4$, $L_O = 9L_K$, the turbulence is completely suppressed and enters the *fossil* region. The case of the stationary Richardson number (△) is interesting because the data lies at the edge of the transition region where the flux Richardson number $R_f = B/P$ of the turbulence is a maximum. Under steady-state conditions, ϵ/DCN^2 can be interpreted as an inverse mixing efficiency.

6. Eddy diffusivity models

If the time rates of change of turbulent kinetic energy and potential energy (see Equations 3 and 4) are small compared with dissipation and production (near-steady state), the vertical eddy diffusivities K_ρ and K_m can be easily estimated using the following methods.

6.1 Dissipation techniques

The dissipation technique makes use of the kinetic energy equation which, under steady-state assumptions, reduces to

$$P = B + \epsilon, \tag{18}$$

is often used to estimate K_m in the atmospheric boundary layer (e.g Busch, 1977). After introducing the flux Richardson number $R_f = B/P$ which is a measure of the mixing efficiency of the flow, Eq. (18) can be rewritten in two ways, depending on whether one wishes to estimate K_m

$$K_m = P/S^2 = \frac{1}{1 - R_f}\frac{\epsilon}{S^2} \tag{19}$$

or K_ρ:

$$K_\rho = B/N^2 = \frac{R_f}{1 - R_f}\frac{\epsilon}{N^2} \tag{20}$$

Figure 8 shows that the assumption of production equal to dissipation (solid line) provides a good estimate of K_m for Richardson numbers slightly larger than the stationary value. Under these conditions, the buoyancy flux and the time rate of

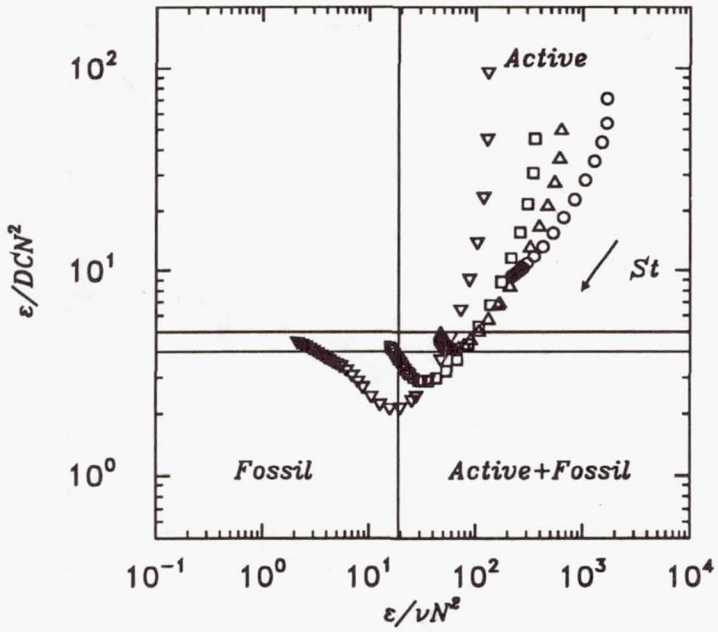

FIGURE 7. Hydrodynamic Phase Diagram for the evolution of turbulence in stably stratified flows. The two horizontal lines $\epsilon = (4,\ 5)DCN^2$ mark the onset of buoyancy effects, while the vertical line $\epsilon = 19\nu N^2$ represents the point where the buoyancy flux goes to zero; ◯ $Ri = 0.0575$; △ $Ri = 0.21$; □ $Ri = 0.37$; ▽ $Ri = 1$. Time increases from right to left.

change of kinetic energy cancel each other out, and production equals dissipation. When $Ri = Ri_s$, the buoyancy flux B adds a 20% contribution and $K_m \approx 1.2\epsilon/S^2$. For Richardson numbers small or large compared to the stationary value, the time rate of change of the kinetic energy becomes of the same order as production and dissipation and the model becomes invalid. However, K_m can still estimated within a factor of 2 from Eq. (19).

Similar results are obtained when the vertical eddy diffusivity is estimated with Eq. (20); on average $K_\rho = 0.16\epsilon/N^2$. However, the low Reynolds number simulations (closed symbols of Fig. 9) appear to have a lower mixing efficiency ($R_f \approx 0.09$) than the high Reynolds number simulations (open symbols in Fig. 9). For these simulations, the mixing efficiency $R_f \approx 0.20$ is a maximum for the stationary case, yielding $K_\rho \approx 0.25\epsilon/N^2$. When $Ri = 0.075$ and $Ri = 0.37$, $K_\rho = 0.16\epsilon/N^2$ is an excellent approximation. The formula proposed by Osborn (1980) $K_\rho = 0.20\epsilon/N^2$ is valid within $\pm 20\%$ for the range of Richardson numbers $0.075 < Ri < 0.37$ when stratified turbulent shear flows are slowly evolving, i.e., the time rate of change of kinetic energy is still small compared to the turbulent production P and the dissipation ϵ.

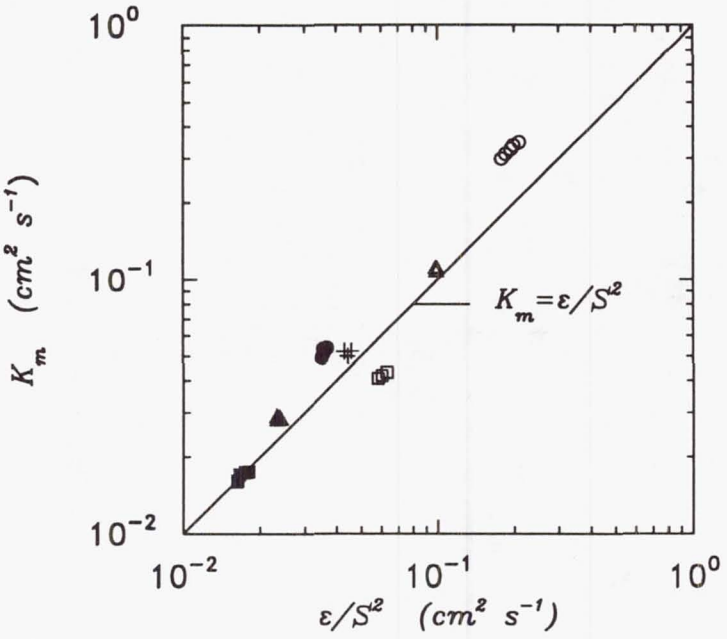

FIGURE 8. Comparison of the true momentum eddy diffusivity K_m to its estimate ϵ/S^2 using the dissipation technique for various Richardson and Reynolds numbers. Open symbols: $R_\lambda = 140$, ○ $Ri = 0.075$, △ $Ri = 0.21 = Ri_s$, □ $Ri = 0.37$; + $R_\lambda = 76$, $Ri = 0.15 = Ri_s$; closed symbols: $R_\lambda = 32$, • $Ri = 0.0575$, ▲ $Ri = 0.0875 = Ri_s$, ■ $Ri = 0.1125$.

6.2 The Osborn-Cox Model (1972)

Under the same steady-state assumptions, Osborn and Cox (1972) proposed that vertical eddy diffusivity K_ρ can be estimated from the potential energy (or temperature) equation (Eq. 4) as:

$$K_\rho = DC \tag{21}$$

Osborn and Cox (1972) originally proposed this diffusivity model for temperature (the major contributor to the density variation in the thermocline), but it can extended to other scalar variables such as salinity and density. Figure 10 shows that the Osborn-Cox model works best (as expected) near Ri_s (triangle and plus symbols). Otherwise, this model estimates the vertical eddy diffusivity K_ρ within $\pm 50\%$ for $0.075 < Ri < 0.37$ in the large Reynolds number simulations. Away from steady-state conditions ($Ri = 0.075$ or 0.37, for example), the time rate of change of potential energy can be about $\pm 0.30B$.

Equations (20) and (21) can be combined to give an alternate expression for the

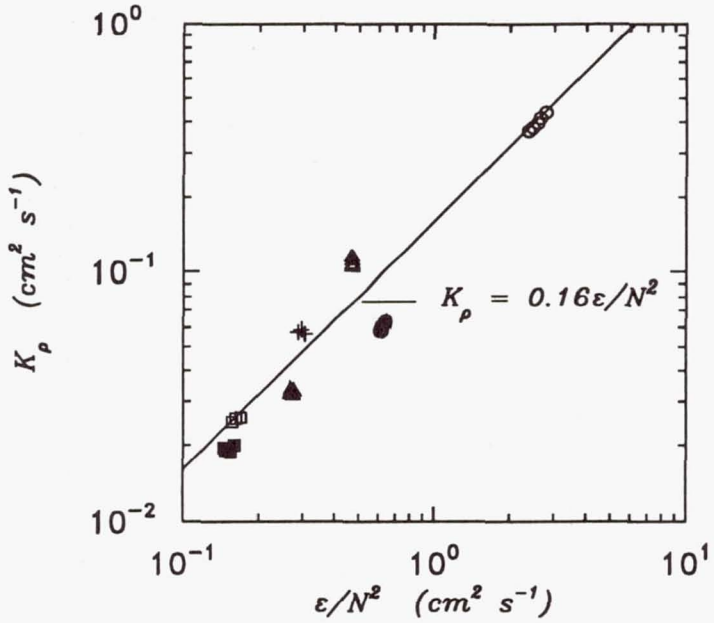

FIGURE 9. Comparison of the true vertical eddy diffusivity K_ρ to its estimate ϵ/N^2 using the dissipation technique for various Richardson numbers, symbols as in Fig. 8.

point of fossilization described in section 5.1:

$$\epsilon = \frac{1 - R_f}{R_f} DCN^2 \tag{22}$$

when it is reasonable to assume that near-steady state conditions exist. The observed mixing efficiency $R_f = 0.20$ at Ri_s yields $\epsilon = 4DCN^2$ in good agreement with Eq. (14). In contrast, Gibson's fossil turbulence model (Eq. 13) implies that the mixing efficiency at fossilization (transition from *active* turbulence to *active+fossil* turbulence) is only 7%, a value much lower than expected.

7. Conclusions

Direct numerical simulations of homogeneous turbulence in stably stratified shear flows by Holt (1990) confirm the length scale evolution observed in laboratory experiments (Stillinger *et al*, 1983; Itsweire *et al*, 1986; Rohr *et al*, 1988). Furthermore, these simulations show that when the Richardson number Ri is less than the stationary Richardson number Ri_s, the turbulence grows at all scales, the growth rate being a function of Richardson number. When $Ri = Ri_s$, there is a net balance between production, buoyancy, and dissipation. The vertical overturns measured by the Thorpe scale L_T remain constant in time, and the mixing efficiency measured

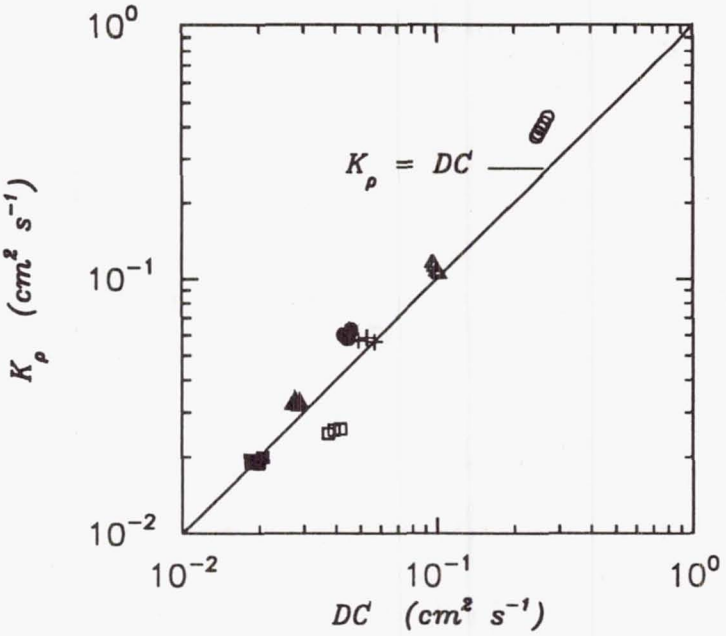

FIGURE 10. Comparison of the true vertical eddy diffusivity K_ρ to its estimate DC using the Osborn-Cox technique for various Richardson numbers, symbols as in Fig. 8.

by the flux Richardson number R_f is between 0.20 and 0.25. Finally, for stable conditions, ($Ri > Ri_s$), the large eddies of the turbulence are affected by buoyancy when $\epsilon = (4 \sim 5)DCN^2$, and the buoyancy flux goes to zero when $\epsilon = 19\nu N^2$. For $Ri \leq 0.5$, the mean shear controls the size of the dissipative scales as predicted by Hunt *et al.* (1988).

Estimates of the eddy diffusivities using dissipative techniques give $K_m = 1.2\epsilon/S^2$ and $K_\rho = 0.16\epsilon/N^2$ in good agreement with the measured diffusivities when the Richardson number is close to the stationary value Ri_s. Under the same conditions, the Osborn-Cox model (1972) can also be used to estimate the vertical eddy diffusivity as $K_\rho = DC$. When considering a broad range of Richardson numbers ($0.0575 < Ri < 0.37$), the dissipation technique formula proposed by Osborn (1980), $K_\rho = 0.2\epsilon/N^2$, provides a more accurate estimate of the vertical diffusivity ($\pm 20\%$) than the Osborn-Cox model.

Acknowledgements

We wish to thank Claude Cambon, Carl Gibson and Derek Stretch for fruitful discussions during the 1990 CTR Summer Program. ECI is very grateful to the CTR summer program for making this work possible. JRK, JHF and SEH were funded by the Office of Naval Research. C-L Lin provided assistance with the

post-processing of the database on the UCSD Cray.

REFERENCES

BUSCH, N. E. 1977 Fluxes in the surface boundary layer over the sea, In *Modeling and Prediction of the Upper Layers in the Ocean* (Ed. E. B. Kraus) pp. 72-91, Pergamon.

CALDWELL, D. R. 1983 Oceanic turbulence: Big bangs or continuous creation?. *J. Geophys. Res.* **88**, 7543-7550.

DILLON, T. M. 1982 Vertical overturns: A comparison of Thorpe and Ozmidov length scales. *J. Geophys. Res.* **87**, 9601-9613.

DILLON, T. M. 1984 The energetics of overturning structures: Implications for the theory of fossil turbulence. *J. Phys. Oceanogr.* **14**, 541-549.

DOUGHERTY, J. P. 1961 The anisotropy of turbulence at the meteor level. *J. Atmos. and Terrestrial Physics.* **21**, 210-213.

ELLISON, T. H. 1957 Turbulent transport of heat and momentum from an infinite rough plane. *J. Fluid Mech.* **2**, 456-466.

GARGETT, A. E., OSBORN, T. R. & NASMYTH, P. W. 1984 Local isotropy and the decay of turbulence in a stratified fluid. *J. Fluid Mech.* **144**, 231-280.

GERZ, T., SCHUMANN, U. & ELGHOBASHI, S. E. 1989 Direct numerical simulation of stratified homogeneous turbulent shear flows. *J. Fluid Mech.* **200**, 563-594.

GIBSON, C. H. 1980 Fossil temperature, salinity and vorticity in the ocean. In *Marine Turbulence* (Ed. J. C. T. Nihoul) pp 221-258, Elsevier.

GIBSON, C. H. 1986 Internal waves, fossil turbulence and composite ocean microstructure spectra. *J. Fluid Mech.* **168**, 89-117.

GREGG, M. C. 1989 Scaling turbulent dissipation in the thermocline. *J. Geophys. Res.* **94**, 9686-9698.

HOLT, S. E. 1990 The evolution and structure of homogeneous stably stratified sheared turbulence. Ph. D. Dissertation, Department of Civil Engineering, Stanford University.

HOLT, S. E., KOSEFF, J. R. & FERZIGER, J. H. 1990 The evolution of turbulence in the presence of mean shear and stable stratification. In *Seventh Symposium on Turbulent Shear Flows*, Stanford. Springer-Verlag, in Press.

HUNT, J. C. R., STRETCH, D. D. & BRITTER, R. E. 1988 Length scales in stably stratified turbulent flows and their use in turbulence models. In *Stably Stratified Flow and Dense Gas Dispersion* (Ed. J. S. Puttock) pp. 285-321, Clarendon.

ITSWEIRE, E. C. 1984 Measurements of vertical overturns in a stably stratified turbulent flow. *Phys. Fluids.* **27**, 764-767.

ITSWEIRE, E. C., HELLAND, K. N. & VAN ATTA, C. W. 1986 The evolution of grid-generated turbulence in a stably stratified fluid. *J. Fluid Mech.* **162**, 299-338.

OSBORN, T. R. 1980 Estimates of the local rate of vertical diffusion from dissipation measurements. *J. Phys. Oceanogr.* **10**, 83-89.

OSBORN, T. R. & COX, C. S. 1972 Oceanic finestructure. *Geophys. Fluid Dyn.* **3**, 321-345.

OZMIDOV, R. V. 1965 On the turbulent exchange in a stably stratified ocean. *Ivz. Atm. Ocean Physics.* **1**, 853-860.

ROGALLO, R. S. 1981 Numerical experiments in homogeneous turbulence . *NASA Tech. Memo. 81315.*

ROHR, J. J., HELLAND, K. N., ITSWEIRE, E. C. & VAN ATTA, C. W. 1987 Turbulence in a stably stratified shear flow: A progress report. In *Fifth Symposium on Turbulent Shear Flows*, (Eds. F. Durst et al.), pp 67-76, Springer-Verlag, New York.

ROHR, J. J., ITSWEIRE, E. C., HELLAND, K. N. & VAN ATTA, C. W. 1988 Growth and decay of turbulence in a stably stratified shear flow. *J. Fluid Mech.* **195**, 77-111.

STILLINGER, D. C., HELLAND, K. H. &VAN ATTA, C. W. 1983 Experiments on the transition of homogeneous turbulence to internal waves in a stratified fluid. *J. Fluid Mech.* **131**, 91-122.

THORPE, S. A. 1977 Turbulence and mixing in a Scottish loch. *Phil Trans. R. Soc. Lond.* **A286**, 125-181.

A numerical evaluation of the dynamical systems approach to wall layer turbulence

By Gal Berkooz[1]

This work attempts to test predictions based on the Dynamical Systems approach to Wall Layer Turbulence. We analyze the Dynamical Systems model for the non linear interaction mechanism between the coherent structures and deduce qualitative behavior to be expected. We then test for this behavior in data sets from D.N.S. The agreement is good, given the sub optimal conditions for the test. We discuss implications of this test and work to be done to deepen the understanding of control of turbulent boundary layers

1. Introduction

The Dynamical Systems approach to wall region turbulence is a methodology for deriving low dimensional Dynamical Systems (which are systems of O.D.E's) to describe the interaction of Coherent Structures in the near wall region. Coherent Structures are defined through the Proper Orthogonal Decomposition (to be described later). See Aubry *et al.* (1988) and Berkooz *et al.* (1990-1). The most significant achievement of the Dynamical Systems approach to date was suggesting a non-linear interaction mechanism that produces the so called "bursting" observed in experiments (Kline *et al.* 1967, Kim *et al.* 1970, Corino and Brodkey 1969). These events were also observed in numerical simulations of wall bounded flows (Moin and Kim, 1985). The reaction to the Dynamical Systems Approach in the Turbulence community ranged from enthusiasm to technical criticism to basic objections. Technical criticism, like Moffat's observations (Moffat 1990), were instrumental in furthering our understanding of the results (Berkooz *et al.* 1990-2, Holmes *et al.* 1990). Basic objections stemmed from previous experience where interesting dynamical behavior of Dynamical Systems models was due to the process which led to the Dynamical System (abbreviated D.S. from now on), and not to physical content of the equation they were modeling. The celebrated Lorenz system is such an example, the original problem it started off as was the Benard convection problem.

This work attempts to establish a connection between the D.S. approach and the "real world" (i.e. computer D.N.S.) by showing that the D.S. models predict non trivial behavior of the wall layer region that may be observed in D.N.S.

There are technical and fundamental difficulties in establishing this connection. A technical difficulty facing a detailed comparison is that the spanwise periodic domain used in the D.S. is small compared to most full size wall bounded D.N.S. In addition

1 Center for Applied Math. Cornell Univ. Ithaca, N.Y. 14853

the D.S. concentrate on a series of events in time, while spatially there is only one event. A full D.N.S. has several events occurring at different spatial locations, sometimes with overlap. This problem was overcome by using the "Minimal Flow Unit of Near Wall Turbulence" studied by Jimenez and Moin (1990). The minimal flow unit is the smallest computational domain, in a channel flow computation that would sustain a turbulent flow. This flow is not ideal for our purpose. Two point velocity correlation functions are not reproduced accurately, thus suggesting that the structures (in a P.O.D. sense) observed will not be the same as a real flow. The effects of the outer layer are not well produced above $y^+ = 40$, as will be outlined later; this effect is of importance to the D. S. models. The box sizes used in the minimal flow unit are smaller then the boxes used in previous studies of D.S. (100^+ for the minimal flow compared to 333^+ for the D.S. The eigenfunctions we had were not computed for this flow. They were derived from a large flow box D.N.S. (see Moin and Moser 1989). This caused us to interpolate the eigenfunctions, thus getting a less then optimal basis. The question of interpolating eigenfunctions, or two point correlation functions, will be addressed in the sequel. The main advantage of the minimal flow unit is that it produces well defined events which is in the spirit of the events produced by the D.S. Overall these data sets were the most readily available and therefore used.

Determining what will constitute a connection is a fundamental question. We suggest that the D.S. model for the non linear interaction mechanism that produces the burst will be analyzed to give qualitative predictions. The predictions will be compared to behavior of the corresponding real world objects to see what parts of the model perform accurately and what parts need improvement. A more quantitative study (i.e. measuring the short time tracking capability of D.S.) is underway.

This work is organized as follows: In section 2. we describe the essential ingredients of the D.S. approach. We describe the non linear interaction mechanism suggested to be the mechanism for the production of bursts. Based on the description we deduce some qualitative predictions that will be tested in the sequel. In section 3. we describe the numerical procedures developed in this work to test the predictions outlined in section 2. and the results of the comparison. Section 4. contains a discussion, conclusions, describes the relevance of this work to control applications, and suggests further topics for work and their contribution. Section 5. contains acknowledgements.

2. The D.S. approach and the Non Linear Interaction Mechanism.

The D.S. approach to the wall layer region of the turbulent boundary layer relies on four distinct elements. These are: The Proper Orthogonal Decomposition, Galerkin projection or truncation, a model to describe the feedback of the evolving coherent structures on what is effectively the local mean velocity profile, and a Smagorinsky type subgrid scale model to model the loss of energy to the unresolved modes. For a more thorough exposition the reader is referred to Aubry *et al.* (1988), Berkooz *et al.* (1990-1) and Berkooz *et al.* (1990-3).

The P.O.D has been described in several references. See Lumley (1970) for the most comprehensive discussion. For our purpose it will suffice to give the following necessary and sufficient condition which characterizes the P.O.D. Given a random signal (assume one dimensionality for simplicity) $u(x,t) : [a,b] \rightarrow I\!R$ such that $u(x,t) \in L^2([a,b])$ for every t. The P.O.D gives an optimal basis for a representation of the signal in the following sense. Let $\{\phi_i(x)\}_{i=1}^{\infty}$ be the P.O.D basis and $\{\psi_i(x)\}_{i=1}^{\infty}$ is any orthonormal basis s.t (equality in L^2 sense)

$$u(x,t) = \sum_{i=1}^{\infty} a_i(t)\phi_i(x) = \sum_{i=1}^{\infty} b_i(t)\psi_i(x)$$

where $a_i(t)$ and $b_i(t)$ are random coefficients. If $< \cdot >$ denotes the time average then

$$\sum_{i=1}^{n} < a_i a_i^* > \geq \sum_{i=1}^{n} < b_i b_i^* >$$

for every n. Recall that in such a representation $< a_i a_i^* >$ represents the average energy content of the i-th mode. Hence for a given number of modes the P.O.D basis captures the most energy. This is due to the fact that the sum of the n largest eigenvalues of an operator are greater than the sum of any n elements on the diagonal w.r.t any basis of the functional space. See Holmes *et al.* (1990). For an application of the P.O.D to the wall region in a pipe flow see Herzog (1986). For an application in a D.N.S see Moin and Moser (1989). The last two sources discuss the application of the P.O.D in three dimensions, where two of the directions are homogenous, which is the case we are interested in.

Galerkin projection, or truncation, is a tool in common use in C.F.D. Basically one picks a finite number of basis functions and gets dynamical equations for their amplitudes from the equations of motion. It is the core of a spectral method code and in a different sense, for a finite difference code. In our context we perform the same operation, the difference being that we retain a very small number of modes, and instead of picking a numerically convenient basis we use a physically relevant one.

The feedback of the evolving coherent structures on the "local" mean velocity profile is given by the formula:

$$U(x_2) = \frac{1}{\nu}\int_0^{x_2} < u_1 u_2 > dx_2 + \frac{u_\tau^2}{\nu}(x_2 - \frac{x_2^2}{2H}) \qquad (1)$$

where H is a channel half width. See Tennekes and Lumley pg 150. It is derived using time stationarity of the flow. It is then used when in place of u_1 and u_2 one puts the dynamical values of these quantities. This proves to be an important element since it provides a feedback that prevents the dynamical coefficients from growing indefinitely as would be the case if one was to put the average value of the mean velocity profile.

The loss to higher modes is modelled by a Smagorinsky type subgrid scale model. The value of the Smagorinsky constant for a given truncation may be computed

in terms of the eigenfunctions and eigenvalues to within an order 1 number. See Berkooz *et al.* (1990-2). The order 1 number gives rise to a parameter in the problem called the bifurcation parameter α. This parameter is used to tune the D.S. to obtain physically relevant behavior, corresponding to proper modeling of loss to higher modes.

At this point we should remark that most models studied by our group at Cornell contained no streamwise variation in the representation of the velocity field. It has been shown (Berkooz *et al.* 1990-2) that this functional subspace has some nice and useful properties. Recently, however, N. Aubry and her student S. Sanghi, have studied higher dimensional models with streamwise variation. See Aubry and Sanghi (1989). Their results show that the essentials of the dynamics described in previous reports persist in these higher dimensional models. A point of nomenclature, we will be discussing dynamics in the functional space, which is of 10 real dimensions if 5 structures are resolved, or the regular physical, 3 dimensional space where the fluid flows. The reader can distinguish between them from the context.

After performing modeling described above and analyzing the resultant D.S. using techniques from bifurcation theory and dynamical systems theory, the following non linear interaction mechanism is suggested. The interaction of the coherent structures is dominated by a spherical type heteroclinic attractor. One can visual this mechanism as follows, imagine a sphere in the real invariant subspace of phase space. On it there are distinct patches that are "pseudo-attractors", i.e. sets which are capable of attracting the dynamics for a while but points eventually escape them with a small perturbation present. The simplest examples of such systems were studied for the case of the "pseudo attractor" being a hyperbolic fixed point. See Holmes and Stone (1990). In the D.S. of the wall region it is the coupling with the outer layer that provides the perturbation term. The behavior of the wall region may be envisioned as a point travelling close to the sphere, lingering for a while in a well defined area, this corresponds to periods of quiescent behavior of the fluid. The point then jumps toward a new attracting patch, this corresponds to the burst and sweep, until the point settles for a while around a new point, only to start the cycle again - see figure 4.

The attractors described in Aubry *et al.* (1988) and Berkooz *et al.* (1990-1) are specific cases of this more general kind of attractor. They consisted of a circle of fixed points, where bursts occurred as jumps from one side of the circle to the other. However, if one wants to describe the general type of attractor that one will find one has to talk about a sphere. In higher dimensions the jumps may occur between different parts of the sphere as different heteroclinic structures may coexist and may be intertwined, thus allowing more freedom in the destination of the jump. This formulation has two advantages. It is independent on the number of modes chosen, and does not produce behavior that might be considered over simplified.

The pressure term that represents the coupling to the outer layer serves to perturb the points and thus prevent them from being attracted to a quiescent state indefinitely. The dynamics of the bursting are thus determined by the dynamics of the large scale structure where the outer layer is a constant source of instability.

C-3

A remarkable observation of Armbruster Guckenheimer and Holmes is that these types of attractors are structurally stable (in the D.S sense) in the context of systems with symmetry like that of the system derived from a boundary layer. This implies that the it is possible to meet such attractors for a non negligible set in "parameter space", and that the occurrence of such dynamical features is robust. The original result was proven for 2 dimensional systems. The principle for generalization to higher dimensions can be deduced from the original proof. Recently Holmes and Campbell (1990) and Berkooz (1990-4) have shown generalizations to higher dimensions.

Based on the model described above we can make the following predictions:

1. The p.d.f of the radius of in functional space of the dynamics should have a well defined peak (for a given flow). This is due to the basic conjecture regarding the shape of the attractor.
2. The distribution of points in phase space should be such that intervals of of time corresponding to the quiescent periods of the flow should be clustered together. This is from the conjecture that the quiescent periods correspond to motion around the "pseudo-attractors" around the sphere .
3. One should be able to correlate between streaky motion in phase space and bursting periods.

3. Numerical Methods and Results

3.1 The Data Set Used.

As mentioned earlier the data sets used were those studied by Jimenez and Moin. The simulation was run so as to keep a constant mass flux through the channel by varying the pressure drop. A Reynolds number was compiled based on channel half width and the center line velocity of a parabolic velocity profile which the same mass flux. Specifically we had a Reynolds number of 2000. The friction velocity was approximately 1/22 of the centerline velocity. The computational domain was $\pi \times 2 \times 0.35\pi$, streamwise, wall normal and spanwise respectively. Our realizations were spaced 0.625 external time units apart, or 3 wall time units. We had 352 realizations totalling 220 external units, or 1056 wall units. The characteristic time between bursts reported by Jimenez and Moin is approximately 100 external time units, thus the flow is expected to contain two bursts. See fig. 1, which contains the time history of the wall shear stress. An increase in the wall shear is associated with the bursting process where low momentum fluid from the near wall region is exchanged with high momentum fluid from higher up, thus increasing the wall shear stress

3.2 The Eigenfunctions and the Projection.

The eigenfunctions used in this study are based on eigenfunctions from a full channel D.N.S. This posed a requirement to fabricate eigenfunctions for the specific box used. The procedure applied was to interpolate the eigenfunctions, where the interpolation is performed according to wave lengths in wall variables. This procedure seemed to produce reasonable results for this case. This is due to the fact that

the eigenfunctions have a distinct shape, fairly robust as a function of wave number. As R. Moser suggested, it is preferable to interpolate the 2 -point velocity correlation tensor and recompute the eigenfunctions. This will also solve the problem that interpolating is not valid for the second eigenfunction, due to loss of orthogonality. The question of interpolating eigenfunctions, or the two point velocity correlation tensor, will be addressed in the sequel.

We decided to choose $y^+ = 39$ as the upper bound for the modeled domain, that gave us 39 grid points. The eigenfunctions were then normalized. The normalized eigenfunctions were used in the study. See fig 5.a, 5.b, 5.c for the streamwise, normal, cross stream components of the eigenfunctions.

Once the eigenfunctions were computed we had to determine which of them correspond to large scale structures. The criterion chosen was that they should have such a shape as to be able to extract energy from interaction with the mean flow (i.e. a positive linear coefficient in the D.S.) and they should also have such a shape that their energy cannot grow without bound, (negative cubic). This selection ruled out eigenfunctions 5,6,7. One can also see by observation that they have fine structure that would generate scales which would not be considered large scale. We also chose not to include the first eigenfunction in the analysis since its average did not go to zero during the period simulated. As Jimenez and Moin point out a long averaging period is needed for the statistics to stabilize. We thus are left with three complex or 6 real variables. See figures 6.a, 6.b, 6.c for the traces used in this study.

3.3 The p.d.f of the Radius in Phase Space.

The p.d.f of the radius in phase space was computed. See figure 2 for the result. The total amount of points was divided into 25 bins. Note that the p.d.f has a very well defined peak. More over it seems to strongly suggest an exponential tail. This is quite remarkable as Holmes and Stone (1990) predicted an exponential tail for the distribution of passage time between bursts. It is conceivable that a similar analysis for the distance from the invariant heteroclinic attractor will also give an exponential tail since the passage time and the distance from the attractor are very intimately linked. (see Holmes and Stone 1990)

3.4 Distribution in Phase Space.

Determining whether points in phase space are clustered together of form a streaky structure is a tricky question. The way we decided to compare "clusters" versus "streaks" is as follows. Given a set of n points in phase space we create a list of distances between all possible pairs $d_1 \dots d_f$ where $f = n(n-1)/2$. We would then compute the flatness factor of this list. A higher flatness would indicate more of a streaky group of points. It is also a dimensionless quantity. The following table summarizes our findings.

t: $20^+ - 40^+$ flat: 2.35 behavior: small burst

t: $55^+ - 75^+$ flat: 1.69 behavior: quiescent

t: $90^+ - 110^+$ flat: 2.09 behavior: small burst

t: $130^+ - 150^+$ flat: 2.61 behavior: start of big burst

t: $165^+ - 185^+$ flat: 2.81 behavior: peak of big burst

t: $200^+ - 220^+$ flat: 2.35 behavior: relaxation after big burst

We see that there is a correlation between the flatness indicator and the wall shear stress, for the few points we have. Another indicator of dynamical activity is the velocity in phase space. Based on the interaction mechanism described previously one would expect the velocity in phase space to be higher at bursting periods. Figure 3, which shows the velocity in phase space as a function of time shows such a correlation.

4. Summary and Discussion

This study was intended to evaluate numerically qualitative predictions of the Dynamical Systems approach to wall layer turbulence. The predictions were reasonably confirmed, considering the amount of data available and the basis used.

The main achievement of the D.S. approach as it comes to light in this study, is that starting with time average quantities (2-point velocity correlations) one is able to make, through the proposed model for non linear interaction of coherent structures, predictions about dynamical behavior of large scale structures and validate them numerically.

This study suggests a follow up in several areas. First it would be desirable to perform this study on a sample size significantly larger, like the ones used by Jimenez and Moin. Better eigenfunctions could also contribute. Second, it would be important to study the variation of the eigenfunctions and the two point velocity correlation as the geometry changes. One could start with different box sizes for the same geometry and go on to a curved channel etc. This is an important question since as seen by the P.O.D the two point correlation contains important structural information.

This study encourages the pursuit of a practical control scheme for drag reduction or increase of mixing. It confirms our basic assumptions about the relation of the dynamical systems objects we have dealing with and real world objects (like wall shear stress). If the control scheme suggested, i.e. holding the dynamics as close as possible to the hyperbolic points, or the pseudo attractors, succeeds, one will indeed reduce drag. We still are pursuing the measurement of the short term tracking. The analysis performed here can be applied to existing drag reduction techniques, i.e. riblets or the control scheme studied by Moin, Kim, and Choi (1989). It would be interesting and important to gauge the effects of those controls on the dynamics and see whether from a dynamical point of view they share the same principals.

Acknowledgements

Professor P. Holmes and Professor J. L. Lumley both contributed with discussions and suggestions about the subject. I would like to thank Mr. H. Choi of CTR for his help in accessing the data bases and the computing environment in general. I would also like to thank Mr. Y. Y. Du of the Center for Applied Math. at Cornell for computing the coefficients of the Dynamical System. I am particularly grateful to Professor P. Moin of CTR for his interest in this work. Partially supported by AFOSR-89-0226.

REFERENCES

ARMBRUSTER, D., GUCKENHEIMER, J. & HOLMES, P. Heteroclinic cycles and modulated traveling waves in systems with O(2) symmetry. Physica D 1989.

AUBRY, N., HOLMES, P., LUMLEY, J. L. & STONE, E. 1988 The dynamics of coherent structures in the wall layer of a turbulent boundary layer. *J. Fluid Mech.* **192,** 115-173

AUBRY, N. & SANGHI, S. 1989 Streamwise and crosstream dynamics of the turbulent boundary layer. *Proc ASME N.Y., July 89.*

BERKOOZ, G., GUCKENHEIMER, J., HOLMES, P., LUMLEY, J. L., MARSDEN, J., AUBRY, N.& STONE, E. 1990 Dynamical Systems Theory Approach to the Wall Region. *AIAA Seattle June 1990.*

BERKOOZ, G., HOLMES, P. & LUMLEY, J. L. 1990 Intermittent Dynamics in Simple Models of the Wall Layer. *Submitted to J. Fluid Mech.*

BERKOOZ, G., HOLMES, P.& LUMLEY, J. L. 1990 Modeling the turbulent boundary layer using empirical eigenfunctions and control. *Preprint.*

BERKOOZ, G. 1990 Higher Dimensional Systems with O(2) Symmetry. *Preprint.*

CORINO, E. R. & BRODKEY, R. S. 1969 A visual investigation of the wall region in turbulent flow. *J. Fluid Mech.* **37,** 1-30.

HOLMES, P., BERKOOZ, G. & LUMLEY, J. L. 1990 On the unreasonable effectiveness of dynamical systems in turbulence. *Proc. 1990 Cong. of Math.*

HOLMES, P. & CAMPBELL, S. 1990 *in preparation*

HOLMES, P. & STONE, E., 1990 Random Perturbations of heteroclinic attractors. *SIAM J. App Math. 90.*

KIM, H. T., KLINE, S. J. & REYNOLDS, W. C. 1971 The production of turbulence near a smooth wall in a turbulent boundary layer. *J. Fluid Mech.* **50,** 133-160.

KLINE, S. J., REYNOLDS, W. C., SCHRAUB, F. A. & RUNSTADLER, P. W. 1967 The structure of turbulent boundary layers. *J. Fluid Mech.* **30,** 641-773.

LUMLEY, J. L. 1971 Stochastic tool in turbulence. Wiley.

MOIN, P. & KIM, J. 1985 The structure of the vorticity field in turbulent channel flow, Part I. *J. Fluid Mech.* **155,** 441-464.

MOIN, P., KIM, J.,& CHOI, H. 1990 On active control of wall bounded turbulent flows. *AIAA-89-09600.*

MOIN, P. & MOSER, R. D. 1989 Characteristic-eddy decomposition of turbulence in a channel. *J. Fluid Mech.* **200**, 471-509.

TENNEKES & LUMLEY 1972 *A First Course in Turbulence.* The MIT Press

Resonant instability of supersonic shear layers

By C. K. W. Tam[1] AND S. K. Lele[2]

A computer simulation of possible resonant instability of a supersonic shear layer is carried out. The resonance of two acoustic duct modes of the flow induced by periodic Mach waves generated by a wavy wall is sought. Results of the simulations are reported. Simulations are unable to document a resonant instability and the mixing characteristics remain unchanged. Possible weakness of the present simulations are discussed. A second set of simulations involving a mixing layer separating a supersonic and a subsonic stream were performed. A wavy wall placed adjacent to the supersonic stream to produce a set of periodic Mach waves terminating at the shear layer is modelled. The entire flow field is similar to that of an imperfectly expanded supersonic jet discharging into a subsonic coflowing stream for which enhanced mixing due to the onset of screech (feedback instability) is known to occur. The purpose of these simulations is to see if enhanced mixing and feedback instability would, indeed, take place. Some evidence of feedback oscillations is found in the simulated flow.

1. Introduction

Recent measurements by Ikawa & Kubota (1975), Bogdanoff (1983), Papamoschou & Roshko (1986, 1988), Chinzei et al. (1986), and Samimy & Elliot (1990) indicate that the mixing rate of shear layers decreases drastically as the convective Mach number becomes supersonic. This is a great detriment for certain types of applications such as supersonic combustion where faster mixing is not only desirable but also a necessity. In the past, various trailing edge mixing devices have been tried (see e.g., Papamoschou, 1989). However, so far no success has been reported.

Papamoschou & Roshko were the first to demonstrate that a strong correlation exists between the mixing rate of shear layers and the maximum growth rate of the instability waves of these flows over a wide range of subsonic and supersonic convective Mach number. The good correlation was reconfirmed by the more recent calculations of Ragab & Wu (1989), Zhuang et al. (1988, 1990), Jackson & Grosch (1989), and Sandham & Reynolds (1989) using improved theoretical models. In the newer works, spatial instability growth rate was used instead of the temporal growth rate, and the wall effects were included. It is known that the instability growth rate of shear layers decreases with an increase in convective Mach number, which is a measure of the effect of compressibility. A simple interpretation of the strong correlation between shear layer spreading rate and instability growth rate

1 Florida State University

2 Stanford University

is that instability is the primary mechanism of mixing in this class of flows. The reduction in instability growth rate with an increase in convective Mach number, therefore, necessarily results in a lower mixing or spreading rate.

In a recent paper, Tam & Hu (1989a) suggested the use of resonant instability to destabilize the flow of ducted supersonic shear layers. When a shear layer is confined inside a rectangular duct, its motion is invariably coupled to the acoustic modes of the ducted flow (see Tam & Hu, 1989b). The resonant instability idea is to introduce a periodic Mach wave system in the supersonic flow by means of a wavy channel wall. The wave length of the wavy wall is carefully chosen so that it allows two of the acoustic wave modes of the ducted flow to interact forcing each other to grow. This resonance condition requires the wave number of the Mach waves to be equal to the difference of the wave numbers of the two acoustic modes. Using a multiple-scales perturbation analysis, Tam & Hu showed that significant growth compared with those of the natural instability waves of the shear layer can be realized over a wide range of flow conditions and frequencies.

The purpose of this work is to perform a numerical simulation of resonant instability of supersonic shear layers. The primary objective is to see if resonant instability does occur in a simulated experimental environment other than the idealized condition of perturbation analysis. Such simulated experiments would also provide quantitative information as to whether such resonant instability has an impact on the shear layer spreading rate.

Another objective of this work is to test the feasibility of using feedback instability as a mechanism for mixing enhancement when the flow on one side is supersonic and the other side is subsonic. The idea is based on the well known jet screech phenomenon of imperfectly expanded supersonic jets. Jet screech is driven by a feedback loop. The energy of the feedback loop is derived from the downstream propagating instability waves in the shear layer of the jet. The instability waves are initiated at the nozzle lip by acoustic excitation. As the instability waves propagate downstream, their amplitudes grow. At a distance of about four to five shock cells from the nozzle exit, they interact strongly with the quasi-periodic shock cell structure in the jet plume. The interaction generates strong acoustic waves, part of which propagate upstream outside the jet where the flow is either subsonic or at rest. Upon reaching the nozzle lip, these acoustic waves excite the shear layer leading to the further generation of instability waves. This completes the feedback loop. For a mixing layer housed inside a rectangular channel separating a supersonic and a subsonic stream, the flow condition is similar to that near the exit of supersonic jet discharging into a coflowing subsonic stream. The equivalent of a quasi-periodic shock structure may be generated by a wavy wall on the supersonic side of the shear layer. In such a flow configuration, it is even possible to control the feedback frequency by selecting an appropriate wave length for the wavy wall. This latitude allows one to tune the feedback frequency to coincide with that of the most unstable wave of the shear layer, thus obtaining maximum mixing enhancement.

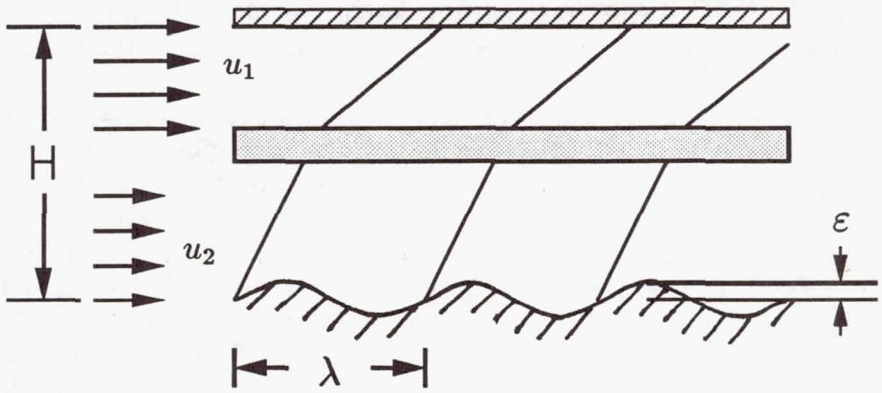

FIGURE 1. Schematic diagram of flow configuration for direct numerical simulation of resonant instability.

2. Simulation of Resonant Instability

Computer simulations of resonant instability of a supersonic shear layer were carried out. The computational procedure and boundary conditions are documented earlier by Lele (1988, 1989). The inviscid walls, inflow perturbations, and the Mach waves due to the wavy walls were introduced following the details described by Poinsot & Lele (1989). The inflow perturbations used the linear stability eigen functions calculated by Tam & Hu, and the Mach wave solutions were used for modeling the wavy wall. The flow configuration is shown in Figure 1. The numerical values of the parameters chosen are:

$$M_1(\text{Mach number of fast stream}) = 2.0 \qquad T_1 = T_2$$
$$M_2(\text{Mach number of slow stream}) = 1.2 \qquad \epsilon/\lambda = 0.015$$

where ϵ and λ are the amplitude and wavelength of the wavy wall.

Two acoustic duct modes are introduced at the inflow boundary of the channel with a peak amplitude of 1% relative to the fast stream velocity. These modes have a nondimensional frequency of $\omega H/u_1 = 6.0$. This first duct mode has a wave number of $k_1 H = 12.39$. According to linear theory, this wave mode has a subsonic phase velocity relative to the slow stream so that the eigenfunction is confined mainly to the fast stream. The second duct mode has a wave number $k_2 H = -4.68$. The eigenfunction of this wave mode spreads over the entire channel. The mixing layer is assumed to have an initial velocity profile in the form of the hyperbolic-tangent function with a vorticity thickness equal to 10% of the channel height. To attain resonance, the wave number of the wavy wall, k_M, is taken to be equal to $(k_1 - k_2)$. The computation domain consists of a 2×16 rectangle divided into a 150×500 cells (the half channel height is the length scale for non-dimensionalization). As the simulation progresses, the pressure and other flow variables are monitored at eleven equally spaced stations in the flow direction (the first and last stations are at the

inflow and outflow boundary respectively) at levels $j = 20$, 110, and 130. Level $j = 1$ corresponds to the mean position of the bottom wall whereas the top wall is at $j = 151$.

Figure 2 shows the pressure variations as functions of time (time unit $= 1.007\, H/u_1$) at the 11 x-stations at level $j = 110$. The bottom one corresponds to that at the inflow boundary ($x = 0$, $i = 1$), and the top one corresponds to that at the outflow boundary ($x = 16$, $i = 501$). These stations are close to the shear layer. As a result, the pressure fluctuations in the downstream stations are dominated by the shear layer instability wave. In Figure 2 the distinct wave front (indicated by a straight line) is the wave front of the instability wave. The propagation velocity, V, of the wave front as calculated from this figure is $V = 0.76\, u_1$. The propagation velocity can also be calculated from the group velocity, $\frac{d\omega}{dk}$, of the linear instability wave theory. It is found to be equal to $0.787\, u_1$. Thus there is good agreement between linear instability wave theory and direct numerical simulation.

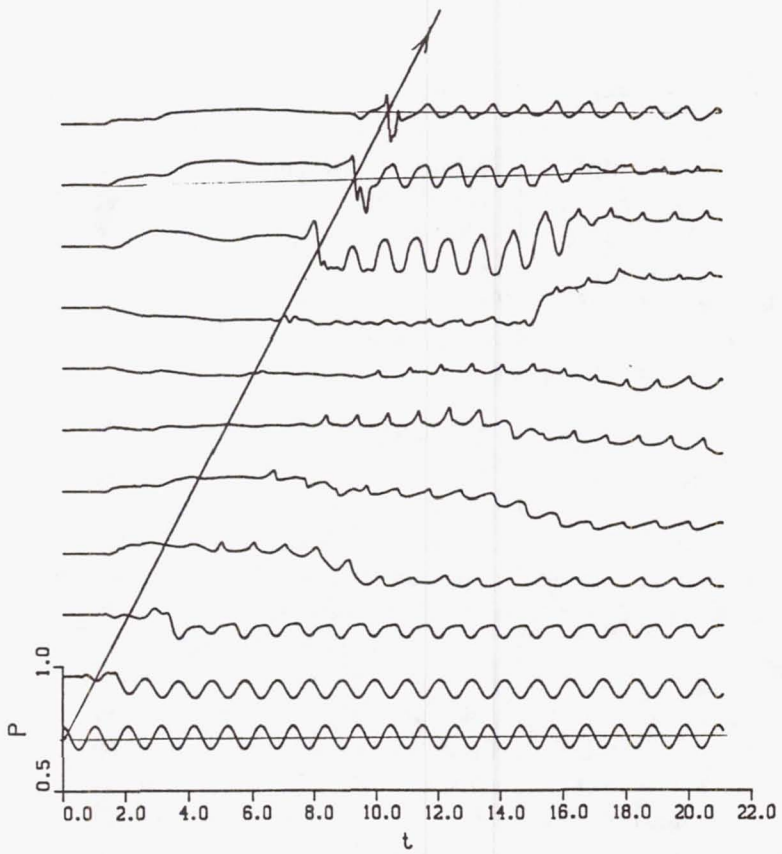

FIGURE 2. Pressure time histories at the eleven monitoring stations at the $j = 110$ level. Wave front of the instability wave is indicated by a straight line. Time histories at the intermediate stations show large-scale shock cell and duct oscillations.

Figure 3 shows the pressure variations at the eleven x-monitoring stations at level

$j = 130$. These stations are close to the top wall quite far from the shear layer. As a result, there is minimal influence from the shear layer instability wave. From the eigenfunctions of the two duct modes, it is found that the contribution from duct mode 2 is also very small. In this figure, two wave fronts can be readily identified. The first wave front is that of the instability wave having the same velocity as that in Figure 2. The second wave front is that of the first duct mode. The wave front velocity as measured from this figure is equal to $0.48\ u_1$. This is in good agreement with the group velocity $\frac{d\omega}{dk} = 0.51\ u_1$ calculated by the linear theory. The amplitude of the duct mode oscillations appears to persist all the way to the end of the computation domain. No significant amplification is detected, although some slight increase is observed at several intermediate monitoring stations. The nonlinear steepening of the waves is also evident from this and the preceding figure. Figures 2 and 3 also show large scale and low frequency oscillation of the flow field. The precise origin of these oscillations is not clear.

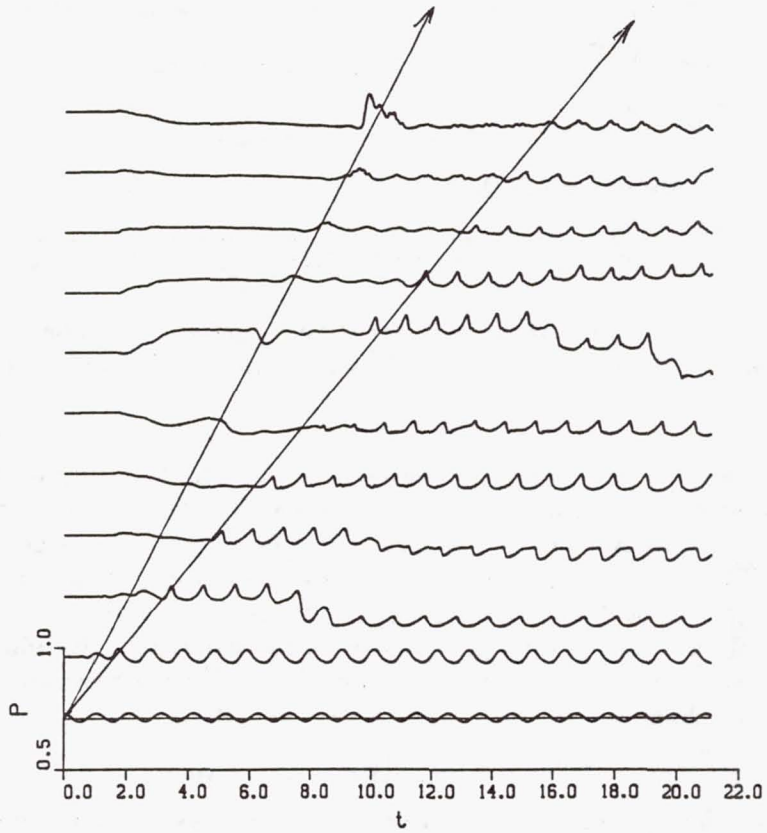

FIGURE 3. Pressure time histories at the eleven monitoring stations at the $j = 130$ level. Wave fronts of the instability wave and the first duct mode are indicated by straight lines.

Figure 4 shows the pressure fluctuations at the $j = 20$ level monitoring stations. These stations are very close to the bottom wall. At this leve,l the influence of the

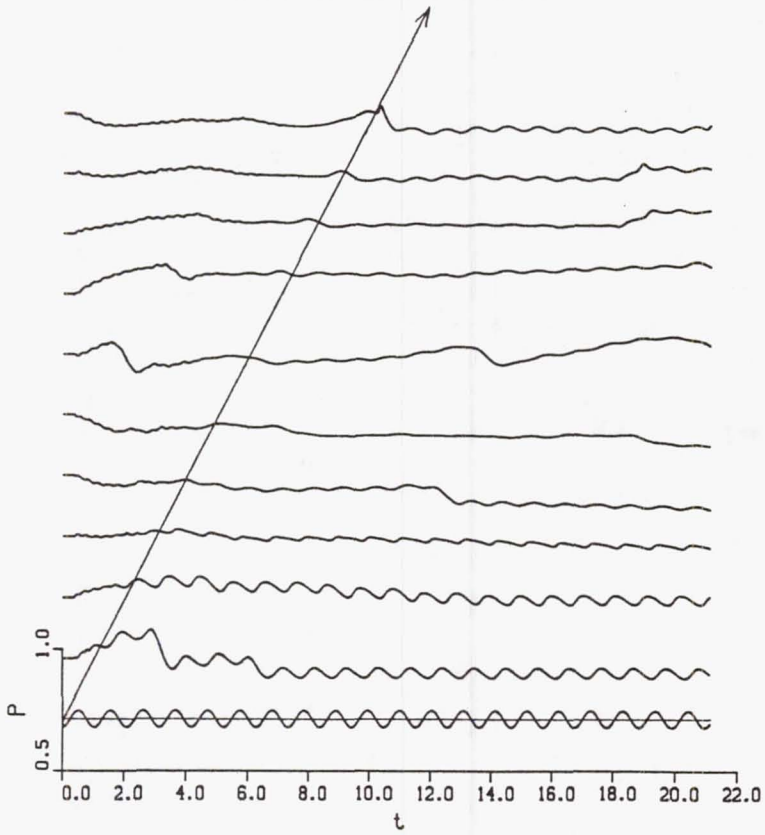

FIGURE 4. Pressure time histories at the eleven monitoring stations at the $j = 20$ level. There appears to be a leakage of the second duct mode from the computation domain.

first duct mode and the instability wave is very small. The output is essentially the pressure oscillations associated with the second duct mode. It is clear from this figure that the amplitude of the second duct mode decreases in the downstream direction. The exact cause of this is not known. But since there is no damping mechanism, it is possible a loss may exist at the bottom wall. In any case, at a distance of two and a half channel height downstream, the second duct mode appears to vanish from the computation domain. It appears to re-emerge towards the end of the channel.

2.1 Interpretation and Conclusion

The simulations performed so far were unable to resolve the question of whether resonant instability can enhance mixing. While the simulations did not show any enhanced tendency for the mixing layer to roll up or pair, the resonance being sought was not directly observed. The possible loss of the second duct mode amplitude may be partly responsible for this. Furthermore, the values of the flow parameters chosen were not optimal for the resonant instability to be the dominant instability of the flow. They were chosen to facilitate the numerical calculations. Future work

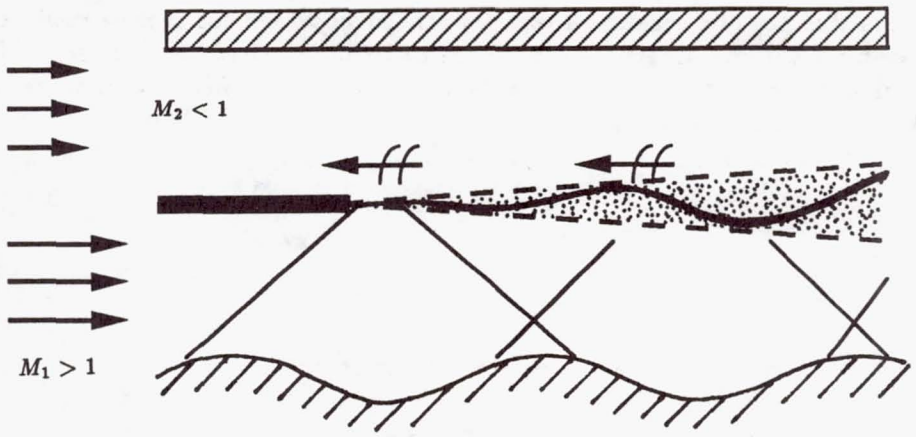

FIGURE 5. Schematic diagram of the flow field for direct numerical simulation of feedback instability.

is needed to resolve these problems.

3. Simulation of Feedback Instability

Simulations of possible feedback instability have been carried out with a flow configuration as shown in Figure 5. In the first simulation, no trailing edge is used. In the second simulation, an inviscid trailing edge is inserted at the inflow boundary extending to 24 mesh cells in the interior. The numerical values of the flow parameters are:

$$\begin{aligned} M_1(\text{subsonic stream}) &= 0.5 \\ M_2(\text{supersonic stream}) &= 1.5 \end{aligned} \qquad \begin{aligned} \lambda/H &= 1/3 \\ T_1 &= T_2 \\ \delta/H &= 1/20 \end{aligned}$$

where δ is the vorticity thickness of the shear layer and H is the channel width. The computational domain consists of a rectangle of 2×7 and a mesh with 150×300 cells and the shear layer is symmetrically placed. Again, the time evolution of the flow and acoustic fields is monitored by eleven evenly spaced stations distributed in the flow direction.

Results of the first simulation are given in Figure 6. Plotted in this figure are the V velocity component (y-component) at the eleven monitoring stations as a function of time. The output of the first station (at the inflow boundary) is given by the bottom curve. The output of the last station (at the outflow boundary) is given by the top curve. It is clear by comparing the output of the first and last station that the instability waves of the mixing layer are excited. The time history of the velocity fluctuation at the outflow station is, however, quite irregular. So

it is not clear whether feedback instability has been established. We remark that similar results due to numerical feedback have been observed for incompressible mixing layer by Buell and Huerre (1988). It is to be noted that the frequency of oscillations is quite close to that of the instability wave of maximum growth rate based on linear instability wave theory.

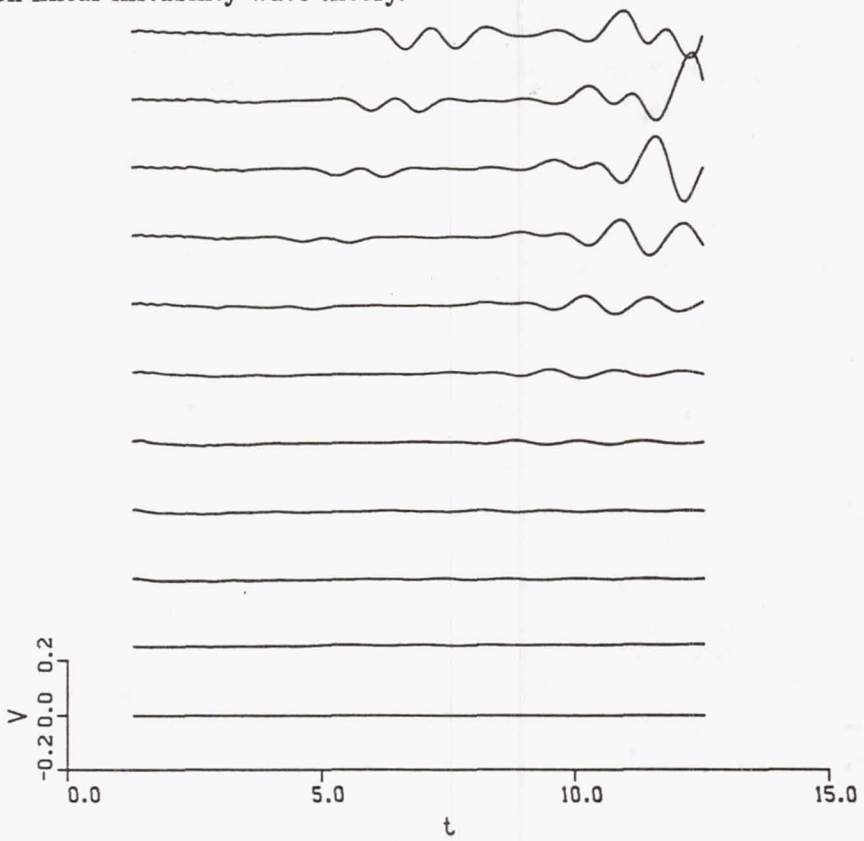

FIGURE 6. Time histories of the v-velocity component at the eleven monitoring stations. No trailing edge in the simulation.

Figure 7 gives the time history of the V-velocity component at the monitoring stations for the second simulation. This simulation includes an inviscid trailing edge. By comparing the output at the last few stations with those in Figure 6, it is evident that the oscillation amplitudes are much larger. In addition, the oscillations appear to be more regular, and the period of oscillation is nearly 1.5 to 2.0 times that without the trailing edge. The observed nondimensional period is approximately equal to $(u_2 T/\delta) = 28.0$ where T is the period. The expected value based on feedback theory is 30.0. Thus, there is a good possibility that the observed oscillations are due to feedback instability. However, because the run time is not long enough, a firm conclusion is premature. Also, it is known that in simulations of this kind, numerical feedback is possible. In this present case, this does not appear to be very significant. To obtain the theoretical feedback oscillation period, the

upstream propagating waves must travel with the speed of sound against the subsonic flow. Note that upstream stream propagating numerical error waves travel at speeds considerately larger than the speed of sound. Further investigation is, nevertheless, needed to rule out with certainty such non-physical feedback loops.

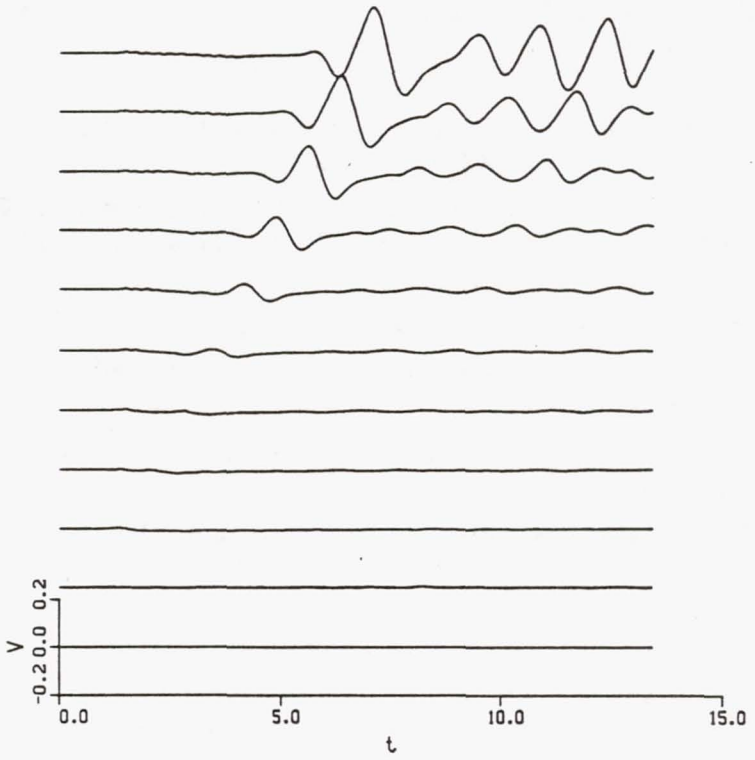

FIGURE 7. Time histories of the v-velocity component at the eleven monitoring stations. Inviscid trailing edge included in the simulation.

3.1 Interpretation and Conclusion

The results of the direct numerical simulation are very encouraging. Because the run time is not long enough, a definitive statement on the existence of feedback instability cannot be made. However, the agreement between the predicted and observed frequency and the fairly regular oscillations measured at the very downstream stations are surely favorable indications of the possible feedback instability. Future work must extend the run time by at least a factor of two. Also, a much longer duct in the direct numerical simulation appears to be very much needed.

REFERENCES

BOGDANOFF, D. W. 1933 Compressible effects in turbulent shear layers. *AIAA J.* **21**, 926–927.

BUELL, J. C. & HUERRE, P. 1988 CTR Report CTR-S88, Stanford University.

CHINZEI, N., MASUYA, G., KOMURO, T., MURAKAMI, A., & KUDEN, K. 1986 Spreading of two-stream supersonic turbulent mixing layers. *Phys. Fluids.* **29**, 1345–1347.

IKAWA, H. & KUBOTA, T. 1975 Investigation of supersonic turbulent mixing with zero pressure gradient. *AIAA J.* **13**, 566–572.

JACKSON, T. L. & GROSCH, C. E. 1989 Absolute/convective instabilities and the convective Mach number in a compressible mixing layer. *ICASE Report 89-38*

LELE, S. K. 1988 Vortex evolution in compressible free shear layers, Workshop on the Physics of Compressible Turbulent Mixing, Princeton, NJ.

LELE, S. K. 1989 Direct numerical simulation of compressible free shear flows. *AIAA paper 89-0374*

PAPAMOSCHOU, D. & ROSHKO, A. 1986 Observation of supersonic free shear layers. *AIAA paper 89-0162*

PAPAMOSCHOU, D. & ROSHKO, A. 1988 The compressible shear layers: an experimental study. *J. Fluid Mech.* **197**, 453–477.

PAPAMOSCHOU, D. 1989 Structure of the compressible turbulent shear layer. *AIAA paper 89-0126*

POINSOT, T. J. & LELE, S. K. 1989 Boundary conditions for direct simulations of compressible viscous reacting flows. *CTR manuscript.* **102**, Stanford Univ., to appear in *J. Computational Physics.*

RAGAB, S. A. & WU, J. L. 1989 Linear instabilities in two-dimensional compressible mixing layers. *Phys. Fluids A.* **1**, 957–966.

SAMIMY, M. & ELLIOT, G. S. 1990 Effects of compressibility on the characteristics of free shear layers. *AIAA Journal.* **28**, 439–445.

SANDHAM, N. D. & REYNOLDS, W. C. 1989 The compressible mixing layer theory and direct simulation. *AIAA paper 89-0371*

TAM, C.K.W. & HU, F. Q. 1989a The instability and acoustic wave modes of supersonic mixing layers inside a rectangular channel. *J. Fluid Mech.* **203**, 51–76.

TAM, C.K.W. & HU, F. Q. 1989b Resonant instability of ducted free supersonic mixing layers induced by periodic Mach waves. *Bull. Amer. Phys. Soc.* **34**, 2285, submitted to *J. Fluid Mech.*

ZHUANG, M., KUBOTA, T., & DIMOTAKIS, P. E. 1989 On the instability of inviscid compressible free shear layers. *AIAA paper, 88-3538*

ZHUANG, M., KUBOTA, T., & DIMOTAKIS, P. E. 1990 The effect of walls on a spatially growing supersonic shear layer. *Phys. Fluids A.* **2**, 599–605.

IV. The small scales mixing group

The study of direct numerical simulations of turbulence has significantly added to the understanding of many turbulent flows. Originally such simulations concentrated on examination of the turbulent velocity and vorticity fields, studying both statistics and the structure of the instantaneous flow fields. More recently there has been increased interest in using direct numerical simulations to examine the ability of turbulence to mix scalar quantities (such as temperature or concentration of a chemical species). This stems partly from the desire to extend the predictive capabilities of direct numerical simulations to chemically reacting flows.

The interaction of turbulence with a chemically-reacting flow field remains one of the most complex and least understood problems of engineering interest. In typical combustion applications the large heat release associated with the chemical reaction can significantly alter the local hydrodynamics. In addition the turbulence can dramatically alter the distribution of the reactant (and product) species. In many practical applications the rate of reaction is controlled primarily by the ability of the turbulence to mix reactant species. By examining the turbulent mixing of a passive scalar quantity (one which does not alter the hydrodynamic flow field) the mixing capability can be studied without the added complications associated with heat-release-induced alterations of the flow field. Such direct numerical simulations of passive scalar mixing thus lend themselves directly to the study of mixing by realistic turbulence, ignoring complex reaction kinetics and the effects of heat release.

In many practical combustion applications the reaction occurs in free shear flows, *e.g.* fuel jets, flame-holder wakes. Perhaps the simplest such free shear flow is the plane mixing layer and it is thus often used as the prototypical free shear flow for the study of turbulent mixing. The development of three-dimensionality and small-scale turbulence in such a plane mixing layer is of crucial importance to its mixing capabilities. Three of the four projects summarized below were directed at studying small-scale turbulence and scalar mixing in this flow. The fourth is more general in nature, directed towards elucidating the basic mechanisms of scalar mixing.

Recent direct numerical simulations have shed substantial insight into the early evolution of plane mixing layers. Despite this, no general theory is available to predict the layer evolution for disturbances that are too large for the results of linear theory to be valid. The fact that this flow is sensitive to slight changes in initial conditions underscores the need for such a model. Daniel Riahi, Bob Moser and Fabian Waleffe investigated various possible weakly-nonlinear theories in an effort to complement the direct numerical simulation results. This proved to be more difficult than initially anticipated due primarily to the time-evolving nature of the base flow under consideration.

Very large direct numerical simulations have just recently been able to simulate through the mixing transition (sudden increase in mixing due to proliferation of small-scale motions) in the plane mixing layer. It is of great interest to ascertain whether this transition resembles that seen in experiments. Yitshak Zohar,

Bob Moser, Jeff Buell and Chih-Ming Ho extensively compared the post-transition numerical simulation velocity and vorticity fields with data taken in experimental mixing layers by Zohar and Ho. They found a high degree of correspondence between the two, with both indicating that the most probable length scale of the small-scale eddies corresponds to the scale associated with the peak of the energy-dissipation-rate spectrum and that the small-scale strains are comparable to the global strain associated with the velocity difference across the layer and the streamwise separation between eddies.

The mixing transition discussed above is associated with development of small-scale three-dimensional eddies by vortex stretching and thus presumably could not occur in a two-dimensional simulation. Javier Jiménez examined passive scalar mixing in very high Reynolds/Peclet number two-dimensional mixing layers to study the mixing behavior in the absence of the three-dimensional structures described above. He found that while a mixing transition of the kind seen in three-dimensional simulations was not observed, there was a definite increase in the complexity of the "reaction sheet" separating two chemical species (as measured by its fractal dimension). This increase was found to occur during the first pairing of the primary Kelvin-Helmholtz rollers and subsequent pairings did not further increase the dimension. The observed fractal dimensions, both before and after the pairing, have been explained in terms of two model structures. The simulations of Jiménez and Martel also confirm that the Peclet number (product of flow Reynolds number and scalar Schmidt number) is the relevant parameter for quantifying the mixing characteristics. Simulations with identical Peclet numbers (but different Reynolds and Schmidt numbers) were found to yield virtually identical scalar mixing behavior.

The final project in the small scales mixing group was a more general examination of the small-scale mixing behavior of a passive scalar quantity in homogeneous isotropic turbulence. In particular Carl Gibson, Mike Rogers, Jeff Chasnov and John Petresky sought to determine by numerical simulation whether the small-scale strain rate is relevant in determining the nature of the scalar field for Prandtl/Schmidt numbers much less than unity. Batchelor has proposed that the small-scale strain (primarily due to scales much smaller than the smallest scalar scales) would be irrelevant to the scalar behavior and predicted a $k^{-17/3}$ (k being the magnitude of the wavevector) decay of the scalar spectrum beginning from the Corrsin-Oboukhov scale. Gibson proposed mechanisms in which the small-scale strain rate is relevant and predicted an intermediate k^{-3} decay of the scalar spectrum between the Corrsin-Oboukhov scale and the Batchelor scale. Results from forced direct numerical simulations were found to scale in the manner proposed by Gibson, but this may be due to the low Reynolds numbers of the simulations. Higher-Reynolds-number simulations, obtained by using a subgrid-scale turbulence model for the velocity field, support the ideas of Batchelor; however it may be that the subgrid-scale model is not accurate enough to account for the small-scale strain-related mechanisms suggested by Gibson.

Mike Rogers

Center for Turbulence Research
Proceedings of the Summer Program 1990

Low order dynamical models for mixing layers

By D. N. Riahi[1], R. D. Moser[2] AND F. Waleffe[3]

The goal of this project was to investigate the feasibility of developing useful low order dynamical systems to allow one to determine cheaply the effect of various initial conditions on the evolution of mixing layers. A mathematically rigorous approach for a time evolving base flow as found in a mixing layer seems to be the *singular value decomposition* of the linear operator transforming some initial perturbations into the solution at a given later time. Unfortunately, this is very costly, if at all feasible, and only deals with the linear evolution of a disturbance. A different approach based on weakly non-linear analysis was attempted, but numerous difficulties were encountered. Several formulations were proposed which may be ill-posed. The reason for this possible failure of the attempted approach is related to fundamental limitations of weakly non-linear analysis. The clarification of these issues is attempted in this report.

1. Introduction

We are concerned with the evolution of a two-stream mixing layer, and for the sake of simplicity, we consider a time-evolving mixing layer, which is periodic in the streamwise (x) and spanwise (z) spatial directions. In a time-evolving mixing layer, one considers two semi-infinite streams moving in opposite direction with equal velocities. The interface region between the two streams is unstable, and we are interested in the evolution of arbitrary perturbations to the flow. It is well known that the fastest growing linear disturbances are two-dimensional modes which lead to the Kelvin-Helmholtz roll-up of the mixing layer. Two-dimensional roll-ups of the mixing layer are commonly observed both experimentally and numerically. It is of great interest to understand the way in which the two-dimensional mixing layer undergoing the Kelvin-Helmholtz roll-up becomes three-dimensional. This problem has been addressed numerically by Moser & Rogers (1990) and Rogers & Moser (1989). However, it is not possible to thoroughly explore the infinite dimensional space of initial conditions numerically. An analytic theory which captures the important features of the full problem is required. Two features of this problem make the analytic theories considered here difficult. First, the critical Reynolds number for the flow is zero (or near zero), so that flows of interest are always far from the critical condition; and second, the base flow (the rolling up mixing layer) on which the perturbations are to evolve is itself evolving in time.

1 University of Illinois
2 NASA Ames Research Center
3 Center for Turbulence Research

In the current effort, an extension of standard methods of weakly non-linear analysis to this problem was attempted. The purpose of weakly non-linear analysis is to shed light on the nature of non-linear processes, especially as to how they modify the development of an instability. Usually, non-linearity induces a saturation of the exponential growth of a perturbation. That non-linear saturation can take many different forms. A weakly non-linear analysis usually leads to significant qualitative insights into the physics of the problem. However, one is in general restricted to an investigation near criticality, i.e. to small departures from the base flow. In that range, the full dynamics can be well described by the evolution of one or a few modes. Of course, one can always heavily *truncate* a representation of the full flow field so as to obtain a low order system of differential equations. With luck, such a severe truncation could be indicative of the behavior of the full system, but there is no guarantee. Severe truncations can lead to extremely interesting non-linear systems, but they are not necessarily representative of the *real* thing. The *Lorenz* equations, for instance, can be obtained from a three-mode truncation of the flow field in the study of convection. The truncated system shows fascinating dynamical behaviors (chaos, *etc.*), but the real flow behaves differently. In a weakly non-linear analysis, one seeks to deduce a simple dynamical system in a range where it will be a faithful representation of the real physics. The ideas involved in the derivation of a low order system and the difficulties encountered for the mixing layer case are illustrated below.

2. Weakly non-linear analysis

Let us consider a non-linear problem (*e.g.* the incompressible Navier-Stokes equations) where the full solution field v is decomposed into a basic state U and a perturbation u: $v = U + u$. Substituting in the governing equations and subtracting out the basic state, one obtains the equation for the perturbation which, for the purpose of illustration, will be written here as:

$$\frac{\partial}{\partial t}u + Lu = \epsilon N(u,u) \tag{1}$$

where L is a linear operator and N is a quadratically non-linear operator. The parameter ϵ has been introduced (after a rescaling perhaps) as a measure of the amplitude of the perturbation (at time 0 say). A straightforward solution technique would be to expand the perturbation as a series in powers of ϵ:

$$u = u_0 + \epsilon u_1 + \epsilon^2 u_2 + \cdots$$

Substituting this series in the equation and equating powers of ϵ yields an infinite sequence of *linear* problems:

$$\begin{aligned}
\frac{\partial}{\partial t}u_0 + Lu_0 &= 0 \\
\frac{\partial}{\partial t}u_1 + Lu_1 &= N(u_0,u_0) \\
\frac{\partial}{\partial t}u_2 + Lu_2 &= N(u_1,u_0) + N(u_0,u_1)
\end{aligned} \tag{2}$$

Unfortunately, such an expansion is, in general, nastily divergent. At best, it is valid in an asymptotic sense, *i.e.* in the limit as $\epsilon \to 0$ (when properly scaled). If any of the u_i is growing in time, the expansion will, furthermore, be valid only for small times. In the mixing layer case, for example, we might simplify the problem by taking a base flow which is independent of time, implying that L is independent of time (as in Pierrehumbert & Widnall 1982). In that case, the solution for u_0 is obtained from the eigenfunctions of the operator L and can be written

$$u_0 = e^{\lambda t}\phi_0,$$

where ϕ_0 is an eigenfunction (normalized) and λ an eigenvalue of L. In the simple case of a time developing mixing layer in an x-periodic domain considered here, there are one (or possibly a few) real positive λ; the rest are in general complex with negative real parts. Taking λ and ϕ_0 to be the most unstable mode, can we follow its non-linear development? The first order problem is

$$\frac{\partial}{\partial t}u_1 + Lu_1 = e^{2\lambda t}N(\phi_0, \phi_0) \tag{3}$$

and admits a separable solution of the form $u_1 = \exp(2\lambda t)\phi_1$. Substituting that form in (3), ϕ_1 is the solution of $(L + 2\lambda)\phi_1 = N(\phi_0, \phi_0)$. As λ is the largest eigenvalue of L, the operator $L + 2\lambda$ is not singular and ϕ_1 exists. One can proceed similarly to arbitrary order and obtain:

$$u = e^{\lambda t}\phi_0 + \epsilon e^{2\lambda t}\phi_1 + \epsilon^2 e^{3\lambda t}\phi_2 + \cdots$$

The linear solution is valid provided $\epsilon e^{\lambda t} \ll 1$. The higher order terms provide an asymptotic expansion in the same limit, *but they do not extend the range of validity (in time) of the expansion.*

It is possible to extend the domain of validity of the expansion if the growth rate is small, a concept to be made precise below (*e.g.* Stuart 1960). The zeroth order solution is written as $u_0 = A(t)\phi_0$, with $(L + \lambda)\phi_0 = 0$. Substituting in (1) shows that $dA/dt - \lambda A = O(\epsilon A^2)$, where ϵ should be considered as an ordering parameter, ϵA is the real measure of the amplitude. The next order problem is

$$\frac{\partial}{\partial t}u_1 + Lu_1 = A^2 N(\phi_0, \phi_0) - \frac{1}{\epsilon}(\frac{dA}{dt} - \lambda A)\phi_0 + O(\epsilon A^3) \tag{4}$$

To extend the range of validity of the solution, at least for the eigenmode ϕ_0, one wants to insure that u_1 will not contain any growing contribution of the form ϕ_0. This is the case if one requires that the right-hand side of (4) be orthogonal to ϕ_0^*, the solution to the adjoint of the linear homogeneous problem. The adjoint ϕ_0^* is the solution of $(L^* + \lambda^*)\phi_0^* = 0$, where the operator $L^* + \lambda^*$ is defined through the relation: $< \phi_0^*, (L + \lambda)\phi_0 > = < \phi_0, (L^* + \lambda^*)\phi_0^* >$. The brackets $< . >$ denote the appropriate inner product. That requirement yields an equation for A:

$$(\frac{dA}{dt} - \lambda A) < \phi_0^*, \phi_0 > - \epsilon A^2 < \phi_0^*, N(\phi_0, \phi_0) > = O(\epsilon^2 A^3)$$

or

$$\frac{dA}{dt} = \lambda A + \epsilon\lambda_2 A^2 + O(\epsilon^2 A^3)$$

The solution for u_1 is then taken to be of the form $u_1 = A^2\phi_1'$. Substituting in (4), it is found that ϕ_1' satisfies:

$$(L + 2\lambda)\phi_1' = N(\phi_0, \phi_0) - \lambda_2\phi_0$$

as stated above ϕ_1' exists. The next order problem becomes:

$$\frac{\partial}{\partial t}u_2 + Lu_2 = A^3[N(\phi_1', \phi_0) + N(\phi_0, \phi_1')] - 2\lambda_2 A^3\phi_1' - \lambda_3 A^3\phi_0 + O(\epsilon A^4) \qquad (5)$$

The constant λ_3 is determined by requiring that the inner product of the right-hand side of (5) with ϕ_0^* be zero. One then looks for a solution of the form $u_2 = A^3\phi_2'$. The procedure can be extended to arbitrary order and yields the solution:

$$u = A(t)\phi_0 + \epsilon A^2(t)\phi_1' + \epsilon^2 A^3(t)\phi_2' + \cdots$$

with

$$\frac{dA}{dt} = \lambda A + \epsilon\lambda_2 A^2 + \epsilon^2\lambda_3 A^3 + \cdots$$

In practice, the expansion is truncated at some finite order. There are two possible outcomes of such an analysis. First, the solution for $A(t)$ may grow rapidly and be unbounded; in this case the solution quickly becomes invalid as A becomes large. Second, the solution for A may saturate and remain bounded; assume, for instance, that λ_2 is negative. Then the second order truncation indicates that there is an equilibrium solution with $A = -\lambda/(\epsilon\lambda_2)$. In this case, the second order truncation is uniformly valid in time in the asymptotic limit $\lambda \to 0$ like ϵ. Thus, the expansion is valid near the (super critical) critical point for the instability under consideration. We are here considering the mixing layer far from critical; however, we proceeded with the analysis and hoped for the best.

During the course of the summer program, an analysis of this sort was applied to the Navier-Stokes equations for the case of the mixing layer. Several added difficulties were encountered and successfully treated. For example, the dependent variable is a divergence-free vector quantity which was treated by using a vector stream function formulation. Also, a spatially growing layer was considered in addition to the time-developing layer discussed here. This required the introduction of two time and space scales to accommodate the traveling wave component of the solution.

The difficulty which could not be so easily overcome is the fact that the base flow is time-evolving. The procedure outlined above is straightforward and well defined when L is independent of time, but L becomes explicitly time dependent when the base flow is time dependent. In this case, there are no longer eigensolutions to the zeroth order linear problem. To obtain a solution to the linear problem, we must

specify an initial condition $u(t = 0)$, which when L was time dependent was taken to be the most unstable eigenfunction. This guaranteed that there would be no faster growing solution that would enter at higher order to invalidate the expansion. Without eigensolutions, we cannot guarantee this except by using singular value decomposition. (see §3). Also, if we are to generalize the solution procedure (as was attempted), the inner product, orthogonality, and the adjoint of the linear problem must be generalized by including an integral in time in the definition of the inner product. Thus we must consider from the outset a finite time interval (say $(0, t_1)$). It is then possible to proceed mechanically with the solution procedure, defining an "adjoint" and determining a "solvability" condition. However, as formulated, the adjoint solution has to satisfy a "temporal boundary condition" $\phi^*(t = t_1) = 0$, which for a diffusive operator L results in an apparently ill-posed problem for ϕ^*. Finally, even if the appropriate adjoint solution(s) were available, it is not clear that the resulting expansion would be valid over the time interval $(0, t_1)$ because the expansion functions ϕ_i are now functions of time, which may or may not exhibit large growth over the time interval.

3. Other generalizations

The generalization of standard weakly non-linear analysis to the time-evolving mixing layer encountered several problems as outlined above. However, the generalization of the linear problem is clear. When the linear operator L is dependent on time, then the general solution of the zeroth order linear problem can be formally expressed as a linear operator which takes arbitrary initial conditions at $t = 0$ to a solution at $t = t_1$. It is the singular value decomposition of this operator and in particular the singular functions associated with the largest singular value which are of interest. Unfortunately, obtaining this decomposition appears computationally intractable at this time. There may also be a generalization of the weakly non-linear analysis making use of a decomposition in terms of the singular functions, but this has not been explored.

Another possibility is to use a technique like that of Riley *et al* (1988), in which some of the difficulties discussed above are overcome by solving for the evolving base flow as well as the perturbations. However, this too suffers from the lack of a uniformly valid asymptotic expansion as a basis for the analysis. Finally, by considering a different problem (*e.g.* a plane wake) and appropriately scaling space and time, one may be able to obtain a model problem which is more amenable to analysis but is still relevant to the study of free shear flows.

REFERENCES

PIERREHUMBERT, R. T. & WIDNALL, S. E. 1982 The two- and three-dimensional instabilities of a spatially periodic shear layer. *J. Fluid Mech.* **114**, 59.

MOSER, R. D. & ROGERS, M. M. 1990 Mixing transition and the cascade to small scales in a plane mixing layer. *Phys. of Fluids.* To appear.

RILEY, J. J., MOURAD, P. D., MOSER, R. D. & ROGERS, M. M. 1988 Sensitivity of mixing layers to three-dimensional forcing. *Proceedings of the 1988 Summer Program of the Center for Turbulence Research.* **CTR-S88,** 91.

ROGERS, M. M. & MOSER, R. D. 1989 The development of three-dimensional temporally-evolving mixing layers. *Seventh International Symp. on Turb. Shear Flows* (Stanford University), 21-23 August 1989.

STUART, J. T. 1960 On the non-linear mechanics of wave disturbances in stable and unstable parallel flows. *J. Fluid Mech.* **9**, 353.

Numerical simulation of low Prandtl number turbulent mixing

By C. Gibson[1], M. Rogers[2], J. Chasnov[3] AND J. Petresky[1]

Numerical simulations of turbulent mixing of strongly diffusive scalar fields were carried out with and without subgrid-scale modeling of the small-scale strain field. For low-Reynolds-number flows, when the rate-of-strain field (determined primarily by the small scales) is fully resolved, the scalar microstructure was found to collapse under Batchelor (1959) rate-of-strain scaling even for small Prandtl numbers, in agreement with Kerr (1990). For high-Reynolds-number flows, when small-scale straining is modeled with a subgrid-scale model, the scalar microstructure follows the Batchelor, Howells and Townsend (1959) prediction that the small-scale rate-of-strain is irrelevant.

1. Introduction

An important problem of turbulent mixing is to determine the mechanisms of small-scale mixing for the case of strongly diffusive scalar properties; that is, properties like temperature with Prandtl number $Pr = \nu/D < 1$, where D is the molecular diffusivity of the scalar θ and ν is the kinematic viscosity of the fluid. Recent contributions that review the theoretical and experimental issues can be found in Gibson, Ashurst and Kerstein (1988) and Kerr (1990).

Oboukhov (1949) and Corrsin (1951) independently inferred an inertial subrange for the scalar spectrum

$$\Gamma = \beta_{si}\chi\epsilon^{-1/3}k^{-5/3}; \quad L_O^{-1} < k < L_C^{-1}; \quad L_C \equiv (D^3/\epsilon)^{1/4} \tag{1}$$

which terminates at the Oboukhov-Corrsin length scale L_C. Here β_{si} is a universal constant, χ is the dissipation rate of scalar variance, ϵ is the dissipation rate of turbulent kinetic energy, k is the wavenumber and L_O is the energy, or Oboukhov, length scale of the turbulence. The spectral form in (1) was inferred by dimensional analysis without reference to any specific physical mechanisms or mathematical models, and is therefore analogous to the velocity inertial subrange

$$\Phi = \alpha\epsilon^{2/3}k^{-5/3}; \quad L_O^{-1} < k < L_K^{-1}; \quad L_K \equiv (\nu^3/\epsilon)^{1/4} \tag{2}$$

that follows by dimensional analysis from the Kolmogorov (1941) universal similarity hypotheses (which also does not assume a particular mechanism or model for

1 University of California at San Diego
2 NASA Ames Research Center
3 NASA Goddard Institute for Space Studies

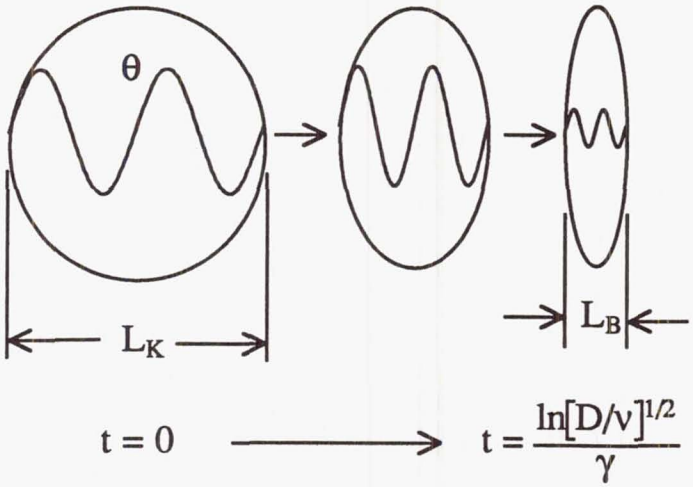

FIGURE 1. Batchelor (1959) wave crest compression model for $Pr \gg 1$. A scalar Fourier element θ smaller than L_K is compressed to the Batchelor scale L_B, without decay, in time $\ln(D/\nu)^{1/2}/\gamma$, by uniform straining γ. At L_B its amplitude begins to decrease by molecular diffusion. This model fails for $Pr \ll 1$.

the flow field) where Φ is the energy spectrum, α is a universal constant, and L_K is the Kolmogorov length scale.

The first specific physical model for scalar mixing by turbulence was the wave crest compression mechanism of Batchelor (1959) for the case of weakly diffusive scalars θ like salt concentration in water, with $Pr \gg 1$. The model is illustrated in figure 1.

Batchelor showed that Fourier elements of the scalar field with wavenumbers $k > L_K^{-1}$ would align with the compressive axis of the rate-of-strain tensor $e_{ij} = 1/2(\partial u_i/\partial x_j + \partial u_j/\partial x_i)$ and would be rapidly convected by strain-mixing, not turbulent mixing, to the Batchelor length scale $L_B \equiv (D/\gamma)^{1/2}$, where γ is the rate of strain $\gamma = (\epsilon/\nu)^{1/2}$. The velocity field acting on scales smaller than L_K consists of locally uniform staining so wave crests would simply be convected together, as shown in figure 1. By this very plausible physical model a viscous-convective subrange was derived for the range of scales smaller than the viscous cutoff Kolmogorov scale but larger than the diffusive cutoff Batchelor scale,

$$\Gamma = \beta_{vc}\chi\gamma^{-1}k^{-1}; \quad L_B^{-1} < k < L_K^{-1}\,, \tag{3}$$

where β_{vc} is another universal constant. Equation (3) can also be derived by dimensional analysis, but the Batchelor (1959) mathematical analysis permits a bound to be placed on the value of the universal constant

$$\sqrt{3} < \beta_{vc} < 2\sqrt{3} \tag{4}$$

as shown by Gibson (1968b), where the form of the spectrum derived by Batchelor (1959) is

$$\Gamma = \beta_{vc}\chi\gamma^{-1}k^{-1}\exp(-\beta_{vc}k^2D/\gamma); \quad k > L_K^{-1} \tag{5}$$

for $Pr \gg 1$. The spectral form given by (5) has been tested experimentally many times, starting with Gibson and Schwarz (1963), and has generally been verified with respect to the form in (5) and the constant in (4). Gargett (1985) finds a large departure from (4), by a factor of 4, in a Fjord, but Gibson (1986) shows the departure may be the result of averaging together fossil turbulence and active turbulence patches without accounting for the extreme intermittency of viscous and scalar dissipation rates usually observed in such stratified flows.

For the case of $Pr \ll 1$, however, the Batchelor wave crest compression mechanism fails because the separation of wave crests for the smallest Fourier elements used to represent the scalar field will be larger than the size of the regions of uniform strain, which should be of order L_K. Consequently, Batchelor, Howells and Townsend (1959) proposed that the rate-of-strain should become irrelevant for turbulent mixing of such strongly diffusive scalars. Based on this hypothesis, they derive an inertial-diffusive cutoff spectrum for $Pr \ll 1$ beginning at the Oboukhov-Corrsin scale $L_C \equiv (D^3/\epsilon)^{1/4}$

$$\Gamma = \frac{\alpha}{3}\chi D^{-3}\epsilon^{2/3}k^{-17/3}; \quad k > L_C^{-1} \tag{6}$$

where α is the inertial subrange constant of the turbulent velocity spectrum in (2).

From an analysis of the velocities of isoscalar surfaces and zero-gradient points, Gibson (1968a) suggested that other physical mechanisms besides the wave crest compression mechanism of figure 1 exist by which the smallest scalar fluctuations for $Pr \ll 1$, or indeed arbitrary Pr, could be mixed to smaller scale by the rate-of-strain tensor e_{ij}, and proposed that probability laws describing the smallest scale features of scalar fields with arbitrary Pr should become universally similar under "Batchelor" coordinate normalization with length L_B, time $T_B \equiv \gamma^{-1}$ and scalar $S_B \equiv (\chi/\gamma)^{1/2}$ scaling of space, time and scalar, respectively. For $Pr \ll 1$, this shifts the beginning of the inertial-diffusive cutoff of (6) to L_B rather than L_C, and results in an intermediate strain-rate-diffusive k^{-3} subrange

$$\Gamma = \beta_{\mathrm{srd}}\chi D^{-1}k^{-3}; \quad L_B^{-1} < k < L_C^{-1} \tag{7}$$

prior to the final inertial-diffusive cutoff, presumably with the form of (6), but with a different constant, an explicit Prandtl number dependence

$$\Gamma = \beta_{\mathrm{id}}Pr^{-2/3}\chi D^{-3}\epsilon^{2/3}k^{-17/3}; \quad L_K^{-1} < k < L_B^{-1}\,, \tag{8}$$

and an exponential cutoff at the Kolmogorov scale L_K. Gibson (1968a) suggested that turbulence produces extremum points, hot spots and cold spots for temperature, by distorting isothermal surfaces until they become diffusively unstable and split up, at scales no smaller than L_C, to form multiply connected surfaces. The extremum points diffuse to positions of symmetry and then tend to be convected as fluid particles so they can be compressed and stretched as fluid particles by the local strain field, with a stretching-diffusion equilibrium length scale L_B for all Pr. Other topological features of the scalar field exhibit similar sensitivity to the

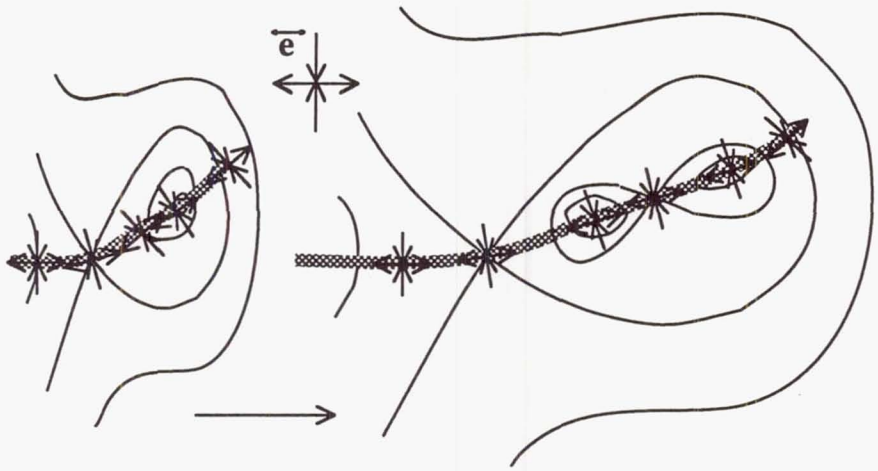

FIGURE 2. Interaction and alignment of the local rate-of-strain tensor $\overleftrightarrow{e}$ with topological features of scalar fields mixed by turbulence that have minimal or zero gradient, according to the Gibson (1968a) strain-mixing model. Extrema and saddle points have zero gradient, and are connected by the checkered minimal gradient line, which tends to be aligned with the stretching axes of the local $\overleftrightarrow{e}$, independent of the Prandtl number of the scalar field.

strain-field history. For example, the lines of minimal gradient that must connect a set of extrema and saddle points (resulting from secondary splitting of an original extremum produced by turbulence) tend to be stretched out as material lines. This is illustrated schematically in figure 2. The steepest scalar gradients occur in the vicinity of the extremum points and the minimal gradient lines are aligned with the compression axes of the strain-rate tensor. Using numerical simulations of two-dimensional turbulence, Gibson, Ashurst and Kerstein (1988) confirmed that this was the case, and suggested a positive feedback mechanism based on the expression

$$\vec{v}_\theta = \vec{v} - \vec{v}_D = \vec{v} - D\left(\frac{\nabla^2\theta}{|\nabla\theta|}\right)\vec{g}; \quad \vec{g} \equiv \frac{\vec{\nabla}\theta}{|\nabla\theta|} \tag{9}$$

for the velocity of isoscalar surfaces $\vec{v}_\theta$ in terms of the fluid velocity $\vec{v}$ and the diffusive velocity $\vec{v}_D$ derived in Gibson (1968a). As shown in (9), the convective velocity of the fluid will dominate the motion of θ surfaces when the diffusive velocity is small, *i.e.* when gradient magnitudes $|\nabla\theta|$ are large and $\nabla^2\theta$ values are small. But gradient magnitudes $|\nabla\theta|$ will be increased by such convection of isoscalar surfaces and this results in a positive feedback mechanism of mixing.

Based on the rate-of-strain mixing mechanisms of figure 2, Gibson (1968b) proposed the universal similarity hypotheses in table 1. According to these hypotheses, the n-joint probability laws $F_{\theta n}$ describing turbulent mixing of scalars θ at n points separated by vectors $\vec{y}_k$, where $k = 1,...,n$, will become universally similar in normalized Batchelor, Corrsin and Kolmogorov spaces (see table 2), depending on the Prandtl number and length scale y_k ranges of the k^{th} separation vector. The

Hypothesis	Length range	Prandtl number, Pr
1a. $F_{\theta n}(\chi, \gamma, D, y_k)$	$y_k < L_B$	all values
	$y_k < L_K$	$\gg 1$
	$y_k < L_C$	$\ll 1$
1b. $F_{\theta n}(\chi, \epsilon, y_k)$	$L_K < y_k < L_O$	$\gg 1$
	$L_C < y_k < L_O$	$\ll 1$
2a. $F_{\theta n}(\chi, \epsilon, D, y_k)$	$L_B < y_k < L_O$	$\ll 1$
2b. $F_{\theta n}(\chi, \epsilon, y_k)$	$L_B < y_k < L_C$	$\ll 1$
3a. $F_{\theta n}(\chi, \epsilon, \nu, y_k)$	$L_B < y_k < L_O$	$\gg 1$
3b. $F_{\theta n}(\chi, \gamma, y_k)$	$L_B < y_k < L_K$	$\gg 1$

Table 1. Universal similarity hypotheses of turbulent mixing

Scale (dimensional parameters)	Batchelor (χ, γ, D)	Corrsin (χ, ϵ, D) $\gamma Pr^{1/2} = (\epsilon/D)^{1/2}$	Kolmogorov (χ, ϵ, ν) $\gamma = (\epsilon/\nu)^{1/2}$
Length: L_B, L_C, L_K	$(D/\gamma)^{1/2}$	$(D/\gamma Pr^{1/2})^{1/2}$	$(\nu/\gamma)^{1/2}$
Time: T_B, T_C, T_K	γ^{-1}	$(\gamma Pr^{1/2})^{-1}$	γ^{-1}
Scalar: S_B, S_C, S_K	$(\chi/\gamma)^{1/2}$	$(\chi/\gamma Pr^{1/2})^{1/2}$	$(\chi/\gamma)^{1/2}$

Table 2. Scales of turbulent mixing

formulation is completely analogous to that proposed by Kolmogorov (1941) for turbulent velocity fields, and has the same limitations due to intermittency of the dissipation rates. In table 1, the largest scale eddy of the turbulence is indicated by the Oboukhov, or energy scale L_O. Dimensional analysis based on the hypotheses, as well as overlapping length scale ranges, leads to overlapping power law subranges $k^{-5/3}$, k^{-3} and k^{-1} from hypotheses 1b, 2b and 3b, respectively, in B, C and K spaces.

Evidence supporting the Gibson (1968a,b) theory has been gradually accumulating from low Pr mixing experiments such as Clay (1973), and numerical mixing experiments of Kerr (1985) and Kerr (1990). However, numerical mixing experiments of Chasnov, Canuto and Rogallo (1988) and Chasnov (1990), using a subgrid-scale model for the small scales of the velocity field, give strong support to the Batchelor, Howells and Townsend (1959) theory and expression (6) in the far-inertial-diffusive subrange, $k \gg L_C^{-1}$. The purpose of this paper is to attempt to clarify possible reasons for the discrepancies between these apparently contradictory results.

2. Numerical experiments

Numerical simulations of turbulent mixing are constrained to relatively small Reynolds numbers by computer speed and memory limitations. The larger the number of mesh points in the grid, the larger the Reynolds number of the simulation but the higher the cost of the calculation in time and money. Clearly it would be advantageous if approximations could be made for the smaller-scale features of turbulence and mixing by means of subgrid-scale modeling, so that the larger-scale features characteristic of high-Reynolds-number turbulence could be explored. The results shown below indicate that if turbulent mixing at low Prandtl number is dominated by direct interactions of the velocity strain rate and scalar fields, then the subgrid-scale model does not capture this effect, at least over a wide range of Pr.

All simulations examined here are of three-dimensional incompressible homogeneous isotropic turbulence. Several low-Prandtl-number passive scalar quantities were mixed simultaneously by each of the velocity fields simulated. The cases considered here fall into three classes. The first employs both forcing of the large scales and a subgrid-scale model to obtain as wide an inertial subrange as possible and statistically stationary turbulence. The second type uses only a subgrid-scale model, thereby permitting the simulation of high-Reynolds-number decaying turbulence. The third class maintains the forcing of the large scales to obtain a statistically stationary flow but fully resolves the small-scale motions, thereby significantly reducing the flow Reynolds number. Scalar fields both with and without mean scalar gradients were considered. Because of the low Prandtl numbers considered, the scalar fields were well-resolved on the computational mesh (*i.e.* no subgrid-scale model was required for the scalar fields in any of the simulations). The simulation results were evaluated in terms of the form of the velocity and scalar variance spectra, mixed skewness statistics, and direct visual inspection of the three-dimensional computed fields. Spectra were normalized with the length, time and scalar scales listed in table 2.

Energy spectra $(k^{5/3}\Phi)_K$ versus $(k)_K$ for the three types of numerical simulations are shown in figure 3, where K subscripts indicate normalization with Kolmogorov length L_K and time T_K from table 2. All have the same 1.5 decades of wavenumber range corresponding to the 64^3 mesh used in the calculations. The direct numerical simulation has only a short inertial subrange (part of the flat portion being associated with the forced modes) but agrees well with the universal spectral form of laboratory and field experiments. The forced subgrid-scale simulation is reasonably flat over all wavenumbers (*i.e.* contains only inertial subrange) whereas the unforced subgrid-scale simulation becomes flat only at the largest wavenumbers.

3. Direct numerical simulations

The direct numerical simulations (no subgrid-scale model) were made for a flow with viscosity $\nu = 0.01$ on a 64^3 mesh with $\Delta x = 2\pi/64 = 0.0982$ (note all dimensional quantities given in this paper are in arbitrary but consistent units). The scalar fields all evolved in the presence of a mean scalar gradient of magnitude

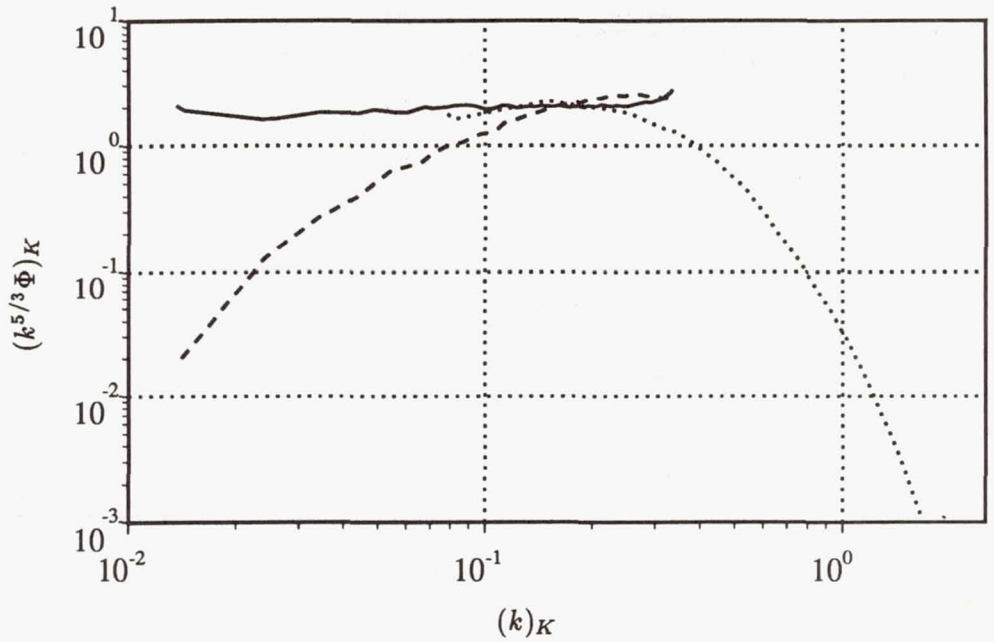

FIGURE 3. Kolmogorov normalized energy spectra for numerical simulations, multiplied by $k^{5/3}$. ——— forced subgrid-scale model, - - - - unforced subgrid-scale model, ····· direct numerical simulation.

$\partial\overline{T}/\partial z = 1.0$. The field examined here has evolved for about 1.5 eddy turnover times and has $\epsilon = 0.0595$ and $L_K = 0.0640$. Four scalars were simultaneously mixed, with Pr values of 0.769, 0.434, 0.172, and 0.118. Spectra multiplied by k^2 and normalized by Batchelor scales of table 2 are shown in figure 4 for the various Pr values. Such spectra must have integrals equal to 1/2 from the Batchelor normalization, as shown by Gibson (1968b). It is readily apparent that the spectra collapse under this scaling.

The longitudinal mixed skewness parameter Σ, with components

$$\Sigma_u \equiv \frac{\overline{\frac{\partial u}{\partial x}\left(\frac{\partial\theta}{\partial x}\right)^2}}{\left(\overline{\left(\frac{\partial u}{\partial x}\right)^2}\right)^{1/2}\overline{\left(\frac{\partial\theta}{\partial x}\right)^2}}, \quad \Sigma_v \equiv \frac{\overline{\frac{\partial v}{\partial y}\left(\frac{\partial\theta}{\partial y}\right)^2}}{\left(\overline{\left(\frac{\partial v}{\partial y}\right)^2}\right)^{1/2}\overline{\left(\frac{\partial\theta}{\partial y}\right)^2}}, \quad \Sigma_w \equiv \frac{\overline{\frac{\partial w}{\partial z}\left(\frac{\partial\theta}{\partial z}\right)^2}}{\left(\overline{\left(\frac{\partial w}{\partial z}\right)^2}\right)^{1/2}\overline{\left(\frac{\partial\theta}{\partial z}\right)^2}} \tag{10}$$

are sensitive indicators of the role of rate-of-strain in turbulent mixing (u, v and w are velocity components in the x, y and z directions, respectively). Note that Σ_w may be different from Σ_u and Σ_v because of the presence of the mean scalar gradient in this direction. Clearly Σ should approach zero as Pr approaches zero if the rate-of-strain becomes irrelevant to the mixing, but if Hypothesis 1a is correct, Σ should be approximately independent of Pr and negative because compressive negative straining should enhance scalar gradient magnitudes. Values of Σ for the

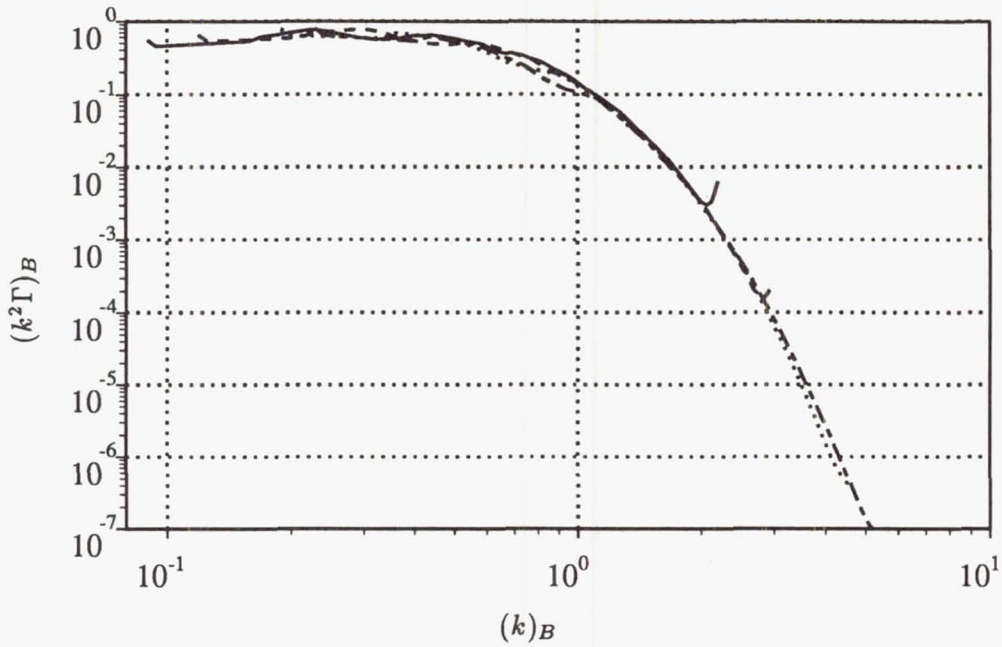

FIGURE 4. Batchelor-scaled scalar dissipation spectra from direct numerical simulation of low Pr mixing. —— $Pr = 0.769$, ---- $Pr = 0.434$, ····· $Pr = 0.172$, —·— $Pr = 0.118$. Convergence of spectra for low Pr values is consistent with Hypothesis 1a of table 1.

Pr	Σ_u	Σ_v	Σ_w
0.769	-0.473	-0.329	-0.518
0.434	-0.426	-0.309	-0.505
0.172	-0.333	-0.262	-0.493
0.118	-0.277	-0.246	-0.478

Table 3. Σ values for the direct numerical turbulence simulation

present numerical simulation are given in table 3.

All the values of Σ in table 3 are negative and significantly nonzero. Differences in magnitude and the tendency to decrease somewhat as Pr decreases may be the result of the small mesh size. Kerr (1985) used a larger mesh of 128^3, and reports no such trend when the Peclet number Pe_λ (here based on the Taylor-microscale Reynolds number) is greater than about 10. For $Pe_\lambda < 10$ he observes a decrease in Σ. The value of $-\Sigma$ is proportional to the integral of $(k^4\Gamma)_B$,

$$\Sigma = \frac{-4\sqrt{15}}{5} \int_0^\infty (k^4\Gamma)_B d(k)_B \,, \tag{11}$$

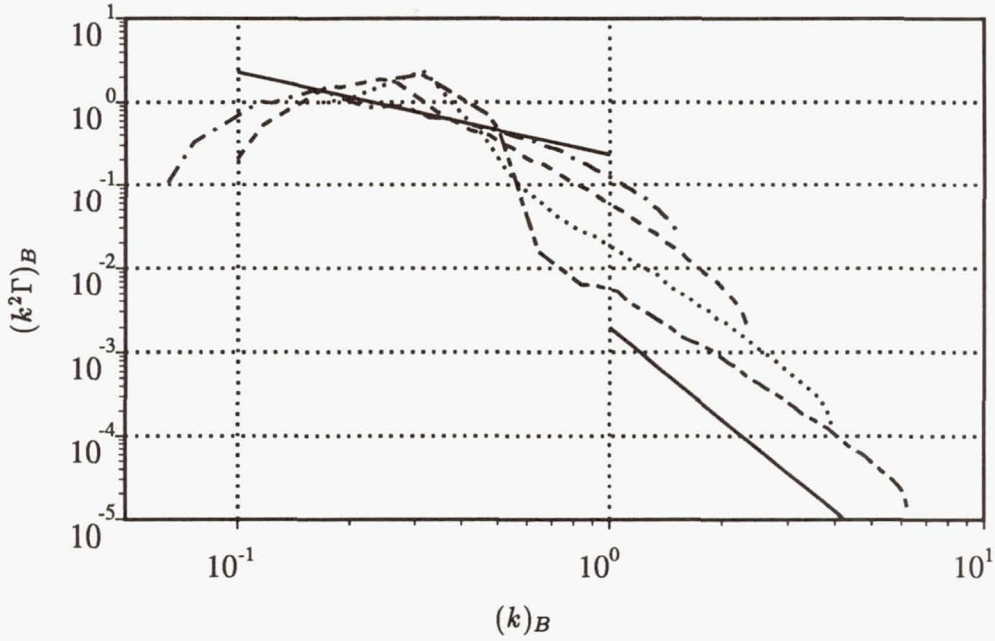

FIGURE 5. Batchelor-normalized scalar dissipation spectra of unforced subgrid-scale modeled simulations. Estimated Prandtl numbers are —·— $Pr = 0.045$, ---- $Pr = 0.019$, ····· $Pr = 0.007$, —-— $Pr = 0.003$. The upper and lower straight solid lines represent k^{-3} and $k^{-17/3}$ behavior of Γ, respectively.

as shown by Wyngaard (1971). Thus the collapse shown in figure 4 implies that Σ should be nearly the same for all four Prandtl numbers. However, for the spectra in figure 4, the value of Σ is primarily determined by the behavior of $(k^4\Gamma)_B$ over the wavenumber range $0.5 < (k)_B < 1.5$ with $(k^4\Gamma)_B$ peaking at about $(k)_B = 0.8$. The value of Σ is thus very sensitive to the details of the spectra for these wavenumbers. The smaller values of Σ for the lower Pr cases in table 3 are a result of the slight drop in the spectra (figure 4) for these cases near $(k)_B = 0.8$.

4. Simulations employing a subgrid-scale model

The subgrid-scale model of Chasnov (1990) was used to generate high-Reynolds-number flow fields with an inertial subrange. Use of such a model, however, implies that the actual small-scale behavior (including that of the strain field) is not resolved. The subgrid-scale model seeks to simulate the case where $\nu = 0$. In reality the large scales feel an "effective" viscosity which is fairly constant away from the cutoff wavenumber. Here this effective viscosity is used to estimate the Prandtl number. Simulations were run with and without forcing of the large-scale motions and with and without a mean scalar gradient (again $\partial\overline{T}/\partial z = 1$ for mean gradient cases). The energy spectra for both the forced and unforced cases are shown in figure 3.

Estimated Pr	Σ_u	Σ_v	Σ_w
0.045	-0.428	-0.383	-0.448
0.019	-0.279	-0.271	-0.247
0.007	-0.121	-0.107	-0.116
0.003	-0.046	-0.052	-0.046

Table 4. Σ values for the unforced subgrid-scale turbulence simulation

The Batchelor-scaled scalar dissipation spectra for scalars of four different molecular diffusivities are shown in figure 5 for the unforced case in the absence of a mean scalar gradient. It is clear that they do not collapse. Spectra for the smaller Pr values in figure 5 approach the $-17/3$ subrange of (6), both in slope and absolute value. The largest Pr value approaches the -3 subrange of (7), and as will be shown below, it approaches the universal Batchelor diffusive cutoff form of figure 4.

The behavior of the lower Pr cases in figure 5 is limited by the computational box size. Visual examination of the $Pr = 0.003$ scalar field shows that essentially only one large structure is in the computational domain and the results are therefore clearly affected by the imposed periodicity. The spectra have significant contributions from a few low wavenumbers, then drop very rapidly (faster than $k^{-17/3}$!) before finally decaying at the expected $k^{-17/3}$ rate. Effectively, the computation is setting up a large structure which provides a mean scalar gradient. A limited range of wavenumbers (about half those in the computation) can then respond to this gradient. Because it is not feasible to dramatically increase the computational domain size, another means of increasing the range of useful wavenumbers is needed. By explicitly imposing a uniform mean scalar gradient the computation does not have to form its own large-scale structures and the entire range of computational wavenumbers becomes useful for the study of the problem considered here.

Table 4 lists Σ values for this flow. As the Pr values of the scalars approach zero in table 4, the correlations $\Sigma_{u,v,w}$ between compressive strain and the scalar gradient also approach zero. However, close examination of the microstructure of the scalar fields revealed that only the field with the largest Pr value of 0.045 possessed significant numbers of zero-gradient points. The conditions for the strain-mixing mechanism of figure 2 were thus not met. The effective Peclet number (product of Reynolds and Prandtl numbers) of the simulated turbulence for smaller Pr values was too small for any extrema to be produced. For the spectra of the lower Pr cases in figure 5 the dominant contribution to Σ comes from $(k)_B = 0.3$ with virtually no contribution from wavenumbers $(k)_B > 0.6$. The value of Σ for the $Pr = 0.045$ case is similar to the values in the direct numerical simulations given in table 3 and the $(k)_B$ wavenumber range which contributes to Σ is also similar to that observed in the direct numerical simulations.

Figure 6 shows the Corrsin/Batchelor-scaled spectra (same scaling for the quantity $k^3\Gamma$) plotted against the Corrsin-scaled wavenumber for several forced cases

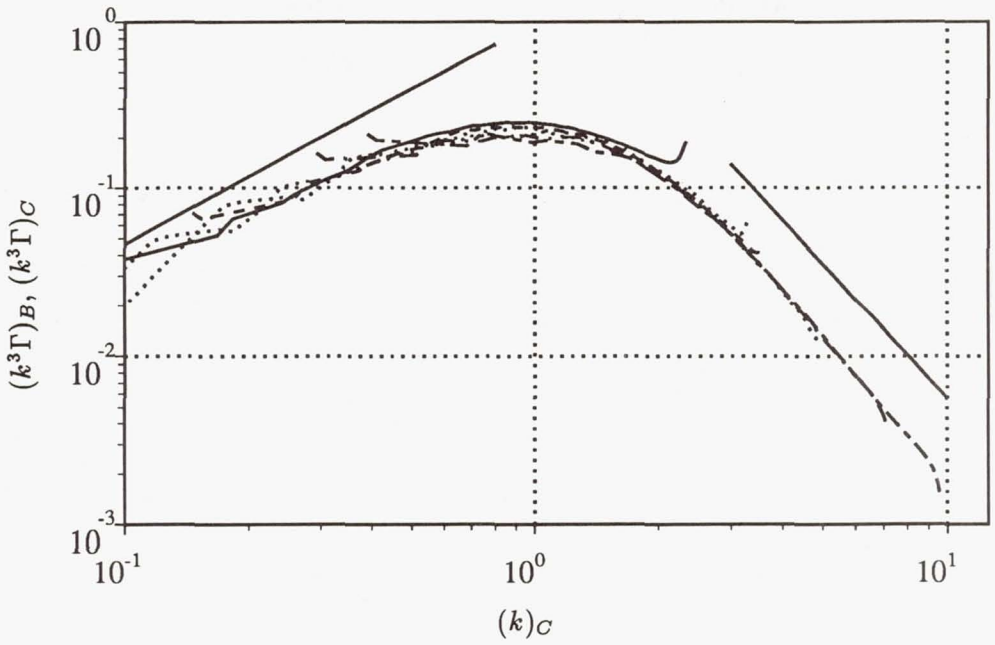

FIGURE 6. Corrsin/Batchelor-normalized $k^3\Gamma$ spectra for forced turbulence with a subgrid-scale model. Estimated Prandtl numbers —— $Pr = 0.069$, ---- $Pr = 0.039$, —·— $Pr = 0.015$, —·— $Pr = 0.011$. ····· curves are results from a 128^3 simulation for $Pr = 0.043$ and $Pr = 0.0251$. The left and right straight solid lines represent $k^{-5/3}$ and $k^{-17/3}$ behavior of Γ, respectively.

with an explicitly imposed mean scalar gradient. Time-averaged spectra (permitted by statistical stationarity and done to smooth the curves) from a 64^3 simulation with four passive scalars are shown along with results for two scalars from a single time of a (different velocity field) 128^3 simulation. All the curves exhibit a good collapse onto an apparently "universal" spectrum when the mean scalar gradient is included in the scalar dissipation used for the normalization (note that for the high Peclet number fields the dissipation due to the mean is insignificant compared to that of the fluctuating field). This collapse is in agreement with the predictions of Batchelor, Howells & Townsend (1959) but may be an artifact of the subgrid-scale model. There is a fairly wide transition region between the $k^{-5/3}$ and $k^{-17/3}$ subranges, the latter occurring for $(k)_C > 2.5$.

When the "universal" subgrid-scale spectrum shown in figure 6 is fitted to a smooth curve (consisting of $k^{-5/3}$ and $k^{-17/3}$ subranges and the fitted transition between them) Σ can be calculated from (11). The existence of a "universal" spectrum in these coordinates implies that Σ decays like $Pr^{1/2}$ for small Pr. Use of the fitted curve yielded $\Sigma \approx -3Pr^{1/2}$ (the exact value of the coefficient being somewhat dependent on wavenumber cutoffs chosen for the different subranges), with the dominant contribution coming from the $k^{-17/3}$ subrange, closely followed by that from the transition region. Contribution to Σ from the $k^{-5/3}$ range was

negligible. Σ values calculated directly from the computed flowfields may not agree exactly with this formula due to the more limited range of wavenumbers captured by any one computation and departures from the fitted curve.

5. Comparison of direct and subgrid-scale modeled simulations

It is interesting to compare the largest Pr value unforced subgrid-scale simulation (with $Pr = 0.045$) to the direct numerical simulations of §3, since this is still a factor of 2.6 smaller than the smallest direct numerical simulation Pr value. Figure 7 shows a comparison of the scalar dissipation spectra. The Batchelor-normalized subgrid-scale spectrum is in excellent agreement with the results from the direct numerical simulations, collapsing onto a single "universal" curve for $(k)_B > 0.3$. The larger effective Reynolds number of the subgrid-scale modeled flow seems to have led to the development of a small region of strain-rate-diffusive k^{-3} subrange, as shown also in figure 5. The subgrid-scale simulation suggests that with still higher Reynolds number simulations, a strain-rate-diffusive k^{-3} subrange might be found. The universal constant β_{srd} indicated by figures 5 and 7 is about 0.23 (note $(k^2\Gamma)_B = \beta_{\mathrm{srd}}(k)_B^{-1}$ in the k^{-3} subrange and therefore β_{srd} equals the value of the k^{-3} line at $(k)_B = 1$). It is also interesting to note the rather strong departures between the Batchelor (5) viscous-diffusive behavior for $Pr \gg 1$ and the numerically computed behavior for $Pr = 0.1$–0.5.

6. Conclusions

Scalar spectra resulting from turbulent mixing by a high-Reynolds-number velocity field generated with a subgrid-scale model collapse under Corrsin scaling as predicted by Batchelor, Howells & Townsend (1959). The "universal" spectrum in this case exhibits a wide transition (nearly a decade) between the $k^{-5/3}$ and $k^{-17/3}$ subranges. The corresponding spectra obtained in low-Reynolds-number direct numerical simulations collapse under the Batchelor scaling of Gibson (1968b). Two possible explanations for this discrepancy exist. The first is that virtually all the scales of the direct numerical simulation are affected by viscosity and are therefore not in the inertial-diffusive subrange but rather in a viscous-diffusive region. In this case the scaling put forth by Batchelor, Howells & Townsend (1959) would be expected to break down. The second is that the subgrid-scale model is not accurate enough to capture the physics of the interaction between the predominantly subgrid-scale strain-rate field and the scalar. It is interesting to note that for moderate Peclet numbers (as opposed to the usually smaller values generated by the extremely low Prandtl numbers considered here) the subgrid-scale simulations produce spectra that collapse with the direct numerical simulation results and show the beginnings of a strain-rate-diffusive k^{-3} subrange in agreement with Gibson (1968b). This case is also the only one of those shown in figure 5 that contains a significant number of scalar extremum points required for the strain-mixing mechanism to be effective.

Future plans include extension to higher Reynolds/Peclet numbers by using 128^3 simulations and direct examination of the direct numerical simulation scalar fields

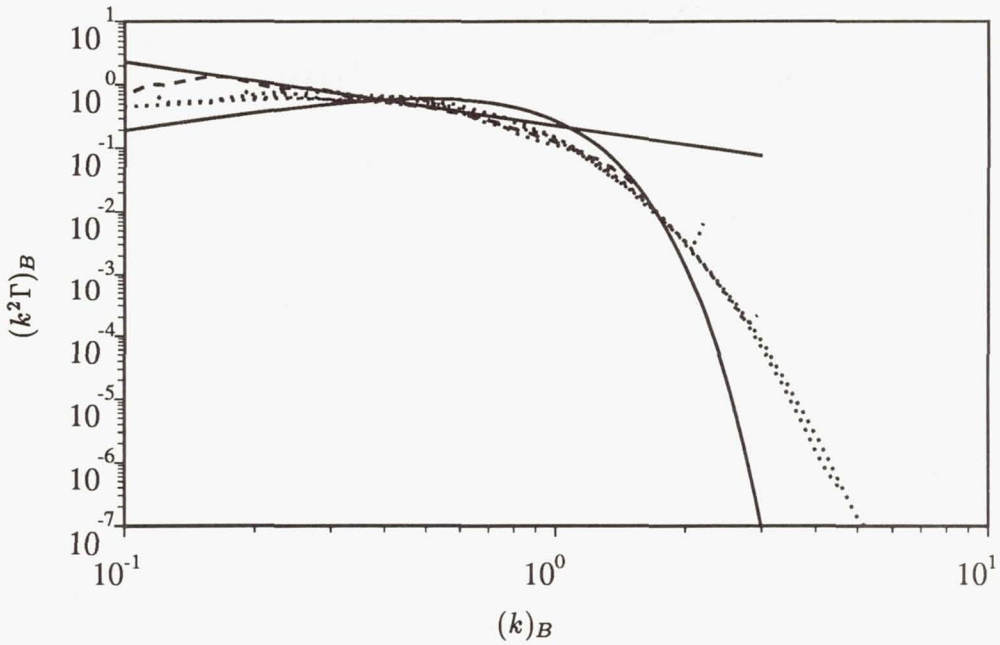

FIGURE 7. Comparison of scalar dissipation spectra from the subgrid-scale simulation with estimated $Pr = 0.045$ (also shown in figure 5), with direct numerical simulation results of figure 4. ---- subgrid-scale model simulation with estimated $Pr = 0.045$, ····· direct numerical simulation results for four values of Pr. The straight solid line is an extended version of the same k^{-3} line shown in figure 5. The curved solid line represents the Batchelor (1959) spectrum (valid for $Pr \gg 1$) given by (5) with $\beta_{vc} = 2.0$.

in an effort to observe the mechanisms suggested by Gibson (1968a). Collapse of scalar spectra from direct numerical simulations on a 128^3 mesh with the 64^3 results presented here would seem to indicate that the scaling proposed by Gibson (1968b) may be correct, whereas a tendency towards the "universal" spectrum of figure 6 would favor the Batchelor, Howells & Townsend (1959) theory.

This work was carried out during the Center for Turbulence Research 1990 Summer School Program. The authors would like to acknowledge many useful conversations with other participants in the program, particularly Robert Rogallo, Parviz Moin and William Reynolds.

REFERENCES

BATCHELOR, G. K. 1959 Small-scale variation of convected quantities like temperature in turbulent fluid. Part 1. General discussion and the case of small conductivity. *J. Fluid Mech.* **5**, 113–133.

BATCHELOR, G. K., HOWELLS, I. D. & TOWNSEND, A. A. 1959 Small-scale variation of convected quantities like temperature in turbulent fluid. Part 2. The case of large conductivity. *J. Fluid Mech.* **5**, 134–139.

CHASNOV, J., CANUTO, V. M. & ROGALLO, R. S. 1988 Turbulence spectrum of a passive temperature field: Results of a numerical simulation. *Phys. Fluids.* **31**, 2065–2067.

CHASNOV, J. 1990 Simulation of the inertial-conductive subrange. *Phys. Fluids*, (in press).

CLAY, J. P. 1973 Turbulent mixing of temperature in water, air and mercury. Ph.D. thesis, University of California at San Diego.

CORRSIN, S. 1951 On the spectrum of isotropic temperature fluctuations in isotropic turbulence. *J. Appl. Phys.* **22**, 469–473.

GARGETT, A. E. 1985 Evolution of scalar spectra with the decay of turbulence in a stratified fluid. *J. Fluid Mech.* **159**, 379–407.

GIBSON, C. H. & SCHWARZ, W. H. 1963 Detection of conductivity fluctuations in a turbulent flow field. *J. Fluid Mech.* **16**, 357–364.

GIBSON, C. H., ASHURST, W. T. & KERSTEIN, A. R. 1988 Mixing of strongly diffusive passive scalars like temperature by turbulence. *J. Fluid Mech.* **194**, 261–293.

GIBSON, C. H. 1968a Fine structure of scalar fields mixed by turbulence: I. Zero-gradient points and minimal gradient surfaces. *Phys. Fluids.* **11**, 2305–2315.

GIBSON, C. H. 1968b Fine structure of scalar fields mixed by turbulence: II. Spectral theory. *Phys. Fluids.* **11**, 2316–2327.

GIBSON, C. H. 1986 Internal waves, fossil turbulence, and composite ocean microstructure spectra. *J. Fluid Mech.* **168**, 89–117.

KERR, R. M. 1985 Higher-order derivative correlations and the alignment of small-scale structures in isotropic numerical turbulence. *J. Fluid Mech.* **153**, 31–58.

KERR, R. M. 1990 Velocity, scalar and transfer spectra in numerical turbulence. *J. Fluid Mech.* **211**, 309–332.

KOLMOGOROV, A. N. 1941 The local structure of turbulence in incompressible viscous fluid for very large Reynolds number. *Dokl. Akad. Nauk SSSR.* **30**, 301.

OBOUKHOV, A. M. 1949 Struktura temperaturnovo polia v turbulentnom potoke. *Izv. Akad. Nauk SSSR Ser. Geofiz.* **3**, 59.

WYNGAARD, J. C. 1971 The effect of velocity sensitivity on temperature derivative statistics in isotropic turbulence. *J. Fluid Mech.* **48**, 763–769.

Length scales and dissipation of fine eddies in a mixing layer

By Y. Zohar[1], R. D. Moser[2], J. C. Buell[3] AND C. M. Ho[1]

It has been shown that small scale turbulence is produced by the interaction of the merging spanwise structures (rollers) and the streamwise vortices (ribs) (Huang & Ho 1990, Moser & Rogers 1990). In this study, we examine the dissipation rate of the three-dimensional kinetic energy and the length scales associated with the dissipation rate in a temporally-evolving mixing layer.

1. Introduction

It has been recognized that entrainment of fluids from the two streams into the shear region of a mixing layer is controlled by the unsteady evolution of the large coherent structures. The fine-scale mixing of the two fluids is accomplished by the random small eddies which produce a larger mixing interface area (Ho & Huerre 1984). This paper presents some properties of these fine-scale eddies.

The small-scale transition characterized by the sudden increase of the roll-off exponent of the energy spectrum near the first vortex merging was reported by Huang & Ho (1990). They used the Peak-Valley-Counting (PVC) technique to directly detect the small-scale velocity fluctuations and found that the small-scale activity was initially concentrated in regions corresponding to the cores of the merging rollers and in the plane containing the streamwise vortices. Hence, they suggested that the interaction between these two deterministic structures during vortex merging leads to the production of small eddies. Zohar & Ho (1990) then further developed the PVC technique to gain more physical insight into the small-scale eddies. They found that the most probable length scale of the fine eddies is equal to the scale of maximum dissipation, suggesting that the structures detected by the PVC technique are responsible for most of the dissipation of kinetic energy. Furthermore, the maximum strain rate associated with the small eddies was found to scale with the global strain rate associated with the coherent structures.

In the experiment, the PVC technique was applied to the streamwise velocity signal recorded by a hot-wire at a single point in the flow field. The length scale was obtained by converting time into length through the Taylor hypothesis. In the flow, the eddies are distributed in space, so the length scale determined from a single point is only a component of the averaged distance between eddies. However, in a numerically simulated mixing layer, the entire velocity field is readily available.

1 University of Southern California
2 NASA Ames Research Center
3 Center for Turbulence Research

It is then possible to extend the PVC technique to a 2-D x–z surface (x is the streamwise and z is the spanwise direction) instead of the 1-D time (or pseudo-x) trace. Furthermore, the PVC technique can be applied to velocity components other than the streamwise, and even to other quantities such as vorticity.

The dissipation of turbulent energy is mainly due to the effect of viscosity on small scales. In experiments, due to the limitation of having only a few sampling points in space, the study of dissipation has concentrated on time-averaged quantities. However, using numerical simulation data, the spatial distribution of the viscous dissipation can be examined.

Several numerically simulated time-evolving mixing layers are available. For the current study we have selected a simulation which undergoes two pairings. By the second pairing, the layer has completed the transition to small-scale turbulence. This simulation is described by Moser & Rogers (1990). The numerical results reported below were all taken from this simulation at the time of the second pairing.

2. The peak-valley-counting (PVC) technique

The study of fine-scale eddies in the past was restricted to statistical analyses, however these techniques do not provide the phase and amplitude information of the small eddies. Huang & Ho (1990) and Hsiao (1985) started to develop a method of registering both the instant and the magnitude of an event whenever the velocity signal exhibits a peak or a valley (PVC technique). Although the concept is simple, it is difficult to distinguish between the actual small eddies and instrument or numerical noise. Recently, Zohar (1990) has significantly alleviated this problem by applying several conditional criteria.

The PVC technique locates the extrema of the velocity fluctuations induced by the small eddies. The interval between a peak-valley pair provides a length scale for the event. Since the velocity difference between the peak and the valley is also registered, the average strain rate associated with that event can be obtained as well.

In the current work, the PVC technique based on the 1-D time trace of velocity fluctuations has been extended to a 2-D plane of velocity data taken from a computational mixing layer. The stationary points of the velocity field on a given surface, (i.e. extrema and saddle points) where both directional derivatives vanish ($\partial/\partial x = \partial/\partial z = 0$) are first identified. Noise effects are minimized by eliminating extraneous stationary points using criteria similar to those used by Zohar (1990). The stationary points are then connected together in an unstructured mesh using the greedy algorithm. The length scales and strain rates can then be calculated from the probability distribution function (pdf) of the distance between stationary points and the velocity difference between these points.

3. Spatial distributions of small-scale turbulence

The spatial distribution of the velocity fluctuations associated with small-scale turbulence is represented by the stationary points determined from the 2-D PVC method. The technique has been applied to all three velocity components. It is

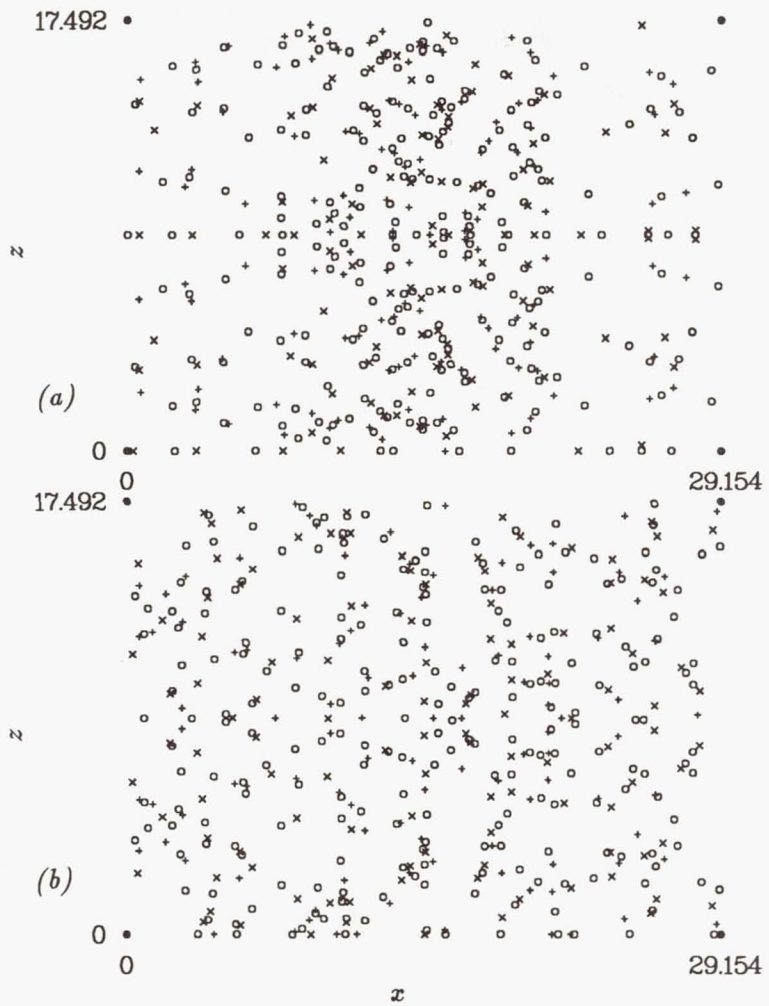

FIGURE 1. Location of two-dimensional stationary points of *(a)* u, and *(b)* v in the x–z plane at $y = 0$. The stationary points are: $\times$, minima; $\circ$, saddles; and $+$, maxima. The spanwise roller is centered in the x domain.

very interesting to note that the patterns of the stationary points in each of the three velocity components are quite different. In figure 1, the streamwise velocity fluctuations, u, show higher concentration of fine eddies along the roller core than in the braid region. Similarly, Zohar & Ho (1990) found in their experiment that the small-scale activity in the roller core is about twice that in the braid region. However, the transverse velocity fluctuations, v, have a uniform distribution in the x–z plane (figure 1*b*). This finding is somewhat surprising and is not yet understood. Farge *et al.* (1990) applied the wavelet analysis to the same velocity field. They also observed that the energy content of the transverse velocity fluctuations at high wavenumbers is evenly distributed. The spanwise velocity fluctuations, w, have a

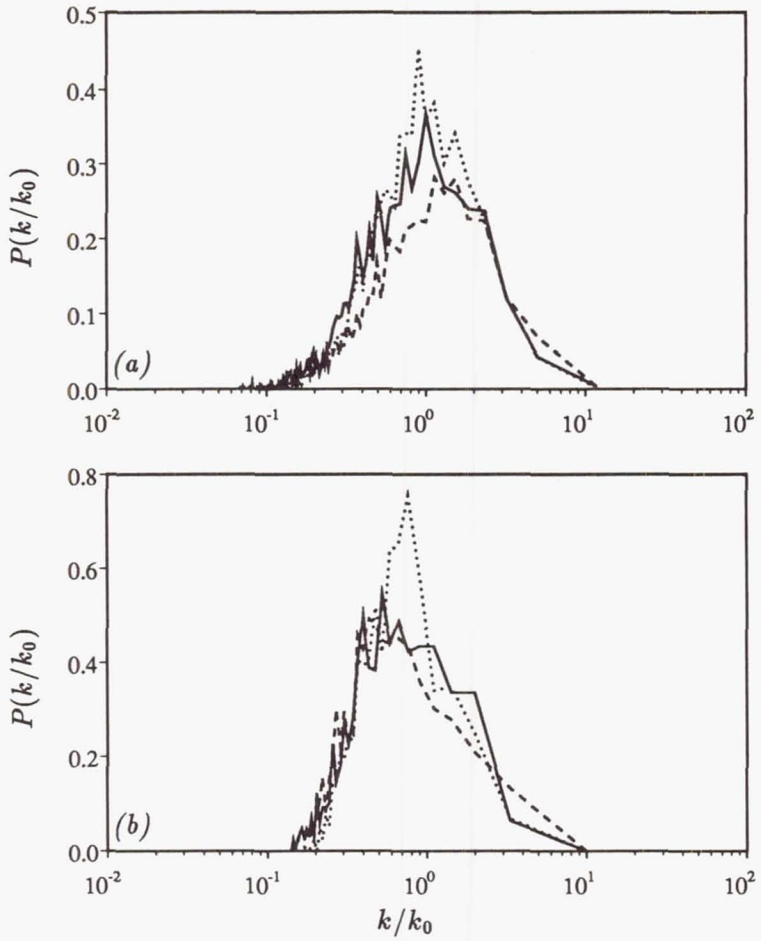

FIGURE 2. Probability density of the wavenumbers $k_i = 2\pi/d_i$, where the d_i are the separations between stationary points in the *(a)* one-dimensional and *(b)* two-dimensional PVC technique based on: ——— , streamwise velocity u; - - - - , cross-stream velocity v; and ····· , spanwise velocity w.

stationary point distribution pattern similar to that of the streamwise fluctuating velocity, but the number of stationary points is about 50% higher than for the streamwise component.

4. Length scales of fine eddies

4.1. Length scales of velocity fluctuations

The distance, d_i, between a peak-valley pair yields a measure for the size of the fine eddies. At the extremum, in the 1-D PVC, the velocity derivative is zero. Therefore, d_i is just the distance between zero crossings of the first velocity derivative. The pdf of the corresponding wavenumbers, $k_i = 2\pi/d_i$, is constructed for the 3 velocity components; u, v and w as shown in figure 2*a*. The pdf curves have a

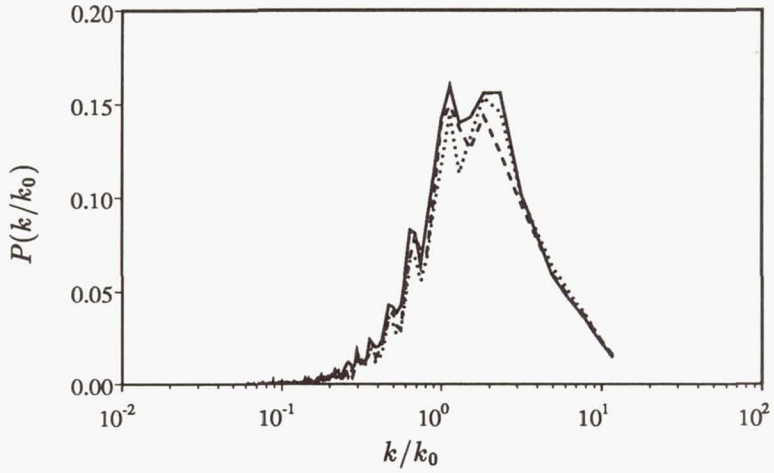

FIGURE 3. Probability density of the wavenumbers $k_i = 2\pi/d_i$, where the d_i are the separations between stationary points in the one-dimensional PVC technique based on: ——— , streamwise vorticity ω_x; - - - - , cross-stream vorticity ω_y; and ····· , spanwise vorticity ω_z.

clear sharp peak. The wavelength at the peaks, denoted as $L_s = 2\pi/k_s$, is used as the length scale to characterize the size of the fine eddies. Based on the numerical data, the pdf curves of the three velocity components peak at $k_s/k_0 \simeq 1$, where $k_0 = 2\pi/\delta_0$ and δ_0 is the initial vorticity thickness of the mixing layer. Experimentally, the value of this ratio, k_s/k_0, was found to be about 5. This difference could be due to the difference in initial Reynolds number between the experiment and simulation. In the numerical simulation, $Re = \Delta U \delta_0/\nu = 500$, but $Re = 2000$ in the experiment. It is expected that the fine eddies should have a smaller length scale in the flow with the higher Reynolds number.

Next, the 2-D PVC technique is applied to the velocity components in a horizontal, x–z plane. The pdf curves of wavenumbers based on the length of the line segments connecting the stationary points are similar to the 1-D results, i.e. there is a clear peak as shown in figure 2*a*. The wavenumber at the peak is smaller than the value for the 1-D case, $k_s/k_0 \simeq 0.7$. The d_i measured by the 1-D technique are projections of the d_i measured by the 2-D technique. Therefore, the d_i obtained from the 1-D PVC are expected to be shorter than those for the 2-D PVC, at least in the case of 2-D isotropy.

4.2. Length scales for vorticity fluctuations

Both the 1-D and the 2-D PVC techniques can be applied to other fluctuating quantities. Vorticity is obviously an interesting quantity to be examined. Due to noise problems in the vorticity signal, only the results of the 1-D PVC technique are presented (figure 3). The peak of the pdf curves of the vorticity peak-valley wavenumbers is at $k_s/k_0 \simeq 1.25$. This value is larger than the peak value of the velocity fluctuations. Vorticity is derived from derivatives of velocity fluctuations.

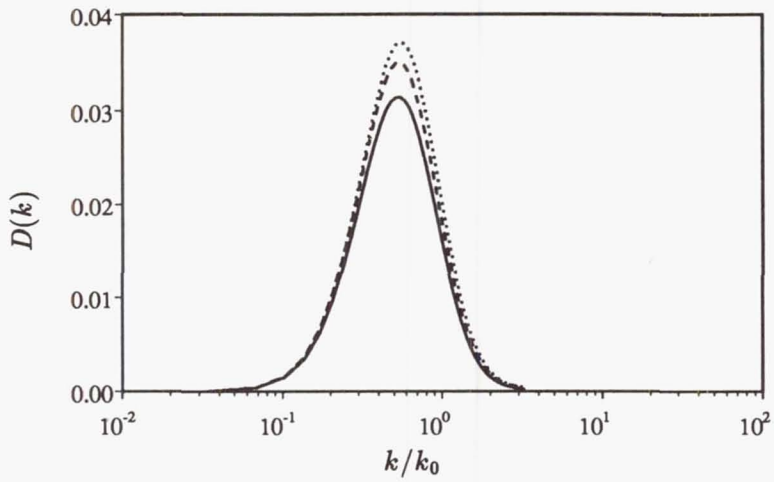

FIGURE 4. Dissipation spectrum $D(k)$ estimated from equation (2), based on the velocity spectrum at: ——— , $y = 0$; - - - - , $y = 1$; and ····· , $y = 2$.

Spatial differentiation emphasizes the high wavenumber end of the spectrum and therefore the vorticity length scale is shorter than the velocity length scale. Moreover, velocity fluctuations are detected in the potential flow regions as well, where the vorticity fluctuations vanish. These potential velocity fluctuations are found to have longer wavelengths compared to the rotational fluctuations. Nevertheless, the most probable length scale of the fluctuating vorticity and the fluctuating velocity components are of the same order of magnitude in this low-Reynolds-number flow.

4.3. A new dissipative scale

The physical significance of the length scale based on the PVC technique has been pointed out by Zohar & Ho (1990). L_s corresponds to the wavelength at the peak of the dissipation spectrum, $D(k)$. In order to verify this for other velocity components the dissipation spectrum should be estimated. First, the 3-D energy spectrum, $E(k)$, is calculated from the 1-D energy spectrum of the streamwise velocity, $F_{uu}(k)$, by using the following isotropic relationship,

$$E(k) = k^3 \frac{d}{dk}\left[\frac{1}{k}\frac{d}{dk}F_{uu}(k)\right] \tag{1}$$

Then, the dissipation spectrum can be obtained from the 3-D energy spectrum as follows,

$$D(k) = k^2 E(k) \tag{2}$$

The peak of the dissipation spectrum, shown in figure 4, appears at $k_s/k_0 \simeq 0.7$. Indeed, it is equal to the most probable length scale obtained from the 2-D PVC technique. This suggests that the small-scale eddies detected by the 2-D PVC scheme dissipate most of the kinetic energy. A similar correspondence between k_s and the peak in the dissipation spectrum was found by Zohar (1990) in his 1-D PVC experiment.

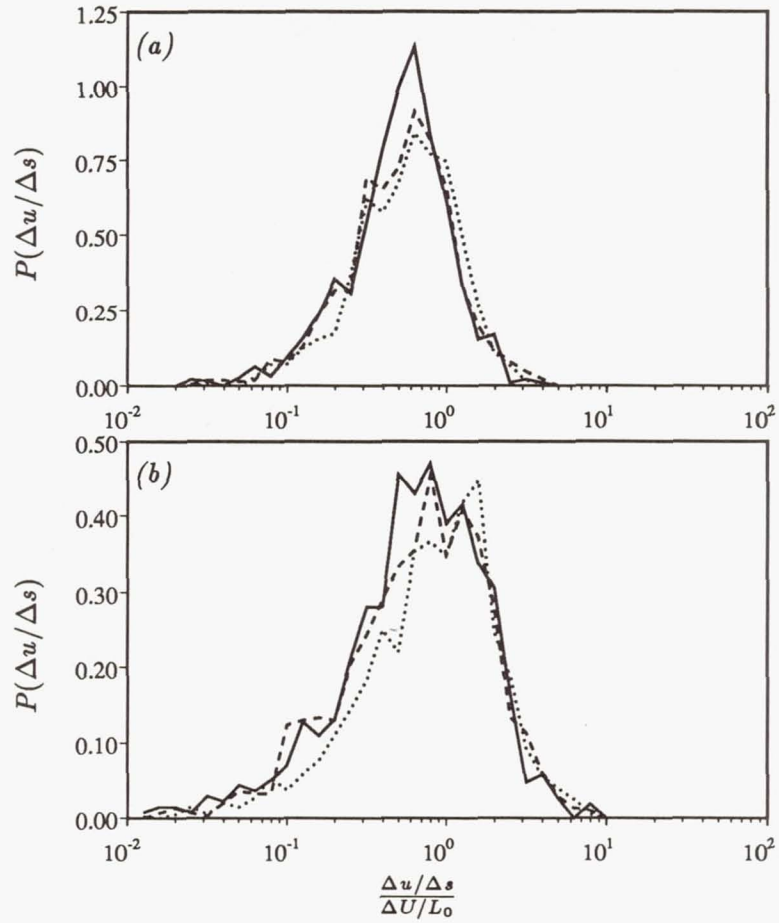

FIGURE 5. Probability density of the average small-scale strain rate $\Delta u/\Delta s$ obtained from the *(a)*, one-dimensional and *(b)*, two-dimensional PVC technique based on the streamwise velocity at —— $y = 0$, - - - - $y = 1$ and ····· $y = 2$.

5. Strain rates

The PVC technique enables one to estimate the average strain rate associated with the small eddies. This estimate is obtained by dividing the velocity difference between adjacent extrema or stationary points, Δu, by the length separating them, Δx in a 1-D trace or Δs in a 2-D plane. Then, the collection of all values of $|\Delta u/\Delta x|$ or $|\Delta u/\Delta s|$ can be used to construct a histogram for the local strain rate. These strain rates are normalized by the total velocity difference across the mixing layer, ΔU, and the initial instability wavelength, L_0. Figure 5*a* shows the pdf of the strain rate based on 1-D traces of the streamwise velocity, where the maximum occurs at a normalized strain rate of 0.6. The pdf based on the 2-D plane of the streamwise velocity peaks around 1, as shown in figure 5*b*. This value agrees with the experimental data based on the 1-D PVC technique.

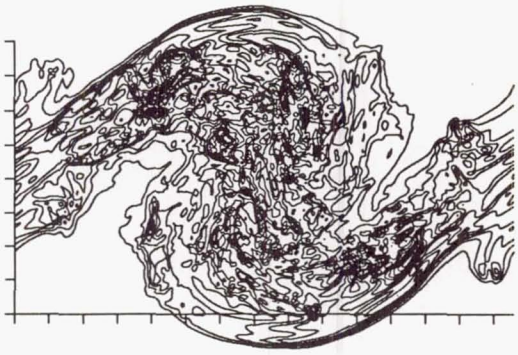

FIGURE 6. Spanwise average of the 3-dimensional strain contraction $2S_{ij}S_{ij} = \epsilon/\nu$. The contour increment is 0.5 and the highest contour level is 8.

6. Spatial distribution of dissipation

Turbulent flow is three dimensional in nature. In order to investigate the dissipation-rate of 3-D kinetic energy, the velocity is first averaged along the spanwise direction to obtain the 2-D averaged velocity field. The 3-D velocity field was obtained by subtracting the 2-D averaged velocity from the total velocity. Dissipation can then be calculated from the resultant 3-D velocity. The instantaneous local dissipation of turbulent kinetic energy can be written $\epsilon = 2\nu S_{ij}S_{ij}$, where S_{ij} is the strain tensor. The spanwise average of ϵ/ν (or strain contraction) is shown in figure 6. The strain contraction (ϵ/ν) in the x–y plane between the rib vortices and through the rib vortices is shown in figure 7. Also shown is the enstrophy ($\omega_i\omega_i$) in the same planes. As would be expected from the spatial location of the small scales, the dissipation occurs largely in the roller. There is however some dissipation associated with the braid-region ribs in the rib plane. The enstrophy contours show that the enstrophy is much more intermittent than the dissipation. Nearly all the enstrophy hot-spots are associated with significant dissipation, though there is also significant dissipation in essentially irrotational regions. It is interesting to note that the volume integral of $S_{ij}S_{ij}$ over the domain is the same as that of the enstrophy. Thus, the smaller regions of support for the enstrophy imply (as is visible in figure 7), that the peak magnitudes are much larger than for ϵ/ν.

7. Conclusions

The PVC signal processing technique is indeed a useful tool for studying small-scale turbulence from a new perspective. The technique has been extended to a two-dimensional velocity field. The data from the 2-D PVC technique are slightly different from that of the 1-D PVC technique. The results derived from the numerical simulations confirm the experimental findings; the most probable length scale of the small-scale eddies is equal to the scale of maximum dissipation and the local strain rates associated with the small-scale activity are comparable to the global strain rate, $\Delta U/L_0$.

The dissipation was seen to occur mostly in the mixing layer rollers, consistent

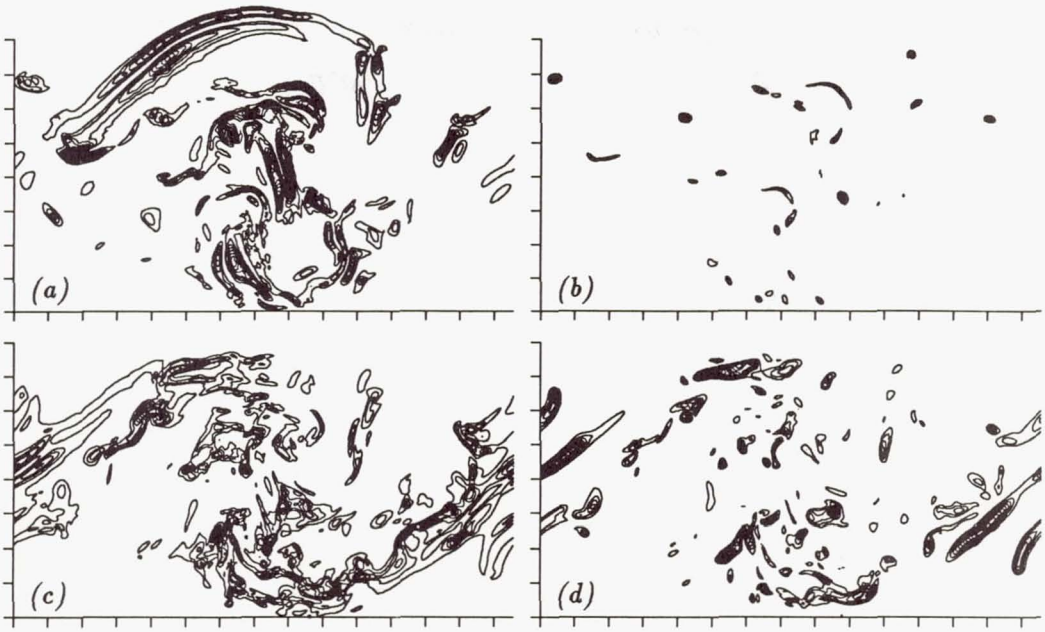

FIGURE 7. The 3-dimensional strain contraction $2S_{ij}S_{ij} = \epsilon/\nu$ (*(a)* and *(c)*) and the enstrophy $\omega_i\omega_i$ (*(b)* and *(d)*) in an x–y plane between the rib vortices (*(a)* and *(b)*) and through the rib vortices (*(c)* and *(d)*). The contour increment in 2.5. The spanwise roller is centered in the domain.

with the observation that the small-scale eddies are located there. The enstrophy is much more intermittent than the dissipation. There were many dissipating regions which were essentially irrotational.

REFERENCES

FARGE, M., GUEZENNEC, Y., HO, C. M. & MENEVEAU, C. 1990 Continuous wavelet analysis of coherent structures. *In this volume.*

HO, C. M. & HUERRE, P. 1984 Perturbed free shear layers. *Ann. Rev. Fluid Mech.* **16,** 365-424.

HSIAO, F. B. 1985 Small scale transition and preferred mode in an initially laminar plane jet. *Ph.D. thesis,*Univ. South. Calif., Los Angeles.

HUANG, L. S. & HO, C. M. 1990 Small scale transition in a plane mixing layer. *J. Fluid Mech.* **210,** 475-500.

MOSER, R. D. & ROGERS, M. M. 1990 Mixing transition and the cascade to small scales in a plane mixing layer. *Proc. IUTAM Symposium on Stirring and Mixing.* La Jolla, Ca., 20-24 August, 1990.

ZOHAR, Y. 1990 Fine scale mixing in a plane mixing layer. *Ph.D. thesis,* Univ. South. Calif., Los Angeles.

ZOHAR, Y. & HO, C. M. 1990 Fine-eddy production and control in a mixing layer. *In preparation.*

Center for Turbulence Research
Proceedings of the Summer Program 1990

A fractal transition in the two dimensional shear layer

By Javier Jiménez[1] AND Carlos Martel[2]

The dependence of product generation with Peclét and Reynolds number in a numerically simulated, reacting, two dimensional, temporally growing mixing layer is used to compute the fractal dimension of passive scalar interfaces. A transition from a low dimension of 4/3 to a higher one of 5/3 is identified and shown to be associated to the kinematic distortion on the flow field during the first pairing interaction. It is suggested that the structures responsible for this transition are non-deterministic, non-random, inhomogeneous fractals. Only the large scales are involved. No further transition is found for Reynolds numbers up to 20 000.

1. Introduction

It has been realized for some time that smooth velocity fields can generate very complicated advective scalar distributions (Aref, 1984) and, in particular, that initially smooth interfaces can become very convoluted. In fact, even if such an interface remains technically rectifiable for any finite amount of time, its geometry becomes more and more complicated, and we shall give below simple examples in which it develops fractal properties over a wide range of length scales. When seen at those scales, its area increases substantially, and if the interface separates two fluids that are to be mixed by molecular diffusion, the stretching results in a enhancement of the mixing efficiency. A convenient measure of the complication of the interface and, indirectly, of its area increase is its fractal dimension (Mandelbrot, 1982).

We will show here that in the *two dimensional* mixing layer, a transition occurs at the location of the first pairing interaction, which results in a change of the dimension of the advected interfaces from approximately 4/3 to a higher value of 5/3. Whether or not this transition results in a increase of mixing depends on other variables such as the Reynolds and Peclét numbers, but the change of dimensionality is intrinsic and does not depend on them. At the highest Peclét numbers computed, the presence of the transition results in a mixing enhancement of a factor of two.

Assume a two dimensional situation in which the interface separating two immiscible fluids can be described by a line with a fractal dimension F. Diffusion will "blur" the interface and generate a mixed region in the form of a strip centered around the original line whose width will, from dimensional considerations, grow in time proportionally to $W = (Dt)^{1/2}$, where D is the molecular diffusivity. The resulting strip will have a length $L(W)$ and an area proportional to $S = W\,L(W)$,

1 Centre for Turbulence Research and Universidad Politécnica Madrid
2 Universidad Politécnica Madrid

where the length is a function of the width, W, because of the fractal properties of the central backbone. In fact, $L \sim W^{1-F}$, and $S \sim W^{2-F}$. If we now repeat the same mixing experiment with all dimensions constant but with different diffusivities, the area of the mixed strip and, therefore, the amount of mixed fluid will be proportional to

$$S \sim D^{1-F/2} \sim Pe^{F/2-1}, \tag{1}$$

where $Pe = UL/D$ is the Peclét number. This equation contains the "practical" implication of the fractal dimension of the fluid interface, and we will use it in the following as a definition for F. An equivalent formulation exist for three dimensional situations, in which the exponent in equation (1) is replaced by $(F-3)/2$.

If the dimensionality of the interface increases at some stage in the flow, nothing in equation (1) guarantees that for a given Pe, the amount of mixing will also increase. However, if the diffusivity is reduced, the amount of mixing will increase faster after the transition and will eventually be enhanced for some sufficiently high Pe. The assumption in this argument is that the immiscible interface itself is independent of Pe, either because the velocity field is kept constant among different experiments, as in the cases in which Pe is increased by varying only the Schmidt number, Sc, or because the changes in the velocity field are small and irrelevant to the global geometry of the interface. This seems to be the case in the two dimensional flows described here but probably does not apply to the mixing transition observed in three dimensional layers (Konrad, 1977, Breidenthal, 1981), in which the flow itself becomes considerably more complex as Re increase (Moser and Rogers, 1990). In those cases, it is still possible to use the arguments given above to explain the variation of the mixing efficiency with Sc, but the discussion of the Reynolds number dependence must include considerations of the flow dynamics.

In this paper we describe some numerical experiments on the generation of product by a simple chemical reaction in a two dimensional, incompressible, temporally growing mixing layer. The amount of product is controlled by diffusion, and it will be taken as representative of the amount of mixing and used as such in equation (1). The initial conditions are held constant as the Reynolds and Peclét numbers are changed, both together and independently, and the variation in product generation is used to deduce the fractal dimension of a theoretical interface separating two immiscible species. The numerical code and the experimental arrangement are discussed briefly in the next section, and the results are then presented and discussed.

2. Experimental arrangements

The numerical code is a full Navier-Stokes simulator, developed at the Universidad Politécnica in Madrid using the vorticity-stream function formulation in conservative form, and includes the transport equation for a passive scalar. It uses a Fourier spectral representation in the streamwise (x) direction and a fourth order (Padé) finite difference scheme in the transverse (y) coordinate. The grid is mapped to infinity, and the nonlinear terms are computed using a fully de-aliased collocation scheme. Typical grids use 512 Fourier modes (341 after de-aliasing) and 400

transverse points. The code solves the initial value problem, starting with a initial velocity distribution, $u(y) = \tanh(y)$. This profile is perturbed initially with a small sinusoidal transverse deformation of amplitude $\Delta y \approx 0.1$ and wavelength $\alpha = 0.4$, which is close to the most amplified one for the initial Kelvin Helmholtz instability. In most of the runs, the computational box contains four initial wavelengths, resulting in the formation of four primary eddies that later interact through pairing. To insure this, small subharmonic and sub-subharmonic components are added to the initial perturbation.

A dimensionless viscosity is defined in terms of a Reynolds number based on the half velocity difference across the layer and on half the initial vorticity thickness, $\delta_\omega = 2$. The initial distribution of the passive scalar is taken as $s = 0.5(1 + \tanh(y/L_s))$, and its evolution is controlled by a Schmidt number, Sc, related to Re and the Peclét numbers by $Pe = Sc\,Re$. In most cases, $Sc = 1$, but some tests were done with Schmidt numbers in the range 0.25 to 4. The evolution of the scalar is used to model the behavior of a fast binary chemical reaction, $A + B \rightarrow P$, between species A and B, each of which is initially assumed to be distributed uniformly in one stream. Later they diffuse through the mixing layer and react immediately. The parameter L_s determines the width of the initial mixed region and should ideally be as small as possible to approximate a sharp interface. Numerical limitations prevent this, and all our experiments have been done with $L_s = 0.3$. At the most unfavorable case of high Peclét number, the memory of this initial thickness seems to be lost by the flow before $t = 20$, approximately the time necessary for the formation of the primary Kelvin-Helmhotz eddies.

In the Burke-Schumann limit assumed here, given the local concentration of the scalar, s, the concentration of product P can be shown to be proportional to

$$P = 2s \quad \text{if} \quad s < 1/2, \qquad P = 2(1 - s) \quad \text{otherwise.}$$

With this normalization, the maximum product concentration is always locally equal to one, and the center of the product distribution follows the $s = 0.5$ isoline. The product thickness,

$$\delta_p = \int_0^{L_x} P\,dx/L_x, \tag{2}$$

is a good measure of the area occupied by the reaction product, and we will take it as a measure of the mixed fluid area to be used in computing the fractal dimension through the arguments leading to eq. (1). L_x is the length of the computational box.

3. Results

Some typical time histories of the vorticity and product thickness are shown in figure 1. There are several bumps in the vorticity thickness evolution which mark the initial roll-up into vortex cores and two consecutive pairings. It is a property of temporal simulations that the time at which each pairing occurs can be controlled by varying the amplitudes of the initial subharmonic perturbations. These were

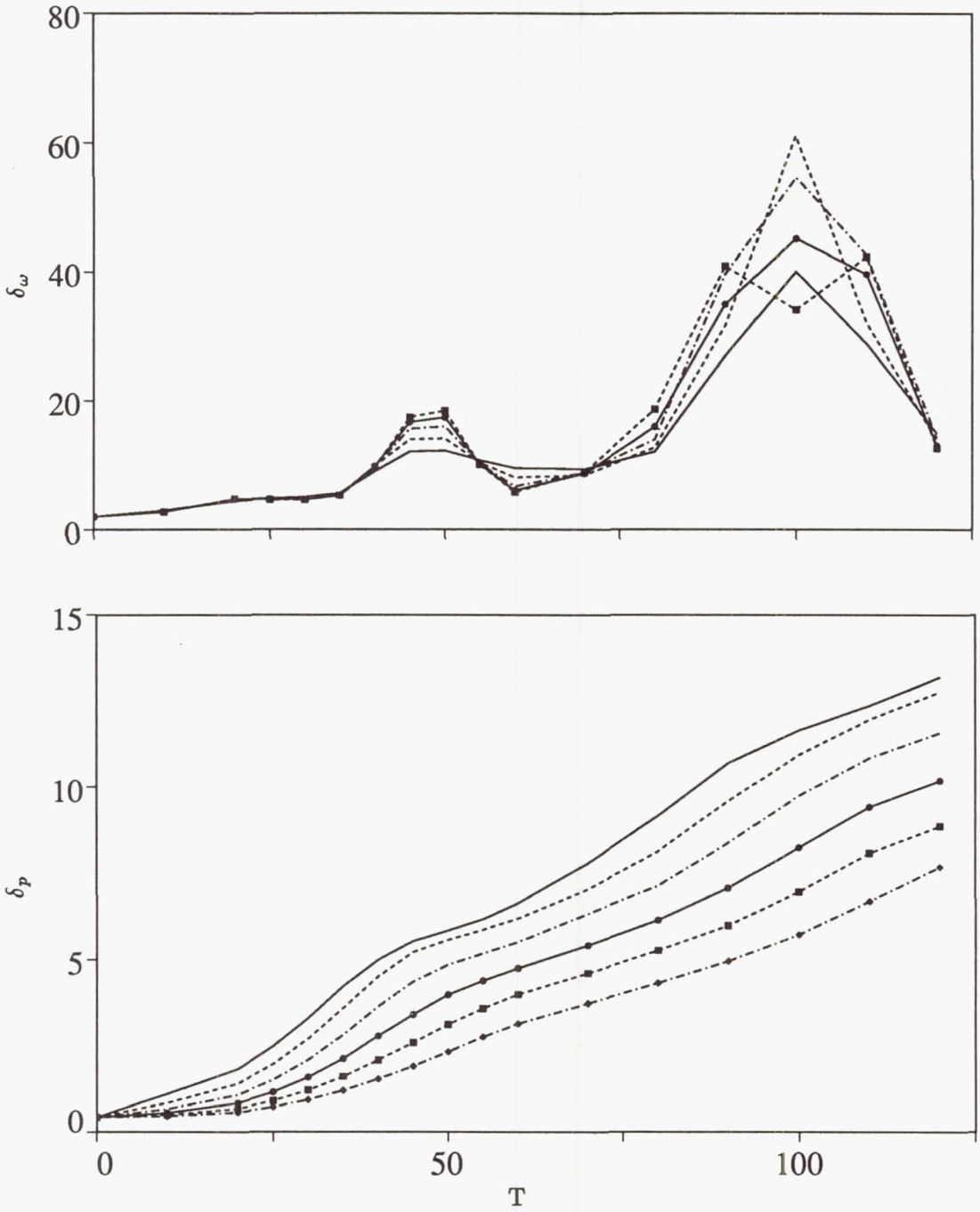

FIGURE 1. Time evolution of vorticity (top) and product thickness (bottom). $Pe =$ 50, 100, 200, 400, 800, 1600, in order of decreasing product generation. All cases $Sc = 1$, except $Pe = 1600$, $Sc = 4$.

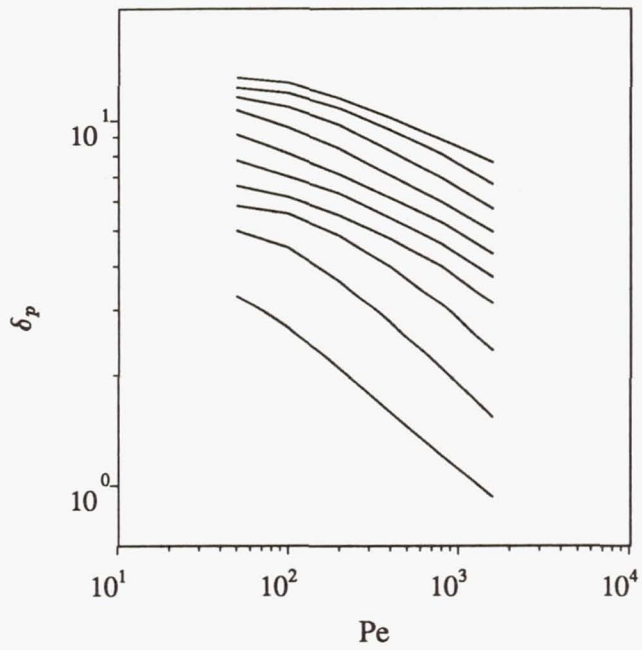

FIGURE 2. Variation of product thickness with Peclét number for different times. $t = 30$, 120, (10), increasing upwards. Data as in figure 1, but see text for other Sc.

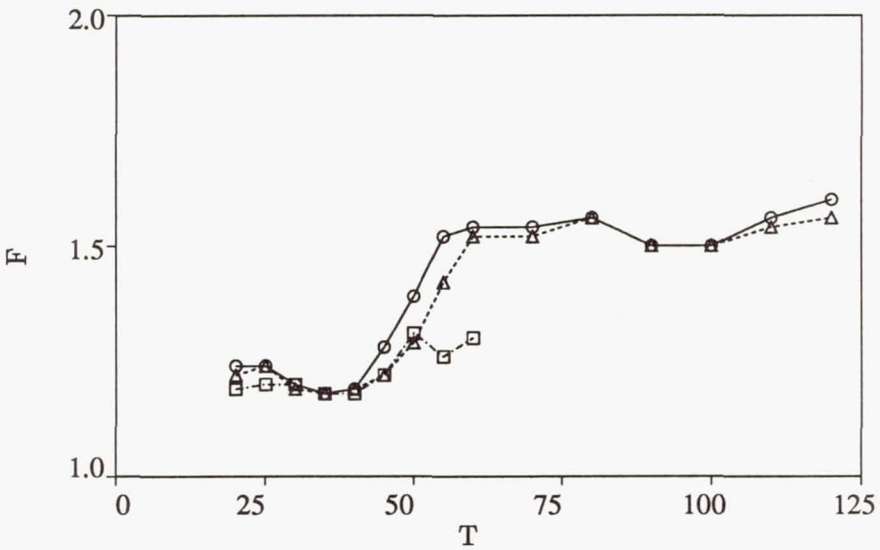

FIGURE 3. Fractal dimension of interface computed from figure 2, and from other similar data sets. ○: Natural layer, two pairings; △: Second pairing inhibited; □ : All pairings inhibited.

chosen so as to reproduce as closely as possible the experimental observations in an unforced half jet (Jiménez, 1983). The evolution of the vorticity thickness is too irregular to be described by a linear growth rate, but a least square fit to the lines in fig. 1a has a slope of 0.22, which is in reasonable agreement with the experimental growth rates for tripped shear layers. The evolution of the momentum thickness also shows bumps, although shallower, and its mean growth rate, 0.14 ± 0.02, is also approximately consistent with experiments. Later we will discuss briefly simulations in which the first and second pairings were purposely inhibited. In those cases, the vorticity thickness grows at the beginning as in the natural case but eventually levels off and oscillates about a fixed value.

Note that the growth of the product thickness is linear and is little affected by the pairing. This behavior is typical of all the simulations that were carried out. The rate of growth is, however, very dependent on Pe, decreasing with decreasing diffusivity. A plot of δ_p against Pe and time is given in figure 2, in which each line represents a point in time for different Peclét numbers, and time increases upwards. The slopes of these lines are the exponents discussed in equation (1) and can be related directly to the dimension of the fractal interfaces. The time evolution of F computed in this way is given by the open circles in fig. 3. It is clear that a transition occurs near $t = 50$, which corresponds to immediately after the first pairing interaction. The second pairing, near $t = 100$, also induces a slight increase in F, but a much weaker one, and the dimension seems to asymptote to a value close to $5/3$. Before $t = 20$, the time of initial roll-up, the measurement of F was prevented by the effect of the finite thickness of the initial condition for s, but the dimension has to approach $F = 1$ for short times. The two other sets of symbols in fig. 3 refer to two different sets of runs, in one of which the second pairing was inhibited, while in the other both pairings were prevented. It is clear that the effect of the second pairing is small, but that the absence of the first pairing prevents completely the appearance of the fractal transition. In fact, this latter case seems to asymptote to a value close to $4/3$. The significance of this number together with the previously cited $5/3$ will be discussed briefly below.

Note that the abscissae in figure 2 refer to Pe instead of to Reynolds number. In fact, several Schmidt numbers are represented in this figure. In most cases, $Sc = 1$, but $Pe = 1600$ was run at $Re = 400$, $Sc = 4$. Also $Pe = 800$ and $Pe = 200$ were both run at $Re = 200$ and $Re = 800$. In these last four runs, even if the Reynolds numbers were quite different and even if the vorticity fields showed appreciably more visual complication at the higher one, the product thickness scaled almost exclusively with Pe with variations below 3% and with no clear systematic trend. Note also that these Re and Pe are actually quite high since they refer to the initial state of the layer. In fact, when they are reduced to local quantities at the last stage in the simulation, $Pe_\omega = \Delta U\, \delta_\omega / D$ is of the order of 40 000 for $Pe = 1600$ (the fitted value, $\delta_\omega = 0.22t$, has been used for this reduction.)

4. Discussion

We have measured the change in time of the fractal dimension of an ideal interface in a two dimensional mixing layer, and we have related it to the scaling properties

of product generation with Peclét number. We have also shown that this scaling laws holds independently of the Reynolds number, even for fairly high values of this latter quantity. Since the effect of Re is mainly on the small scales, this suggests that mixing in this two dimensional case is controlled predominantly by the large coherent eddies. This is confirmed by inspection of the flow fields at high Re and Pe. The structure of the product is dominated by large folds and structures, with few small scales in the sense of fine random corrugations. This is also confirmed by the relatively low values of the fractal dimensions measured. Several investigators have studied and measured the fractal dimensions of interfaces in *three dimensional* turbulence (Sreenivasan and Meneveau, 1988), arriving at $F \sim 7/3$, and have justified this value using models based on random homogeneous fractals. The same arguments when applied to two dimensional turbulence (Meneveau, private communication) result in $F = 2$. This would correspond to horizontal lines in figure 3 and is inconsistent with our observations.

In fact, the assumptions of randomness and homogeneity are not necessary for a fractal model. It is shown in (Jiménez and Martel, 1990) that both the spirals generated by the deformation of initially plane interfaces by point vortices and the "stacks" resulting from the stretching those spirals by a plane strain are fractals. In fact, the dimension associated to the spirals is 4/3, while that associated to the stacks is 5/3, which are reasonably close to those found in figure 3 before and after the pairing. Both structures are common in the product distributions of the two dimensional layer. Spirals are generated trivially near the centre of the large coherent eddies, while stacks appear when the spirals are strained during the pairing interaction. As soon as the stacks appear, of course, their higher fractal dimension dominates the product generation of the whole field. It is, therefore, tempting to conclude that these are the structures responsible for the fractal behavior of the interface in the two dimensional mixing layer and that the fractal transition is caused by the straining of the original mixing eddies during the pairing.

Note that this picture is very different from that of the wrinkled interface of a homogeneous fractal. The fractional dimension comes in this case from the accumulation of turns near the center of the spirals and from the accumulation of sheets in the central part of the stacks. Note also that this picture is very similar to that arising from the *tendril-whorl* mapping studied in (Khakar *et al.*, 1986).

5. Conclusions

In summary, we have shown that the scalar interfaces in a two dimensional plane mixing layer acquire fractal properties, we have measured their fractal dimensions, and we have related them to the Peclét number dependence of product generation in a fast binary, diffusion controlled chemical reaction. We have also shown that those dimensions and the generation of product are fairly independent of Reynolds number (for $\Delta U \delta_\omega / \nu \leq 20\,000$), although they are strongly dependent on molecular diffusivity, suggesting that the mixing is mostly due to "chaotic advection" from the large scale eddies. This is contrary to the behavior of the three dimensional mixing layer, in which a large part of the mixing seems to be associated to longitudinal vorticity and small scales.

The fractal dimension undergoes a transition from $F \approx 4/3$ to $F \approx 5/3$, which coincides in time with the first pairing and which is inhibited when this pairing is inhibited. The effect of the second pairing is not as marked. We have presented a model for these dimensions in terms of non-random, non homogeneous, fractal structures. The transition is then explained as the kinematic distortion during pairing of structures of one kind ("spirals") into those of another ("stacks"). Finally, up to the Reynolds numbers quoted above and Peclét numbers twice as high, we found no further transition either in the mixing efficiency, or in the structure of the vorticity field.

REFERENCES

AREF, H. 1984 Stirring by chaotic advection. *J. Fluid Mech.* **143**, 1-21.

BREIDENTHAL, R. 1981 Structure in turbulent mixing layers and wakes, using a chemical reaction. *J. Fluid Mech.* **109**, 1-24.

JIMÉNEZ, J. 1983 A spanwise structure in the plane mixing layer. *J. Fluid Mech.* **132**, 319-336.

JIMÉNEZ, J. & MARTEL, C. 1990 Fractal properties of interfaces in two dimensional shear layers, *Proc. IUTAM Symp. Stirring and Mixing.* La Jolla, 20-24 August, 1990.

KHAKHAR, D. V., RISING, H. & OTTINO, J. M. 1986 An analysis of chaotic mixing in two chaotic flows. *J. Fluid Mech.* **172**, 419-451.

KONRAD, J. H. 1977 An experimental investigation of mixing in two dimensional turbulent shear flows with applications to diffusion limited chemical reactions, *Ph.D. Thesis.* Caltech.

MANDELBROT, B. B. 1982 *The fractal geometry of nature.* W. H. Freeman.

MOSER,R. D. & ROGERS,M. M. 1990 Mixing transition and the cascade to small scales in a plane mixing layer, *Proc. IUTAM Symp. Stirring and Mixing.* La Jolla, 20-24 August, 1990.

SREENIVASAN, K. R. & MENEVEAU, C. 1986 The fractal facets of turbulence. *J. Fluid Mech.* **173**, 357-386.

V. The Combustion Group

This group conducted five projects. The goals were to improve understanding of the fundamental mechanisms controlling turbulent combustion and to use this knowledge to construct better models for reacting flows. The bases for these studies were a two-dimensional code including heat release and three-dimensional codes that ignore the hydrodynamic effects of chemical reaction.

W. Ashurst used a finite-difference 3D passive scalar code to study the propagation of a premixed flame in three-dimensional turbulence. In this approach, the flame is a zero-thickness interface located on a level surface of a passive scalar whose value is computed from a field equation. The turbulence is forced in order to produce a constant energy flow. Runs were performed on 16^3 grids to allow fast post-processing. Statistics of the curvature indicate that most flame fronts are nearly cylindrical in shape, justifying two-dimensional studies of flame-vortex interactions. It was also shown that out-of-plane strain tends to counteract viscous effects. The existence of vortical cores which interact strongly with the flame front was also demonstrated.

Two studies (C. Rutland and S. Cant) used a modified version of the Rogallo (3D incompressible spectral) code to produce direct simulations of flames propagating in three-dimensional turbulence with a 128^3 grid. This code treats turbulent flames via passive scalars, thereby limiting it to constant density and precluding consideration of the effect of the flame on the turbulent flow. Their purpose was to gather statistics needed to validate and improve models of the Bray-Moss-Libby type for premixed turbulent combustion. Shape factors of the flame front were computed and indicate the predominance of cylindrical flames, in agreement with a result of Ashurst (see above). PDFs of strain rate and curvature on surfaces of constant progress variable (flame surfaces in this formulation) were computed. Rutland and Trouvé studied the effect of curvature and Lewis number on flame structure. Most of the results were not unexpected but provided quantitative data for the first time; an unanticipated finding is that the temperature behind a flame is affected by the local curvature, a result of considerable potential importance in the prediction of pollutant production.

Two projects (D. Haworth and G. Kosály) used a two-dimensional finite difference program which solves the compressible Navier-Stokes equations. This code takes into account heat release, variable temperature and density, and variable transport properties using up to 400^2 gridpoints; it was developed at CTR by T. Poinsot in 1989. D. Haworth wrote a post-processing program to analyze fields produced by this code. The dominant effect of Lewis number on the local flame structure was demonstrated. Quenching induced by inhomogeneities representing imperfect mixing of the gases were investigated in 1D and 2D cases.

The two studies just described were directly comparable and complementary. Many common results were obtained. For example, both studies show that curvature is more important than strain in controlling the local instantaneous reaction

rate, but that strain determines the mean reaction rate. PDFs of burnt gases temperature were obtained and reveal large temperature differences when the Lewis number is not equal to unity.

Only one project (G. Kosály, *et al.*) related to diffusion flames. It studied the validity of the flamelet assumption for diffusion flames using 2D direct simulations made with the compressible flow code. Flamelet models assume that the reaction rate as a function of the conserved scalar and scalar dissipation can be computed from laminar flames. It was found that for large Damköhler numbers (small chemical times), this assumption is accurate. For more intense turbulent fields (smaller Damköhler numbers), the relationship is no longer as precise but remains accurate enough to be applied in practical situations; Kosály and Mell intend to continue this investigation. The effect of heat release on these conclusions was examined.

The comparison between 2D variable density and 3D constant density codes for similar situations was an important feature of this workshop. The results obtained from the two codes on certain issues eg., the effects of molecular transport and of thermodiffusive instabilities (Lewis number effects) were quite comparable, justifying the use of the simpler incompressible flow code for many situations. The use of direct simulations to investigate turbulent combustion is practiced at only a few laboratories worldwide and the Summer Program added considerably to the body of results available and contributed to the confidence of the combustion community in the approach; many original and important results were obtained.

The Combustion Group met twice a week; many of the results are direct consequences of the animated and fruitful discussions that took place at these meetings. The participants also enjoyed the opportunity to work together on a daily basis.

Thierry Poinsot and Joel H. Ferziger

Geometry of premixed flames in three-dimensional turbulence

By Wm. T. Ashurst[1]

Constant density premixed flame propagation in three-dimensional Navier-Stokes turbulence has been simulated. The zero-thickness flame model of Kerstein *et al.* (1988) has been used. There are two aspects to this study: 1) adjustment of the large-scale strain rate in order to achieve a constant energy system, and 2) determination of flame curvature. The sampled distribution of curvature indicates that in most cases the flame has a cylindrical shape, with one curvature at least three times larger than the other. This implies that realistic chemical reactions in a flame-vortex interaction may be simulated in two-dimensions.

1. Constant Energy Turbulence

Simulation of turbulent flow at constant energy allows flame propagation in a statistical steady state. To achieve a constant energy system, a large-scale forcing scheme was developed. Normal strain-rates in each octant of a periodic cube are determined at each time-step. Let

$$a = \frac{\partial < u >_x}{\partial x}$$

where the subscript on the brackets indicate that the velocity is averaged over the octant face normal to the x direction; each octant is a cube with $L/2$ edge length within a periodic cube with edge length L. Notice that in each direction, the periodic boundary condition makes the strain in one octant the negative of the adjacent octant. Let b, c be the strain rates in the y, z directions in the same octant, then for incompressible flow the sum of strains is zero, $a + b + c = 0$. Adjustment of these strains is done in order to maintain constant energy on the fine-scale grid. If the velocity within the octant is modified by a fraction of the strain rate, $(fa + fb + fc)$ then the flow will still be incompressible. The new x component of velocity within the octant is

$$u(x, y, z) = u_o(x, y, z) + f\ a\ x, \quad 0 < x < L/2$$

and in the adjacent octant

$$u(x, y, z) = u_o(x, y, z) - f\ a\ (x - L), \quad L/2 < x < L$$

1 Combustion Research Facility, Sandia National Laboratories

and corresponding adjustments of $f\ b$ and $f\ c$ in the y and z velocity components. The adjustment factor f is the same for all eight octants and is determined by a predictor-corrector procedure so that the kinetic energy is constant. Adjustment with a relaxation time could also be done, in which case the system energy would have a time variation. This adjustment, the value of f, is small: about one-half percent change in the octant strain-rate is needed for a 32-cubed system with Taylor Reynolds number of fifty. (The turbulent kinetic energy is $q^2/2 = 1.5$, the reference velocity and length scale L is unity, the kinematic viscosity is $\nu = 0.002$.)

These finite-difference simulations yield small-scale strain rates in agreement with those obtained with the pseudospectral method (Ashurst *et al.*, 1987). The strain-rate tensor, with eigenvalues of $\alpha \geq \beta \geq \gamma$ and magnitude $e^2 = \alpha^2 + \beta^2 + \gamma^2$, has a shape characterized by the intermediate strain rate, β. The shape is expressed as $\beta/\sqrt{e^2/6}$, a parameter with bounds of ± 1. (For the large-scale normal strains we use $b/\sqrt{(a^2 + b^2 + c^2)/6}$.) The shape of the strain-rate tensor at a single point changes from a symmetric distribution of β to an asymmetric one as the strain magnitude increases, the change described by $A(e)$. In the 32^3 finite-difference simulations, a value of $\nu = 0.002$ matches the trend of $A(e)$ in the 128^3 results, whereas a value of 0.001 does not. Thus, the resolution of the finite-difference work is deemed adequate. These distributions have the character that the limit case of two equal strains has vanishing probability. The most probable value for $(\alpha : \beta : \gamma)$ is (1, 0, -1) at low strain and (3, 1, -4) at high strain. For the large-scale normal strains this is not so. It appears that the large scale has uniform probability for all possible shapes.

It is thought that the small-scale strain rate is dictated by the flow pattern associated with a stretching vortex when the strain is large and by a shearing flow when the strain is small. The uniform probability of the large-scale is an indication that all possible flow patterns exist. From a limited investigation, it appears that one-sixth of the possible directions have very large extensive strains. These strains appear to be created by a large-scale rotation: two adjacent faces of an octant have large velocities (inflow, outflow), while the velocities on the respective opposite faces are small. The differencing and averaging of these face velocities result in large strain and small convection. The apparently small convection may be misleading if the actual convection is rotational and not unidirectional. We have attempted to compare the vorticity structure with the large-scale extensive strains in order to determine if there is a causal connection. It appears that there may be, as described below, but larger system calculations should be done. (There is a possibility that the periodic boundary condition creates a strain which enhances the vorticity structure in comparison to non-periodic turbulence.)

There are two aspects of the large-scale strain which affect the small-scale flow patterns: 1) magnitude of the extensive strain and 2) lifetime of this strain. Thus, the vorticity within those octants will amplify in the extensive directions during the lifetime of these strains, providing that the vorticity is not convected out of the octant before significant growth occurs. The vorticity growth caused by a large-scale

strain $a(\tau)$ over a time period of t is

$$\omega(t) = \omega(0)\exp(\int_o^t a(\tau)\, d\tau)$$

These normal strains have a numerical range of $\pm$ 3, while the average of the octant face velocity, corresponding to the large-scale convection within the octant, has a range of $\pm$ 0.7. Because strain is a derivative of velocity, it has more variation than the convective velocity.

Displacement of the vorticity is the time-integral of the convection velocity and is an indication of how long a particular vorticity region may reside within the octant under consideration. The transverse spatial correlation of velocity gives an estimated integral time of approximately 0.16, or 120 time-steps. The longitudinal velocity correlation decays to 0.3 at a separation of $L/2$, while a similar correlation of the octant face velocity has a value of only 0.035. At an octant face, the time correlation indicates a zero-crossing at approximately three times the integral time. So the large-scale strain has a long life compared to the integral time.

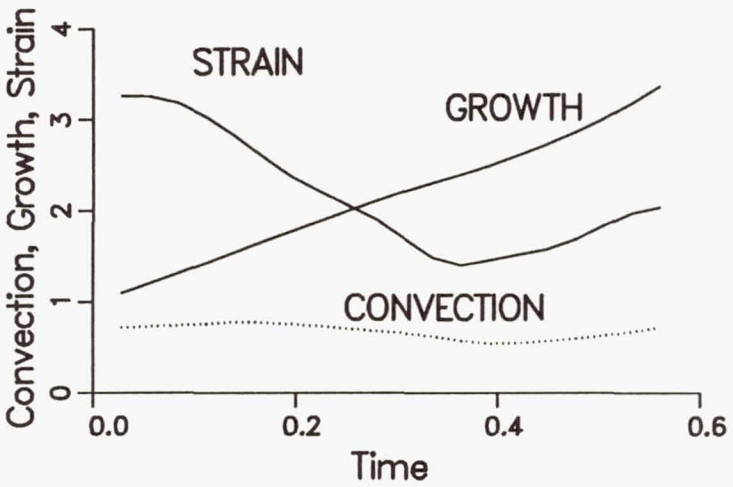

FIGURE 1. Evolution of large-scale normal strain in an octant during a 400 time-step period. The growth of a material line subjected to this strain is also shown. The convection (dotted line) is more constant than the strain.

Figure 1 presents the time variation of an octant normal strain and the resulting growth factor over a period of 400 time-steps. For this particular octant, the strain changes from extensive to compressive during the next 400 step period, and so negative growth occurs. Examination of the vorticity structure during the first period reveals that intensification of vorticity does occur. Examination was done by viewing the vorticity surface which has a magnitude of one-half the maximum vorticity value, using the program TURB3D (developed at NASA-Ames). Over intervals of

30 time-steps it is easy to see the changing vortex structure, and in some cases, the plotting of surfaces with lower enstrophy reveal how the structure is developing during a growth phase. Over intervals of 100 time-steps it becomes difficult in some cases to decipher which structure evolved from the previous arrangement of vorticity.

Observation of the intense vorticity structures in the computed flow field indicates that their creation may be a result of the extensional large-scale strain, but more work is needed before this can be considered a firm conclusion.

Flame Model

The zero-thickness, constant-density premixed flame model described in Kerstein *et al.* (1988) has been used. A continuous scalar G is convected by the flow and the flame propagation is accomplished by Huygens mechanism where the flame speed is a function of strain and curvature

$$\frac{\partial G}{\partial t} + \mathbf{u} \cdot \nabla G = u_F |\nabla G| + \nu' \nabla^2 G$$

The flame speed is $u_F = u_L \exp(-L_M \kappa)$ where $L_M = 0.025L$ is the Markstein length and κ is the local flame stretch. An exponential form is used so that large stretch can only reduce the flame speed to zero (and not create negative values if the linear version is used). To insure an upper bound on flame speed for advancement in the explicit finite difference method, a limit of four is placed on the exponential term, $-L_M \kappa < 1.39$. With respect to any value of G, the unburnt fluid is located at smaller values of G. Flame motion can create pockets of unburnt fluid, but not pockets of burnt. The latter case does occur in the discrete numerics when a local maximum of G is created; however, these false maxima are not numerous if the flame speed u_L is comparable to the rms velocity q, which is $\sqrt{3}$. To help suppress the false maxima, a dissipation term is added, $\nu' = \nu/4$, see discussion in Ashurst *et al.* (1988). This model has the advantage that each numerical grid point contributes statistical information about the flame since any constant value of G represents a flame.

3. Intense Vortex Effect on Flame Geometry

Intense vorticity has a tube-like shape, one dimension is greater than the other two. The cover of *Physics Today*, January 1990 presents a nice view of the intense vorticity. As a flame approaches such a structure, it becomes wrapped around the vortex, and so the flame surface is more often like a cylinder than a sphere.

We examine two aspects of the flame surface: 1) curvature and 2) direction of flame normal with respect to the most compressive strain rate. The flame surface is described by the unit normal vector $\mathbf{n} = -\nabla G/|\nabla G|$ and the two principal curvatures of the surface are $h_1 = 1/R_1$ and $h_2 = 1/R_2$. Negative curvature represents a concave flame with respect to the reactants and the local flame speed u_F is increased but limited to $4u_L$ in these simulations. At each grid point, the first

and second spatial derivatives of G are calculated and the elements of the curvature tensor are formed

$$h_{ij} = -\frac{\partial^2 G}{\partial x_i \partial x_j}\frac{1}{g} + \frac{1}{g^3}\sum_{k=1}^{3}\frac{\partial G}{\partial x_i}\frac{\partial G}{\partial x_k}\frac{\partial^2 G}{\partial x_j \partial x_k}$$

where $g = |\nabla G|$. This tensor has two real eigenvalues h_1, h_2 and one eigenvalue equal to zero. Thus, the determinant is zero and the two principal curvatures may be found from a quadratic equation. The calculated determinant of h_{ij} is zero to within machine round-off. The divergence of the surface unit vector is $\nabla \cdot \mathbf{n}_G = h_1 + h_2$, where the subscript G indicates the normal for a particular value of G. Note that the divergence of the field variable unit vector $\nabla \cdot \mathbf{n}(\mathbf{x}; G)$ is not the same quantity, and so the expression given above for h_{ij} must be used. The flame stretch is $\kappa = -(\mathbf{n} \cdot \mathbf{e} \cdot \mathbf{n})/u_L + h_1 + h_2$ where $\mathbf{e}$ is the strain-rate tensor.

A convenient way to describe the local flame shape is a ratio of the principal curvatures: the smallest curvature (in magnitude) is divided by the larger, yielding a result bounded by ± 1. A spherical shape has equal curvatures, a zero value is that of a cylinder (one curvature is zero), and a spherical saddle point has curvatures of equal magnitude but opposite sign. Pope *et al.* (1989) have calculated and displayed the curvature ratio of material elements in this manner. Figure 2 presents the distribution of curvature shape for a laminar flame speed of $u_L = 1$; the rms velocity is 1.73. The distribution is from four realizations, 200 time-steps apart, in a 32^3 flow. The flow at zero time for the scalar has already evolved 4,700 time steps from a random initial condition. Changing the value of q/u_L from 0.87 to 3.5 does not change the shape of the distribution. The flame results agree with the behavior of material points in having a vanishing probability for spherical shapes and a most probable shape to be that of a cylinder. Fifty-six percent of the flame data have a shape factor within $\pm$ 0.3, indicating that one radius is at least three times larger than the other.

The distribution in Fig. 2 overlays the distribution obtained by Cant *et al.* (1990) from the spectral simulation of constant-density, finite-rate, finite-thickness flame propagation. The best match is with the curvature that occurs on the surface that has a progress variable value of 0.1, the non-reacting, preheat zone of the flame. In comparison, the larger progress values have higher probability on the negative side and lower on the positive, but all results have the same peak probability. This trend indicates a different response when reaction, diffusion and convection operate as opposed to only diffusion and convection. The assumed strain-curvature effect on the propagation of G appears to describe the response of the leading edge of a finite-thickness flame.

To explore the principal curvature in more detail, we sort the data by increasing h_1 value and carry along the associated h_2 value. Breaking the data set into 16 bins of h_1 and averaging yields the curve shown in Fig. 3. The rms value of h_2 in each bin is not small, ~ 8 over most of the data range. Because of the ordering of the eigenvalues $h_1 > h_2$, there are no points above the line $h_1 = h_2$, shown dotted in Fig. 3. Each symbol represents 1/16 of the data and we can see that about 2/3

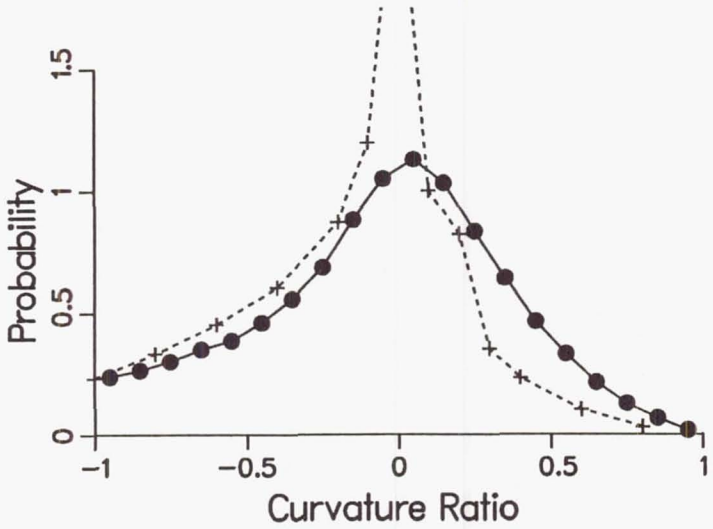

FIGURE 2. Distribution of flame surface shape, accumulated in bin widths of 0.1. The curvature ratio is the smaller (absolute value) divided by the larger ($h_{min}/h_{max} = R_{min}/R_{max}$). A ratio of unity corresponds to a sphere and a ratio of zero is that of a cylinder. Material element results from Pope *et al.* are shown by dashed line.

of the data falls along a line of $h_2 = h_1 - c$, where the values of c are 7.7, 9.9 and 11.2 for flame speeds of $u_L = 2$, 1 and 1/2, all with $q = 1.73$. The offset from the origin increases with the ratio of q/u_L. The cylindrical shapes are associated with results along the two axes – about twenty percent are from the region where $h_1 \approx 0$, with $h_2 < 0$ which corresponds to a flame concave to the unburnt gas. There is also a smaller contribution for cylindrical shape at large h_1, where the average h_2 is approximately zero. This would be flames concave to the burnt gas. The saddle shape is given by points close to the line $h_2 = -h_1$. The data crosses almost normal to this line. The conclusion from Fig. 3 is that when one curvature is large, then the average value of the second component is small.

A previous investigation of strain rate revealed that vorticity is more likely to be in the intermediate strain direction while the pressure gradient and a passive scalar gradient align in the most compressive strain direction (Ashurst *et al.* 1987). Figure 4 presents distributions of alignment of vorticity and the flame normal. The vorticity alignment agrees with the previous pseudospectral results.

The propagating flame appears to have properties similar to a passive scalar. Similar to the behavior of the scalar gradient, the normal to the flame surface has a high probability to align with the most compressive strain-rate direction. This probability increases if the alignment is conditioned on the large strain regions, but decreases if the condition is based on having a large vortical magnitude. This effect indicates that the large enstrophy regions have small strain rates and so, as the flame propagates through the vortex core, it loses alignment with the strain

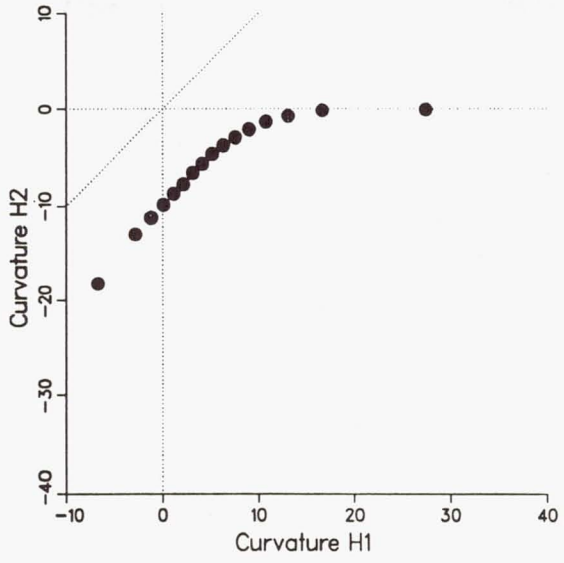

FIGURE 3. Principal curvature of flame indicates that when one curvature is very large, the other is small. By definition, $h_1 > h_2$. Averages were obtained by sorting data according to value of h_1, each symbol represents 1/16 of the data set.

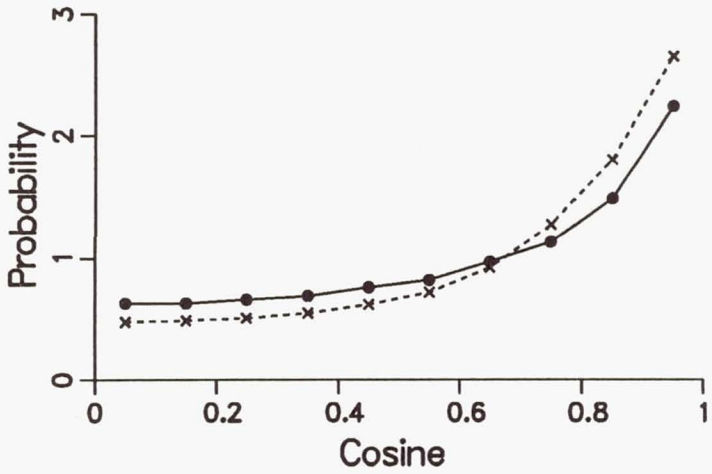

FIGURE 4. Distribution of alignment with strain rate for vorticity ($\beta \cdot \omega$, solid line) and for flame normal ($\gamma \cdot \mathbf{n}$, dashed line); gathered in bins of 0.1 in cosine of the angle.

directions because the strain magnitude is weak at the vortex center.

The conceptual picture is that of a stretching vortex with the large strain rate in an annular region outside the vortex core. Thus the large curvature of the flame occurs outside the vortical core, the location where the shearing strain is largest.

4. Conclusions

The implications of this three-dimensional constant-density flame propagation simulation is that detailed chemistry may be simulated in two-dimensional flow because in most of the sample points the flame has a cylindrical shape. In a two-dimensional simulation, there should be a weak out-of-plane strain to represent the three-dimensional stretching effect. This stretching effect counteracts the diffusive nature of viscosity upon the vorticity, and so the vortical core can remain intense and small during the propagation of the flame in the neighborhood of the vortex. Simple single-step, finite-rate reaction were used in the two-dimensional work by Rutland & Ferziger (1989) and that by Ashurst & McMurtry (1989). Detailed chemical kinetic simulations would reveal if curved, strained flames have a different structure than steady-state plane strained flames.

Acknowledgement

Discussions with S. Cant, T. Poinsot, C. Rutland and A. Trouvé during the Summer Program of the Center for Turbulence Research have been very helpful. Work supported by United States Department of Energy, through the Office of Basic Energy Sciences, Division of Chemical Sciences and Center for Turbulence Research, Stanford University & NASA Ames.

REFERENCES

ASHURST, WM. T., CHEN, J.-Y. & ROGERS, M. M. 1987 Pressure gradient alignment with strain rate and scalar gradient in simulated Navier-Stokes turbulence. *Phys. Fluids.* **30**, 3293.

ASHURST, WM. T., KERSTEIN, A. R., KERR, R. M., & GIBSON, C. H. 1987 Alignment of vorticity and scalar gradient with strain rate in simulated Navier-Stokes turbulence. *Phys. Fluids.* **30**, 2343.

ASHURST, WM. T. & MCMURTRY, P. A. 1989 Flame Generation of Vorticity: Vortex Dipoles from Monopoles. *Combust. Sci. and Tech.* **66**, 17.

ASHURST, WM. T., SIVASHINSKY, G. I. & YAKHOT, V. 1988 Flame Front Propagation in Nonsteady Hydrodynamics Fields. *Combust. Sci. and Tech.* **62**, 273.

CANT, R. S., RUTLAND, C. & TROUVÉ, A. 1990 Statistics for laminar flamelet modeling. *Center for Turbulence Research Report CTR-S90.* Stanford University & NASA Ames

KERSTEIN, A. R., ASHURST, WM. T. & WILLIAMS, F. A. 1988 Field equation for interface propagation in an unsteady homogeneous flow field. *Phys. Rev. A.* **37**, 2728.

POPE, S. B., YEUNG, P. K. & GIRIMAJI, S. S. 1989 The Curvature of Material Surfaces in Isotropic Turbulence. *Phys. Fluids A.* **1**, 2010.

RUTLAND, C. & FERZIGER, J. 1989 Interaction of a Vortex and a Premixed Flame, AIAA Paper 89-0127.

Laminar flamelet modeling of turbulent diffusion flames

By W. E. Mell[1], G. Kosály[1], O. Planche[2], T. Poinsot[3], AND J. H. Ferziger[2]

In modeling turbulent combustion, decoupling the chemistry from the turbulence is of great practical significance. In cases in which the equilibrium chemistry model breaks down, laminar flamelet modeling (LFM) is a promising approach to decoupling. This report investigates the validity of this approach using direct numerical simulation of a simple chemical reaction in two-dimensional turbulence.

1. Introduction

Modeling turbulent combustion is a formidable task since the equations satisfied by the mass fractions and temperature are coupled with the Navier-Stokes equations, and the nonlinearity is very strong. The laminar flamelet model (LFM) is a powerful technique for decoupling the chemistry problem from the turbulence problem (Williams 1985, Peters 1984,1989). Our goal was to investigate the validity of LFM in turbulent diffusion flames via direct numerical simulations.

Recent laboratory results of Barlow et al. (1990a,b) offer new insight into the validity of LFM in hydrogen and methane flames. These measurements provide simultaneous point data on species mass fractions and temperature. The interpretation of the data is, however, hindered by lack of simultaneous information on the scalar dissipation field (χ). Information on the latter quantity is of fundamental importance for LFM validity investigations (Bilger, 1989a,b.) Since in direct simulations the scalar dissipation field is calculated along with all other relevant quantities, DNS provides a unique tool for studying LFM validity.

2. Background

In what follows, $Y_i (i = 1, 2, \ldots, N)$ and T stand for species mass fractions and temperature, respectively. Z is the mixture fraction defined, for instance, via element mass fractions and $\chi = 2D\nabla Z \cdot \nabla Z$ is its dissipation (Bilger 1982). The present investigations are restricted to the chemical scheme

$$F + rO \rightarrow (r+1)P.$$

1 University of Washington
2 Stanford University
3 Center for Turbulence Research

The reactants are initially segregated. Since the initial mass fractions of F and O are assumed equal, the stoichiometric value of the mixture fraction is $Z_{st} = 1/(1+r)$. The instantaneous stoichiometric surface x is implicitly defined by $Z(x,t) = Z_{st}$.

LFM can be derived by introducing a local orthogonal coordinate system attached to the instantaneous stoichiometric surface (Peters, 1984). By a change of independent variables, the normal coordinate becomes Z. The other two variables are perpendicular to the mixture fraction coordinate and tangent to the stoichiometric surface. Following Williams (1985), we can write the equation satisfied e.g. by the temperature in these coordinates as

$$\rho\frac{\partial T}{\partial t} + \rho\mathbf{v}_\perp \cdot \nabla_\perp T = w_T + \frac{1}{2}\rho\chi\frac{\partial^2 T}{\partial Z^2} + \nabla_\perp \cdot (\rho D \nabla_\perp T) \qquad (1)$$

$$- \rho D \nabla_\perp \big(\ln|\nabla Z|\big) \cdot \nabla_\perp T.$$

The subscript $\perp$ identifies two-dimensional vectors locally perpendicular to ∇Z. If the reaction takes place in a thin layer in the vicinity of the stoichiometric surface, then the first two terms on the RHS of equation (1) become dominant, i.e.,

$$w_T \cong -\frac{1}{2}\rho\chi\frac{\partial^2 T}{\partial Z^2}. \qquad (2)$$

and, locally, $\chi = \chi(Z,t)$ (Peters, 1984).

The production term (w_T) can be expressed in terms of the variables T and Z. Peters (1984) assumes that in the coordinate system fixed to a point on the instantaneous stoichiometric surface, χ depends on t only through Z and writes the scalar dissipation as

$$\chi = \chi_{st} f(Z), \qquad (3)$$

where χ_{st} is the value at $Z = Z_{st}$. The function $f(Z)$ represents the dependence of χ on Z. In the LFM approximation, eq.(3) is modeled by

$$\chi = \chi_{st} f_l(Z). \qquad (4)$$

where $f_l(Z)$ is the distribution of χ along the stagnation point streamline in laminar counterflow combustion in terms of the coordinates introduced above (Peters, 1984). Eq.(2) is then identical to the ODE satisfied by the temperature along the stagnation point streamline in laminar counterflow (Spalding, 1961). Its solution is, therefore, the laminar one which can be written

$$T = T^l(Z, \chi_{st}). \qquad (5a)$$

The same argument shows that the mass-fractions can be approximated by

$$Y_i = Y_i^l(Z, \chi_{st}). \qquad (5b)$$

Equations (5a,b) can be rewritten using eq.(4) as

$$T = \hat{T}^l(Z,\chi), \quad Y_i = \hat{Y}_i^l(Z,\chi). \tag{6}$$

Equation (6) says that in a turbulent flame T and Y_i depend on $\mathbf{x}$,t *through* Z and χ. While in the turbulence $Z(\mathbf{x},t)$ and $\chi(\mathbf{x},t)$ are random functions, the Z and χ dependence of T and Y_i is modeled identically in turbulent and laminar cases (Peters, 1984).

Several authors (Bilger, 1989a; Kuznetsov and Sabelnikov, 1990) arrive at a similar, but not equivalent, result:

$$T = T(Z,\chi), \quad Y_i = Y_i(Z,\chi). \tag{7}$$

Equation (7) also states that T, Y_i depend on $\mathbf{x}, \mathbf{t}$ through Z, χ. However, it is not assumed that the dependence of T, Y_i on Z, χ is related to laminar flow. For various predictions regarding the functional forms of $T(Z,\chi)$ and $Y_i(Z,\chi)$, refer to the works of Bilger (1989a) and Kuznetsov and Sabelnikov (1990). Physically, the scalar dissipation in eq.(7) represents the influence of the local Damköhler-number (Da_χ) defined in terms of the local turbulent time scale $\tau = 1/\chi$ (Peters, 1984; Pope, 1990). For $\chi \to 0, Da_\chi \to \infty$, therefore, both eqs.(6) and (7) become the equilibrium chemistry result.

Equations (2) and (4) become valid if the flame is "sufficiently thin". (For thin flames $\chi \cong \chi_{st}$.) This means that LFM validity improves with increasing values of the Damköhler (Da) and Zeldovich (Ze) numbers. (Throughout this paper Da denotes the Damköhler-number defined via the initial large eddy time. This Da is a global parameter to be distinguished fromDa_χ, the local parameter defined above.)

It is important to distinguish between the equilibrium (fast) chemistry approach and LFM modeling. LFM modeling is intended to *replace* equilibrium modeling when Da is not large enough to justify use of the latter. A typical LFM application is the modeling of the free-radical superequilibrium close to the nozzle in a H_2/air jet flame (Bilger, 1989a). From a practical point of view, researching LFM validity involves determination of the conditions under which Da is large enough for LFM validity but too small for application of the equilibrium chemistry approach.

In order to derive eq.(2) from eq.(1), one has to assume that the radius of curvature of the flame is much larger than its thickness (L_R). The condition of LFM applicability should compare L_R to another length-scale. Bilger (1989a) suggests that $L_R \ll \eta$ is necessary (η = Kolmogorov-scale, $Sc \cong 1$). Peters (1989) formulates a validity condition which appears not to be related to turbulence length scales. The present work represents a first step in the investigation of LFM validity via DNS.

3. The basic equations. Numerical method

The direct numerical simulations were made using a direct numerical simulation code for reacting flows. The original version (Poinsot and Lele, 1989) was extended to diffusion flames. The Mach-number was kept low ($u_{rms}/c \leq 0.05$) so that dilatation is predominantly due to heat release of chemical reaction. The code solves the

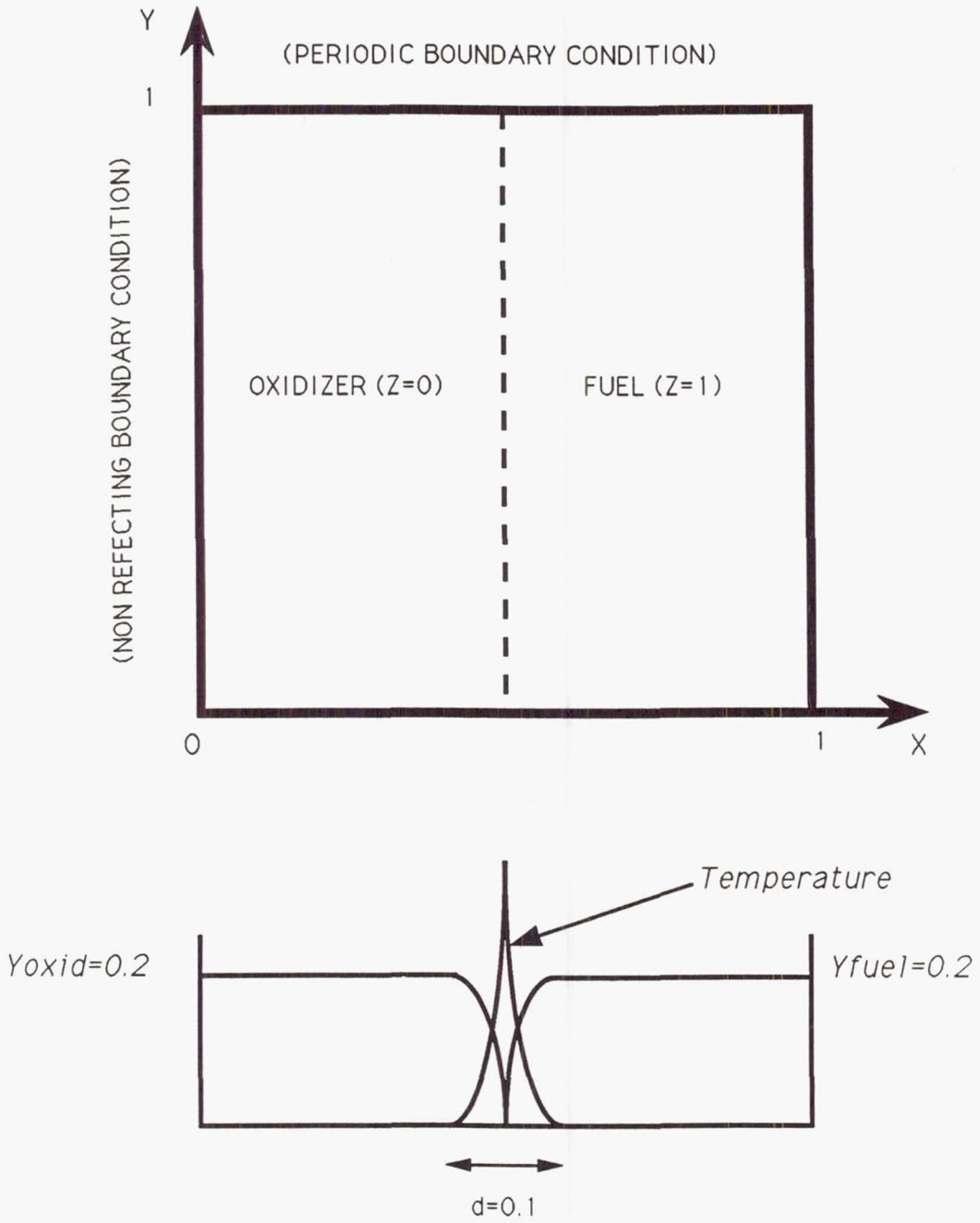

FIGURE 1. Initial scalar field and boundary conditions. a) boundary conditions. b) initial scalar distributions.

full Navier-Stokes equations in 2D using an explicit scheme with accuracy of sixth order in space and third order in time. In the present application, $Sc = Pr = Le = 1$ and $\mu = \mu_o(T/T_o)^b$ where $b = 0$ for constant transport properties and $b = .76$ for variable properties. The chemical scheme is single step and irreversible.

The fluid dynamics equations solved are:

$$\frac{\partial \rho}{\partial t} + \frac{\partial \rho u_i}{\partial x_i} = 0,$$

$$\frac{\partial \rho u_i}{\partial t} + \frac{\partial \rho u_i u_j}{\partial x_i} + \frac{\partial p}{\partial x_i} = \frac{\partial \tau_{ij}}{\partial x_j},$$

$$\frac{\partial \rho h_t}{\partial t} + \frac{\partial \rho u_i (h_t + p)}{\partial x_i} = \frac{\partial u_i \tau_{ij}}{\partial x_j} - \frac{\partial q_j}{\partial x_j} + Ce\dot{w},$$

$$\frac{\partial \rho Y_f}{\partial t} + \frac{\partial \rho u_i Y_f}{\partial x_i} = \frac{\partial}{\partial x_i}(\rho D \frac{\partial Y_f}{\partial x_i}) - \dot{w},$$

$$\frac{\partial \rho Y_o}{\partial t} + \frac{\partial \rho u_i Y_o}{\partial x_i} = \frac{\partial}{\partial x_i}(\rho D \frac{\partial Y_o}{\partial x_i}) - r\dot{w}.$$

All of the notation is standard.

The reaction rate is:

$$\dot{w} = A\rho^2 Y_f Y_o e^{-Ze/T}. \tag{8}$$

The mixture is a perfect gas with constant molar mass and γ (ratio of specific heats)= 1.4. All velocities are non-dimensionalized by the speed of sound in the unburnt gas, and the temperature is non-dimensionalized by $(\gamma - 1)T_0$, where T_0 is the temperature of the fresh gases. The heat release parameter Ce is the heat of reaction per unit mass of fresh gases. Ze is the nondimensional activation temperature. The heat flux is q_j, h_t is the total energy density, and Y_f and Y_o are the mass fractions of fuel and oxidizer. All the calculations are performed on a regular mesh of 271x271 points in a square domain whose side is the reference length.

The code simulates a 2D, isotropic, decaying turbulent velocity field whose initial energy spectrum is determined by the initial value of u_{rms} and the wavelength of the energy containing eddies (k_e).

$$E(k) = \frac{32}{3}\sqrt{\frac{2}{\pi}}\frac{u_{rms}^2}{k_e}(\frac{k}{k_e})^4 \quad exp(-2(\frac{k}{k_e})^2)$$

The initialization of the scalars is performed in two steps. First the analytical solution of the one dimensional diffusion equation with infinitely fast chemistry is used to specify the initial species and temperature distribution. The velocity and scalar fields are initialized after the initial pressure wave has left the domain.

The boundary conditions are periodic in the y direction and non-reflective in the x direction (Poinsot and Lele, 1989). Figure 1 illustrates the initial conditions of the scalars and the boundary conditions. The initial large eddy Reynolds number is 200.

The mixing process in two dimensional turbulence differs from that in three dimensional flow (Lesieur, 1987). This means that caution must be held in extending conclusions drawn from diffusion-flames from 2D studies to 3D. Our results will demonstrate that some important features connected with LFM validity can be captured in 2D. The present 2D studies are preliminary investigations.

There are advantages to 2D simulations of turbulent reacting flows. With the computer facilities presently available, it is not feasible to perform 3D calculations which account for dilatation, complex chemistry, non-unity Lewis-number, and temperature dependent transport coefficients. We believe, therefore, that 2D simulations -if interpreted carefully- can offer valuable insights.

4. Results and Discussion

Figures 2a and 2b are scatter plots of product mass-fraction (Y_p) versus mixture fraction (Z) for a flow without heat release ($r = 1, Z_{st} = 0.5$) for $Da = 5000$ and $Da = 400$, respectively (Da is defined with the initial large eddy time). In the equilibrium chemistry limit, $Y_p = Y_p(Z)$ and $Y_p(Z = 0.5) = 0.2$. (The mass fraction of the diluent is 0.8). The vertical width of the cloud of points and the deviation of the peak of the envelope from 0.2 measure the deviation from equilibrium. As expected, the higher Da case is closer from equilibrium.

The internal structure of the two clouds can be seen more closely in Figs. 3a and 3b. The symbols indicate different values of $\chi/2D$, the scalar dissipation (see legend in Fig. 2a). Fig. 3a exhibits, from top to bottom, a characteristic layering according to the local dissipation. The layers correspond to increasing values of χ . This behavior is plausible since the local Damköhler-number (Da_χ) decreases with increasing scalar dissipation. The behavior in Fig. 3a is consistent with eq.(7). We believe, however, that further research is needed for full corroboration of eq.(7). The layering of the data points is present in Fig. 3b but less conspicuous than in Fig. 3a, which is consistent with Fig. 3b representing a lower Da case.

We now turn to the discussion of whether our data are consistent with the LFM prediction of eq.(6). In order to investigate this problem, one has to compute the mass fractions along the stagnation point streamline in laminar counterflow. In the isothermal, incompressible case (r=1) the equations read (Spalding, 1961):

$$\frac{1}{2}\chi\frac{d^2Y_F^l}{dZ^2} = AY_O^lY_F^l,$$

$$\frac{1}{2}\chi\frac{d^2Y_O^l}{dZ^2} = AY_O^lY_F^l, \tag{9a}$$

$$\frac{1}{2}\chi\frac{d^2Y_P^l}{dZ^2} = -2AY_O^lY_F^l,$$

$$\chi = \chi_{st}exp\{-2[erfc^{-1}(2Z)]^2\}. \tag{9b}$$

Here A is the reaction rate constant appearing in eq.(8) . The strain rate a ($u = ax, v = -ay$) is related to χ_{st} via $a = \pi\chi_{st}$.

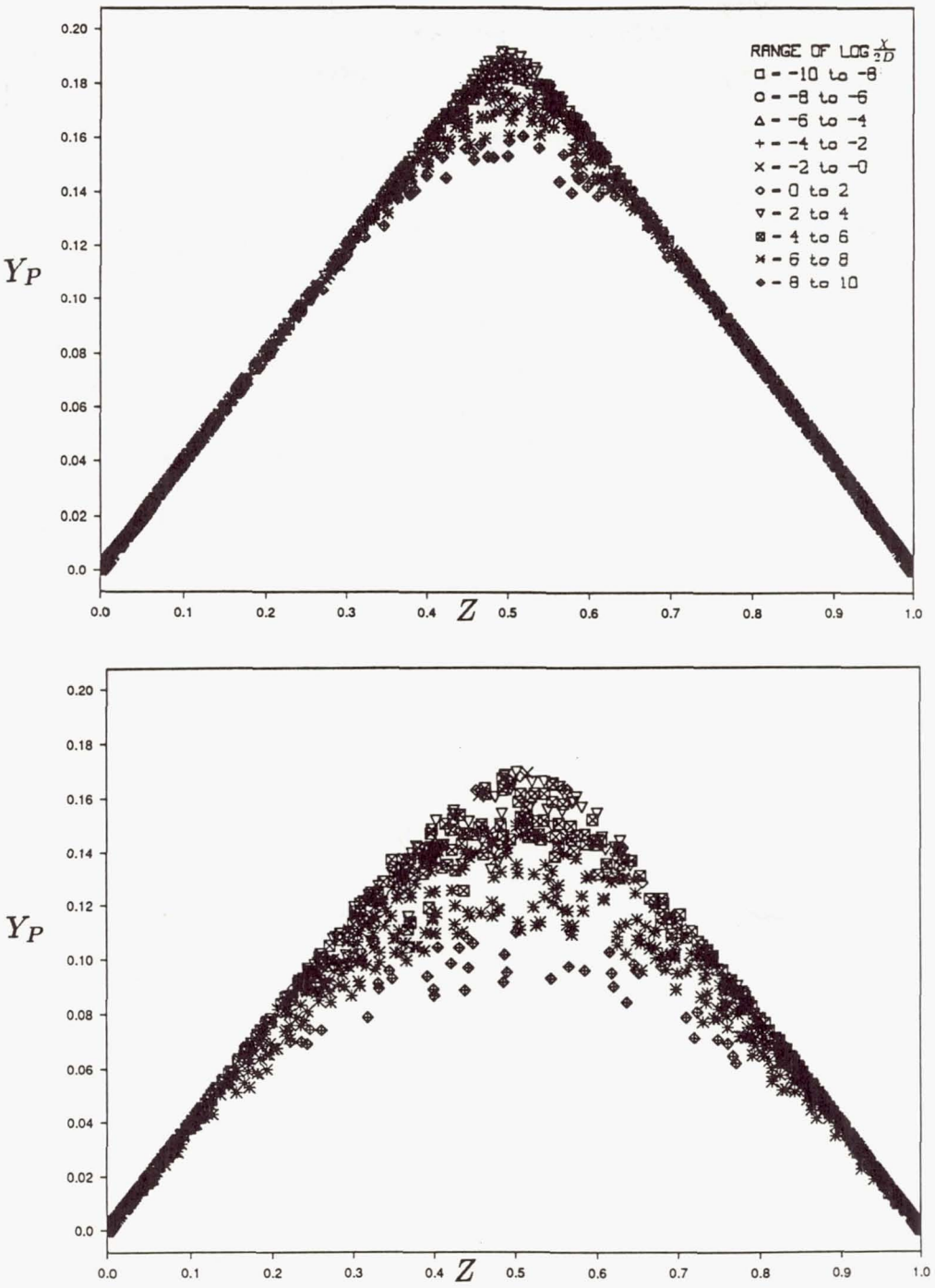

FIGURE 2. Product mass fraction vs. mixture fraction for different values of $\frac{\chi}{2D}$ at $\frac{tu}{\ell} = 0.5$ with r = 1. (Here $\frac{\ell}{u}$ is the initial large eddy time.) (a) $Da = 5000$, legend shows the values of $\frac{\chi}{2D}$ (b) $Da = 400$.

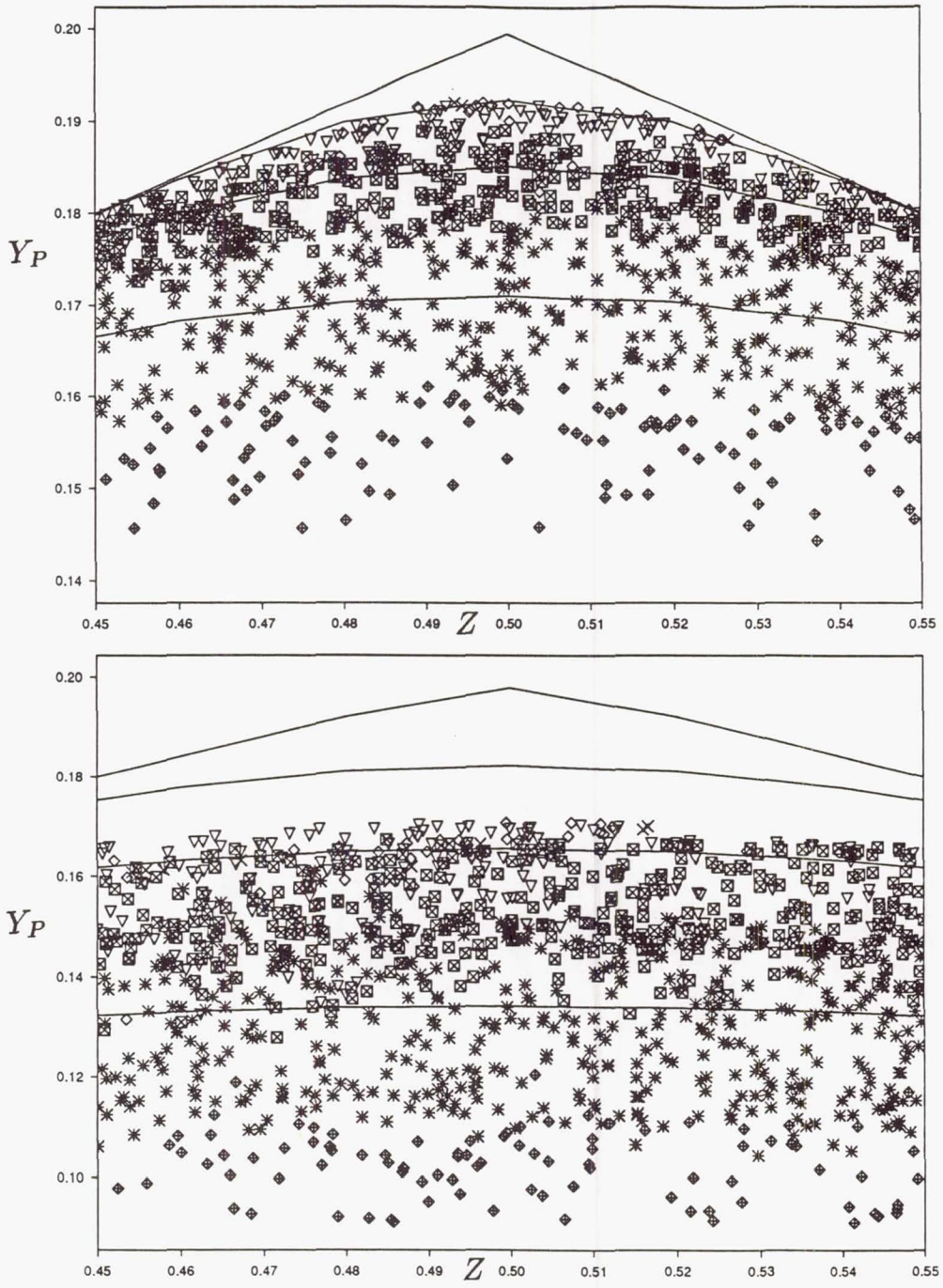

FIGURE 3. Product mass fraction vs. mixture fraction for the cases in Figure 2 near $Z = Z_{st} = 0.5$ (a) $Da = 5000$, (b) $Da = 400$. The lines show the laminar counterflow prediction $Y_P^l(Z, \chi)$ for different values of $\chi/2D$. The bottom, middle and top lines correspond to $\chi/2D = e^8$, $\chi/2D = e^6$, $\chi/2D = e^4$ respectively.

Solution of eqs.(9a,b) with boundary conditions at $Z = 0$ and $Z = 1$ provide Y_O^l, Y_F^l, Y_P^l versus Z for a given value of χ_{st}. In order to compare the laminar counterflow predictions to the Fig. 3a,b data, we need Y_P^l versus Z parameterized with χ rather than χ_{st}. $\hat{Y}_P^l(Z,\chi)$ can be generated from $Y_P^l(Z,\chi_{st})$ from eq.(9b) which computes χ from a given pair Z, χ_{st} pair.

The lines in Figs. 3a,b indicate $\hat{Y}_P^l(Z,\chi)$ for different values of $\chi/2D$. According to the LFM approximation, the laminar result for $\chi/2D = e^8$ should approximately coincide with the boundary between the lowest and the next lowest layer. Contrary, all the laminar lines lie *above* the boundaries where LFM expects them to appear. The deviation between the data and the LFM expectation is smaller in Fig. 3a than in Fig. 3b. Figure 4 shows the reaction rate contours for $Da = 5000$ and $Da = 400$. Naturally, the flame is thicker at lower Da. This accounts for the worse LFM prediction in Fig. 3b than in Fig. 3a. However, the reaction regions in both cases are much wider than the smallest turbulence scale in these flows (Lesieur, 1987). Bilger's (1989a) validity criterion is not satisfied; there are turbulent eddies within the flame. The deviations from laminar behavior are, therefore, not unexpected. While Fig. 3 shows that LFM predictions are not in perfect accord with the data, it also shows that the laminar model may contain a sufficient portion of the truth to predict the average mass fraction with reasonable accuracy.

It is important to distinguish clearly between *physical* and *predictive* validity. Physical validity means that the turbulent flame indeed consists of laminar flamelets; predictive validity means that the model is robust enough to predict correct averages. The discussion based on Figs. 3a,b concerns the physical validity of the model. One measure of the predictive validity is the correlation between the average product mass-fraction ($< Y_P >_t$) and its LFM estimate:

$$\int_0^\infty \int_0^1 Y_P^l(Z,\chi) P(Z,\chi;t) dZ d\chi.$$

Here $P(Z,\chi;t)$ is the joint pdf of the mixture fraction and its dissipation. Investigation of the robustness of the model is an important task for the future.

LFM should improve with increasing Damköhler number. Since for any given value of A in eq.(8), the Damköhler number increases in time, one expects better agreement between LFM and the data at later times. Since LFM is intended to replace equilibrium chemistry modeling, it is critical to investigate whether LFM becomes valid *before* the equilibrium limit sets in.

Figure 5 shows Y_P vs. Z for different values of $\chi/2D$ at $Da = 5000$ for a case with $r = 3$, ($Z_{st} = 0.25$) . Since the initial distribution of the scalars is the same as before (cf. Fig.1), globally the fuel and oxidizer are not in stoichiometric proportion. The layering which appears in Fig. 3a is also present here. Comparison of Fig. 5 to Fig. 3a shows, however, that the highest values of χ are less important when $r \neq 1$ (Note, for instance, the different number of points in the $e^8 < \chi/2D < e^{10}$ interval in the two graphs). To clarify this result, in Fig. 6 we show the joint pdf of Z and χ at approximately the time of the previous figures. For this no heat release case, the instantaneous spatial distributions of the mixture fraction and the dissipation

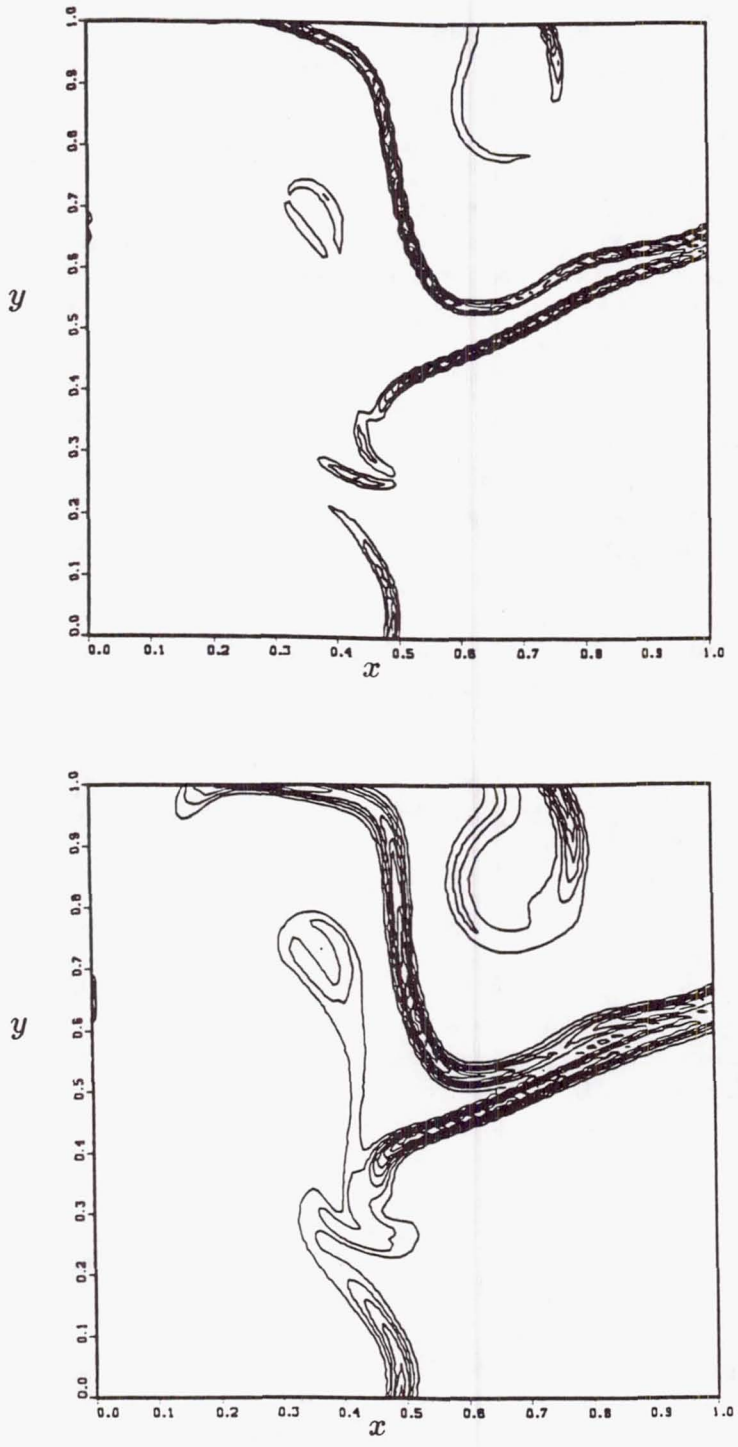

FIGURE 4. Typical reaction rate contours for the two zero heat release cases, ($\frac{tu}{\ell} = .5$) (a) $Da = 5000$ and (b) $Da = 400$.

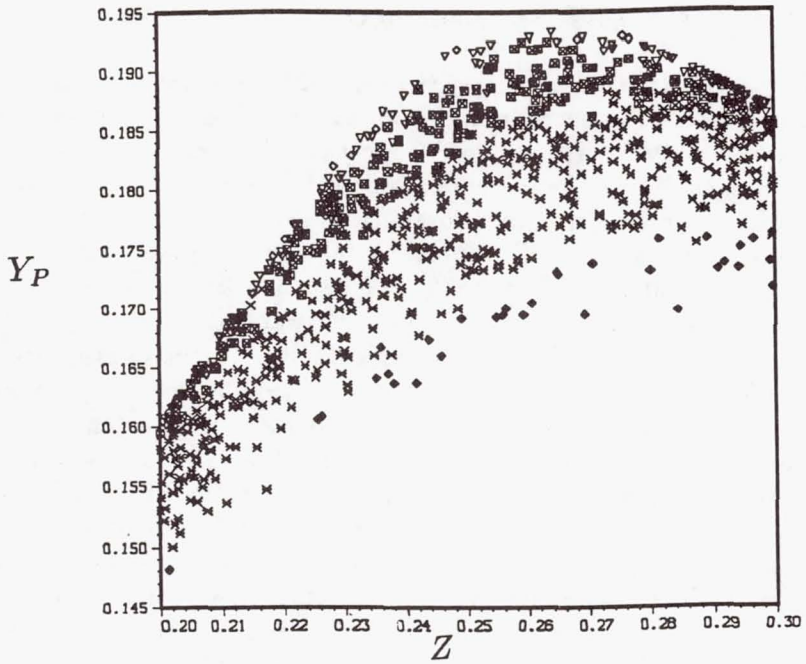

FIGURE 5. Product mass fraction vs. mixture fraction for different values of $\frac{\chi}{2D}$ for the $r = 3, Z_{st} = .25$ case ($\frac{tu}{\ell} = 0.5$). $Da = 5000$.

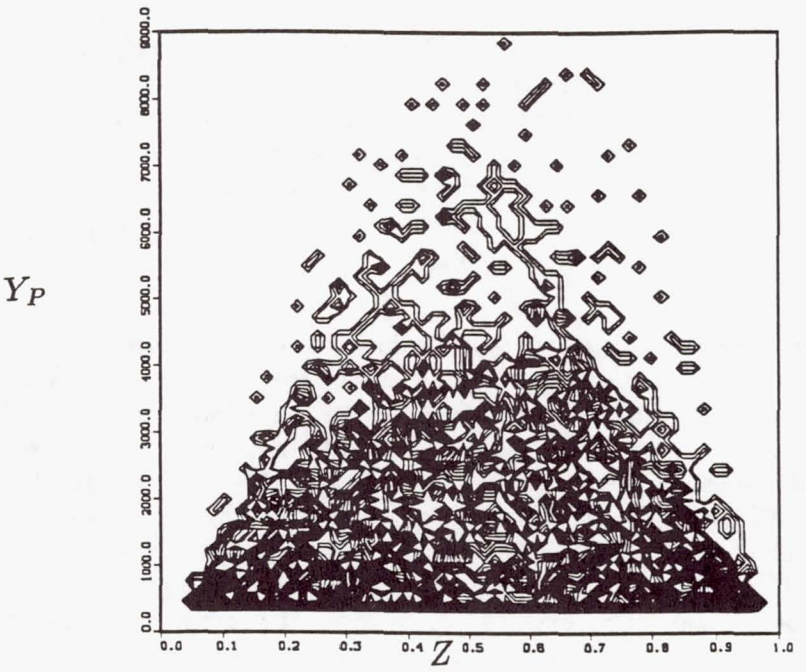

FIGURE 6. Contour plot of the joint probability density function of Z and χ at $\frac{tu}{\ell} = 0.5$.

are independent of the chemistry. The joint pdf of Z and χ is independent of the chemistry as well.

Figure 6 demonstrates that the mixture fraction and its dissipation are not independent random variables. Higher values of χ appear with higher probability near $Z = 0.5$ than near $Z = 0.25$. The reduced importance of the highest dissipation values in Fig. 5 vis-à-vis Fig. 3a is, therefore, due to the change in Z_{st}. This means that the Damköhler number within the reaction zone is larger for $Z_{st} = .25$ than for $Z_{st} = .5$. This effect may have an important influence on LFM validity. Since for real flames, Z_{st} is usually quite small ($Z_{st} = 0.0284$ for H_2/air, $Z_{st} = 0.055$ for CH_4/air), further investigation of this issue is clearly warranted.

Figure 7a shows a scatter plot of product mass fraction versus mixture fraction for a zero heat release case with $Da = 260$ and $Z_{st} = 0.5$. Fig. 7b exhibits a corresponding compressible heat release case ($Ce = 3, Ze = 7$). The chemical rate constant A used in the case shown in Fig. 7b is such that $Da(T_c) = 260$, where T_c is the adiabatic flame temperature. Since $T \leq T_c$ and $Da(T)$ is proportional to $exp\{-\frac{Ze}{T_c}\frac{T_c}{T}\}$, the heat release case is farther from equilibrium chemistry than the no heat release case. The most striking difference between the two cases lies in the influence of the high dissipation values. Dilatation due to the exothermicity evidently diminishes the gradients, thereby decreasing the probability of high values of χ (Spalding, 1961; McMurtry, Riley and Metcalfe, 1989). The probability density functions shown in Fig. 8 further demonstrate this effect. It seems, therefore, that heat release increases the local Damköhler number within the reaction layer and thereby enhances LFM validity. While this effect can be important, its investigation in two dimensions is questionable. The distribution of the scalar dissipation is strongly dependent on the turbulent mixing process. This effect should be investigated further using a 3D simulation code which accounts for dilatation.

The case shown in Fig. 7b accounts for dilatation due to heat release but does not consider the temperature dependence of the transport coefficients. Figure 9 exhibits a case with temperature dependent viscosity otherwise identical to the Fig. 7b case. The flow is less turbulent which reduces the largest values of χ.

5. Conclusions

The incompressible results indicate that the deviation of the species mass fractions from their equilibrium behavior depends on $\mathbf{x}$ and t through the Z and χ variables. In the LFM approximation, the dependence of the mass fraction on Z and χ is modeled via laminar counterflow. The data for a 2D turbulent non-premixed flow show systematic deviations from the LFM predictions. However, the results show that LFM modeling improves as the width of the reaction layer becomes thinner.

It was also found that the maximum scalar dissipation in the reaction zone decreases as Z_{st} decreases. Since lower values of the dissipation correspond to higher values of the local Damköhler-number ($Da_\chi = A/\chi$), it is expected that LFM will improve with decreasing Z_{st}. This effect is desirable since Z_{st} is quite small in real flames.

It is important to realize that LFM may predict the averages accurately even when

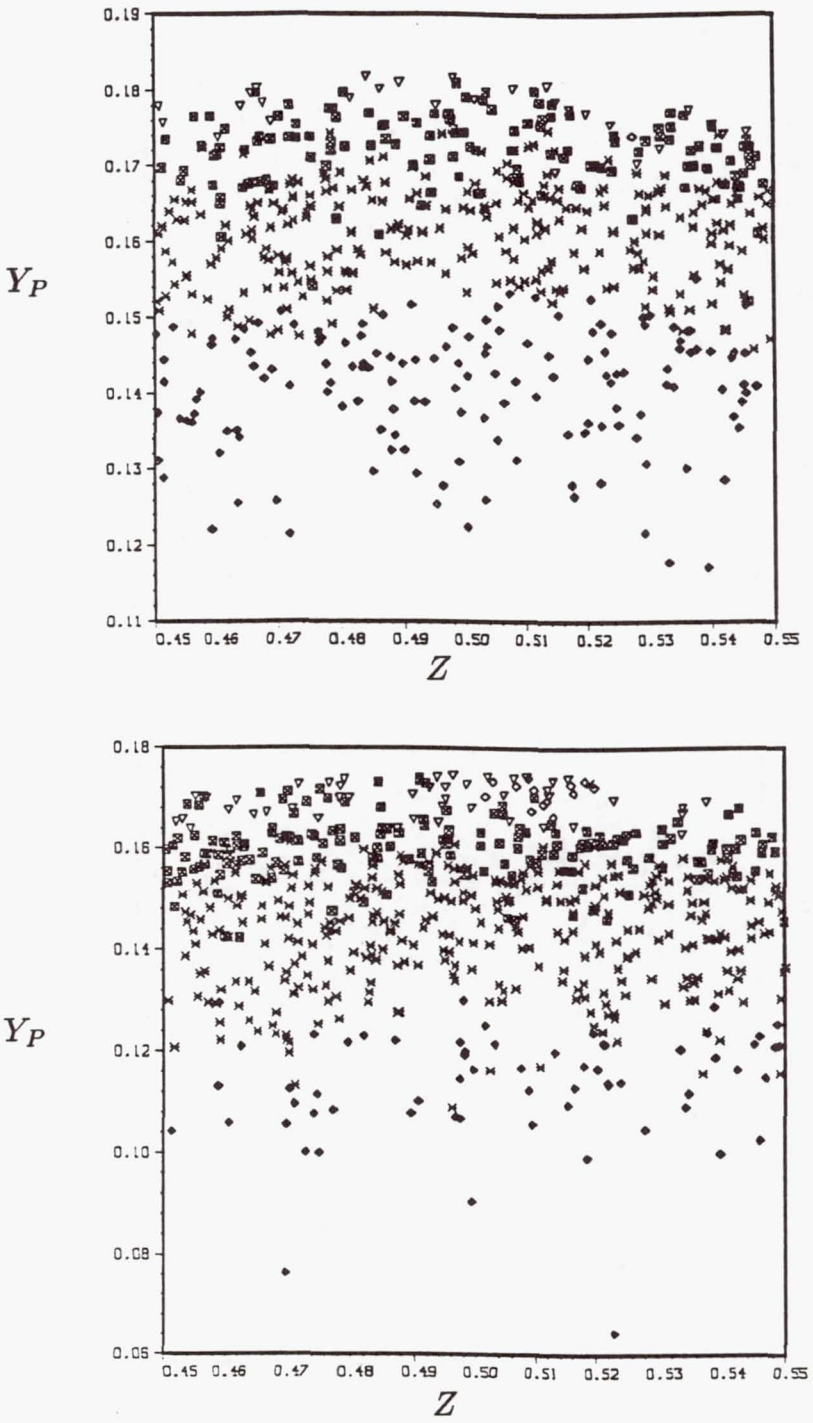

FIGURE 7. Product mass fraction vs. mixture fraction ($Da \cong 260, \frac{tu}{\ell} = 0.5$) (a) without heat release, (b) with heat release.

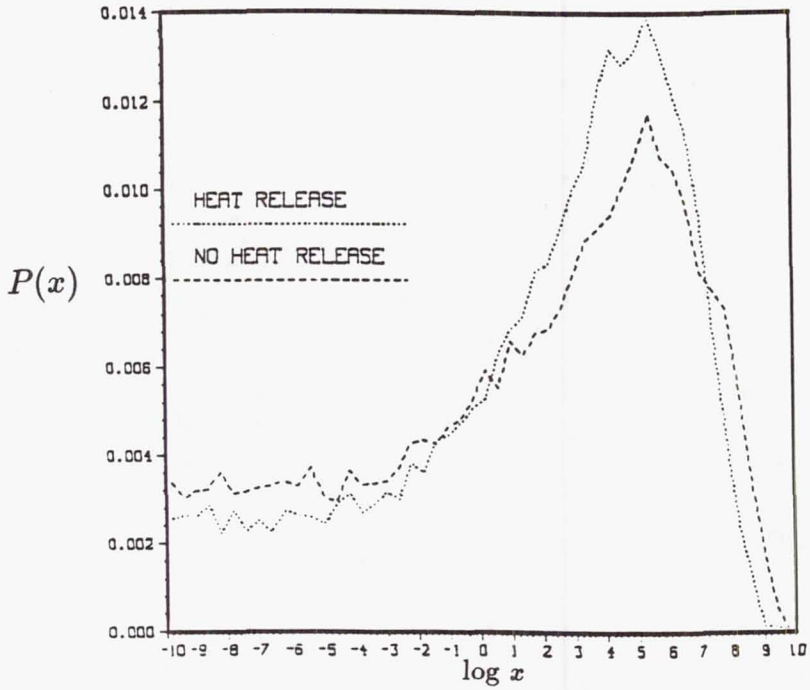

FIGURE 8. Probability density function of the scalar dissipation for the two cases of Figure 7.

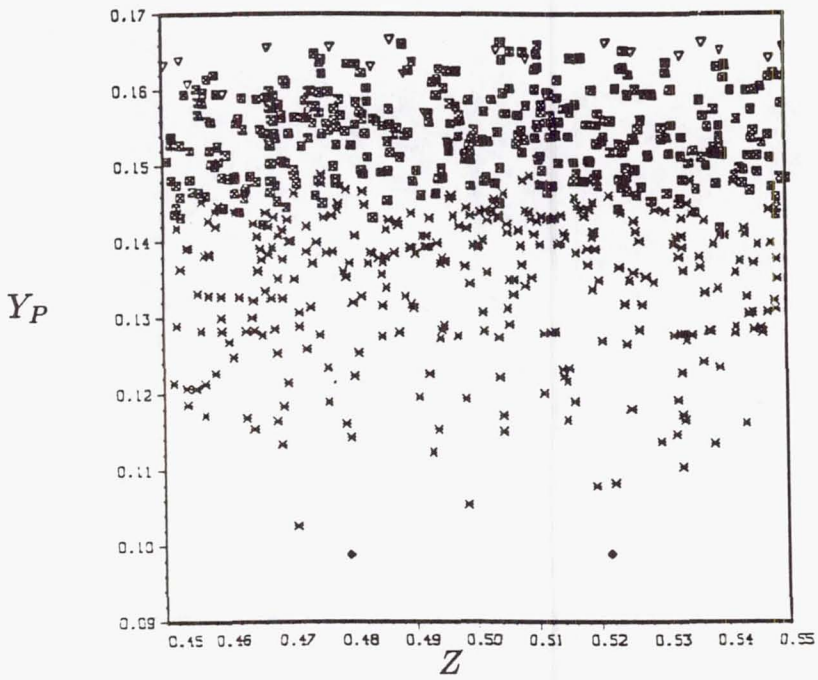

FIGURE 9. Product mass fraction vs. mixture fraction for a case with heat release and temperature dependent viscosity ($Da \cong 260, \frac{tu}{l} = 0.5$).

the turbulent flame does not consist entirely of laminar flamelets. The investigation of the robustness of LFM is one of our major future tasks.

Comparison of the incompressible results to compressible high-heat release results confirms the expectation that dilatation smooths the gradients and thereby diminishes the probability of appearance of large values of χ. This increases the local Damköhler number in the reaction zone. While this effect may enhance the validity of LFM, we believe its study requires 3D investigation.

Acknowledgement

The contribution of Mr. Christopher Montgomery (UW) is appreciated.

REFERENCES

BARLOW, R. S., DIBBLE, R. W. CHEN, J.-Y., & LUCHT, R. P. 1990a Effect of Damköhler number on superequilibrium OH concentration in turbulent nonpremixed jet flames. *Combustion and Flame.* in press.

BARLOW, R. S., DIBBLE, R. W., STARNER, S. H., & BILGER, R. W. 1990b Piloted diffusion flames of nitrogen-diluted methane near extinction: OH measurement. *Twenty-Third Symposium (International) on Combustion.*

BILGER, R. W. 1982 Turbulent flows with nonpremixed reactants. *Turbulent Reacting Flows.* (P. A. Libby, F. A. Williams, eds.), Springer–Verlag, 65-113.

BILGER, R. W. 1989a The structure of turbulent non premixed flames. *22nd Symp. (Intl.) Combustion,* 475.

BILGER, R. W. 1989b Turbulent diffusion flames. *Ann. Rev. Fluid Mech.* **21,** 101.

KUZNETSOV, V. R., & SABELNIKOV, V. A. 1990 *Turbulence and Combustion.* Hemisphere Publishing Co.

LESIEUR, M. 1987 *Turbulence in Fluids.* Martinus Nijhoff Publishers

MCMURTRY, P. A., RILEY, J. J. & METCALFE, R. W. 1989 Effects of heat release on the large scale structures in turbulent mixing layers. *J. Fluid Mech.* **199,** 297.

PETERS, N. 1984 Laminar diffusion flamelets models in non-premixed turbulent combustion. *Prog. Energy Combust. Sci.* **10,** 319.

PETERS, N. 1989 Length scales in laminar and turbulent flames. *Numerical Approaches to Combustion Modeling.* (E.S. Oran & J. P. Boris, eds.), to appear.

POINSOT, T. & LELE, S. 1989 Boundary Conditions for Direct Simulation of Compressible Viscous Reacting Flows. *CTR Report No. 102.* Center for Turbulence Research, NASA Ames Research Center/Stanford University

POPE, S. B. 1990 "Computations of Turbulent Combustion: Progress and Challenges", Plenary Lecture. *23rd Symp. (Intl.) Combustion.*

SPALDING, D. B. 1961 *Journal of the American Rocket Society.* **31,** 763.

WILLIAMS, F. A. 1985 *Combustion Theory.* Benjamin-Cummings, 2nd Edition.

Statistics for laminar flamelet modeling

By R. S. Cant[1] & C. J. Rutland[2] & A. Trouvé[3]

Statistical information required to support modeling of turbulent premixed combustion by laminar flamelet methods is extracted from a database of the results of Direct Numerical Simulation of turbulent flames. The simulations were carried out previously by Rutland (1989) using a pseudo-spectral code on a three-dimensional mesh of 128 points in each direction. One-step Arrhenius chemistry was employed together with small heat release. A framework for the interpretation of the data is provided by the Bray-Moss-Libby model for the mean turbulent reaction rate. Probability density functions are obtained over surfaces of constant reaction progress variable for the tangential strain rate and the principal curvatures. Further results reveal details of the interaction between strain and curvature. New insights are gained which will greatly aid the development of modeling approaches.

1. Introduction

It is widely recognized that in most cases of practical interest premixed turbulent combustion occurs in the flamelet regime, in which all chemical reaction is confined to thin, highly-wrinkled interfaces separating unburned reactants from fully-burned products. When the thickness of the interface is smaller than the smallest length scales present in the embedding turbulence the internal structure is that of a laminar flame subjected to the effects of straining and curvature. Models exploiting the laminar flamelet approach have been available for some time and have achieved some success in the representation of experimental data. Among these is the Bray-Moss-Libby model (Bray, Moss and Libby, 1985; Cant and Bray, 1988) in which the laminar flamelet approach is used to build up a formalism capable of simplifying the closure of a full second-moment transport model. A consequence of the strict application of the laminar flamelet approximation is that the model for the mean turbulent reaction rate becomes decoupled from that for the turbulent transport and may be considered as an essentially separate modeling problem.

Information required for the reaction rate model includes the behavior of the flame surface area and the response of the laminar flamelet chemistry under the influence of strain and curvature. A balance equation for the former quantity is currently the subject of much modeling activity (Cant, Pope and Bray, 1990; Candel and Poinsot, 1990) while the latter is obtained in idealized circumstances using full-chemistry laminar flame calculations. The results of such calculations may be stored in a

1 Cambridge University Engineering Department, Cambridge, U.K.
2 University of Wisconsin-Madison
3 Center for Turbulence Research

laminar flamelet library for later interpolation by a turbulent model code (Cant, Rogg and Bray, 1990). Once again, the parameterization of the library requires that the strain and curvature be well characterized in turbulent flows of interest.

Experimental techniques are not yet sufficiently advanced to probe a flow field in three dimensions for the velocity and for indicators of the chemistry, but Direct Numerical Simulations offer the possibility for complete information albeit on small samples of the field at low Reynolds numbers. Additional compromises are necessary in large-scale sampling where the main objective is to resolve the flame to a degree sufficient to measure its response to turbulence (Rutland, 1989). The limitations of Direct Simulation do not present a serious obstacle where the information required relates essentially to the small scales. This is the case in flamelet combustion where the flame thickness is by definition smaller than the smallest scales present in the embedding turbulence and small-scale straining and curvature are expected to play an important role. This view is supported by the Direct Simulation results of Pope (1989,1990) for the straining and curvature of material surface elements in a turbulent flow. The present calculations are similar but make use of a fully-connected flame surface with chemical reaction and a finite propagation speed.

2. Model formulation

The Bray-Moss-Libby model formalism may be divided into two distinct parts linked through the consistent application of the laminar flamelet approximation. The transport model involves first-moment equations for pressure (continuity), momentum and reaction progress variable together with a full second-moment closure involving separate balance equations for the six independent Reynolds stress components and for the three components of the Reynolds flux of reaction progress variable. Details of the development and application of the transport model may be found in Bray, Moss and Libby (1985) and in Cant and Bray (1988). The model for the mean turbulent reaction rate model is based on the flamelet expression

$$\rho_R S_L^0 I_0(a,h)\Sigma$$

where Σ is the flamelet surface area per unit volume and $\rho_R S_L^0 I_0$ is the reaction rate per unit surface area composed of the unburned density ρ_R, the unperturbed laminar flame speed S_L^0 and a correction factor $I_0(a,h)$ accounting for the effects on the laminar flame speed of strain a and curvature h. A balance equation for Σ based on an exact equation (Pope, 1988; Candel and Poinsot, 1990) and consistent with the remainder of the model is currently under development (Cant, Pope and Bray, 1990). For the moment this quantity is modelled by an exact expression derived by considering the spatial analogue to a time series obtained by measuring instantaneous progress variable at a fixed point in the flame brush. A square-wave is formed by the transitions between burned and unburned states encountered in passing along a mean contour of progress variable superimposed on a single realization. The expression is (Bray, Libby and Moss, 1984)

$$\Sigma = \frac{g\bar{c}(1-\bar{c})}{\bar{\sigma}_y \hat{L}_y}$$

where $\tilde{c}$ is the mean progress variable, g is a constant derived from the pdf of crossing lengths and $\bar{\sigma_y}$ is the mean cosine of the angle between the mean contour and the instantaneous flame at the crossing point. The length scale $\hat{L}_y$ is the integral length scale of the flamelet crossing process and may be interpreted as the principal large length scale of the flame.

Modeling of the reaction rate per unit surface area currently involves the use of a laminar flamelet library (Cant, Rogg and Bray, 1989) containing S_L^0 as a function of pressure and reactant temperature, and I_0 as a function of the strain rate a_T in the plane of the flame. The data for S_L^0 and I_0 has been obtained by calculations of one-dimensional laminar flames in a fresh-counter-to-burnt counterflow geometry using full chemical mechanisms. It is implicitly assumed in the present model that strain alone is sufficient to characterize the combined effects of strain and curvature on the laminar flamelet. The local mean strain rate is modelled using the conventional expression

$$a \propto \left(\frac{\tilde{\varepsilon}}{\nu}\right)^{\frac{1}{2}}$$

where the mean viscous dissipation $\tilde{\varepsilon}$ is obtained from a standard balance equation and ν is the viscosity in the reactants. Libraries have been assembled for methane and propane over a range of conditions and model calculations have been carried out. Preliminary comparison with experiment is encouraging (Bray, 1990).

Areas in which Direct Simulation results are likely to prove particularly valuable are in the characterization of the strain on the flame surface both for modeling of Σ and for controlling the parameterization of the flamelet libraries. Similarly, information on the curvature of the flame surface is required to assist in the modeling of area creation and destruction by propagation, and to assess the extent to which pure curvature effects contribute to the laminar flame response.

3. Datasets and Postprocessing

Data available at CTR includes several large sets of results obtained from direct simulation of the propagation of a premixed flame in isotropic turbulence (Rutland, 1989). The simulations were carried out in three dimensions on a 128^3 grid using a pseudo-spectral method with periodic boundary conditions. Two flames were started back-to-back near a central plane of the grid and were allowed to propagate outwards. One-step Arrhenius kinetics were employed and near-zero heat release was assumed. The turbulence was allowed to decay naturally and the simulation was terminated when either the flames had reached the edge of the domain or the turbulence integral length scale had grown too large. Considerable distortion of the initially planar flames was observed, and the turbulent flame speed was found to rise rapidly to a maximum value before decaying in time with the background turbulence.

The datasets were made available together with a skeleton postprocessing program written in the local language Vectoral. Further postprocessing software was written in both Vectoral and Fortran and a powerful tool was developed for the extraction of relevant statistical data.

4. Results and discussion

Results were extracted from individual datasets chosen from four separate runs of the pseudo-spectral code denoted by Rutland (1989) as Cases 1 to 4 in order of rising initial u'. In all of these the domain Reynolds number was set to 30, the unperturbed laminar flame speed was 0.39 and the unperturbed laminar flame thickness was 0.45. The list of cases considered is:

Case	1,	set	g:	Re_λ	=	1.9,	Ka	=	0.18,	u'/S_L^0	=	0.26
Case	2,	set	g:	Re_λ	=	5.2,	Ka	=	0.64,	u'/S_L^0	=	0.79
Case	2,	set	l:	Re_λ	=	4.2,	Ka	=	0.24,	u'/S_L^0	=	0.43
Case	3,	set	m:	Re_λ	=	7.2,	Ka	=	0.73,	u'/S_L^0	=	0.97
Case	3,	set	p:	Re_λ	=	6.4,	Ka	=	0.41,	u'/S_L^0	=	0.72
Case	4,	set	p:	Re_λ	=	8.6,	Ka	=	0.75,	u'/S_L^0	=	1.10

Visualization of the flame surfaces in three dimensions revealed the extent of the wrinkling. The periodic boundary conditions ensured that the surfaces of mean progress variable were planes oriented perpendicular to the direction of propagation and the locations $x_{mean}(\bar{c} = \bar{c}^*)$ of these planes were found for $\bar{c}^* = 0.1$, 0.3, 0.5, 0.7 and 0.9 during the first pass through the data. A second pass was then made to localize points on the instantaneous flame surface $x_s(c = c^*)$ for the same values of *instantaneous* progress variable. This produced a list of points on the surface spaced regularly in the plane perpendicular to the direction of mean propagation and randomly in the propagation direction. Quantities of interest were interpolated onto the flame surface points using cubic splines, and statistics were obtained on the surface with a sample size of at least 128^2 points.

4.1 Square Waves

The intersection of each mean plane with the instantaneous flame surface (defined by the location of the maximum laminar reaction rate) produced a two-dimensional square wave of progress variable 128^2 points in extent. Each line in the mean plane produced a one-dimensional square wave, all such lines being equivalent due to isotropy. Unfortunately the number of flame crossings in each mean plane was severely limited in all Cases (max. 8 per line, mean about 2) and it was not possible to obtain a reliable estimate of $\hat{L}_y$ by autocorrelation. A similar restriction applies to the collection of statistics of burned (or unburned) packet sizes. Insufficient numbers of such packets precluded the formation of a pdf of packet length and hence the estimation of g, but statistics of the crossing direction $\bar{\sigma}_y$ were obtained, indicating values of $\bar{\sigma}_y$ ranging from 0.37 for Case 4, set p to 0.87 for Case 1, set g, but with only weak dependence on mean progress variable. This is in agreement with the weakly-turbulent Bunsen flame data of Chew (1989) who obtained $\bar{\sigma}_y$=0.5 independent of progress variable. The inability to collect large-scale statistics is a reflection of the poor large-scale sampling inherent in the Direct Simulations and does not represent a serious limitation since these statistics are among the most easily obtained from experiment. In contrast the three-dimensional direction $\bar{\sigma}_y$ is

extremely difficult to obtain experimentally and is found quite naturally here.

4.2 Strain rate

The rate-of-strain tensor s_{ij} on the flame surface was evaluated from velocity derivatives taken in spectral space, and the tangential strain rate a_T in the flame surface was obtained by rotating the tensor to align the 3-direction with the flame normal. A pdf of tangential strain is shown in Figure 1 for Case 3, set p. The strain axis is normalized by the Kolmogorov time-scale and the pdf reveals that the mean strain is positive, having a value of about $0.28/\tau_\eta$ independent of progress variable. There is also very significant probability of negative straining (compression) of the flame. Variation of the normalized pdf with Reynolds number is slight.

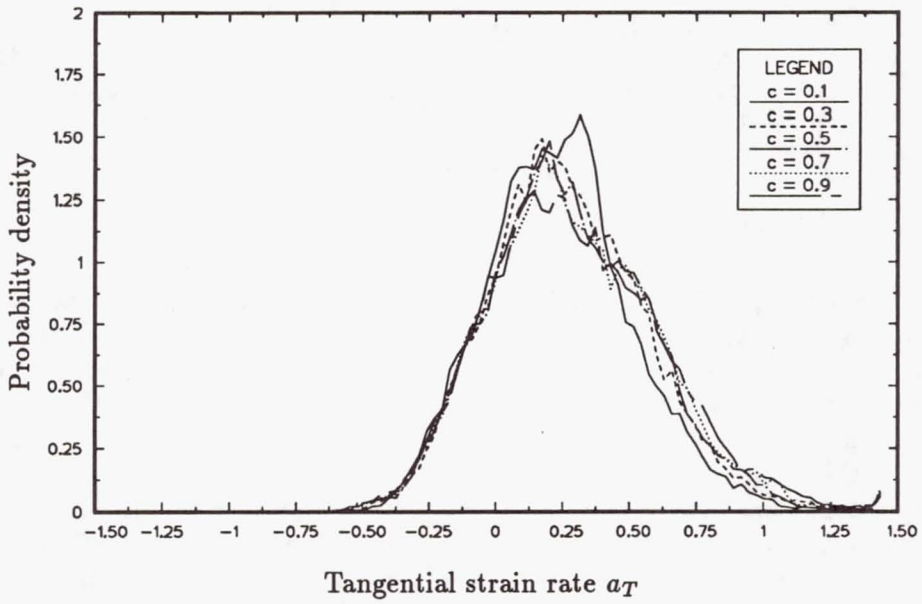

FIGURE 1. Pdf of tangential strain rate a_T. Case 3, set p.

These results agree well with those of Pope (1990) and are of fundamental importance in modeling.

4.3 Curvature

Flame surface curvature was calculated by forming the tensor of the derivatives of the normal to the surface $N_{i,j}$ and rotating it to align the 3-direction with the normal. Solution of the eigenvalue problem in the plane then yields the two principal curvatures h_1 and h_2. Positive curvature here is in the sense of convex towards the reactants. The mean curvature h is plotted in Figure 2 for Case 2, set l and shows a slight skewness towards positive curvature although the mean is zero. This may be interpreted as a propagation effect, with positively-curved wrinkles growing while negatively-curved wrinkles shrink to the minimum allowed by diffusion. The

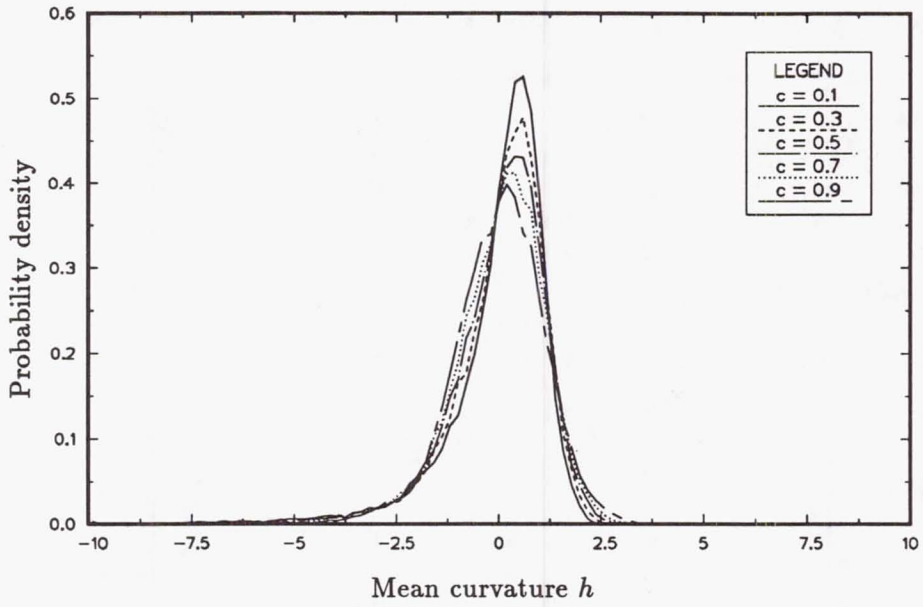

FIGURE 2. Pdf of mean curvature h. Case 2, set 1.

curvatures corresponding to the inverse flame thickness $1/\delta_L$ and to the inverse Kolmogorov scale $1/\eta$ are indicated.

There appears to be some systematic variation with progress variable leading to narrower pdf's near the front of the flame. Again, there is little variation between cases of different Reynolds number.

A slightly different perspective is given by Figure 3 which shows the curvature shape factor defines as $s_h = h_l/h_u$ where h_l is the smaller of the two principal curvatures by magnitude and h_u is the other. Then $s_h = 1$ denotes spherical curvature, $s_h = 0$ denotes cylindrical curvature and $s_h = -1$ denotes spherical saddle points. Evidently cylindrical curvature predominates and this is true for all Cases considered, as well as for material surfaces at much higher Reynolds number (Pope, 1989). Spherical curvature simply does not occur, while spherical saddle points occur only with relatively small probability. The implication for modeling is that only single (or mean) curvature needs to be considered in the treatment of laminar flamelets.

4.4 Interaction between strain and curvature

Strain and curvature do not occur in isolation and their interaction is illustrated in Figure 4 as contours of their joint pdf taken from Case 3, set p for progress variable 0.5.

Maximum strain is found where the curvature is zero, while maximum positive and negative curvature occurs near where the strain is zero. Strain and curvature occur together only at moderate values of both. Further illustration is provided by Figure 5 which shows the cosine of the angle θ_{sh} between the direction of maximum

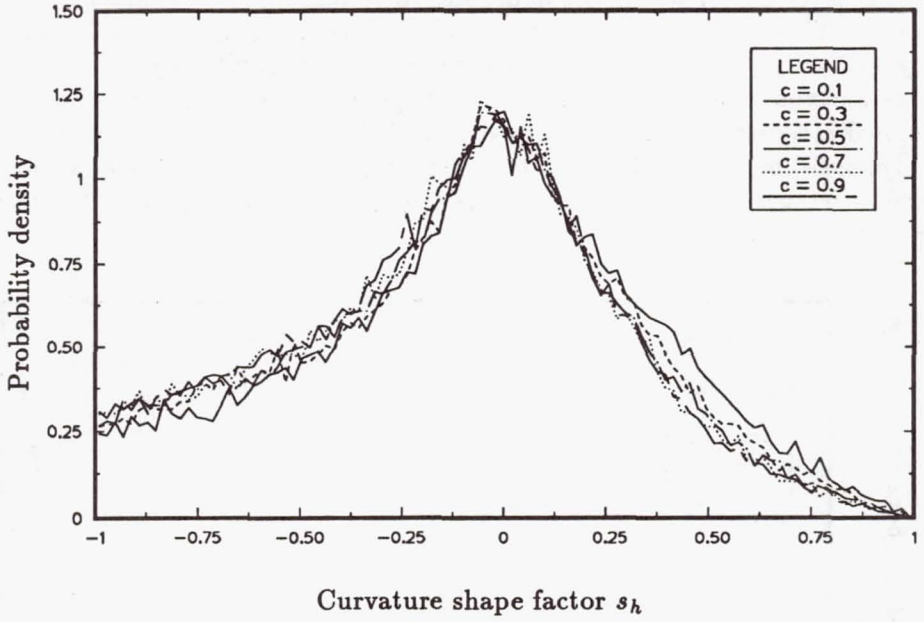

FIGURE 3. Pdf of curvature shape factor s_h. Case 4, set p.

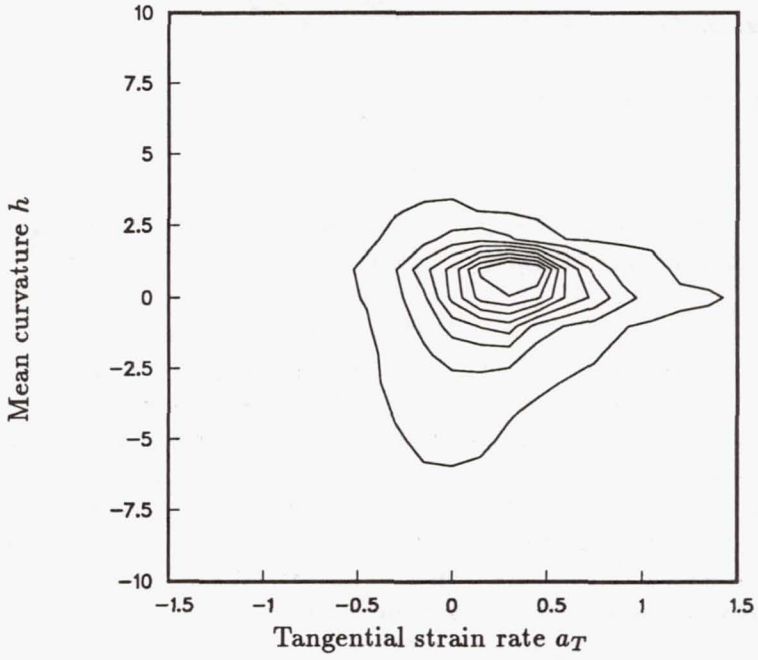

FIGURE 4. Joint pdf of mean curvature h and tangential strain rate a_T. Case 3, set p.

C-4

strain in the tangent plane of the flame and the direction associated with minimum curvature. There is a high probability of alignment which appears to indicate that the cylindrically curved portions of the flame are being pulled out by strain. This observation would also support the idea that spherically curved pieces of the surface are immediately strained into a more cylindrical shape, while spherical saddles result from changes in the direction of straining on an already cylindrical surface. In general curvature appears to be associated with strain history (see, for example, Pope, 1988).

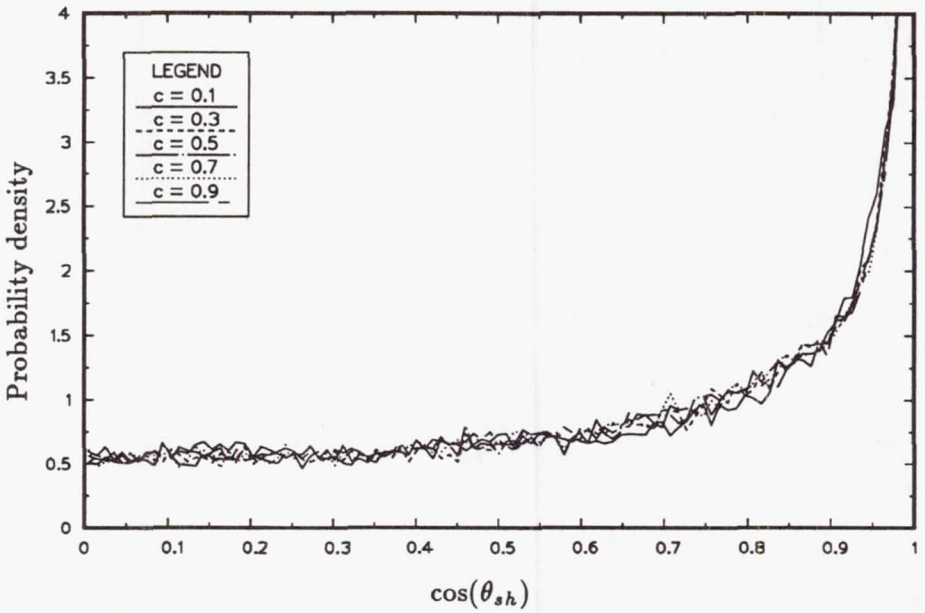

FIGURE 5. Pdf of cosine of the angle θ_{sh} between the direction of maximum strain in the surface and the direction of minimum curvature. Case 1, set g.

4.5 Other results

Several other quantities were evaluated during the collection of the principal results given above. The pdf of the velocity u' on the surface was assembled and agrees well with the volume-averaged statistics, yielding zero mean, variance of u'^2 and isotropy. The pdf of the flame normal yields a mean of zero in the transverse directions, about 0.92 for Case 1, set g and about 0.37 for Case 4, set p in the direction of propagation independent of progress variable. The principal strain rates on the surface yield magnitudes in the familiar ratio 3:1:-4 in the mean, while the flame normal demonstrates strong preference for alignment with the direction of maximum compressive strain (Rutland, 1989).

5. Conclusions

Statistics of interest in the modeling of turbulent premixed combustion by a laminar flamelet approach have been gathered from a database of the results of

Direct Numerical Simulation of turbulent flames. A reasonable range of Taylor-scale Reynolds number, Karlovitz number and u'/S_L has been covered. Statistical results, mainly in the form of pdf's, have been obtained for strain, curvature and associated quantities and show features which have been observed previously only for material surfaces at considerably higher Reynolds numbers. A great deal of insight has been gained into the processes governing the propagation of turbulent flames and sound foundations have been laid for future modeling activity.

REFERENCES

BRAY, K. N. C. 1990 Studies of the Turbulent Burning Velocity. *Proc. Roy. Soc. Lond.* to appear.

BRAY, K. N. C., LIBBY, P. A., MOSS, J. B. 1984 Flamelet Crossing Frequencies and Mean Reaction Rates in Premixed Turbulent Combustion. *Comb. Sci. Tech.* **41**, 143-172.

BRAY, K. N. C., MOSS, J. B., LIBBY, P. A. 1985 A Unified Model of Premixed Turbulent Combustion, Part 1: General Formulation. *Combust. Flame.* **61**, 87-102.

CANDEL, S. M., POINSOT, T. J. 1990 Flame Stretch and the Balance Equation for Flame Area. *Comb. Sci. Tech.* **70**, 1-15.

CANT, R. S., BRAY, K. N. C. 1989 A Theoretical Model of Premixed Turbulent Combustion in a Closed vessel. *Combust. Flame.* **76**, 243-263.

CANT, R. S., POPE, S. B., BRAY, K. N. C. 1990 Modeling of Flamelet Surface-to-Volume Ratio in Turbulent Premixed Combustion. *23rd Symposium (International) on Combustion.* To appear.

CANT, R. S., ROGG, B., BRAY, K. N. C. 1990 On Laminar Flamelet Modeling of the Mean Reaction Rate in a Premixed Turbulent Flame. *Comb. Sci. Tech.* **69**, 53-61.

CHEW, T. C. 1989 Aspects of Premixed Turbulent Combustion. *Ph. D. Thesis.* University of Cambridge.

POPE, S. B. 1988 The Evolution of Surfaces in Turbulence. *Int. J. Engr. Sci.* **26**, 445-500.

POPE, S. B., YEUNG, P. K., GIRIMAJI, S. S. 1989 The Curvature of Material Surfaces in Isotropic Turbulence. *Phys. Fluids A.* **1(12)**, 2010-2018.

RUTLAND, C. J. 1989 Effects of Strain, Vorticity and Turbulence on Premixed Flames. *Ph. D. Thesis.* Stanford University.

YEUNG, P. K., GIRIMAJI, S. S., POPE, S. B. 1990 Straining and Scalar Dissipation on Material Surfaces in Turbulence: Implications for Flamelets. *Combust. Flame.* **79**, 340-365.

The Influence of Lewis number and nonhomogeneous mixture on premixed turbulent flame structure

By D. C. Haworth[1] AND T. J. Poinsot[2]

The structure of a premixed flame front in two–dimensional turbulence is investigated using full numerical simulation including heat release, variable fluid properties, and one–step Arrhenius chemistry. Non–unity Lewis number (Le) effects are described by comparing the local instantaneous turbulent flame structure to the steady one–dimensional laminar flame structure for the same thermochemical parameters. Flame surface area, mean reactant consumption rate per unit area of flame (mean "flamelet speed"), turbulent flame speed, and statistical descriptions of the flame geometry (pdf's of curvature and strain) also are reported. Principal findings are that the local flame structure correlates strongly with the local flame curvature, while global properties (e.g., turbulent flame speed) depend both on strain and on curvature.

Preliminary results for cases with nonhomogeneous reactant mixture strength are reported. Here the emphasis is on the ability of a propagating flame to recover after encountering a fuel–lean pocket in an otherwise homogeneous mixture. Both one–dimensional and two–dimensional cases are described.

1. Introduction

The structure of premixed flames in turbulent flows is an important fundamental and practical question in turbulent combustion. In applications such as reciprocating internal combustion engines, accurate modeling of turbulent premixed combustion is an essential step in formulating truly predictive multidimensional models that can be used to study in–cylinder processes and optimize engine designs.

Because flame structure information is difficult to obtain experimentally, numerical simulations have become an important tool in complementing experimental investigations of turbulent combustion. For the foreseeable future, numerical simulation of the full three–dimensional governing partial differential equations with variable density and transport properties and complex chemistry will remain intractable; thus various levels of simplification will remain necessary. On one hand, the requirement to simplify is not necessarily a handicap: numerical simulations allow the researcher a degree of control in isolating specific physical phenomena that is inaccessible in experiments. For example, one can "turn off" heat release to study

1 General Motors Research Laboratories, Warren, MI

2 Center for Turbulence Research, and C. N. R. S., Ecole Centrale de Paris

the influence of turbulence on chemical reaction without the confounding effects of chemistry on the flow field through density and fluid property variations. On the other hand, the highly coupled nonlinear nature of the governing partial differential equations demands that one remains wary when extrapolating results obtained in such idealized modeled systems to practical turbulent premixed flames. A judicious balance of experiment and computation remains the most fruitful approach.

In the present study, the modeled system includes heat release, variable fluid properties, and simple chemistry in two–dimensional turbulence. While it is recognized that two–dimensional turbulence differs from three–dimensional turbulence (e.g., Herring *et al.*, 1974; Lesieur, 1987), it is our feeling that the response of the physical flame structure to straining and curvature should be generic, even if detailed statistical correlations (especially of small–scale quantities) differ quantitatively from what would be found in three dimensions. Restricting the simulations to two dimensions also permits a wider dynamic range of scales to be computed, so that, for example, higher turbulence Reynolds numbers can be simulated while still resolving the flame structure. In any case, the present results can be compared with three–dimensional constant–density computations (e.g., Pope *et al.*, 1989; Rutland, 1989; Yeung *et al.*, 1990; Cant *et al.*, 1990; Rutland & Trouvé, 1990) to better understand the limitations and similarities of the two approaches.

If chemical times are short enough compared to turbulence times, the flame zone is "thin" and may be treated, in the limit, as an interface separating fresh unburnt reactants from hot burnt products. This mode of combustion is called the *flamelet* regime. It has been invoked widely as a framework for the construction of turbulent combustion models (e.g., Bray & Libby, 1986; Candel *et al.*, 1988; Pope & Cheng, 1988; Cant & Bray, 1988; El Tahry, 1990). Of primary importance for flamelet models are two quantities: 1) the total flame surface (the area of the interface between fresh and burnt gases); and, 2) the local structure of the individual flamelets. Although these flame elements are thin, their internal structure may be influenced by the flow characteristics and may have an influence on the global consumption rate of reactants.

The objective of this work is to investigate the dependence of these two quantities on the Lewis number Le (ratio of thermal to species diffusivities) and on the spatial distribution of reactant mass fraction. The Lewis number has been identified in asymptotic analyses of laminar flames as an important parameter influencing premixed flame structure and stability; we wish to assess its importance in determining the local and global structure of turbulent flames. Nonhomogeneous combustion is an important mode of burning in practical devices including direct–injection or stratified–charge internal combustion engines. There is, however, relatively little analysis or experimental results to guide the modeling of this mode of combustion with turbulence. Most of the discussion will focus on Lewis number effects; only preliminary results for nonhomogeneous cases will be given.

2. Numerical method

We consider a compressible viscous reacting flow. The chemical reaction is represented by a single–step mechanism,

$$R \quad \text{(reactants)} \quad \rightarrow P \quad \text{(products)}, \tag{1}$$

and the reaction rate $\dot{w}_R$ is expressed as,

$$\dot{w}_R = B\rho Y_R \ \exp\left(-\frac{T_a}{T}\right). \tag{2}$$

This can be interpreted as a binary reaction where one of the reactants (Y_R) is always deficient. It is convenient to follow Williams (1985) and cast this expression in the form,

$$\dot{w}_R = \mathcal{B}\rho Y_R \exp\left(\frac{-\beta(1-\Theta)}{1-\alpha(1-\Theta)}\right). \tag{3}$$

Here Θ is the reduced temperature, $\Theta = (T - T_1)/(T_2 - T_1)$, where T_1 is the fresh gas temperature and T_2 is the adiabatic flame temperature for unity Lewis number. The activation energy is T_a, and the coefficients $\mathcal{B}$, α, and β are, respectively, the reduced pre–exponential factor, the temperature factor and the reduced activation energy,

$$\mathcal{B} = B\exp(-\beta/\alpha), \quad \alpha = (T_2 - T_1)/T_2, \quad \text{and} \quad \beta = \alpha T_a/T_2. \tag{4}$$

The mass fraction of the reactants Y_R may be conveniently nondimensionalized by the initial mass fraction of reactants Y_R^o in the fresh gases, $\widetilde{Y} = Y_R/Y_R^o$, so that $\widetilde{Y}$ varies from 1 in the fresh gases to 0 in the burnt gases. Fluid properties follow the equations of state,

$$\rho = \rho_1(pT_1/p_1T)\ ,\ \mu = \mu_1(T/T_1)^b\ ,$$

$$Le = \lambda/\rho D c_p = \text{constant}\ ,\ Pr = \mu c_p/\lambda = \text{constant}\ , \tag{5}$$

where μ, λ, and D are molecular diffusivities of momentum, internal energy, and species, respectively. Here a subscript 1 refers to reference properties in the fresh gases. Heat losses can be included in the energy equation: a dimensionless heat loss coefficient c expresses the magnitude of the heat loss (Poinsot *et al.*, 1990). For the homogeneous runs, $c = 0$ (adiabatic).

Using these assumptions and a Cartesian frame of reference, the conservation equations for compressible flows are solved using a high–order finite difference scheme. The numerical accuracy is sixth–order in space and third–order in time (Lele, 1990). Spatial derivatives are computed using a compact scheme and the time advancement is produced by a minimal–storage third–order Runge–Kutta method (Wray, 1990). Boundary conditions are specified using the NSCBC method (Poinsot

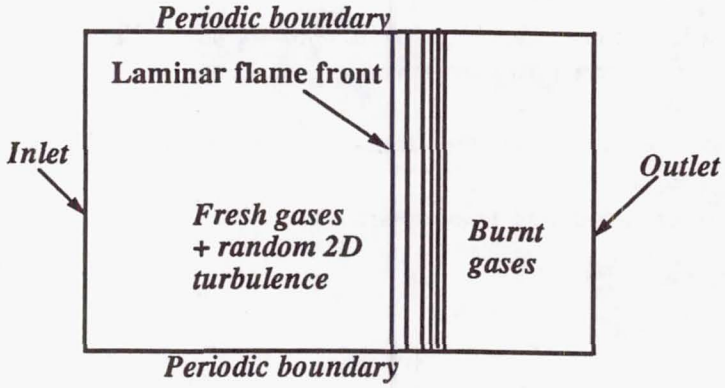

FIGURE 1. Schematic of two–dimensional computational configuration.

& Lele, 1990). Details concerning the system of equations solved and the numerical methods can be found in these papers. Typical grids contain 160000 points.

A schematic of the computational configuration is given in Figure 1. The calculations are initialized with reactants on one side of the computational domain and products on the other; these are separated by a laminar premixed flame. The initial velocity field (turbulence spectrum) and spatial distribution of reactant mass fraction is specified at $t = 0$: the system is then allowed to evolve in time. The initially planar flame is convected and strained by the turbulence while the combustion influences the fluid mechanics through dilatation and temperature–dependent properties (Eq. 5). Typical contours of temperature, reactant mass fraction, reaction rate, and vorticity are shown in Figure 2 for a homogeneous reactant, $Le = 1.2$ case. There it can be seen that the initially planar flame has been strongly distorted and stretched by the turbulence. There is very little vorticity behind the flame in the hot products: the high viscosity there (Eq. 5) suppresses most turbulent velocity fluctuations.

Relevant dimensionless parameters in the homogeneous reactant simulations are:
– ratio of rms turbulence intensity u' to the undisturbed laminar flame speed s_l^0;
– ratio of turbulence integral length scale l to laminar flame thickness δ_{l1}, where $\delta_{l1} = (T_2 - T_1)/(dT/dx)_{max}$;
– turbulence Reynolds number $Re_l = u'l/\nu$;
– ratio of turbulence time scale $\tau = l/u'$ to flame time scale $\tau_f = \delta_{l1}/s_l^0$;
– strain Karlovitz number $Ka_{st} \equiv \langle s_t \rangle \cdot \tau_f$, where $\langle s_t \rangle$ is the area–averaged mean strain rate tangent to the flame;
– ratio of turbulence micro–length–scale l_η to laminar flame thickness δ_{l1}; and,
– ratio of turbulence micro–time–scale τ_η to flame time scale τ_f.
The values of these parameters as functions of time for three cases are given in Table I (τ_0 is the initial value of the turbulence time scale τ). Table II contains the fixed parameters for the homogeneous reactants cases. Initial turbulence specification is (statistically) the same for all three cases in Table I; runs made with

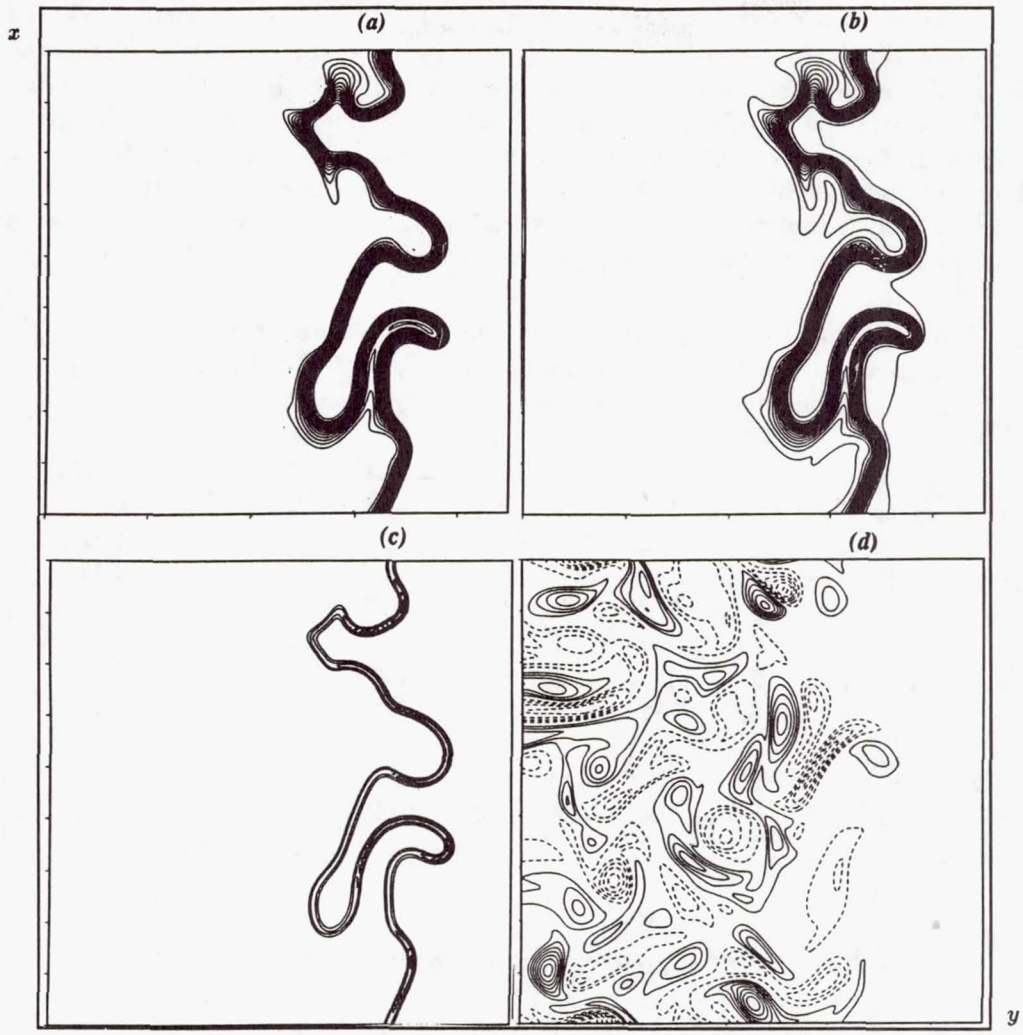

FIGURE 2. Contours at dimensionless time $t/\tau_0 = 1.8$ for $Le = 1.2$ with homogeneous reactants: a) temperature; b) reactant mass fraction; c) reaction rate; and d) vorticity.

different initial spectra have been made, but are not reported here.

The microscales l_η and τ_η are based on the dissipation rate of enstrophy; presumably, this is the most appropriate definition of the scales of the smallest motions in two–dimensional turbulence (Herring *et al.*, 1974; Lesieur, 1987). The enstrophy Ω (mean–square vorticity) and its dissipation rate η are given by,

$$\Omega = .5\,\overline{|\nabla \times \underline{v}|^2}, \tag{6}$$

$$\eta = \overline{\nu|\nabla \times (\nabla \times \underline{v})|^2}, \tag{7}$$

where the overbar denotes a spatial average. The ratios of the enstrophy–based microscales $l_\eta = (\nu^3/\eta)^{1/6}$, $\tau_\eta = \eta^{-1/3}$, to the more conventional Kolmogorov microscales appropriate for three–dimensional turbulence ($l_k = (\nu^3/\epsilon)^{1/4}$, $\tau_k = (\nu/\epsilon)^{1/2}$, where ϵ is the dissipation rate of turbulence kinetic energy) are also given in Table I. There it can be seen that the length microscales differ by 50%–60%, while the time microscales differ by up to nearly a factor of three. It should be noted that all turbulence scales (u', l, τ, l_η, τ_η, l_k, and τ_k) are volume–averaged mean quantities conditional on being in the fresh gases in front of the flame.

Table I. Dimensionless parameters for three homogeneous mixture cases. First row for each Lewis number is the initial condition ($t = 0$), second row is at normalized time $t/\tau_0 \approx 1.8$.

Le	t/τ_0	u'/s_l^0	l/δ_{l1}	Re_l	τ/τ_f	Ka_{st}	l_η/δ_{l1}	τ_η/τ_f	l_η/l_k	τ_η/τ_k
0.8	0.00	6.44	2.57	81	0.40	0.00	0.19	0.18	1.63	2.43
	1.83	4.82	5.29	126	1.10	1.47	0.24	0.28	1.49	2.23
1.0	0.00	6.11	2.68	81	0.44	0.00	0.20	0.20	1.64	2.69
	1.85	4.68	5.80	132	1.24	1.25	0.25	0.30	1.48	2.20
1.2	0.00	5.69	2.91	77	0.52	0.00	0.22	0.23	1.64	2.68
	1.84	4.32	6.46	124	1.50	1.09	0.27	0.37	1.48	2.34

Table II. Fixed parameters for homogeneous reactant cases.

α	β	Λ	b	Pr	c
0.75	8.00	146.	0.76	0.75	0.00

3. Diagnostics

For homogeneous cases, postprocessing of the two–dimensional computed fields (snapshots at fixed times) begins by defining a flame front as an isocontour of either temperature T or of reactant mass fraction Y_R. The choice of dependent variable and the value of isocontour selected to identify the flame have been seen to have little influence on the results. Unless otherwise specified, the $Y_R = 0.3$ isocontour has been used to define the flame in the results that follow; this contour lies slightly in front of the reaction zone towards the fresh gases.

Once the flame front has been located, the local normal and local flame curvature are readily computed: curvatures concave towards the hot products are assigned positive values. One–dimensional cuts normal to the flame are taken; it is these profiles that define the local "structure" of the turbulent flame. We compare the local turbulent flame profiles with the steady one–dimensional laminar flame profile for the same chemistry and fluid properties. Of particular interest is the distribution along the flame of the normalized local flame speed ("flamelet speed") s_n defined by,

$$s_n = \int \dot{w}\, dn \,/\, s_l^0 \,, \tag{8}$$

that is, the integral of the reaction rate profile in a direction locally normal to the isocontour defining the turbulent flame, normalized by the undisturbed laminar flame speed. If the local turbulent reaction rate profile is identical to that of an undisturbed laminar flame, then $s_n = 1$. The isocontour curvature and the components of the strain rate normal to $(\nabla_n \cdot \underline{v})$ and tangent to $(\nabla_t \cdot \underline{v})$ the flame contour are also computed along the flame front. Area–weighted (arclength–weighted in two dimensions) statistics of s_n, curvature, and components of the strain rate are calculated. The mean consumption rate of reactants per unit area of flame surface ("mean flamelet speed"), normalized by the laminar flame value, is computed as,

$$\langle s_n \rangle = \int s_n\, dA \,/\, \int dA. \tag{9}$$

For nonhomogeneous reactant cases, appropriate diagnostics are still being developed.

4. Non–unity Lewis number effects in turbulent premixed flames

Results for $Le = 0.8$, 1.0, and 1.2 are reported (see Table I). We begin in Section 4.1 with a brief review of analytic and earlier computational results for nonunity Lewis numbers in premixed flames. Next, we describe the local flame structures found in the present simulations. In Section 4.3, global quantities of interest are discussed. And finally, in Section 4.4, statistics of flame front curvature and strain rate are given; these are compared with results obtained in three–dimensional uniform–property simulations.

4.1. Review of Lewis number influence in premixed flames

Textbook discussions of thermodiffusive effects for premixed flames with nonunity Lewis numbers reveal the following behavior (e.g., Williams, 1985). For $Le = 1$ (and subject to other assumptions consistent with those made here in Section 2), only one of Y_R or T is independent ($\widetilde{Y} + \theta = 1$ everywhere), and the reaction rate is a unique function of the reactant mass fraction or temperature. Flame curvature is not expected to influence the local flame structure. Straining can thin the flame (for positive, or extensive, straining in the tangent plane) or thicken the flame (for negative, or compressive, straining in the tangent plane), but the maximum reaction rate remains unaffected. Thus the local flamelet speed (Eq. 8) is expected

to (slightly) decrease/increase for a flame element subjected to positive/negative tangential strain.

For Lewis numbers other than unity, differential diffusion between heat and species leads to richer possibilities in flame structure. In particular, flame front curvature influences the local burning rate. For $Le > 1$, elements of flame surface that are concave towards the reactants are expected to burn faster, while elements that are concave towards the products are expected to have a lower burning rate compared to that of a planar flame. Positive (extensive) tangential strain will decrease the flamelet speed relative to that of an undisturbed laminar flame for $Le > 1$. On the other hand, Lewis numbers less than unity are expected to display the opposite behavior: lower burning rate for elements concave towards reactants; higher burning rates for elements concave towards products; and, increasing flamelet speed with extensive strain.

Ashurst *et al.* (1987) reported two–dimensional numerical simulations of premixed flames with nonunity Lewis numbers in the limit of zero heat release. The thermodiffusive effects described above for nonunity Lewis number were observed in their simulations. Results were expressed in terms of the excess enthalpy relative to an undisturbed laminar flame; a correlation between strain rate and excess enthalpy was reported. Here, we calculate cases with higher turbulence intensity (Table I), variable properties, and heat release. The local flame structure is found to correlate more strongly with the local flame curvature than with strain rate, while global flame behavior depends on both strain and curvature.

4.2. Simulation results: local flame structure

The local flame structure, as illustrated through one–dimensional cuts of reaction rate, is shown in Figure 3 for each of the three Lewis numbers simulated. There, it is clear that the local flame structure is everywhere nearly identical to that of an undisturbed laminar flame for $Le = 1$ (Figure 3b), while for nonunity Lewis numbers, there is no collapse of the local turbulent flame profiles onto the one–dimensional undisturbed laminar flame profile (Figures 3a and 3c). From the discussion given in Section 4.1 above and the sample reaction rate contours shown in Figure 2, we expect to see a correlation between local flame curvature and the local flamelet speed; indeed, this is the case. Figures 4a, 4b, and 4c illustrate this correlation for each of the three Lewis numbers computed. For $Le = 0.8$ (Figure 4a), flame elements concave towards reactants tend to have lower local flamelet speeds, and conversely for elements concave towards products; for $Le = 1.0$ (Figure 4b), there is no apparent correlation between local curvature and local flame structure; and, for $Le = 1.2$ (Figure 4c), the correlation is opposite to that shown in Figure 4a.

If instead, we attempt to correlate the local flamelet speed in the turbulent flame with the strain rate tangent to the flame, then the scatter plots of Figure 5 result. There is no apparent systematic correlation evident for the nonunity Lewis number cases. For $Le = 1$, a small negative slope can be seen. This presumably is a reflection of flame thickening/thinning resulting from compressive/extensive tangential straining. The strain Karlovitz number Ka_{st} at this time is greater than unity (Table I) so that it is reasonable to expect that turbulent straining could affect the

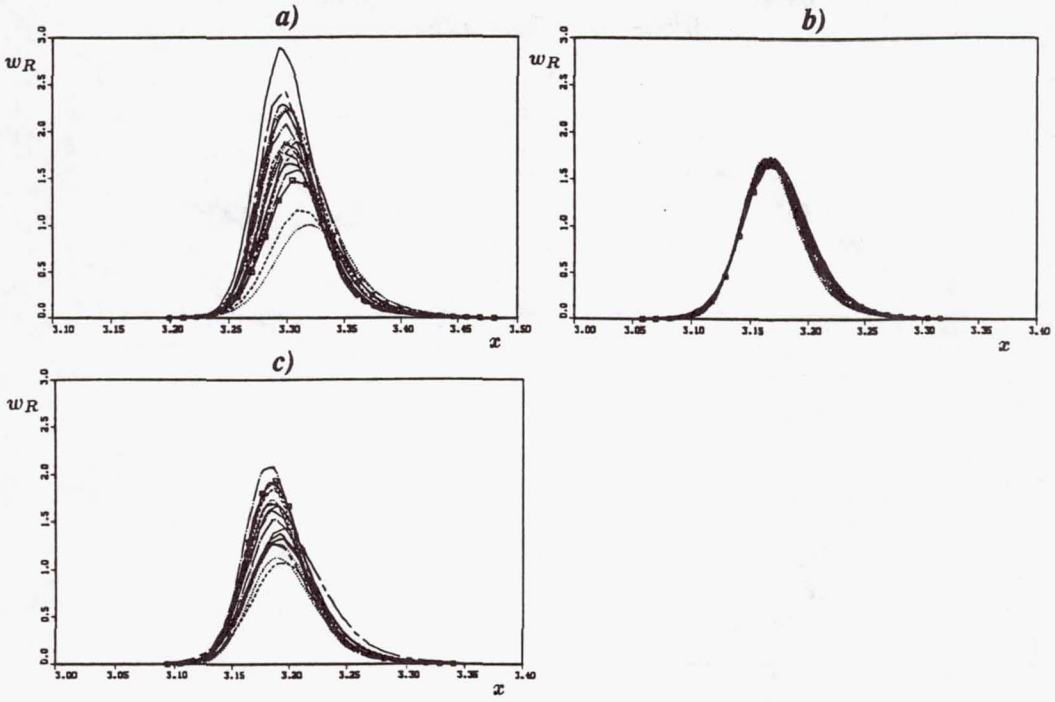

FIGURE 3. Local reaction rate profiles normal to the turbulent flame (lines) and laminar reaction rate profile (symbols) for three Lewis numbers at normalized time $t/\tau_0 = 1.8$: a) $Le = 0.8$; b) $Le = 1.0$; c) $Le = 1.2$.

local flame structure.

4.3. Simulation results: global quantities

The mean reaction rate along the turbulent flame (mean flamelet speed) and the flame surface area are quantities of interest in constructing flamelet models for turbulent premixed combustion. In Figure 6, probability density functions (pdf's) of the normalized local flamelet speed in the turbulent flame are shown for each of the three Lewis numbers at time $t/\tau_0 = 1.8$. For nonunity Lewis numbers, it can be seen that the pdf of flamelet speed is broadened and shifted relative to $Le = 1.0$. The unity Lewis number case shows a small spread about the undisturbed laminar flame speed, presumably reflecting the influence of tangential strain. The area–averaged mean flamelet speeds, referred to that of an undisturbed laminar flame at the same Lewis number, are 1.14 ($Le = 0.8$); 1.00 ($Le = 1.0$); and, 0.86 ($Le = 1.2$).

Figure 7 illustrates the Lewis number effects in a different way. There, the variation with time of the turbulent flame speed (computed from the volume–averaged mean reaction rate over the entire two–dimensional computational domain), normalized by the laminar flame speed, is shown for each of the three cases. Superimposed on this is the flame area (or length, in two dimensions), normalized by the initially planar flame length. The turbulent flame speed is (normalizations aside) the product of the mean flamelet speed and the flame area. The interesting finding is that

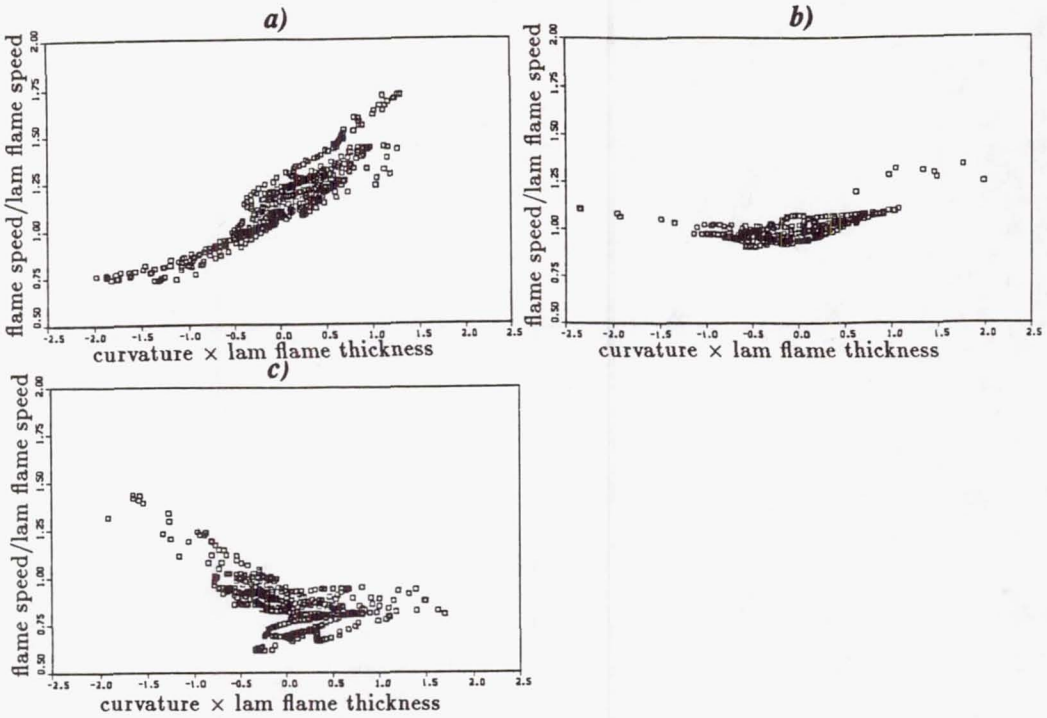

FIGURE 4. Scatter plots of normalized local flamelet speed in the turbulent flame (Eq. 8) versus local flame curvature (normalized by the laminar flame thickness δ_{l1}) for three Lewis numbers at normalized time $t/\tau_0 = 1.8$: a) $Le = 0.8$; b) $Le = 1.0$; c) $Le = 1.2$. Profiles are for various y locations.

the turbulent flame speed increases more rapidly than the flame area for $Le = 0.8$; that for $Le = 1.0$, these two quantities evolve identically; and, that for $Le = 1.2$, the flame surface increase exceeds the turbulent flame speed augmentation. Figure 7d repeats the turbulent flame speed curves for the three Lewis numbers to emphasize the decrease in turbulent flame speed with increasing Lewis number.

Comparison of Figures 7a–7c reveals that, for $Le = 0.8$, the turbulence creates more flame surface than for $Le = 1.0$. This results from the interaction between flame curvature and thermodiffusive effects for nonunity Lewis numbers. Thus the higher turbulent flame speed relative to flame area for $Le = 0.8$ can be seen to result from two complementary effects: more flame surface, plus higher mean flamelet speed (Figure 6). Similarly, for $Le = 1.2$, the lower turbulent flame speed is a consequence of less flame area being generated, coupled with a lower mean flamelet speed.

4.4. Simulation results: flame curvature and strain rate

Typical pdf's of flame curvature (normalized by the laminar flame thickness δ_{l1}) are shown in Figure 8. It may be seen that the pdf is nearly symmetric, with a mean value near zero, and with few curvatures exceeding one over the laminar flame thickness. The smallest radii of curvature are equal to about one–half of δ_{l1}. The

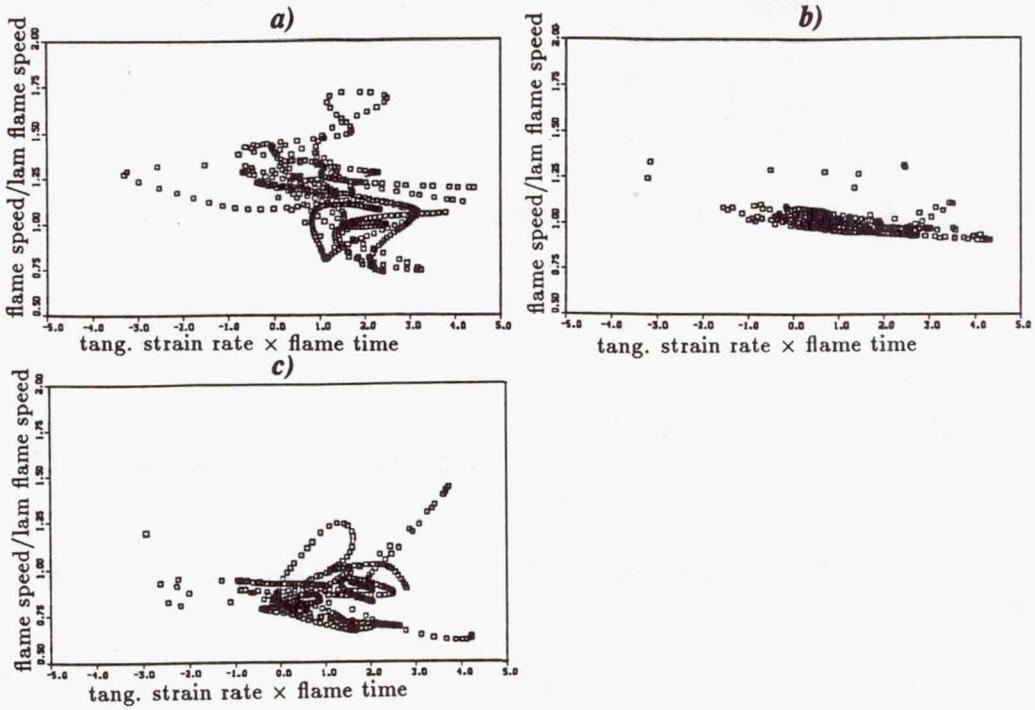

FIGURE 5. Scatter plots of normalized local flamelet speed in the turbulent flame (Eq. 8) versus local flame tangential strain rate (normalized by the laminar flame timescale $\tau_f = \delta_{l1}/s_l^0$) for three Lewis numbers at normalized time $t/\tau_0 = 1.8$: a) $Le = 0.8$; b) $Le = 1.0$; c) $Le = 1.2$.

near symmetry of the pdf suggests that the differences in mean flamelet speed with Lewis number seen in Figure 6 are primarily attributable to strain.

For simulations with heat release and variable properties, it is important to distinguish between the normal and tangential components of the strain rate on the flame. Here the normal component is dominated by the velocity divergence through the flame resulting from the change in fluid density. Pdf's of tangential strain rate are given in Figure 9. There it can be seen that extensive strain rates are dominant – that is, the flame aligns preferentially with extensive strains; there is no apparent systematic dependence on Le. This is again consistent with the notion that the differences in normalized mean flamelet speeds for the three Lewis numbers is principally a strain effect. The dominance of extensive strain rates is also seen in three–dimensional simulations (Yeung *et al.*, 1990 – for material surfaces; Rutland, 1989; Cant *et al.*, 1990; Rutland & Trouvé, 1990). The mean tangential strain rate in Figure 9 has been scaled with the flame time τ_f to emphasize interactions between chemistry and turbulence. If, instead, we scale the mean tangential strain rate with the enstrophy micro–time–scale τ_η as,

$$\langle \nabla_t \cdot \underline{v} \rangle = C_\eta / \tau_\eta, \tag{10}$$

then it is found that the value of C_η varies from a zero value at the beginning of

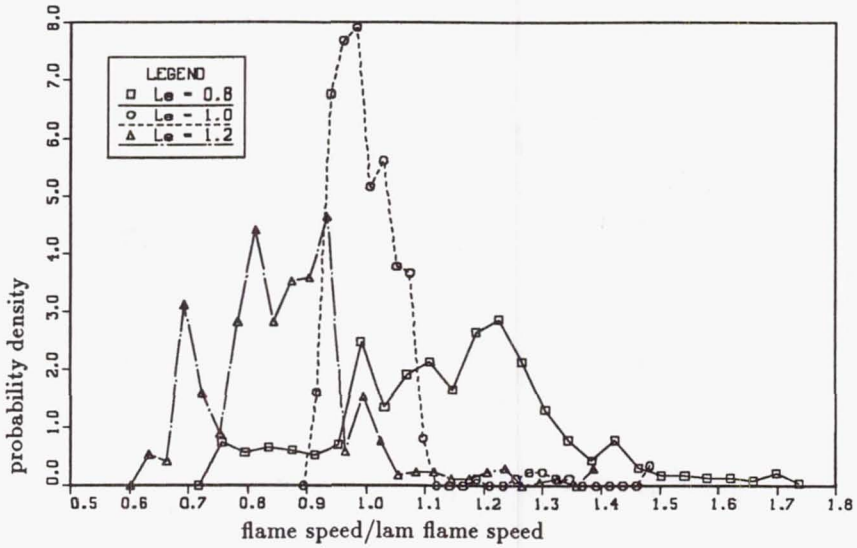

FIGURE 6. Pdf's of normalized local flamelet speed s_n (Eq. 8) for three Lewis numbers at normalized time $t/\tau_0 = 1.8$.

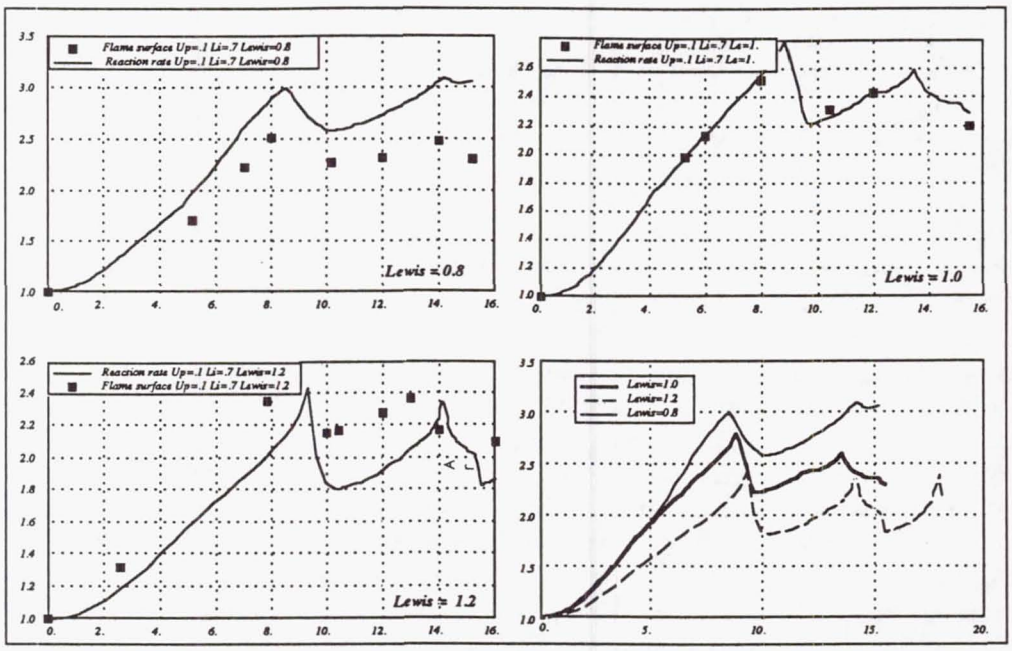

FIGURE 7. Normalized turbulent flame speed (lines) and flame area (symbols) for three Lewis numbers as a function of time. Both quantities are normalized by their $t = 0$ values: a) $Le = 0.8$; b) $Le = 1.0$; c) $Le = 1.2$; d) turbulent flame speeds for all three Lewis numbers.

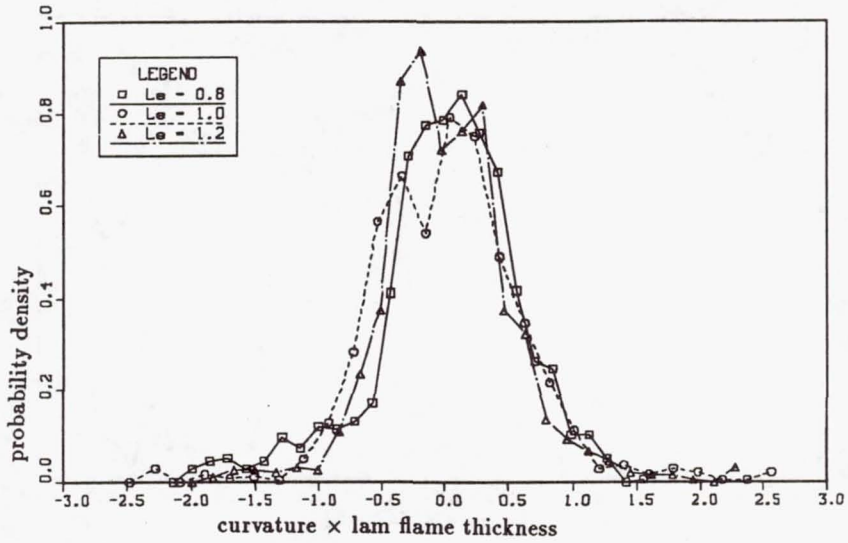

FIGURE 8. Normalized pdf's of flame curvature for three Lewis numbers at normalized time $t/\tau_0 = 1.8$.

the computations (no preferential alignment of the initially planar flame with the fluid strain rate) to a more or less steady value of $0.40 - 0.50$. We can also scale the mean tangential strain rate with the Kolmogorov time scale τ_k,

$$\langle \nabla_t \cdot \underline{v} \rangle = C_k/\tau_k = C_k(\epsilon/\nu)^{1/2}. \tag{11}$$

In this case, values of C_k range from 0.15 to 0.20 once the flame has become sufficiently wrinkled ($t/\tau_0 >\approx 1$). In three–dimensional simulations, C_k is found to be $0.25 - 0.28$ (Yeung *et al.*, 1990 – for material surfaces; Cant *et al.*, 1990). It should be emphasized that τ_k is probably not a physically meaningful scale for two–dimensional turbulence; it is shown here only for comparison with three–dimensional results.

5. Nonhomogeneous reactants

As a first step towards understanding and modeling the behavior of turbulent flames in nonuniform mixtures, we have modeled the case of a laminar flame propagating through a "hole" or pocket of lean ($Y_R = 0$) reactants in an otherwise homogeneous ($Y_R = 1$) mixture. We first briefly review related previous work concerning nonhomogeneous combustion, then show preliminary results for the cases that we have calculated.

5.1. Background

Several configurations of laminar combustion in nonhomogeneous mixtures have been investigated analytically using high–energy asymptotics. These include cases of one–dimensional laminar flames propagating into gradients in reactant mass fraction normal to the flame (e.g., Bissett & Reuss, 1986; Mikolaitis, 1984), and cases

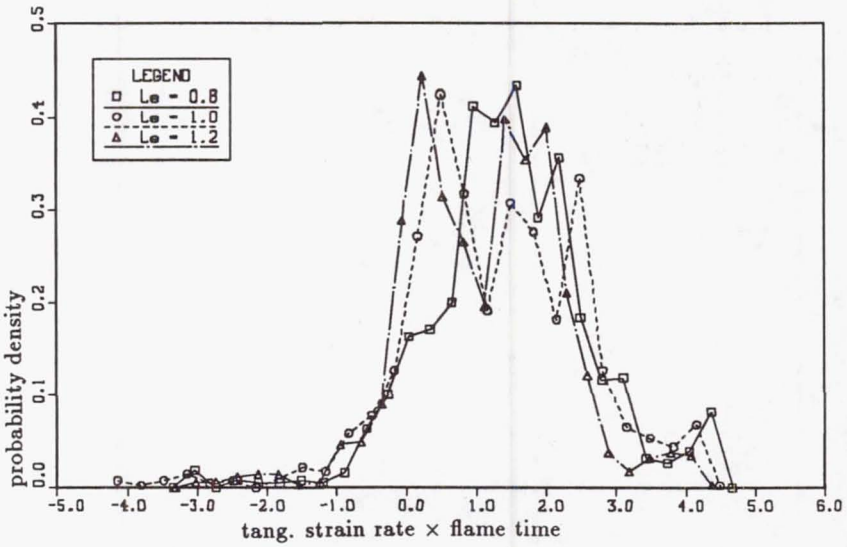

FIGURE 9. Normalized pdf's of tangential strain rate for three Lewis numbers at normalized time $t/\tau_0 = 1.8$.

where there is a gradient in reactant concentration parallel to the premixed flame front (Buckmaster & Matalon, 1988). In these analyses, it is principally the mass consumption rate of the transient flame compared to that of an undisturbed steady laminar flame at the same local mixture strength that is of interest.

Nonhomogeneous mixtures also have been incorporated into models for turbulent combustion by Veynante *et al.* (1989) within the framework of the modified coherent flame model of Marble and Broadwell (1977). This model uses two modeled equations for flame surface–to–volume ratio, one for premixed burning and the other for post–flame diffusion burning.

Here, nonhomogeneous combustion is addressed in two simple configurations. The single–step Arrhenius chemistry of Eqs. (1)–(4) is retained, but heat losses are allowed ($c > 0$) so that extinction effects can be modeled. The Lewis number is unity, and all chemistry parameters are as in Table II. Since we monitor a single reactant mass fraction, we are restricting our attention to cases where one of the reactants is always deficient (i.e., the mixture is everywhere rich or lean). This precludes some interesting behavior that can be expected when equivalence ratios on both sides of stoichiometric are present (Buckmaster & Matalon, 1988). A planar laminar flame propagating in a homogeneous mixture ($Y_R = 1$) encounters a pocket of zero fuel mass fraction ($Y_R = 0$). As a first step, we seek to quantify the parameters that govern whether the flame will reignite or extinguish following its encounter with the hole. The governing parameter is expected to be a ratio of a length scale characteristic of the post–flame temperature gradient resulting from the heat loss to a characteristic hole size.

5.2. One–dimensional laminar calculations

Typical initial profiles of reactant mass fraction and temperature are shown in

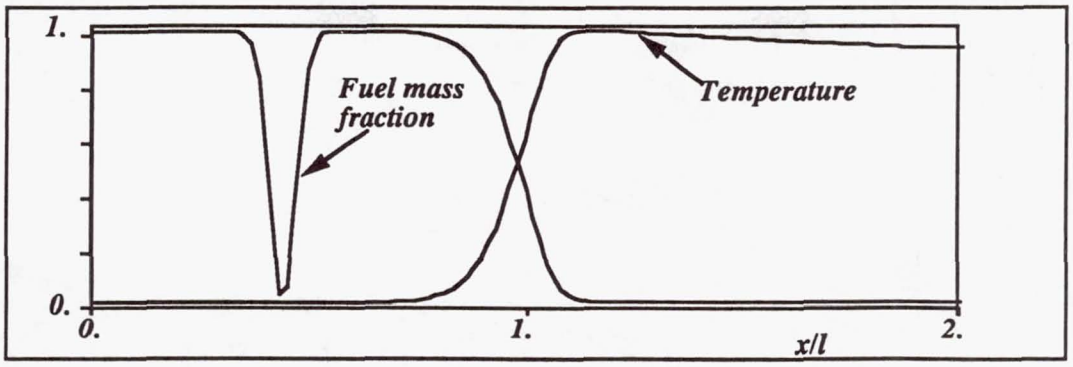

FIGURE 10. Initial profiles of reactant mass fraction and temperature for a one–dimensional laminar case with a reactant "hole."

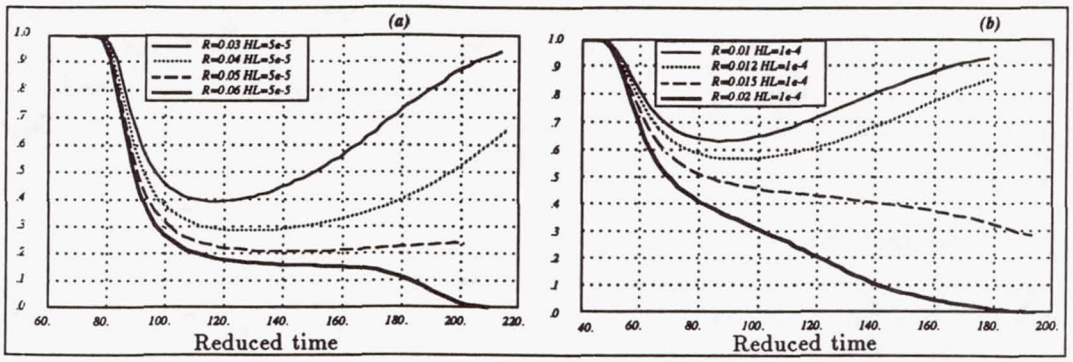

FIGURE 11. Normalized total reaction rate versus time as a function of hole half–width R for two values of the heat loss coefficient c: a) $c = 5 \cdot 10^{-5}$; b) $c = 1 \cdot 10^{-4}$.

Figure 10. As the flame propagates, the reaction rate drops as the flame encounters the hole. The half–width of the hole, R, is taken as a characteristic dimension of the disturbance.

Figure 11 shows the transient behavior of the flame (normalized total reaction rate versus time) as it passes through the hole as a function of R for two values of the heat loss coefficient c. There is a critical value of R, $R_{crit} = R_{crit}(c)$, such that for $R > R_{crit}$, the flame extinguishes and for $R < R_{crit}$, the flame reignites. For $c = 5 \cdot 10^{-5}$, Figure 11 shows that $R_{crit} \approx 0.05$; and, for $c = 1 \cdot 10^{-4}$, $R_{crit} \approx 0.014$. In the limit of zero heat loss ($c = 0$), the flame will always reignite.

5.2 Two–dimensional laminar calculations

Similar calculations have been repeated in two spatial dimensions for a round hole of lean ($Y_R = 0$) reactants embedded in a $Y_R = 1$ mixture. Compared to the one–dimensional case, the flame now can travel around the hole to reignite on the other side. An example of a case where the flame failed to reignite after passing the hole is shown in Figure 12.

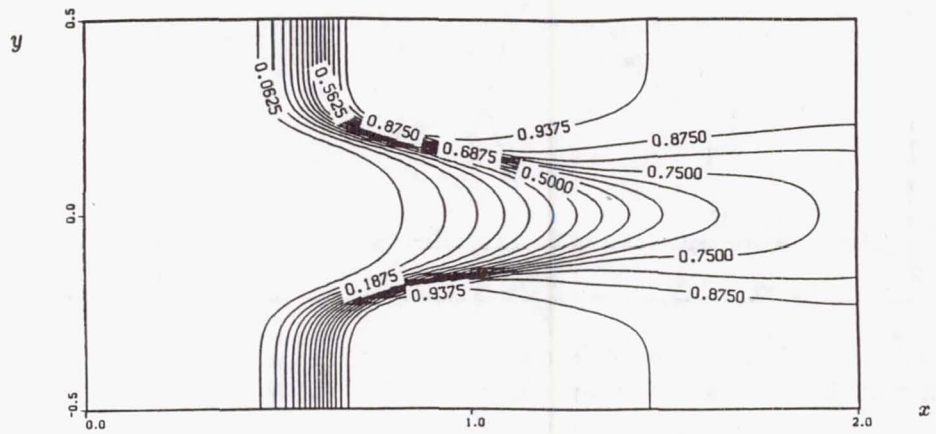

FIGURE 12. Contours of temperature for a two–dimensional laminar calculation with a lean hole in the reactants. The flame has failed to reignite after passing through the hole.

6. Summary and conclusions

Calculations of premixed turbulent flame structure in two–dimensional turbulence have been reported. Quantitative results have been presented illustrating the effect of Lewis number on the local and global flame structure. Pdf's of flame strain rate and curvature have also been shown. Conclusions are that: 1) the local flamelet speed in the $Le = 1$ flame is everywhere nearly identical to that of an undisturbed laminar flame; 2) for $Le \neq 1$, the local flamelet speed differs from that of the undisturbed laminar flame and correlates strongly with local flame curvature; 3) flame strain results in a mean flamelet speed that is higher than the laminar value for $Le < 1$, is identical to the laminar value for $Le = 1$, and is lower than the laminar value for $Le > 1$; 4) straining and curvature effects result in more flame surface for $Le < 1$ than for $Le > 1$ – this, combined with the dependence of mean flamelet speed on Le, results in a strong dependence of turbulent flame speed on Le; 5) pdf's of flame curvature are nearly symmetric with a near–zero mean value – the maximum curvatures found are of the order of one over the laminar flame thickness; and, 6) pdf's of strain rate tangent to the flame are skewed towards positive (extensive) strains with a mean strain rate of the order of the inverse of the time scale of the smallest turbulent motions. These results imply that, for the range of parameters investigated, curvature is more important than strain rate in determining the local flame structure. Turbulent flame speed, however, is influenced both by curvature (through the flame surface area) and by strain (through the flame surface area and mean flamelet speed), and is strongly Lewis number dependent.

These results may have implications for the implementation of flamelet models of turbulent premixed combustion. The prototype laminar configuration for which

flamelet libraries have been generated is generally that of a one–dimensional laminar stagnation–point burner. This configuration accounts, in some sense, for the effect of tangential strain, but does not account for flame front curvature. A second important result for modeling is that the flame surface area, the mean flamelet speed, and the turbulent flame speed all are functions of Lewis number: this dependence has been neglected in most models.

Questions remaining to be addressed include: further comparisons between two–dimensional and three–dimensional calculations to quantify the limitations and virtues of each; relative contributions of straining versus curvature to the total flame stretch; and, quantitative correlations between global quantities such as turbulent flame speed, turbulent rms velocity, and Lewis number.

For nonhomogeneous mixture cases, the bulk of the data reduction remains to be done. Here, we need to: quantify the recovery limits for flames propagating through lean holes, add at least one additional species so that both fuel–rich and fuel–lean regions can be modeled, include turbulence in the calculations, and try more complex (random) initial spatial distributions of the reactants.

REFERENCES

ASHURST, W. T., PETERS, N. & SMOOKE, M. D. 1987 Numerical simulation of turbulent flame structure with non–unity Lewis number. *Combust. Sci. Technol.* **53**, 339–375.

BISSETT, E. J. & REUSS, D. R. 1986 Analysis of a nonadiabatic flame propagating through gradients of fuel or temperature. *Twenty–First Symp. (International) on Combust.* 531–538. The Combustion Institute.

BRAY, K. N. C. & LIBBY, P. 1986 Passage times and flamelet crossing frequencies in premixed turbulent combustion. *Combust. Sci. Tech.* **47**, 253.

BUCKMASTER, J. & MATALON, M. 1988 Anomalous Lewis number effects in tribrachial flames. *Twenty–Second Symp. (International) on Combust.* 1527–1535. The Combustion Institute.

CANDEL, S., MAISTRET, E., DARABIHA, N., POINSOT, T., VEYNANTE, D., & LACAS, F. 1988 Experimental and numerical studies of turbulent ducted flames. *Marble Symposium.* CALTECH.

CANT, R. S. & BRAY, K. N. C. 1988 Strained laminar flamelet calculations of premixed turbulent combustion in a closed vessel. *Twenty–Second Symp. (International) on Combust.* 791. The Combustion Institute.

CANT, R. S., RUTLAND, C., & TROUVÉ, A. 1990 Statistics for laminar flamelet modeling. *Center for Turbulence Research Report CTR–S90, Stanford University & NASA Ames.*

EL TAHRY, S. H. 1990 A turbulence combustion model for premixed charge engines. *Combust. Flame* (to appear).

HERRING, J. R., ORSZAG, S. A., KRAICHNAN, R. H., & FOX, D. G. 1974 Decay of two–dimensional homogeneous turbulence. *J. Fluid Mech.* **66**, 417–444.

LELE, S. 1990 Compact finite difference schemes with spectral–like resolution. *J. Comp. Phys.* (submitted for publication).

LESIEUR, M. 1987 *Turbulence in Fluids.* Martinus Nijhoff.

MARBLE, F. E. & BROADWELL, J. 1977 The coherent flame model for turbulent chemical reactions. *Project SQUID Report TRW–9–PU.*

MIKOLAITIS, D. W. 1984 The unsteady propagation of premixed flames through nonhomogeneous mixtures and thermal gradients. *Combust. Flame.* **57**, 87–94.

POINSOT, T. & LELE, S. 1990 Boundary conditions for direct simulations of compressible viscous flows. *J. Comp. Phys.* (submitted for publication).

POINSOT, T., VEYNANTE, D., & CANDEL, S. 1990 Quenching processes and premixed turbulent combustion diagrams. *J. Fluid Mech.* (submitted for publication).

POPE, S. B. & CHENG, W. 1988 The stochastic flamelet model of turbulent premixed combustion. *Twenty–Second Symp. (International) on Combust.* 781–789. The Combustion Institute.

POPE, S. B., YEUNG, P. K., & GIRIMAJI, S. S. 1989 The curvature of material surfaces in isotropic turbulence. *Phys. Fluids A.* **1**, 2010–2018.

RUTLAND, C. J. 1989 Effect of strain, vorticity and turbulence on premixed flames. *Ph.D. Thesis, Stanford University.*

RUTLAND, C., & TROUVÉ, A. 1990 Premixed flame simulations for nonunity Lewis numbers. *Center for Turbulence Research Report CTR–S90.* Stanford University & NASA Ames.

VEYNANTE, D., LACAS, F., MAISTRET, E., & CANDEL, S. 1989 Coherent flame model in nonuniformly premixed turbulent flames. *Seventh Symp. on Turb. Shear Flows.* 26.2.1–26.2.6. Stanford University.

WILLIAMS, F. A. 1985 *Combustion theory, 2nd ed.* Benjamin Cummings.

WRAY, A. 1990 Minimal storage time–advancement schemes for spectral methods. *J. Comp. Phys.* (submitted for publication).

YEUNG, P. K., GIRIMAJI, S. S., & POPE, S. B. 1990 Straining and scalar dissipation on material surfaces in turbulence: implications for flamelets. *Combust. Flame.* **79**, 340–365.

Pre-mixed flame simulations for non-unity Lewis numbers

By C. J. Rutland[1] AND A. Trouvé[2]

A principal effect of turbulence on premixed flames in the flamelet regime is to wrinkle the flame fronts. For non-unity Lewis numbers, the local flame structure is altered in curved regions. This effect is examined using direct numerical simulations of three dimensional, constant density, decaying isotropic turbulence with a single step, finite rate chemical reaction. Simulations of Lewis numbers 0.8, 1.0 and 1.2 are compared. The turbulent flame speed, S_T , increases as Le decreases. The correlation between S_T and u' found in previous $Le = 1$ simulations has a strong Lewis number dependency. The variance of the pdf of the flame curvature increases as Le decreases, indicating the flames become more wrinkled. A strong correlation between local flame speed and curvature was found. For $Le > 1$, the flame speed increases in regions concave towards the products and decreases in convex regions. The opposite correlation was found for $Le < 1$. The mean temperature of the products was also found to vary with Lewis number. For $Le = 0.8$, it is less than the adiabatic flame temperature and for $Le = 1.2$ it is greater.

1. Introduction

Premixed flame propagation in many technologically important flows is essentially a front propagation problem. The flame is a propagating surface separating regions of unburnt reactants from burnt products. Such flames are classified as being in the flamelet regime characterized by large Damkohler numbers, Da, which is the ratio of inverse strain rate to chemical time scale. For large Da, the flame responds quickly to strain, and its local structure is maintained sufficiently so that the flame is a propagating front.

In the flamelet regime, the important issues concern the total area and local propagation speed of the front. This information gives the total consumption rate of reactants which defines the turbulent flame speed. The first of these issues, total flame area, in a sense incorporates the second issue since it is controlled by the complete interaction of turbulence and flame. The turbulence convects, stretches, and wrinkles the flame while it propagates forward tending to reduce the wrinkling. Most current approaches to understanding this issue involve relating the time evolution of the area to turbulence effects (convection, strain, diffusion) and propagation effects (collisions, dewrinkling) (Cant *et al.*, 1990; Candel *et al.*, 1990).

1 University of Wisconsin - Madison
2 Center for Turbulence Research

The second issue in the flamelet regime, the local propagation speed, depends on local strain and curvature effects. For moderate values of Da less than unity, the flamelet regime is still valid, but the local structure is altered. The most likely result is that the flame is compressed and the local speed is reduced (Libby and Williams, 1982). In unity Lewis number flames, this is the primary effect of turbulence on flames in the flamelet regime.

However, most real reactants have non-unity Lewis numbers, and curvature of the flame surface becomes important. The Lewis number, Le , is the ratio of thermal diffusivity to reactant mass diffusivity. The effect of curvature for $Le \neq 1$ can be described with reference to Figure 1. Thermal energy and reactant diffuse in opposite directions along their respective gradients. For the case $Le < 1$, the reactant diffuses more rapidly than thermal energy. In region A, the curvature of the flame front results in a 'focusing' of reactant. This, in turn, results in an enhancement of reaction and local propagation speed. The opposite situation occurs in region B with reactant being 'defocused' and the local speed decreasing. Hence, for $Le < 1$, a wrinkled flame is unstable, and we expect to see a wrinkled, cusped front. For $Le > 1$, the situation is the opposite: thermal energy is 'defocused' in A and 'focused' in B. This results in slower speeds at A and higher speeds at B - a stable situation leading to less wrinkled flame fronts. This thermo-diffusive mechanism is well-known for laminar flames. Its importance in turbulent flows remains an open question.

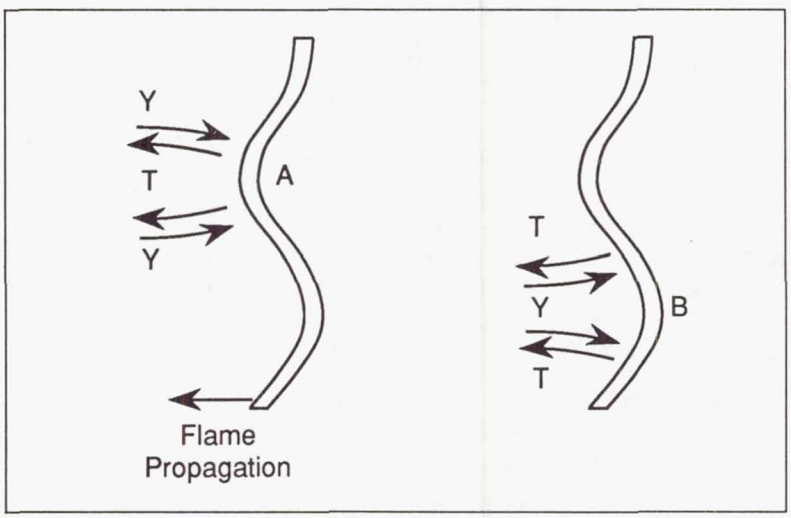

FIGURE 1. The influence of flame curvature on diffusion directions for temperature, T, and reactant mass fraction Y.

In the present work, we examine the effects of Lewis number on turbulent flames using direct numerical simulations. The objectives are: (1) begin a data base of three dimensional, non-unity Lewis number, turbulent premixed flame simulations, (2) examine the effects of Lewis number on global flame characteristics such as

the turbulent flame speed and examine various correlations with global turbulence parameters, (3) study the local flame structure and investigate the thermo-diffusive mechanism presented in Figure 1. Two cases were run, each with $Le = 1.2$ and 0.8. The present work is an extension of the $Le = 1$ simulations of Rutland *et al.* (1989), which should be referred to for more detailed information. The turbulent velocity fields are referred to as cases 2 and 3 because they were previously labelled this way in the $Le = 1$ simulations. These velocity fields simulate decaying homogeneous turbulence. A modified version of the Rogallo code (1981) was used, and the flame chemistry is represented by a single step, finite rate (Arrhenius law) kinetic scheme. The simulations are constant density, and no feedback from the flame to the flow field is allowed. The code uses spectral methods in a three-dimensional cubic domain with periodic boundary conditions. Two flame fronts, propagating outwards from the center of the domain, are required to satisfy the (periodic) boundary conditions. The unperturbed plane laminar flame speeds, S_L , are: 0.390 for $Le = 1$, 0.416 for $Le = 1.2$, and 0.361 for $Le = 0.8$.

2. Results

2.1. Turbulent flame speed

The turbulent flame speed, S_T , is calculated by integrating the reaction rate over the volume and normalizing by the laminar flame speed. This measures the total consumption rate of the reactants. Figure 2 shows the effect of Lewis number on S_T . The flame speed is decreased for $Le > 1$ and increased for $Le < 1$. This is consistent with the effect of unequal diffusivities in curved regions of the flame. The $Le > 1$ flame is stable and tends to flatten out wrinkled regions, while the $Le < 1$ flame is unstable and wrinkles are accentuated. The effect of Lewis number on S_T is opposite to the effect on S_L . Thus, in these simulations the variation of S_L is masked by the turbulence effects even though the ratio $\frac{u'}{S_L}$ is of order unity.

Commonly, S_T is correlated with u' based on the idea that the wrinkling effect of the turbulence on the flame front is controlled by u' . The correlations are presented in Figure 3. Previously, (Rutland *et al.*, 1989) a correlation with u' was found in $Le = 1$ simulations but only after flame-turbulence equilibrium is achieved. In our terminology, equilibrium is reached when the flame speed begins to decay along with the decaying turbulence. In Figure 3, the different Lewis number curves have similar shapes which, according to previous work, indicates a correlation exists. However, there is a definite Lewis number effect. Often these correlations contain a correction for Reynolds number (Williams, 1985) but not one for Lewis number. The Reynolds number is identical for the three Lewis numbers in each case, so all of the variation is due to Le .

2.2. Flame curvature

As the Lewis number varies, changes in the curvature characteristics of the flame are expected. Curvature is defined in planes tangent to constant progress variable surfaces, positive curvature being convex towards the reactants. The progress variable, c , varies monotonically from 0 in the reactants to 1 in the products, and is defined as $1 - Y$, where Y is the normalized reactant mass fraction.

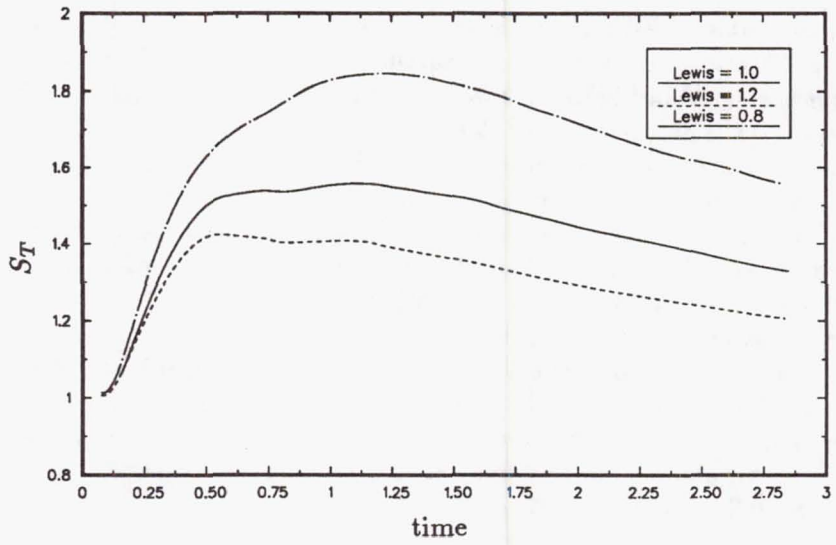

(a)

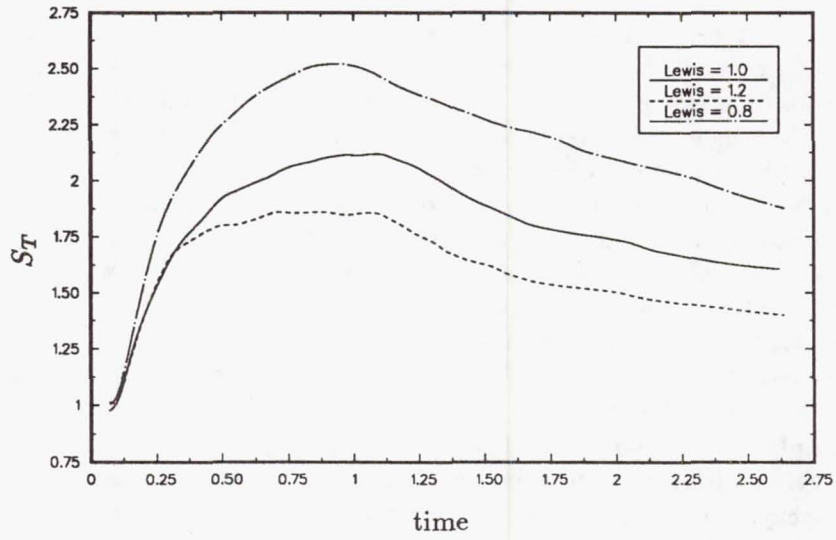

(b)

FIGURE 2. Turbulent flame speeds (normalized by S_L) vs. time; (a) Case 2, (b) Case 3

Probability density functions of curvature are presented in Figure 4. Curvature is defined as the half-sum of the local principal radii of curvature. For all Lewis numbers shown, the pdf's are centered around zero (means vary from -0.003 to 0.001) and skewed towards negative values. As c increases, the skewness decreases to values less than -0.61 for $c = 0.9$. There is also a tendency for the skewness to decrease as Le increases.

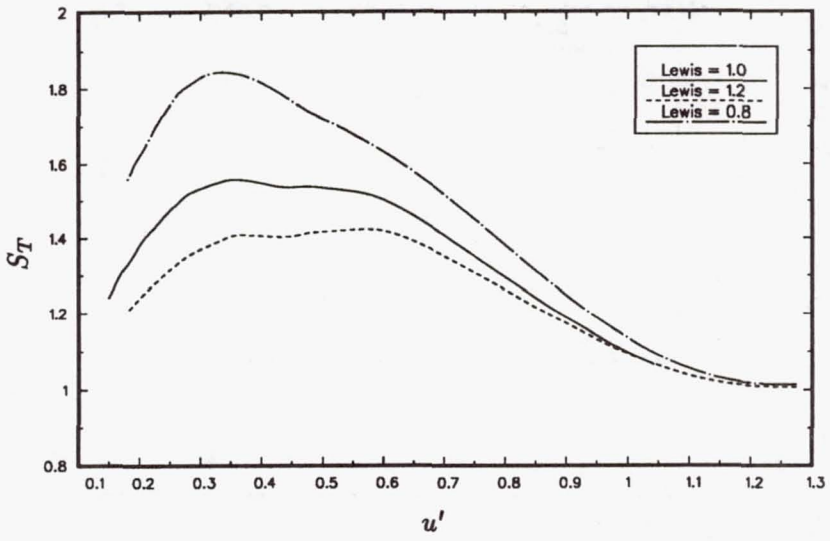

(a)

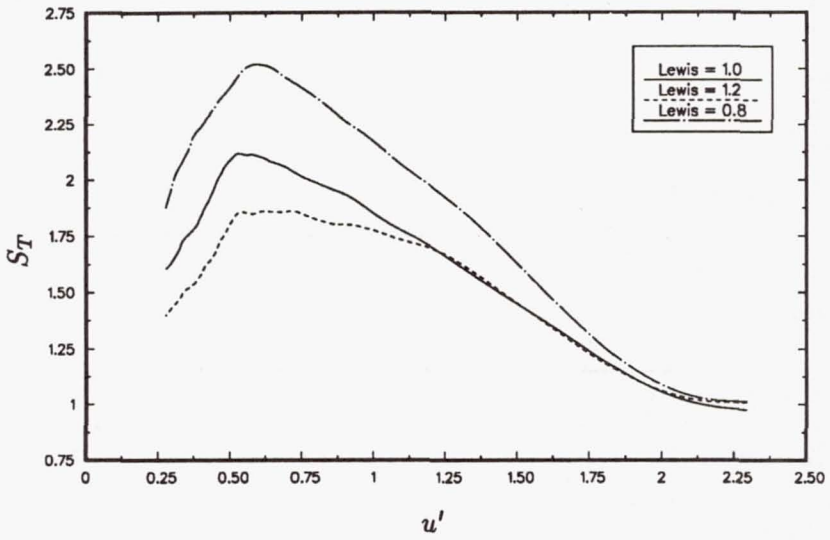

(b)

FIGURE 3. Turbulent flame speed vs. u'; (a) Case 2, (b) Case 3

The main effect of Lewis number on the curvature pdf's is for the peak values in the hot side of the flame to decrease as Le decreases. This is indicated by an increase in the variances. Evaluated at $c \geq 0.5$, the variances are 0.06, 0.08, and 0.11 in order of decreasing Le . This indicates the reaction zone becomes more curved as the Lewis number decreases, which is consistent with our expectations of thermal-diffusive effects.

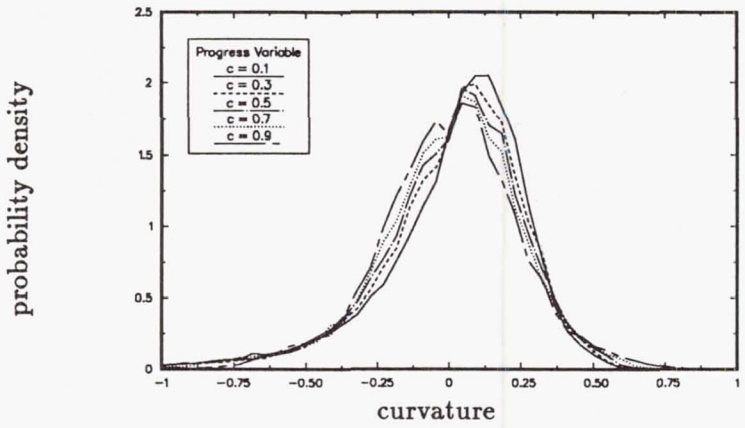

(a)

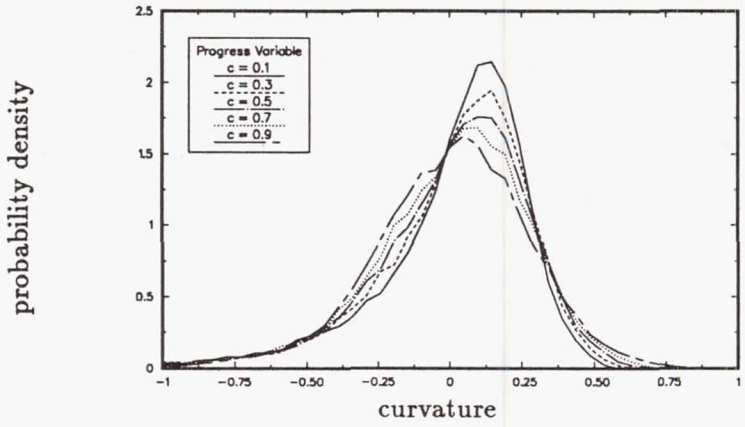

(b)

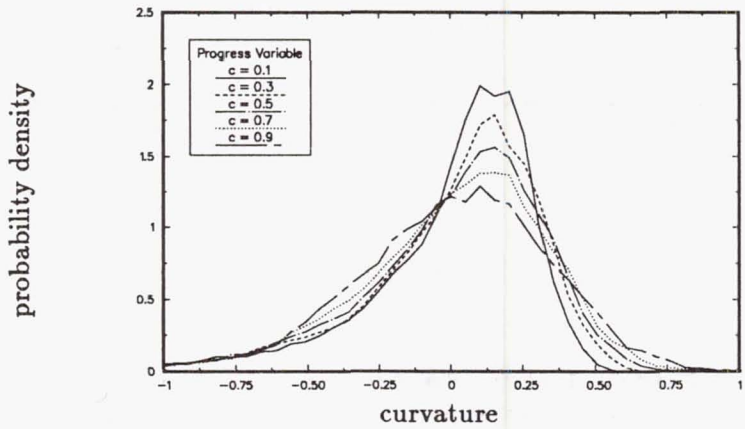

(c)

FIGURE 4. Probability density function of curvature normalized by the one-dimensional flame thickness: $\delta = (T_{burned} - T_{unburned})/\frac{dT}{dx}_{max}$; (a) $Le = 1.2$, (b) $Le = 1.0$, (c) $Le = 0.8$

A principal issue for non-unity Lewis number flames is what effect flame curvature has on local flame speed. In order to focus on curvature effects, the simulations were examined at times when $Da > 1$ and strain effects are relatively minor. Contour plots of reaction rate taken in x, z planes show the local reaction rate depends on curvature, and the dependence is opposite for $Le > 1$ and $Le < 1$ (Figure 5).

More quantitative results are obtained by calculating the local flame speed. This is accomplished by interpolating the temperature and reactant mass fraction along the gradient of c and integrating the resulting reaction rate across the flame. The results are shown in a joint pdf of flame curvature and flame speed (Figure 6). For $Le > 1$, the local flame speed is increased in regions of negative curvature and decreased in regions of positive curvature. The opposite effect occurs for $Le < 1$. The local flame speeds and curvature are well correlated, and the approximate slopes of lines drawn through the maximum regions are -0.6 for $Le = 1.2$ and $+0.5$ for $Le = 0.8$. These results are consistent with the qualitative explanation of Lewis number effects.

Another effect of Lewis number on local flame structure is for strain effects to qualitatively vary for $Le > 1$ and $Le < 1$. Even though the Damkohler number is 1.3 for data presented in Figure 6 and strain effects are small, they are still present. This is seen in the pdf's when the curvature is zero and only strain effects remain. Then the local flame speed is shifted from unity: decreased for $Le > 1$ and increased for $Le < 1$. This is consistent with one-dimensional asymptotic analysis (Libby *et al.*, 1983) in which the compressive strain is aligned with the flame normal. Examination of the non-unity Lewis number simulations show this alignment to be the most common, similar to the $Le = 1$ simulations.

2.3. Product temperatures

For an $Le = 1$ adiabatic system, the temperature and reactant mass fraction sum to unity at every point. In the product region behind the flames, the reactant mass fraction is zero and the temperature is unity ($T = 1$ is the non-dimensional adiabatic flame temperature). However, for non-unity Lewis numbers, the point-wise constraint on temperature and reactant mass fraction does not exist, and the temperature varies behind the flame. This occurs in curved regions consistent with the local reaction rates in Figure 5. Contour plots of temperature (not shown) reveal local hot spots behind negatively curved regions for $Le > 1$ and behind positively curved regions for $Le < 1$. This effect was also found in two dimensions by Haworth and Poinsot (1990) and Ashurst *et al.* (1987). In the present work, this is shown in Figure 7 in a plot of the pdf of the temperature conditioned on the progress variable being unity. For $Le < 1$, the average temperature is less than unity, and for $Le > 1$, it is greater than unity. These local deviations in the burnt gas temperature can have important consequences on pollutant formation with hot regions contributing to NOx production and cool regions contributing to unburnt hydrocarbon production. On initial inspection, Figure 7 may appear to violate the adiabatic constraints on the system. However, the sample obtained by conditioning on $c = 1$ does not define an adiabatic system since temperature gradients exist at the flames. In addition, the pdf's in Figure 7 consider only the fully burnt gases

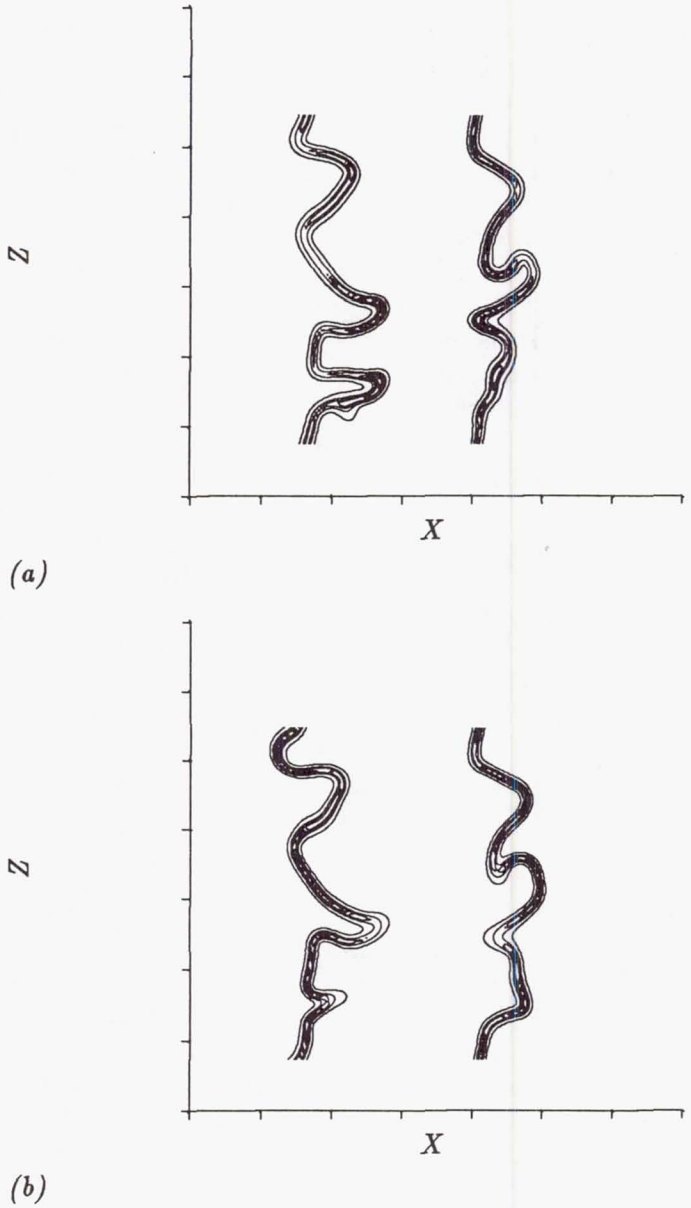

FIGURE 5. Contours of reaction rate; (a) $Le = 1.2$, (b) $Le = 0.8$

and ignore the partially burnt regions within the flame zones.

3. Conclusion

The direct numerical simulations of turbulent premixed flames with non-unity Lewis numbers generally show the flames behaving in an expected manner. Differential diffusion represented by the Lewis number affects local reaction rates, which in turn affects the global character of the flames. Most notable in these results is

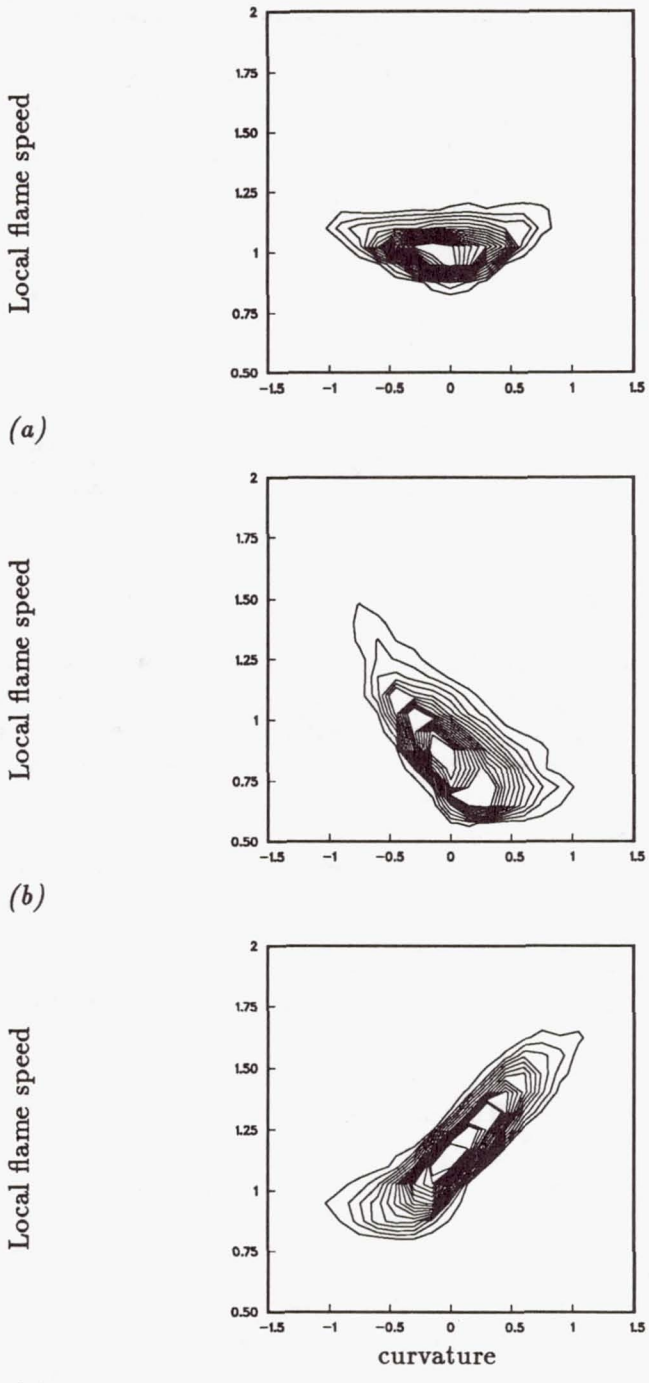

FIGURE 6. Joint pdf of local flame speed and local flame curvature. Flame speeds are normalized by the one-dimensional, laminar flame speeds; (a) $Le = 1.0$, (b) $Le = 1.2$, (c) $Le = 0.8$.

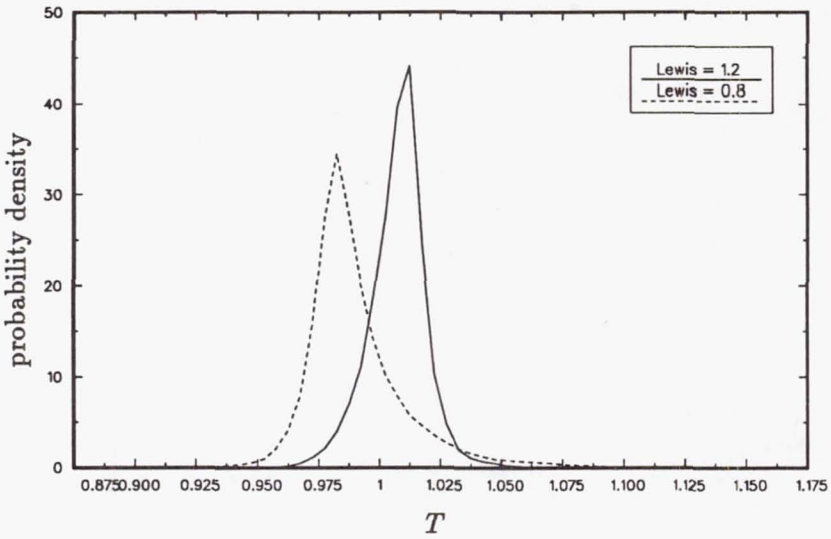

FIGURE 7. Probability density function of temperature conditioned on $c = 1$.

the strong correlations between local flame speed and curvature. Indications are that Lewis number effects could be much more important than strain effects for determining the local flame speed. Future work will address this issue directly since it has major implications for flamelet libraries used in turbulent flame models.

An unexpected finding was the strong variation in product temperature with Lewis number. This is especially significant because of its potential effect on pollutant formation. Further study is required to clarify, characterize, and quantify this result.

This work expands the previous work of $Le = 1$ flames. A data set covering all of the major aspects of single step, constant density turbulent premixed flames now exists. Future work will endeavor to put together a complete picture of these flames.

REFERENCES

ASHURST, W. T., PETERS, N. & SMOOKE, M. D. 1987 Numerical simulation of turbulent flame structure with non-unity Lewis number. *Combust. Sci. and Tech.* **53**, 339-375.

CANDEL, C., VEYNANTE, D., LACAS, F., MAISTRET, E., DARABIHA, N., & POINSOT, T. 1990 *Coherent flamelet model: applications and recent extensions*, Recent Advances in Combustion Modeling, B. Larrouturou ed., World Scientific, Singapore.

CANT, R. S., POPE, S. B., & BRAY, K. N. C. 1990 Modeling of flamelet surface-to-volume ratio in turbulent premixed combustion. *Twenty Third Symposium (International) on Combustion, The Combustion Institute.*

HAWORTH, D. C., & POINSOT, T. J. 1990 The influence of Lewis number and nonhomogeneous mixture on premixed turbulent flame structure. *Center for Turbulence Research Report CTR-S90*, Stanford University and NASA Ames.

LIBBY, P., LINAN, A. & WILLIAMS, F. 1983 Strained premixed laminar flames with non-unity Lewis number. *Combust. Sci. and Tech.* **34**, 257.

LIBBY, P. & WILLIAMS, F. 1982 Structure of laminar flamelets in premixed turbulent flames. *Combus. and Flame.* **44**, 287.

RUTLAND, C. J., FERZIGER, J. H., & CANTWELL, B. J. 1989 *Effects of strain, vorticity, and turbulence on premixed flames*, Report TF-44 Thermosciences Division, Dept. of Mech. Engineering, Stanford University.

ROGALLO, R. S. 1981 *Numerical experiments in homogeneous turbulence*, NASA Technical Memorandum 81315.

WILLIAMS, F. A. 1985 *Combustion theory, 2nd ed.*, Benjamin Cummings, Menlo Park.

VI. The turbulence theory group

The projects of the "Theory" group deal with the most fundamental aspects of turbulence dynamics: the source, transfer, and dissipation of turbulent kinetic energy, and their structure in space and scale. These aspects are of intrinsic interest, and an understanding of them is required for the development of accurate and robust subgrid (and supergrid) models for large-eddy simulation.

Chasnov analyzes the short-time evolution from rest of the velocity field produced by the action of gravity on an initially homogeneous isotropic density perturbation. The resulting large-scale energy spectrum is then used as the initial state for a *linear* analysis of the final period of decay. The solution indicates that some of the energy lost to viscous dissipation is replaced by the action of buoyancy forces, and the net energy decay rate is reduced to the point that the growth of the length scale is more rapid than the decay of the velocity scale. The turbulence Reynolds number then increases with time, the assumption of linearity fails, and the final decay is presumed to be nonlinear, and possibly self similar. The rapid growth of length scales presents a challenge to the Fourier spectral numerical methods employed for homogeneous simulations because the spatial period is fixed to adequately resolve the largest scales initially present and the turbulence scales are soon constrained by this fixed length. At present we do not have an acceptable solution to that problem.

Domaradzki, in a continuation of his work at the 1988 summer program, investigated inter-scale interactions and energy transfer in homogeneous turbulence. The processes observed in homogeneous shear flow were the same as those observed previously in the isotropic case. The physical-space distribution of transfer by nonlocal interactions is observed to be intermittent and to coincide more closely with regions of high large-scale energy than with those of high large-scale strain rate. The transfer spectra also collapse better when scaled with large-scale energy rather than with strain rate. This is counter to what one would expect from a disparate-scale analysis in which the large scales are expanded locally in Taylor series. There the lowest term, uniform velocity, would not contribute to transfer and the next term, a uniform velocity gradient, would be the relevant large-scale parameter. The notion that transfer among the small scales is directly influenced, at high Reynolds numbers, by the large scales is counter to the classical hypothesis of Kolmogorov and its acceptance will require a convincing explanation. At present, analyses based on triad interactions (EDQNM and the works of Brasseur & Corrsin (1987, *Advances in Turbulence*, Springer-Verlag) and Yeung & Brasseur (1990, submitted to *Physics of Fluids A*) do predict the observed nonlocal interaction, but the corresponding analyses in physical space have not appeared. In view of the increasing interest in this problem, I expect that it will soon be resolved.

Farge *et al.* use a continuous wavelet analysis to study the space-scale structure of two basic inhomogeneous flows. Wavelet analysis allows one to move between physical space and scale space in a systematic way that provides access to spatial and scale information simultaneously. It is then possible to measure such fundamental

quantities as the spatial intermittence of energy transfer and the spatially local flow Reynolds number. The latter is related to the question of whether the spatially local transfer is the result of local instability, or simply the result of straining by larger scales. The computational evidence suggests the latter, but this may be simply because the achievable local Reynolds numbers are too low to allow the former. This question is obviously related to the conflict mentioned above between the local cascade hypothesis of Kolmogorov and the transfer measured in simulations. Wavelets also provide an alternative closure space for large-eddy simulation where today there is some debate about whether one should close (model) in physical or wave space.

Bob Rogallo

Generation of large-scale density fluctuations by buoyancy

By J. R. Chasnov[1], and R. S. Rogallo[2]

The generation of fluid motion from a state of rest by buoyancy forces acting on a homogeneous isotropic small-scale density field is considered. Nonlinear interactions between the generated fluid motion and the initial isotropic small-scale density field are found to create an anisotropic large-scale density field with spectrum proportional to k^4. This large-scale density field is observed to result in an increasing Reynolds number of the fluid turbulence in its final period of decay.

1. Introduction

Consider a random homogeneous density distribution created in a large body of fluid at rest. As a physical example, one can envision the creation of such a distribution in the ocean by melting ice. The buoyancy force acting on the random density distribution can result in turbulent motion of the fluid. Turbulence enhances mixing, so that subsequent generation of smaller-scale density and velocity fluctuations is expected, with a corresponding increase in the rates of viscous dissipation and diffusion. Hence, the scenario we envision is the initial creation of velocity fluctuations through buoyancy forces, a subsequent transfer of energy and scalar variance to smaller scales where molecular processes are more effective, and the ultimate smoothing of density fluctuations and return of the fluid to rest. Large-eddy simulations of highly-turbulent buoyancy-generated flows have quantitatively confirmed this picture of self-induced mixing (Batchelor *et al.*, 1990).

However, in this report we will be concerned with a more subtle effect. Whereas the dominant feature of three-dimensional turbulence is the cascade of energy and scalar variance to smaller scales, non-linear interactions can also result in a significant backscatter of energy and scalar variance to larger scales. In isotropic flows with steep initial spectra this backscatter gives rise to characteristic k^4 energy and scalar spectra at small k (Lesieur, 1987). Buoyancy-generated turbulence is axisymmetric rather than isotropic, and in this report we derive the resulting backscattered spectrum of the density fluctuations. We further show that the power law of this density spectrum at small wavenumbers can have important consequences for the final period of decay.

1 NASA Goddard Institute for Space Studies
2 NASA Ames Research Center

2. Equations of motion

Using the Boussinesq approximation, the fundamental equations for this flow are

$$\nabla \cdot \mathbf{u} = 0 \tag{1}$$

$$\frac{\partial \mathbf{u}}{\partial t} + \mathbf{u} \cdot \nabla \mathbf{u} = \mathbf{g}\theta - \nabla P + \nu \nabla^2 \mathbf{u} \tag{2}$$

$$\frac{\partial \theta}{\partial t} + \mathbf{u} \cdot \nabla \theta = D \nabla^2 \theta \ , \tag{3}$$

where $\mathbf{u}$ is the fluid velocity, $\theta = \rho'/\rho_0$, ρ_0 is the mean density, ρ' is the density fluctuation, $\nabla P = \nabla p - \rho_0 \mathbf{g}$, p is the pressure, $\mathbf{g} = (0, 0, -g)$ is the gravitational acceleration, ν is the kinematic viscosity, and D is the diffusivity of the fluid. It should be noted that we are considering situations in which the mean density gradient is zero.

3. Backscatter of scalar variance

We proceed to calculate the spectrum of large-scale density fluctuations created from an initial small-scale density disturbance. First, (1)-(3) are Fourier transformed, and the continuity equation is used to eliminate the pressure. We assume that the effects of ν and D may be neglected for sufficiently small times and large scales. Equations (1)-(3) then become

$$\frac{\partial u_i(\mathbf{k}, t)}{\partial t} = g P_{i3}(\mathbf{k}) \theta(\mathbf{k}, t) - i k_j P_{il}(\mathbf{k}) \int u_j(\mathbf{p}, t) u_l(\mathbf{q}, t) \delta(\mathbf{k} - \mathbf{p} - \mathbf{q}) \, \mathrm{dpdq} \tag{4}$$

$$\frac{\partial \theta(\mathbf{k}, t)}{\partial t} = -i k_j \int u_j(\mathbf{p}, t) \theta(\mathbf{q}, t) \delta(\mathbf{k} - \mathbf{p} - \mathbf{q}) \, \mathrm{dpdq}, \tag{5}$$

where $P_{ij}(\mathbf{k}) = \delta_{ij} - k_i k_j / k^2$. It is possible to expand $\theta(\mathbf{k}, t)$ and $u_i(\mathbf{k}, t)$ in Taylor series in time, substitute these expansions into (4) and (5), and explicitly solve for the $\mathbf{k}$-dependent coefficients (Batchelor, private communication). Such an approach will formally yield an exact expression for $u_i(\mathbf{k}, t)$ and $\theta(\mathbf{k}, t)$. However, in this report, we restrict our attention to the generation of large-scale density fluctuations. These fluctuations arise from non-linear interactions between the initial density fluctuations and the subsequent buoyancy-generated velocity fluctuations. Accordingly, we neglect the non-linear term in (4) and further consider only wavenumbers k smaller than wavenumbers, say of order k_*, at which the initial density field $\theta_0(\mathbf{k})$ is appreciable. The resulting equations may then be integrated for small times. Integration of (4) yields

$$u_i(\mathbf{k}, t) = t g P_{i3}(\mathbf{k}) \theta_0(\mathbf{k}) \tag{6}$$

to order t, and integration of (5), using (6), yields

$$\theta(\mathbf{k},t) = -\frac{i}{2}t^2 g k_j \int P_{j3}(\mathbf{p})\theta_0(\mathbf{p})\theta_0(\mathbf{q})\delta(\mathbf{k}-\mathbf{p}-\mathbf{q})\ \mathrm{d}\mathbf{p}\mathbf{q}, \tag{7}$$

for $k << k_*$ to order t^2. After multiplication of both sides of (7) by $\theta(\mathbf{k}',t)$, taking the ensemble average, and integrating over $\mathbf{k}'$, we obtain

$$\int \langle\theta(\mathbf{k},t)\theta(\mathbf{k}',t)\rangle d\mathbf{k}' = -\frac{1}{4}t^4 g^2$$

$$\times \int k_j k_l' P_{j3}(\mathbf{p})P_{l3}(\mathbf{p}')\langle\theta_0(\mathbf{p})\theta_0(\mathbf{p}')\theta_0(\mathbf{q})\theta_0(\mathbf{q}')\rangle$$

$$\times\delta(\mathbf{k}-\mathbf{p}-\mathbf{q})\delta(\mathbf{k}'-\mathbf{p}'-\mathbf{q}')d\mathbf{p}d\mathbf{q}d\mathbf{p}'d\mathbf{q}'d\mathbf{k}'. \tag{8}$$

Some assumptions about the statistics of the initial density distribution are necessary to close (8). We assume that the initial density distribution is isotropic, and more importantly, that the phases of $\theta_0(\mathbf{k})$ are randomly distributed. The fourth-order moment appearing in (8) may then be reduced to products of second-order moments (by means of the quasi-normal approximation), and the second-order moments may be expressed in terms of the initial scalar spectrum $G_0(k)$:

$$\langle\theta_0(\mathbf{p})\theta_0(\mathbf{p}')\theta_0(\mathbf{q})\theta_0(\mathbf{q}')\rangle = \frac{G_0(p)G_0(q)}{(4\pi)^2p^2q^2}[\delta(\mathbf{p}-\mathbf{p}')\delta(\mathbf{q}-\mathbf{q}')+\delta(\mathbf{p}-\mathbf{q}')\delta(\mathbf{q}-\mathbf{p}')]$$

$$+\frac{G_0(p)G_0(p')}{(4\pi)^2p^2q^2}\delta(\mathbf{p}-\mathbf{q})\delta(\mathbf{p}'-\mathbf{q}'). \tag{9}$$

Substituting (9) into (8) and integrating over $\mathbf{p}'$, $\mathbf{q}'$, $\mathbf{p}$ and $\mathbf{k}'$ yields (the third term in (9) integrates to zero)

$$\int \langle\theta(\mathbf{k},t)\theta(\mathbf{k}',t)\rangle d\mathbf{k}' = \frac{1}{4}t^4 g^2 k_m k_j$$

$$\times \int [P_{m3}(\mathbf{k}-\mathbf{q})+P_{m3}(\mathbf{q})]P_{j3}(\mathbf{k}-\mathbf{q})\frac{G_0(|\mathbf{k}-\mathbf{q}|)G_0(q)}{(4\pi)^2|\mathbf{k}-\mathbf{q}|^2q^2}d\mathbf{q}. \tag{10}$$

The wavenumber k has already been assumed to be much less than values of q for which the integrand is appreciable so that (10) reduces to the simpler expression

$$\int \langle\theta(\mathbf{k},t)\theta(\mathbf{k}',t)\rangle d\mathbf{k}' = \frac{1}{2}t^4 g^2 k_m k_j \int P_{m3}(\mathbf{q})P_{j3}(\mathbf{q})\frac{G_0(q)^2}{(4\pi)^2q^4}d\mathbf{q}. \tag{11}$$

The integration over the angles of $\mathbf{q}$ can now be performed. Using

$$\int_0^{2\pi} d\phi \int_0^{\pi} d\theta sin\theta P_{m3}(\mathbf{q})P_{j3}(\mathbf{q}) = \frac{4}{15}\pi(\delta_{m1}\delta_{j1}+\delta_{m2}\delta_{j2}+8\delta_{m3}\delta_{j3}), \tag{12}$$

(11) becomes

$$\int \langle \theta(\mathbf{k},t)\theta(\mathbf{k}',t)\rangle d\mathbf{k}' = \frac{t^4 g^2}{120\pi}[k_\perp^2 + 8k_3^2]\int_0^\infty \frac{G_0(q)^2}{q^2}dq. \tag{13}$$

Equation (13) explicitly displays the axisymmetric nature of the generated large scale density distribution. The spectrum $G(k,t)$ may be obtained by integrating (13) over a spherical shell of radius k :

$$G(k,t) = \frac{1}{9}t^4 g^2 k^4 \int_0^\infty \frac{G_0(q)^2}{q^2}dq, \tag{14}$$

so that $G(k,t) \propto k^4$ for small k.

4. The Flow at Large Time

We will see that the generation of a large-scale density distribution has important consequences for the flow evolution at large times. In particular, we will examine the behavior of the statistics of the velocity field as $t \to \infty$. Now, for isotropic turbulence, the final period of decay is adequately described by the linearized Navier-Stokes equations (Batchelor, 1953), and we proceed here under the *tentative assumption* that the asymptotic flow evolution of buoyancy-generated turbulence can also be so described. The linear equations that we assume to govern the final period of decay may be obtained from (1)-(3):

$$\frac{\partial u_i(\mathbf{k},t)}{\partial t} = gP_{i3}(\mathbf{k})\theta(\mathbf{k},t) - \nu k^2 u_i(\mathbf{k},t) \tag{15}$$

$$\frac{\partial \theta(\mathbf{k},t)}{\partial t} = -Dk^2\theta(\mathbf{k},t)\ . \tag{16}$$

If we further assume that this linear final period of decay begins at a time t_f, and write $\theta(\mathbf{k},t_f) = \theta_f(\mathbf{k})$, then (15) and (16) are easily solved for $t > t_f$:

$$\theta(\mathbf{k},t) = \theta_f(\mathbf{k})\exp[-Dk^2(t-t_f)] \tag{17}$$

$$u_i(\mathbf{k},t) = u_i(\mathbf{k},t_f)\exp[-\nu k^2(t-t_f)]$$

$$+gP_{i3}(\mathbf{k})\frac{1}{(\nu-D)k^2}\left[\exp[-Dk^2(t-t_f)] - \exp[-\nu k^2(t-t_f)]\right]\theta_f(\mathbf{k})\ . \tag{18}$$

For the following, we restrict our attention to times $t >> t_f$. It is evident from (18) that the dominant contributions to $\langle u^2\rangle$ will come from small wavenumbers. Furthermore, if we assume that the kinetic energy spectrum follows the same power law behavior at small k as the density spectrum (which can be shown analytically by a careful computation of the kinetic energy backscatter spectrum), then the second

term on the right side of (18) dominates the first term due to the presence of the factor k^{-2}. Accordingly, we neglect the first term on the right side of (18), multiply (18) by $u_i(\mathbf{k}', t)$, and integrate over $\mathbf{k}'$ and $\mathbf{k}$ to get

$$\langle u^2 \rangle = \frac{\xi g^2}{(\nu - D)^2} \int_0^\infty dk \frac{\left[\exp[-Dk^2 t] - \exp[-\nu k^2 t]\right]^2}{k^4} G_f(k) \,, \tag{19}$$

where we have performed the angular integration over k and have introduced the constant ξ, of order unity, that arises from this integration. The behavior of $\langle u^2 \rangle$ as $t \to \infty$, may now be obtained from (19) by changing variables of integration from k to $\eta = k\sqrt{t}$:

$$\langle u^2 \rangle = \frac{\xi g^2 t^{3/2}}{(\nu - D)^2} \int_0^\infty d\eta \frac{\left[\exp[-D\eta^2] - \exp[-\nu\eta^2]\right]^2}{\eta^4} G_f(\eta/\sqrt{t}) \,. \tag{20}$$

For large η, the contribution to the integrand in (20) decreases rapidly, so that when $t \to \infty$, $G_f(\eta/\sqrt{t})$ may be expanded in a Taylor series around zero. If we assume that

$$G_f(k) \propto k^n \text{ near } k = 0, \tag{21}$$

then to lowest-order in $\eta/\sqrt{t}$

$$G_f(\eta/\sqrt{t}) \propto t^{-n/2}, \tag{22}$$

so that as $t \to \infty$,

$$\langle u^2 \rangle \propto t^{(3-n)/2} \,. \tag{23}$$

For the backscatter spectrum computed in §3, n is equal to 4 yielding a mean-square velocity decaying like $t^{-1/2}$. A divergence in the mean-square velocity occurs for $n < 3$. Obviously, the assumption that the linear analysis is valid at asymptotically large times must be false for $n < 3$, *i.e.*, if the initial density spectrum has a power law behavior near wavenumber zero less steep than k^3. However, we must also consider the validity of the linear analysis for the case $n = 4$. A length scale L associated with the energy containing eddies may be calculated from (18) (Batchelor, private communication), and it can be shown that all reasonable definitions yield

$$L \propto t^{1/2}, \tag{24}$$

independent of n, at large times. Hence, for $n = 4$, the Reynolds number R behaves asymptotically like

$$R = \frac{\sqrt{\langle u^2 \rangle} L}{\nu} \propto t^{1/4} \,, \tag{25}$$

which is also at odds with the assumption that the final period of decay is linear. The asymptotic scaling given by the linear analysis is therefore invalid and the

determination of the correct asymptotic behavior of $\langle u^2 \rangle$ in the final period of decay requires consideration of the full non-linear equations. Such numerical simulations of the full equations will be presented elsewhere.

5. Conclusions

We have shown that an initially isotropic small-scale density distribution will generate an anisotropic large-scale density distribution with a small wavenumber spectrum proportional to k^4. Furthermore, this large-scale density distribution has important consequences. In particular, it results in an increasing Reynolds number of the flow in the final period of decay. A decreasing Reynolds number implies the eventual validity of the linear analysis, yielding a *reductio ad absurdum*. Remarkably then, the motion thus generated by any initial density disturbance, no matter how weak, approaches an infinite Reynolds number flow asymptotically. This is true, even though the kinetic energy of the flow decays to zero.

Acknowledgments

This research is part of a continuing collaboration between JRC, Prof. G. K. Batchelor, and Dr. V. M. Canuto. In particular, JRC would like to thank Prof. Batchelor for his aid in clarifying the significance of the results obtained during the 1990 CTR Summer Program. Part of this work was done while JRC held a National Research Council — NASA Goddard Institute for Space Studies Research Associateship.

REFERENCES

Batchelor, G. K., Canuto, V. M., & Chasnov, J. R. 1990 Homogenous buoyancy-generated turbulence and mixing. in *Abstracts of the IUTAM Symposium on Fluid Mechanics of Stirring and Mixing.*

Batchelor, G. K. 1953 *The Theory of Homogeneous Turbulence*, Cambridge University Press.

Lesieur, M. 1987 *Turbulence in Fluids*, Martinus Nijhoff Publishers.

Interscale energy transfer in numerically simulated turbulence

By J. A. Domaradzki[1], R. S. Rogallo[2], and A. A. Wray[2]

Energy transfer is investigated for flows obtained by direct numerical simulations of low Reynolds number homogeneous-shear and isotropic turbulence and by large-eddy simulations of high Reynolds number isotropic turbulence. The transfer in spectral space is found to be local but results from interaction between separated scales. The transfer among small scales is highly intermittent in physical space. The measurements suggest an important correlation between transfer among small scales and the energy of large scales.

1. Introduction

Using results of low-Reynolds-number direct numerical simulations (DNS), Domaradzki and Rogallo (1988, 1990) analyzed the energy transfer in isotropic turbulence and concluded that beyond the energy containing range the energy was transferred among scales of motion similar in size but that the interactions responsible for this local energy transfer were nonlocal in k-space. The same transfer mechanism was also found when the eddy-damped quasinormal Markovian (EDQNM) approximation was applied to high Reynolds number flows which are inaccessible to the DNS technique.

The conclusions concerning the apparent universality of this transfer mechanism are extended in this work to homogeneous shear flows and to high Reynolds number isotropic flows obtained by large-eddy simulation. We also devise a physical-space representation of the spectral energy transfer calculated in k space that allows us to estimate the spatial intermittency of the energy transfer and the spatial correlation between quantities defined using only large-scales flow information and the dynamically important energy transfer among different scales. In particular, this is useful in evaluating the performance of subgrid-scale models formulated in physical space, e.g. the classical Smagorinsky eddy viscosity model.

2. Numerical Velocity Fields

We have used velocity fields generated by numerical simulations that were run for sufficiently long times to fully establish nonlinear interactions.

The velocity field C128U8 is the result of a DNS of uniformly sheared homogeneous turbulence performed by Rogers (1986), and LES128 is the result of a

1 University of Southern California
2 NASA Ames Research Center

large-eddy simulation of forced isotropic turbulence, at nominally infinite Reynolds number, performed by Chasnov (1990). The energy spectrum of LES128 exhibits a $k^{-5/3}$ law over the entire range of simulated wavenumbers. The field K128 is obtained from a DNS of isotropic turbulence performed by Rogallo (unpublished). Its use is motivated primarily by the fact that the two dynamically important processes that determine the evolution of the energy spectrum, i.e. viscous dissipation and nonlinear transfer, are very well resolved. This resolution is obtained at the expense of lowering the Reynolds number as compared with the two other cases.

3. Basic Quantities

The Navier-Stokes equations, in the Fourier spectral representation, for the fluctuating velocity field u_n subjected to uniform shear $\mathbf{U} = (sx_2, 0, 0)$ are

$$\left(\frac{\partial}{\partial t} + \nu k^2\right) u_n(\mathbf{k},t) = (-i/2)P_{nlm}(\mathbf{k}) \int u_l(\mathbf{p},t)u_m(\mathbf{k}-\mathbf{p},t)d\mathbf{p}$$

$$+2s\frac{k_1 k_n}{k^2}u_2(\mathbf{k},t) + sk_1\frac{\partial}{\partial k_2}u_n(\mathbf{k},t) - s\delta_{n1}u_2(\mathbf{k},t) \tag{1}$$

$$ik_n u_n = 0 \tag{2}$$

where

$$P_{nlm}(\mathbf{k}) = k_m(\delta_{nl} - k_n k_l/k^2) + k_l(\delta_{nm} - k_n k_m/k^2), \tag{3}$$

ν is the kinematic viscosity, and the summation convention is assumed. In subsequent formulae explicit time dependence will be omitted.

The equation for the energy amplitudes $\frac{1}{2}|u(\mathbf{k})|^2 = \frac{1}{2}u_n(\mathbf{k})u_n^*(\mathbf{k})$ is obtained from (1)

$$\frac{\partial}{\partial t}\frac{1}{2}|u(\mathbf{k})|^2 = -2\nu k^2\frac{1}{2}|u(\mathbf{k})|^2 + T(\mathbf{k}) + sk_1\frac{\partial}{\partial k_2}\frac{1}{2}|u(\mathbf{k})|^2 - sRe\{u_1(\mathbf{k})u_2^*(\mathbf{k})\} \tag{4}$$

where the asterisk denotes complex conjugate.

The nonlinear energy transfer is

$$T(\mathbf{k}) = \frac{1}{2}Im\left[u_n^*(\mathbf{k})P_{nlm}(\mathbf{k})\int u_l(\mathbf{p})u_m(\mathbf{k}-\mathbf{p})d\mathbf{p}\right] \tag{5}$$

and the following two terms in (4) containing s describe energy transfer due to the mean shearing deformation of turbulent eddies and turbulent energy production by the mean shear respectively. A detailed description of these effects is given by Deissler (1961), Fox (1964), and Lumley (1964), and is summarized in Hinze's (1975) monograph. Note that the corresponding equations for isotropic turbulence are obtained from (1) by taking $s = 0$. In particular, the nonlinear transfer term (5) has the same form for both homogeneous shear turbulence and isotropic turbulence.

The principal quantity of interest here is the energy exchange between a given mode $\mathbf{k}$ and all pairs of modes $\mathbf{p}$ and $\mathbf{q} = \mathbf{k} - \mathbf{p}$ that form a triangle having $\mathbf{k}$ as one of the legs and where $\mathbf{p}$ and $\mathbf{q}$ lie in prescribed regions $\mathcal{P}$ and $\mathcal{Q}$ of the spectral space respectively. For a given $\mathbf{k}$, confining $\mathbf{p}$ and $\mathbf{q}$ to $\mathcal{P}$ and $\mathcal{Q}$ is equivalent to selecting a specific set of triangles from all of the possible triangles contributing to the energy transfer at the wavevector $\mathbf{k}$ in (5).

In this work, we choose $\mathcal{P}$ and $\mathcal{Q}$ as shells in the wavenumber space $k - \frac{1}{2}\Delta k < |\mathbf{k}| < k + \frac{1}{2}\Delta k$ with a shell thickness Δk. This choice is natural for isotropic turbulence and is also convenient for other homogeneous fields as first suggested by Batchelor (1953).

The net nonlinear energy transfer to wavenumber band k is denoted by $T(k)$, and the contribution to this transfer resulting from nonlinear interactions between wavenumbers in the band k and wavenumbers in the bands p and q is denoted by $T(k|p,q)$. According to this definition

$$T(k) = \sum_p \sum_q T(k|p,q) = \sum_p P(k|p) \tag{6}$$

where the $P(k|p)$ is the result of summation of $T(k|p,q)$ over all bands q and is interpreted as the contribution to the net energy transfer into band k due to all interactions involving band p.

The functions $T(k)$, $P(k|p)$, and $T(k|p,q)$ give progressively more detailed information about energy transfer among different scales of motion in a turbulent field. The method of computing these functions is described by Domaradzki and Rogallo (1990).

4. Analysis of Energy Transfer in Spectral Space

All of the contributing terms of (4), computed for the field C128U8 and averaged over spherical shells with thickness $\Delta k = 1$, are plotted in figure 1. The calculation of the linear transfer $sk_1 \frac{\partial}{\partial k_2} \frac{1}{2}|u(\mathbf{k})|^2$ suffers from low accuracy due to the coarse resolution of $\mathbf{k}$, and we believe that this term is close to zero for $k > 40$, contrary to the plotted results. Despite this numerical error, a few important conclusions can be drawn from these results. Nonlinear transfer, viscous dissipation, and mean shear all make significant contributions to the energy balance for wavenumbers $k < 40$ which comprise the energy containing range and a significant fraction of the dissipation range. Energetics of the smaller eddies ($k > 40$) is affected only by nonlinear transfer and viscous dissipation which are roughly in balance. Thus, the energetics of turbulence in about half of the spectral domain ($k > 40$) is not affected directly by the large scale mean shear.

The triad structure of the nonlinear energy transfer term is illustrated by plotting $P(k|p)$ in figure 2a as a function of k for p fixed in a wavenumber band beyond the peak of the energy spectrum. The contributions $T(k|p,q)$ to $P(k|p)$, from all significant bands q, are also included. The peaks of $P(k|p)$ are located in the vicinity of the band p, indicating that the energy transfer is primarily between comparable scales of motion. However, the decomposition into functions $T(k|p,q)$ reveals that

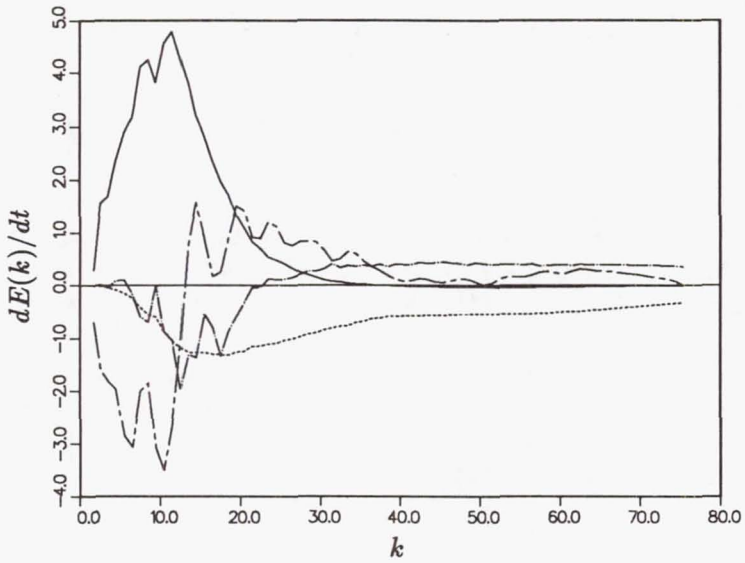

FIGURE 1. Spectral energy balance for the field C128U8. —— production, ---- dissipation, —·— nonlinear transfer, —-— linear transfer. The linear transfer data has been smoothed.

the largest contributions to this local transfer come from the interactions involving a scale in the energy containing range $5 < q < 20$. Thus, for homogeneous shear flow we obtain the same result as previously reported by Domaradzki and Rogallo (1988, 1990) for isotropic flows: local energy transfer between two scales beyond the energy containing range results from nonlocal interactions with scales in the energy containing range.

Analysis of the nonlinear transfer for the two remaining velocity fields, LES128 and K128, provided the same qualitative results.

An attempt was made to find a similarity scaling for the functions $T(k|p,q)$. For a given energy spectrum, the following transformation collapses reasonably well all curves $T(k|p,q)$ for a band p beyond the energy containing range.

$$T(k|p,q) = pE(p)E(q)T_s(\frac{k-p}{q}) \tag{7}$$

The similarity variable $\xi = (k-p)/q$ is deduced from geometric relations for a triad with legs k, p, and q and the scaling factor $pE(p)E(q)$ is *ad hoc* (but is found in the EDQNM theory for power-law spectra in the disparate-scale limit). In figure 2b we show the result of scaling (7) applied to the measured functions $T(k|p,q)$ of figure 2a. Interestingly, the transfer scales with the energy $E(q)$ of the large eddies rather than with their rate-of-strain $qE(q)^{1/2}$ which is the scaling postulated by a number of classical closure hypotheses (Monin and Yaglom, 1975). We have not been able to propose a convincing dynamical model of transfer processes which would provide scaling (7).

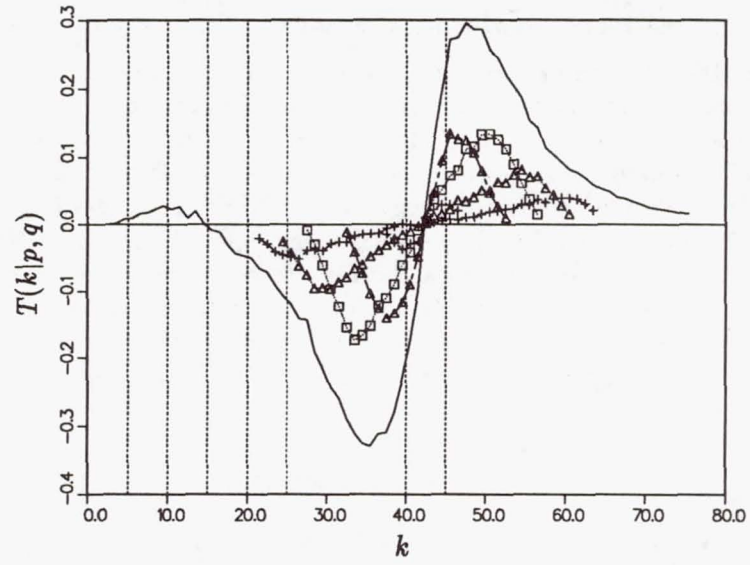

(a)

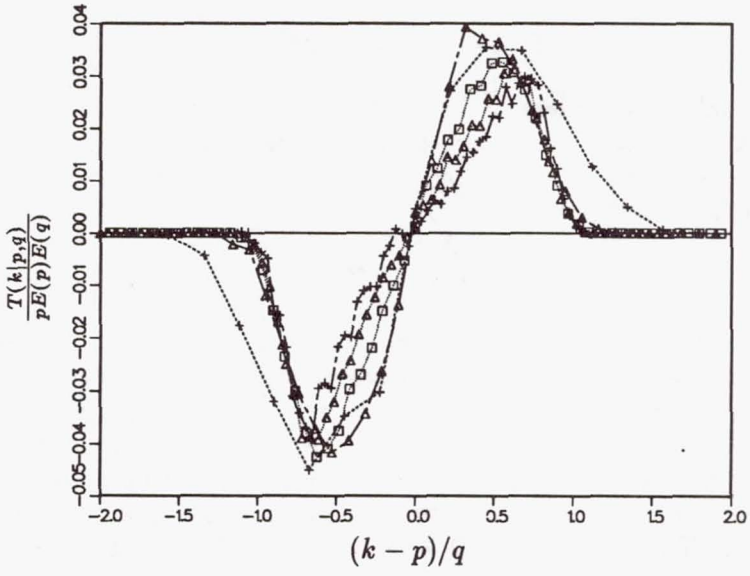

(b)

FIGURE 2. Detailed triad contributions to energy transfer for case C128U8: (a) unscaled, (b) scaled by (7). The transfer spectra $T(k|p,q)$ are shown for band $40 < p < 45$, and all bands q that make a significant contribution to $P(k|p)$. +---- $0 < q < 5$, △ —-- $5 < q < 10$, □ ····· $10 < q < 15$, △ ····· $15 < q < 20$, +—-- $20 < q < 25$, —— $P(k|p)$.

5. Physical Space Representation of Spectral Energy Transfer

Let us denote by $N_n^{\mathcal{P}\mathcal{Q}}(\mathbf{k})$ the contribution to the integral (the nonlinear term) in (1) from only those interactions between modes $\mathbf{p}$ and $\mathbf{q} = \mathbf{k} - \mathbf{p}$ such that each of them is confined to one of the two prescribed wavenumber bands $\mathcal{P}$ and $\mathcal{Q}$. This quantity is computed using the method described by Domaradzki and Rogallo (1990). Its Fourier transform to physical space, $N_n^{\mathcal{P}\mathcal{Q}}(\mathbf{x})$ say, gives the contribution to the rate of change of velocity in physical space $u_n(\mathbf{x}, t)$ caused by the nonlinear interactions involving two scales from the respective wavenumber bands $\mathcal{P}$ and $\mathcal{Q}$ in the spectral space. Note that these interactions influence all modes $\mathbf{k}$ that can form a triangle with modes such that one is in $\mathcal{P}$ and the other in $\mathcal{Q}$. Consider next a velocity field truncated to a prescribed wavenumber band $\mathcal{K}$, i.e.

$$u_n^{\mathcal{K}}(\mathbf{k}) = \begin{cases} u_n(\mathbf{k}), & \text{if } \mathbf{k}\epsilon\mathcal{K} \\ 0, & \text{otherwise.} \end{cases} \tag{8}$$

The Fourier transform of (8) to physical space, $u_n^{\mathcal{K}}(\mathbf{x})$ say, represents the contribution in physical space that scales from band $\mathcal{K}$ make to the total velocity. The contracted product of these two physical space quantities

$$T^{\mathcal{K}\mathcal{P}\mathcal{Q}}(\mathbf{x}) = u_n^{\mathcal{K}}(\mathbf{x}) N_n^{\mathcal{P}\mathcal{Q}}(\mathbf{x}) \tag{9}$$

gives a physical space representation of the energy transfer to/from modes in the k-band due to their nonlinear interactions with modes in the p- and q-bands.

An interesting case is obtained by dividing wavenumber space into two disjoint regions $\mathcal{K}$ ($k < k_c$) and $\mathcal{P}$ ($k > k_c$). The quantity

$$T_{SGS}(\mathbf{x}|k_c) = T^{\mathcal{K}\mathcal{P}\mathcal{P}}(\mathbf{x}) + T^{\mathcal{K}\mathcal{K}\mathcal{P}}(\mathbf{x}) \tag{10}$$

provides a physical space representation of the rate of change of energy of large scales $k < k_c$ due to nonlinear interactions involving small scales $k > k_c$. This is precisely the energy transfer process which is the subject of subgrid-scale modeling.

We have computed transfer functions (9) and (10) for various wavenumber bands of the field K128. The low wavenumber band $\mathcal{Q}$ is chosen to cover the entire energy containing range $0 < q < 10$. Figure 3a shows one plane from the full transfer (9) representing in physical space the energy transfer to eddies in the band $23 < k < 28$ caused by their interactions with eddies in the bands $20 < p < 25$ and $0 < q < 10$. The transfer function is spatially intermittent and is predominantly positive, indicating a flow of energy from the larger scales p to the smaller scales k. In figure 4b, we plot the same function for $17 < k < 22$. The transfer is now predominantly negative as expected and occurs at roughly the same locations as the transfer of figure 3a. We thus conclude that the local energy transfer between similar wavenumber modes in spectral space is intermittent in physical space.

We have attempted to correlate this spatial distribution of energy transfer with a number of simpler quantities (rate-of-strain, dissipation, energy, etc.) calculated from the velocity field truncated to contain only either large or small scales. In

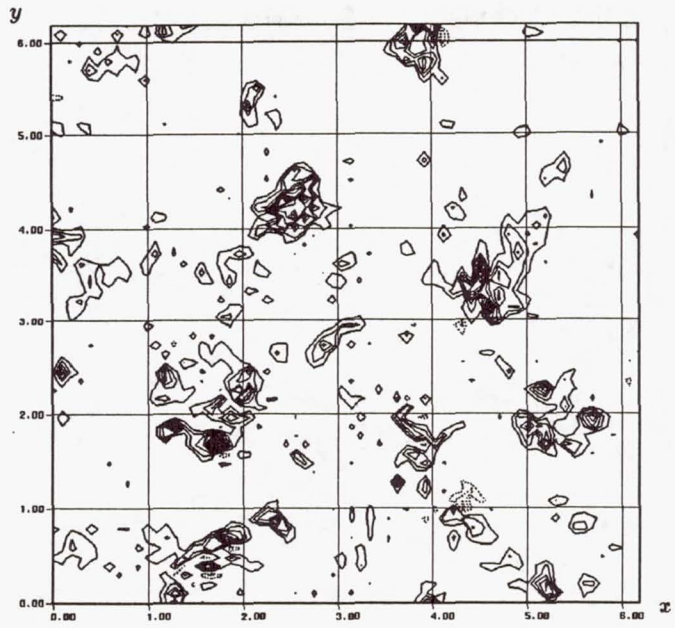

(a)

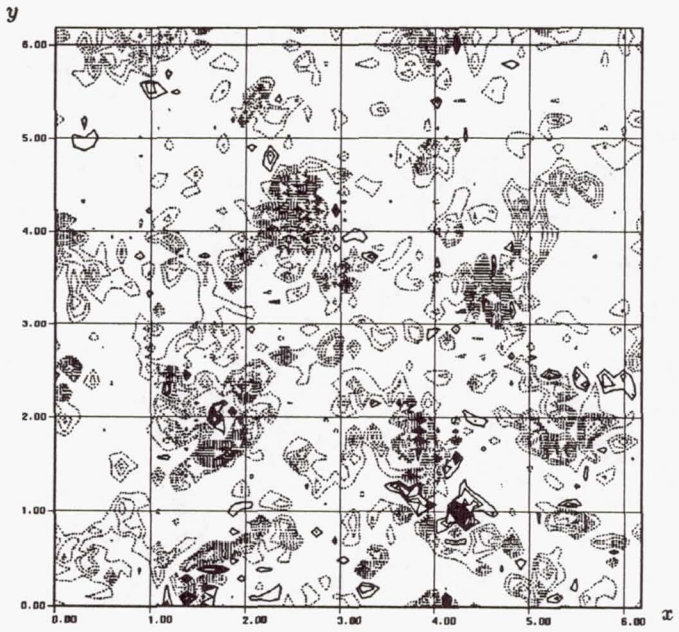

(b)

FIGURE 3. Energy transfer $T^{\mathcal{KPQ}}(\mathbf{x})$ of K128 in physical space for $20 < p < 25, 0 < q < 10$: (a) $23 < k < 28$, (b) $17 < k < 22$.

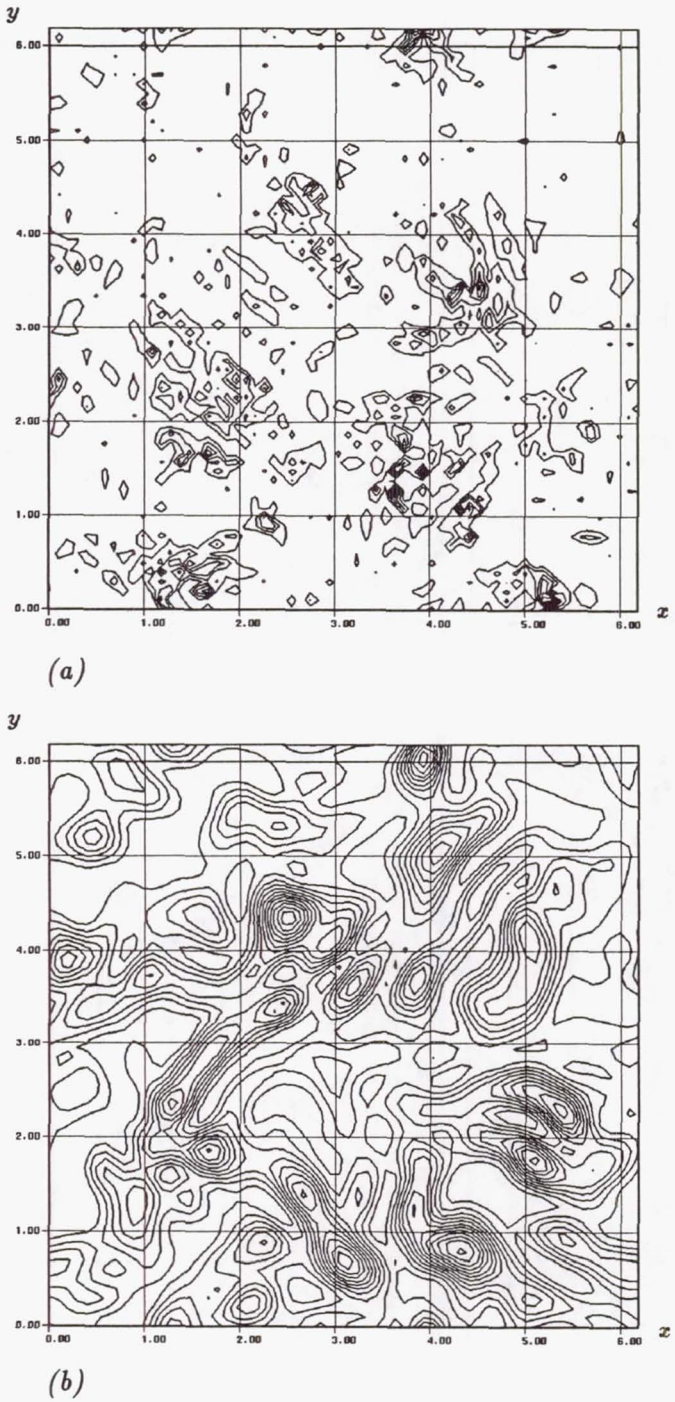

FIGURE 4. Turbulent energy in physical space for the velocity field truncated in spectral space to wavenumber band: (a) $23 < k < 28$, (b) $0 < k < 10$.

figures 4a and 4b, we show the physical-space distribution of energy for the velocity field truncated to $23 < k < 28$ and $0 < k < 10$, respectively. Both energy fields correlate very well with the energy transfer among small scales shown in figure 3. Correlation of other calculated quantities with the energy transfer, notably the square of the rate-of-strain tensor, was generally much worse. Therefore, we conclude that the energy transfer among small scales occurs mostly at those physical locations that contain large amounts of turbulent energy rather than at the locations of high strain rate. This correlation is the physical space counterpart of the observed importance of the nonlocal triads in the energy transfer process in spectral space.

We have used formula (10) to calculate subgrid-scale (SGS) energy transfer for the field K128 with the cutoff wavenumber $k_c = 10$. The full SGS transfer field, plotted in figure 5a for a typical plane, is characterized by the presence of both negative and positive regions. These indicate energy flux from and to the large scales respectively due to subgrid-scale interactions. The classical Smagorinsky model (Smagorinsky, 1963) for this transfer, based on the velocity field truncated to the large scales $0 < k < 10$, is plotted in figure 5b. Note that the model captures properly the locations of the regions where the transfer is most intense but fails completely to predict the inverse energy transfer from small to large scales.

6. Conclusions

Using results of direct numerical simulations of homogeneous shear turbulence, we have shown that the nonlinear energy transfer in spectral space beyond the energy containing range has the same character as reported previously for isotropic turbulence: *local* energy transfer caused by *nonlocal* triad interactions. The same conclusion was reached for velocity fields obtained in large-eddy simulations of isotropic turbulence at high Reynolds numbers.

An *ad hoc* scaling roughly collapses the transfer $T(k|p,q)$ to a self-similar form. This scaling implies an important role which the energetic scales play in the energy transfer among small scales, but the process does not appear to be simply straining of the small scales by the large ones.

We have devised a physical space representation of the energy transfer processes among scales of motion belonging to three distinct wavenumber bands in spectral space and conclude from it that the energy transfer among small scales is highly intermittent in physical space. Furthermore, regions of significant transfer appear to correlate better with regions of significant large-scale energy than with those of significant large-scale strain rate.

As a particular case, we have calculated the subgrid-scale energy transfer in isotropic turbulence. This SGS transfer exhibits regions of energy drain from large to small scales as well as significant regions of reversed energy transfer from small to large scales. The Smagorinsky eddy viscosity model captures the locations of the most intense transfer but predicts that it is always from large to small scales, contrary to the measurements from direct calculations.

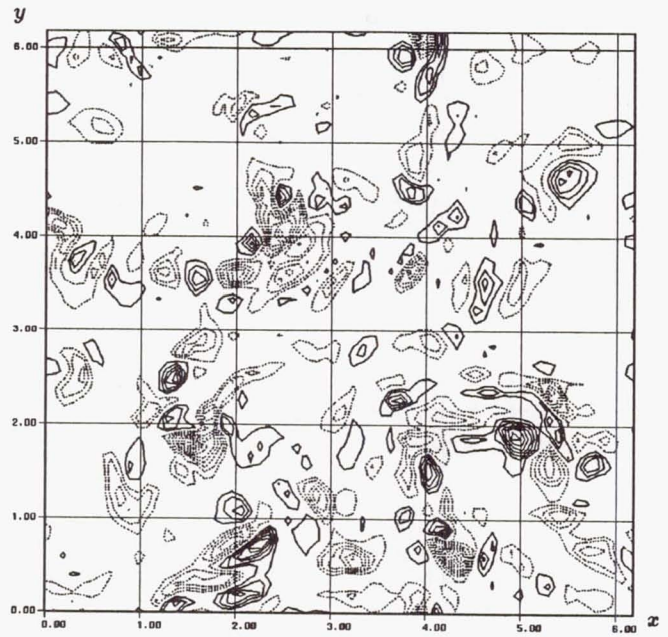

(a)

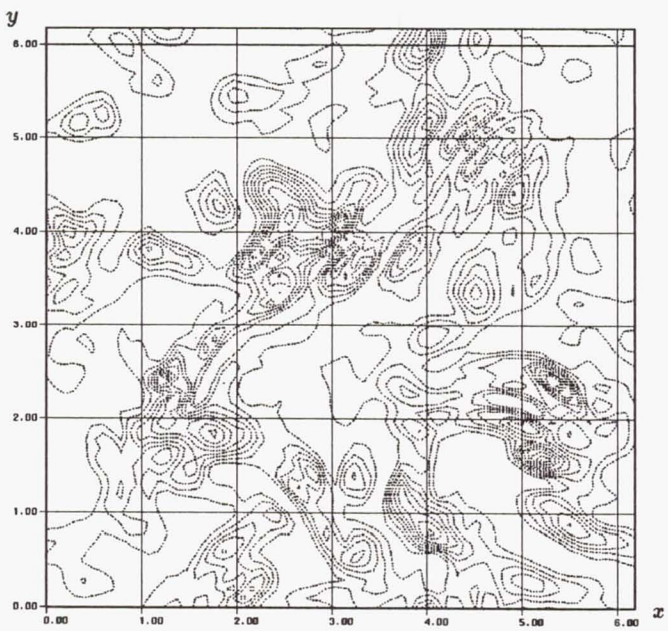

(b)

FIGURE 5. Subgrid scale energy transfer in physical space $T_{SGS}(\mathbf{x}|k_c)$ for $k_c = 10$: (a) measured, (b) computed using the Smagorinsky eddy viscosity model for the velocity field truncated to wavenumber band $0 < k < 10$.

REFERENCES

BATCHELOR, G. K. 1953, *The Theory of Homogeneous Turbulence*, Cambridge University Press.

CHASNOV, J. R. 1990 Ph.D. Dissertation, Columbia University

DEISSLER, R. G. 1961, *Phys. Fluids* **4**, 1187.

DOMARADZKI, J. A. & ROGALLO, R. S. 1988, in *Proceedings of Center for Turbulence Research, Summer Program 1988.*

DOMARADZKI, J. A. & ROGALLO, R. S. 1990, *Phys. Fluids* A**2**, 413.

FOX, J. 1964, *Phys. Fluids* **7**, 562.

HINZE, J. O. 1975, *Turbulence*, McGraw-Hill.

LUMLEY, J. L. 1964, *Phys. Fluids* **7**, 190.

MONIN, A. S. & YAGLOM, A. M. 1975, *Statistical Fluid Mechanics*, Vol. 2, The MIT Press, pp.212-241.

ROGERS, M. M., MOIN, P., & REYNOLDS, W. C. 1986 Report TF-25, Department of Mechanical Engineering, Stanford University

SMAGORINSKY, J. 1963, *Mon. Weath. Rev.* **91**, 99.

Continuous wavelet analysis of coherent structures

By M. Farge[1], Y. Guezennec[2], C. M. Ho[3] AND C. Meneveau[4]

We perform an analysis of planar cuts through three-dimensional turbulent fields (planar channel flow and mixing layer) using the 2D continuous wavelet transform. We propose two new diagnostics: (a) a measure of intermittency $I(r, \vec{x})$, which is the ratio of local energy and average energy at a given scale r. (b) a local Reynolds number, defined on the local velocity contribution at a given scale, computed from the wavelet transform of the three velocity components, the scale of the transform, and molecular viscosity; this gives a representation of the local non-linearity of the flow viewed in both space *and* scale. We find, for all the analyzed flows, strong small-scale intermittency located in the ejection regions for the channel flow and in the vortex core for the mixing layer.

1. Introduction

The wavelet transform is a new technique, first introduced by Grossmann and Morlet (1984), which allows the decomposition of a signal into contributions of both space (or time) *and* scales (or frequencies). Therefore, it is particularly well suited for the study of transients or possible singular behavior of a signal. The interesting feature of the wavelet transform, as opposed to the traditional Fourier transform, is to use an analyzing function (called wavelet) which is localized in space. The scale decomposition is performed by dilating or contracting this wavelet before convolving it with the signal to be analyzed. This procedure is an optimal compromise in view of the uncertainty principle: the wavelet transform gives a very good spatial resolution for the small scales and a very good scale resolution for the large scales. As for the Fourier transform, the original signal can be reconstructed from the wavelet transform, and the energy can be computed in the wavelet space (Parseval).

Several orthonormal wavelet bases exist (Lemarie & Meyer (1986), Daubechies (1988), Mallat (1989)), which conserve information and which are, therefore, convenient from a computational point of view, especially in higher dimensions (for an application to turbulence, see Meneveau (1990)). In the present work, we explore the use of the continuous wavelet transform (which is non-orthonormal and, therefore, redundant) for the analysis of turbulent flows (Farge & Rabreau 1988). The idea is to benefit from this redundancy and observe the signal for both scale and

1 CNRS-Ecole Normale Superieure
2 The Ohio State University
3 Univ. Southern California
4 Johns Hopkins University

position in a continuous fashion; this is expected to highlight coherent structures which should display some coherence not only in physical space but also across a range of scales (for a review of the continuous wavelet transform and its applications to turbulence, see Farge (1990)). Since the continuous wavelet transform adds one more dimension to the representation, at present we will study two-dimensional cuts through three-dimensional flow fields.

The objective is to compute the wavelet transform of flow-fields resulting from direct numerical simulations of turbulent flows. First we study the velocity and temperature fields in a plane channel flow near the wall in order to measure its intermittency and to try to correlate the active regions (where energy is still high even at the small scales) with some dynamical features such as the ejections from the sublayer. We will also study the isotropy of the flow at all scales *and* locations.

Then we study the simulations of the temporal mixing layer, where the objective is to also locate the small-scale activity in the flow and to measure its intermittency. For this we study not only the wavelet transform of vorticity, velocity, and a passively convected scalar, but we also compute the local Reynolds number. This gives a good picture of the local instability of the flow, measuring the ratio of non-linearity and dissipation at every scale *and* location.

For all turbulent flows studied here, we will try, using the continuous wavelet transform, to answer the three following questions:

(1) Where are the small scales of the flow, and how intermittent are they?

(2) What is the local scaling of energy or enstrophy, and is it different from one structure to another?

(3) What is the topology of the iso-Reynolds number manifold and what is its scale extension at the dissipative level?

2. The Continuous Wavelet Transform

The discussion of the wavelet transform is done in a general setting in n dimensional space. The only constraint imposed on a function

$$\psi(\vec{x}) \in L^2(R^n),$$

(R=real numbers) to be a wavelet is the admissibility condition:

$$C_\psi = \int_{-\infty}^{\infty} \ldots \int_{-\infty}^{\infty} |\, \hat{\psi}(\vec{k}) \,|^2 \, \frac{d^n \vec{k}}{|\, \vec{k} \,|^n} \; < \; \infty. \tag{1}$$

The function $\psi(\vec{x})$ can be either a real or complex-valued function. If $\psi(\vec{x})$ is integrable, Eq. (1) actually implies that it has zero mean:

$$\int_{-\infty}^{\infty} \ldots \int_{-\infty}^{\infty} \psi(\vec{x}) d^n \vec{x} = 0, \quad or \quad \hat{\psi}(\vec{k} = 0) = 0. \tag{2}$$

From this basic wavelet, we generate the family of dilated, rotated, and translated wavelets:

$$\psi_{r,\Omega,\vec{x}'}(\vec{x}) = c(r)^{-n}\psi(\Omega^{-1}\frac{\vec{x}-\vec{x}'}{r}), \tag{3}$$

where $r \in R^+$ is a scale dilation parameter, $\Omega \in (R^n \times R^n)$ is the (unitary) rotation tensor, $\vec{x}' \in R^n$ is the translation vector, and $c(r)$ is a normalization constant. Such normalization is actually the L^2 norm if $c(r) = r^{-1/2}$, and it is the L^1 norm if $c(r) = r^{-1}$.

The analysis of the signal $f(\vec{x})$ is then given by

$$\tilde{f}(r,\Omega,\vec{x}') = \frac{1}{\sqrt{C_\psi}} \int_{-\infty}^{\infty} \cdots \int_{-\infty}^{\infty} f(\vec{x})\psi^*_{r,\Omega,\vec{x}'}(\vec{x})d^n\vec{x}. \tag{4}$$

Here ψ^* denotes the complex conjugate of ψ. In two dimensions, the rotation tensor can be characterized by a single angle θ, and there the reconstruction formula reads:

$$f(\vec{x}) = \frac{1}{\sqrt{C_\psi}} \int_{r=0+}^{\infty} \int_{\theta=0}^{2\pi} \int_{x'=-\infty}^{\infty} \int_{y'=-\infty}^{\infty} \tilde{f}(r,\Omega(\theta),\vec{x}')\ \psi_{r,\Omega,\vec{x}'}(\vec{x})\ \frac{dr\ d\Omega(\theta)dx'dy'}{r^3}. \tag{5}$$

More of the basic properties of the wavelet transform are listed below. Here we denote the wavelet transform of a function $f(x)$ in the operator notation $W[f(x)]$ or with the tilde notation, $\tilde{f}(r,\Omega,\vec{x})$.

Linearity:

$$W[\alpha f_1(\vec{x}) + \beta f_2(\vec{x})] = \alpha\tilde{f}_1(r,\Omega,\vec{x}') + \beta\tilde{f}_2(r,\Omega,\vec{x}'). \tag{6}$$

Translation property:

$$W[f(\vec{x}-\vec{x}_0)] = \tilde{f}(r,\Omega,\vec{x}'-\vec{x}_0). \tag{7}$$

Dilation property:

$$W[f(\frac{\vec{x}}{r_0})] = \frac{1}{r_0}\tilde{f}(\frac{r}{r_0},\Omega,\frac{\vec{x}'}{r_0}). \tag{8}$$

Energy conservation:

$$\int_{-\infty}^{\infty} \cdots \int_{-\infty}^{\infty} [f(\vec{x})]^2 d^n\vec{x} =$$

$$\frac{1}{C_\psi} \int_{0+}^{\infty} \int_{\theta_1} \cdots \int_{\theta_{n-1}} \int_{x_1'=-\infty}^{\infty} \cdots \int_{x_n'=-\infty}^{\infty} [\tilde{f}(r,\Omega,\vec{x}')]^2 \frac{dr\ d^{n-1}\Omega\ d^n\vec{x}'}{r^{n+1}}. \tag{9}$$

Characterization of the local regularity of a function:

$$|| \tilde{f}(r, \Omega, \vec{x}_0) ||_{L^1} \sim r^{\alpha}, \quad for \quad r \to 0^+, \tag{10}$$

α is the degree of differentiability of the function at $\vec{x}_0$ if $\alpha \geq 1$, or the Lipschitz exponent of the singularity present in $\vec{x}_0$ if $-1 < \alpha < 1$.

Besides the necessary admissibility condition, the choice of the analyzing wavelet is determined largely by the condition of good localization as well as smoothness in both physical and spectral space. These conditions can be expressed as

$$| \psi(\vec{x}) | < \frac{1}{1 + | \vec{x} |^n} \tag{11.a}$$

and

$$| \hat{\psi}(\vec{k}) | < \frac{1}{1 + | \vec{k} - \vec{k}_0 |^n}, \tag{11.b}$$

$\vec{k}_0$ being the dominant frequency of the wavelet, and n should be as large as possible. For instance, the Haar wavelet (similar to a French hat) is irregular in space and does not decay fast enough in spectral space; the Maar wavelet (mexican hat) is smooth in physical space, but it is not regular enough is spectral space. For the purpose of this work, we also prefer to use a complex-valued wavelet. This is because for the analysis of one-dimensional signals the phase has proven to be rich in information, e.g. to detect singularities or to compute the instantaneous frequency (Escudier & Torresani, 1988). The local energy density at every scale can then be obtained from the modulus of the complex wavelet transform.

A good compromise in terms of both space (11.a) and scale (11.b) localization is attained with the Morlet wavelet, which is a complex valued function:

$$\hat{\psi}(\vec{x}) = e^{i\vec{k}_0 \cdot \vec{x}} e^{-\frac{|\vec{x}|^2}{2}} - C_1. \tag{12}$$

Here $\vec{k}_0$ is related to the number of oscillations of the basic wavelet within the modulated region, and C_1 is a correction term that guarantees admissibility (1) by forcing the mean of ψ to be equal to zero. In our code, the wavelet is sampled in physical space, then transformed to spectral space via FFT, and the admissibility condition is satisfied by setting $\hat{\psi}(\vec{k} = 0) = 0$. The convolutions needed to evaluate the wavelet transform (Eq. (4)) are performed in Fourier space (using FFT).

Figure 1 is a plot of the 2-D Morlet wavelet for $| \vec{k}_0 | = 6$ and $\theta = 0$.

3. Intermittency function and local Reynolds Number

An unambiguous characterization of the local 'activity' of a scalar field $f(\vec{x})$ is given by the intermittency function $I(r, \vec{x})$. It is defined in terms of the wavelet transform of $f(\vec{x})$ as follows:

$$I(r, \vec{x}) = \frac{| \tilde{f}(r, \vec{x}) |^2}{< | \tilde{f}(r, \vec{x}') |^2 >_{\vec{x}'}}, \tag{13}$$

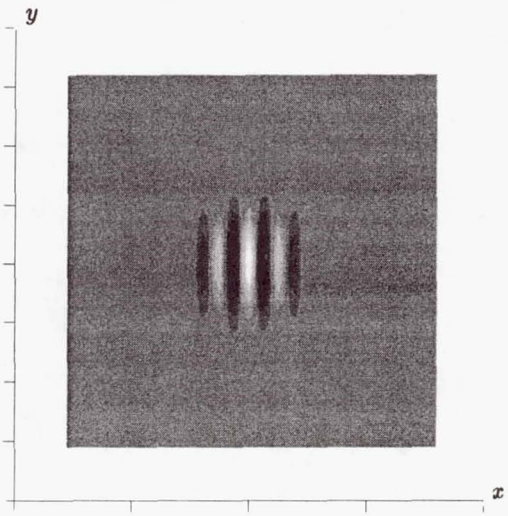

FIGURE 1. The two-dimensional Morlet wavelet, with $\theta = 0$ and $k_0 = 6$.

where the averaging extends over all points $\vec{x}'$. $I(r, \vec{x})$ then measures local deviations from the mean spectrum of a field, at every scale.

Another measure of interest is the local Reynolds number, defined in terms of the scale parameter r, the kinematic viscosity of the fluid ν, and some local root-mean-square value of the velocity field. This rms value should only correspond to contributions to the velocity field at that particular scale r. We concentrate on planar cuts through three-dimensional fields, but still consider all three velocity components on that cut. Let $\tilde{u}_i(r, x, y, \theta)$ be the continuous (2D) wavelet transform of the ith component of the fluctuating part of the velocity field in the plane of the cut, defined as follows:

$$\tilde{u}_i(r, x, y, \theta) = \frac{1}{\sqrt{C_\psi}} \int_{-\infty}^{\infty} \int_{-\infty}^{\infty} u_i(x', y')\, \psi^*_{r,\theta,x,y}(x', y')\, dx'\, dy'. \tag{14}$$

From here on we concentrate on a single angle, say $\theta = 0$, $\theta = \pi/2$, or the value of the wavelet coefficients averaged over 16 different angles equally sampled in $[0, 2\pi]$. The total kinetic energy can be obtained from

$$\frac{q^2}{2} = \frac{1}{2} \int_{r=0+}^{\infty} \int_{x=-\infty}^{\infty} \int_{y=-\infty}^{\infty} \tilde{u}'(r, x, y)^2\, \frac{dx dy dr}{r^3}, \tag{15}$$

where

$$\tilde{u}'(r, x, y) = \sqrt{\frac{1}{3C_\psi}[\tilde{u}_1(r, x, y)^2 + \tilde{u}_2(r, x, y)^2 + \tilde{u}_3(r, x, y)^2]}. \tag{16}$$

Here $\tilde{u}'(r,x,y)$ is the characteristic rms velocity at scale r and at location (x,y) in the plane being analyzed. Now we can define the local Reynolds number at every scale, according to

$$Re(r,x,y) = \frac{\tilde{u}'(r,x,y)\ r}{\nu}. \tag{17}$$

The expectation is that at large scales $r \sim L$, the Reynolds number should roughly coincide with the usual large-scale Reynolds number $Re = u'L/\nu$, where u' is the rms turbulent velocity and L is some integral scale of the flow. At the smallest scales (say $r \sim \eta$, where η is the Kolmogorov scale of the flow), one would expect this Reynolds number to be close to unity. The question we want to address here is about the variability of such a Reynolds number defined locally in space *and* scale. That is, are there locations where such a Reynolds number at some small scale is much larger than in others, and how such regions correlate with regions of small-scale activity in the flow? If so, then this could be a measure of the non-linearity at small scales (or at any desired scale); it is unambiguous because it is based on energy considerations. Such regions of high local Reynolds number could then also be interpreted as regions of strong non-linearity within the flow.

As mentioned in section 2, we utilize the Morlet wavelet to perform the analysis. In addition to location *and* scale, the angle of the wavelet can also be prescribed. For notational convenience we omit explicit reference to this angle when using $\theta = 0$ (with respect to the x-axis). When using another angle, we indicate this by adding another variable, e.g. $Re(r,x,y,\theta)$. Another issue of importance when computing the local Reynolds number is the precise value of the constant C_ψ. In the continuous case it is given by Eq.(1). However, in practice the convolutions needed to obtain the wavelet transform will be done discretely, which means that some discretization error is unavoidable. To obtain an effective constant C_ψ such that energy is the same in the physical and wavelet spaces, we compute C_ψ from

$$C_\psi = \frac{\int_{0+}^{\infty}\int_{-\infty}^{\infty}\int_{-\infty}^{\infty} [\tilde{u}_1(r,x,y)^2 + \tilde{u}_2(r,x,y)^2 + \tilde{u}_3(r,x,y)^2]\ \frac{dxdydr}{r^3}}{\int_{-\infty}^{\infty}\int_{-\infty}^{\infty} [u_1(x,y)^2 + u_2(x,y)^2 + u_3(x,y)^2]\ dxdy}. \tag{18}$$

This is then used to obtain $\tilde{u}'(r,x,y)$ (16) and $Re(r,x,y)$ (17).

4. Analysis of near-wall dynamics in turbulent channel flow

In this section, we analyze a turbulent channel flow at a Reynolds number $Re_\tau = 180$. In addition to the velocity field, three passive scalars (heat for $Pr = 0.1$, 0.7, 2.0) are also computed for the case where one wall is uniformly hot and the other is uniformly cold. Both the hydrodynamics and the scalar fields are fully developed. For more details about the flow characteristics and the computation, see Kim and Moin, 1989. In this report, we will concentrate solely on the analysis of the velocity component normal to the wall, the temperature for $Pr = 0.7$ and the pressure.

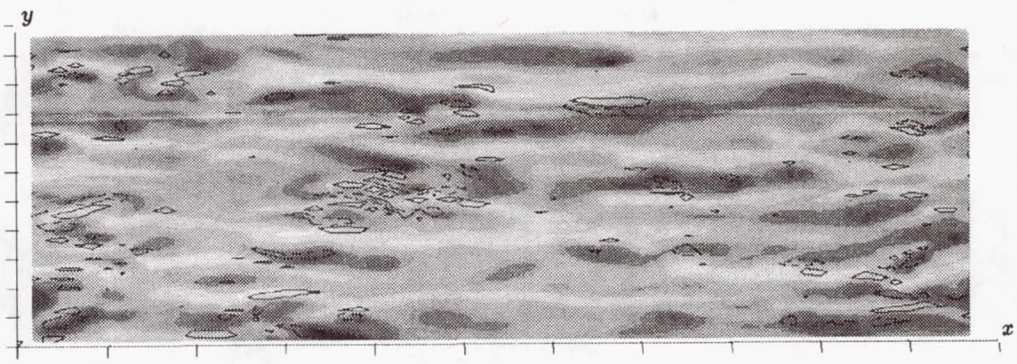

FIGURE 2. Iso-temperature lines in a horizontal x-z plane at $y^+ = 10$, in the plane channel flow simulation. Black spots indicate regions of high values of the normal velocity.

Since the wall region is the most active dynamically, the analysis is focused on one single plane, parallel to the wall at $y^+ = 10$. Figure 2 shows iso-lines of temperature in that plane. Black regions indicate the maxima of the normal velocity field. While the normal velocity is the one responsible for the advection of heat from the wall, the two fields exhibits a very different character. The temperature field is very streaky, while the regions of active transfer from or to the wall are very localized.

Next we compute the continuous wavelet transform of the temperature field for $\theta = 0$ and for scales ranging from $r = 64$ to $r = 4$ (in units of the elementary computational grid). In all subsequent figures, the r-axis is logarithmic (the small scale r=4 on the top and the large scales r=64 on the bottom). We consider 40 steps for the discretization of r, which means a base of 1.074 for the logarithmic increments. In Fig. 3, we show the intermittency factor $I(r, x, z)$, defined as the energy (modulus squared) of the wavelet coefficients normalized at every scale on the average energy at that scale (13). We observe the following features:

(a) In the large scales, the energy is evenly distributed in space.

(b) On the contrary, the temperature field at the small scales is highly intermittent; in four locations at the smallest scale, the local energy is about 15-20 times the average energy at that scale.

(c) The flow remains anisotropic, with similar elongation factor at all scales.

Let us then compare the wavelet transform of the temperature field with the one of normal velocity. Figures 4 and 5 show the wavelet transforms in the x-z plane, where the r-dependence has been compressed; this representation is analogous to viewing the wavelet coefficients as in Fig. 3 from 'above', parallel to the r-axis. In Fig. 4, we use the transform with $\theta = 0$, which selects the streamwise contributions, while in Fig. 5, we use $\theta = \pi/2$, which selects the spanwise contributions to the fields. In both figures, we plot the transform of the temperature (4(a) and 5(a)) and the transform of the normal velocity (4(b) and 5(b)).

We observe that regions of activity in the temperature field are correlated with

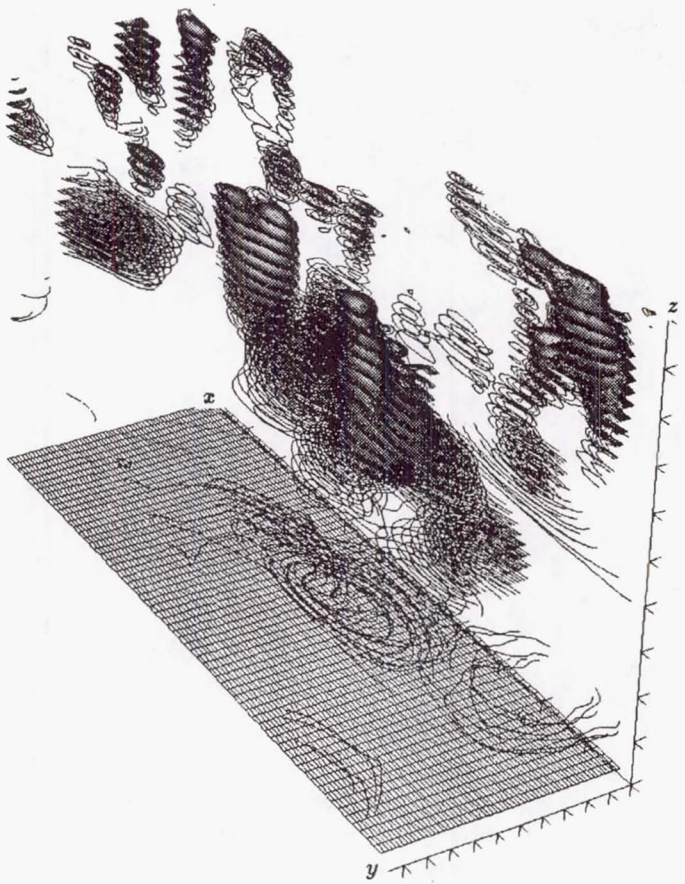

FIGURE 3. Wavelet transform of temperature field for $\theta = 0$ in plane channel flow at $y^+ = 10$.

the spots where vertical velocity is high. These regions correspond to ejections from the viscous sublayer. In the case $\theta = 0$, it is interesting to notice that even though the streaks are elongated in the streamwise direction, the wavelet transform shows some very localized active regions. This, therefore, indicates strong local changes in the x-direction inside or at the end of the streaks. These events are also correlated with the peaks of vertical velocity (Fig. 2). This is probably due to the fact that the temperature, as the streamwise velocity streaks, are very passive almost everywhere, except in very localized regions associated to the ejection mechanism. In other words, this intermittency function allows to locate very precisely the regions characterized by strong dynamics.

In the spanwise direction (considering $\theta = \pi/2$) we observe similar correlation between temperature and normal velocity; however, the activity is less intermittent. The maximum value of $I(r, x, z)$ for this case is 13 for the temperature, and 18 for

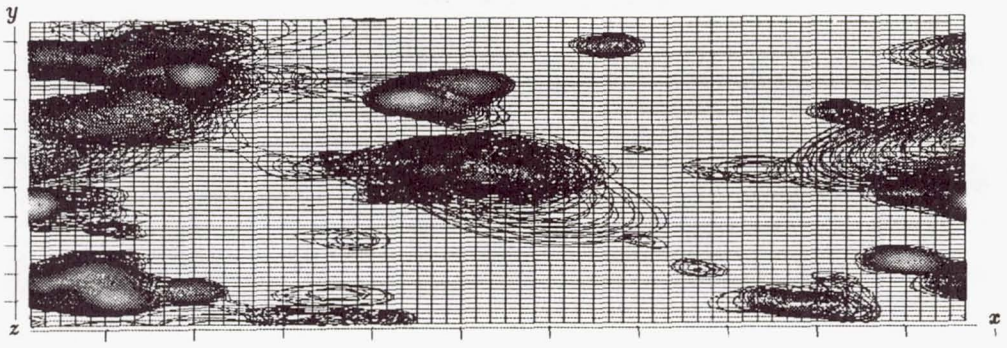

FIGURE 4(A). Intermittency function $I(r, x, z)$ of temperature field in plane channel flow at $y^+ = 10$, in the direction $\theta = 0$. Shown are iso-lines of $I(r, x, z)$ ranging from $I = 2$ to $I = 20$.

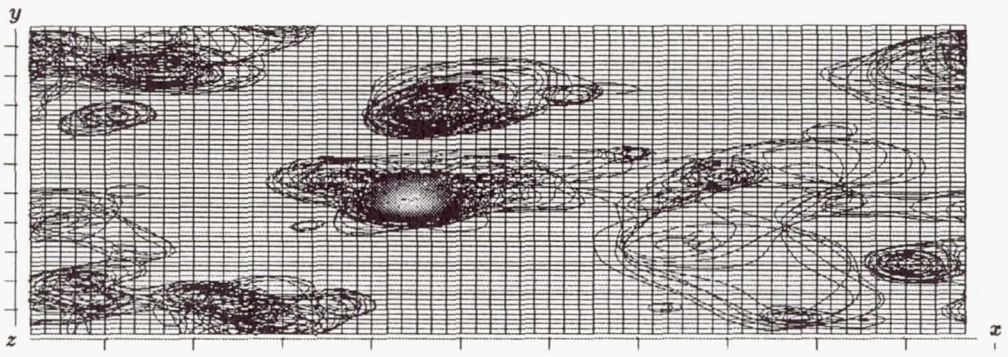

FIGURE 4(B). Intermittency function $I(r, x, z)$ of normal velocity field in plane channel flow at $y^+ = 10$, in the direction $\theta = 0$. Shown are iso-lines of $I(r, x, z)$ ranging from $I = 2$ to $I = 46$.

the vertical velocity, while for the streamwise direction it is respectively 20 and 46.

We now turn our attention to the pressure field in the same plane. Fig. 6 depicts the pressure fluctuations at $y^+ = 10$, highlighted with the regions of strong normal velocity. Despite the integral character of the pressure, the pressure fluctuations tend to be very spotty and concentrated primarily in the regions with strong normal velocity perturbations.

The transform of the pressure field is shown in Figure 7a and 7b for the streamwise ($\theta = 0$) and spanwise ($\theta = \pi/2$) directions, respectively.

The intermittency values in the spanwise and streamwise directions are similar in distribution and magnitude. As noted before, the pressure fluctuations are relatively homogeneous at the large scales and highly intermittent at the small scales.

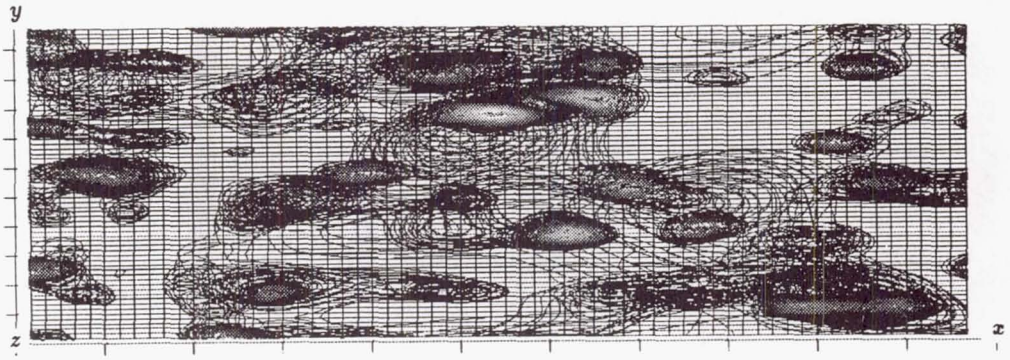

FIGURE 5(A). Intermittency function $I(r, x, z)$ of temperature field in plane channel flow at $y^+ = 10$, in the direction $\theta = \pi/2$. Shown are iso-lines of $I(r, x, z)$ ranging from $I = 1$ to $I = 13$.

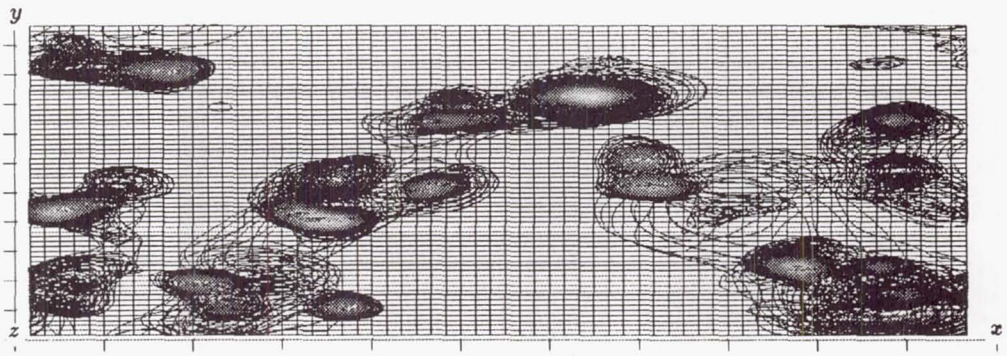

FIGURE 5(B). Intermittency function $I(r, x, z)$ of normal velocity field in plane channel flow at $y^+ = 10$, in the direction $\theta = \pi/2$. Shown are iso-lines of $I(r, x, z)$ ranging from $I = 2$ to $I = 18$.

Furthermore, the anisotropy of the small scales observed for the temperature and normal velocity is also present for the pressure fluctuations, and it appears that the elongation in the streamwise direction remains similar over a significant range of scales. Again, regions of high intermittency for the pressure can be correlated with regions of strong ejections (normal velocity away from the wall) which set up strong streamwise and spanwise local pressure gradients. This confirms the importance of these localized pressure gradients for "momentum mixing" as discussed by Guezennec *et al.* (1990). As pointed out earlier, this intermittency is very useful in pinpointing the regions dominated by strong dynamics.

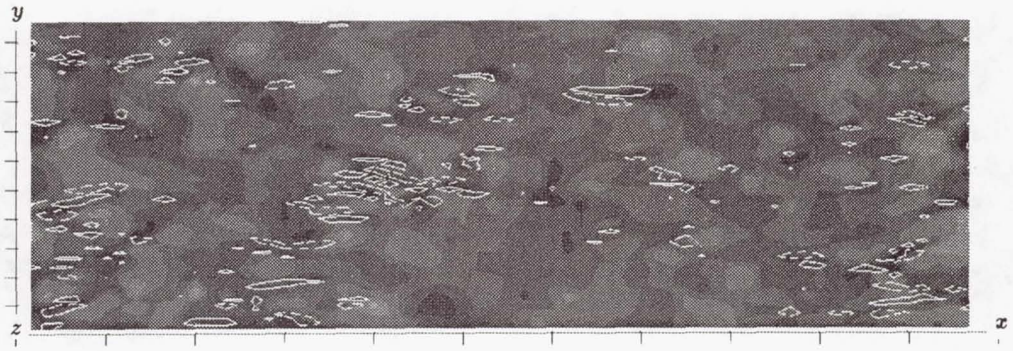

FIGURE 6. Iso-lines of pressure in the x-z plane at $y^+ = 10$ in the plane channel simulation. Black spots indicate regions of high values of the normal velocity.

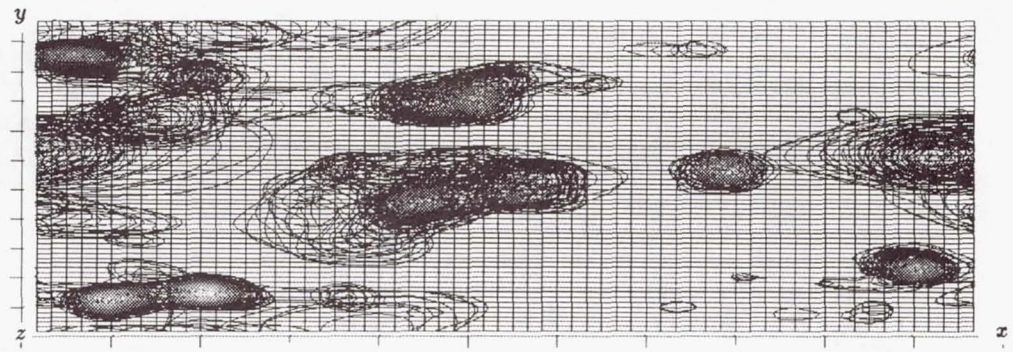

FIGURE 7(A). Intermittency function $I(r, x, z)$ of pressure field in plane channel flow, in the direction $\theta = 0$. Shown are iso-lines of $I(r, x, z)$ ranging from $I = 2$ to $I = 22$.

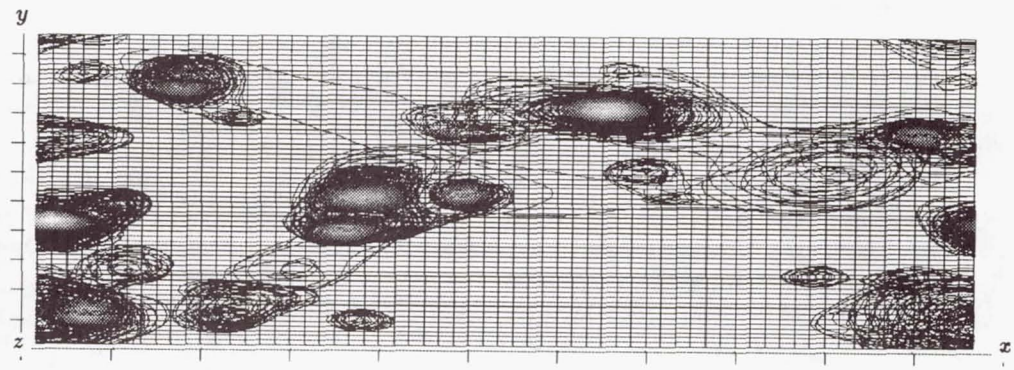

FIGURE 7(B). Intermittency function $I(r, x, z)$ of pressure field in plane channel flow, in the direction $\theta = \pi/2$. Shown are iso-lines of $I(r, x, z)$ ranging from $I = 2$ to $I = 26$.

5. Analysis of mixing layer

In this section, we perform the continuous wavelet analysis of numerical simulations of the temporally evolving mixing layer by Rogers & Moser (1990). The fields analyzed correspond to the vortex produced after the first merging (namely after the mixing transition). We consider a cut in the horizontal direction going through the center of the core region. Iso-lines of vertical (w_y) vorticity are shown in Fig. 8. The center of the plot corresponds to the spanwise vortex core. The alternating sign vortical structures seen on either side of the plot represent cuts through the "ribs" (the streamwise vortices formed between the vortex cores).

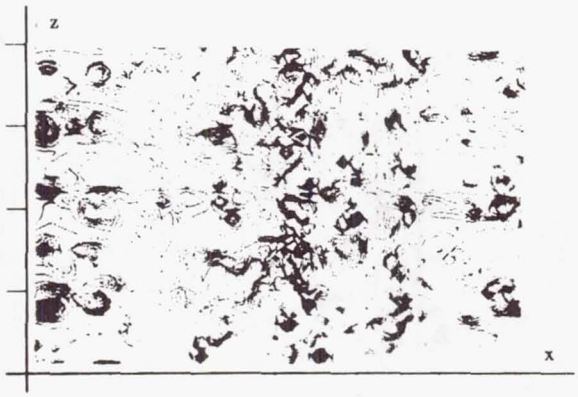

FIGURE 8. Vorticity contours in a x-z plane in the mixing layer (Rogers & Moser, 1990).

We compute $\tilde{u}_1(r,x,z)$, $\tilde{u}_2(r,x,z)$ and $\tilde{u}_3(r,x,z)$, the two-dimensional wavelet transform of this field for each velocity component u_1 (streamwise), u_2 (vertical) and u_3 (spanwise).

We also compute the wavelet transform of the vertical vorticity component, for which we plot the intermittency function $I(r,x,y)$ defined in section 2 (13) giving for each scale the local deviations of the modulus around the spectral mean value. Such representations of the transform are shown in Fig. 9.

The following conclusions regarding vorticity can be reached:

(a) The large-scales are evenly distributed in space.

(b) There is a very strong intermittency (reaching a factor $I = 120$) of the small scales and these are localized in the vortex core.

(c) We observe return to isotropy at the small scales (such a conclusion is drawn from combining both figures 9(a) and 9(b))

We now analyze the velocity fields. Figures 10(a), (b) and (c) show $I(r,x,z)$ for each velocity component, again viewed by 'collapsing' the r-axis. It is clear that the active zones of the streamwise velocity (Fig. 10(a)) are localized in a narrow region along the centerline of the vortex core and they are highly intermittent (the maximum value of $I(r,x,z)$ reaches 145). The spanwise component (Fig. 10(b)) has

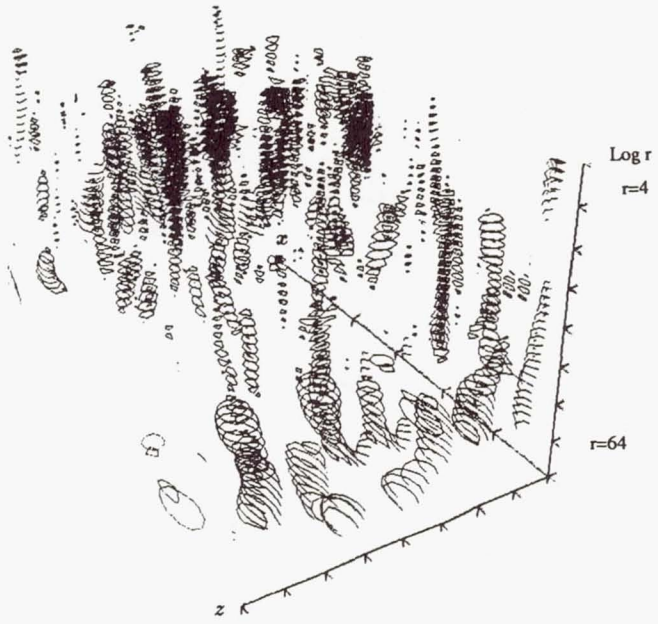

FIGURE 9(A). Intermittency function $I(r, x, z)$ of the vertical vorticity component in the mixing layer.

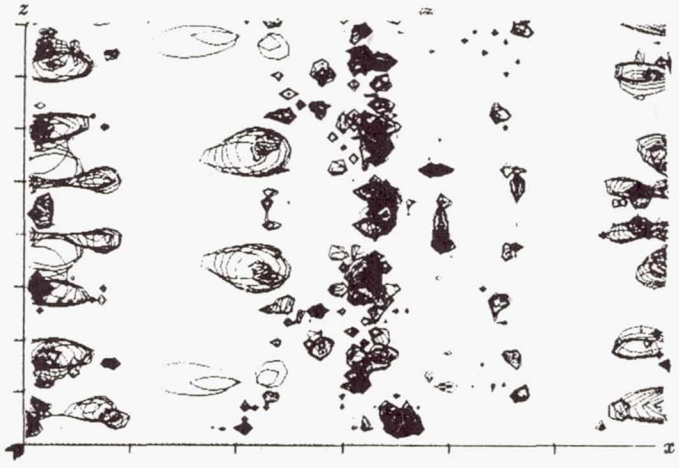

FIGURE 9(B). Intermittency function $I(r, x, z)$ of the vertical vorticity component in the mixing layer, viewed from 'above'. Shown are iso-lines of $I(r, x, z)$ ranging from $I = 0$ to $I = 125$.

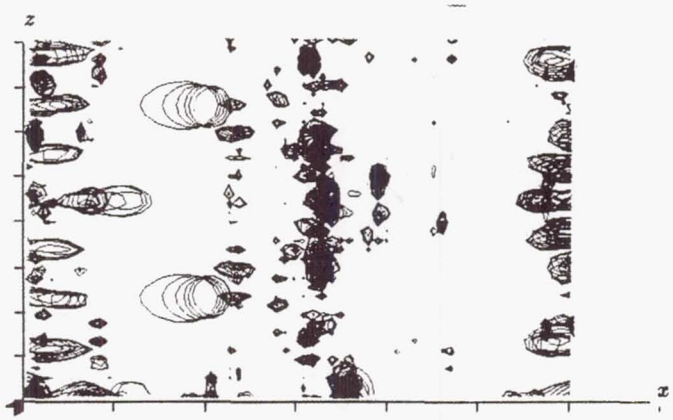

FIGURE 10(A). Intermittency function for the streamwise (u_1) velocity component in the mixing layer (top view, parallel to r-axis). Shown are iso-lines of $I(r, x, z)$ ranging from $I = 0$ to $I = 145$.

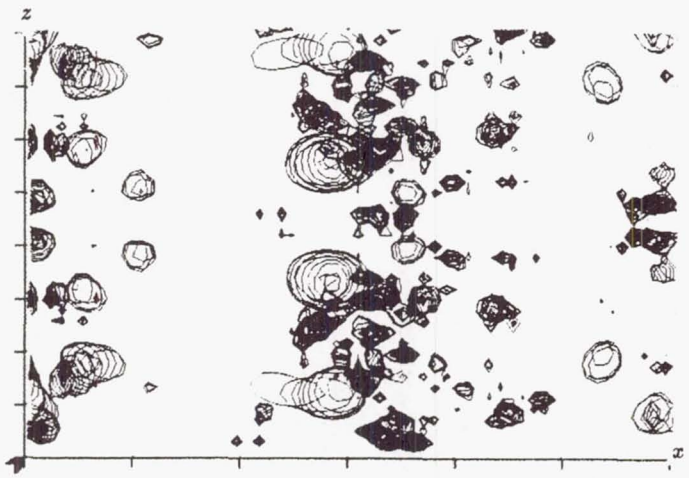

FIGURE 10(B). Intermittency function for the spanwise (u_2) velocity component in the mixing layer (top view, parallel to r-axis). Shown are iso-lines of $I(r, x, z)$ ranging from $I = 0$ to $I = 90$.

activity also localized in the vortex core, but in a wider zone, and it is less intermittent ($I(r, x, z)$ reaches at most 90). On the contrary, the vertical velocity component (Fig. 10 (c)) is much more space-filling and considerably less intermittent ($I(r, x, z)$ maximum is 40).

Now we consider two spanwise cuts (constant x) of the intermittency function. The first cut is located in the braid region, while the second corresponds to the vortex core. These cuts (not shown here) were obtained for each velocity component.

FIGURE 10(c). Intermittency function for the vertical (u_3) velocity component in the mixing layer (top view, parallel to r-axis). Shown are iso-lines of $I(r, x, z)$ ranging from $I = 0$ to $I = 40$.

As a first conclusion, we state that the intermittency in the braid regions is very low (between 0 and 5), this at every scale. Second, in the vortex core we observe different features comparing the three velocity components:

(a) For the streamwise component, only one relevant small-scale structure is visible, for which $I(r, x, z) = 85$. Its fluctuations exist on a band of scales corresponding to $r \sim 16$ to the smallest resolved scales ($r = 4$).

(b) For the spanwise component, the small-scale activity is more distributed, occurring only at the smallest scales (around $r \sim 4$. The maximum intermittency there is 40, and is encountered at three different locations, possibly corresponding to some ribs (Moser & Rogers 1990) engulfed into the vortex core.

(c) For the vertical velocity component, we observe a very different behavior: The intermittency is weak (maximum value of I is 9), and is encountered in two distinct bands of scales (around $r \sim 16$ and $r \sim 4$), separated by a clear gap with no activity there. Within the active bands, we can distinguish several features which we interpret tentatively as the cups region (Moser & Rogers 1990), or again ribs engulfed into the vortex core.

Similar conclusions concerning the small scale activity concentrated in the core region and the difference between different velocity components were reached with a technique called 'peak-valley counting' utilized by Zohar *et al.* (1990). This technique provides information about the geometry of scales but not about their energy content.

From the computation of the wavelet coefficients, we can also plot local spectra, defined as $\mid \tilde{f}(r, x_0, z_0) \mid^2$ the energy or enstrophy at some location (x_0, z_0) as a function of scale, plotted in terms of inverse scale r^{-1}. As an example, we study the local spectra of the vertical vorticity at three different points: The two points where vorticity is largest (these are actually located in the vortex core), and a point

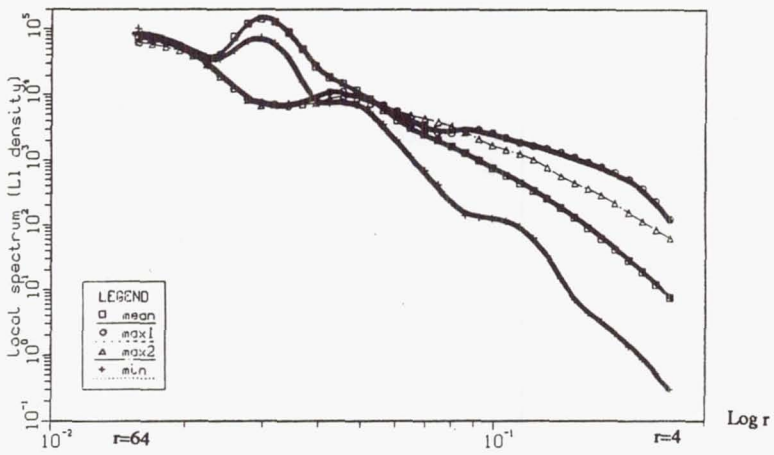

FIGURE 11. Comparison of global and local spectra of vertical vorticity in the mixing layer. The squares correspond to the spectral mean over all locations. The crosses correspond to the local spectrum at the location of very small vorticity in the braid region. The circles correspond to the local spectrum at the location of maximum vorticity (in the core region), and the triangles correspond to the second maximum of vorticity, also located in the core region.

(located in the braid region) where vorticity is very low. We also compute the average enstrophy (average over all points (x, z) for each scale). The results are plotted in Fig. 11.

For scales smaller than r=20, we observe a rapid departure from average, a sign of the strong intermittency. At the scale $r = 4$, the difference is 1.4 decades in enstrophy. Extrapolating the spectra using the observed slopes, we conjecture that the larger the Reynolds number, the larger the degree of intermittency.

As a next step, we analyze the distribution of local Reynolds number, which is defined combining all three velocity components. In Fig. 12 we show a iso-Reynolds number surface corresponding to $Re = 25$. This can be interpreted as a surface of iso-level of nonlinearity in the flow. It is not flat and it presents a scale extension over 4 octaves ($r = 64$ to 4). Its peaks, corresponding to the most unstable regions, are located in the vortex core, clearly confirming our previous conclusions concerning the small-scale activity there.

In the vortex core, relatively high local Reynolds numbers are attained at much smaller scales in the braid region (we notice that $Re = 25$ even reaches the smallest computed scale $r = 4$). Due to the limited resolution of the data, we have not obtained the manifolds for Reynolds numbers smaller than 5. Therefore, we have not attained the dissipative manifold $Re = 1$, but it is safe to argue that the dissipative manifold would also fluctuate, meaning that the Kolmogorov scale varies with location, being much smaller in the vortex core than in the braid regions.

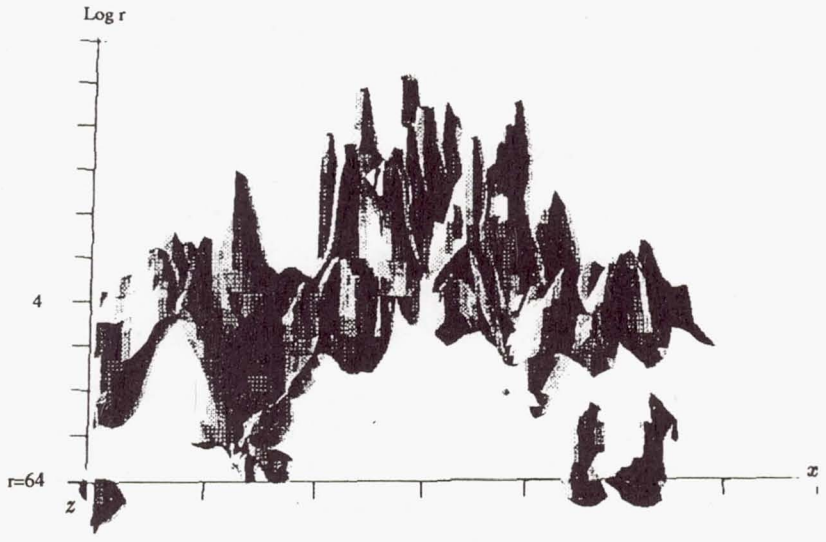

FIGURE 12. Local Reynolds number behavior in the mixing layer. Shown is a surface corresponding to $Re(r, x, z) = 25$. The peaks are located in the vortex core.

6. Conclusions

In conclusion, the wavelet transform allows us to:

(1) Localize the dynamically active regions of a turbulent flow.

(2) In varying the wavelet angle θ, we are able to separate the streamwise contributions (for $\theta = 0$) from the spanwise contributions (for $\theta = \pi/2$) of the flow field we analyze.

(3) In comparing the isotropy of the flow at different scales, we can test the return to isotropy in the small scales.

In order to answer the three questions we have asked in the introduction, we have defined three new diagnostic tools:

(1) A measure of intermittency, defined as the ratio of local energy to average energy at a given scale,

(2) A local spectrum giving the energy or enstrophy distribution versus scale in the vicinity of a given point, which can then be compared to the total spectrum,

(3) A local Reynolds number, defined in terms of the local velocity contribution, the scale of the transform, and molecular viscosity. This gives a representation of the local non-linearity of the flow viewed in both space *and* scale. The surface $Re = 1$ corresponds to the 'dissipative manifold' and its topology (flat or not) indicates how much the Kolmogorov scale varies in space.

For all flows considered we have found that:

(1) In the large scales, the energy density is homogeneous,

(2) In the small scales, the energy density is very inhomogeneous, and there is a strong intermittency associated to some coherent structures, namely the "bursts"

for the channel flow and the vortex core for the mixing layer,

(3) The topology of iso-Reynolds number surfaces is not flat and their peaks, corresponding to the most unstable regions, are encountered in the vortex core of the mixing layer, where the Kolmogorov scale is, therefore, much smaller than in the rest of the flow.

Finally, as future development, the continuous wavelet transform in two dimensions (as opposed to the one-dimensional case which has received much attention) needs to be tested more in detail in some simple test cases. One needs to better understand the information given by the phase, define better techniques to average over angles, and compare results using different wavelets (orthogonal or not).

Acknowledgements

The authors wish to thank: M. Holschneider, from the Center for Theoretical Physics, CNRS-Luminy, who has contributed to the writing of the two-dimensional wavelet code; R. Moser and M. Rogers, NASA Ames, for making their mixing-layer database available for analysis, and J. Kim and P. Moin for sharing the channel-flow data.

REFERENCES

DAUBECHIES, I. 1988 *Comm.Pure Appl. Math.* **XLI,** 909

FARGE, M. 1990 in Annual Conference of the Societe de Mathematiques de France

FARGE, M. AND RABREAU, G. 1988 *C. R. Acad. Sci. Paris* **II 307,** 1479

GROSSMANN, A. AND MORLET, J. 1984 *SIAM J. Math. Anal.* **15,** 723

GUEZENNEC, Y., STRETCH, D. AND KIM, J. 1990 This Volume (see also APS Abstracts)

MALLAT, S. J. 1989 *IEEE Patt. Anal. and Mach. Int.* **11,** 674

KIM, J. AND MOIN, P. 1989 Turbulent Shear Flow **6,** 85

LEMARIE, P. G. & MEYER, Y. 1986 *Rev. Mat. Ibero-americana* **2,** 1

MENEVEAU, C. 1990 *CTR Manuscript 120,* Center for Turbulence Research NASA Ames/Stanford

MOSER, R. D.& ROGERS, M. M. 1990 IUTAM Symp. on Stirring and Mixing

ZOHAR, Y., BUELL, J. C., MOSER, R. D., & HO, C. M. 1990 This Volume (see also APS Abstracts)